Modeling Observed Differential Frost Heave Within Non-Sorted Circles in Alaska

D.J. Nicolsky, V.E. Romanovsky
Geophysical Institute, University of Alaska Fairbanks PO Box 757320, Fairbanks, AK 99775, USA
G.S. Tipenko, D.A. Walker
Institute of Environmental Geosciences, Russian Academy of Science, PO Box 145, 101000 Moscow, Russia

Abstract

We investigate bio-geophysical processes causing differential frost heave in non-sorted circles north of Alaska's Brook Range. The main question to be addressed is, "How doest heterogeneity in soil properties and ground surface conditions cause the differential frost heave observed within the non-sorted circle?" We address this question by developing a numerical thermo-mechanical model of a non-sorted circle. A sensitivity study of predicted differential frost heave, with respect to soil physical properties and vegetation characteristics, shows that hydrological and thermal properties, as well as the local heterogeneity in distribution of surface vegetation, have a decisive role in formation of differential frost heave. We applied this model to simulate differential frost heave at the Franklin Bluffs site and obtained a good quantitative agreement with observed soil temperatures, water content, and frost heave. For other locations, such as at the Sagwon Bluffs and Howe Island sites, we obtained qualitative agreement with frost heave measurements.

Keywords: freezing and thawing; frost heave; numerical modeling; patterned ground**;** permafrost.

Introduction

Extensive areas of the Arctic landscape are characteristically patterned into small-scale ground features called non-sorted circles. Non-sorted circles are 0.5–3.0 m diameter patches of barren or sparsely vegetated soil formed by frost action (van Everdingen 2002) and ordinarily develop on poorly drained tundra sites (Fig. 1).

Changes to these features in relation to changes in climate could affect energy and carbon mass exchange at the tundra surface with possible feedbacks to the climate. However, formation, development, and maintenance of such ground patterns and their interaction with vegetation is poorly understood (Walker et al. 2004). The objective of this study is to numerically model observed frost heave in non-sorted circles and gain an understanding of interactions between water fluxes, temperature dynamics as influenced by the plant canopy and the motion of soil particles resulting from the heave of ground surface.

As part of the biocomplexity of the patterned-ground project (Walker 2004), we observed non-sorted circles at several locations near the Dalton Highway in Alaska. We instrumented several non-sorted circles at these sites with sensors that measure soil temperature, moisture content, and the maximum frost heave (Walker et al. 2004). Our measurements revealed that the maximum frost heave in a circle interior was 2–8 times greater compared to frost heave surrounding the circle tundra. This phenomenon is referred to as the differential frost heave.

Our field observations support the idea that the frost heave of saturated soil very often cannot be explained solely by the expansion of liquid water transforming into ice crystals. In this study,we apply a general thermo-mechanical model (Mikkola & Hartikainen 2001) of frost heave to simulate the observed frost heave in non-sorted circles. In this work, we assume that the soil is a homogeneous mixture of liquid water, ice, and soil skeleton. We assume that the skeleton and ice undergo small deformations described by linear elasticity, and the linear momentum conservation principles can be exploited in the quasi-static form. In our model, we also neglect ice flow relative to the soil skeleton. The liquid water is an incompressible and non-viscous fluid that changes its phase and is always in thermodynamical equilibrium with ice. The chemical potential of the liquid water is modified due to adsorption to the soil skeleton.

Based on observations from field experiments and results of our numerical simulations, we conclude that heterogeneity in surface characteristics and soil properties (due to the presence of a heterogeneous plant canopy together with presence of waterlogged conditions) are among the primary requirements necessary for occurrence of differential frost heave observed in non-sorted circles.

Physical Description

In this section, we highlight key physical processes and mechanisms presumably causing the differential frost heave in non-sorted circles. The area surrounding the circle is called the inter-circle area and has a relatively thick mat of vegetation as well as a layer of organically enriched soil (Fig. 1). Incorporation of the organic material into soil leads to heterogeneity in thermal properties, structure, and water-holding capacity of soil. For example, different soil textures indicate distinctive thermal conductivities, soil porosity, and dependence of the unfrozen liquid water content on temperature. Besides variances in thermal and hydrological properties, the non-sorted circle has heterogeneous rheological properties due to structural change that takes place during annual freeze-thaw cycles. This structural change is caused by freezing water that creates a microscopic structure in the form of a sequence of ice lenses.

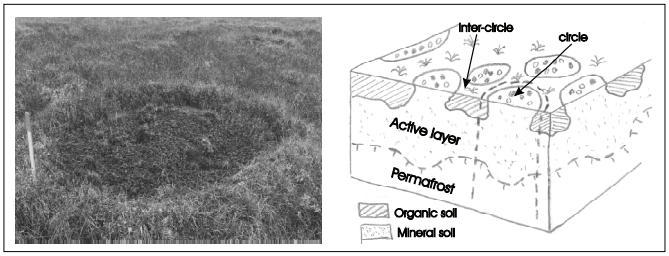

Figure 1. A photography (left) and schematic description (right) of the non-sorted circle.

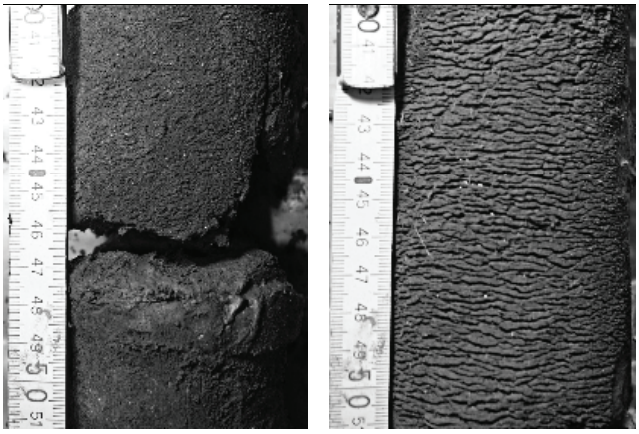

Figure 2. Core samples obtained from the inter-circle area (left photo) and circle (right photo) at the Franklin Bluffs site during winter. On the right photograph, a sequence of horizontally oriented ice lenses can be observed. The vertical scale is in centimeters.

Figure 2 shows the ice lenses in soil core samples from a non-sorted circle at the Franklin Bluffs site, Alaska. Each ice lens separates soil particles, causes the observed lenticular soil structure, and hence lessens structural solidity of soil. In Graham & Au 1985 and Qi et al. (2006), it was shown that soil has a long-term memory of its previous freeze/thaw cycles, which in particular reduces bonding between soil particles. To account for reduction in the bonding, we assume that soil is more structurally solid if it has fewer ice lenses. From a soil core obtained by drilling in winter, we observed that the circle has many more ice lenses than in the inter-circle area, and these lenses can be found even at the significant depth of 0.5 m (Fig. 2). Therefore, we assume that soil in the inter-circle is more structurally solid than in the circle. Despite these heterogeneities, the difference between observed active layer depths (maximum depth of summer thaw) of the circle and inter-circle does not exceed 0.3 m in the majority of cases.

It is well known that frost heave is caused by volumetric water expansion during freezing. However, as mentioned earlier, the observed frost heave heights do not seem to be exclusively dependent on the active layer depth, and on volumetric water content in the soil before freezing. From field observations at the Franklin Bluffs site, we know that the active layer thicknesses for the circle and inter-circle areas are 0.9 and 0.8 m, respectively, and volumetric water content in these areas during summer is almost the same. Thus, if water does not migrate, the frost heave is computable and its height is about 3.0–3.5 cm for both circle

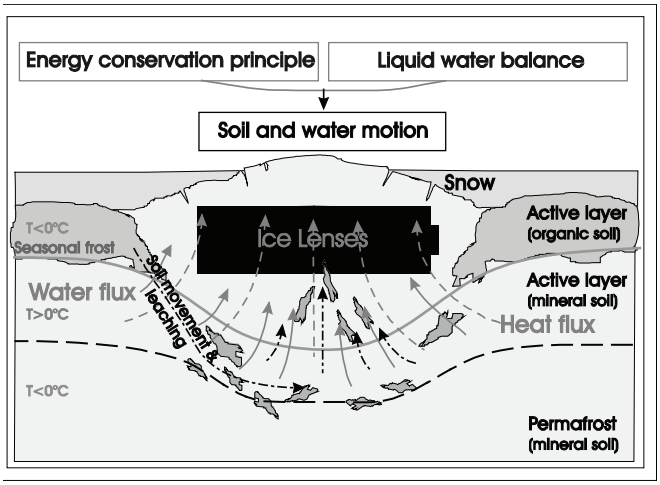

Figure 3. A diagram of fundamental physical processes taking place in a non-sorted circle when it freezes during the fall. Directions of the water flow, heat flux, and soil displacement are marked by solid, dashed, and dot-dashed lines, respectively. Location of the upper 0ºC isotherm is marked by the solid line, whereas location of the permafrost table by the dashed line.

and inter-circle areas. The latter values of the frost heave contradict observations at Franklin Bluffs site, at which the ground heaves by 15 cm in the center of a circle and only by 3 cm in the inter-circle. This significant variation on the local-scale frost heave is called the differential frost heave. We hypothesize that the key physical process responsible for the differential frost heave within non-sorted circles is water redistribution between the circle and inter-circle. The water redistribution is caused by lateral components in the cryogenic suction that pulls water from thawed soil to partially frozen soil. The lateral components in the cryogenic suction are due to heterogeneity in soil properties and in ground surface conditions, first of all in vegetation cover. Figure 3 shows fundamental physical processes occurring in the non-sorted circle in the fall when it freezes.

We describe the nature of these processes and their implications to the observed values of the differential frost heave as follows. When the ground surface temperature becomes lower than 0ºC, water trapped in soil pores starts to freeze. In Figure 3, the direction of the heat flux during freezing is shown by dashed arrows. In several classical works, it was demonstrated that temperature gradients in the freezing ground create cryogenic suction, inducing flow of water towards a freezing region along the temperature gradient (O`Neill & Miller 1985). Since the circle lacks an organic layer, the frost propagates through it faster, causing stronger water migration into the circle, consequently resulting in more intensive ice lens formation and thus higher frost heave in the circle. Over a period of time, the circle heaves significantly higher than the inter-circle area. A secondary consequence of the heave is the reduced thickness of the snowpack above the circle compared to the inter-circle area (Fig. 3). The heterogeneous snow distribution further enhances the thermal heterogeneity of the soil surface. An absence of a vegetation mat within the heaving areas in conjunction with difference in the snow thickness results in

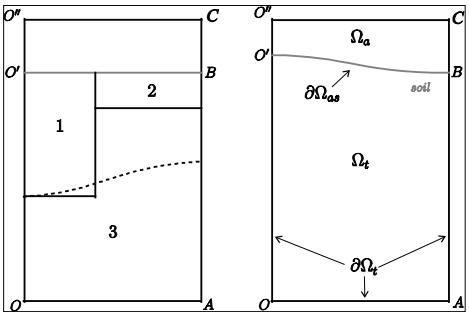

Figure 4. Schematic cross section (left) of the non-sorted circle and its computational domain (right). Segment OO″ is the axis of rotation, AB is the external boundary, and the dotted line on the left shows the upper permafrost boundary.

observed lower winter soil temperatures in the circle than in the inter-circle. The thermal difference between the circle and inter-circle areas creates cryogenic suction and drives water from the inter-circle to the circle (the direction of liquid water motion is shown by solid arrows). Reaching a freezing region, water forms ice lenses, which exert uplifting forces causing deformation of the soil skeleton. We highlight directions of soil particle velocities by dash-dotted arrows (Fig. 3). In our model we exploit a simple rheological model of the soil skeleton and assume that its deformations are well simulated by linear elasticity theory in which the soil stiffness takes into account structural differences and loss in soil bonding caused the ice lenses.

Besides the thermal differences, which cause liquid water migration towards the circle, hydraulic properties of the soil also determine water flux affecting the liquid water migration. One of the key hydraulic parameters is a coefficient of hydraulic conductivity and its dependence on liquid water content, θ_w, for partially frozen ground. According to Konrad & Duquennoi (1993), the hydraulic conductivity increases with an increase of unfrozen water content that is a function of both temperature and porosity. Another hydrological aspect that is important in sustaining water migration is the availability of water inside the non-sorted circle or at its boundary. We note that observations reveal higher values of frost heave that have been measured at poorly drained sites. Hence, lateral boundary conditions play an important role in allowing water to migrate into the circle due to cryogenic suction and to create ice lenses. In our model, we simulate the non-sorted circles either as hydrologically opened or closed systems by setting to zero either the water flux or pressure, respectively, on external boundaries. In the next section, we will briefly describe a general thermo-mechanical model of freezing soil. An interested reader can consult Mikkola & Hartikainen (2001), where the theory is discussed in detail.

Numerical Model

We consider a mixture of several constituents—water, ice, and soil particles—occupying a change in time region. Since a non-sorted circle has an axial symmetry, we solve governing equations in an axisymmetrical domain. In Figure 4, we show the cross-section of the computational domain consisting of three regions. Soil properties for each region are listed in Table 1.

Table 1. Description of soil properties for non-sorted circles along the Dalton Highway in Alaska.

Domain	Soil	Ice lenses	Unfrozen water
1	Mineral	Many	High content
2	Organic	Many	Low content
3	Mineral	Few	High content

We solve the energy conservation principle for the mixture by using two mass conservation principles for soil particles and liquid water, and a quasi-elasticity principle for the soil particles.

Based on the energy conservation principle, we compute the soil temperature T. The temperature consecutively defines the magnitude of the cryogenic suction, f, that forces liquid water from a thawed region towards the partially frozen one. The flux of liquid water, F, is defined such that

$$F \approx \nabla\left(p + \rho_w L \frac{T}{T_0} \frac{\partial f}{\partial \theta_w} \right) + \rho_w L \frac{T}{T_0} \nabla f , \qquad (1)$$

where L is the latent heat of fusion, ρ_w is the water density, and $T_0 = 273.15$ºC. Consequently, the flux F is used in the water conservation principle, i.e., Darcy's Law, and to calculate the pressure, p (Mikkola & Hartikainen 2001). The latter is used to define a force in the quasi-linear elasticity law in order to compute displacement of soil particles. The system is coupled, since the soil particle displacement is used to compute the temperature and the pore pressure. We note that the system pore pressure/soil displacement (up to the coefficients) is common in the poro-elasticity theory. On the ground surface, we specify the temperature and zero pressure. On the lateral boundary, we set zero heat flux, zero pressure/water flux (open/closed system). At some depth (in our case 2.0 m), we set zero heat and water flux.

The system of equation is discretized by a finite element method in a fixed-in-time domain that embeds ground material OABO′ in a heaving non-sorted circle (Fig. 4). The fictitious domain method is used to set physically realistic boundary conditions on the moving ground surface O′B, lateral boundaries AB, OO′ and bottom OA of the non-sorted circle.

In nature, we observe that the maximum frost heave is larger at sites where near-surface ground water is abundant (Walker et al. 2004). To explain this phenomena, we show that liquid water migration towards the partially frozen region as well as the unlimited water supply are both essential to simulate the observed frost heave. Hence, we model two cases. In the first case, we model the zero-pressure boundary condition on AB, and hence water is allowed to pass through this boundary. In the second case, the zero-flux boundary condition is placed on the segment AB, resulting in a hydraulically isolated system.

Due to presence of the cryogenic suction, during freezing there is an induced flow of liquid water from the thawed

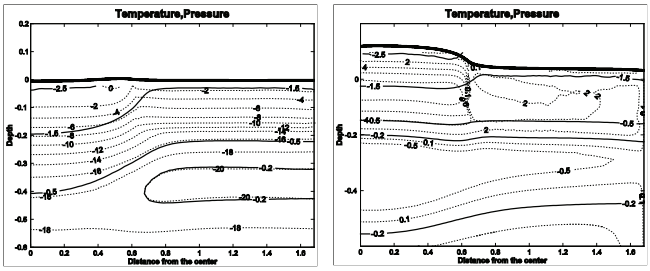

Figure 5. Contours of the temperature in ºC (solid lines) and pressure in 10^5Pa (dotted lines) at the 30th days after beginning of freezing, for hydraulically closed and open systems, in the left and right plots, respectively.

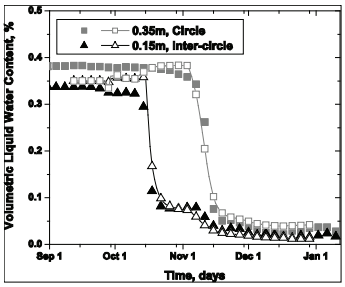

Figure 6. Dynamics of the measured (filled symbols) and calculated (hollow symbols) liquid water content at the Franklin Bluffs site in the center of the circle and in the inter-circle.

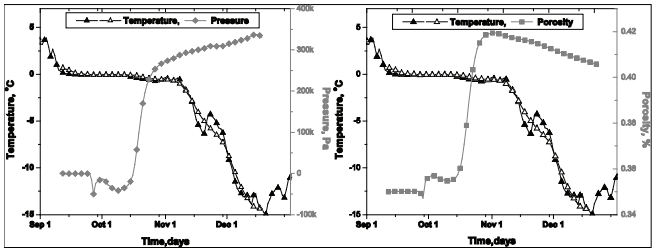

Figure 7. Dynamics of the measured (filled triangles) and calculated (hollow triangles) temperature at 0.35 m depth in the circle. The dynamics of pressure and porosity are marked by filled squares in the left and right plots, respectively.

region to the partially frozen zone. As a result, the pressure in the thawed region decreases. In the hydraulically closed system without internal sources of water, the boundaries are not water-permeable, and hence no additional water can appear in the non-sorted circle. Consequently, the pressure can decrease (Fig. 5).

In the hydraulically open systems with suction, the cryogenic suction creates similar effects as in the closed systems. Namely, it forces the flow of water and creates a low pressure zone in the thawed region. However, unlike the closed systems, the pressure on the external boundary is equal to zero, and water can flow through the boundary and compensate deficiency in water volume and, associated with it, negative pressure. Therefore, in the hydraulically open systems, the pressure in the thawed region is slightly negative compared to the closed system (Fig. 5). We observe that the positive-pressure increase exists in the partially frozen region and it creates the uplifting forces which produce the frost heave.

We conclude that the cryogenic suction forces create water flow. The pressure dynamics and the uplifting forces strongly depend on the pressure boundary condition. These results show that the model qualitatively predicts typical physical behavior of hydraulically closed and open systems occurring in nature. An interested reader is referred to Nicolsky et al. (in review) and to references therein, where the governing system of equations is described.

Frost Heave Modeling at the Franklin Bluffs Site

In this section, we apply the general model to a non-sorted circle located at the Franklin Bluffs site (148.7°W, 69.6°N) on the Dalton Highway in Alaska. The non-sorted circle is approximately 0.6 m in radius and is developed in waterlogged non-acidic tundra. In the inter-circle, the organic layer is 0.2 m in depth (Walker et al. 2004). An array of sensors measuring temperature and moisture dynamics in time are installed at several depths and at several locations across it.

The cryogenic suction is calibrated by matching the simulated unfrozen water content to the observed one at 0.35 m depth in the circle and 0.15 m depth in the inter-circle, respectively. Thermal conductivities of the frozen mineral and organically enriched soil are set to be 1.9 and 0.9 W/(mK), respectively. The Young's modulus for the mineral soil inside and outside the circle is $2 \cdot 10^6$ and $2 \cdot 10^7$ Pa, respectively, which are typical values for weakly consolidated and consolidated silt-clay mixture. Since the non-sorted circle is located in a waterlogged area, we model it as a hydraulically open system. Initial soil temperature distribution with depth was approximated by measured temperature on September 12, 2002, and the soil porosity was set to be 0.35. On this day the active layer depths in the center of the non-sorted circle and in the surrounding tundra were 0.80 and 0.60 m, respectively.

We simulated the soil freezing from September 12, 2002, through December 18, 2002, when the temperature in the non-sorted circle became less than -5ºC. On the circle and inter-circle ground surface, we prescribed a 5-day-running average of the corresponding measured ground surface temperature. The calculated liquid water content at 0.35 m depth in the circle and 0.15 m depth in the inter-circle is compared to the measured data (Fig. 6). The difference in freeze-up timing between the observed and modeled ground is less than three days.

In general, the discrepancy between the measured and computed temperature at the depth of 0.35 m in the circle is less than 1ºC (Fig. 7).

In addition to comparing the measured and computed soil temperatures, we show the calculated pressure dynamics at the same point; i.e., at the depth of 0.35 m. Note that initially when the ground surface temperature was above 0ºC, the pressure was zero (we assume there is no gravity and that the pressure on the lateral boundary is zero). However, as soon as ground freezing begins, the cryogenic suction starts

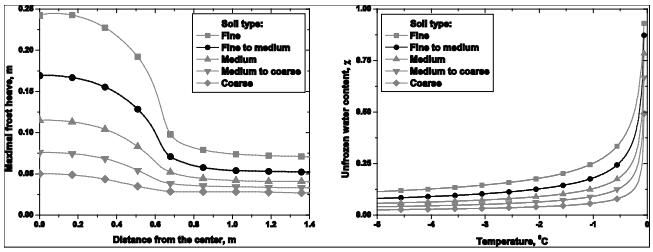

Figure 8. Sensitivity of the frost heave (left) on parametrization of the unfrozen water content (right).

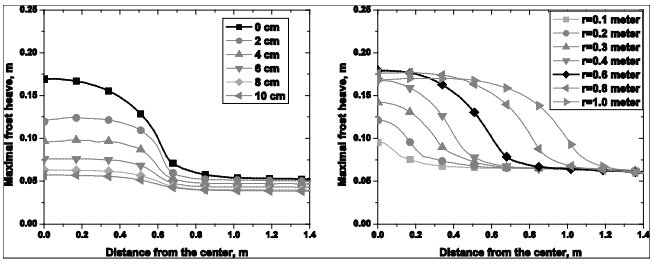

Figure 9. Sensitivity of the maximum frost heave to an addition of organically enriched soil (left) and to the radius (right) of the non-sorted circle.

to force water migration from a still-unfrozen part of the active layer to a partially frozen one. Therefore, the pressure lowers in the entire thawed part of the active layer, and the pressure dynamics have slightly negative pressure at this time (Fig. 7).

When the freezing front reaches the depth/region at which the pressure and temperature dynamics are shown (0.35 m), the cryogenic suction starts to force water migration into this still partially frozen region. Soil porosity consecutively increases (Fig. 7). Due to an increase of the water mass, and due to its expansion while freezing, the pressure continues to increase (Fig. 7). Note that the increased porosity is associated with formation of ice lenses and development of the frost heave (the small decrease in soil porosity is due to numerical regularization of the soil mass conservation principle). The value of the computed frost heave in the center of the non-sorted circle is approximately 0.18 m, whereas in the inter-circle it is 0.045 m. These computed values are in a good agreement with field observation circles heave by 0.15–0.2 m.

Sensitivity Analysis

In this section, we present results from the sensitivity study of the frost heave with respect to unfrozen water content, changes in the organic layer, and geometric dimensions. We define the calculated maximum frost heave at the Franklin Bluffs site as a reference point against which we compare a series of numerical experiments. To simplify comparison, we show the calculated frost heave for the Franklin Bluffs site by a line with circle symbols.

In the first series of experiments, we analyze dependence of the maximum frost heave on the unfrozen water content for the mineral soil. Note that parameterization of unfrozen water content depends on mineralogy, solute concentration, texture, and other factors. For example, the high unfrozen water content is associated with fine-grained ground material. For coarse-grained materials, such as sand, the unfrozen water content depends sharply on temperature near 0ºC (Fig. 8). For each shown parameterization, we simulate freezing of the non-sorted circle and compute the maximum frost heave (Fig. 8). In these numerical experiments, all model parameters except for the parameterization of the unfrozen water content were fixed and equal to the values related to the Franklin Bluffs site.

From the computed results, we observe that the largest frost heave occurs when the soil has a high unfrozen water content. This effect has the following explanation. Hydraulic conductivity of the partially frozen soil increases if the unfrozen water content θ_w becomes higher, and hence more water migrates through the partially frozen region due to cryogenic suction flow F (non-linearly dependent on θ_w) and forms ice lenses. The above-mentioned dependence of the frost heave on unfrozen water content is commonly observed in nature; i.e., that sand and gravel are not frost-heave susceptible soils whereas silt is. Note that clays, which have an even higher unfrozen water content, are typically not capable of developing significant frost heave since they have very small hydraulic conductivity.

In our field experiments, we observe that a thin organic layer is typical on top of some circles. From the physical point of view, this layer represents an additional thermal resistance and changes mean temperatures in the soil. Therefore, in the third series of experiments, we analyze dependence of the maximum frost heave on presence of organically enriched soil in the non-sorted circles. We consider several configurations of organic layers varying in their thicknesses. We additionally place on top of the non-sorted circle an organic layer, which uniformly covers the circle and inter-circle. The soil thermal, hydraulic, and rheological properties of this additional layer are identical to the properties of the original organically enriched soil in the inter-circle for the Franklin Bluffs site. Note that an increase in insulation layer causes a decrease in the active layer thickness. From our field studies, we observed that each additional 0.02–0.03 m of the organic material results in 0.04–0.05 m decrease of the active layer. In the left plot in Figure 9, we show the maximum frost heave developed for various thicknesses of the additional organic layer.

We emphasize that observed results are in agreement with observations at non-sorted circles along the Dalton highway in Alaska. For example, the scarcely vegetated circles at the Franklin Bluffs area heave by 0.15–0.2 m, whereas moderately vegetated circles at the Happy Valley site develop only 0.07–0.1 m of heave during winter. Also, field experiments (Kade et al. 2006, Kade & Walker, in press) at Sagwon Bluffs involved both the removal and addition of vegetation on non-sorted circles. The removal of vegetation at this location resulted in a 1.4ºC increase in mean summer mineral soil surface temperature compared to control, a 6%

increase in the depth of the thaw layer, and a 26% increase in frost heave. The addition of a 0.1 m thick moss layer results in the opposite effect; i.e., a 2.8ºC decrease in the mean summer mineral soil surface temperature, a 15% reduction in the thaw layer, and a 52% decrease in heave. Despite the fact that the numerical model is focused on non-sorted circles at the Franklin Bluffs site, and the field experiments were conducted at the Sagwon Bluffs site, results from these studies show qualitative agreement, and almost similar quantitative behavior of frost heave reduction.

In the fourth series of experiments, we investigate sensitivity of frost heave to the radius of the non-sorted circles. We calculate the frost heave for circles which have 0.1, 0.2, ... 1.0 m radius. Our calculations support observations which reveal that small-scale non-sorted circles heave less compared to the large-diameter ones. The maximum computed frost heave is for circles with the radius of 0.6 m (Fig. 9). For circles with a radius larger than 0.6 m, the maximum frost heave decreases slightly, since liquid water has to migrate to the center of the non-sorted circle longer from the lateral boundary where water is abundant. Smaller values of frost heave computed in the center of the non-sorted circle with a large radius can promote development of live vegetation as observed in nature.

Conclusions

We present a numerical thermo-mechanical model of differential frost heave with special emphasis on simulating biocomplexity of non-sorted circle ecosystems. Unlike many other models that study 1-D ice lens formation, we are concerned with 2-D effects of soil freezing. Heterogeneity in soil properties and surface conditions results in curved frost penetration and 2-D temperature fields. Therefore, the cryogenic suction results in horizontal water redistribution inside the non-sorted circle.

The model was tested using observational data obtained from several sites within the Permafrost/Ecological North American Arctic Transect. We obtained a good comparison between simulated and observed dynamics of physical processes in the non-sorted circle at the Franklin Bluffs. The model also qualitatively represents “non-heaving” non-sorted circles at the Howe Island site.

The simulated frost heave is sensitive to hydrological soil properties, and to changes in the vegetative insulation layer within the circle and inter-circle areas. The results of our sensitivity analysis, with respect to addition/removal of vegetation layer to/from the surface of a circle, are well correlated with field observations where a layer of organic material was either added or removed from the non-sorted circle.

The most active development of differential frost heave takes place for non-sorted circles within waterlogged areas with strong upper-soil-layer heterogeneity caused by living vegetation. The most important driver of the non-sorted circle ecosystem is the presence of vegetation that, over a significant time, changes the soil mineralogy and thermal and hydrological soil properties. This then changes the amount of differential frost heave and reduces or enhances all bio-geophysical processes responsible for the formation and evolution of the non-sorted circles.

Acknowledgments

We thank J. Hartikainen and J. Stroh for their advice along the way. This research was funded by ARCSS Program and by the Polar Earth Science Program, Office of Polar Programs, National Science Foundation (OPP-0120736, ARC-0632400, ARC-0520578, ARC-0612533, IARC-NSF CA: Project 3.1 Permafrost Research), by NASA Water and Energy Cycle grant, and by the State of Alaska.

References

Fremond, M. & Mikkola, M. 1991. Thermomechanical modeling of freezing soil. *The Sixth International Symposium on Ground Freezing, Rotterdam*.

Graham, J. & Au, V.C.S. 1985. Effects of freeze-thaw and softening on a natural clay at low stresses. *Canadian Geotechnical Journal* 22(1): 69-78.

Kade, A., Romanovsky, V.E. & Walker, D.A. 2006. The N-Factor of Nonsorted Circles Along a Climate Gradient in Arctic Alaska. *PPP* 17: 279-289.

Kade, A. & Walker, D.A. 2007. Experimental alternation of vegetation on non-sorted circles: effects on cryogenic activity and implications for climate change in the Arctic. *AAAR* (in press).

Konrad, J.M. & Duquennoi, C. 1993. A model for water transport and ice lensing in freezing soils. *Water Resources Research* 29(9): 3109-3124.

Mikkola, M. & Hartikainen, J. 2001. Mathematical model of soil freezing and its numerical application. *Inter. J. Num. Meth. in Engineering* 52: 543-557

Nicolsky, D.J., Romanovsky, V.E., Tipenko, G.S. & Walker, D.A. 2008. Modeling biogeophysical interactions in non-sorted circles in the Low Arctic. *JGR, Biogeosciences*. (accepted).

O`Neill, K. & Miller, R.D. 1985. Exploration of a rigid ice model of frost heave. *Water Resources Research* 21: 281-296.

Qi, J., Vermeer, P.A. & Cheng, G. 2006. A Review of the Influence of Freeze-thaw Cycles on Soil Geotechnical Properties. *PPP* 17: 245-252.

Van Everdingen, R. 2002. Multi-Language Glossary of Permafrost and Related Ground-Ice Terms.

Walker, D.A., Epstein, H.E., Gould, W.A., Kelley, A.M., Kade, A.N., Knudson, J.A., Krantz, W.B., Michaelson, G., Peterson, R.A., Ping, C., Raynolds, M.K., Romanovsky, V.E. & Shur, Y. 2004. Frost-Boil Ecosystems: Complex Interactions Between Landforms, Soils, Vegetation and Climate. *PPP* 15: 171-188.

Engineering-Induced Environmental Hazards in Permafrost Regions of the Qinghai-Tibet Plateau

Fujun Niu
State Key Laboratory of Frozen Soil Engineering, Cold and Arid Regions Environmental and Engineering Research Institute, CAS, Lanzhou, China 730000

Jian Xu
State Key Laboratory of Frozen Soil Engineering, Cold and Arid Regions Environmental and Engineering Research Institute, CAS, Lanzhou, China 730000

Zhanju Lin
State Key Laboratory of Frozen Soil Engineering, Cold and Arid Regions Environmental and Engineering Research Institute, CAS, Lanzhou, China 730000

Ping Wang
The First Railway Survey and Design Institute of China, Xi'an, China 710043

Abstract

The permafrost in the Qinghai-Tibet Plateau is characterized by massive ground-ice and high ground temperature. Under the influence of global warming, the permafrost is degrading. At the same time, many linear structures, including highways, gas pipelines, cable lines, electrical transfer lines, and railways, have been constructed during the past 50 years. Such engineering activities along with the rising air temperature have changed the permafrost environment along the Qinghai-Tibet Corridor. Field investigation shows that the main environmental hazards related to permafrost changes have widely developed, such as thaw slumping, thawing settlement, thermokarst, icing, frost mound, etc. The main factors causing these hazards include changes of conditions of the ground surface, the groundwater, and natural slope stability. Engineering treatment for preventing the hazards needs to be based on a good understanding of possible changes of ground thermal regime and water movement, along with their processes.

Keywords: engineering activity; hazard; linear structure; permafrost; Qinghai-Tibet Plateau.

Introduction

Permafrost covers 1,500,000 km^2 of area on the Qinghai-Tibet Plateau (Zhou et al. 2000). On the plateau, many linear structures such as highways, railways, gas pipelines, electricity-transmitting lines, and optical fiber cables have been constructed since the 1950s. The permafrost was initially discovered during construction of the Qinghai-Tibet Highway. Though permafrost was encountered at that time, no special engineering treatment was adopted, and the road embankment was just paved with side soils. During the construction, possible changes to the permafrost were not considered, and the seed for roadbed engineering problems was planted thereby. Environmental change caused by engineering activities can lead to environmental hazards, which simultaneously affect engineering stability. These hazards include thawing settlement, thaw slumping, thawing grooves, thermokarsts, frost heave, etc. The purpose of this paper is to introduce the permafrost situation in the Qinghai-Tibet Plateau, to describe some main thawing hazards and frost hazards along the Qinghai-Tibet Highway (QTH) and the Qinghai-Tibet Railway (QTR), to analyze formations of the hazards, and to discuss their treatments.

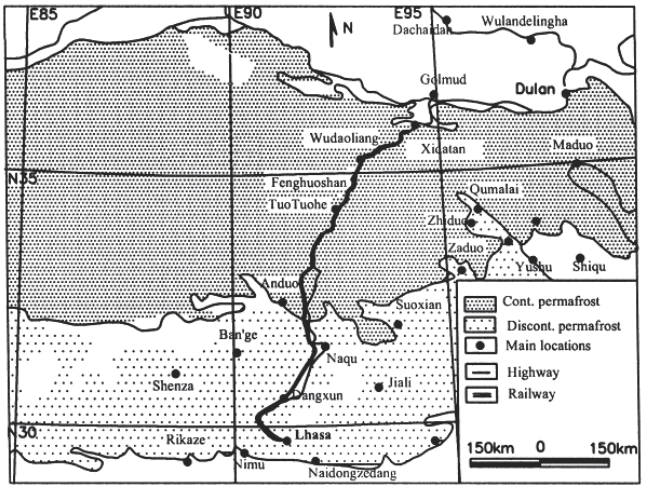

Figure 1. Permafrost distribution and the position of the highway and railway on the Qinghai-Tibet Plateau.

Permafrost and Engineering Activities in the Qinghai-Tibet Plateau

Permafrost comprises 75% of the total land of the plateau; its distribution is shown in Figure 1. The figure shows that along the highway and railway from Golmud to Lhasa, the northern limit of the permafrost is located in the Xidatan Basin north to the Kunlun Mountains. The southern limit is located in the Anduo Basin south to the Tanggula Mountains. The permafrost of the plateau features rich ice and high ground temperature. Take the 550-km-long continuous permafrost along the railway, for example. The section of

Figure 2. Thaw slumping at K3035 mileage of QTH.

permafrost with volume ice content higher than 20% is 221 km. The section with mean annual ground temperature (MAGT) higher than -1.0ºC (warm permafrost) is 221 km. On the whole, the warm and ice-rich permafrost is 124 km long (Liu et al. 2000, Wu et al. 2004).

As the permafrost of the plateau is warm and rich in ground-ice, it is sensitive to global warming and engineering activities. Monitored data from boreholes in the natural ground along the highway showed that the ground temperature at the permafrost table increased by a value of 0.08ºC/a from 1996 to 2001. The table was lowered 2.6 to 6.6 cm/a. According to investigations in past 30 a, the MAGT of the seasonal frozen ground, and the island permafrost along the QTH increased 0.3 to 0.5ºC from the 1970s to 1990s. The MAGT of the continuous permafrost increased 0.1 to 0.3ºC within the period. Under natural conditions, the permafrost area shrunk 0.5 to 1.0 km at the north edge and 1 to 2 km at the south edge. While affected by highway construction, it shrunk 5 to 8 km at the north edge and 9 to 12 km at the south edge (Wang & Mi 1993, Zhu et al. 1995, Nan et al. 2003). Therefore, the degradation influence of engineering activities on the permafrost was much more serious than that of natural forces.

To engineering projects, thawing settlement is the first response to degradation, and some phenomena related to the thawing easily occur, such as thaw slumping and thermokarst. On the other hand, in some cases when the hydrological conditions are changed in permafrost regions, other environmental hazards related to freezing can also occur, such as icing and frost heaving. On the plateau, all projects including highway, railway, cable line and pipe line are near parallel and concentrated in a region called the Qinghai-Tibet Corridor. The earliest project was the Qinghai-Tibet Highway. It was constructed in the 1950s, and repaired in large scale three times, mainly for treating problems caused by permafrost. From 1973 to 1977, a gas pipeline was constructed. The pipeline crossed 560 km of permafrost regions. In 2001, the Qinghai-Tibet Railway began to be constructed after nearly 30 years of intermittent planning, discussion, and investigation. The construction was finished in 2006, and the railway was opened to service in 2007. The electricity-transmitting line was constructed along the railway in 2006. We know that the highway has many problems in the permafrost section, but the railway, in service for one year, was constructed based on cooling-roadbed principles and cost much more than the highway. The railway's roadbed was stable according to our investigation from July to September in 2007. However, some environmental hazards along the railway related to construction activities in the permafrost section have occurred and might influence the roadbed stability in future. Here in this paper, some typical environmental hazards caused by engineering activities were introduced.

Main Environmental Hazards Along the Highway and the Railway

Thawing induced hazards

(1) Thaw slumping

Thaw slumping is commonly caused by slope toe disturbance in ice-rich permafrost regions. On the plateau, well-developed thaw slumping exists on the west side of the highway at K3035 mileage (Fig. 2) in the Kekexili Hill Region between Wudaoliang and the Fenghushan Mountains. In the slope, massive ground-ice with thickness of about 1 m was well developed and buried 2 m deep. The slumping was initially caused by cutting for embankment of the highway during 1990–1992. The failure showed as detachment of the active layer, and consisted of sand and silty clay. After years of repetition of the thawing-collapse-slide, the current 110 m long and 72 m wide landslide area was formed.

To survey the retrogressive process of the landslide area, some monitoring points and boreholes for monitoring the ground temperature, as shown in Figure 3, were installed in 2002. Monitored data of the 8 points near the back wall indicated that, from 2002 to 2006, the longest retrogressive distance at point 1 was 8.0 m. The collapse mainly occurred within a period from July to September, which is the main thawing period of a year. As the grass surface and the soil layers were destroyed when collapse occurred, the ground thermal status was also changed. Figure 4 was drawn with annually averaged ground temperature data obtained from borehole A in the undisturbed natural ground, and borehole B, in the failed zone. The figure shows that the temperature of natural ground at a depth of 0.0 m to 4.5 m was lower than that of the failed zone. Also, the thermal gradient in borehole B was very low, indicating that thermal exchange between the atmosphere and the ground in the failed zone was very limited. This might lead the permafrost in the zone to degrade.

As slope failure of thaw slumping is strikingly influenced by frozen soil, temperature, and groundwater, engineering treatments should fully consider these factors. Reasonable methods should be based on decreasing thermal energy entering the soil and draining groundwater, such as covering the collapsing zone with crushed stone, stacking grass bags filled with earth, re-vegetation, and so on.

(2) Thawing groove

A thawing groove is normally caused by linear cutting or

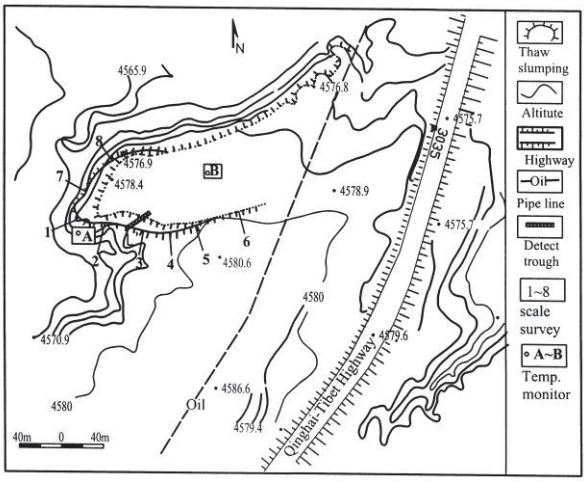

Figure 3. Relief map of the thaw slumping and the monitored positions.

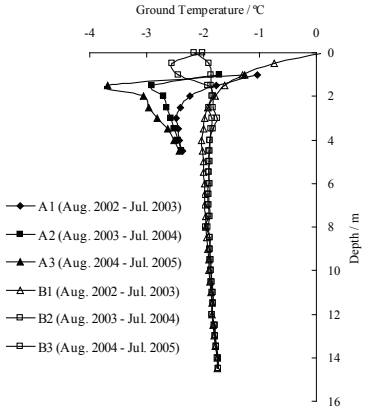

Figure 4. Annually averaged ground temperatures in borehole A and B.

even ground surface disturbance by truck or car driving in wet land in permafrost regions. Figure 5 shows a thawing groove developed along the QTR at K980 mileage south to the Kunlun Mountain. The strata here consisted of 10 m thick fine sand with gravels and the underlying silty clay. The permafrost table was 1.5 m in depth and the permafrost was ice-rich or ice-saturated. The embankment was constructed in 2003, and the slopes were covered with crushed stone in 2006. On the west side a 1.5 m high water barrier and drainage ditch were constructed in 2003. But in 2006, as surface water was gathered between the barrier and the embankment, the barrier was removed and the ditch was covered. According to our investigation, a 180 m long thawing groove along the former ditch developed with a depth of 20 cm in July 2007 (Fig. 5[a]) and then subsided to 40 cm in September (Fig. 5[b]). The gathered water shown in Figure 5(a) was mainly from ground-ice melting according to pit investigations, indicating that the subsidence was caused by thawing of the underlying frozen soils. Figure 6 shows the cross- section of the groove and its relative position to the embankment. Because of the settlement in the groove, many parallel fissures developed along the groove. The nearest fissure

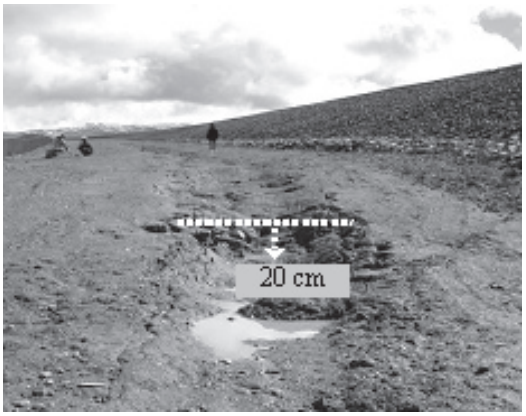

(a)

(b)

(Figure 5. Thawing groove developed on the west side of QTR: (a) Status in July 2007; (b) Status in September 2007.

was 3.5 m from the embankment. Such a hazard needs to be remedied soon, otherwise it continues to develop and even worsen when surface water moves into the fissures and the groove. As it has laterally thermal erosion to the roadbed of the railway, its long existence ultimately affects roadbed stability.

The thawing grooves in some sections along the railway mainly resulted from insufficient understanding of the interaction among the earth surface, ground temperature regime, ground-ice, and melted water. To avoid such problems, engineering construction should be restricted so as not to disturb the surrounding environment. When thawing grooves occur, earth refilling, grass sheet covering, and even sunshine shielding, along with efficient drainage, can be adopted to stop groove development. Basically, the objective is to stop melting of the ground-ice

(3) Thermokarst

Thermokarst results from the thawing of ice-rich permafrost or the melting of massive ice. On the plateau, normal thawing or melting is caused by change or disturbance of the ground surface, as that makes the surface absorb more energy than before. We mentioned above that the embankment of the QTH was initially just stacked with

two side soils. That not only changed the original ground surface, but also left many pits along the way. Now many of the pits show as small thermokarst lakes or where water

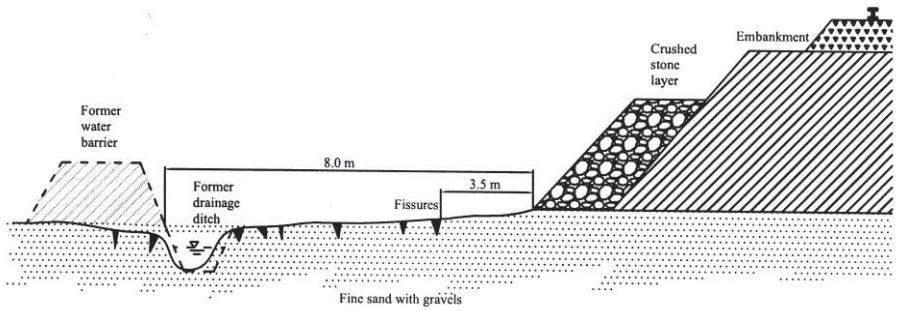

Figure 6. Cross-section of the thawing groove and the embankment

Table 1. Surface waters on the two sides of the QTH within 150 km in the permafrost regions.

Region	Mileage of the QTH /km	Kind of permafrost	MAGT / ºC	Small thermokarst lake		Accumulated water pit	
				Number	Area / m^2	Number	Area /m^2
Xidatan Basin	K2886~K2895	Icy soil	-3.0~-1.5				
Kunlun Mountain	K2895~K2910	Ice-saturated soil and massive ice	-3.0~-1.5	1	1,200	15	949
Unfrozen Spring Valley	K2810~K2920	Ice-rich soil and seasonal frozen soil	-3.0~-1.5; >0			3	400
Xieshuihe Plateau	K2920~K2941	Ice-saturated soil and massive ice	-1.5~-0.5	11	2,405	25	1,134
Xieshuihe Plateau	K2941~K2946	Ice-rich soil	-1.5~-0.5				
Qingshuihe Basin	K2946~K2956	Massive ground-ice	>-0.5	14	2,710		
Qingshuihe Basin	K2956~K2959	Icy soil and ice-saturated soil	-1.5~-0.5				
Chuma'erhe Plateau	K2959~K2963	Ice-saturated soil	-1.5~-0.5	5	2,700	3	21
Chuma'erhe Plateau	K2963~K2970	Massive ground-ice	-1.5~-0.5	4	790	21	721
Chuma'erhe Plateau	K2970~K2978	Massive ground-ice and ice-saturated soil	-1.5~-0.5			20	1,655
Chuma'erhe Plateau	K2978~K2983	Massive ground-ice	-1.5~-0.5	5	610	13	468
Chuma'erhe Plateau~Wudaoliang Hill	K2983~K3006	Icy soil and massive ground-ice	-1.5~-0.5	1	100	27	364
South Wudaoliang Hill region	K3006~K3017	Ice-rich soil and ice-saturated soil	-1.5~-0.5	10	685	20	814
Kekexili Hill region	K3017~K3027	Massive ground-ice	-3.0~-1.5	11	1,120	30	420
Honglianghe Hill region	K3027~3036	Ice-saturated soil	-1.5~-0.5	7	1,015	57	1,488

accumulates. Thermokarst lakes with characteristic collapses of the shore land were different to surface accumulated water. We investigated the surface waters along the two sides of the highway and classified them into small thermokarst lakes and accumulated water in Table 1. The statistical data in the table show that 69 small thermokarst lakes developed mainly in the regions with ice-saturated permafrost or massive ground-ice. In the regions with low ice content permafrost, no thermokarst lake developed within the investigated 150 km zone. At the same time, surface water did not readily accumulate either.

To intensively investigate the thermal regime of the ground under a thermokarst lake, we drilled boreholes in a lake near the Fenghuoshan Mountain region, where permafrost is rich in ground-ice. The lake shown as Figure 7 was approximately elliptic, 150 m long and 120 m wide. The water in the lake was 2.0 m deep. Figure 7 shows that the shore edge collapsed during thawing time, which is a characteristic of a thermokarst lake. Six boreholes were drilled in the lake and in the shore land, and temperature probes were installed in 2006. Figure 8 shows positions of the boreholes and the local strata. Borehole investigation revealed that the permafrost table was buried 2.1 m deep. Under the table, the massive ground-ice existed with a

thickness of about 3 m, which supplied a water source for the formation of the lake by melting.

Figure 9 shows the temperatures of the water and the humus deposits in the lake. The curves in the figure indicate that the lake water at a depth of 0.5 m processed phase change between water and ice. In fact the maximum ice thickness in winter was 0.7 m. The temperatures at other depths were all above 0ºC. The ground temperatures of the six boreholes at maximum-thawed-depth time were drawn in Figure 10. The figure indicates that the ground temperature in borehole 6, which was in the center of the lake, was higher than 0ºC. The permafrost table in boreholes 3–6 was 2.0 m deep, while in borehole 2, it was 7.2 m deep, as the borehole was in the lake area. The figure also shows that the ground temperature decreased from the lake to the land. Also, the ground thermal gradients were different. Such a situation was the same with the lakes studied by Burn at the west Arctic coast, Canada (Burn 2005). In that region, if lake ice freezes to the bottom sediments, it may be underlain by permafrost. Otherwise the thermal talik may penetrate through permafrost. Here, the thermokarst lake was somewhat similar to lakes in the Arctic region. Table 2 lists the calculated thermal gradient and estimated depth of the permafrost base in the different boreholes. The data in the table indicate that no permafrost existed, and there was a negative thermal gradient under the center area of the lake, hinting that the lake water provided a heat source to the underlying sediments. In the other boreholes, the temperature gradients were positive as normal. The permafrost base in the lake near the bank was 32.2 m deep, while far from the lake, the base depth lowered. Such differences revealed that the thermokarst lake has greatly influenced the existence of local permafrost. It also seriously laterally eroded neighboring permafrost. Therefore, if thermokarst existed near a roadbed, with time it would influence the thermal stability of the roadbed along permafrost regions. Engineering experience in permafrost regions of the plateau shows that good drainage systems and no-excavation are effective ways to avoid thermokarst.

Freezing induced hazards

In the engineering constructions in the permafrost regions of the plateau, thaw settlement was paid much more attention than frost problems. As the permafrost degraded in the past years and the degradation continues, thaw settlement problems are becoming more serious than frost heave problems. However, when the groundwater seepage conditions are changed, outflow or new movement of the groundwater might cause frost heave problems.

Figure 11 shows an icing incorporated with a frost mound along the QTH in the Unfreezing Spring region (Budongquan region), where both permafrost and seasonal frozen ground exist. Springs are widely distributed and are the main

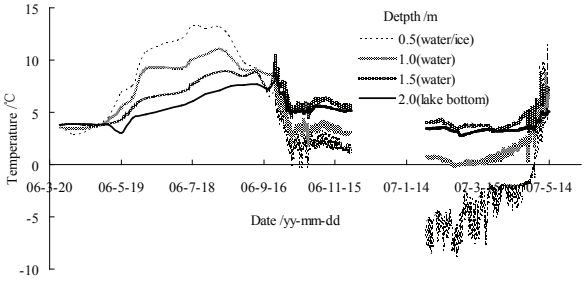

Figure 9. Temperature of the water and shallow depth of the thermokarst lake.

Figure 7. Thermokarst lake near Fenghuoshan Mountain.

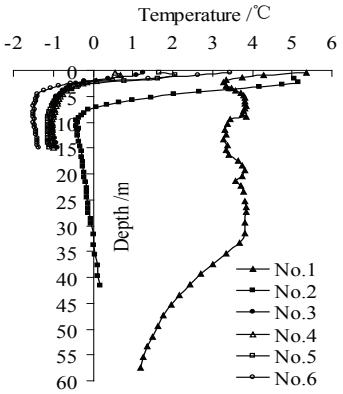

Figure 10. Ground temperatures in the six boreholes at beginning of October, 2006.

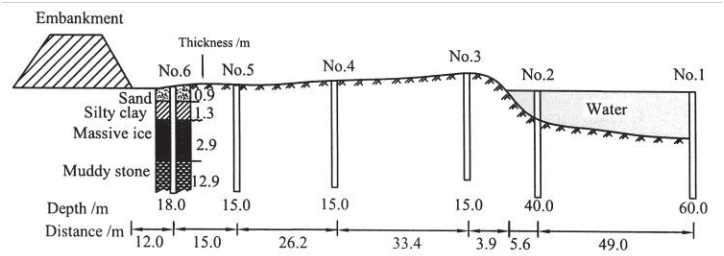

Figure 8. Borehole distribution and the local strata around the thermokarst lake.

Table 2. Thermal gradient and estimated permafrost base depth in different boreholes.

Hole number	Thermal gradient / ºC/100m	Depth of permafrost base /m	Depth range for calculation /m
No.1	-6.3		45~60
No.2	1.8	32.2	30~40
No.3	3.2	52.7	11~15
No.4	2.0	64.3	11~15
No.5	1.8	75.5	11~15
No.6	1.8	89.7	11~15

Figure 11. Icing and frost mound along the QHT.

source of the local river. After the QTH embankment was constructed and some of the groundwater discharge was blocked, icings along with frost mounds resulted. Every winter several icings formed at the two sides of the highway within a 3 km section. Some of them even covered the road surface shown as Figure 11. At the same time, when icings and frost mounds thawed, the roadbed subsided unevenly. To solve such a hazard, groundwater migration routes need to be investigated, and seepage structures are necessary. In a road structure, sometimes a bridge is the final choice.

Conclusions

(1) Permafrost in the Qinghai-Tibet Plateau is in degradation under the influence of global warming. Moreover, in the narrow Qinghai-Tibet corridor, dense engineering projects have intensified the degradation and caused secondary hazards. These hazards mainly show as thawing settlement, thaw slumping, thawing grooves, thermokarst, frost heave, etc.

(2) Thaw slumping is commonly caused by slope toe disturbance in ice-rich permafrost regions. Well-developed thaw slumping along the QTH has developed to about 7500 m^2 in scale in the past 15 years. The permafrost in the slumping zone is under degradation, characterized by ground-ice melting and temperature-rising.

(3) Thawing grooves are mainly caused by linear cutting or even ground surface disturbance. A thawing groove which exists along the QTR subsided 40 cm in 2 years. Long-time development of the groove finally affects the roadbed stability by parallel cracks and lateral thermal erosion.

(4) Thermokarst results from the thawing of ice-rich permafrost or the melting of massive ice. There were 69 small thermokarst lakes in an ice-saturated permafrost section within 150 km along the QTH. Permafrost under a typical thermokarst lake near the Fenghuoshan region has totally thawed. Therefore, lateral thermal erosion of a thermokarst lake needs to be considered if it is near an engineering project.

(5) An icing incorporated with a frost mound along the QTH was cause by embankment blocking of groundwater discharge. The road surface was hard to keep even because the roadbed suffered frost heave and thaw settlement every year.

(6) Restricting ground surface disturbance and excavation, ensuring an efficient drainage system, and keeping the ground frozen are suggested ways to avoid the secondary hazards in permafrost regions of the plateau.

Acknowledgments

This work was supported in part by the Chinese Natural Science Fund (No. 40471023), the grant of the Knowledge Innovation Program of the CAS (No.KZCX1-SW-04, KZCX-XB-10) and the National Science Supporting Project of the Ministry of Science and Technology of China (2006BAC07B02).

References

Burn, C.R. 2005. Lake-bottom thermal regimes, western Arctic coast, Canada. *Permafrost and Periglacial Progresses* 6: 355-367.

Liu, Y.Z., Wu, Q.B., Zhang, J.M. et al. 2000. Study on ground temperature field in permafrost regions of Qinghai-Tibet Plateau. *Highway* 2: 4-8.

Nan, Z.T., Gao Z.S., Li, S.X. et al. 2003. Permafrost Changes in the Northern Limit of Permafrost on the Qinghai-Tibet Plateau in the Last 30 Years. *ACTA Geographic SINICA* 586): 817-823.

Wang, S.L. & Mi, H.Z. 1993. The Change of Permafrost under Roadbed with Asphalt Pavement along the Qinghai-Tibet Highway. *Journal of Glaciology and Geocryology* 15(4): 566-573.

Wu, Q.B., Cheng, G.D. & Ma, W. 2004. The impact of climate warming on Qinghai-Tibetan Railroad. *Science in China, Series D* 47 (Supp.I): 122~130.

Zhou, Y.W., Cheng, G.D., Qiu, G.Q. et al. 2000. *Permafrost in China*. Beijing: Science Press, 403-404.

Zhu, L.N., Wu, Z.W. & Liu Y.Z. 1995. Permafrost Degeneration in the East of Tibetan Plateau. *Journal of Glaciology and Geocryology* 17(2): 120-124.

Comparison of Simulated 2D Temperature Profiles with Time-Lapse Electrical Resistivity Data at the Schilthorn Crest, Switzerland

Jeannette Noetzli
Glaciology, Geomorphodynamics, Geochronology, Geography Department, University of Zurich, Switzerland
Christin Hilbich
Department of Geography, University of Jena, Germany
Christian Hauck
Institute for Meteorology and Climate Research, University of Karlsruhe/Forschungszentrum, Karlsruhe, Germany
Martin Hoelzle
Glaciology, Geomorphodynamics, Geochronology, Geography Department, University of Zurich, Switzerland
Stephan Gruber
Glaciology, Geomorphodynamics, Geochronology, Geography Department, University of Zurich, Switzerland

Abstract

The Schilthorn Crest in the Bernese Alps, Switzerland, is a prominent permafrost research site. Topographic and transient effects influence the temperature field below the east-west oriented crest. Measured T(z)-profiles in boreholes, however, do not provide sufficient information for a comprehensive description of the subsurface temperature distribution. We combine ground temperature measurements, electric resistivity tomography (ERT) monitoring, and numerical modeling to investigate the 3-dimensional thermal regime below the crest. The modeled temperature field of a north-south oriented cross section agrees well with ERT results along the same profile. The simulated thermal regime below the Schilthorn is characterized by generally warm permafrost, with the coldest zone below the upper part of the north-facing slope, and permafrost a little below the surface on the south-facing slope. The combination of temperature modeling and measurements and geophysical monitoring bears potential to improve simulation and validation strategies.

Keywords: alpine permafrost distribution; electrical resistivity; thermal modeling; tomography monitoring; transient and topographical temperature effects.

Introduction

Permafrost was first found on Schilthorn summit, Switzerland, when the facilities for the cable car were built between 1965 and 1967. During the construction of the buildings, several ice lenses with a thickness of up to 1 m were encountered. Since then, extensive research has taken place on Schilthorn (e.g., Imhof 2000, Vonder Muehll et al. 2000, Hauck 2001, Mittaz et al. 2002, Hilbich et al. 2008), making it to one of the most intensively investigated permafrost sites in the European Alps. Three boreholes in perennially frozen ground were drilled within the PACE-project between 1998 and 2001 (Harris 2001). These boreholes provide the basis for monitoring and quantification of changes in the permafrost thermal regime.

In mountain areas, the interpretation of T(z)-profiles measured in boreholes with respect to climate signals is complicated by topographic effects (Gruber et al. 2004). The Schilthorn represents an east-west oriented ridge with a warm south-facing and a colder north-facing slope. Even though measured temperature profiles in boreholes enable an initial assessment of topography related and transient effects, they are only representative of isolated local spots. A comprehensive analysis of permafrost distribution and evolution below the crest can only be achieved by integrating additional subsurface data

Figure 1. View of the Schilthorn Crest in the Bernese Alps looking eastward. The ERT-Profile starts just below the meteo station in the northern slope and reaches across the crest approximately to the southern border of the photo.

In this paper, we combine measurements of surface and subsurface temperatures, electric resistivity tomography (ERT), and numerical modeling of a subsurface thermal field for a 2-dimensional investigation of permafrost conditions below the Schilthorn crest. A 2D heat transfer model is forced by measured near-surface temperatures at the upper boundary to simulate the thermal field of a north-south cross section of the ridge. An ERT monitoring system was installed across the same profile, which provides additional information on subsurface conditions, and enables comparison of modeling results for a qualitative validation.

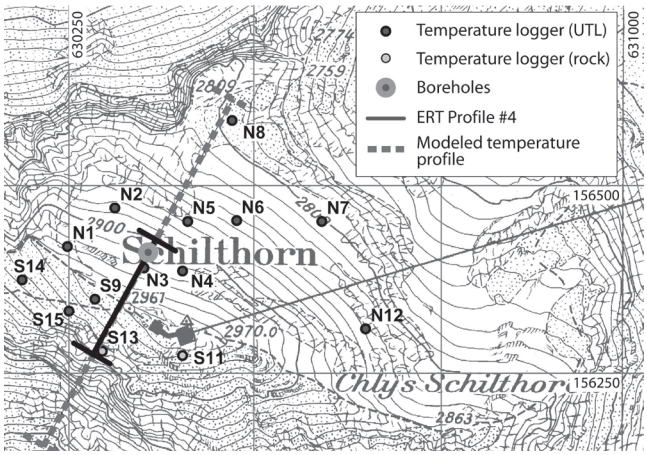

Figure 2. Overview of the field site Schilthorn Crest showing the locations of the near-surface temperature loggers, the boreholes, the measured ERT profile, and the modeled north-south cross section. Map: Swisstopo.

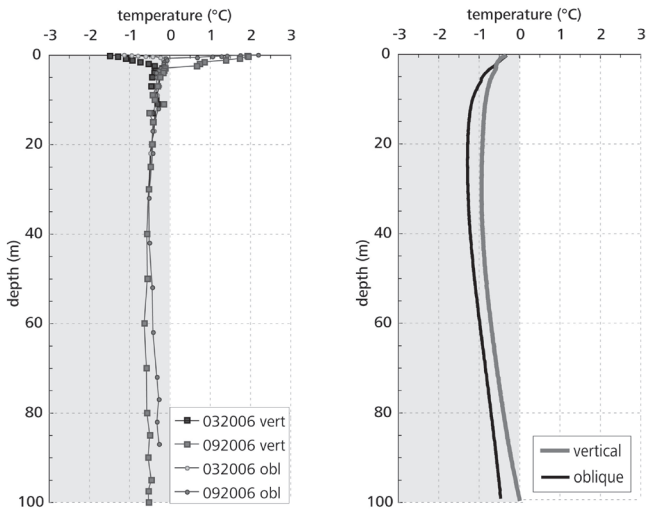

Figure 3. T(z)-profiles for the 101 m vertical (vert, black) and oblique (obl, gray) boreholes on the Schilthorn for spring and autumn 2006 (left). Modeled T(z)-profiles extracted from the temperature field in Fig. 4 at the locations of the two boreholes (right; colored illustration available on CD-Rom).

The Field Site

The Schilthorn (2970 m a.s.l., 46.56°N/7.83°E, Figs. 1, 2) is located in the Bernese Oberland in the Northern Swiss Alps. The three boreholes are located on a small plateau on the north-facing slope approximately 60 m below the summit. Air temperatures recorded at the meteo station close to the boreholes indicate an annual mean of -2.8 °C for the years 1999–2007 (Hoelzle and Gruber 2008). The annual precipitation is estimated to 2700 mm and about 90% of it falls as snow (Imhof 2000). As the precipitation maximum occurs during summer and due to additional snow input through wind transport, the snow cover on the northern slope usually persists from October until June or even July (Hauck 2001). The average snow depth since the beginning of measurements at the meteo station in 1999 is around 80 cm. The Schilthorn consists of dark micaceous shales that weather to form a fine-grained debris layer of up to several meters in thickness covering the entire summit region. The ice content of the subsurface material is assumed to be generally low (around 5–10% in the upper meters, as reported from direct observations, Imhof et al. 2000, Vonder Mühll et al. 2000).

Temperature Measurements

Boreholes

In the scope of the PACE project, a 14 m borehole was drilled in 1998 and complemented by two 101 m boreholes in 2000. Today, these boreholes are part of the Permafrost Monitoring Switzerland (PERMOS). The deeper boreholes were drilled vertical and with an angle of 60° to the vertical in order to account for topography-related effects. Temperatures measured in these boreholes point to warm permafrost conditions with temperature values between -1 and 0°C below depth of the zero annual amplitude (ZAA) at approximately 20 m, and to a very small temperature gradient with depth (Fig. 3, left). The temperature gradient in the oblique borehole is slightly greater than in the vertical borehole. Ground temperatures are considerably higher compared to other sites at similar altitude and exposition, which is probably due to the low bedrock albedo, thick snow cover, and low ice content at the site (Hauck 2001).

Ground surface temperatures

In addition to the borehole measurements, 14 temperature loggers were distributed on both sides of the crest in summer 2005 and 2006 to measure near surface-temperatures (see Fig. 2). The loggers were installed at a depth of 30 cm (UTL mini loggers) and 10 cm (rock temperature loggers), respectively, and temperatures are recorded every 2 hours. The accuracy of the temperature loggers is given as ±0.25°C and ±0.1°C, respectively. As the lower parts of the steep southern slope are difficult to access, loggers were only placed in the upper part of the slope. These near-surface temperature measurements provide the upper boundary condition for the numerical heat transfer model presented in the following section. In addition, they can be used to constrain the interpretation of the geophysical results concerning the subsurface thermal regime.

Numerical Modeling of Subsurface Temperatures

General approach

We considered a purely conductive transient thermal field under variable topography in an isotropic and homogeneous medium according to Carslaw and Jaeger (1959). In steep topography, heat transfer at depth mainly results from conduction, driven by the temperature variations at the surface. Processes such as fluid flow are not included in this first step. Subsurface temperatures are calculated for conditions in the hydrological year 2006/2007 (i.e., 1 Oct. to 30 Sept.) based on mean annual conditions at the surface. That is, seasonal variations at the surface are not included, and temperature variations above the ZAA are not simulated.

Ice contained in the pore space and crevices delays the

response to surface warming by the uptake of latent heat during warming. This is addressed in our finite-element heat transport model by apparent heat capacity, which substitutes the volumetric heat capacity in the heat transfer equation and includes energy consumed during phase change. We used the approach described by Mottaghy & Rath (2006).

The resulting temperature pattern is expected to be similar for any north-south oriented cross crest profile. Hence, simulations are conducted for a 2D section across the crest and the borehole site on the northern slope. The assumption of symmetry in an east-west direction is supported by first results of a quasi-3D geoelectrical investigation including four parallel and two orthogonal ERT-profiles in the Schilthorn summit area (Krauer 2008). The selected profile was extracted from a digital elevation model (DEM) with 10 m horizontal resolution (Data Source: Swissphoto). The finite element (FE) mesh was generated for this geometry with corresponding 10 m resolution at the surface, and lower resolution at greater depth. The mesh consists of 1468 elements. The software package COMSOL Multiphysics was used for forward modeling of subsurface temperatures.

Boundary conditions

For all near-surface temperature loggers the mean annual temperature for the hydrological year 2006/2007 was calculated and set as an upper boundary condition at the corresponding elevation and side of the modeled profile. The measured thermal offset between the ground surface and TTOP is small at Schilthorn (about 0.3°C; cf. Hoelzle & Gruber 2008) and is, hence, neglected in the simulations.

The years 2006 and 2007 were very warm and clearly above the long-term average. Therefore, measured near-surface temperatures are not representative for the thermal conditions at the surface during the past decades and century. Transient effects are likely to occur and, therefore, initialization of the heat conduction model is required in order to perform a realistic simulation of the current subsurface temperature field. Based on the assumption that surface temperature fluctuations mainly follow air temperatures, we used mean annual air temperatures (MAAT) from the meteo station on Jungfrauoch (3576 m a.s.l., Data source: MeteoSwiss) some 10 km east of Schilthorn to describe the evolution of the upper boundary. For Jungfraujoch, air temperature data is available back to 1933. The total difference in MAAT between 2006 and the mean of the period 1933–1950 is +1.52°C. We additionally assumed a difference in air temperature of +0.5°C between the start of the data recordings and the Little Ice Age (ca. 1850). The model initialization was started in 1850, and daily time steps were taken. A uniform lower boundary heat flux of 0.08 W m^{-2} was set at sea level, and thermal insulation was assumed for the lateral boundaries of the geometry.

Subsurface properties

Subsurface material properties were assigned on the generated FE mesh. In purely diffusive and transient simulations, thermal conductivity, volumetric heat capacity, and the ice/water content are the petrophysical parameters of importance. However, only little is known on the subsurface characteristics below steep topography and the parameters were set based on published values: Thermal conductivity was assumed as 2.5 W K^{-1} m^{-1}, and heat capacity to 2.0 x 10^6 J m^{-3} K^{-1} for the bulk material (Cermák & Rybach 1982).

Based on estimations from geophysical measurements (cf. Hauck et al. 2008) for the upper layers, a uniform ice content of 5% for the entire profile was assumed in the model simulations. The unfrozen water content is described by an exponential function, and the steepness factor was set to 0.2 (cf. Mottaghy & Rath 2006).

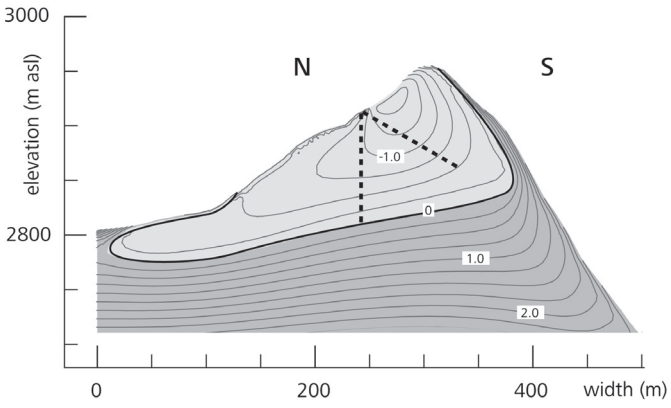

Figure 4. Isotherms of the modeled subsurface temperature field for a north-south cross section of the Schilthorn crest. The 0°C isotherm is depicted in black, and the dashed black lines indicate the boreholes. Light gray areas are permafrost, darker shaded areas are outside permafrost (colored illustration available on CD-ROM).

Modeling results

The resulting temperature field for the Schilthorn profile is depicted in Figure 4. Maximum permafrost thickness amounts to roughly 100 m below the northern slope and the top of the crest. Isotherms are steeply inclined in the top part, and a lateral heat flow exists from the warm south to the colder north face. Simulated permafrost temperatures are higher than -2°C for the entire profile.

The coldest temperatures exist below the northern and central part of the ridge. The reason is that coldest surface temperatures are found in the steep part of the northern slope (mainly due to reduced solar radiation and longer snow cover duration), and that surface temperatures are higher on the small plateau where the boreholes are located, as well as on the southern side. The southern slope is mainly permafrost-free at the surface. However, due to the cold, northern slope permafrost can be found below the surface. In addition, this is caused by the fact that 20th century warming has not yet penetrated to greater depth in the model, which lowers the temperatures a few tens of meters below the surface compared to present-day steady-state conditions. Similarly, permafrost remains below the surface at the foot of the northern slope. These results point to the importance of transient 2D/3D modeling, as such transient and topography related effects could not be detected using steady state 1D models.

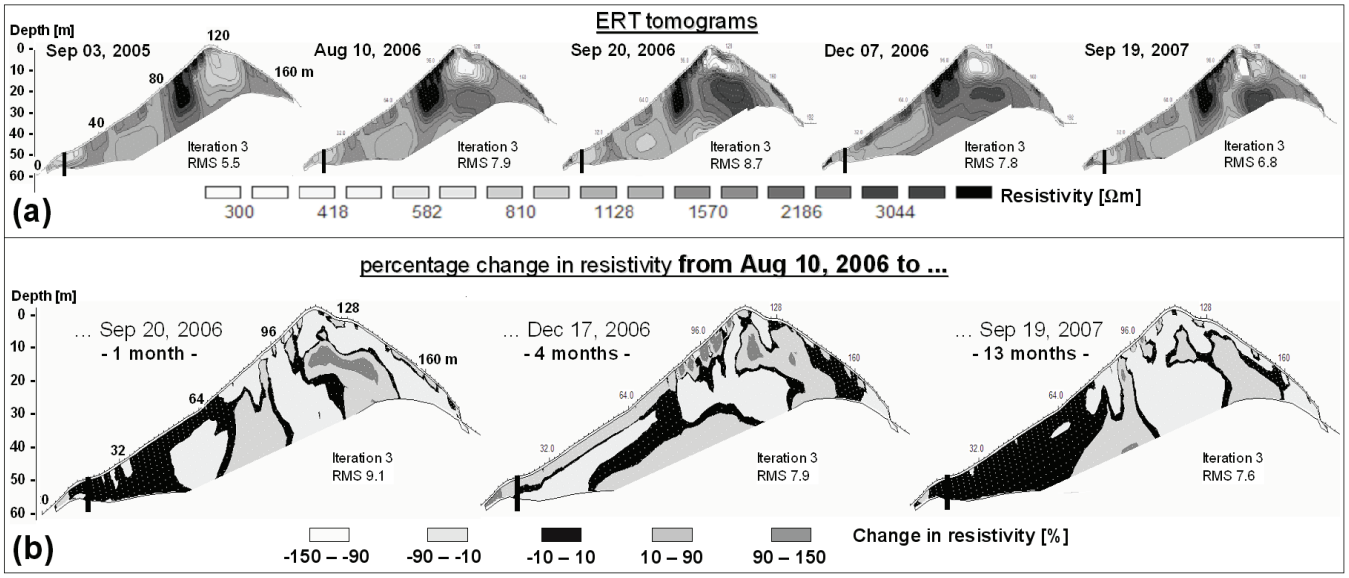

Figure 5. ERT monitoring data illustrated as individual resistivity tomograms for subsequent measurements (a), and as calculated change in resistivity based on the reference profile from August 10, 2006 over one, four, and 13 months (b; colored illustration available on CDRom).

In contrast to ERT profiles (c.f. next section), which mainly allow for a qualitative validation of the general pattern of temperature distribution, comparison with extracted T(z)-profiles at the locations of the boreholes shows the accuracy of the modeled temperature values (Fig. 3). In general, the modeled profiles correspond to the measured data in Figure 3 as temperatures are below -1.5°C for the entire profile, and temperature gradients with depth are small. For both measured and modeled profiles, the oblique borehole shows a slightly more curved profile. However, temperatures of the modeled profile average about 0.2°C colder than the measured values, but range up to 1°C in the upper half of the profile. Further, in the lower parts, the oblique profile is warmer than the vertical profile, which could not be reproduced in the simulation. The results are encouraging given the model error sources, which include: (1) subsurface properties (i.e., ice content, thermal conductivity) are assumed as homogenous for the entire profile and are hardly known at depth; (2) the temperature evolution at the surface may be influenced by effects of solar radiation and snow cover, and, hence, not exactly follow air temperature. In addition, the higher ice content in the limestone scree in the upper meters can slow down the reaction of the subsurface to changing surface temperatures by the uptake of latent heat; (3) small scale variability at the site may cause random errors in logger measurements, and (4) processes such as heat transport by convection are not taken into account.

Geophysical Measurements

Electrical Resistivity Tomography (ERT)

In 1999, a semi-automatic ERT monitoring system was installed on a 60 m line close to the three boreholes in the north facing slope to observe subsurface resistivity changes with respect to ground ice and water content (Hauck 2001, Hilbich et al. 2008). In summer 2005, a second ERT monitoring line (188 m) was installed across the crest, complemented by a quasi-3D ERT survey along four transects across the crest in 2006. Datasets across the crest can be used to analyze the 3D permafrost distribution.

The measured signal is sensitive to temporally variable properties such as temperature, via the unfrozen water, and ice content, as well as unchanging material characteristics, such as lithology and porosity. Repeated ERT measurements, therefore, yield information on the changes occurring in the physical properties of the ground with changing temperature and time (Fortier et al. 1994).

ERT monitoring data of the cross-crest profile (Fig. 2) are available on different time scales: (a) annual measurements in late summer (August/September) for 2005, 2006, and 2007, and (b) seasonal-scale measurements between August and December 2006. Whereas the annual resolution provides interannual resistivity changes between 2005 and 2007, the seasonal scale helps to identify zones with pronounced resistivity changes to delineate ice-free from ice-rich regions. ERT data were processed with the software RES2DINV (Loke & Barker 1995). Besides a qualitative comparison of individual tomograms, a so-called time-lapse inversion of time series of ERT data allows for a quantitative assessment of the resistivity changes.

Results

Figure 5 shows the results of the ERT monitoring across the Schilthorn Crest. In general, measured resistivities are quite low compared to other permafrost sites and do not exceed 4000 Ωm. This is mainly due to the thick fine-grained debris layer covering the summit region. Outcrops of the underlying bedrock also indicate strongly weathered conditions of the micaceous shales with crevices, where water can percolate. In addition to the comparably conductive host material, the low ice content is in accordance with the low resistivity values.

A number of features can be observed in all tomograms (cf. Fig. 6): (A) a relatively homogeneous zone with resistivities between 700 and 1600 Ωm in the lower part of the northern slope, (B) a high resistive zone (>3000 Ωm) in the upper part of the northern slope, (C) a homogeneous intermediary zone in the southern slope with resistivities from 1200 to 1700 Ωm, and (D) a very low resistive anomaly (<500 Ωm) with an underlying high resistive anomaly (>2300 Ωm) at the summit.

The high resistive anomaly in the northern slope (B) may indicate the presence of ground ice and/or firm bedrock. Both possibilities would result in increased resistivity values compared to regions with lower ice contents or more weathered bedrock occurrences, respectively. The low resistive anomaly at the crest (D) is difficult to interpret. In comparable terrain, such low resistivity values are normally associated with very high amounts of unfrozen water or conductive man-made structures (e.g., cables). The presence of such a large amount of water is very unlikely since the crest consists of firm bedrock without a superficial debris cover, whereas metallic remnants from the construction of the summit station (e.g., anchors) are found all over the crest. A man-made low resistive anomaly can therefore, not be excluded. The high resistive anomaly directly below this feature is believed to be an inversion artifact, which is often generated during inversion below a zone of anomalously high or low resistivity values (Rings et al. 2007).

Apart from the high and low resistive anomalies close to the crest, the characteristics of the northern (A) and southern (B) slope seem to be similar. From the qualitative analysis of the individual tomograms no clear indication of differences in permafrost occurrence and ice content between the two slopes is apparent. Calculating the percentage change of resistivities between subsequent measurements (Fig. 6), the tomograms can be transferred into information on seasonally changing properties. From this, zone (A) in the northern slope can be seen as a region with little change in the deeper parts but with pronounced resistivity changes within the upper 4–5 m. This clearly indicates the presence of permafrost with active layer freezing in winter. The deeper parts tend to exhibit slightly lower resistivities in winter, which we interpret as delayed advance of the summer heating (increasing unfrozen water content and therefore decreasing resistivities) into the ground. Zone (B) only yields systematic resistivity changes near the surface, that can be attributed to thawing (decreasing resistivities) between August and September and freezing (increasing resistivities) processes until December. Both processes are similar to the features in zone (A) but seem to be more pronounced. Zone (C) is characterized by a homogeneous resistivity decrease during summer, but shows almost no changes between August and December, i.e., no active layer freezing can be observed. In contrast to the very similar absolute resistivity values, seasonal changes are different in the northern and southern slope. This can be related to differences in subsurface material properties, i.e., permafrost or ice content.

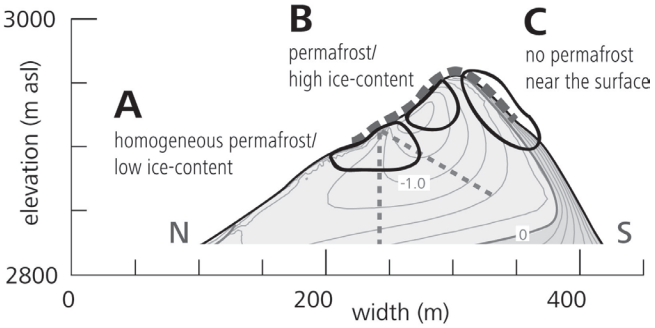

Figure 6. Three features that are addressed in the discussion section are highlighted by black circles: (A) A homogeneous permafrost zone in the lower northern slope with low ice content, (B) a cold zone in the north slope with a high ice content, and (C) no permafrost near the surface on the southern slope. Additionally, grey dashed lines indicate the boreholes and the extent of the ERT profile (colored illustration available on CD-ROM).

Discussion

In both the modeled temperature field and the ERT profiles, three zones in the investigated cross section of the Schilthorn Crest can be distinguished that are particularly interesting (Fig. 6). Cross validation of the results of the two complementary approaches enables an interpretation as follows.

(A) In the lower part of the northern slope, a zone of homogeneous temperatures and resistivities exits. The small variations in temperature in this area may be explained by the fact that temperature values are only little below the melting point and the energy input of the recent warming is consumed by latent heat. Also, the results from ERT monitoring suggest high amounts of unfrozen water and only little ice content (Hauck et al. 2008).

(B) In the upper part of the northern slope a zone of cold temperatures exists. The corresponding zone of high resistivity in the ERT profile is, hence, probably caused by higher ice content rather than by geological characteristics. This is also supported by the larger seasonal resistivity changes pointing to higher contents of ice and unfrozen water than in the lower part of the northern slope.

(C) The permafrost boundary on the southern slope is likely situated only a little below the surface, an effect that can be mainly attributed to surface warming of the past century that has not yet affected greater depths. Seasonal resistivity changes support the hypothesis that there is no permafrost near the surface in the southern slope.

The results of this qualitative validation corroborate the assumption that the general pattern of the subsurface temperature field can be modeled using diffusive and transient 2D and 3D simulations. Using such an approach enables the simulation of temperature fields at greater depths that cannot be reached by geophysical measurements or direct measurements in boreholes. Additionally, the numerical model can be used to calculate scenarios of the evolution of subsurface temperatures and of future permafrost occurrence below the Schilthorn Crest by prescribing the evolution of

the upper boundary condition or by coupling the model to a surface energy balance model and/or using regional climate model output (cf. Noetzli et al. 2007).

Conclusions and Perspectives

The subsurface thermal field of a 2D-section across the Schilthorn was modeled assuming a purely conductive and homogenous underground in a first approach. Comparison with measured ground temperatures and ERT profiles leads to the following conclusions:

- The subsurface thermal regime of the Schilthorn Crest is predominantly influenced by both topography and transient effects. The cold northern slope and the recent 20th century warming induce permafrost on the southern side of the crest only a little below the surface.
- The thermal regime of the profile can be characterized by a cold zone below the upper part of the northern slope, permafrost occurrence only a little below the surface on the southern slope and in the lowest part of the northern slope, and rather homogeneous conditions at and below the area of the boreholes.
- The modeled temperature field agrees with the results from ERT monitoring. The three zones mentioned above can be distinguished in the results of both methods.

ERT monitoring on Schilthorn is being continued in the scope of PERMOS. The combination of thermal modeling, temperature measurements in boreholes and geophysical surveys bears potential to further improve modeling and validation strategies. These may include (1) quantitative comparison of numerical results and measured data to estimate model performance, (2) extending single point temperature data to larger scales using 2D or 3D resistivity values, and (3) improving the representation of the subsurface physical properties in the model by incorporating subsurface information (e.g., geological structures, water/ice content) detected by geophysical surveys.

Acknowledgments

We are indebted to Michael Krauer for making available the ERT data measured within his M.S. thesis. Further, we'd would like to thank the motivated students that helped us in the field and the Schilthornbahnen AG for generous logistic support. Part of this study (JN) was financed by the Swiss National Science Foundation as part of the NF 20-10796./1 project, and geophysical fieldwork (CH) was partly financed by PERMOS.

References

Carslaw, H.S. & Jaeger, J.C. 1959. Conduction of heat in solids. In *Oxford Science Publications*. Oxford: Clarendon Press, 510 pp..

Cermák, V. & Rybach, L. 1982. Thermal conductivity and specific heat of minerals and rocks. In G. Angeneister, (ed.), *Landolt-Börnstein Zahlenwerte und Funktionen aus Naturwissenschaften und Technik, Neue Serie, Physikalische Eigenschaften der Gesteine*. V/1a. Berlin: Springer Verlag, 305-343

Gruber, S., King, L., Kohl, T., Herz, T., Haeberli, W. & Hoelzle, M. 2004. Interpretation of geothermal profiles perturbed by topography: The Alpine permafrost boreholes at Stockhorn Plateau, Switzerland. *Permafrost and Periglacial Processes* 15(4): 349-357.

Fortier, R., Allard, M. & Seguin, M.K. 1994. Effect of physical properties of frozen ground on electrical resistivity logging. *Cold Regions Science and Technology* 22: 361-384.

Harris, C., Haeberli, W., Vonder Muehll, D., & King, L. 2001. Permafrost monitoring in the high mountains of Europe: The PACE project in its global context, *Permafrost and Periglacial Processes* 12: 3-11.

Hauck, C. 2001. *Geophysical methods for detecting permafrost in high mountains*. Ph.D. Thesis. Zürich, Switzerland: ETH-Zürich, 204 pp.

Hauck, C., Bach, M. & Hilbich, C. 2008. A 4-phase model to quantify subsurface ice and water content in permafrost regions based on geophysical datasets. *Proceedings of the Ninth International Conference on Permafrost, Fairbanks, Alaska, June 29–July 3, 2008* (this proceedings).

Hilbich, C., Hauck, C., Hoelzle, M., Scherler, M., Schudel, L., Völksch, I., Vonder Mühll, D. & Mäusbacher, R. 2008. Monitoring of mountain permafrost evolution using electrical resistivity tomography: A seven-year study of seasonal, annual and long-term variations at Schilthorn, Swiss Alps. *Journal of Geophysical Research* 113:F01S90, doi:10.1029/2007JF000799.

Hilbich, C., Hauck, C., Delaloye, R. & Hoelzle, M. 2008. A geoelectric monitoring network and resistivity-temperature relationships of different mountain permafrost sites in the Swiss Alps. *Proceedings of the Ninth International Conference on Permafrost, Fairbanks, Alaska, June 29–July 3, 2008* (this proceedings).

Hoezle, M & Gruber, S. 2008. Borehole measurements and ground surface temperatures and their relationship to meteorological conditions in the Swiss Alps. *Proceedings of the Ninth International Conference on Permafrost, Fairbanks, Alaska, June 29–July 3, 2008* (this proceedings).

Imhof, M. 2000. Permafrost investigation in the Schilthorn massif, Bernese Alps, Switzerland. *Permafrost and Periglacial Processes* 11(3): 189-206.

Krauer, M. 2008. Versuch einer 3-dimensionalen Erfassung des Peramfrosts in der Gipfelregion des Schltohrns mittels Geoelektrik, M.S. Thesis. University of Zurich, 112 pp.

Loke, M.H. & Barker, R.D. 1995. Least-squares deconvolution of apparent resistivity. *Geophysics* 60: 1682-1690.

Mottaghy, D. & Rath. V. 2006. Latent heat effects in subsurface heat transport modeling and their impact on paleotemperature reconstructions, *Geophysical Journal International* 164: 236-245.

Noetzli, J., Gruber, S., Kohl, T., Salzmann, N. & Haeberli, W. 2007. Three-dimensional distribution and evolution of permafrost temperatures in idealized high-mountain topography. *Journal of Geophysical Research* 112: doi:10.1029/ 2006JF000545.

Rings, J., Preko, K., Scheuermann, A. & Hauck, C. 2007. Soil water content monitoring on a dike model using electrical resistivity tomography. *Near Surface Geophysics* (in press).

Stocker-Mittaz, C. 2002. *Permafrost distribution modeling based on energy balance data*. Ph.D Thesis. Zurich, Switzerland: University of Zurich, 122 pp.

Vonder Mühll, D., Hauck, C. & Lehmann, F. 2000. Verification of geophysical models in Alpine permafrost by borehole information. *Annals of Glaciology* 31: 300-306.

The Effect of Fines Content and Quality on Frost Heave Susceptibility of Crushed Rock Aggregates Used in Railway Track Structure

Antti Nurmikolu and Pauli Kolisoja
Tampere University of Technology, Tampere, Finland

Abstract

The high smoothness requirement of rails does not allow frost action in the structural layers of the track. Long-term experience with the use of crushed rock aggregates in the uppermost layer of the track, the ballast bed, indicates that the aggregates degrade substantially with accumulating traffic loading. In Finland, the use of crushed rock aggregates has recently extended to the lower structural layers (subballast). For the purpose of setting optimal material requirements for crushed rock aggregates, their degradation and its impacts on frost susceptibility have been studied at TUT. Sampling, a total of 132 frost heave tests, and a large number of laboratory index tests revealed that in certain crushed rock aggregate the frost susceptibility at under 15% fines content was directly proportional to the fines content. In the combined analysis of various aggregates, the observation of quality of fines improved the correlation.

Keywords: ballast; crushed rock aggregate; fines; frost heave test; frost susceptibility; pore size distribution.

Introduction

The smoothness requirement of railway tracks is extremely high and is tightening along with increasing train speeds. Even relatively small deviations in track geometry limit the competitiveness of environmentally friendly rail traffic, as travel times increase and traffic capacity diminishes. In cold climates frost action is an essential factor behind the vertical deviations of track geometry. Because structural layers are generally considered to be built of "non-frost-susceptible" materials, the frost action of traffic routes is commonly associated with problems in the frost-susceptible subgrade. However, in the severe loading environment of the track structure, crushed rock aggregates degrade as a consequence of traffic loading, maintenance operations, and environmental loadings. The tendency towards higher axle loads and train velocities further increases the loading applied to structural layers.

Coarse-grained and uniformly graded crushed rock aggregate, ballast (Fig. 1), is traditionally used in the uppermost structural layer of a track. A literature review by Nurmikolu (2005) showed that many studies dealing with the degradation of ballast have been published. As a result of ballast degradation, its water retention, frost susceptibility, and deformations increase. Finally, the effectiveness of the maintenance performed to keep the track geometry at an acceptable level decreases to the extent that the most economical alternative is to clean the ballast with a special sieving machine in the field. Published research data dealing directly with the frost susceptibility of ballast are scarce, though at least in Finland, maintenance operators have distinct experiences of frost action in ballast causing deviations in track geometry. In a recent field study Akagawa (2007) found that degraded ballast causes significant frost heave in a track. Studies dealing with the frost susceptibility of other coarse-grained materials, such as the base course aggregates of roads, have been published in recent years, perhaps due to the increased smoothness requirements, for example, by Guthrie & Hermansson (2003) and Konrad & Lemieux (2005). It is obvious that the frost susceptibility criteria for the crushed rock aggregates of modern railway track structure cannot be determined on the basis of that literature.

Unlike in the case of ballast, there is no experience of the long-term behavior of crushed rock aggregates in the structural layers below the ballast bed. The use of crushed rock aggregates in the intermediate and frost protection layers (subballast) started in Finland with the 74 km Kerava-Lahti double track line finished in 2006. From the degradation point of view, the stress levels in the lower parts of the structure are of course lower than in the ballast but, on the other hand, cleaning of the lower layers in the same manner as the ballast bed is practically impossible. Therefore, a 100-year service life is required of the substructure (Finnish Rail Administration 2005). In order to distribute the loading applied to the subgrade, to diminish deformations and to prevent convective heat transfer (Goering et al. 2000), the material of the frost protection layer must be more fine grained and more broadly graded than ballast. Consequently, the material can become frost susceptible as a result of lesser degradation than ballast.

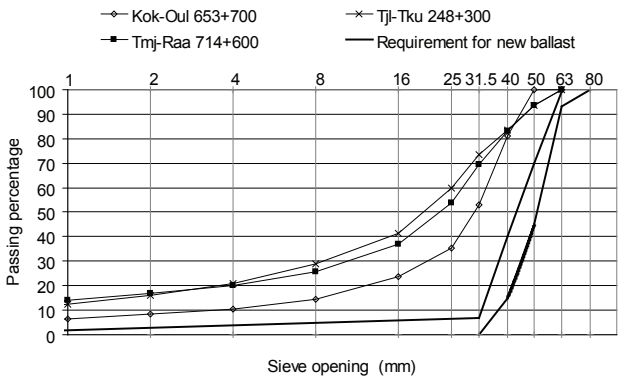

Figure 1. Finnish grading requirement for fresh ballast and examples of degraded samples taken from track structure.

Experimental Studies

Test materials and methods

The degradation of the crushed rock aggregates used in the structural layers of tracks and the quality of the produced fines was studied by long-term cyclic loading tests, ballast bed sampling, and laboratory tests of the samples. The studies concerning degradation have been described elsewhere (Nurmikolu et al. 2001, Nurmikolu 2005) as well as those dealing with the evaluation of the ballast bed's degradation stage by GPR (e.g., Silvast et al. 2007). The samples of the degradation examinations were utilized also in frost susceptibility studies.

The fines generated from ballast in an actual loading environment of a track structure were considered to be the best approximation of the quality of fines possibly produced by degradation of crushed rock aggregates in the lower structural layers. Frost susceptibility examinations were focused on 36 degraded ballast bed samples that had been in service without cleaning for a long time (mainly over 30 years or subject to 40–340 million gross tons of train loading). The sampling points were also decentralized geographically across as much of the rail network as possible to ensure a comprehensive sample of different parent rocks. Also, seven fresh, unused crushed rock aggregates from the quarries and eight natural gravels and sands, mostly from the substructure of the track, were examined. Of the fines of the samples, grain-size distribution (Sedigraph equipment), mineralogy (X-ray diffraction), specific surface area (nitrogen adsorption), pore size distribution (mercury porosimeter), water adsorption, humus content (ignition method), and surface texture (Scanning Electron Microscope) were examined. Of the coarse particles several properties were studied, too, water adsorption being the most important in terms of frost action. A total of 132 frost heave tests were done with the samples with various fines contents and grain-size distributions in the arrangement described next.

Frost heave test arrangement

The frost heave test method has not been internationally standardized. Thus, the results yielded by various arrangements, some of them listed (e.g., by Chamberlain 1981) are difficult to compare. Based on a literature review of the test methods (Nurmikolu 2005), the step freezing test arrangement was considered the most suitable for this research and was set up. In this arrangement the specimens were prepared by the Intensive Compactor Tester (ICT 150RB) into a PVC pipe (inside diameter 150 mm) which served as the specimen mould in the test. The intention was to achieve sample height of 150 mm but, due to fixed compaction effort, specimen heights varied mainly from 145–155 mm. The key decision with regard to minimizing technical testing constraints was to use a cut-up mould pipe (Fig. 2) in the test arrangement, as also recommended by ISSMFE (1989). The frictional force operating at the interface between the mould walls and the aggregate, which is increased by the freezing of water, limits the occurrence of frost heave. Different solutions have been sought for the problem such as discussed by Kujala (1991). In the cut-up mould pipe individual mould rings can separate from each other during frost heave. Then, there is movement between the mould and aggregate only within part of one mould ring, whereby the frictional force resisting frost heave is considerably less compared to a continuous mould pipe. This was obvious also based on the experimental results which showed the frost heave in a cut-up mould pipe to be 2- to 4-fold compared to a continuous pipe using identical sample materials.

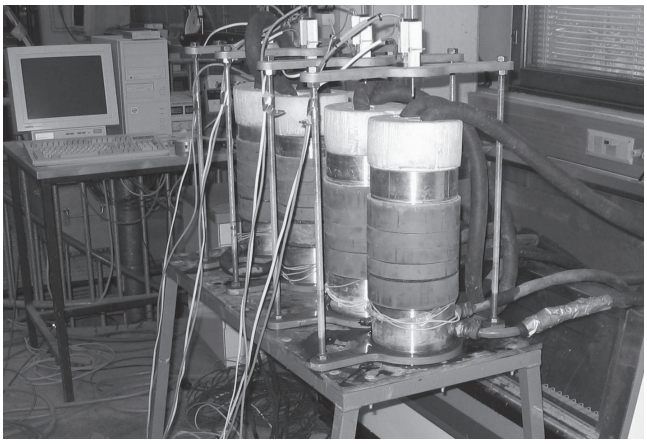

Figure 2. Frost heave test arrangement at TUT.

The equipment built for frost heave testing enabled freezing four samples simultaneously. Before starting the test, seven thermocouples were attached to a specimen at 25 mm intervals. At the beginning of the test the specimens were saturated by keeping them submerged in water for a day. At the same time the specimens were cooled to 1°C–2°C. Then the water level was lowered to about 12 mm above the bottom level of the specimen material, and the specimens were thermally insulated in order to minimize radial heat flows. The specimens were frozen in the natural freezing direction from top to bottom. The temperature of the top surfaces of specimens was controlled by circulation of a cooling agent to -3°C, and the bottom surfaces of specimens with water circulation to +1°C. The supply of additional water for specimens was secured during freezing in line with the view of Konrad and Lemieux (2005), who considered free water flow important in testing the materials of traffic routes. Frost heave was measured during the test by displacement transducers attached to specimen frames. The freezing phase was continued for a minimum of four days. The only load resisting frost action in the tests was the 3 kPa pressure from the caps.

The frost heave specimens made from ballast layer samples were, for the most part, made by proportioning the grain-size distributions (Fig. 3) from sieved fractions as desired to allow comparing the impact of fines quality. The selection of frost heave specimen grain-size distributions was tied to the typical grain-size distributions of degraded ballast bed samples and the recommended grain-size distribution of subballast material and likely progress of degradation (Nurmikolu 2005). Due to the test scale, the maximum grain

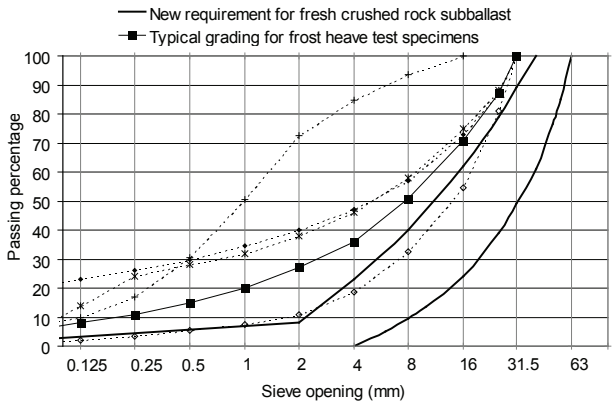

Figure 3. Typical grading curves of crushed rock samples proportioned for frost heave test specimens. Dashed curves depict variation range of tested gradings. New Finnish requirement for grading of fresh crushed rock subballast is presented, too.

size of frost heave specimens was limited to 31.5 mm. Frost heave tests on gravel and sand samples, as well as some of ballast bed samples, were done using their natural grain-size distribution of under 31.5 mm.

Parameters depicting frost susceptibility

Several parameters depicting frost susceptibility were among the analyzed results of the frost heave tests, such as accumulated frost heave, frost heave ratios, and frost heave rates after various freezing periods. A parameter independent of freezing conditions, the segregation potential (presented by Konrad 1980), was not determined, because the flow rate of the additional water into the sample was not measured. Instead, the "frost heave coefficient," which is similar in principle and is used commonly in Finland in frost dimensioning of road structures, was determined. The frost heave coefficient, *SP*, (mm/Kh) is determined from Equation 1, where *v* is the frost heave rate (mm/h) and *gradT_* is the average temperature gradient in the frozen sample section (K/mm).

$$SP = \frac{v}{gradT\_} \tag{1}$$

The primary difference in principle between the frost heave coefficient and segregation potential is that the *v* in Equation 1 indicates the flow-rate of water into the freezing zone instead of the frost heave rate when determining segregation potential (Konrad 1980). Thus, in water saturated material the frost heave coefficient can, in principle, be considered about 1.09-fold compared to segregation potential with the assumption that all the water flowing to the freezing zone ends up thickening the ice lens. However, the in situ frost heave occurring in completely or nearly water-saturated material is accounted for in the frost heave coefficient but not in the segregation potential, which increases the above-mentioned difference in water-saturated material. In an unsaturated state the difference is more difficult to assess since, according to Guthrie and Hermansson (2003), ice segregation may take place due to a material's internal water flow in the absence of external additional water. This kind of frost action cannot be depicted based on the flow rate of additional water into the material, but it is considered by the frost heave coefficient. Another difference in principle between the concepts is that when determining the segregation potential, the temperature gradient should be observed in the partly frozen zone at the frost front, not throughout the frozen layer, which is easier to measure.

As suggested by Konrad (1980) for the segregation potential, the reference value for the frost heave coefficient was determined at the moment the transient freezing phase changes into the stationary freezing phase, that is, as the frost front stops migrating in the sample. Due to the large variations in the frost heave coefficient during the test, it is highly important to follow a systematic practice, although sometimes the moment is hard to determine, as the frost front continues migrating very slowly.

Test Results and Discussion

The impact of grain-size distribution on frost susceptibility

The amount of fine-grained material coarser than fines (>0.063 mm) was observed to have an insignificant effect on the frost susceptibility of crushed rock aggregates within the range of variation normally occurring in the case of materials of the track structure. The impact of the other features of grain-size distribution on frost heave was also found insignificant in practical terms with the examined crushed rock aggregates and the grain-size distribution variation range allowed by the test method (Fig. 3). Observations (e.g., by Konrad 1999) suggest that the frost susceptibility of uniformly graded material may be lower than that of broadly-graded material containing an equal amount of fines. In crushed rock aggregates, however, especially in the case of uniform grain-size distribution and large maximum grain size which allow internal sorting, as with ballast, the finest fraction accumulates at the bottom of the material layer. In fact, internal sorting may result in a non-frost-susceptible material becoming locally frost-susceptible.

The impact of fines content on frost susceptibility

It is natural to start an analysis of the effect of fines content on frost susceptibility with test results on a specific aggregate with different fines contents. Figure 4a shows that after 4 days of freezing *(h_{96h}),* the frost heave of a specific fresh crushed rock aggregate is fully linearly dependent on the amount of fines in the material within the estimated repeatability limits of the test (Nurmikolu 2005). This applies to fines contents below 15%. The dependence is about the same as regards the frost heave coefficient *(SP_o)* (the subindex indicates the unloaded nature of the tests) in Figure 4b. Based on all the tests with fines content below 15%, the mutual correlation coefficient (R) between h_{96h} and SP_o was as high as 0.95, but yet h_{96h} correlated generally slightly more closely with the fines content, which is why the following figures only include h_{96h}.

When the analysis of Figure 4a is widened by including

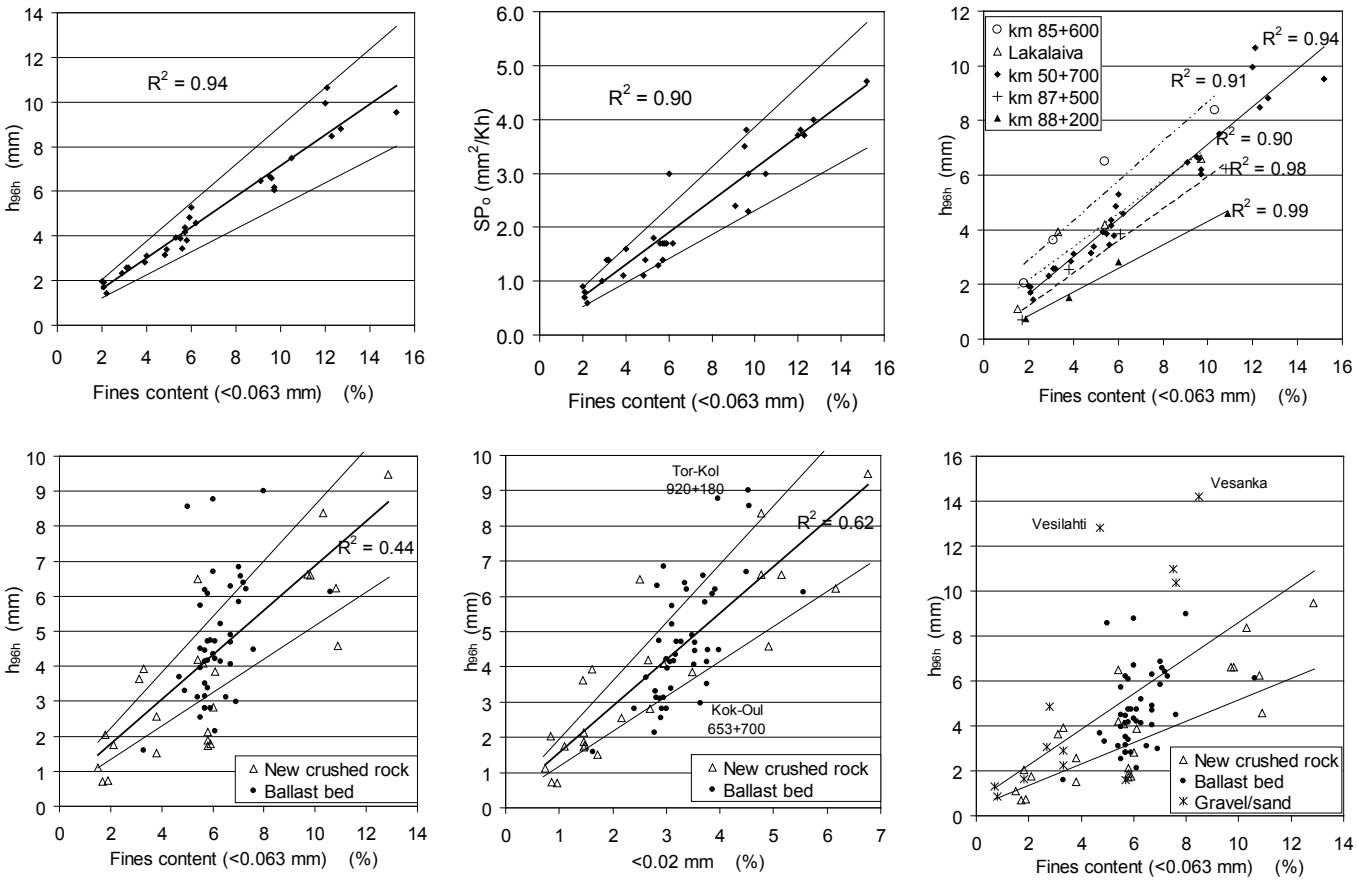

Figure 4. Correlation of parameters depicting frost susceptibility (h_{96h}, SP_o) with fines (or under 0.02 mm material) content applied to: (a & b) only tests on specific (km 50+700) aggregate, (c) different unused crushed rock aggregates, (d & e) all new crushed rock aggregates and degraded ballast bed samples from track, and (f) new crushed rock aggregates, ballasts as well as gravel and sand materials.

the corresponding results for four other fresh crushed rock aggregates, we find that the correlations between h_{96h} and fines content were strong with each aggregate as shown by Figure 4c. The location of the correlation line varied slightly depending on the aggregate, indicating slight qualitative differences in aggregates or their fines.

Figure 4d also includes the results from the tests on degraded ballast bed samples. The large number of observations made during tests on the material of Figure 1 was reduced in order to eliminate its excessive weighting. The correlation between h_{96h} and fines content is clearly weaker than in the above examinations of individual aggregates. This is explained partly by the different internal grain-size distribution of fines as seen in Figure 4e, where the correlation of h_{96h} is much stronger in the content of the finer portion of fines (<0.02 mm). This view is also supported by observations on the frost susceptibility of natural soils by, for example, Kujala (1991) and Vinson et al. (1987). Regression Equations 2 and 3, where $P_{0.02mm}$ is the content of under 0.02 mm material, could be obtained from this combined analysis of all tested crushed rock aggregates.

$$h_{96h} = 1.32 \cdot (P_{0.02mm}) + 0.24 \qquad (R^2=0.62) \qquad (2)$$

$$SP_o = 0.57 \cdot (P_{0.02mm}) + 0.14 \qquad (R^2=0.53) \qquad (3)$$

In Figure 4f the results from the tests on natural gravel and soil materials were added to show that if frost heave is assessed on the basis of fines content, there seems to be considerably more deviation in the case of gravels and sands than with crushed rock aggregates. The frost susceptibility of some gravels and sands was remarkably higher than that of crushed rock aggregates with a corresponding fines content. This can only partly be explained by the internal grain-size distribution of fines.

The impact of particle quality on frost susceptibility

The frost susceptibility of some crushed rock aggregates in Figures 4d and 4e and especially that of gravels and sands (Fig. 4f), which deviated from that evaluated on the basis of fines content, can be largely explained by divergent surface properties of particles. For example, the water adsorptions of the fines of the most divergent materials in Figure 4f (Vesilahti gravel and Vesanka sand) were almost 3-fold compared to the average level of crushed rock aggregates (Nurmikolu 2005). Corresponding differences could be noted, for example, in relation to the specific surface area or pore size distribution of fines as shown by Figure 5. The differences are clearly revealed by the SEM images in Figure 6.

The porosity and water retaining properties of some gravel and sand materials that deviated clearly from those

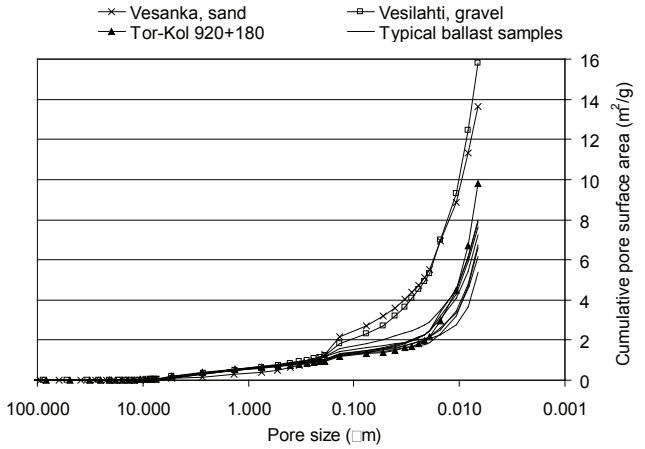

Figure 5. Cumulative pore surface areas in relation to pore size with regular ballast samples and with samples diverging the most from the analyzed fines.

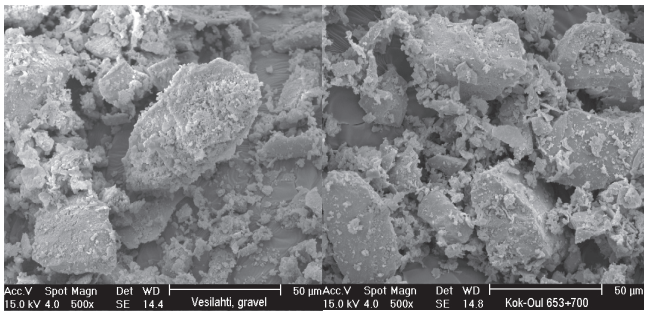

Figure 6. SEM images of the fines of (a) non-frost-susceptible ballast bed sample and (b) weathered, highly frost-susceptible gravel.

of crushed rock aggregates indicate their slight weathering. As a result, their frost susceptibility was higher than that of the examined crushed rock aggregates with corresponding fines content. The environmental loading on the particles of naturally sorted coarse-grained soils over millennia is of a different magnitude than the loading on crushed rock aggregate particles over the few decades since their crushing.

Distinct chemical weathering after crushing could be observed only in one ballast bed sample, where opaque minerals and mica had weathered, causing deposits of iron compounds on grain surfaces. In general, most of the fines in the ballast samples consisted of the most common rock minerals, quartz, feldspars, and amphiboles, whose average share in the mineral fines of the samples was established at about 80% (Fig. 7). This was a positive finding as it proved that despite the thousands of times larger specific surface area of fines compared to coarse grains, hard minerals appear to be resistant to chemical weathering in the structure even in the form of fines. The findings support the idea (Nurmikolu 2005) that degradation of ballast aggregates in the Finnish railway network is mainly the result of mechanical fragmentation and attrition caused by traffic loads and tamping (maintenance), or in a few cases possibly by frost weathering.

The significance of particles' quality on frost heave

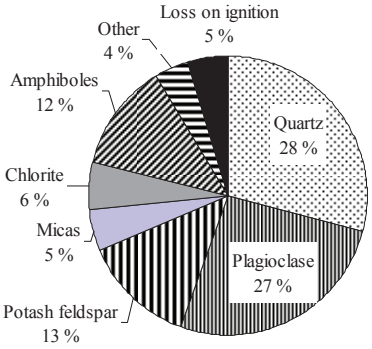

Figure 7. Indicative average mineral content of the fines of 36 ballast samples based on X-ray diffraction analyses.

susceptibility was examined statistically with stepwise regression analysis. The examined determining variables alongside the amounts of fines fractions (<0.063 mm, <0.02 mm and <0.002 mm) were water adsorption, specific surface area, total pore volume and total pore area of fines, as well as water absorption of coarse particles. The outcome of the stepwise regression analysis was clear. Based on the index properties of aggregate particles, the predictability of each parameter depicting frost susceptibility could be improved significantly compared to examinations based solely on the contents of fines fractions. The best correlation was achieved by using as independent variables the content of under 0.002 mm material, $P_{0.002mm}$, water absorption of coarse particles, WA_{24}, and total pore volume of fines measured with the mercury porosimeter, V_{tot}. Both water absorption and total pore volume clearly improved the coefficient of determination. In the case of parameters h_{96h} and SP_o this yielded regression Equations 4 (R^2=0.86) and 5 (R^2=0.80), which explained frost susceptibility in this combined analysis of aggregates nearly as well as fines content in the analyses of individual aggregates. Other independent variables did not improve the attained coefficients of determination.

$$h_{96h} = 6.9 \cdot P_{0.002mm} + 15.8 \cdot WA_{24} + 10.6 \cdot V_{tot} - 8.0 \quad (4)$$

$$SP_o = 2.8 \cdot P_{0.002mm} + 10.0 \cdot WA_{24} + 4.6 \cdot V_{tot} - 3.8 \quad (5)$$

Concluding Remarks

Degradation of the crushed rock aggregates used in the track structure affects their frost susceptibility. Some problems due to frost action can therefore be explained by frost heave in the structural layers instead of the freezing of frost-susceptible subgrade.

The results obtained from various frost heave test arrangements are hard to compare. The test method should be internationally standardized and made rather easy to perform while yet minimizing the technical restraints preventing frost heave from occurring. The arrangement with cut-up mould pipes worked well in this study.

The frost susceptibility of a certain crushed rock aggregate was found to be at the examined under 15% fines

contents directly proportional to its fines content. In the combined analysis of various crushed rock aggregates, frost susceptibility correlated better with the very finest, under 0.02 mm and under 0.002 mm, fractions of fines than with the total fines content.

Because significant chemical weathering could not be observed even in ballast bed samples that had been in service for a long time except in one case, the surface properties of mineral particles of crushed rock aggregates varied relatively little with a few exceptions. With the rock types typically used in Finland, the impact of fines on the performance of the ballast bed can, thus, be largely assessed on the basis of their amount.

The porosity and water retaining properties of some gravel and sand materials, clearly more disadvantageous than those of crushed rock aggregate, indicated their weathering and caused their higher frost susceptibility compared to crushed rock aggregates with the same fines content.

Of the examined qualitative properties of particles, water absorption of coarse particles and total pore volume of fines correlated best with frost susceptibility. The regression model building on the under 0.002 mm material content, the water absorption of coarse particles and the total pore volume of fines explained frost susceptibility in the combined analysis of aggregates nearly as well as fines content in the analyses of individual aggregates.

The concept of the non-frost susceptibility of aggregate is mainly theoretical, since minor frost heave, not explained by in-situ frost heave, actually occurs in many materials generally assumed to be non-frost-susceptible. Therefore, it would be more important to deal with the concept of practical non-frost susceptibility. Establishing the limits of it would require field observations or large-scale tests. In their absence, and as a result of the investigations and consideration of the high smoothness requirement of railway tracks, it is suggested that a frost heave coefficient of 1.0 mm^2/Kh and frost heave of 2.2 mm after four days, attained in the described test, be applied to the track structure as the limits of practical non-frost susceptibility. In fines content-based frost heave models of crushed rock aggregates, the suggested limits corresponded to an under 0.02 mm fraction content of 1.5%. In the case of typical crushed rock aggregate this corresponded to a fines (<0.063 mm) content of 2.7%.

Acknowledgments

The authors want to thank the Finnish Rail Administration for financing the research and participating in its steering. Thanks go also to the Academy of Finland for their partial funding (Finance decision 73664).

References

Akagawa, S. 2007. Frost heave susceptibility of ballast containing fines. *Proceedings of 8th International Symposium on Cold Region Development (ISCORD 2007), Tampere, Finland, September 25–27, 2007.*

Chamberlain, E.J. 1981. *Frost Susceptibility of Soil, Review of Index Tests.* Hanover, New Hampshire: CRREL Monograph 81-2, 110 pp.

Finnish Rail Administration 2005. *Track Technical Regulations and Instructions (RAMO) Part 3, Track Structure.* Helsinki, Finnish Rail Adminstration, 44 pp. (in Finnish).

Goering, D.J., Instanes, A. & Knudsen, S. 2000. Convective heat transfer in railway embankment ballast. *Ground Freezing 2000, Louvain-La-Neuve, Belgium, September 11–13:* 31-36.

Guthrie, W.S. & Hermansson, Å. 2003. Frost heave and water uptake relations in variably saturated aggregate base materials. *Transportation Research Board 82nd Annual Meeting, Paper No. 03-4391, Washington, DC, January 12–16*: 22 pp.

ISSMFE Technical Committee on Frost, TC-8 1989. Work report 1985–1989. *VTT Symposium 94, Frost in geotechnical engineering, Saariselkä, Finland, March 13–15, 1989, Vol 1:* 15-70.

Konrad, J.-M. 1980. *Frost Heave Mechanics.* Ph.D. Thesis. Edmonton, University of Alberta, 405 pp.

Konrad, J.-M. 1999. Frost susceptibility related to soil index properties. *Canadian Geotechnical Journal* 36: 403-417.

Konrad, J-M. & Lemieux, N. 2005. Influence of fines on frost heave characteristics of well-graded base-course material. *Canadian Geotechnical Journal* 42: 515-527.

Kujala, K. 1991. *Factors Affecting Frost Susceptibility and Heaving Pressure in Soils.* Ph.D. Thesis. ACTA Universitatis Ouluensis Series C 58, 99 pp.

Nurmikolu, A., Uusinoka, R., Niskanen, P. & Kuula-Väisänen, P. 2001. Effects of aggregate strength on the life cycle of railway ballast. *Proceedings of Aggregate 2001 – Environment and Economy, Helsinki, August 6–10, 2001, Vol. 1:* 213-218.

Nurmikolu, A. 2005. *Degradation and Frost Susceptibility of Crushed Rock Aggregates Used in Structural Layers of Railway Track.* Doctoral Thesis. Publication 567. Tampere University of Technology.

Silvast, M., Nurmikolu, A., Kolisoja, P. & Levomäki, M. 2007. GPR technique in the analysis of railway track structure. *Proceedings of 14th European Conference on Soil Mechanics and Geotechnical Engineering, Madrid, Spain, September 24–27, 2007.*

Vinson, T.S., Ahmad, F. & Rieke, R. 1987. Factors important to the development of frost heave susceptibility criteria for coarse-grained soils. *Transportation Research Record* 1089: 124-131.

Contemporary Permafrost Degradation of Northern European Russia

Naum Oberman
Mining Geological Joint-Stock Company MIREKO, Syktyvkar, Russia

Abstract

This paper discusses the results of permafrost temperature monitoring. Temperatures were recorded over recent decades at a depth of zero annual amplitude at eight geocryological field stations located between the Ural Mountains and the lower reaches of the Pechora River. It is shown that almost all permafrost within this region has been warming. Permafrost temperature increases during the last 20 to 30 years ranged from 0.22°C to 1.56°C. Regional patterns of mean annual permafrost temperature dynamics are analyzed. During the period of observations, new closed taliks appeared, and those existing prior to climate warming increased in thickness by 0.6 to 6.2 m depending on a number of factors. Data presented in this paper suggest that permafrost of this region is more vulnerable to recent climate warming than that in Central Yakutia and West Siberia.

Keywords: monitoring; northern European Russia; permafrost; taliks; temperature; warming.

Introduction

Global climate warming leads to increases in permafrost temperature in many northern regions (Gravis et al. 1988, Haeberli et al. 1993, Pavlov 1994, Osterkamp et al. 1994, Romanovsky & Osterkamp 2001). A number of publications were devoted to the impacts of this warming on permafrost in northern European Russia (Oberman 1996, Pavlov 1997, Kakunov 1999, Oberman 2001, Oberman & Mazhitova 2003, Kakunov & Sulimova 2005, Pavlov & Malkova 2005). Most of the cited publications analyze long-term permafrost monitoring records that were obtained from one or two long-term geocryological field stations in operation during the last two to three decades. The stations are located near the city of Vorkuta in the eastern part of the studied region (Fig. 1, Station #2) and close to the Pechora River delta at Cape Bolvansky in its western part (Fig. 1, Station #11). Data obtained from these two areas are rather different. In the Vorkuta area a rapid warming of permafrost was observed while the permafrost temperatures at Cape Bolvansky remained relatively stable. Given this difference, the interpolation of these data onto the entire region is hardly possible. It was necessary to include in the analysis additional data from other sites within the region where permafrost had been monitored over recent decades.

Therefore, in 2006-2007, the MIREKO Stock Company resumed measurements at six geocryological field stations where measurements were conducted in the past. As a result, the number of field stations where 20 to 38 year-long records are available increased to eight (Fig.1). In this paper we discuss the data from these eight stations. Shorter (10 to 12 years) records from other stations that have not been published before are also included in this analysis. Original observational data used in the paper are from (Kakunov et al. unpublished, Glavatskikh et al. unpublished, Karpovich et al. unpublished, Malkova & Vasiliev unpublished, Romenskaya et al. unpublished, Oberman unpublished).

Study Area and Methods

The study region (Fig.1) is characterized by rather diverse environmental conditions. The Pechora lowland (Bolshezemelskaya Tundra), bordered by the Ural and Pai-Khoi Mountains and their foothills to the east, occupies most of the region. The geological section is represented mostly by Quaternary loam, loamy sand, and sand often overlain with peat. Landscapes with various geneses have different ages that vary from Middle Pleistocene to Holocene. They are dominated by one of these types of deposits or by the combination of different types. Climatic conditions vary within the region. Mean annual air temperature averaged over 1950-2005 declines from -2.4°C in the southwest to -7.5°C in the northeast of the region. Annual precipitation increases from 300-400 mm at the seacoast to 400-500 mm in the continental part of Bolshezemelskaya Tundra and to 500-600 mm and more in the Ural foothills. The long-term means of annual maximum snow depths increase in the same direction from 44 cm at the coast to 59 cm in Bolshezemelskaya Tundra and 78 cm in the Ural foothills. Recent trends in the mean annual air temperature are characterized by higher rates of warming in continental areas and lower rates towards the coast. In the continental areas the rates also decline from east to west (Pavlov & Malkova 2005). Our analysis showed that trends in precipitation and snow depths were similar to those in air temperature, yet better expressed. Excessive humidity is typical for the entire region. Climate is responsible for the region belonging mostly to the tundra zone. Permafrost spatial distribution ranges from isolated patches to continuous permafrost. In the 1970s, permafrost temperatures at the depth of zero annual amplitude varied mostly from -1°C to -3°C, reaching in some places -5.5°C, and permafrost thickness varied from 10 to 700 m, rarely more.

Long-term changes in permafrost temperatures were monitored using mercury thermometers with a scale factor from 0.05°C to 0.1°C. The thermometers were put in cases

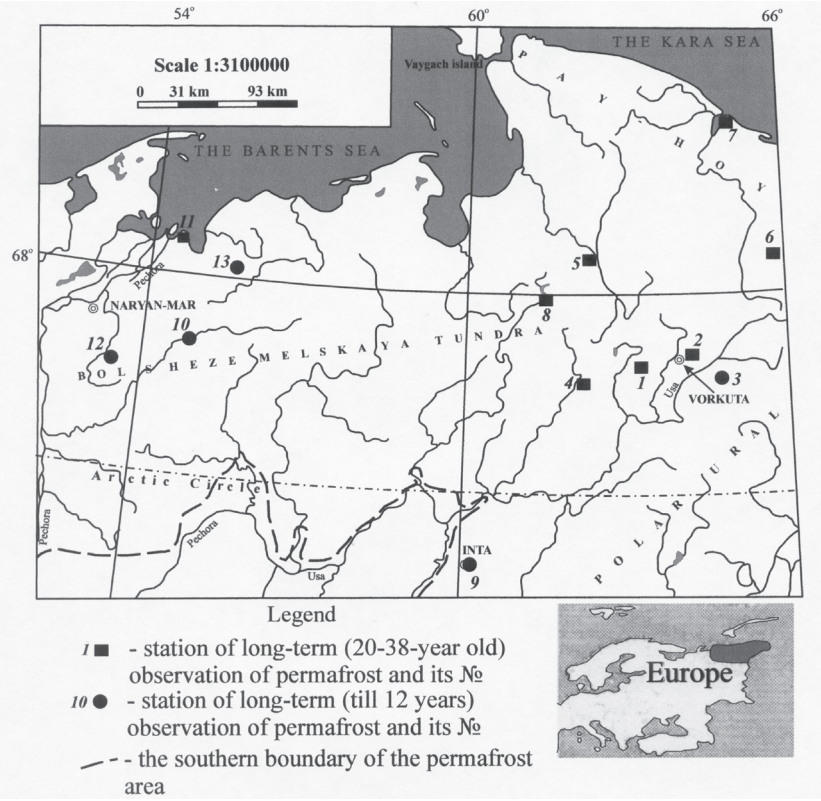

Figure 1. Survey map of the region.

filled with an inert material such as, for example, grease. In 2007, together with a representative from the Geophysical Institute, University of Alaska Fairbanks, temperatures were measured simultaneously with mercury thermometers and dataloggers. Readings differed in average by 0.05°C. Since 2007, boreholes are being equipped with temperature dataloggers. In the past, measurement frequency varied from one to three times monthly to four times annually.

Long-Term Permafrost Dynamics

Multi-year trends in permafrost characteristics were derived from 20-and-more-year-long monitoring records. The record lengths allowed averaging the short-term (decadal) temperature fluctuations (for example, Boreholes ZS-124/124a and ZS-14/227 in Figure 2). These relatively long-term records showed that permafrost temperatures at the depth of zero annual amplitude increased during the period of observations at all eight reference field stations in the region (data from most of them are given in Table 1). At the beginning of monitoring, only one of eight stations (#2) was located in the sporadic permafrost zone, two stations (#1 and #4) were in the discontinuous permafrost zone and the rest of the boreholes were in the continuous permafrost zone (Fig.1).

Permafrost warming over the recent 20 to 50 years has been reported by a number of authors who conducted occasional repeating temperature measurements on certain topographic surfaces in 10 areas within the studied region. The reported rates of warming were similar to those registered at our reference field stations. All available data suggest that permafrost warming from 1950-2000 took place mostly in the second half of this period.

The total increase in the mean annual permafrost temperature varies for different stations from 0.22°C to 1.56°C (Table 1) and depends first of all on the length of observational period. To overcome the effect of different record lengths, the average annual warming rates were calculated. These rates range from 0.01°C to 0.08°C per year. At each field station the maximum rates were usually observed in peatlands and minimum rates were typical for loamy deposits, with sand deposits showing intermediate values.

Generally, the rates of increase in mean annual permafrost temperatures decrease towards the seacoast. In loamy deposits that dominate the region, the rates were 0.031°C to 0.034°C per year at the distance of 165-170 km from the Barents Sea coast. At the same time, these rates were only 0.02°C to 0.028°C per year in the area located 80-85 km from the coast (Fig.1, Table 1: Stations #4 and #1, and Stations #5 and #8, Boreholes KT-5 and 37-6). Similarly, the rates were higher in the continental east of the region and lower in the coastal west, decreasing from 0.031°C-0.034°C per year at Stations #4 and #1 to 0.01°C per year in Borehole 49 (Table 1). The rates of increase in mean annual permafrost temperature (calculated for 1982-1993 at Station #10) decreased from the eastern continental Station #1 to the western continental Station #10, from 0.034°C to 0.013°C per year. Both stations are located at about the same latitude. Owing to the tendencies, the permafrost warming is most

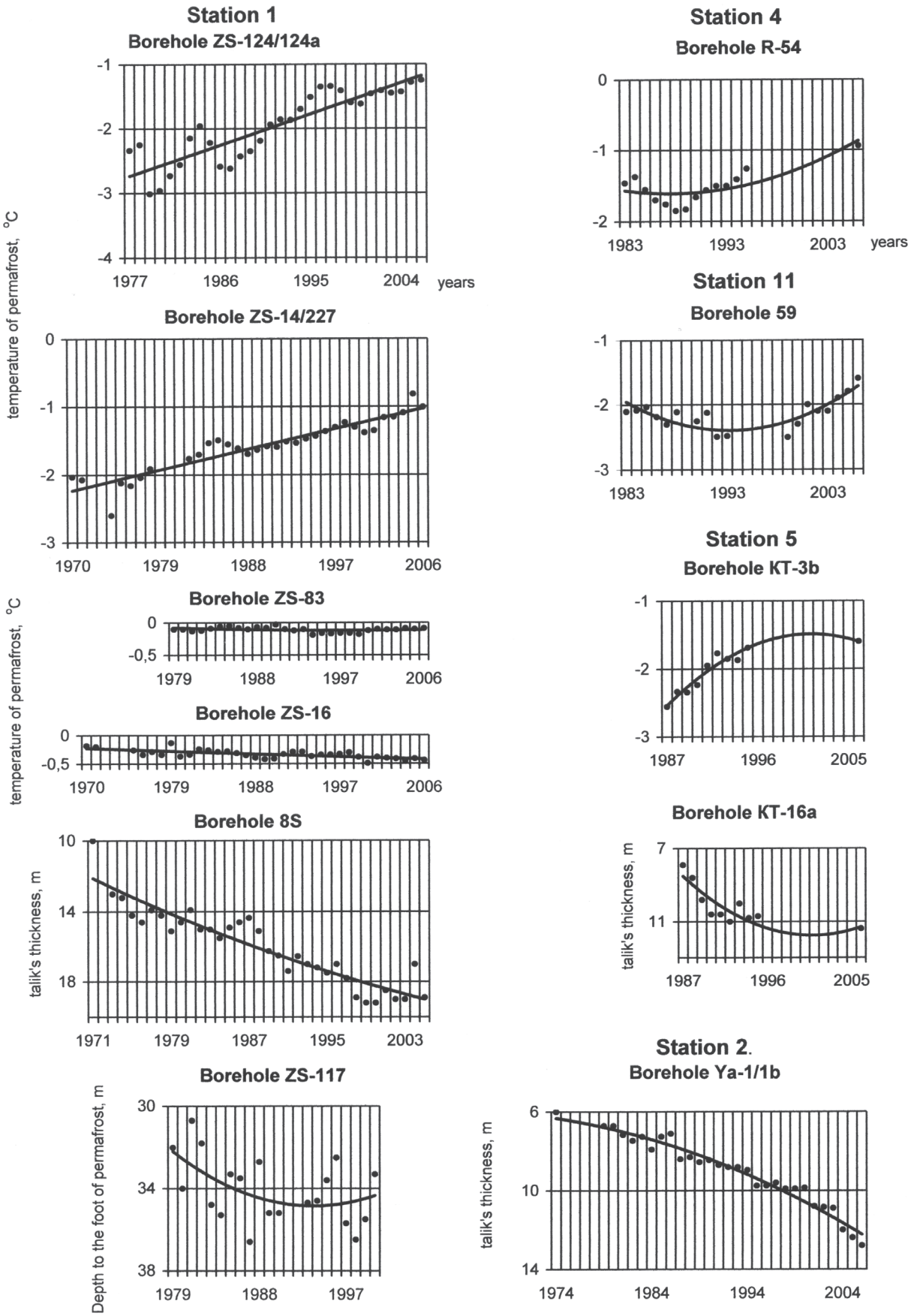

Figure 2. Long-term trends in permafrost characteristics.

pronounced in the eastern continental areas and least in the western coastal regions. The least significant permafrost warming was observed at the westernmost coastal Station #11 (Cape Bolvansky) and was due to the later initiation of climatic warming in this area compared to the rest of the region (Oberman 2007).

The regional pattern of permafrost warming correlates closely with the above discussed pattern of recent trends in major meteorological parameters.

While permafrost warming was a dominant process, permafrost cooling was observed locally, mostly in the areas of complete or partial drainage of thermokarst lakes. Cooling

Table 1. Long-term changes of permafrost in the region.

Landscape*	№ of the station; borehole	Relief; microrelief at the start of observations	Rock's lithology	Period, years	Depth, m	Ground temperature, °C:		
							changes	
						initial	during the period	°C/yr
1	1; ZS-124/124a	slope; polygonal	peat, loam, sandy loam	1977-2006	10	-2.78	+1.56	0.054
	1; ZS-14/227	watershed; spot-medallion	loamy sediments	1970-2006	15	-2.23	+1.20	0.034
1a	11; 59	ridge's crest; spot-medallion	loams	1983-2006	12	-1.95	+0.22	0.01
2	8; 100-6	slope; polygonal	peat, sands, loams	1987-2007	10	-4.30	+1.56	0.078
	8; 35-6	watershed; polygonal	sands, gravel	1987-2007	15	-2.85	+1.09	0.055
	8; 37-6	foot of slope	loams	1988-2007	14	-2.10	+0.52	0.028
3	4; R-54	side of the stream's valley	loam, sand, varved clay	1983-2006	10	-1.56	+0.71	0.031
4	5; KT-5	by watershed; bog	loamy sediments	1986-2006	15	-2.87	+0.41	0.021
	5; KT-3b	I above flood-plain terrace	sands, gravel	1987-2006	15	-2.55	+0.95	0.05
5	2; UP-35	slope's foot; frost small mound	peat, loam	1986-2006	10	-1.72	+0.69	0.035
	7; K-2	marine terrace	sand, loam	1982-2007	10	-3.93	+0.97	0.039
Closed taliks								
		Talik's type				Talik's thickness, m		
							changes	
						initial	during the period	m/yr
1	1; EK-67	snow-made talik	loams, sandy loams, pebble	1980-2006		0	+15.8	0.61
	1; ZS-83	ground water transient talik	loams, sands	1976-2006		0	+8.6	0.29
	1; 8S	snow-made talik	loamy sediments	1971-2005		12.1	+6.7	0.20
3	4; R-53	near-channel talik	sandy loam, varved clay	1983-2006		8.8	+0.6	0.03
4	5; KT-8	near-channel talik	loams, sandy loam	1986-2006		13.2	+2.8	0.14
	5; KT-16a	snow-made talik	loamy sediments	1987-2006		8.6	+2.8	0.15
5	2; UP-34	ground water made talik	loams, limestones	1975-2006		43.5	+24.8	0.80
	6; 23	snow-made talik	sandy loam, gravelly sandy loam	1978-2007		4.9	+6.1	0.21
	6; 32	lake talik	sands, sandy loams	1977-2007		5.0	+6.2	0.21
	7; K-41	snow-made talik	sands, loam	1982-2007		5.3	~ +3.7	0.15

Note: * - plains: 1 and 1a – glacial-marine of Middle Pleistocene age (continental areas and sea coast); 2 – marine, Middle Pleistocene; 3 – lacustrine-alluvial, Late Pleistocene; 4 – lacustrine-alluvial, alluvial-marine, Late Pleistocene; 5 – piedmont areas.

with the rate of 0.006°C per year (during 1970-2006) was observed in the frozen basal peat layer below the floor of one of the lakes that drained before 1969; i.e., before the onset of pronounced warming (Fig. 2, Borehole ZS-16). Cooling rates observed in the thawed peaty sediments of the lakes drained during the climatic warming were much higher. At an initial mean annual ground temperature of 1.5°C, the rates were -0.042°C per year during 1974-2005 and, at an initial temperature of 2.87°C, they were -0.082°C per year during 1980-2006 (Stations #1 and #4, respectively). The duration of periods of thawed lake sediments rapid cooling prior to relative stabilization was equal for both lakes and totaled 14 years. This similarity in temperature regime between these two lakes occurred in spite of different drainage dates and significant differences in the initial enthalpy of bottom deposits. Similar permafrost temperatures in the surrounding terrain of both lakes can possibly explain the phenomenon.

Anomalous permafrost temperatures that persist during the time of recent climatic warming were observed at the sites where permafrost degradation resulted in the development of closed taliks (Fig. 2, Borehole ZS-83, Table 1). Here, the permafrost table lowered to 8.6 m in 30 years. It lowered even deeper, to almost 16 m, in an area where a newly developed closed talik coalesced with a preexisting lateral talik (Table 1, Borehole EK-67). Taliks existing prior to the recent climatic warming also increased in thickness, though to a smaller degree than newly developed taliks. Reduced rates of ground temperature changes in these taliks were probably due to a deeper permafrost table position and, hence, weakened effects of air temperatures on ground temperatures. Total increases in thickness of the closed taliks developed in Quaternary deposits ranged from 0.6 to 6.7 m (Table 1) depending on the geographical location, genetic type of the particular talik, ice content and lithological characteristics of the bearing sediments, hydrological, hydrogeological and other factors. The thickness of newly-developed taliks decreases northward (towards the sea coast), in accordance with the increasing severity of geocryological conditions and in accordance with already mentioned regional distribution of the recent climatic trends (see the Borehole pairs 8S & KT-16a and 23 & K-41, in Table 1). Thawing of the very ice-rich varved clays (Station #4, Borehole R-53) is accompanied by high heat consumption, and therefore total increases in thickness of closed taliks were minimal (only around 0.5 m) in this kind of deposit. On the other hand, a ground-water-formed closed talik in bedrock with practically zero ice content demonstrated a 25-meter increase in thickness in 31 years (Station #2, Borehole UP-34).

As a result of climatic warming, permafrost patches 10 to 15 m thick (Stations #1 and #2) thawed completely. In the patches where Quaternary deposits were perennially frozen to a depth of around 35 m, the base of the permafrost tended to rise (Fig. 2, Borehole ZS-117). Comparison of small-scale maps based on 1950-1960 data with those based on 1970-1995 data shows a shift of the southern limit of permafrost by several tens of kilometers northwards (Oberman 2001). This also indicates that permafrost is degrading in the southernmost part of the region.

At the same time, newly formed permafrost developed within the bottom of completely or partially drained lakes. This new permafrost was confined either by the elevated parts of the lake floor or by the bottom sections adjoining the frozen lakeshores. At one such site, permafrost developed from 1974 to 2001 to a depth of 14.5 m. To assess the extent of new permafrost formation, an analysis of satellite remote sensing data was performed by I.O. Smirnova (Research Institute for Cosmo-Aero-Geological Methods) for the entire region under discussion. According to her results, the area of lakes drained between 1988 and 2000 comprises only a fraction of a percent of the total area. Moreover, only an insignificant part of the drained area has been freezing recently and forming permafrost. Hence, on a regional scale, the significance of the formation of new permafrost is very limited compared to the predominant permafrost degradation.

Finally, the material presented indicates that permafrost dynamics could be very different within different Russian permafrost regions. Recent long-term increases in mean annual air temperature were several-fold smaller in northern European Russia than in Central Yakutia and West Siberia (Pavlov & Malkova 2005). However, an increase in permafrost temperatures at the depth of zero annual amplitude was several-fold larger than those in Central Yakutia and comparable to those in West Siberia. One reason for these differences could be the two-fold increase in atmospheric precipitation in the discussed region. This, in turn, was associated with an increase in the warming effect of ground waters on permafrost (Oberman 2006a, b). The maximum snow depth increase in recent decades was also reported for the western part of the Russian Arctic (Bulygina & Razuvaev 2007). This increase also contributed to the observed warming of permafrost. Taken together with the relatively high temperatures of permafrost in northern European Russia, all the above-discussed evidence indicate that this region is one of the most vulnerable to further warming. A large extent of permafrost degradation can be expected in this region in the foreseeable future.

Conclusions

In all geocryological zones and major landscapes of northern European Russia, the long-term (20 to 38 years) warming trend in permafrost temperatures at the depth of zero annual amplitude were recently observed. Short-term permafrost temperature fluctuations are superimposed on this trend. Total temperature increases vary from 0.22°C to 1.56°C with annual rates ranging between 0.01°C and 0.08°C per year. The observed warming rates decrease from continental areas towards the coast, and from eastern regions toward the west of the study area. These tendencies correlate closely with the recent intra-regional trends in mean annual air temperature, annual precipitation, and snow depth. Permafrost warming led to formation of new closed taliks and to an increase in thicknesses of pre-existing taliks. The

increase in thickness of these taliks range from 0.6 to 6.7 m and depend on the location and genesis of the talik, as well as on ice content in the bearing deposits and other factors. Some thin permafrost patches completely thawed.

Excessive humidity and a recently observed steep increasing trend in snow depths, together with relatively high permafrost temperatures, cause higher vulnerability of permafrost to climate warming in this region as compared to Central Yakutia and, to a lesser degree, to West Siberia.

Acknowledgments

This investigation became possible due to financial support coming from the Russian Federal Agency for Mineral Resources Management (№АМ-18/35 pr, 30.01.2006) and, since 2007, from the Geophysical Institute, University of Alaska Fairbanks, USA (the Polar Earth Science Program, Office of Polar Programs, National Science Foundation; ARC-0632400, ARC-0520578).

I wish to thank Prof. Vladimir Romanovsky and Dr. Galina Mazhitova for translating the paper into English and Roman Makov for computer design and formatting of this manuscript.

References

Bulygina, O.N. & Razuvaev, V.N. 2007. Recent snow cover variability in Northern Eurasia. *Proceedings of the International Conference "Cryogenic resources of polar regions", Salekhard, Russia, June 17-21, 2007* 1: 201-204.

Gravis, G.F., Moskalenko, N.G. & Pavlov, A.V. 1988. Perennial changes in natural complexes of the cryolithozone. *Proceedings of the Fifth International Conference on Permafrost, Trondheim, Norway, August 2-5, 1988* 1: 165-169.

Haeberli, W., Cheng, G., Gorbunov, A.P. & Harris, S.A. 1993. Mountain permafrost and climate change. *Permafrost and Periglacial Processes* 4: 165-174.

Kakunov, N.B. 1999. Monitoring of the active/seasonally frozen layer and upper layers of cryolithozone during the ongoing half-century climatic cycle in the European northeast of Russia. *Abstracts of the International Conference "Monitoring of Cryosphere", Pushchino, Russia, April 20-23, 1999*: 120-121.

Kakunov, N.B. & Sulimova, E.I. 2005. The results of observing grounds temperatures in the European Northeast of Russia during the 1970-2003 warming-up period. *Proceedings of the 3rd Conference of Geocryologists of Russia, Moscow, Russia, June 1-3, 2005* 2: 84-90.

Oberman, N.G. 1996. Geocryological specificity and current trends in natural and anthropogenic dynamics of the cryolithozone of the East-European Subarctic. *Proceedings of the 1st Conference of Geocryologists of Russia, Moscow, Russia, June 3-5, 1996* 2: 408-417.

Oberman, N.G. 2001. Intra-century dynamics of the permafrost zone in the European Northeast of Russia. *Proceedings of the 2nd Conference of Geocryologists of Russia, Moscow, Russia, June 6-8, 2001* 2: 212-217.

Oberman, N.G. & Mazhitova, G.G. 2003. Permafrost mapping of Northeast European Russia based on the period of climatic warming 1970-1995. *Norwegian Journal of Geography* 57, No. 2: 111-120.

Oberman, N.G. 2006a. Long-term tendencies of natural cryolithozone evolution the European Northeast. *Proceedings of International Conference "Earth cryosphere assessment: theory, applications and prognosis of alterations", Tyumen, Russia, May 29-31, 2006* 1: 93-96.

Oberman, N.G. 2006b. Permafrost monitoring. In: I.S. Zektser (ed.), *Geology and Ecosystems*. Boston/ Dordrecht/London: Springer. Kluwer Academic Publishers, 341-354.

Oberman, N.G. 2007. Some peculiarities of current degradation of permafrost in the Pechora-Ural region. *Proceedings of the International Conference "Cryogenic resources of polar regions", Salekhard, Russia, June 17-21, 2007* 1: 96-99.

Osterkamp, T.E., Zhang, T. & Romanovsky, V.E. 1994. Evidence for a cyclic variation of permafrost temperatures in Northern Alaska. *Permafrost and Periglacial Processes* 5: 137-144.

Pavlov, A.V. 1994. Current changes of climate and permafrost in the Arctic and Sub-Arctic of Russia. *Permafrost and Periglacial Processes* 5: 101-110.

Pavlov, A.V. 1997. Geocryological-climatic monitoring in Russia: methodology, results and forecast. *Cryosfera Zemli (Earth Cryosphere)* 1: 47-58.

Pavlov, A.V. & Malkova, G.V. 2005. *Contemporary changes of climate in northern Russia: Album of small-scale maps*. Novosibirsk: Academic Publishing House "Geo", 54 pp.

Romanovsky, V.E. & Osterkamp, T.E. 2001. Permafrost monitoring system in Alaska (structure and results). *Cryosfera Zemli (Earth Cryosphere)* 4: 59-68.

MAGST in Mountain Permafrost, Dovrefjell, Southern Norway, 2001–2006

Rune Strand Ødegård
Gjøvik University College, P.O.Box 191, NO-2802 Gjøvik, Norway
Ketil Isaksen
Norwegian Meteorological Institute, P.O.Box 43 Blindern, NO-0313 Oslo, Norway
Trond Eiken, Johan Ludvig Sollid
Department of Geosciences, University of Oslo, P.O.Box 1047 Blindern, NO-0316 Oslo, Norway

Abstract

A monitoring program to measure ground and air temperatures was started in autumn 2001 in Dovrefjell (62°15′N, 9°20′E), a mountainous area in southern Norway. Ground temperatures are measured in a transect from deep seasonal frost at 1039 m a.s.l. to discontinuous mountain permafrost at 1505 m a.s.l. in 11 boreholes 9 m deep. This is the first transect of this type set up in Scandinavia. Preliminary results are presented including measurements at 0.2 m and 8.5 m depth. The collected ground surface temperatures (GST) show pronounced fluctuations and large interannual variability. A simple normalization procedure is suggested to relate the observed GST to the reference period 1961-1990. The results suggest that even with an averaging period of 5 years the MAGST could deviate more that 1°C from the 30-year average. The period 2001–2006 is generally found to be warmer than the reference period, suggesting thawing permafrost at sites with discontinuous or thin snow cover.

Keywords: MAGST; monitoring; mountain permafrost; Norway.

Introduction

Permafrost is known to be widespread in the world mountain ranges, but scientific investigations only started during the past few decades (Haeberli 1973, Haeberli & Patzelt 1982, Ødegård et al. 1992, Haeberli et al. 1993). The focus of these investigations has been on degrading permafrost and reduction in the stability of mountain slopes (e.g. Harris et al. 2001). Slow thaw of deeper subsurface materials may provoke larger-scale instability on steeper slopes in areas previously considered stable (Dramis et al. 1995). Other studies are related to buildings and other installations directly affected by ground thawing (Haeberli 1992, Haeberli et al. 1993). Permafrost is sensitive to changes in surface energy exchange; it is therefore important to investigate the marginal permafrost areas. Equally important is an understanding of the dominant processes for permafrost development and degradation in mountain areas.

The use of miniature temperature data loggers (MTDs, Fig. 1) for mountain permafrost studies has greatly increased during the last decade. Large amounts of ground surface temperature data now exist from many mountain areas. Continuous temperature recordings make it possible to determine, for example, the mean monthly and annual ground surface temperature (MMGST and MAGST) at selected sites.

This paper presents preliminary results from a monitoring program to measure ground and air temperatures in Dovrefjell (62°15′N, 9°20′E), a mountainous area in southern Norway (Fig. 2). Ground temperatures are measured in a transect from deep seasonal frost at 1039 m a.s.l. to discontinuous mountain permafrost at 1505 m a.s.l. in 11 boreholes 9 m deep in the period 2001–2006. This is the first transect of this type set up in Scandinavia. The analysis includes measurements at 0.2 m and 8.5 m depth. The collected ground surface temperatures (GST) show pronounced fluctuations and large interannual variability. A simple normalization procedure is suggested to relate the observed GST to the reference period 1961–1990.

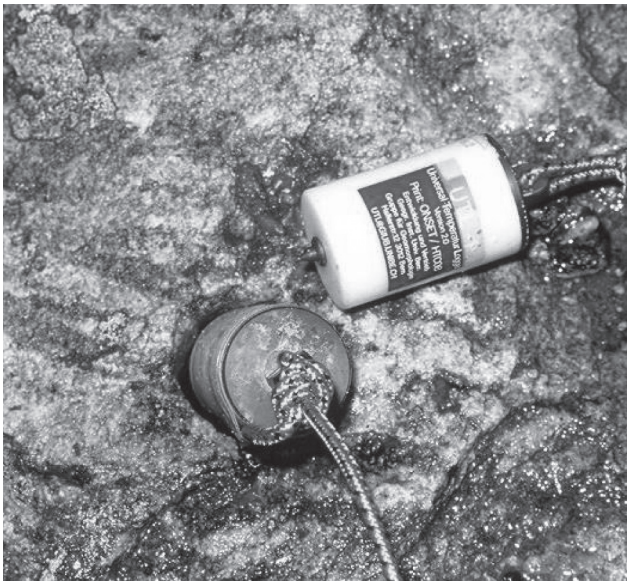

Figure 1. Miniature temperature datalogger (MTD) used in this study. This tool is especially designed for rough field conditions. The thermistor in the MTDs is a TMC-1T with a temperature range of −30°C to +40°C and with accuracy given by the manufacturer to be ±0.13°C. The loggers are available from GEOTEST in Switzerland.

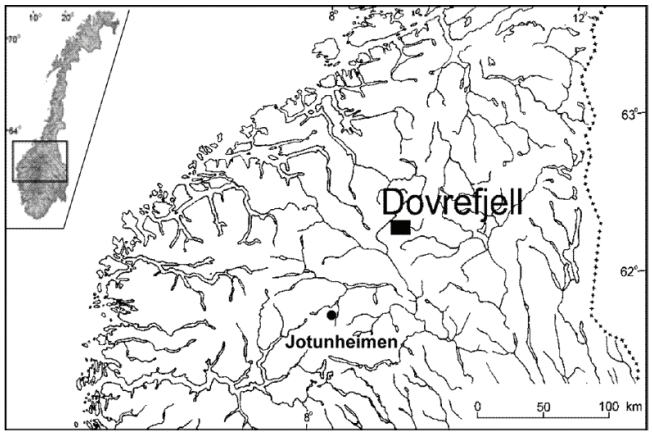

Figure 2. The research area in central southern Norway.

Table 1. Mean ground temperatures 2001–2006, column 2 shows normalized temperatures described in the next section.

BH-nr	Mean 2001-2006 0.2m depth	Normalised 0.2m depth	Mean 2001-2006 8.5m depth
DB1	-1.1	-1.9	-0.2
DB2	-1.0	-2.1	-0.3
DB3	0.7		0.2
DB5	-0.8	-1.7	0.6
DB6	-0.7	-1.7	-0.3
DB7	0.5		1.4
DB8	0.8		2.0
DB10	1.5	0.9	2.6
DB11	1.4	0.8	2.1

Research Area and Previous Studies

The setting and overall scope of the monitoring program in Dovrefjell were presented by Sollid et al. (2003). Key information from the boreholes like position, altitude, surface material, and snow depth are described in this paper.

Ground temperatures are correlated with elevation. The lower limit of the mountain permafrost in Dovrefjell is about 1500 m a.s.l., mapped using the BTS (Bottom Temperature of Snow) method (Ødegård et al. 1996, Isaksen et al. 2002). This limit is representative for areas with a stable snow cover of 1–2 m. Sporadic permafrost is present at elevations down to 1000 m a.s.l. in some palsa bogs (Sollid & Sørbel 1998)

Regression based on 18 climate stations in the vicinity (Aune 1993) indicates that the 0°C isotherm is located at 910 m a.s.l. The mean temperature lapse rate is 0.44°C/100 m (Tveito et al. 2000). The average yearly precipitation is 600 mm (Østrem et al. 1988). Unstable and stormy weather are common in winter, and the dominant wind direction is from the southwest.

Field Data

This study is based on analysis of a subset of the observations including monthly averages from 9 boreholes at 0.2 m depth and 8.5 m depth (Table 1, Figs. 3, 4). DB1, 2, and 6 are located at exposed sites, at main ridge-crest or plateau

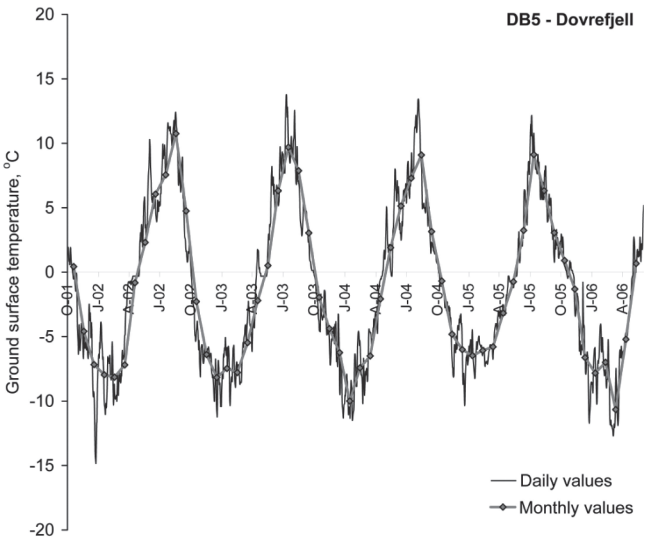

Figure 3. Daily and monthly time series of ground surface temperature at monitoring site DB5 in Dovrefjell, 2001–2006. The temperature series shows large interannual variability.

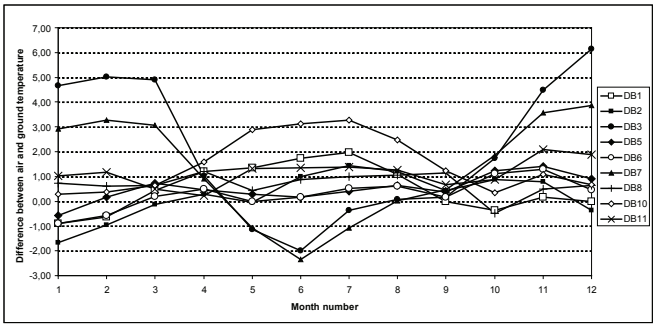

Figure 4. Difference between air temperatures and observed MAGST at the monitoring sites (0.2 m depth–averages 2001–2006).

locations, where winter snow accumulation is minimal. Sites DB5, DB10, and DB11 have discontinuous snow cover in the vicinity of the boreholes. DB 3, 7 and 8 have a maximum snow cover between 0.3 m and 1.0 m as measured in late winter. DB1, DB2, and DB6 are in permafrost; the other boreholes have deep seasonal frost.

Normalization Procedure

In the normalization procedure the monthly scale was selected. The monthly scale improves the correlation between air and ground temperatures (Fig. 5), and captures the overall seasonal variations (Fig. 4). The World Meteorological Organization (WMO) established a standard for a "normal" period to ensure that calculations of climate averages (the "normals") are calculated on a consistent period. A 30-year period is considered long enough to calculate a representative average, and to reduce the impact that one-off, extreme events have on the average. Thus, in this study the official standard normal period 1961–1990 is used.

The normalization procedure starts with the calculation of the MMGST from MTDs by averaging the observations. The second and more complicated step is to obtain mean

Table 2. Difference between observed and normalized air temperatures at Fokstugu (1961–1990).

	JAN	FEB	MAR	APR	MAY	JUN	JUL	AUG	SEP	OCT	NOV	DEC	JUN-AUG	OCT-APR	YEAR
2002	3.2	2.1	1.4	3.9	2.2	1.2	1.1	4.7	1.9	-3.8	-3.4	-3.1	2.3	0.0	1.0
2003	2.1	2.2	3.1	2.2	-1.0	1.1	3.3	0.6	0.8	-2.5	2.0	1.8	1.7	1.6	1.3
2004	-1.6	2.5	1.7	3.5	0.5	-1.1	-0.2	2.0	1.1	-0.5	0.5	3.0	0.2	1.3	1.0
2005	4.3	0.8	0.0	2.2	-2.0	-2.4	2.4	-0.2	1.5	2.0	3.4	0.8	-0.1	1.9	1.1
2006	2.4	1.1	-4.0	-0.3	-0.6										
Average	2.1	1.7	0.4	2.3	-0.2	-0.3	1.7	1.8	1.3	-1.2	0.6	0.6	1.0	1.2	1.1

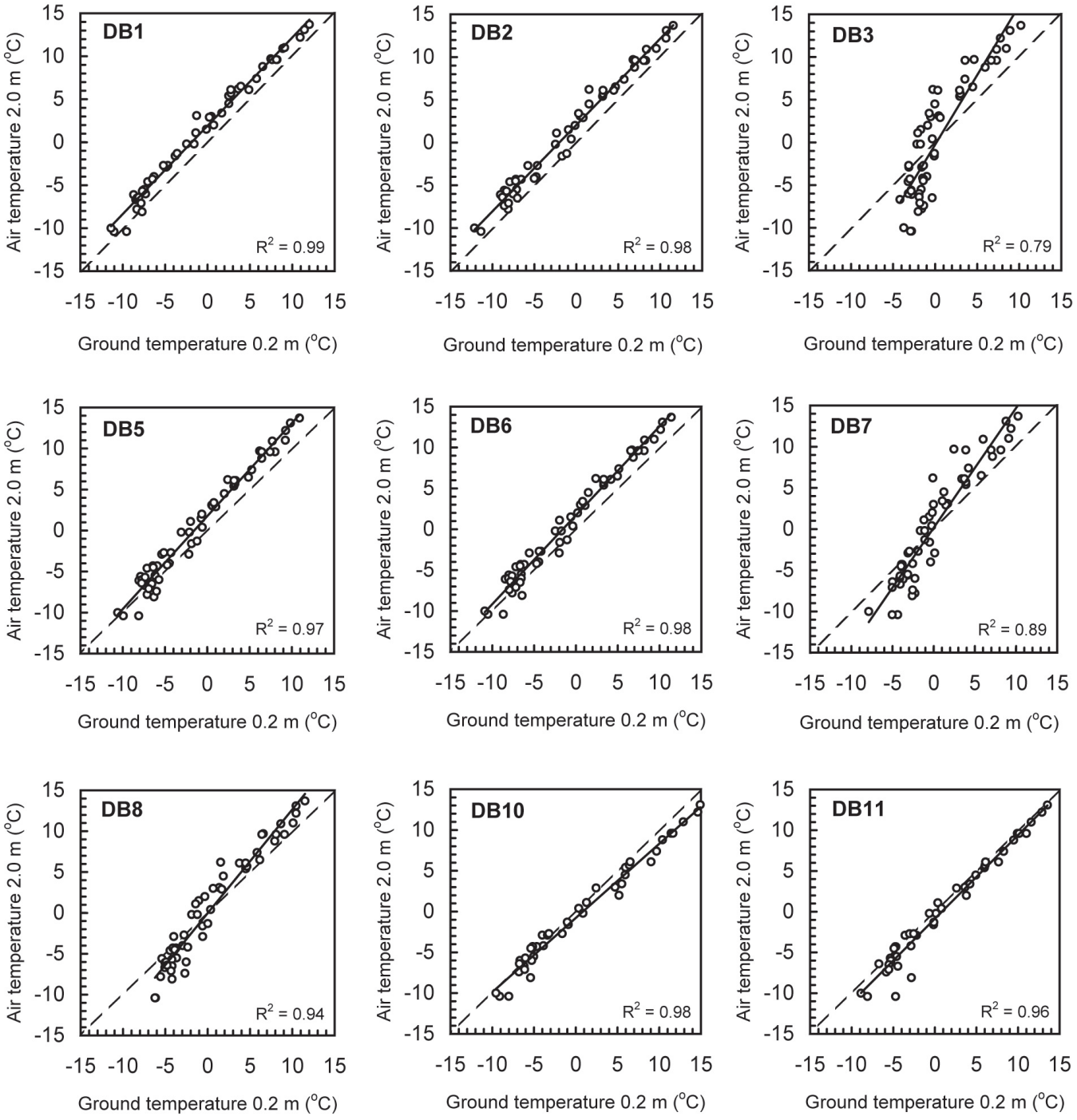

Figure 5. Recorded monthly ground surface temperature for monitoring sites in Dovrefjell vs. monthly air temperature for the weather station at Fokstugu. The snow thickness at several of the monitoring sites is low and for DB1, DB2, and DB6 most of the time snow is completely absent, due to redistribution by wind. Monitoring sites DB3, DB7, and DB8 are highly influenced by snow.

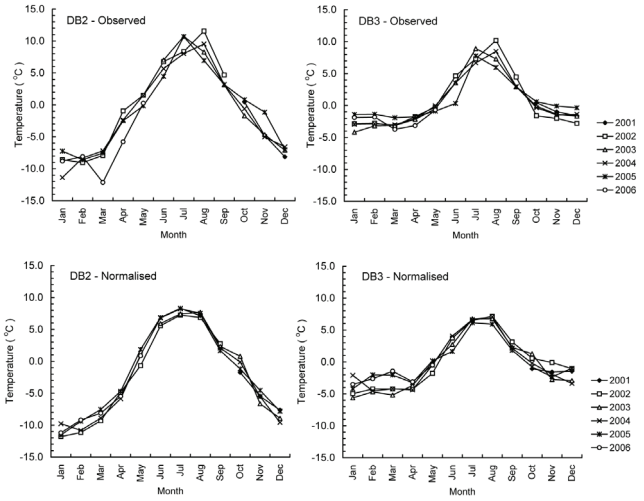

Figure 6. The upper graphs show observed ground surface temperature at selected monitoring sites DB-2 (left) and DB-3 (right). The lower graphs show normalized values for the ground surface temperatures at the same two sites.

monthly air temperature maps and monthly anomaly maps of the air temperature with reference to a standard normal period, in this study 1961–1990.

In Norway 1 km gridded temperature maps and anomaly maps are available from the Norwegian Meteorological Institute (Tveito et al. 2000). The spatial analyses were based on 1247 stations in Fennoscandia using residual kriging. The trend components were defined by a stepwise linear regression.

One alternative method is to obtain air temperature data from a nearby meteorological station having a long time series (e.g. 30-year period or more). A monthly mean temperature anomaly field in a radius of, for example, 30–50 km tends to be quite homogenous, typically within in the range of ±0.3°C.

A high correlation between air and ground temperatures suggests low influence of snow and latent heat effects, which suggests a strong coupling between the air temperatures and the ground surface temperatures. At these sites the monthly air temperature anomalies are simply applied to the MMGST to obtain a normalized estimate.

Results

The normalization procedure outlined above was applied to 6 boreholes (DB1, DB2, DB5, DB6, DB10, and DB11) to obtain the first estimate of MAGST based only on a few years of measurements. The normalization procedure reduces the monthly and interannual variability in the dataset (Fig. 6), especially during summer. At exposed sites with a thin snow cover, the variability in the normalization results during autumn and winter is mainly due to problems with the extrapolation of data obtained from the meteorological stations. For some time periods during autumn and winter, the air temperature in valleys is often lower than in the surrounding mountains because of temperature inversions. This is the case at the Fokstugu meteorological station approximately 15 km from the research area.

For the monitoring period autumn 2001 to spring 2006 the MAGST at exposed sites are on the range 0.6ºC to 1.1°C higher than the 1961–1990 average (Table 1, column 1 and 2).

For determination of MAGST for sites having a thick snow cover the suggested method is not applicable during winter due to the insulating effect of the snow (DB3, DB7, and DB8).

Except DB3 the average ground temperatures observed at 8.5 m depth are higher than MAGST at 0.2 m depth. The averages during the monitoring period range from 0.4°C to 1.2°C higher than MAGST. At DB3 the average at 8.5 m depth is 0.5°C colder than MAGST. This is a good illustration of the complexity of the ground thermal regime in mountain permafrost/deep seasonal frost. The distance between DB2 and DB3 is only 55 m.

Discussion and Conclusions

Observations in 9 shallow boreholes, in warm permafrost (3 boreholes) and deep seasonal frost (6 boreholes), in the period from autumn 2001 to spring 2006 show the limitations of surface measurements in the validation of mountain permafrost models. The results suggest that even with an averaging period of 5 years the MAGST could deviate more that 1°C from the 30-year average (1961–1990). This study shows that a simple normalization procedure based on air temperature anomaly maps could be applied at some sites with a good coupling between air and ground temperatures. A more general normalization procedure would require more sophisticated methods.

The period 2001–2006 is generally found to be warmer than the reference period, suggesting thawing permafrost at sites with discontinuous or thin snow cover.

The ground temperature averages at 8.5 m depth are generally found to be higher than the averages at 0.2 m depth. This is surprising because the conductivity ratio between unfrozen and frozen surface material (Kt/Kf) will cause an offset between the MAGST and the ground temperature at the top of the permafrost. The thermal offset is caused by different thermal properties in the thawed and frozen states (Romanovsky & Osterkamp 1995). These conductivity controlled models show good performance in arctic low-land applications when compared with borehole data (Smith & Riseborough 2002, Wright et al. 2003).

In mountain terrain the surface is often covered with blocks, introducing a top surface layer where non-conductive heat transfer mechanisms are important. Another complication is the redistribution of snow due to wind drift, resulting in a highly variable snow cover, even on scales of just a few meters. This is

definitely the case at the observed boreholes and needs to be considered in order to obtain modeling results that can be compared with borehole data. There is also a possibility for lateral heat transfer in a complex soil-water system, but conclusive statements cannot be made based on this study.

The plan is to continue the monitoring for several decades, for the study of permafrost temperatures under future climate development and probable accelerated warming in the mountains of southern Norway.

Acknowledgments

The monitoring program was initiated by J.L. Sollid, University of Oslo, in co-operation with K. Isaksen, Norwegian Meteorological Institute, R.S. Ødegård, Gjøvik College and T. Eiken, University of Oslo. Forsvarsbygg at Hjerkinn by O.E. Martinsen partly financed the drilling operation and assisted in organizing the field work. The authors give their thanks to Mr. Martinsen and to the institutions involved.

References

Aune, B. 1993. Temperaturnormaler, normalperiode 1961–1990. DNMI. Report 2/93 *Klima.* 63 pp.

Dramis, F., Govi, M., Guglielmin, M. & Mortara, G. 1995. Mountain permafrost and slope instability in the Italian Alps: the Val Pola Landslide. *Permafrost and Periglacial Processes* 6: 73–81.

Haeberli, W. 1973. Die Basis Temperatur der winterlichen Schneedecke als möglicher Indikator für die Verbreitung von Permafrost. *Zeitschrift für Gletscherkunde und Glazialgeologie* 9: 221–227.

Haeberli, W. 1992. Construction, environmental problems and natural hazards in periglacial mountain belts. *Permafrost and Periglacial Processes* 3: 111–124.

Haeberli, W. & Patzelt, G. 1982. Permafrostkartierung im Gebiet der Hochebenkar – Blockgletscher , Obergurgl, Ötztaler Alpen. *Zeitschrift für Gletscherkunde und Glazialgeologie* 18: 127–150.

Haeberli, W., Guodong, C., Gorbunov, A.P. & Harris, S.A. 1993. Mountain permafrost and climate change. *Permafrost and Periglacial Processes* 4: 165–174.

Harris, C., Davies, M.C.R. & Etzelmüller, B. 2001. The assessment of potential geotechnical hazards associated with mountain permafrost in a warming global climate. *Permafrost and Periglacial Processes* 12: 145–156.

Isaksen, K., Hauck, C., Gudevang, E., Ødegård, R.S. & Sollid, J.L. 2002. Mountain permafrost distribution in Dovrefjell and Jotunheimen, southern Norway, based on BTS and DC resistivity tomography data. *Norwegian Journal of Geography* 56: 122-136.

Ødegård, R.S., Sollid, J.L. & Liestøl, O. 1992. Ground temperature measurements in mountain permafrost, Jotunheimen, southern Norway. *Permafrost and Periglacial Processes* 3: 231–234.

Ødegård, R.S., Hoelzle, M., Johansen, K.V. & Sollid, J.L. 1996. Permafrost mapping and prospecting in southern Norway. *Norsk Geografisk Tidsskrift* 50: 41–53.

Østrem, G., Dale Selvig, K. & Tandberg, K. 1988. Atlas over breer in Sør-Norge. *Meddelser nr. 61 fra Hydrologisk avdeling* . Norwegian Water Resources and Energy Directorate (NVE). Oslo. 45 pp.

Romanovsky, V.E. & Osterkamp, T. E. 1995. Interannual variations of the thermal regime of the active layer and near-surface permafrost in Northern Alaska. *Permafrost and Periglacial Processes* Vol. 6.: 313-335.

Smith, M.W. & Riseborough, D.W. 2002. Climate and the Limits of Permafrost: A Zonal Analysis. *Permafrost and Periglacial Process* 13: 1-15.

Sollid, J.L. & Sørbel, L. 1998. Palsa bogs as a climate indicator – examples from Dovrefjell, southern Norway. *Ambio* 27: 287-291.

Sollid, J.L., Isaksen, K., Eiken, T. & Ødegård, R. 2003. The transition zone of mountain permafrost on Dovrefjell, southern Norway. M. Phillips, S.M. Springman & L.U. Arenson (eds.), *Proceedings Eighth International Conference on Permafrost*: 1085-1089.

Tveito, O.E., Førland, E., Heino, R., Hanssen-Bauer, I., Alexandersson, H., Dahlström, B., Drebs, A., Kern-Hanssen, C., Jónsson, T., Vaarby Laursen, E. & Westman, Y. 2000. *Nordic Temperature Maps*. DNMI-report 09/00. 54 pp.

Wright, J.F., Duchesne, C. & Côté, M.M. 2003. Regional-scale Permafrost Mapping using the TTOP Ground Temperature Model. *Proceedings Eighth International Conference on Permafrost*: 1241-1246.

Effects of Changing Climate and Sea Ice Extent on Pechora and Kara Seas Coastal Dynamics

S.A. Ogorodov
Lomonosov Moscow State University, Faculty of Geography, Moscow, Russia

Abstract

About half of the Eurasian Arctic coastline consists of ice-rich deposits. The dynamic response of this coastal type is forced mainly by thermal and wave-energy mechanisms. The role of the thermal factor increases with ground ice content. Low ice content makes the wave-energy factor more significant. We present a comparison of the changing influence that wave energy and temperature regimes can exert on coastal dynamics for two types of Pechora and Kara seas coasts. The first type is represented by barriers and spits, which are expressed by sandy deposits with low ice content. For such coasts, a clear dependence between the seasonal wave energy magnitude directed landward and the coastal retreat rate was found. The second type represents the typical thermo-erosion bluff coast composed of sandy and clayey deposits with medium ice content. The dynamic regime of this type of coast is determined by both thermal and wave-energy factors.

Keywords: climate change; coastal dynamics; sea ice; wave energy.

Introduction

The evolution of Arctic coasts over the coming decades will be governed by changes in the natural environment caused by the effects of climate warming. Rising temperatures are altering the Arctic coastline by reducing sea ice and thawing permafrost, and larger changes are projected to occur as this trend continues. In September, 2007, the area of sea ice in the northern hemisphere achieved its historical minimum for the period of satellite observation (since 1978; http://arctic.atmos.uiuc.edu/cryosphere). Less extensive sea ice creates more open water, allowing stronger wave generation by winds, thus increasing wave-induced erosion along Arctic coasts. Therefore, the acceleration of erosion and thermo-abrasion of the coast is attributable to both an increase of air and water temperatures and a possible intensification of wind-generated wave activity. This is an important topic to pursue given the direct impacts to human communities and infrastructure already being felt along Arctic coasts.

In spite of a short active period, dynamic processes in the coastal zone of the Arctic seas are characterized by a very high intensity. The intensity is due to low coastal stability, which is composed of frozen dispersive sediments and is evolving under the influence of thermal-erosion process. About half of the Eurasian Arctic coastline is exposed to coastal erosion processes and undergoes coastal destruction at rates of 1–5 m per year. In general, which processes

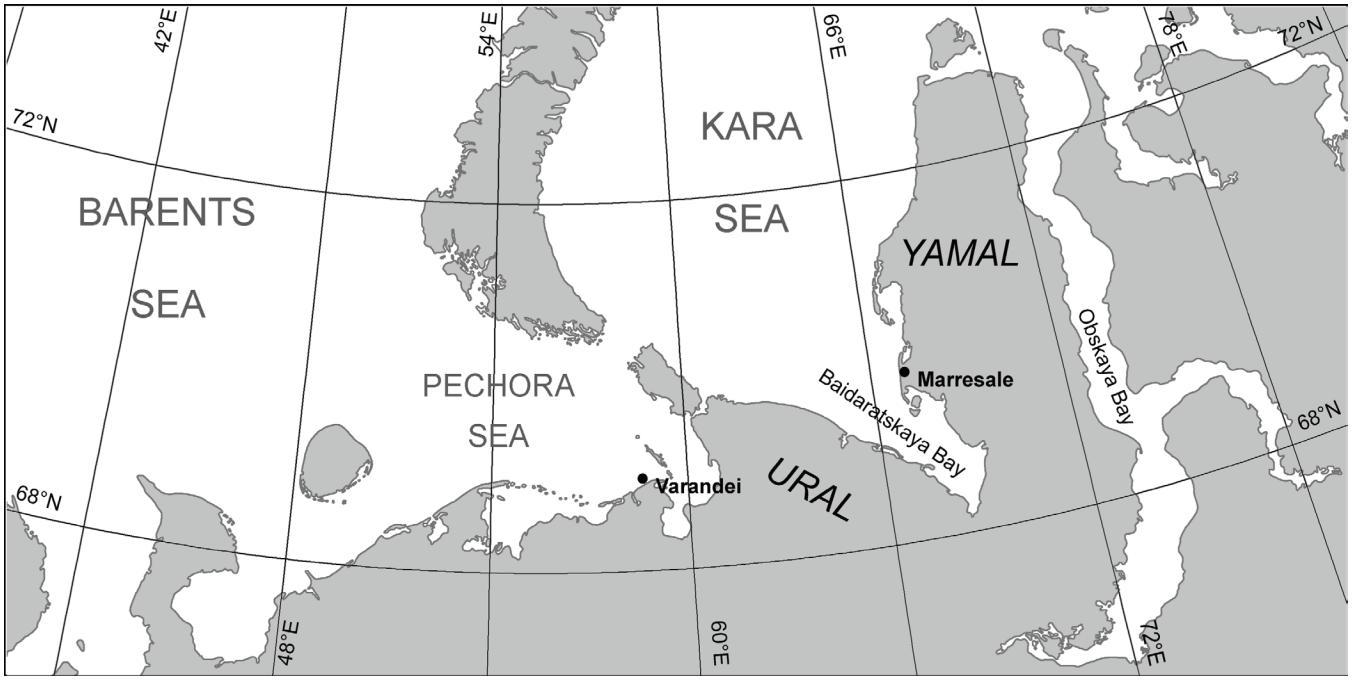

Figure 1. The research area.

affect thermal-erosion coasts, and with what intensity, is determined by a combination of and interaction between thermal and wave-energy factors.

The thermal influence shows itself as energy transmission to the coast, which is composed of frozen sediments, via radiative and sensible heat fluxes from air and water. Accordingly, higher air and water temperatures, together with a longer ice-free period and longer period with positive air temperature, affect the stability of frozen coasts. The role of the thermal factor usually increases with increasing ice content in coastal deposits. In turn, low ice content renders the wave-energy factor more significant.

The wave-energy factor acts via the direct mechanical impact of sea waves on the shore. Correspondingly, the effectiveness of this factor is determined by storm-driven sea surge intensity, as well as by the length of the stormiest period. Conversely, surge intensity substantially depends on the fetch, which is intrinsically linked to sea ice extent since less extensive sea ice creates more open water, allowing stronger wave generation by wind.

We present a comparison of the changing influence of wave energy and temperature regimes on coastal dynamics for two types of coast. These results are drawn from work conducted along the Barents (Pechora) and Kara Sea coasts (Fig. 1), but have much broader implications to coastal regions throughout the Eurasian Arctic.

Methods

Microsoft Excel was used for statistics and correlation analysis. Wave energy flux was calculated using the Popov-Sovershaev (1981, 1982) wind-energy method (Ogorodov 2002). The method is based on the theory of wave processes and takes established correlations between wind speed and parameters of wind-induced waves into account.

For deep-water conditions, when the sea floor does not influence the wave formation, the wave energy flux per second (for 1 m of wave front) at the outer coastal zone boundary is calculated by the equation similar to the one used in Longinov's method (1966):

$$E_{0dw} = 3\times10^{-6} V_{10}^{3} x \quad (1)$$

where V_{10} is the real wind speed measured by anemometer at 10 m above sea level [*m/s*], x is the real or extreme distance of wave racing [*km*];, and the dimension of the coefficient 3×10^{-6} corresponds to the dimensions of ρ/g, where ρ is density [g/*m*^{3}], g is gravitational acceleration [*m/s*^{2}], i.e., $\frac{t/m^3}{m/s^2}$. Thus, E_{0dw} has dimensions, $\frac{tm}{ms}$ or *t/s*, as is the convention in coastal dynamics.

The same equation for the shallow sea zone appears in the following form:

$$E_{0sw} = 2\times10^{-6}\left(\frac{gH}{V_{10}^{2}}\right)^{1.4} V_{10}^{5} \quad (2)$$

where E_{0sw} has the same dimensions as in equation (1). Equation (2) is valid under two conditions: for shallow sea basins, i.e., for most of the arctic seas, wave energy is determined in accordance with kinematic index of shallowness, $\frac{gH}{V_{10}^{2}}$, between water depth H along the wind direction and wind speed V_{10}. At $\frac{gH}{V_{10}^{2}} \le 3$ water depth hampers formation of wind-induced waves.

Another condition is determined by the following: a wave starts to interact with the sea floor when it becomes high enough after it has covered a certain ideal distance without touching the sea floor, when it has developed in the deep-sea basin where equation (1) is valid. Hence, at the boundary between deep-sea and shallow zones both equations should be valid. From this it follows that the ratio between the minimum wave fetch at which the interaction between waves and sea floor begins and the water depth at the distance of that wave fetch is:

$$\frac{x_{\min}}{H} \ge 6.5\left(\frac{gH}{V_{10}^{2}}\right)^{0.4} \quad (3)$$

where $x_{\min}$ is expressed in kilometers, and H is in meters.

At $\frac{gH}{V_{10}^{2}} = 3$ equation (3) becomes

$$\frac{gx_{\min}}{V_{10}^{2}} \ge 30 \quad (4)$$

From (4) we can get the value of the extreme wave fetch for deep-sea conditions equal to the value obtained by other means:

$$x_{\lim} = 3V_{10}^{2} \quad (5)$$

This value could be neglected if other factors limiting wave fetch are absent, for example by sea ice or islands.

To calculate the sum of wave energy of a certain direction from the energy flux per second, E_0 calculated for all wind speeds by wind direction is multiplied by the overall wind duration, for wind of a certain speed range on a monthly or monthly ice-free period, expressed in seconds. The values obtained are summarized for each rhumb line. The rhumb fluxes of wave energy, E_r, are represented by the wave energy sum for all wind speed gradations within a certain rhumb during the dynamically active period.

For delimitation of an ice extent boundary and determination of duration ice-free period http://arctic.atmos.uiuc.edu/cryosphere data are used.

Figure 2. Pesyakov Island, the first type coast.

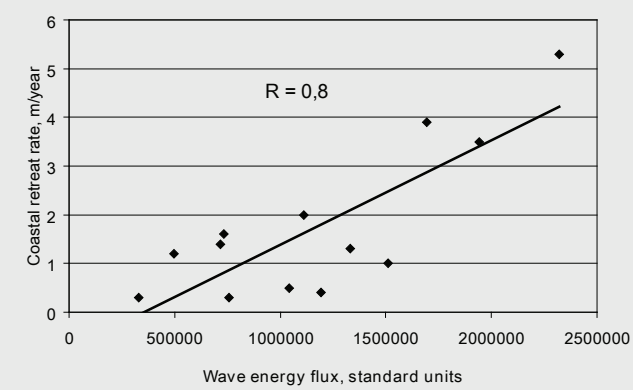

Figure 3. Correlation between wave energy and coastal retreat rate.

Results and Discussion

The Varandei Coast, Barents Sea example

It is a wide-spread opinion that sea coasts consisting of frozen deposits must develop as thermoerosion (thermoabrasion) type coasts. At the same time, coastal bluffs formed of frozen deposits with low ice content (*the first type*) are not subject to thaw slumping, permafrost creep (solifluction), gully thermoerosion, and thermokarst (Fig. 2). Periodicity of extreme storm surges and the total wave energy activity in the coastal zone during the active dynamic period are the main factors which determine the dynamics of coasts with low ice content. Based on the Actualism method, we can suppose that, in the case of climate warming, low ice content coastal dynamics will have similar features to those which they have in the warmest years and decades at the present. Thus, to forecast the dynamics of similar coasts under conditions of climate change, it is only necessary to predict changes in the regional wind-wave regime. As basic coastal retreat values, one may use the values obtained by direct stationary observations during the period with certain wind-wave parameters.

To substantiate this hypothesis, we performed correlation analysis of the results of stationary observations on coastal dynamics and hydrometeorological data. For Varandei area (Pechora Sea), wave energy fluxes at the external border of the coastal zone were calculated using wind direction and speed for each year between 1981 and 2002. The total value of the wave energy flux from the all wave-dangerous rhumbs for dynamically active period (from July to October) was obtained. Then we calculated correlation indices between the value of the wave energy flux and temperature characteristics, and the value of coastline retreat near the Varandei settlement.

Figure 4. Ural Coast of Baidaratskaya Bay, the second type coast.

The obtained results permit us to conclude that for coasts of *the first type*, consisting of low ice content deposits (Varandei site), there is a clear dependence between the wave energy volume at the external border of the coastal zone and the coastal retreat rate. The correlation index (R) is 0.8 (Fig. 3).

At the same time, a significant correlation between the temperature regime and the coastal retreat rate was not observed (Ogorodov 2005). There was no determined interrelationship between average temperatures of active dynamic period and wave activity.

Thus, the conditions of the climate change dynamics of coasts formed by deposits with low ice content will be determined more by wind-energetic than temperature regimes.

The Baidaratskaya Bay and Marresale Coasts, Kara Sea example

The second coastal type represents the typical, thermo-erosion bluff coast composed of sandy and clayey deposits with medium ice content (Baidaratskaya Bay and Marresale Coasts, Kara Sea; Fig. 4). The dynamic regime of coasts of *the second type* is defined by both thermal and wave-energy factors. Thermodenudation processes, caused by the thawing of frozen deposits, result in the mass-wasting of unconsolidated sediments that are loosely deposited at the foot of the coastal bluff. This material is easily washed away by the waves and water-level surges that accompany storm events. In the absence of significant melting, a given wave energy level cannot act with the same efficiency on the coastal bluff to remove material, and hence should result in lower coastal retreat rates. Correspondingly, the persistence of the thawed, loose material at the base of the bluff when wave activity is low should reduce the rate of the thermodenudation processes and also coastal bluff retreat.

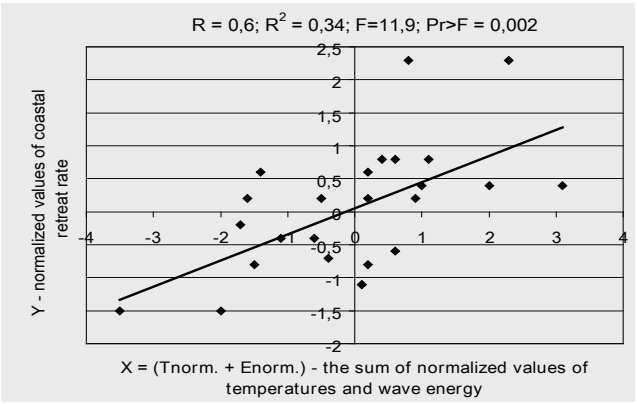

Figure 5. Seasonal erosion response at the second type coast, 1977–2004, with respect to an index combining a representation of seasonal thermal and wave energies (their normalized seasonal values were added and plotted against the normalized erosion response). Results considering the influence of temperature and wave action together showed superior explanatory capacity than temperature or wave energy alone.

For a region with the *second type* of coast (Baidaratskaya Bay and Marresale sites, Kara Sea), we have calculated the sums of temperatures averaged monthly for the mild season (from June to September) for the period from 1977 to 2004, as well as the total value of the wave energy flux. We performed correlation analyses of these data and the results of monitoring of the coastal dynamics. We observed that both factors influence the coastal retreat rate equally. Seasonal indicators of temperature and wave energy returned correlation coefficients (against seasonal erosion) of 0.41 and 0.39, respectively, while together they returned 0.6 (Fig. 5). The maximal coastal retreat rate (2.0–3.5 m/year) corresponds to the years when both average temperature and wave-energy flux approach the maximum values. Such behavior corresponds to the years 1982, 1983, 1988, 1989, 1994, and 1995 (Vasiliev et al. 2005), in particular. The coincidence of minima of these parameters corresponds to the lowest rates of coastal recession (0.5 m/year, for example, during the years 1978 and 1999).

The combined analysis of coastal retreat rate and hydrometeorological parameters specifying the temperature and wave regime seems to be difficult because of the discreteness of monitoring of coastal dynamics. For example, the measurement of the position of the brow of the coastal bluff is usually performed at the end of August and beginning of September, while the high wave energy activity occurs at the end of September and in October. As a result, these measurements give information on the retreat rate of the brow of coastal bluff under the action of thermodenudation processes during the summer of a given year and wave erosion during autumn of the previous year.

Dynamics of coasts consisting of frozen deposits is mainly caused by the two environmental forcing factors, namely, by the thermal and wave-energy mechanisms. As a rule, the role of the thermal factor increases with the ground ice content of the coastal deposits. In turn, low ground ice content renders the wave-energy factor more significant.

Conclusions

Thus, temperature regime and waves, as the major environmental forcing agents determining dynamics of arctic coastal margins have been considered. Rising temperatures are altering the arctic coastline and much lager changes are projected to occur during this century as a result of reduced sea ice, thawing permafrost. Less extensive sea ice creates more open water, allowing stronger wave generation by winds, thus increasing wave-induced erosion along arctic shores. Therefore, the acceleration of erosion and thermo-abrasion of the coast can be caused by both increase of the air and water temperature and possible increasing of wind-wave activity.

Acknowledgments

I am grateful to Dr. David Atkinson (International Arctic Research Center, University of Alaska) for wind data and scientific assistance, and also to the Russian Foundation of Basic Research, projects 07-05-12072, for financial support.

References

Longinov, V.V. 1966. Energetic method of estimating alongshore sediment drift in coastal zone. Proceedings of SoyuzmorNIIproekt, 12 (8): 13-28. (in Russian).

Ogorodov, S.A. 2002. Application of wind-energetic method of Popov-Sovershaev for investigation of coastal dynamics in the Arctic. In: V. Rachold et al. (eds.), *Arctic Coastal Dynamic. Report of an International Workshop. Potsdam (Germany) 26–30 November 2001, Reports on Polar and Marine Research*. Bremerhaven. 413: 37-42.

Ogorodov, S.A. 2005. Peculiarities of Dynamics of Barents Sea Coasts Formed by Deposits with Low Ice Content, TERRA NOSTRA: *2nd European Conference on Permafrost, Potsdam, Germany, June 12–16, 2005:* 164.

Popov, B.A., Sovershaev, V.A. 1981. Principles in distinguishing data for calculating wave energy fluxes. Beregovaya zona morya (Coastal zone). Moscow, Nauka, 47-53 (in Russian).

Popov, B.A., Sovershaev, V.A. 1982. Nekotoryie cherty dinamiki arkticheskikh beregov Azii (Some features of the coastal dynamics in arctic Asia). Voprosy geografii, 119. Morskie berega (Sea coasts). Moscow, Mysl', 105-116 (in Russian).

Vasiliev, A., Kanevskiy, M., Cherkashov, G., Vanshtein, B. 2005. Coastal dynamics at the Barents and Kara Sea key sites. In: *Geo-Marine Letters. An International Journal of Marine Geology*. Vol. 25, N 2-3, 110-120.

Solifluction Lobes in Sierra Nevada (Southern Spain): Morphometry and Palaeoenvironmental Changes

Marc Oliva
Department for Physical and Regional Geography and Landscape Research Laboratory, University of Barcelona, Spain
Lothar Schulte
Department for Physical and Regional Geography and Landscape Research Laboratory, University of Barcelona, Spain
Antonio Gómez Ortiz
Department for Physical and Regional Geography and Landscape Research Laboratory, University of Barcelona, Spain

Abstract

This paper presents a morphometric and spatial approach, the aim of which is to classify solifluction lobes in Sierra Nevada in southern Iberian Peninsula, to understand the involved geomorphic processes, and to reconstruct their evolution during the Late Holocene. Under the present climatic conditions, solifluction is inactive to weakly active in this massif. According to our findings, water availability in the semiarid environment of Sierra Nevada is the main factor controlling solifluidal dynamics. Only lobes near water channels and those influenced by water supply from late-lying snow patches show displacements. By contrast, thermal and topographic monitoring of a solifluction lobe in the Rio Seco Valley showed that, despite a seasonal frozen layer of 70 cm thickness, solifluction processes remain inactive. However, sedimentological studies on solifluction lobes indicate that during the Late Holocene, periods of increased solifluction processes (e.g., Little Ice Age) alternated with periods of geomorphic stability (e.g., Medieval Warm Period). Present climate may not be cold and/or wet enough to trigger important solifluction processes from 2500 to 3000 m altitude.

Keywords: Late Holocene; seasonal frozen layer; Sierra Nevada; solifluction lobes.

Introduction

Solifluction has been defined as the slow mass wasting associated with freeze–thaw action (Andersson 1906, Ballantyne & Harris 1994). During the last decades, research on present and past solifluction processes was undertaken mostly in high-latitude (polar and subpolar regions) and in mid-latitude mountain environments, where periglacial processes affect settlements, infrastructures, and equipment (Matsuoka 2001).

By contrast, solifluction features in the Mediterranean region have attracted less attention from geomorphologists and geophysicists due to the reduced extension of the periglacial belt and lower demographic pressure at high altitudes. However, studies on present solifluction dynamics in Spanish mountains were carried out by Gómez Ortiz et al. (2005) in Sierra Nevada, by Grimalt & Rodríguez (1994) on the Balearic Islands, by Palacios et al. (2003) in the Peñalara massif, and by Chueca & Julián (1995) in the Central Pyrenees**.**

Since the beginning of the research on solifluction phenomena, studies focused on morphometry and spatial pattern of the lobes (Andersson 1906, Rapp 1960, Washburn 1979), but during the last years, research turned towards the active layer, particularly on chronostratigraphy, processes, sediment flux, and ground temperature monitoring (Harris et al. 1997, Matsuoka 2001, Jaesche et al. 2003). In order to understand the nature of mechanisms, processes, and evolution of solifluction landforms, it is crucial to deal with the causes of solifluction being active in some periods and inactive in others (Gamper 1983, Veit 1988, Matthews et al. 2005).

The purpose of the present paper is to examine the morphometry and palaeoenvironmental changes of solifluction lobes in two study areas on the northern and southern slopes of Sierra Nevada.

Regional Setting

Sierra Nevada, the highest massif in the Iberian Peninsula (Mulhacén, 3478 m), is located at latitude 37ºN between the subtropical high-pressure belt and the mid-latitude westerlies. Mean annual temperature at 2500 m records 4.4ºC, and annual precipitation reaches only 702 $mm^{-1}yr$

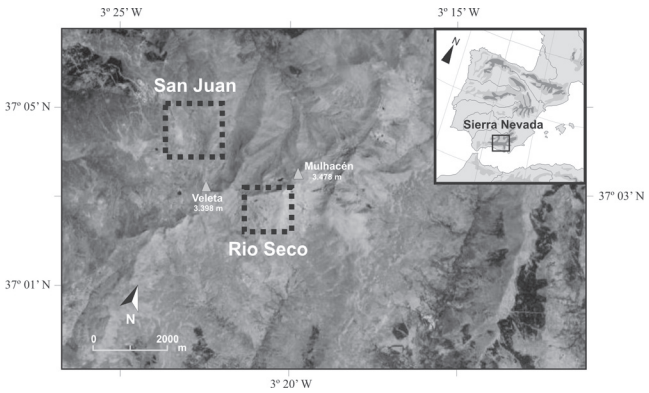

Figure 1. Study area and Sierra Nevada in the Iberian Peninsula (Google Earth).

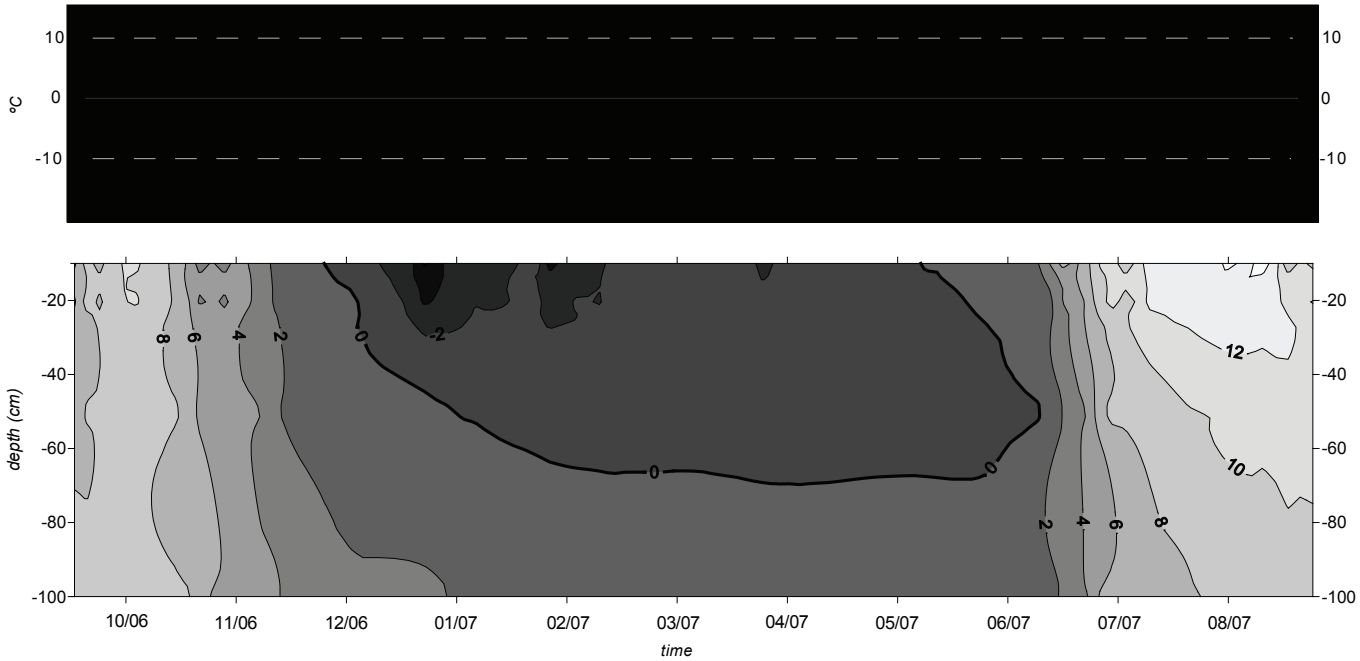

Figure 2. Mean daily air temperature at Veleta Peak, 3398 m (figure above), and ground temperatures of a solifluction lobe of the Rio Seco cirque at 3001 m (figure below) from September 2006 to August 2007.

(1965–1992). 80% of the total precipitation falls between October and April, mainly as snow.

As a consequence of global warming since the end of the Little Ice Age (LIA), the southernmost glacier of Europe located in the Veleta cirque disappeared (Schulte 2002). However, local discontinuous permafrost and active rock glacier dynamics are closely related to remnants of dead ice located in the highest northern cirques of the massif (Gómez Ortiz et al. 2001, Schulte et al. 2002, Gómez Ortiz et al. 2005).

The vegetation cover of the alpine belt in Sierra Nevada is very low, but includes a large number of endemic species (Molero Mesa & Pérez Raya 1987). This sparse vegetation and the low resistance schist, the dominant bedrock in the highest part of Sierra Nevada, enhance solifluction and erosion processes, hence the headwaters of Rio Seco and San Juan valleys show frequent solifluction lobes. In the Rio Seco cirque (southern slope), they are located between 2930 and 3005 m a.s.l. and in the U-shaped valley of San Juan (northern slope) between 2474 and 2911m. Vegetation cover ranges from 1.6% in the Rio Seco cirque to 3.8% in the San Juan valley.

Materials and Methods

More than two hundred solifluction lobes were morphometrically analysed according to the nomenclature of Hugenholtz and Lewkowicz (2002) and Matsuoka et al. (2005), considering 8 variables: altitude, slope, orientation, typology, vegetal cover, length, width, and front height. Universal Temperature Loggers (UTL-1) were installed to measure the ground temperatures continuously every two hours at different depths (2, 10, 20, 50, and 100 cm).

Table 1. Mean stake displacements of monitored solifluction lobes from August 2006 to August 2007.

Valleys	Heights (m a.s.l.)	n	Moving stakes (%)	Horizontal ($cm^{-1}yr$)	Vertical ($cm^{-1}yr$)
San Juan	2793–2911	47	61.8	0.31	0.41
Rio Seco	2935–3001	40	11.8	0.05	0.14

Sedimentological laboratory standard methods were carried out on soil samples extracted from several lobes. Organic carbon was determined with a CN Elemental Analyzer and grain size was measured according to Scheffer & Schachtschabel (2002).

Thermal and Dynamic Control of Solifluction Lobes

From August 2005 to August 2007, displacements of 16 solifluction lobes at different heights were monitored by up to 9 wooden stakes each (50 cm long x 3 cm wide), inserted 45 cm into the lobes. The measurements of the stakes at the lobe fronts and sides may provide sensitive records of active solifluction processes nowadays in Sierra Nevada.

In San Juan, 38.2% of 47 installed stakes did not show any horizontal displacement, reaching 88% out of 40 in the Rio Seco cirque. Furthermore, grass cover, intact root network, soil formation (thin A horizons), and micro-scale geomorphology (clearly defined, steep-sloping lobe fronts) support the interpretation of the inactivity pattern of these lobes.

The rest of the stakes indicate horizontal movement of less than 0.5cm/yr (Table 1) indicating solifluction processes.

Table 2. Different types and characteristics of solifluction lobes in Sierra Nevada.

Type	Characteristics	Nº of lobes (monitorized lobes)	Active / stable	Length (m)		Width (m)		Front height (m)		Slope (º)	
				Range	Mean	Range	Mean	Range	Mean	Range	Mean
Stone-banked lobe-1 STL-1	Abundance of gravels/ rocks > 50%	6 (1)	1 / 0	3-10	5,1	2-5	3,4	0,6-1	0,39	9-19	13,0
Stone-banked lobe-2 STL-2	Abundance of gravels/ rocks < 50%	34 (2)	1 / 1	2-8	5,4	2-8	4,5	0,3-0,9	0,52	7-16	10,3
Low solifluction lobe LSL	Dominance of turf with a frontal height < 80 cm.	104 (4)	2 / 2	1,5-6	4,4	1-5	3,6	0,2-0,7	0,47	7-15	9,8
High solifluction lobe HSL	Dominance of turf with a frontal height ≥ 80 cm	32 (5)	1/ 4	2-10	6,6	2-10	5,3	0,8-1,2	0,9	6-18	11,5
Solifluction terrassettes ST	Low solifluction terrasses	3 (2)	0 / 1	0,6-2	1,1	0,3-1	0,8	0,2-0,3	0,24	6-18	10,0
Stone-mantled lobes MSS	Stone-dominance large lobe ≥ 8 m length	11 (0)	0 / 0	9-15	9,9	8-13	9,5	0,6-1,4	0,86	7-19	14,0
Turf-mantled lobes MST	Turf dominance large lobe ≥ 8 m length	6 (1)	0 / 1	10-18	13,3	10-19	12,7	0,5-1,5	0,78	9-19	13,1
Block STL (block)	Lobe with a rock above	4 (1)	1 / 0	3,5-6	5,0	2-3,5	2,8	0,5-0,9	0,67	6-10	8,0
Mudflow-affected solifluction lobes MSL	Irregular-shaped lobes with muddy matrix	2 (1)	0 / 1	1-6	5,5	5-10	7,5	0,2-0,7	0,67	8-9	8,5

The higher vertical movement rates are due to freeze-thaw uplift. However, the measured surface velocity of the Sierra Nevada lobes is relative slow compared with rates recorded in polar and subpolar regions (Matsuoka 2001).

According to our findings, water availability in the semiarid environment of Sierra Nevada is the main factor controlling solifluidal dynamics. Only lobes near water channels and those influenced by water supply from late-lying snow patches show displacements. Therefore, we expect higher displacement rates during periods of moister climate conditions.

Figure 2 shows mean daily air temperature of Veleta Peak (3398 m a.s.l.) and ground temperature at 10, 20, 50, and 100 cm depth of an inactive solifluction lobe in the Rio Seco cirque at 3001 m a.s.l. from September 2006 to August 2007. The Universal Temperature Logger (UTL-1) at 2 cm depth failed, and no data were obtained.

The formation of the 70 cm thick frozen layer started at the end of November and persisted until the beginning of June. Increased frost penetration was recorded during mid December, the end of January, and the end of March.

This relatively sensitive response of the ground temperature at 10 and 20 cm depth results mainly from reduced snow cover during the winter of 2006–2007. Nevertheless, the persistent conservation of the seasonal frozen layer is due to quite cold late-spring temperatures and a continuous snow cover until the end of May. In contrast to the local permafrost detected in the 3000 m high Veleta (Gómez Ortiz et al. 2005) and Mulhacén cirques (Schulte et al. 2002), the observed pattern of the ground temperature in Figure 2 does not indicate any permafrost regime at the key site of the southern exposed Rio Seco cirque (3001 m a.s.l.).

Morphometry of Solifluction Lobes

In the San Juan valley, 156 lobes were mapped, and 46 were mapped in the Rio Seco Valley. This difference in numbers results from the different amount of water supply and tectonically-influenced valley topography, which explains why there are no solifluction lobes between 2550–2750 m a.s.l. (Fig. 3).

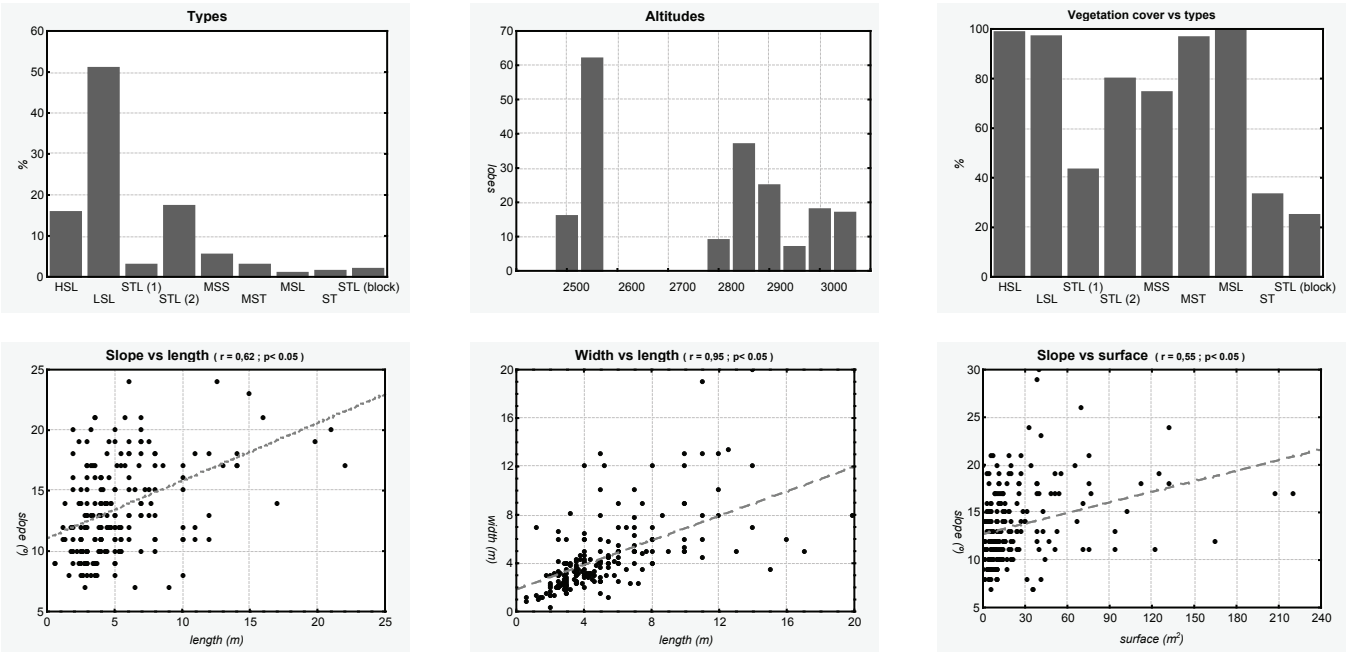

Figure 3. Relations between lobe morphometry, topography and vegetation cover in Sierra Nevada..

In general, a wide range of solifluction lobes can be observed in Sierra Nevada. Types with principal morphometrical and pedological characteristics are listed in Table 2 and can be integrated into two main groups: peat-topped lobes and uncovered stone and block-rich lobes.

There is no evidence that lobe size or other features such as front height, slope gradient, orientation, etc. listed in Figure 3, are related to present solifluction processes. Neither external factors (altitude, slope, and orientation), nor internal characteristics of solifluction lobes correlate with active lobes.

Only vegetation cover may explain the stability or mobility of solifluction lobes, with positive correlations with stable lobes (r = 0.58). Although two well-vegetated LSL also show small horizontal displacements, vegetation seems to impede movement in peat lobes but not in block-rich lobes, which tend to show higher displacement rates**.**

A correlation matrix for lobe morphometry, topography and vegetation cover of solifluction lobes from Sierra Nevada is given in Table 3.

Regarding the lobe morphology, the matrix shows a positive correlation between length and width with slope (r = 0.63; r = 0.54). The height of the riser also shows good correlation with length (r = 0.74) and width (r = 0.71). The surface area is mainly controlled by slope gradient (r = 0.63) and vegetation cover (r = 0.46).

However, orientation does not seem to be an important criterion explaining lobe morphology in Sierra Nevada (r between -0.26 and 0.32). Vegetation cover is mostly controlled by drainage and temperature, showing negative correlations with slope (r = -0.70): the steeper solifluction lobes are, the sparser vegetation cover they have.

Solifluidal Activity During the Late Holocene

Several solifluction lobes in both study areas were examined by macroscopic soil description and geochemical laboratory standard analysis. Figure 4 shows the lithostratigraphy, water content, grain size, and organic carbon content (OC) of a HSL lobe in the Rio Seco cirque at 2945 m a.s.l.

The stratigraphy of the lobe is defined by the alternation of coarse grained stone-rich layers with peat and organic-rich (OC up to 30%). The aggradation of the lobe finished with the development of an organic A horizon. The coarse-grained and sometimes cryoturbated layers are interpreted as solifluidal deposits, whereas the organic-rich horizons represent soil formation under stable geomorphic conditions. Several solifluction lobes in Rio Seco and San Juan valley show a similar lithostratigraphy.

Based on tentative correlations with a solifluction lobe, radiocarbon-dated by Esteban (1994) from 1100 ± 120 yr BP (basal organic layer) to 170 ± 120 yr BP (uppermost organic horizon), we argue that our profile could cover the Late Holocene, from the Medieval Warm Period at the bottom, to the 20th century warming at the top.

The two solifluction layers could correlate with the two main cooler climate pulses of the Little Ice Age reconstructed by Schulte (2002) from ^{210}Pb-dated glacier advances at the nearby Veleta cirque. Historical climate research from documentary data undertaken by Rodrigo et al. (1999) considers that the coldest and wettest phase of the LIA occurred from 1590 to 1650. Radiometric dating and further research is needed to support our chronological model.

Conclusions

This paper presents a morphometric and spatial approach, the aim of which is to classify solifluction lobes in Sierra Nevada in

Table 3. Correlation matrix for lobe morphometry, topography, and vegetation cover of solifluction lobes from Sierra Nevada ($p < 0.05$).

	Orientation	Slope	Vegetation cover	Length	Width	Front height	Surface area	L/W
Orientation								
Slope	0.03							
Vegetation cover	0.31	0.18						
Length	0.05	0.63	0.49					
Width	0.32	0.54	0.61	0.95				
Front height	-0.09	0.29	0.52	0.74	0.71			
Surface area	0.29	0.63	0.46	0.96	0.95	0.62		
L/W	-0.26	-0.22	-0.83	-0.59	-0.74	-0.49	-0.54	

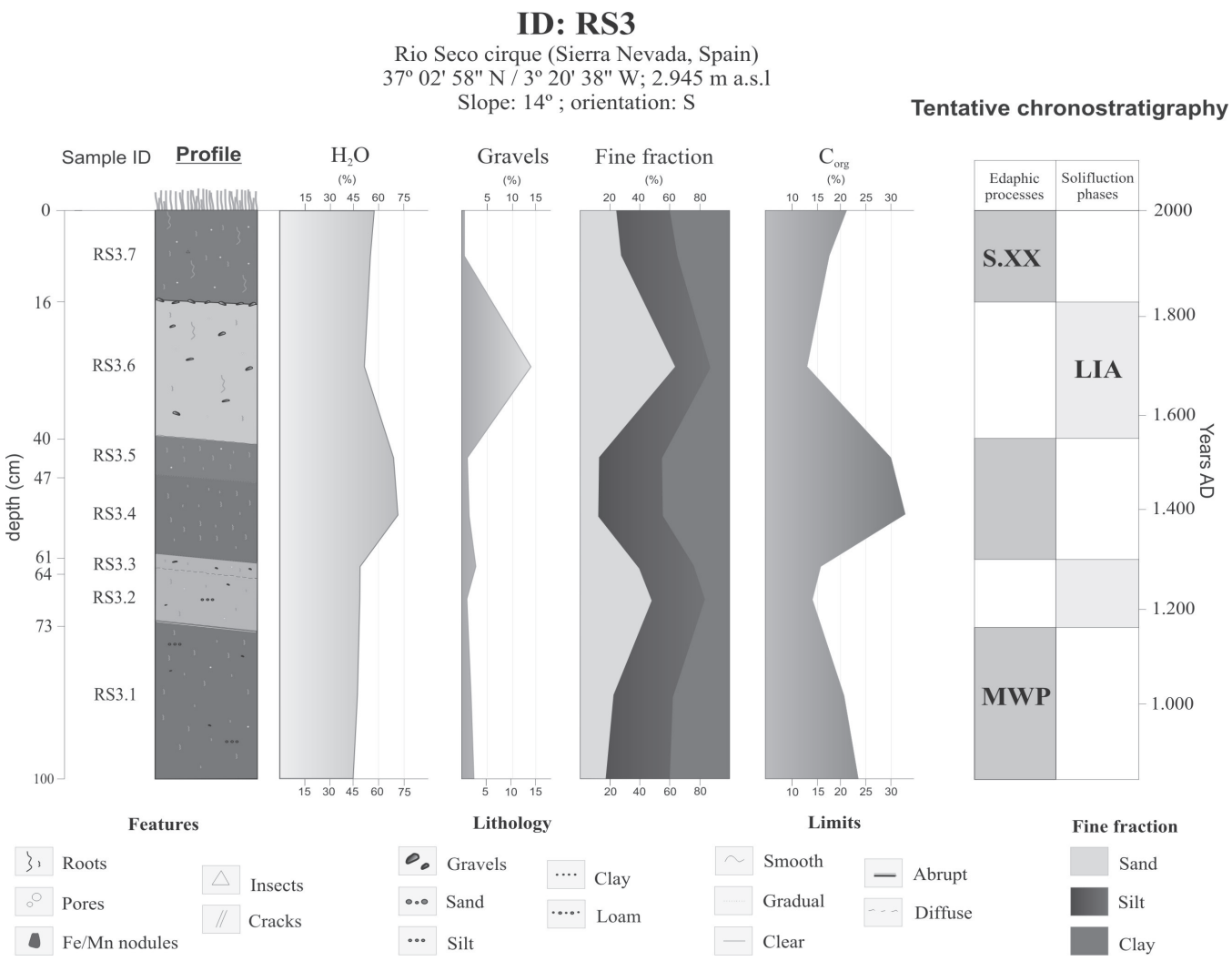

Figure 4. Lithostratigraphy and soil properties of a solifluction lobe of the Rio Seco cirque

southern Iberian Peninsula. Under the present climatic conditions, solifluction is mostly inactive, and only some lobes present small displacements. Thermal and topographic monitoring in the Rio Seco Valley showed that, despite a seasonal frozen layer of 70 cm thickness, solifluction processes were inactive. However, sedimentological studies on solifluction lobes indicate that during the Holocene, periods of increased solifluction processes (e.g., Little Ice Age) alternated with periods of geomorphic stability (e.g., Medieval Warm Period).

We assume that cooler periods in Sierra Nevada could promote solifluction, whereas warmer periods induce soil formation. Present climate may not be wet and/or cold enough to trigger important solifluction processes from 2500 to 3000 m altitude. Future radiocarbon dating will improve our solifluction chronostratigraphy and provide data to precisely identify the timing and environmental conditions of solifluction processes in the alpine belt of Sierra Nevada.

Acknowledgments

This research was financially supported by the Spanish Ministery of Education, project AP-2004-4548 and the Fluvalps-3000 Project (CGL2006-01111). Sedimentological analyses were undertaken at the laboratory of the Department of Geography, University of Berne.

References

Andersson, J.G. 1906. Solifluction, a component of subaerial denudation. *Journal of Geology* 14: 91-112.

Ballantyne, C.K. & Harris, C. 1994. *The Periglaciation of Great Britain.* Cambridge: Cambridge Univ. Press.

Chueca, J. & Julián, A. 1995. Cuantificaclón de movimientos en masa lentos en medios de montaña: Pirineo Central. *Lurralde* 18:173-196.

Esteban, A. 1994. *Evolución del paisaje durante los útimos 10.000 años en las montañas del Mediterráneo occidental: ejemplos del Pirineo Oriental y Sierra Nevada*. University of Barcelona, Master Thesis.

Gamper, M.V. 1983. Controls and rates of movement of solifluction lobes in the eastern Swiss Alps. *Proceedings of the Fourth International Permafrost Conference, Fairbanks, Alaska, July 18–22, 1983:* 328-333.

Gómez Ortiz, A., Palacios, D., Ramos, M., Tanarro, L.M. & Salvador Franch, F. 2001. Location of permafrost in marginal regions: Corral Del Veleta, Sierra Nevada, Spain. *Permafrost Periglac. Process.* 12(1): 92-110.

Gómez, A., Schulte, L., Salvador, F., Palacios, D., Sanz de Galdeano, C., Sanjosé, J.J., Tanarro, L.M. & Atkinson, A. 2005. Field trip to Sierra Nevada Massif Glacial Geomorphology and Present Cold Processes. *Sixth International Conference on Geomorphology. September 7–11, 2005 Zaragoza (Spain)*. Field trip guides, Vol. II: 309-354.

Grimalt, M. & Rodríguez, A. 1994. El modelado periglacial en Baleares. Estado de la cuestión. *Periglaciarismo en la Península Ibérica, Canarias y Baleares*. Servicio de Publicaciones Universidad Granada: 189-201.

Harris, C., Davies, M. & Coutard, J.P. 1997. Rates and processes of periglacial solifluction: an experimental approach. *Earth Surface Processes and Landforms* 22: 849–868.

Hugenholtz, C.H. & Lewkowicz, A.G. 2002. Morphometry and environmental characteristics of turf-banked solifluction lobes, Kluane Range, Yukon Territory, Canada. *Permafrost and Periglacial Processes* 13(4): 301-313.

Jaesche, P., Veit, H. & Huwe, B. 2003. Snow cover and soil moisture controls on solifluction in an area of seasonal frost, Eastern Alps. *Permafrost Periglac. Proces.* 14: 399-410.

Matsuoka, N. 2001. Solifluction rates, processes and landforms: a global review. *Earth-Science Reviews* 55: 107-134.

Matsuoka, N., Ikeda, A. & Date, T. 2005. Morphometric analysis of solifluction lobes and rock glaciers in the Swiss Alps. *Permafrost Periglac. Process* 16: 99-113.

Matthews, J.A., Seppälä, M. & Dresser P.Q. 2005. Holocene solifluction, climate variation and fire in a subartic landscape Al Pippokangas, Finnish Lapland based on radiocarbon-dated buried charcoal. *Journal of Quaternary Science* 20: 533-548.

Molero Mesa, J. & Pérez Raya, F. 1987. *La flora de Sierra Nevada*. Granada, Spain. University of Granada.

Palacios, D., Andrés, N. de, Luengo, E. 2003. Distribution and effectiveness of nivation in Mediterranean mountains: Peñalara (Spain). *Geomorphology* 54, 157-178.

Rapp, A. 1960. Recent development of mountain slopes in Kärkevagge and surroundings, Northern Scandinavia. *Geografiska Annaler* 42a: 65-200.

Rodrigo, F.S., Esteban-Parra, M.J., Pozo-Vázquez, D. & Castro-Diaz, Y. 1999. A 500-year precipitation record in Southern Spain. *International Journal of. Climatology* 19: 1233-1253.

Scheffer, F. & Schachtschabel, P. (2002). Lehrbuch der Bodenkunde. *Spektrum Akademischer Verlag*, 462 pp.

Schulte, L., 2002. Climatic and human influence on river systems and glacier fluctuations in southeast Spain. *Quaternary International* 93-94: 85-100.

Schulte, L., Marcos Garcia-Blanco, J. de, Gómez Ortiz, A, Palacios Estrema, D., Tanarro Garcia, M., Fernández Fernández, A. & Ramos Sainz, M. 2002. Evolución Glaciar y periglaciar del Circo del Mulhacén (Sierra Nevada, Península Ibérica). Publicaciones del Instituto Geológico y Minero de España. *Serie Geología* 1: 491-499.

Veit, H.. 1988. Fluviale und solifluidale morphodynamik des spät- und postglazials in einem zentralalpinen flusseinzugsgebiet (Südliche Hohe Tauern, Osttirol). *Bayreuther Geowissenschaftliche Arbeiten* 13:1-167.

Washburn, A. 1979. *Geocryology: a survey of periglacial processes and environments*. London: Arnold, 406 pp.

Cyanobacteria Within Cryptoendolithic Habitats: The Role of High pH in Biogenic Rock Weathering in the Canadian High Arctic

Christopher R. Omelon
Department of Geological Sciences, The University of Texas at Austin, Austin, Texas, USA
Wayne H. Pollard
Department of Geography, McGill University, Montréal, Québec, Canada
F. Grant Ferris
Department of Geology, University of Toronto, Toronto, Ontario, Canada
Philip C. Bennett
Department of Geological Sciences, The University of Texas at Austin, Austin, Texas, USA

Abstract

Cryptoendolithic microorganisms are widespread in the Canadian High Arctic and show differences in microbial community composition and pH conditions. Laboratory experiments measuring changes in pH and DIC of 15 strains of phototrophic microorganisms (both cyanobacteria and algae) representative of species found in High Arctic cryptoendolithic habitats show clear differences in their ability to generate high pH conditions and uptake HCO_3^- during photosynthesis. Surveys of cryptoendolithic habitats show that microorganisms capable of producing high pH conditions are found within sandstone outcrops that experience rapid exfoliative weathering under water-saturated conditions, suggesting that these microorganisms play a direct role in chemical erosion of the host rock. This is possibly the only known chemical weathering mechanism directly related to photosynthesizing microorganisms in terrestrial silicate rocks, and may have a profound impact on landscape evolution in polar desert environments such as the Canadian High Arctic.

Keywords: biogenic weathering; carbon concentrating mechanism; cyanobacteria; pH shifting; silica dissolution.

Introduction

The abundance and diversity of microorganisms in the subsurface reflect not only their ability to grow under a wide range of natural conditions, but also their capacity to harvest energy from light as well as organic and inorganic substrates. The complexity of these microbial communities depends upon the suitability of a given habitat for colonization, which in many cases exhibit extremes in physical and/or chemical conditions to effectively limit the number of species that can exist within any given ecological niche. An example of this natural selection is found in cryptoendolithic habitats, where microbial colonization is restricted to those organisms able to acquire the necessary resources for growth within the physical confines of pore spaces of rocks. Communities are normally found directly beneath the rock surface (Fig. 1) that consist of primary producers such as algae and/or cyanobacteria as well as consumers and decomposers, including fungi and heterotrophic bacteria (Friedmann et al. 1980, Friedmann et al. 1981, Friedmann 1982, Friedmann & Ocampo-Friedmann 1984, Hirsch et al. 1988, De La Torre et al. 2003, Selbmann et al. 2005, Omelon et al. 2007). They are found in both hot and cold deserts around the world (Friedmann et al. 1987, Bell 1993, Cockell et al. 2003, Bungartz et al. 2004, Omelon et al. 2006) and local areas in temperate regions where climatic extremes limit epilithic colonization (Bell et al. 1986, Ferris & Lowson 1997, Gerrath et al. 2000, Casamatta et al. 2002, Sigler et al. 2003).

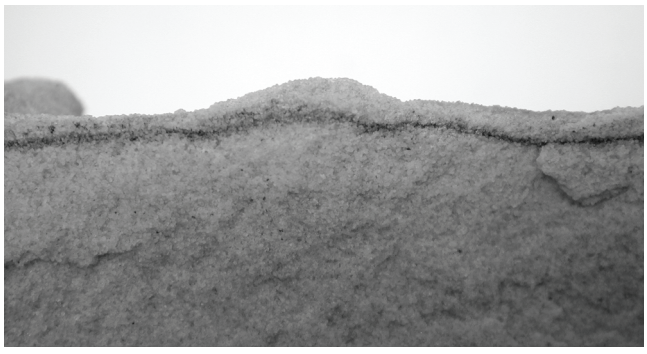

Figure 1. Example of cryptoendolithic microorganisms colonizing a sandstone rock, Ellesmere Island, Canadian High Arctic. Note limited vertical extent of biomass.

Location and site characteristics

Cryptoendolithic colonization of sandstone outcrops are found around Eureka, Ellesmere Island, Nunavut in the Canadian High Arctic (80°00′N, 85°55′W). Microbial communities show marked differences in composition and diversity despite similarities in microclimate, pore space availability, and host rock mineralogy (Omelon et al. 2006). More recently, Omelon et al. (2007) showed that cyanobacteria-dominated communities exist under higher pH conditions in contrast to communities dominated by fungi and algae that are characterized by lower pH conditions, suggesting that the activity of the dominant microorganism(s) controls the pH of the surrounding environment.

It is believed that differences in pH within these cryptoendolithic habitats control weathering rates of the

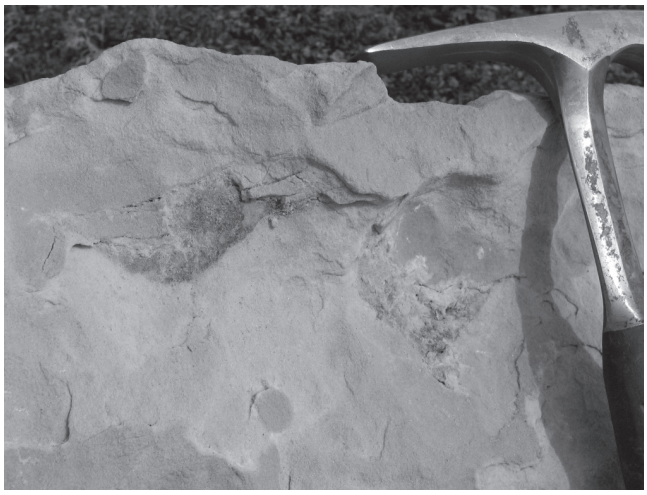

Figure 2. Exfoliative weathering of sandstone rock, with the detachment boundary occurring along the horizon of microbial colonization.

host rock (Omelon et al. 2007). Outcrops dominated by the cyanobacterial species *Leptolyngbya* sp. and *Gloeocapsa* sp. exhibit exfoliated rock weathering through flaking off of surface material, with the origin of detachment occurring along the colonized boundary (Fig. 2). This is in contrast to uncolonized sandstones and those dominated by algae and fungi, which do not exhibit these weathering patterns. This study attempts to relate these observations to cryptoendolithic microbial community structure by examining how microbial activity influences pH, and therefore how cyanobacteria and algae are involved in biogenic weathering of silicate rocks in this polar desert environment.

Biogenic weathering: background

The traditional view of biogenic weathering of sedimentary rocks links the solubilization of cementing minerals to the production of inorganic and organic acids by cryptoendolithic lichens (Friedmann 1982, Hirsch et al. 1995, Wierzchos & Ascaso 1996, Ascaso et al. 1998, Burford et al. 2003, Gaylarde & Gaylarde 2004). Decreasing pore water pH accelerates dissolution of primary silicates and increases solubility (Knauss & Wolery 1986, Knauss & Wolery 1988), while organic acids complex aluminum, and in some cases silica (Bennett & Siegel 1987, Bennett & Casey 1994, Stillings et al. 1996). The net result is the removal of both framework silicates and cements, with the mobilization of nutrients that benefit the microbial community (Bennett et al. 2001).

Bioalkalization

In contrast, cyanobacteria are not known to produce organic acids or acid pore water environments but rather may contribute to silicate dissolution via *bioalkalization* (Budel et al. 2004), whereby high pH conditions are generated in pore waters during cyanobacterial photosynthesis. As with acidic environments, high pH conditions also increase both quartz and feldspar solubility and dissolution kinetics (Brady & Walther 1989, Bennett 1991), resulting in accelerated mineral dissolution that leads to enhanced cycling of elements and nutrients within cryptoendolithic habitats (Johnston & Vestal 1989, Johnston & Vestal 1993, Ferris & Lowson 1997, Blum et al. 2002), and influences residence times of these microbial communities (Omelon et al. 2007).

Cyanobacteria have adapted to changes in temperatures and atmospheric CO_2 and O_2 levels over the past 2.5 billion years (Giordano et al. 2005), which enables them to survive under a wide range of environmental conditions (Badger et al. 2006). Most notable is the evolution of a carbon concentrating mechanism (CCM) to maintain high rates of CO_2 fixation for photosynthesis under conditions of low dissolved CO_2 concentrations (<15 μM) normally found in aquatic habitats (Kaplan & Reinhold 1999, Price et al. 2002, Badger & Price 2003).

The CCM consists of active transport systems to accumulate dissolved inorganic carbon (DIC) within the cell. Specifically, the CCM involves distinct modes of DIC uptake as either HCO_3^- or CO_2 by transporters (Omata et al. 1999, Shibata et al. 2001, Price et al. 2002, Price et al. 2004), to accumulate HCO_3^- within the cell for carbon fixation. A consequence of activation of HCO_3^- transporters for carbon fixation is the production of excess OH^- that is expelled from the cell, resulting in a high pH in the surrounding environment as shown in the equation:

$$HCO_3^- + H_2O \rightarrow (CH_2O) + O_2 + OH^- \quad (1)$$

In the case of silica-rich cryptoendolithic habitats, this mechanism can lead to accelerated weathering of the lithic substrate (Chou & Wollast 1985, Knauss & Wolery 1986, Knauss & Wolery 1988, Brady & Walther 1989, Budel et al. 2004). Observations of pH values >9 in cultures of cyanobacteria from High Arctic cryptoendolithic habitats suggest that these microorganisms use HCO_3^- transporters and are therefore capable of bioalkalization.

Materials and Methods

Cyanobacterial and algal species

Experiments were conducted on a total of 15 species of phototrophic microorganisms; these include 2 species cultured from field samples as well as cultures obtained from the Culture Collection of Algae at the University of Texas at Austin (Table 1) that correspond to the same genus' as those found in the High Arctic cryptoendolithic habitats as described by Omelon et al. (2007). Despite the fact that many algae and cyanobacteria are cosmopolitan in nature, an attempt was made to select cultures from similar habitats (i.e., cold and/or desert conditions) as these species may have adapted their mode of DIC uptake to specific climate and/or microenvironmental conditions. Species were cultured in designated liquid media, aerated with normal air and continuously illuminated at ~60 $\mu mol \cdot m^{-2} \cdot s^{-1}$ at 20°C.

Table 1. Phototrophic microorganisms (cyanobacteria and algae) used for pH drift and DIC experiments. Field samples in bold.

Taxa	Origin
Cyanobacteria	
***Leptolyngbya* sp.**	**Ellesmere Island, Canada**
Gloeocapsa sp.	N/A
Synechococcus sp.	Atacama Desert, Chile
Aphanothece sp.	Great Salt Plains, Oklahoma, USA
Leptolyngbya sp.	Great Salt Plains, Oklahoma, USA
Eukaryotic Algae	
***Cladophorella* sp.**	**Ellesmere Island, Canada**
Stichococcus sp.	Battleship Promontory, Antarctica
Chlorella antarctica	Antarctica
Chlorosarcinopsis negevensis	Negev Desert, Israel
Bracteacoccus minor var. desertorum	Negev Desert, Israel
Chlorococcum aegyptiacum	El Tahir, Egypt
Botrydiopsis alpina	Unterengadin, Switzerland
Cladophora kosterae	Jarden des Plantes, Paris, France
Tetracystis sp.	Ganzu, Wuwei City, China
Chroococcus turgidus	Bloomington Indiana, USA

pH drift experiments

Experimental liquid medium contained 0.25 mmol $CaCl_2$, 0.15 mmol $MgSO_4$, 1 mmol NaCl, 50 µmol KCl, and 1 mmol $NaHCO_3$. Cells were harvested and washed three times in experimental medium by centrifugation at 1000 g for 5 minutes to remove culture media, resuspended in 30 ml of experimental medium in 50 ml Erlynmeyer flasks double-sealed with Parafilm, and incubated at 20°C under saturated photosynthesis light levels (~100 µmol·m^{-2}·s^{-1}) and constant stirring. The pH of the medium was measured periodically, concurrent with the removal of 1 ml subsamples for DIC measurements that were analyzed using a Dohrmann DC-180 carbon analyzer. Experiments were monitored until pH values stabilized, which corresponded to only small changes in DIC concentrations.

Results and Discussion

pH drift

In all cases, the pH of the solution increased from initial pH values (~7–8) as a result of microbial uptake of CO_2 or HCO_3^- for photosynthesis until the pH compensation point (pH_c) was reached, normally within 24 hours of initiation of experiments (Fig. 3). The highest pH_c value recorded was 10.89 by the coccoid cyanobacteria *Gloeocapsa* sp., followed by a pH_c of 10.80 by the filamentous alga *Chladophera kosterae*; similarly high pH_c values were associated with High Arctic cryptoendolithic filamentous cyanobacterial and algal species *Leptolyngbya* sp. (10.34) and *Cladopherella* sp. (10.02). Six species produced pH_c values ranging between 9–10 (two cyanobacteria, four algae), with the remaining five species (one cyanobacteria, four algae) reaching pH_c values <9 that rose only slightly from initial pH values.

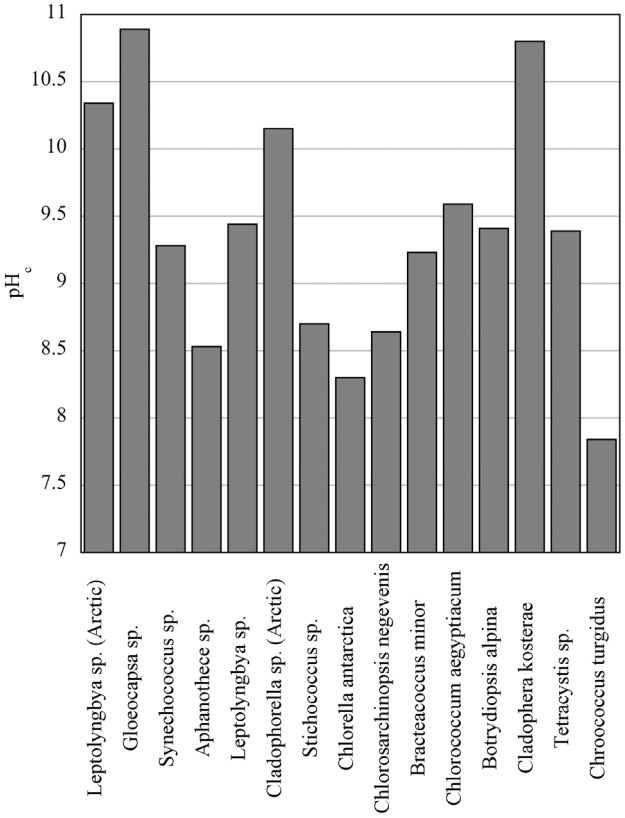

Figure 3. pH compensation points for 15 phototrophic microorganisms. Cultures were incubated at 100 µmol·m^{-2}·s^{-1} and 20°C; pH was monitored until values stabilized.

DIC measurements

As with pH, uptake of HCO_3^- or CO_2 led to decreases in DIC concentrations in all samples (Fig. 4), with the same species that generated high pH_c values removing the largest amount of available DIC. Uptake by *Gloeocapsa* sp. was the most dramatic, with the removal of 98.9% of DIC, followed by *Cladophera kosterae* (80.2%), the High Arctic *Leptolyngbya* sp. (66.0%), and the High Arctic *Cladopherella* sp. (60.1%). The remaining species removed less that 50% of available DIC from the experimental solution.

A pH_c >9 is the suggested lower limit for activation of a CCM (Kevekordes et al. 2006), however a more definitive value may be a pH of 10, as the concentration of CO_2*(aq)* at this level is <0.06% of total DIC (Banares-Espana et al. 2006) and suggests the use of HCO_3^- transporters over CO_2 transporters.

Based on these guidelines, all species in the current study are able to activate a CCM and therefore utilize HCO_3^- during photosynthesis. *Gloeocapsa* sp., *Cladophera kosterae*, *Leptolyngbya* sp. and *Cladopherella* sp. were the most efficient at removing HCO_3^- from solution with concurrent generation of high pH conditions; in all cases, changes in pH and DIC concentrations occurred within 24 hours. In contrast, the remaining species showed initial increases in pH corresponding to uptake of CO_2 followed by slow changes in pH and lower final pH_c values, suggesting these microorganisms are less efficient in their ability to uptake HCO_3^-.

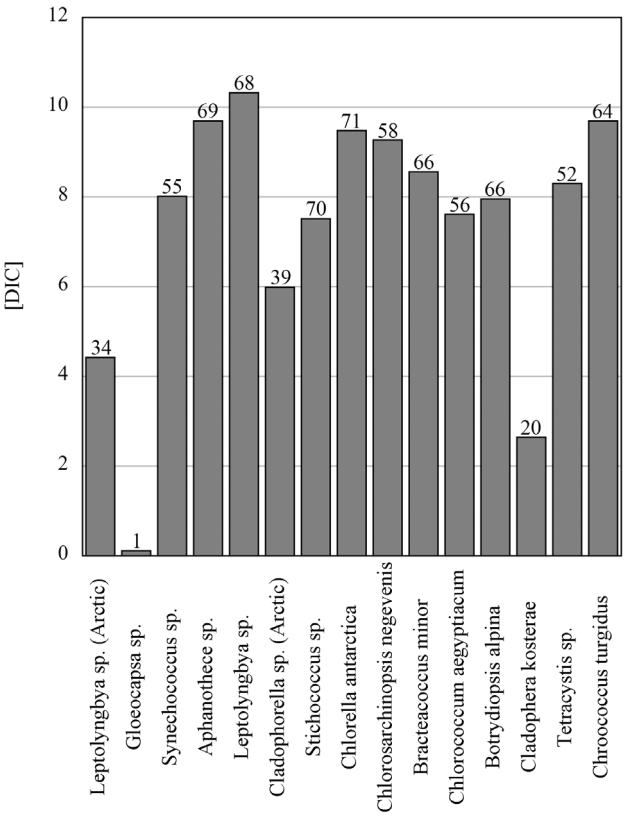

Figure 4. DIC concentrations remaining for 15 phototrophic microorganisms. Cultures were incubated at 100 $\mu mol \cdot m^{-2} \cdot s^{-1}$ and 20°C; DIC was measured until no further changes occurred. Numbers above columns represent % DIC remaining.

A comparison of these results to the microbial survey of cryptoendolithic communities around Eureka, Nunavut (Omelon et al. 2007) shows that the dominant microorganisms found at sites with high rates of weathering through exfoliation of the overlying rock surface (*Leptolyngbya* sp. and *Gloeocapsa* sp., and to a lesser extent *Cladophorella* sp.) are the same microorganisms capable of producing high pH conditions in laboratory experiments. In contrast, sites with the lowest measured pH values in the field were populated by microorganisms that produced pH_c values <10 (*Chlorella antarctica*, *Bracteacoccus minor var. desertorum*) as well as limited removal of DIC in the current study, suggesting that these microorganisms do not readily uptake HCO_3^- for photosynthesis through a CCM. Although the majority of microorganisms used in this study were not cultured directly from cryptoendolithic habitats in the Canadian High Arctic, many of these microorganisms are widely distributed in nature and likely possess similar physiological traits, such as the presence or absence of a CCM. It is interesting to note, however, differences in pH_c and DIC uptake between the two *Leptolyngbya* spp., suggesting that microorganisms may evolve to adapt to conditions within their specific environment.

Silicate weathering in the cryptoendolithic environment

Although high pH conditions can be generated in aquatic habitats where cyanobacteria and algae consume all available $CO_2(aq)$ and must therefore use HCO_3^- for photosynthesis, there is little knowledge or understanding of the impact of high pH-generated conditions in terrestrial habitats. The data presented here provides information that, when coupled with an understanding of microenvironmental conditions within cryptoendolithic habitats, can explain observations of exfoliative weathering of rocks colonized by microorganisms generating high pH conditions. Previous work by Omelon et al. (2006) showed that High Arctic cryptoendolithic habitats experience warmer temperatures and wetter conditions than the exposed outcrop surface. Temperatures can reach up to 30°C within the cryptoendolithic habitat and were found to exceed 10°C and 20°C for substantial periods of time (753 and 93 $h \cdot yr^{-1}$, respectively) during summer months, which is likely correlated to substantial net growth in these environments (Omelon et al. 2006). Furthermore, evidence of water infiltration into the subsurface resulting from rainfall or snowmelt and subsequent retention of this moisture in pore spaces leads to increased rates of photosynthesis due to increased light penetration and continuous irridation. The combination of these microenvironmental conditions generates elevated pH within pore waters, whereby rates of OH^- production by cyanobacteria and algae with an effective CCM exceeds rates of diffusion of $CO_2(g)$ into the water-saturated microenvironment. These high pH conditions greatly enhance silicate and quartz dissolution rates—for example, at pH 9.8, the solubility of quartz doubles, and at pH 10.8 it is almost five times the solubility at pH 7—resulting in the solubilization of the rock matrix near these photosynthesizing organisms. In contrast, sites dominated by microorganisms that do not produce high pH conditions experience increased rates of photosynthesis but with apparently negligible production of OH^-.

The sporadic nature of this rock exfoliation highlights the fact that generation of high pH conditions within these habitats requires the presence of liquid water that effectively limits CO_2 diffusion from the atmosphere, thereby requiring activation of microbial CCMs. Given the low number of precipitation events that occur in this region of the Canadian High Arctic, rapid solubilization of intergranular silica-rich cements is restricted to those periods of moisture infiltration into the subsurface. In contrast, during periods of arid conditions, all photosynthesizing microorganisms uptake atmospheric CO_2, resulting in little change in pH in the cryptoendolithic environment.

Direct evidence for silica dissolution through bioalkalization has been found in preliminary ESEM observations of etch pits on quartz grain surfaces overlain by cyanobacterial communities. Further documentation of such features will provide additional evidence for chemical weathering of silica-rich intergranular cements through the generation of high pH conditions by these microorganisms, and will be of interest to studies focusing on mechanisms that lead to the creation of terrestrial biosignatures.

Conclusions

The global ubiquity of cyanobacteria and algae in cryptoendolithic habitats and the generation of high pH conditions by those microorganisms with efficient CCMs suggests that bioalkalization could play a fundamental role in the chemical weathering of silica minerals (Schwartzman & Volk 1989). In addition, this pH shift has important implications for porosity development, release of essential nutrients, and mobilization of metals under high pH conditions. Understanding the biogeochemical dynamics of cryptoendolithic microorganisms is an important step towards a broader understanding of how phototrophic microorganisms control silica dissolution in terrestrial landscapes.

Acknowledgments

The authors wish to thank Canada's Atmospheric Environment Service and the Polar Continental Shelf Project for lodging and logistical support during field seasons. This work is supported by the Jackson School of Geosciences at the University of Texas at Austin, the Natural Sciences and Engineering Research Council of Canada, and the Canadian Space Agency. We sincerely thank the staff of the Eureka Weather Station for their dedicated field support, and Lisa Nguyen of UT Austin's Culture Collection of Algae for laboratory assistance.

References

Ascaso, C., Wierzchos, J. & Castello, R. 1998. Study of the biogenic weathering of calcareous litharenite stones caused by lichen and endolithic microorganisms. International *Biodeterioration and Biodegradation* 42: 29-38.

Badger, M.A., Price, G.D., Long, B.M. & Woodger, F.J. 2006. The environmental plasticity and ecological genomics of the cyanobacterial CO_2 concentrating mechanism. *Journal of Experimental Botany* 57: 249-265.

Badger, M.R. & Price, G.D. 2003. CO_2 concentrating mechanisms in cyanobacteria: molecular components, their diversity and evolution. *Journal of Experimental Botany* 54: 609-622.

Banares-Espana, E., Lopez-Rodas, V., Salgado, C., Costas, E. & Flores-Moya, A. 2006. Inter-strain variability in the photosynthetic use of inorganic carbon, exemplified by the pH compensation point, in the cyanobacterium *Microcystis aeruginosa*. *Aquatic Botany* 85: 159-162.

Bell, R.A. 1993. Cryptoendolithic algae of hot semiarid lands and deserts. *Journal of Phycology* 29: 133-139.

Bell, R.A., Athey, P.V. & Sommerfeld, M.R. 1986. Cryptoendolithic algal communities of the Colorado plateau. *Journal of Phycology* 22: 429-435.

Bennett, P.C. 1991. The dissolution of quartz in organic-rich aqueous systems. *Geochimica et Cosmochimica Acta* 55: 1781-1797.

Bennett, P.C. & Casey, W.H. 1994. Organic acids and the dissolution of silicates. In: E.D. Pittman & M. Lewan (eds.), *The Role of Organic Acids in Geological Processes*. Springer-Verlag.

Bennett, P.C., Rogers, J.R., Hiebert, F.K. & Choi, W.J. 2001. Silicates, silicate weathering, and microbial ecology. *Geomicrobiology Journal* 18: 3-19.

Bennett, P.C. & Siegel, D.I. 1987. Increased solubility of quartz in water due to complexation by dissolved organic compounds. *Nature* 326: 684-687.

Blum, J.D., Klaue, A., Nezat, C.A., Driscoll, C.T., Johnson, C.E., Siccama, T.G., Eagar, C., Fahey, T.J. & Likens, G.E. 2002. Mycorrhizal weathering of apatite as an important calcium source in base-poor forest ecosystems. *Nature* 417: 729-731.

Brady, P.V. & Walther, J.V. 1989. Controls on silicate dissolution rates in neutral and basic pH solutions at 25 C. *Geochimica et Cosmochimica Acta* 53: 2823-2830.

Budel, B., Weber, B., Kuhl, M., Pfanz, H., Sultemeyer, D. & Wessels, D. 2004. Reshaping of sandstone surfaces by cryptoendolithic cyanobacteria: bioalkalization causes chemical weathering in arid landscapes. *Geobiology* 2: 261-268.

Bungartz, F., Garvie, L.A.J. & Nash III, T.H. 2004. Anatomy of the endolithic Sonoran Desert lichen *Verrucaria rubrocincta* Breuss: implications for biodeterioration and biomineralization. *The Lichenologist* 36: 55-73.

Burford, E.P., Fomina, M. & Gadd, G.M. 2003. Fungal involvement in bioweathering and biotransformation of rocks and minerals. *Mineralogical Magazine* 67: 1127-1155.

Casamatta, D.A., Verb, R.G., Beaver, J.R. & Vis, M.L. 2002. An investigation of the cryptobiotic community from sandstone cliffs in southeast Ohio. *International Journal of Plant Science* 163: 837-845.

Chou, L. & Wollast, R. 1985. Steady-state kinetics and dissolution mechanisms of albite. *Amer. J. Sci.* 285: 963-993.

Cockell, C.S., McKay, C.P. & Omelon, C. 2003. Polar endoliths - an anti-correlation of climate extremes and microbial diversity. *International Journal of Astrobiology* 1: 305-310.

de la Torre, J.R., Goebel, B.M., Friedmann, E.I. & Pace, N.R. 2003. Microbial diversity of cryptoendolithic communities from the McMurdo Dry Valleys, Antarctica. *Applied and Environmental Microbiology* 69: 3858-3867.

Ferris, F.G. & Lowson, E.A. 1997. Ultrastructure and geochemistry of endolithic microorganisms in limestone of the Niagara Escarpment. *Canadian Journal of Microbiology* 43: 211-219.

Friedmann, E.I. 1982. Endolithic microorganisms in the Antarctic cold desert. *Science* 215: 1045-1053.

Friedmann, E.I., Friedmann, R.O. & McKay, C.P., 1981. Adaptations of cryptoendolithic lichens in the Antarctic desert. In: P. Jouventin, L. Masse &

P. Trehen (eds.), *Colloque sur les Ecosystemes Subantarctiques*. Paris: Comite National Francais des Recherches Antarctiques.

Friedmann, E.I., Kappen, L. & Garty, J. 1980. Fertile stages of cryptoendolithic lichens in the dry valleys of Southern Victoria Land. *Antarctic Journal of the United States* 15: 166-167.

Friedmann, E.I., McKay, C.P. & Nienow, J.A. 1987. The cryptoendolithic microbial environment in the Ross Desert of Antarctica: satellite-transmitted continuous nanoclimate data, 1984 to 1986. *Polar Biology* 7: 273-287.

Friedmann, E.I. & Ocampo-Friedmann, R. 1984. Endolithic microorganisms in extreme dry environments: Analysis of a lithobiontic habitat. In: M.J. Klug & C.A. Reddy (eds.), *Current Perspectives in Microbiology.* Washington, DC: American Society of Microbiology.

Gaylarde, P. & Gaylarde, C. 2004. Deterioration of siliceous stone monuments in Latin America: Microorganisms and mechanisms. *Corrosion Reviews* 22: 395-415.

Gerrath, J.F., Gerrath, J.A., Matthes, U. & Larson, D.W. 2000. Endolithic algae and cyanobacteria from cliffs of the Niagara Escarpment, Ontario, Canada. Canadian *Journal of Botany-Revue Canadienne De Botanique* 78: 807-815.

Giordano, M., Beardall, J. & Raven, J.A. 2005. CO_2 concentrating mechanisms in algae: mechanisms, environmental modulation, and evolution. *Annual Reviews of Plant Biology* 56: 99-131.

Hirsch, P., Eckhardt, F.E. W. & Palmer, R.J. 1995. Fungi active in weathering of rock and stone monuments. *Canadian Journal of Botany-Revue Canadienne De Botanique* 73: S1384-S1390.

Hirsch, P., Hoffmann, B., Gallikowski, C.C., Mevs, U., Siebert, J. & Sittig, M. 1988. Diversity and identification of heterotrophs from Antarctic rocks of the McMurdo Dry Valleys (Ross Desert). *Polarforschung* 58: 261-269.

Johnston, C.G. & Vestal, J.R. 1989. Distribution of inorganic species in two Antarctic cryptoendolithic microbial communities. *Geomicrobiology Journal* 7: 137-153.

Johnston, C.G. & Vestal, J.R. 1993. Biogeochemistry of oxalate in the Antarctic cryptoendolithic lichen-dominated community. *Microbial Ecology* 25: 305-319.

Kaplan, A. & Reinhold, L. 1999. CO_2 concentrating mechanisms in photosynthetic microorganisms. *Annual Rev. Plant Physiol. Plant Mol. Biol.* 50: 539-570.

Kevekordes, K., Holland, D., Haubner, N., Jenkins, S., Koss, R., Roberts, S., Raven, J.A., Scrimgeour, C. M., Shelly, K., Stojkovic, S. & Beardall, J. 2006. Inorganic carbon acquisiton by eight species of *Caulerpa* (Caulerpaceae, Chlorophyta). *Phycologia* 45: 442-449.

Knauss, K.G. & Wolery, T.J. 1986. Dependence of albite dissolution kinetics on pH and time at 25°C and 70°C. *Geochim. Cosmochim. Acta* 50: 2481-2497.

Knauss, K.G. & Wolery, T.J. 1988. The dissolution kinetics of quartz as a function of pH and time at 70°C. *Geochimica et Cosmochimica Acta* 52: 43-53.

Omata, T., Price, G.D., Badger, M.R., Okamura, M., Gohta, S. & Ogawa, T. 1999. Identification of an ATP-binding cassette transporter involved in bicarbonate uptake in the cyanobacterium *Synechococcus* sp. strain PCC 7942. *Proceedings of the National Academy of Sciences of the United States of America* 96: 13571-13576.

Omelon, C.R., Pollard, W.H. & Ferris, F.G. 2006. Environmental controls on microbial colonization of High Arctic cryptoendolithic habitats. *Polar Biology* 30: 19-29.

Omelon, C.R., Pollard, W.H. & Ferris, F.G. 2007. Inorganic species distribution and microbial diversity within High Arctic cryptoendolithic habitats. *Microbial Ecology.*

Price, G.D., Maeda, S.-i., Omata, T. & Badger, M.A. 2002. Modes of active inorganic carbon uptake in the cyanobacterium, *Synechococcus* sp. PCC7942. *Functional Plant Biology* 29: 131-149.

Price, G.D., Woodger, F.J., Badger, M.A., Howitt, S.M. & Tucker, L. 2004. Identification of a SulP-type bicarbonate transporter in marine cyanobacteria. *PNAS* 101: 18228-18233.

Schwartzman, D.W. & Volk, T. 1989. Biotic enhancement of weathering and the habitability of Earth. *Nature* 340: 457-460.

Selbmann, L., de Hoog, G.S., Mazzagalia, A., Friedman, E. I. & Onofri, S. 2005. Fungi at the edge of life: cryptoendolithic black fungi from Antarctic desert. *Studies in Mycology* 51: 1-32.

Shibata, M., Ohkawa, H., Kaneko, T., Fukuzawa, H., Tabata, S., Kaplan, A. & Ogawa, T. 2001. Distinct constitutive and low-CO_2-induced CO_2 uptake systems in cyanobacteria: genes involved and their phylogenetic relationship with homologous genes in other organisms. *PNAS* 98: 11789-11794.

Sigler, W.V., Bachofen, R. & Zeyer, J. 2003. Molecular characterization of endolithic cyanobacteria inhabiting exposed dolomite in central Switzerland. *Environmental Microbiology* 5: 618-627.

Stillings, L.L., Drever, J.I., Brantley, S.L., Sun, Y. & Oxburgh, R. 1996. Rates of feldspar dissolution at pH 3-7 with 0-8 mM oxalic acid. *Chemical Geology* 132: 79-90.

Wierzchos, J. & Ascaso, C. 1996. Morphological and chemical features of bioweathered granitic biotite induced by lichen activity. *Clays and Clay Minerals* 44: 652-657.

—Plenary Paper—

Thermal State of Permafrost in Alaska During the Fourth Quarter of the Twentieth Century

T. E. Osterkamp
Geophysical Institute, University of Alaska, Fairbanks, Alaska, U.S.A.

Abstract

Permafrost temperatures in Alaska increased during the fourth quarter of the twentieth century at sites north of the Brooks Range from the Chukchi Sea to Canada, south along a transect from Prudhoe Bay to Gulkana, and at other sites. Tentative results are presented concerning the characteristics of the warming. Meteorological records, permafrost temperature measurements, thermokarst studies, and modeling efforts suggest the warming occurred statewide. Its magnitude along the transect was 3 to 4°C for the Arctic Coastal Plain, 1 to 2°C for the Brooks Range, and 0.3 to 1°C south of the Yukon River. The warming was seasonal, primarily in winter. Active layer thicknesses on the Arctic Coastal Plain did not increase. Thawing at the permafrost surface and base is occurring and new thermokarst terrain has developed. Probable causes of the warming and thawing include changes in air temperatures, snow cover effects, and combinations of these.

Keywords: borehole temperatures; climate warming; permafrost; thermokarst

Introduction

Air temperatures in Alaska warmed from the late 1800s until near the end of the second quarter of the twentieth century (Hansen & Lebedev 1987). There was a cooling during the third quarter and, in the permafrost regions of Alaska, a step-like increase in air temperatures during the fourth quarter (1976/1977, Hartmann and Wendler 2003). This warming peaked in the early 1980s and was followed by decreased air temperatures into the mid-1980s. Temperature trends from the late 1970s to the end of the 20th century were sometimes warmer although many sites had little or no warming or a cooling. From the cooler mid-1980s to the end of the century, most sites showed a warming trend. The first 6 years of the 21st century have been consistently warm, typically about the same as the period around 1980. Snow covers were generally thick during the third quarter and relatively thin during the early 1980s. Snow cover thicknesses during the 1990s were typically much greater than during the 1980s. The recent warming may be the continuation of the long term warming or a new unrelated warming event.

The thermal state of Alaskan permafrost has responded to these climatic changes and perhaps to other factors. It appears there were two permafrost warming events; a long-term warming that was initiated in the early 1900s and a recent warming (since 1976/1977).

Past international conferences on permafrost have examined climate-permafrost interactions and have documented permafrost warming in Alaska. This paper reiterates, updates, and extends reviews of the thermal state of permafrost in Alaska by the U.S. Geological Survey and University of Alaska (Lachenbruch et al. 1982, Lachenbruch & Marshall 1986, Osterkamp et al. 1984, 1987, Lachenbruch et al. 1988, Clow et.al 1991, Lachenbruch 1994, Osterkamp & Romanovsky 1999, Romanovsky et al. 2003, Osterkamp 1983, 2003a, b, 2005, & 2007a, b). The data used herein are from the U.S. Geological Survey studies (Lachenbruch & Marshall 1986, Clow & Urban 2002) and the University of Alaska studies (Fig.1). (See Osterkamp (2003b) for methods and site information.) The paper is primarily concerned with the characteristics, impacts, and causes of permafrost warming during the last quarter of the twentieth century and attempts to provide at least tentative answers to questions regarding this warming. The effort is hampered by the lack of data even in the northwest and along a north-south transect of Alaska where most of the data are concentrated. This makes it difficult to arrive at definitive conclusions about the thermal state of the permafrost. However a better understanding of permafrost conditions is emerging from efforts that combine modeling, weather data, and thermokarst studies with temperature measurements.

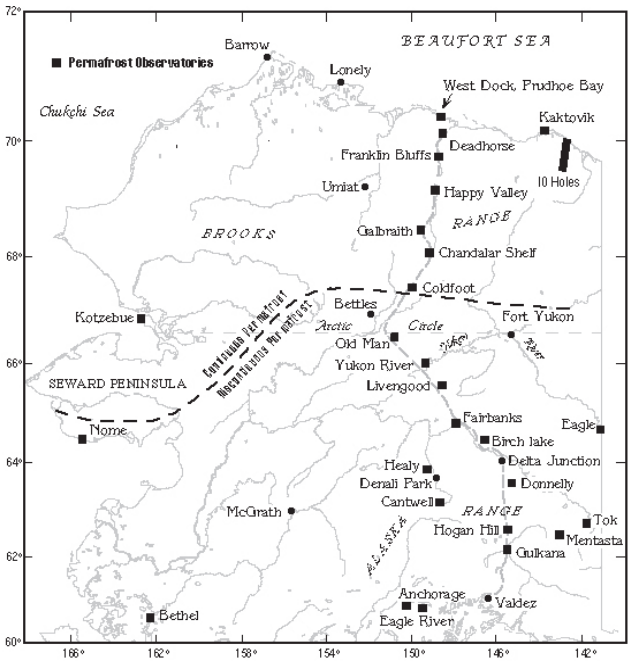

Figure 1. Location of the Alaskan transect and other sites. USGS sites are primarily in northwest Alaska.

Review and Discussion

Effects of climate on permafrost

The effects of climate (here the averaged weather, primarily air temperature and precipitation) on permafrost are difficult to determine because of sparse data and a multitude of non-climatic factors that can influence the thermal state of permafrost. These factors include terrain (topography, slope, aspect, geomorphology), hydrology (surface drainage, site wetness, proximity of nearby water bodies, presence of underground water), vegetation (succession, insulation, insolation, snow interception), geology (type of soil and rock, tectonic setting and geothermal heat flow), and disturbances (human, animal, fire, and flooding events) (Osterkamp & Jorgenson, in press). The factors operate at different time scales (days to millennia) and spatial scales (local to continental). The effects of changes in some of them (e.g., geomorphology, vegetation (succession), disturbances) have the potential for being mistaken for changes in climate as do other related factors (e.g., rapid sedimentation at the ground surface, three dimensional heat flow, and vertical variations in thermal conductivity).

The permafrost surface is separated from effects of air temperatures and other climatic factors by vegetation, snow cover in winter, and an active layer that freezes and thaws annually. Heat and mass transport processes, including coupled and advective processes, and phase change in these materials influence the surface temperature of the permafrost (Outcalt et al. 1975, Goodrich 1982, Smith & Riseborough 1983, Lachenbruch 1994, Zhang et al. 1996, 1997). There are also intricate thermal feedback effects such as the effects of air temperature and moisture on vegetation, the ensuing effects of vegetation and wind on snow cover, and the effects of the resulting snow cover on permafrost surface temperatures. Consequently, the relationships between climate and permafrost surface temperature are exceedingly complex. Even the case of air temperature is not straightforward. Warming of annual mean air temperatures can be a result of a general change in all seasons or seasonal changes such as warmer or longer summers (defined here as the period when the ground is snow free) or warmer or shorter winters (when snow is on the ground). Since winters are longer than summers in permafrost areas, cooler summer temperatures can be offset by warmer winter temperatures resulting in a net warming.

The net result of a snow cover is that it increases mean annual ground surface temperatures. The magnitude of the warming depends on the timing and duration of the snow cover, its accumulation (thickness) and melting history, and the effects of macrostructure (wind slab, depth hoar) on its properties (Goodrich 1982, Goodwin et al. 1983, Zhang et al. 1996, Zhang 2005). Interactions of wind, microrelief, and vegetation with the snow cover also influence the surface temperature of permafrost (Zhang et al. 1997).

The above considerations suggest that, when permafrost warms, the warming cannot be automatically attributed to increasing air temperatures and/or the effects of changes in snow cover thickness. Nevertheless, modeling studies confirm the primary role of air temperatures and the effects of changes in snow cover on the surface temperature of permafrost (Outcalt 1975, Goodrich 1982). Applications of models to field conditions show that, using measured daily air temperatures and snow cover thicknesses as input data to drive calibrated site specific conductive numerical models that include phase change and use realistic thermal parameters taking into account site conditions (wetness and others), typically produces remarkable agreement between calculated and measured active layer and permafrost temperatures (Zhang et al. 1997, Osterkamp & Romanovsky 1997, Osterkamp and Romanovsky, 1999; Romanovsky and Osterkamp 2000). While mass transport, advective, and coupled processes are known to occur in the snow cover, vegetative mat, and active layer, they appear to be of secondary importance in influencing long-term permafrost surface temperatures except in certain settings. The reasons for this are not known but may include cancellation of effects, shortness of their duration, and others.

Characteristics of the warming

For the long-term event, temperature profiles in deep boreholes generally indicate an increase at the permafrost surface of 2 to 4°C in northwest Alaska. Warming did not begin synchronously at all sites, not all sites showed a warming, and the results were not readily contourable (Lachenbruch & Marshall 1986, Lachenbruch et al. 1988, Clow et al. 1991).

For the recent warming during the last quarter of the twentieth century, observations show that permafrost in warmed north of the Brooks Range from the Chukchi Sea Coast to the Alaska-Canada border, south along a transect from Prudhoe Bay to Gulkana and up to 300 km from the transect (Fig. 1, Clow & Urban 2002, Osterkamp 2003a, 2005, 2007a, Osterkamp & Jorgenson 2005). Borehole temperatures at Prudhoe Bay (Fig. 2), thermokarst observations, basal thawing measurements, and modeling investigations elsewhere suggest that permafrost temperatures increased statewide coincident with the increase in air temperatures that began in 1976/1977 in Alaska (Osterkamp 2007a). The initial permafrost warming peaked in the early 1980s and then cooled into the mid-1980s. Arctic sites began warming again about 1986 and Interior sites about 1988 (Fig. 2). The timing of this warming was somewhat later in the western Arctic (Chukchi Sea to the Colville River), not long before 1989 (Clow, personal communication, 2006). Warming generally continued through the 1990s although some sites leveled off or cooled near the end of the century while some continued to warm. The magnitude of the total warming at the permafrost surface through 2003 falls into three latitudinal groups; an average of 3°C for the western Arctic and a range of 3 to 4°C for the Arctic Coastal Plain near Prudhoe Bay, 1 to 2°C along the transect through the Brooks Range including its northern and southern foothills, and 0.3 to 1°C south of the Yukon River (Osterkamp 2005). On the Arctic Coastal Plain, the magnitude of the recent warming is comparable to that of the long term warming but it occurred over a much shorter time period.

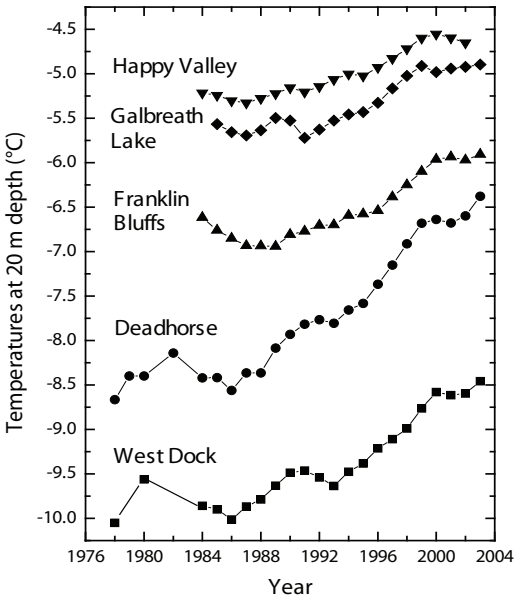

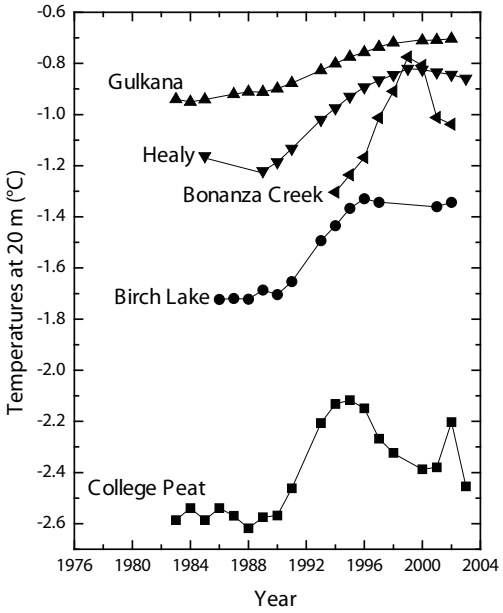

Figure 2. Temperatures (20 m depth) for selected sites.

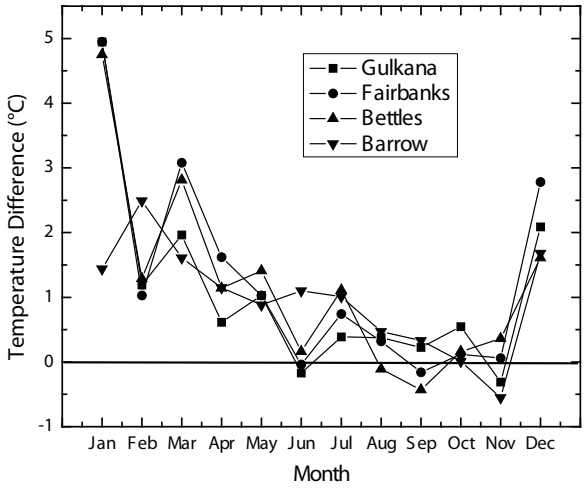

Figure 3. Increases in mean monthly air temperatures for the period after (1977-1996) compared to before (1957-1976) the recent warming.

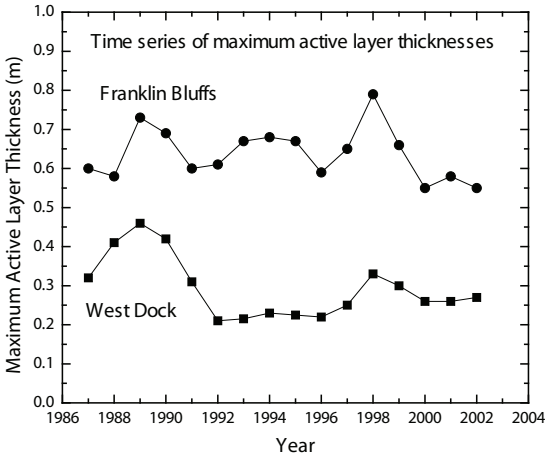

Figure 4. Time series of maximum active layer thicknesses for two sites on the Arctic Coastal Plain.

Measurements show that permafrost warmed north of Kotzebue, near Cantwell, and at Eagle River; sites that are 300 km or more from the transect (Osterkamp 2007a). These observations from widely separated areas coupled with weather data and other observations suggest that the scenario developed above for northern Alaska and the transect may also hold, with some differences in timing and magnitude, in other permafrost areas in the state (Osterkamp 2007a). However, some sites cooled over the same period and a site near Eagle had not warmed by 1994 indicating that there may be other areas that are exceptions to the warming.

The regime shift that occurred in 1976/1977 was seasonal, characterized by increased air temperatures for mid to late winter months (Hartmann & Wendler 2003). There was little change in summer and early winter air temperatures (Fig. 3). This seasonality also occurred in permafrost surface temperatures at the Deadhorse and Franklin Bluffs sites. Again, the general nature of the warming (Fig. 3) suggests a similar statewide seasonality for the permafrost warming with possible exceptions (Osterkamp 2005).

While the permafrost warmed 3 to 4°C, maximum active layer thicknesses at nearby sites on the Arctic Coastal Plain did not show increasing trends from 1987 to 2002 (Fig. 4, Osterkamp 2005). This is a direct result of the observed seasonality in air temperatures. Since the warming occurred primarily in winter, active layer thicknesses would not be expected to be significantly influenced by the warming and cannot be used as an indicator of the warming. The widespread seasonality of the air temperature increases (Fig. 3) suggests that statewide active layer thicknesses may not have been generally influenced significantly by the warming.

Natural thawing of the permafrost from the top downward has been observed to occur in a tundra and a forest site at a rate of about 0.1 m/yr in response to the permafrost warming (Osterkamp 2005). Basal thawing is occurring at four sites with shallow (<40 m thickness) discontinuous permafrost.

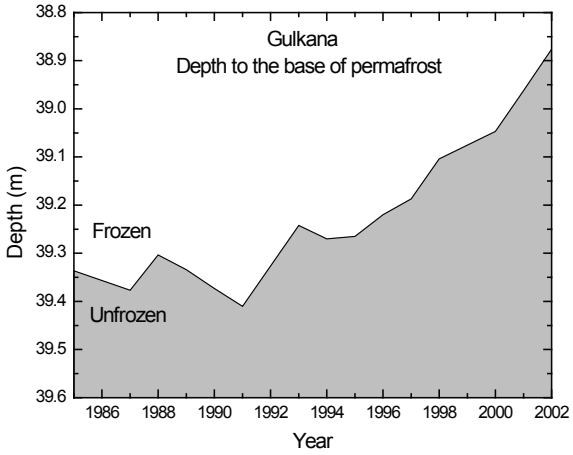

Figure 5. Thawing at the base of the permafrost at Gulkana.

Sites with thicker permafrost (>60 m) are generally warming at depth. At Gulkana, thawing at the base of the permafrost began about 1992 and proceeded at a mean rate of ~ 0.04 m/yr until 2000 when it accelerated to ~ 0.09 m/yr (Fig. 5, Osterkamp 2005). These basal thawing rates are much greater than predicted theoretically. If basal thawing at Gulkana was the result of a step change in permafrost surface temperature, the change would have occurred in 1976 coincident with the statewide warming of air temperatures. Thawing at the boundaries of unfrozen ground with permafrost (taliks in the continuous permafrost and isolated permafrost masses elsewhere) as a result of permafrost warming is predicted (Osterkamp 2003, 2005) but has not been investigated.

Thermokarst terrain was absent at a site near Healy, when the site was established (1985) but now exists in several places throughout the area (Fig. 6). Maximum thaw settlement was about 1.1 m in a pit at the borehole pipe and up to about 1½ m in the surrounding area (Osterkamp et al., submitted). New thermokarst terrain, formed by thawing ice-rich permafrost, has been observed, not only in Interior Alaska, but also in Northern Alaska where old ice wedges have been thawing since 1989 (Osterkamp et al. 2000, Jorgenson et al. 2001, Jorgenson et al. 2006).

Causes

For the recent warming, the data reviewed above suggest that permafrost generally warmed statewide coincident with increasing air temperatures in 1976/1977. There was not a pattern of corresponding changes in snow cover at this time suggesting this initial warming may have been primarily a result of increased air temperatures. Increasing permafrost temperatures in the late 1980s and into the 1990s may have been in response to a series of winters with thick snow covers (Osterkamp & Romanovsky 1999). This appears to be the case for Healy (Osterkamp 2007b) and Gulkana (Fig. 7) and, at least partially, for other sites. At some sites, air temperatures increased less than permafrost surface temperatures implicating snow cover effects in the observed warming. At Barrow, modeling results have shown that snow cover effects were involved in the century-long warming and

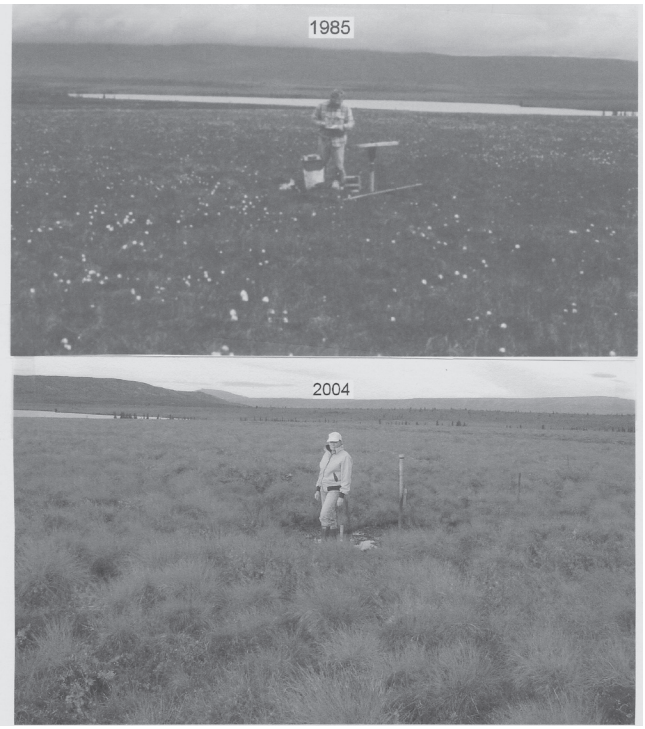

Figure 6. Photos showing thermokarst and changes in surface mophology over two decades at the Healy site.

the recent warming (Zhang & Osterkamp 1993). Stieglitz et al. (2003) have shown that about half the recent warming there was due to air temperature changes and half due to snow cover effects.

Since new thermokarst was observed at Healy coincident with warming permafrost, it appears that permafrost thawing and development of thermokarst terrain was also a result of snow cover effects there (Osterkamp et al. submitted).

Summary

This paper uses borehole temperature measurements, basal thawing measurements, thermokarst observations, modeling results, and weather data in an attempt to reconstruct the thermal state of permafrost in Alaska during the last quarter of the twentieth century. This effort is hindered by the sparsity of long-term permafrost temperature data and the lack of interpretive studies which make the conclusions tentative.

During the last quarter of the twentieth century, permafrost warmed north of the Brooks Range from the Chukchi Sea to the Alaska-Canada border, south along a transect from Prudhoe Bay to Gulkana and up to 300 km from the transect. Sporadic measurements also show that permafrost warmed at other widely separated sites including north of Kotzebue, near Cantwell, and at Eagle River. It appears likely that permafrost temperatures increased statewide coincident with the statewide increase in air temperatures that began in 1976/1977. Some sites did not warm indicating there may be other sites that are exceptions to the warming.

The initial permafrost warming peaked in the early 1980s

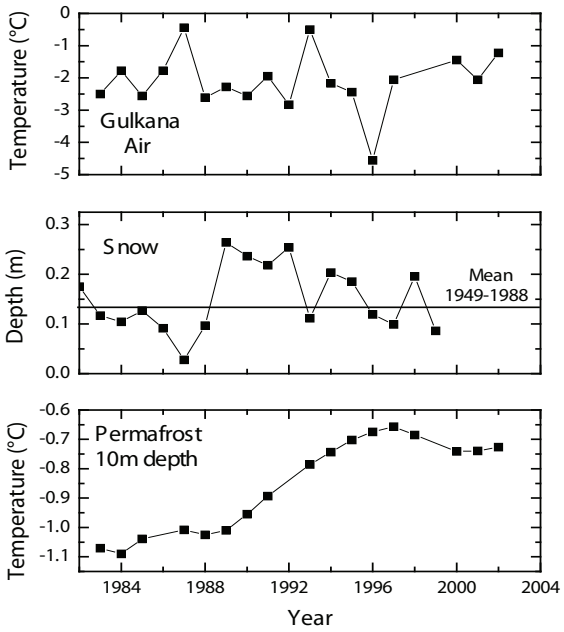

Figure 7. There was a trend of increasing permafrost temperatures at the Gulkana site (1989-1997) while air temperatures decreased and snow covers were thicker than the long term average.

and then cooled into the mid-1980s. Arctic sites began warming again about 1986 (Western Arctic prior to 1989) and Interior sites about 1988. Warming generally continued through the 1990s although some sites leveled off or cooled near the end of the century while some continued to warm.

The magnitude of the total warming at the permafrost surface was up to 4°C for the Arctic Coastal Plain, 1 to 2°C along the transect through the Brooks Range including its northern and southern foothills, and 0.3 to 1°C south of the Yukon River.

Increased air temperatures in the two decades after 1976/1977 were seasonal, a result of warmer winter temperatures with little change in summer conditions. This seasonality also occurred in permafrost surface temperatures at the Deadhorse and Franklin Bluffs sites. It is suggested that this was likely the case for other areas of the state. While permafrost temperatures increased by 3 to 4 °C, maximum active layer thicknesses did not show an increasing trend.

Thawing at the permafrost table and base has been observed in shallow permafrost and new thermokarst terrain has been observed.

Warming of the permafrost in the Arctic Coastal Plain in the late 1970s was probably caused primarily by increased air temperatures and, in Interior Alaska during the late 1980s and into the 1990s, primarily by increased snow cover thicknesses. At a few sites in Interior Alaska and for certain time periods, the permafrost warmed entirely because of snow cover effects. Generally, both air temperatures and snow cover effects appear to have contributed to the permafrost warming.

A thorough study of the effects of past snow conditions is needed. However, due to the complex and non-linear nature of snow cover effects, calibrated site-specific numerical models are required to quantify the relative contributions of snow and air temperatures to warming and thawing of the permafrost.

Acknowledgments

This research was supported by the Arctic Natural Sciences Program (most recently #0520578) and ARCSS, Office of Polar Programs at NSF, Army Research Office, U. S. Dept. of Energy, NIGEC (Western Regional Center), Asahi Beer Company, NSF and USDA Long Term Ecological Research Program and by the State of Alaska. The data are available on-line for use by other researchers at http://nsidc.org/data/arcss034.html and http://nsidc.org/data/arcss106.html. The data, through 2003, are of high quality with a resolution of 3 to 5 mK and an accuracy better than 10 mK. Contact the author if you need further information (ffteo@uaf.edu).

References

Clow, G.D., Lachenbruch, A.H. & McKay, C.P. 1991. Inversion of borehole temperature data for recent climatic changes: Examples from the Alaskan Arctic and Antarctica. *Proc. Int. Conf. on the Role of Polar Regions in Global Change*, 11-15 June, ed. by G. Weller, C.L. Wilson, and B.A.B. Serverin, Geophysical Institute, Univ. of Alaska, Fairbanks, AK.

Clow, G.D. & Urban, F.E. 2002. Largest permafrost warming in northern Alaska during the 1990s determined from GTN-P borehole temperature measurements. *EOS, Trans. AGU*, 83, (47): F258.

Goodrich, L.E. 1982. The influence of snow cover on the ground thermal regime. *Can. Geotech. J.*, 19: 421-432.

Goodwin, C.W., Brown, J. & Outcalt, S.I. 1983. Potential responses of permafrost to climatic warming. *Conf. Proc.: Potential effects of carbon dioxide-induced climatic changes in Alaska, Misc. Pub*. 83-1: 92-105, edited by J.H. McBeath, Univ. of Alaska, Fairbanks, AK.

Hansen, J. & Lebedev, S. 1987. Global trends of measured surface air temperatures. *J. Geophys. Res*., 92(D11): 13,345-13,372.

Hartman, B. & Wendler, G. 2003. Manifestation of the Pacific decadal oscillation shift of 1976 in Alaskan climatology. *Proc. AMS 7th Conf. Polar Meteorology and Oceanography and Joint Symp. on High-Latitude Climate Variation*, 12-16 May, Hyannis, MA.

Jorgenson, M.T., Racine, C.H., Walters, J.C. & Osterkamp, T.E. 2001. Permafrost degradation and ecological changes associated with a warming climate in central Alaska. *Climatic Change*, 48(4): 551-579.

Jorgenson, M.T., Shur, Y.L. & Pullman, E.R. 2006. Abrupt increase in permafrost degradation in Arctic Alaska. *Geophys. Res. Letters*, 33, (L02503): doi:10.1029/2005GL024960.

Lachenbruch, A.H. 1994. Permafrost, the active layer, and changing climate. *Open file report* 94-694, U.S. Geological Survey, Menlo Park, CA, 43 pp.

Lachenbruch, A.H., Sass, J.H., Marshall, B.V. & Moses, T.H. 1982. Permafrost, heat flow and the geothermal regime at Prudhoe Bay, Alaska, *J. Geophys. Res*., 87(B11): 9301-9316.

Lachenbruch, A.H. & Marshall, B.V. 1986. Changing climate: Geothermal evidence from permafrost in the Alaskan Arctic. *Science* 234: 689-696.

Lachenbruch, A.H., Cladouhos, T.T. & Saltus, R.W. 1988. Permafrost temperature and the changing climate. *Proc. 5th Int. Conf. on Permafrost*, 3: 9-17, 2-5 August, edited by K. Senneset, Tapir Publishers, Trondheim, Norway.

Osterkamp, T.E. 1983. Response of Alaskan permafrost to climate, *Final Proc., 4th Int. Conf. on Permafrost,* p. 145-152, 17-22 July, NAS, Washington D.C.

Osterkamp, T.E. 1994. Evidence for warming and thawing of discontinuous permafrost in Alaska, *EOS, Trans. AGU*. 75(44): 85.

Osterkamp, T.E. 2003a. A thermal history of permafrost in Alaska, *Proc. 8th Int. Conf. on Permafrost*, 2: 863-868, edited by M. Phillips, S.M. Springman, L.U. Arenson, A.A. Balkema, Lisse, The Netherlands.

Osterkamp, T.E. 2003b. Establishing long-term permafrost observatories for active layer and permafrost investigations in Alaska: 1977-2002. *Permafrost and Periglacial Proc.* 14 (4): 331-342.

Osterkamp, T.E. 2005. The recent warming of permafrost in Alaska. *Global and Planetary Change*, 49: 187-202.

Osterkamp, T.E. 2007a. Characteristics of the recent warming of permafrost in Alaska. *J. Geophys. Res*., 112, F02S02, doi:10.1029/2006JF000578.

Osterkamp, T.E. 2007b. Causes of warming and thawing permafrost in Alaska. *EOS*, 88(48): 3-4, 27 November.

Osterkamp, T.E. & Payne, M.W. 1981. Estimates of permafrost thickness from well logs in northern Alaska. *Cold Regions Science and Technology* 5: 13-27.

Osterkamp, T.E. & Romanovsky, V.E. 1997. Freezing of the active layer on the Coastal Plain of the Alaskan Arctic. *Permafrost and Periglacial Proc*. 8: 23-44.

Osterkamp, T.E. & Romanovsky, V.E. 1999. Evidence for warming and thawing of discontinuous permafrost in Alaska. *Permafrost and Periglacial Proc*. 10: 17-37.

Osterkamp, T.E. & Jorgenson, J.C. 2005. Warming of permafrost in the Arctic National Wildlife Refuge. *Permafrost and Periglacial Proc*. 16: 1-5.

Osterkamp, T.E. & Jorgenson, M.T., in press, Permafrost conditions and processes, *Geological Monitoring Manual*, Geological Society of America.

Osterkamp, T.E., Gosink, J.P. & Kawasaki, K. 1984. Permafrost temperature measurements in an Alaskan transect: Preliminary results. *Workshop on Permafrost Geophysics*, Spec. Rept. 85-5, U.S. Army CRREL, Hanover, NH.

Osterkamp, T.E., Gosink, J.P. & Kawasaki, K. 1987. Measurements of permafrost temperatures to evaluate the consequences of recent climate warming. Final report, Contract 84 NX 203 F 233181, Alaska Dept. of Transportation and Public Facilities, Fairbanks, Alaska.

Osterkamp, T.E., Viereck, L., Shur, Y., Jorgenson, M.T., Racine, C.H., Doyle, A.P. & Boone, R.D. 2000. Observations of thermokarst in boreal forests in Alaska. *Arctic, Antarctic, and Alpine Res*. 32(3): 303-315.

Outcalt, S.I., Goodwin, C., Weller, G. & Brown, J. 1975. Computer simulation of snowmelt and soil thermal regime at Barrow, Alaska. *Water Resour. Res*. 11(5): 709-715.

Romanovsky, V.E. & Osterkamp. T.E. 1997. Thawing of the active layer on the coastal plain of the Alaskan Arctic. *Permafrost and Periglacial Proc*. 8(1): 1-22.

Romanovsky, V.E. & Osterkamp, T.E. 2000. Effects of unfrozen water on heat and mass transport processes in the active layer and permafrost. *Permafrost and Periglacial Proc.* 11: 219-239.

Romanovsky, V.E., Sergueev, D.O. & Osterkamp, T.E. 2003. Spatial and temporal variations in the active layer and near-surface permafrost temperatures in Northern Alaska, *Proc. 8th Int. Conf. on Permafrost*, 2: 989-994, edited by M. Phillips, S.M. Springman, L.U. Arenson, A.A. Balkema, Lisse, The Netherlands.

Shur, Y.L., Hinkel, K.M. & Nelson, F.E. 2005. The transient layer: Implications for geocryology and climate change science. *Permafrost and Periglacial Proc.* 16: 5-17.

Smith, M.W. & Riseborough, D.W. 1983. Permafrost sensitivity to climate change. *Proc.4th Int. Conf. on Permafrost*, pp. 1178- 1183, NAS, Washington, D.C.

Stieglitz, M., Dery, S.J., Romanovsky, V.E. & Osterkamp, T.E. 2003. The role of snow cover in the warming of arctic permafrost. *Geophys. Res. Letters* 30(13): 1721, doi:10.1029/2003GL017337.

Zhang, T. 2005. Influence of the seasonal snow cover on the ground thermal regime: An overview. *Rev. Geophys*. 43, RG4002, doi:10.1029/2004RG000157.

Zhang, T. & Osterkamp, T.E. 1993. Changing climate and permafrost temperatures. *Proc. 6th Int. Conf. on Permafrost*, p. 783-788, 5-9 July, South China University of Technology Press, Wushan, Guangzhou, PRC.

Zhang, T., Osterkamp, T.E. & Stamnes, K. 1996. Influence of the depth hoar layer of the seasonal snow cover on the ground thermal regime. *Water Resour. Res*. 32(7): 2075-2086.

Zhang, T., Osterkamp, T.E. & Stamnes, K. 1997. Effects of climate on the active layer and permafrost in Alaska north of the Brooks Range. *Permafrost and Periglacial Proc*. 8(1): 45-68.

Field Trials of Surface Insulation Materials for Permafrost Preservation

James M. Oswell
Colt Worley Parsons Ltd./Naviq Consulting Inc., Calgary, Canada
Jack R. Everts
Exxon Mobil Development Company./Imperial Oil Resources Ventures Limited, Calgary, Canada

Abstract

Two test sites were initiated to examine the use of several insulating-type materials for potential use as thermal mitigation strategies on the Mackenzie Gas Project. The Woodenhouse test site, located northeast of Slave Lake, Alberta, was constructed in March 2005. The Norman Wells, Northwest Territories, test site was constructed in March 2006. At both sites, flax straw bales and white reflective surfaces were being tested. A test cell of shredded wood was also tested at the Woodenhouse test site. Each test cell was approximately 20 m by 20 m in plan area. A control cell was also present. Temperatures were measured at the ground surface and at selected depths to 10 m. All temperatures were recorded on dataloggers. The performance of the test materials was examined from several perspectives including thermal performance, degradation/deterioration, and imported weed growth. Compared to the control cell, straw bales provided the best thermal protection, followed by shredded wood. The reflective surface was marginally better than the control.

Keywords: monitoring; pipeline; surface insulation; thermal mitigation.

Introduction

The Mackenzie Gas Project (MGP) is intended to transport natural gas from the Mackenzie Delta area in northern Canada through the Northwest Territories to connect with distribution pipelines in northern Alberta. The proposed pipeline will have an initial capacity of about 0.8 billion cubic feet per day (bcfd), with a fully expanded capacity of nearly 1.8 bcfd. Along the route, the pipeline will traverse approximately 200 km of continuous permafrost and about 1000 km of discontinuous permafrost. The pipeline will be designed as a fully buried system.

Right-of-way clearing and pipeline construction will alter the geothermal character of the permafrost within the right-of-way, which if not mitigated, will inevitably result in permafrost warming, deepening of the active layer and other effects. For sloping terrain along the route, these geothermal changes could result in instability of the slopes, if not mitigated. There are approximately 160 identified slopes along the route that may require mitigation to ensure long-term stability.

Slope stability issues along pipeline routes underlain by permafrost have been addressed in the past. Perhaps the most important case history for mitigation of the effects of thawing permafrost on slope stability was the Norman Wells oil pipeline, owned and operated by Enbridge Pipelines (NW) Inc. This pipeline is fully buried in discontinuous permafrost along its 868 km route that somewhat parallels the proposed Mackenzie gas pipeline between Norman Wells and Alberta. To address the thawing of permafrost on slopes and related instability that could result, a layer of wood chips was installed on approximately 33% of Norman Wells pipeline slopes. The design and performance of the wood chip-covered slopes was documented by Hanna and McRoberts (1988), Hanna et al. (1994) and Oswell et al. (1998).

Given the design, construction and operational differences between the Mackenzie gas project and the Norman Wells pipeline project (for example, right-of-way width, pipeline operating temperatures, diameters, ground temperatures), the MGP decided to conduct field tests to assess the thermal properties of several surface insulation materials that may be useful in mitigating permafrost degradation.

Surface Insulation Field Trials

Test materials

The field trials tested the following three different materials:

- Shredded wood
- Straw bales
- Reflective surface (geotextile)

The shredded wood material consists of well-graded wood fibers ranging in lengths from about 200 mm to about 50 mm. This material differs from the wood chips used on the Norman Wells pipeline, which were typically flat wood particles being circular to elongated and up to about 25 mm to 40 mm in diameter.

The straw bales were standard rectangular flax straw bales sized at about 0.4 m high, 0.51 m wide and 1.1 m long, and weighing about 30 kg. Flax was selected because it was very slow to decompose and it was of low palatability to animals such as moose and caribou.

The reflective surface material consisted of a white geotextitle, intended to reflect the summer solar radiation from the ground surface while allowing the cold winter temperatures to penetrate the ground. Reflective materials have been used to reduce snow and ice ablation (Poplin et al. 1991).

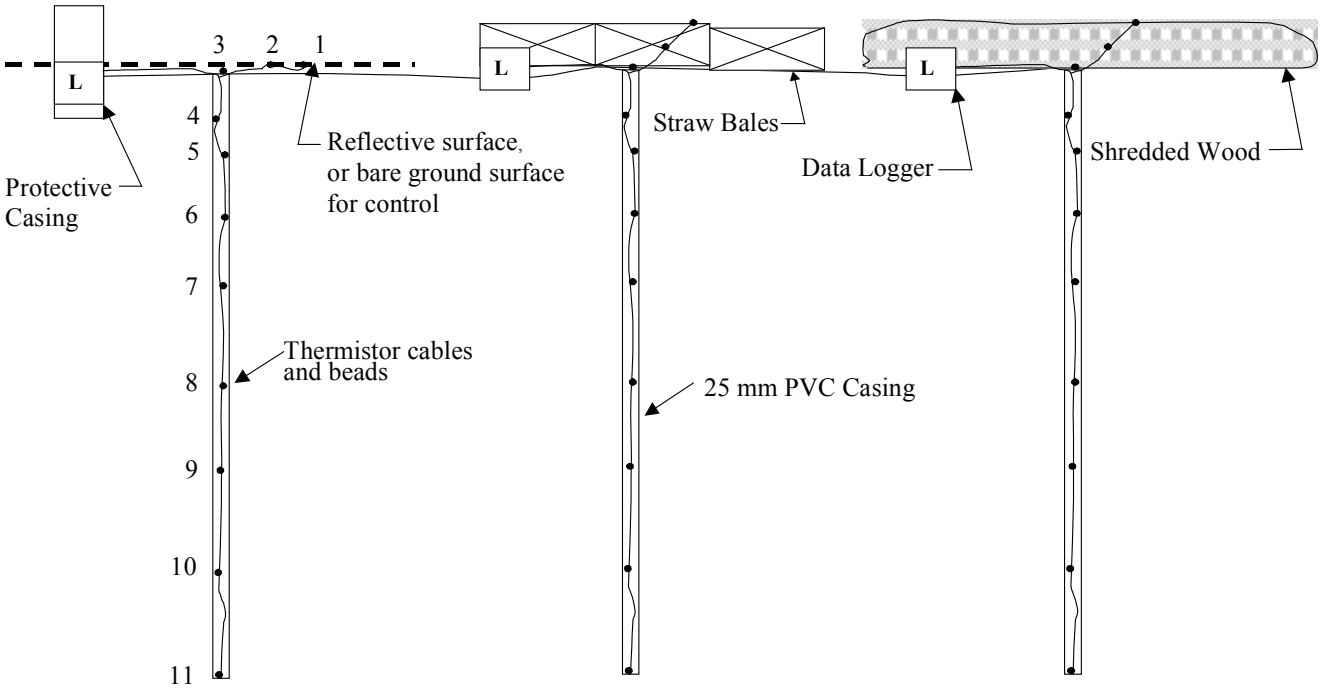

Figure 1. Layout of test cells (not to scale) and associated instrumentation.

Test site and set-up

Two test sites were established; the first site was in northern Alberta, near the community of Slave Lake, at a compressor station site named Woodenhouse. The mean annual air temperature was about +1.3°C. The test site area was previously cleared of all vegetation and the ground surface consisted of granular fill over unfrozen mineral soil. The second test site was in Norman Wells, Northwest Territories, which has a mean annual air temperature of about -5.5°C. This site was initially forested with sparse spruce trees, but was cleared of trees at the start of the test program. The ground surface consisted of the native organic mat underlain by mineral soils that was frozen, but considered to be warm permafrost.

The Woodenhouse test site consisted of three test cells plus a control. The test cells were straw bales, shredded wood and a reflective surface, each 20 m by 20 m in plan dimensions. A control cell was installed to provide baseline data for comparison. The Norman Wells test site was the same as the Woodenhouse site except that there was no shredded wood test cell.

The ground temperatures were monitored using an eleven bead thermistor cable attached to a data logger, recording temperatures at 12-hour intervals. The temperatures were measured at the following depths: 0 m, 0.5 m, 1.0 m, 2.0 m, 3.0 m, 4.5 m, 6.0 m, 8.0 m, and 10.0 m. In addition, two thermistor beads were attached to a "pig-tail" that would monitor the temperatures at the mid-point and top surface of the straw bales and shredded wood layers. Air temperatures were monitored at 1.0 m above the ground surface at the control cell.

The Woodenhouse site was installed in February 2005 and the Norman Wells site was installed in February 2006. The sites were prepared by site clearing, including snow clearing, installing the test cells and then drilling boreholes to install the thermistor cables. Figure 1 presents the typical test cell and thermistor cable lay-out showing the thermistor bead numbering.

Initial thermal performance

This paper only reports initial results from the Woodenhouse test site in northern Alberta. Data collection from the Norman Wells site has experienced a number of challenges, and as a result full analysis of these datahas not been completed. For the Woodenhouse test site, temperature data has been regularly downloaded since testing began.

Thermistor beads 3 (0 m), 4 (0.5 m depth) and 5 (1.0 m depth) provided the most representative data on the near surface geothermal reaction of the surface cover. Bead 9 (6.0 m depth) provided ground temperatures at a moderate depth.

Figure 2 shows ground surface temperatures for all of the test cells at Woodenhouse. The ground surface temperatures at the control test cell and the reflective surface test cell were similar to each other. The ground surface temperatures for the straw bales and shredded wood materials were dampened compared to the atmospheric temperatures. That is, the effect of the straw bale and shredded wood layers was to reduce the day-to-day temperature variation in ground temperature compared to the air temperatures. Furthermore, the straw bales and shredded wood materials experienced a time lag in responding to atmospheric variations. This time lag was about one month, although more data is necessary to more accurately quantify the lag-period.

The time lag experienced for temperatures under the straw bale and shredded wood test cells compared to the control test cell was more apparent at depths of 0.5 m (see Fig. 3)

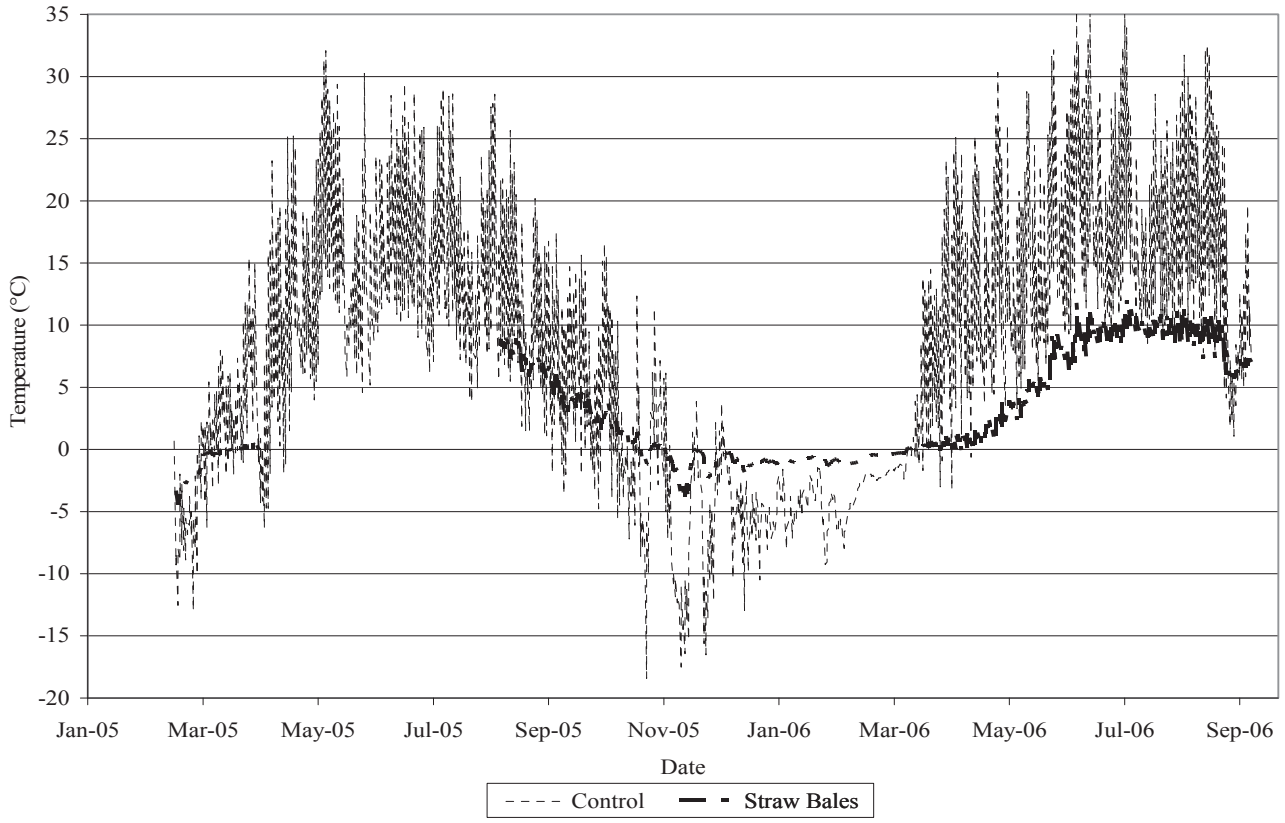

Figure 2a.

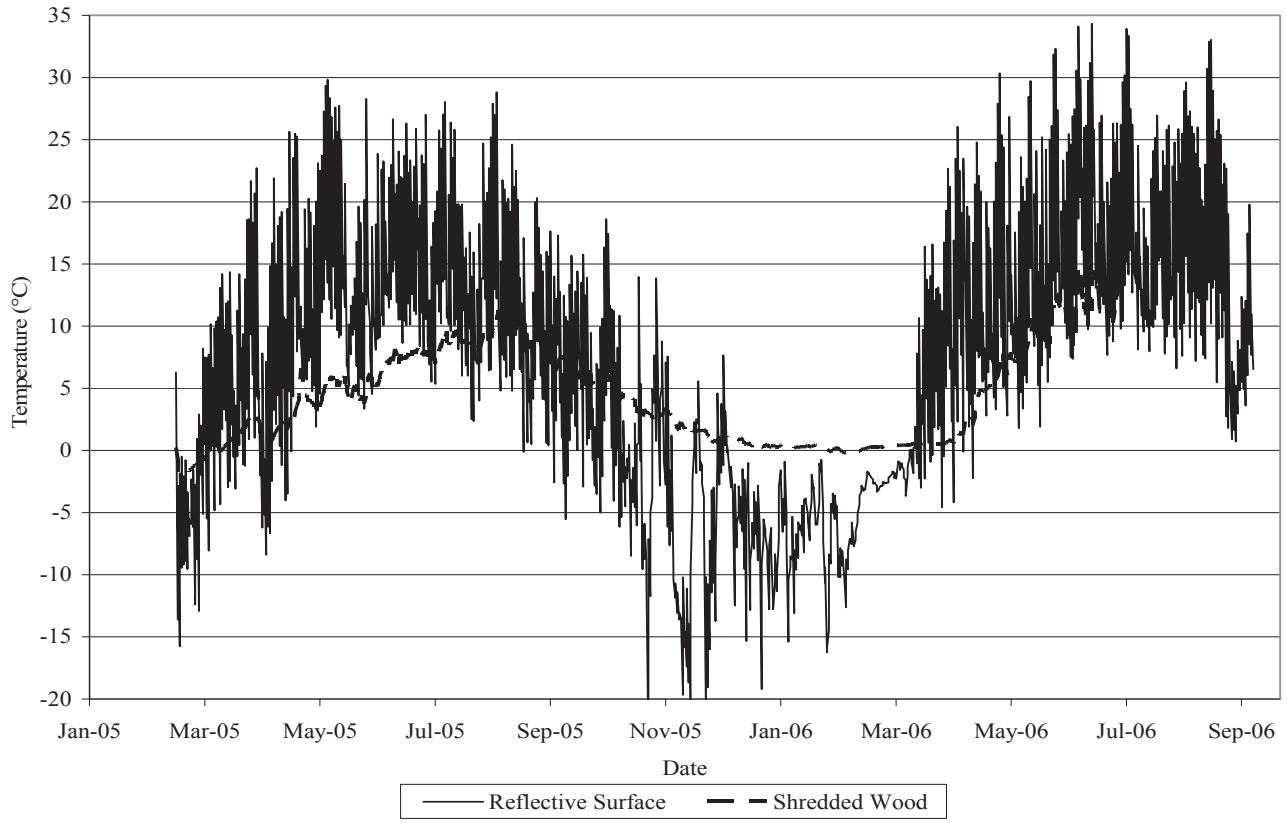

Figure 2b.

Figure 2. Temperature data from Woodenhouse test site, at ground surface.

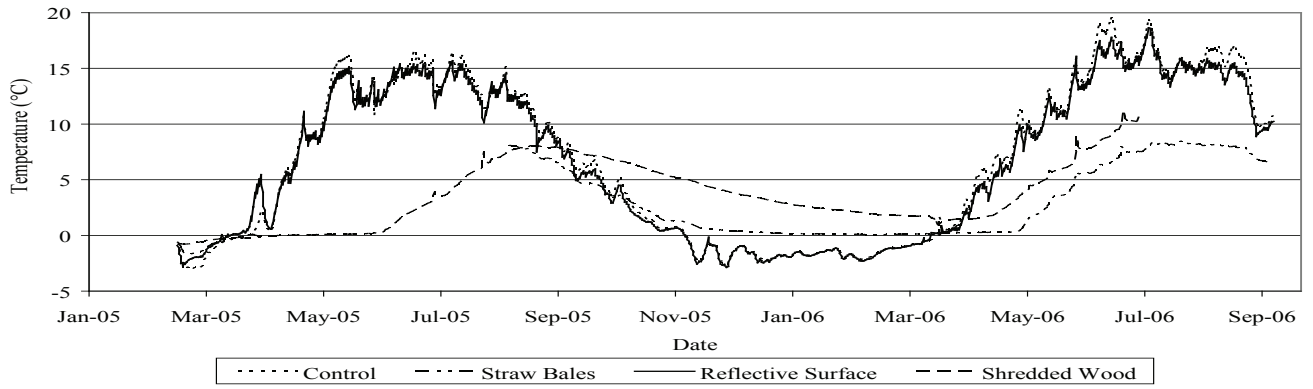

Figure 3. Temperature data from Woodenhouse test site, at 0.5 m below ground surface.

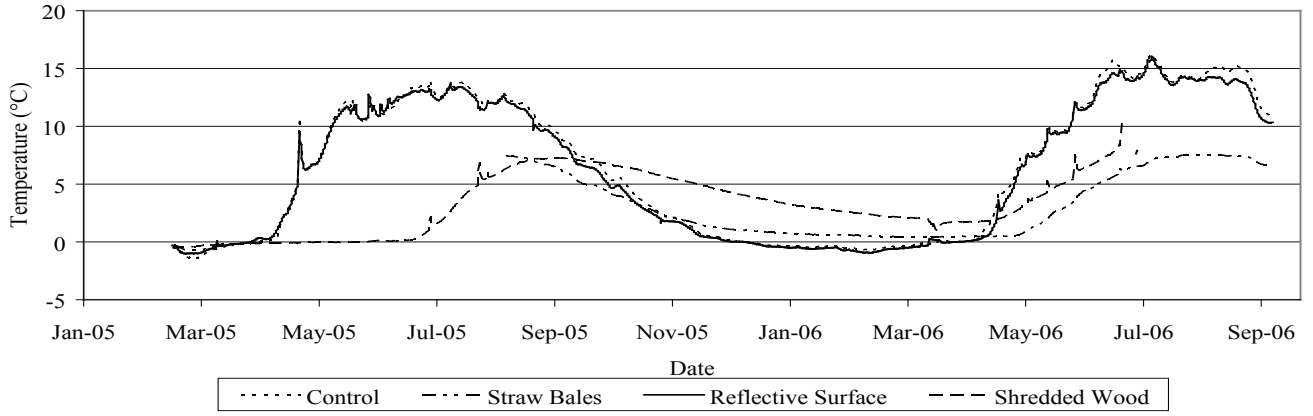

Figure 4. Temperature data from Woodenhouse test site, at 1.0 m below ground surface.

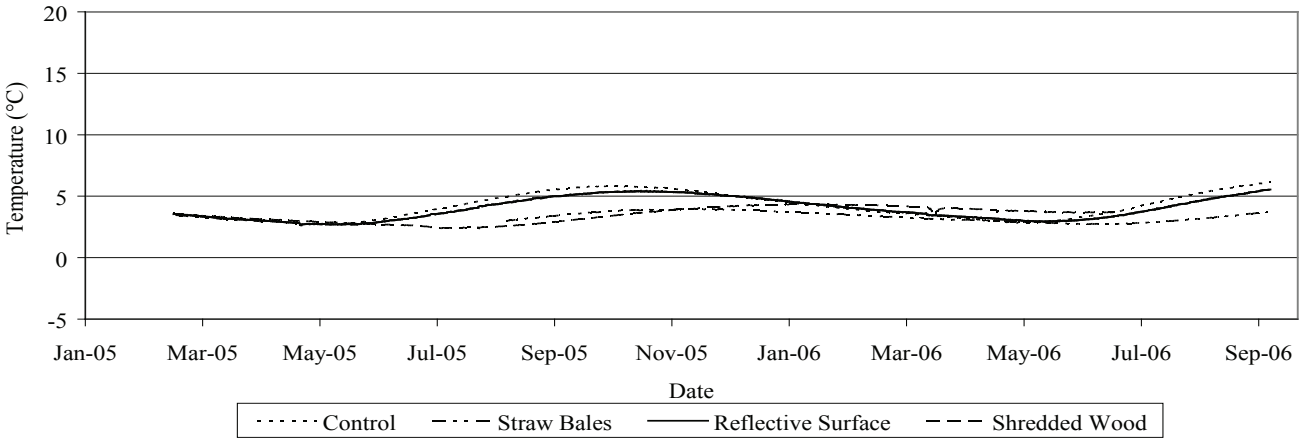

Figure 5. Temperature data from Woodenhouse test site, at 6.0 m below ground surface.

Table 1. Annual degree-day analysis of Bead 3, ground surface temperatures at Woodenhouse.

Test Cell Section	Analysis Period	Calculated Annual °C-Days	Percent of Control	Efficiency Compared to Control
Control	August 31, 2005 – August 30, 2006	2,174	100	1.0
Straw bales	August 31, 2005 – August 30, 2006	1,090	50	2.0
Reflective surface	August 31, 2005 – August 30, 2006	1,945	89	1.1
Shredded wood	July 17, 2005 – July 16, 2006	1,711	79	1.3

and 1 m (see Fig. 4). The time lag was particularly evident during the summer of 2005 and 2006 and lasted about one month. At the end of the winter of 2006, the shredded wood test cell showed a minimal time lag in May 2006 in terms of responding to warmer air temperatures, while the straw bales experienced a time lag of about two weeks before the ground started to warm.

With depth, all ground temperature responses to air temperature changes are dampened. This dampening is a result of the thermal resistance of the mineral soil. Based on the temperature data from thermistor Bead 9 at a depth of 6 m (see Fig. 5), it appears that the influences of the surface insulation material are nearly completely moderated by the overlying soil cover. That is, the temperature response at 6 m depth for each of the test cells and the control are nearly the same.

There were only small differences in the average winter temperatures for any of the test cell materials at Woodenhouse, compared to the control cell temperatures. Between November 2005 and April 2006 winter temperatures measured as follows:

- Under the straw bale and shredded wood test cells, ground temperatures were several degrees warmer than the temperatures under the control cell.
- In the cell containing the reflective surface material, ground temperatures were slightly colder than the temperatures under the control cell.

The warmer average winter temperatures experienced by the shredded wood test cell was because of the long time lag in the response of the ground temperature to the seasonal change in air temperature. This was most apparent in thermistor Bead 5 at 1 m depth (see Fig. 4) and thermistor Bead 9 at 6 m depth (see Fig. 5). In summer 2005, the ground temperatures under the shredded wood lagged behind the ambient temperatures by at least one month. The warmer ground temperatures developed in the summer and early fall of 2005 were carried well into the late fall and early winter 2005–2006, which caused an overall warmer average winter soil temperature.

Ground temperature responses in the summers of 2005 and 2006 also showed differences between the straw bale and shredded wood test cells, and the control cell. The ground temperatures under the reflective surface test cell during the summer of 2005 and 2006 appeared to be close to those of the control cell. Both the straw bales and shredded wood cells recorded average ground surface and near surface (0.5 m depth) temperatures that were less than one-half of those measured in the control cell.

The effectiveness of the test materials could be further examined by a degree-day analysis using Bead 3, which measured the ground surface temperature. This analysis is shown in Table 1.

The data from the degree-day analysis reinforced the observations from the temperature plots. The straw bales achieved one-half the number of annual degree-days of the control section, whereas the shredded wood achieved only 79% of the annual degree-days. The reflective surface material had a minimal effect on the ground temperatures.

Physical performance of test materials

The examination of physical performance of the test materials focused on degradation and loss of integrity of the materials, as these issues will ultimately affect the long-term suitability of the insulation materials used. Observations from the Woodenhouse and Norman Wells test sites were both considered.

Visual examination of the straw bales at both the Woodenhouse and Norman Wells test sites revealed that the bales had shrunk since their initial installation. This shrinkage was first identified at the Woodenhouse test site in the summer of 2005. Consequently, for the Norman Wells straw bale test cell, a thin layer of loose straw was spread over the test cell prior to placement of the bales so that if shrinkage occurred, bare earth (or the organic mat) would not be exposed.

The shrinkage of the straw bales probably resulted from moisture loss from the straw. It would be reasonable to expect that drying would cause the straw bales to shrink in height and length, but less in width because of the anisotropic structure of the straw stalks.

One concern expressed in the planning phase of the study was that foraging by animals, particularly ungulates, would damage the straw bales. However, visual observations at the Woodenhouse and Norman Wells test sites indicated that animals were not eating the straw bales.

The physical performance of the reflective surface materials at the Woodenhouse and Norman Wells test sites appeared to be good. Inspection of the material in the fall of 2006 did not reveal any substantive deterioration of the geotextile reflective material. Some discolouration at the Woodenhouse site had occurred likely associated with airborne dust from adjacent exposed areas. The Norman Wells test site did not have exposed mineral soil near the test cells. Consequently, this site provided a good contrast to the Woodenhouse test site in terms of darkening of the reflective fabric.

Visual observations at Woodenhouse indicated that animal traffic, if any, had not damaged the reflective surface material. No evidence of animal traffic has been found at the Norman Wells test site.

Importation of noxious weeds at test sites

The importation of noxious weeds to sites in the Northwest Territories should be avoided. As part of the initial program to establish the test sites, the straw bales were tested for weeds by an agricultural laboratory. The test results for noxious weeds were negative.

Plants have started to grow on and between the straw bales at Woodenhouse. The weeds observed at the site were stinkweed and tartary buckwheat, species that were common in Alberta, but were not on the noxious weed list. These plants were annuals that were reproducing from seed on new surface disturbances. However, they are not expected to persist more than a few years on the bales at Woodenhouse. If these weeds were imported to the Mackenzie Valley, they would not likely produce seed because of the short growing season and would likely die out after the first year.

Plants were also observed to be growing through seams of the reflective surface material at the Woodenhouse test site. These plants are likely the result of airborne seeds or regeneration of rootstocks that were present on the ground surface when the reflective surface material was installed.

Observations and Conclusions

From the preliminary field testing and analysis, one can conclude the following:

• Although the straw bales shrunk in volume during testing, further temperature measurement and analysis is necessary to determine whether this shrinkage is sufficient to materially affect their thermal insulation properties when used as an insulation system.

• The anchoring system proposed by the manufacturer of the reflective surface material was inadequate for the application at the Woodenhouse test site, where there was exposed mineral soil. However, a revised anchoring system was successfully implemented at the Woodenhouse site but was then found to be inadequate for the Norman Wells test site, which consists of an organic layer overlying hard or frozen mineral soil. The "third generation" anchoring system used at Norman Wells appears to be performing well.

• As measured in terms of ground surface annual degree-days, a single layer of straw bales provided the best thermal performance compared to the control, being about twice as effective as the control cell. The 0.5 m layer of shredded wood performed about 1.3 times better than the control cell. Both materials showed value as ground surface insulation materials.

• Both the shredded wood and straw bales experienced a time lag in response to seasonal ambient temperature changes. In the case of the shredded wood test cell, this time lag appears to help increase the average winter temperature of the ground surface above the average air temperatures measured.

• In comparing the ground surface temperatures of the reflective surface material to the control cell, the reflective material experienced a small, but measurable reduction in ground surface temperature during the thawing period compared to the control cell at the Woodenhouse test site. A reduction of about 10% in ground surface annual degree-days was achieved by the reflective surface compared to the control cell. However, additional monitoring from one or more thaw seasons is needed to confirm the effectiveness. If long-term reduction in ground surface heating can be confirmed, then the applicability of reflective surfaces can be evaluated from a cost-benefit perspective.

Acknowledgments

The authors acknowledge the assistance of their colleagues at Colt Worley Parsons Limited, Imperial Oil Resources Ventures Limited and ExxonMobil Development Company who worked on the Mackenzie Project. Permission to publish this paper has been granted by Imperial Oil Resources Ventures Limited and ExxonMobil Development Company.

References

Hanna, A.J. & McRoberts, E.C. 1988. Permafrost slope design for a buried oil pipeline. *Proceedings of the Fifth International Conference on Permafrost, Trondheim, Norway, August 2–5, 1988*. Volume 2: 1247-1252

Hanna, A.J., Oswell, J.M., McRoberts, E.C., Smith, J.D. & Fridel, T.W. 1994. Initial performance permafrost slopes: Norman Wells pipeline project, Canada. *Proceedings of the Seventh International Cold Regions Engineering Specialty Conference, Edmonton Alberta, March 7–9, 1994*: 369-395.

Oswell, J.M., Hanna, A.J. & Doblanko, R.M. 1998. Update of performance of slopes on the Norman Wells pipeline project. *Proceedings, Seventh International Conference on Permafrost, Yellowknife, Canada.*

Poplin, J.P., Weaver, J.S., Gulati, K.C., Lord, S. & Sisodiya, R.G. 1991. Experimental field study of spray ice ablation. *Proceedings, International Conference on Port and Ocean Engineering under Arctic Conditions, POAC*. Volume 1: 259-272.

The State of Subsea Permafrost in the Western Laptev Nearshore Zone

P.P. Overduin
Alfred Wegener Institute for Polar and Marine Research, Potsdam, Germany
V. Rachold
International Arctic Science Committee, Stockholm, Sweden
M.N. Grigoriev
Permafrost Institute Siberian Branch, Russian Academy of Sciences, Yakutsk, Russia

Abstract

Permafrost in the nearshore zone is affected by sea bottom temperatures, formation of bottom-fast ice, ice movement, formation of brines through freezing, and diffusion of salt water into the sediment. Subsea permafrost drilled on- and offshore along a north-south transect in the Laptev Sea yields sediment temperature, state and pore-water salinity to show salt diffusion into the sediment and its effect on phase state. Since inundation, the permafrost has been separated from atmospheric temperature and radiation fluctuations by a 0 to 6 m water column and, in winter, by sea ice. Nearshore development of bottom-fast ice concentrates brines at the sea bottom and leads to the penetration of a saline front that exceeds seawater salinity by a factor of at least 2. Subsea permafrost pore space can contain a mix of ice and pore-water solution that is primarily determined by salinity.

Keywords: brine; coastal zone; continental shelf; permafrost; subsea.

Introduction

Permafrost beneath the ocean floor is the result of relative sea level rise inundating the land surface. Inundation changes the heat flux at the upper boundary of the permafrost, generally leading to warming and eventual degradation. Nearshore seabed temperature records covering the annual cycle are rare, but measured temperatures are usually negative. Sufficiently saline pore waters can thaw subsea permafrost at negative temperatures. Methods of estimating permafrost distribution include bathymetric delineation (Brown et al. 1998) and heat transfer modeling (Romanovskii et al. 2005). Modeling uses inferred climate histories and simplified heat transfer. Models of permafrost evolution after inundation have been refined by including salinity effects (Swift & Harrison 1984, Hutter & Straughan 1999, Outcalt 1985), but these have not resulted in improvements to regional or global permafrost distribution estimates. Unknowns affecting distribution include regional glacial and sea level histories, the effect of spatial heterogeneity in terrestrial permafrost (esp. thermokarst) on subsequent degradation, and processes affecting sea bottom temperature and salinity (esp. bottom-fast ice). Based on the consequent spatial variability (Overduin et al. 2007b), public domain direct observations of the distribution of ice-bearing subsea

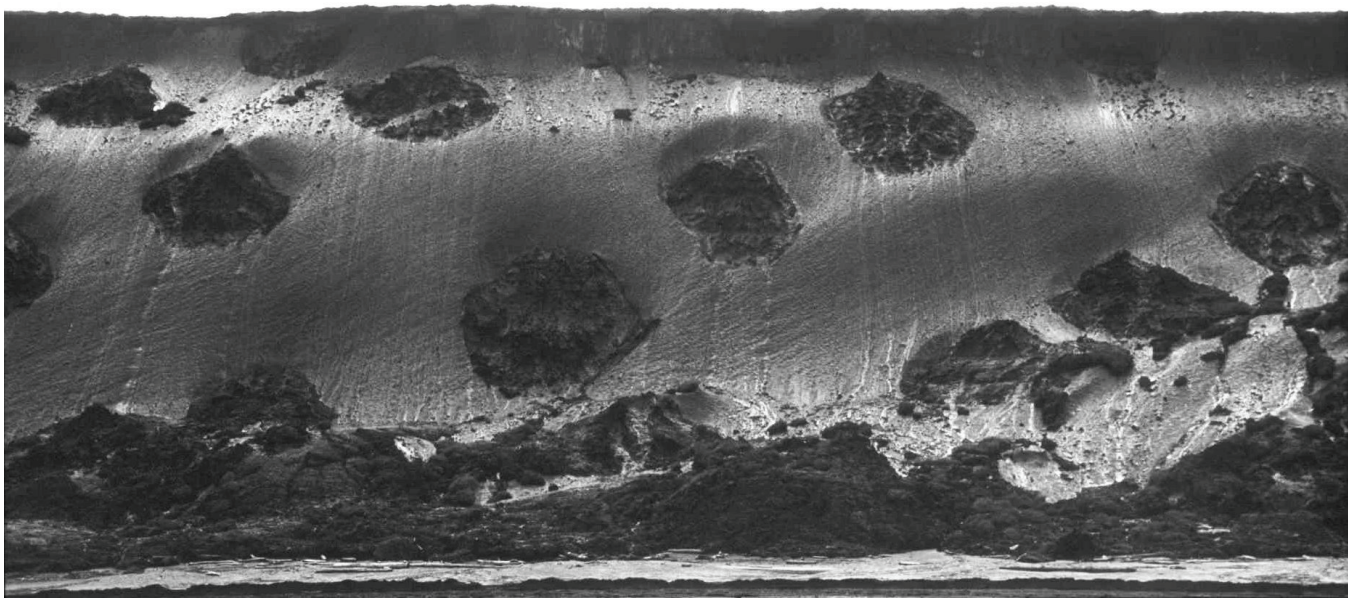

Figure 1. A straight-on view of the eroding Laptev Sea coastal bluff at Cape Mamontov Klyk. The bluff is about 20 m high and is composed mostly of ice with inclusions of organic-rich soil (photograph by Hanno Meyer, 2003).

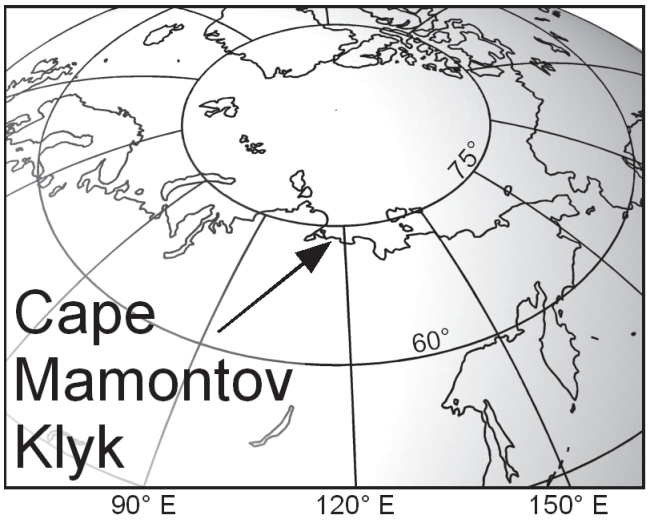

Figure 2. Map showing the location of Cape Mamontov Klyk (above) in the Western Laptev Sea.

permafrost, particularly at water depths shallower than 10 m, provide poor predictive capability for regions where no observations have been made.

In this study, sediment from the Laptev Sea is examined to determine changes in permafrost following submergence. Modeled subsea permafrost is thick (700-1000 m) and ice-bearing and extends over 400 km from the modern coastline (Romanovskii et al. 2005). The shallow inclination of the shelf and the absence of localized glaciation during the last glacial interval create a suitable test bed for subsea permafrost studies. We seek to identify processes determining the rate and distribution of permafrost degradation in the nearshore zone.

Site Description

Located midway between the Anabar and Olenek Rivers, Cape Mamontov Klyk was named for the discovery of mammoth tusks emerging from its thawing coastal bluffs (Figs. 1, 2), which currently reach over 25 m in height with a ground ice content up to over 80% by volume. The bluff stratigraphy is part of the Siberian ice complex deposits formed during the Late Pleistocene (Romanovskii 1993). The coastal bluff contains mostly silty sand, with relatively high organic content (Schirrmeister et al. submitted). The coastal plain stretches from the Pronchishev Ridge about 30 km to the south of the coast, lies 25 to 55 m a.s.l. and inclines to the north-northeast at 0.1°-0.2° at the cape. Thermokarst depressions and lakes up to several km across cover about 50% of the coastal plain in the region (Grosse et al. 2006). The coastline bisects some of these features, and they likely affect the bathymetry and subsea permafrost table (Romanovskii 2000). Available nearshore bathymetry is not precise enough to show these features, but the seafloor continues at less than 0.05° for at least 13 km from shore (Fig. 3). Modeling of permafrost development suggests that thermokarst terrain extends out to at least the 55 m isobath, and probably much further (Romanovskii & Hubberten 2001). Based on bathymetry from Russian maps and field data, the sea level rise inundated the shelf from a point over 200 km north of Mamontov Klyk over the past 11 ka (Bauch et al. 2001). Sea level rise over the past 2 ka was less than 2 mm a^{-1}, but there is little information on recent changes in coastline position, which is currently retreating at about 4.5 m a^{-1} (Arctic Coastal Dynamics Project Team 2008), and average erosion rates of ice complex coastlines in the Laptev Sea are about 2.5 m a^{-1} (Grigoriev & Rachold 2003).

Methods

In April 2005, a coastal and offshore drilling program drilled five cores along a north-south transect (Overduin et al. 2007a). Coring sites extended from onshore (core C1) to 12.5 kilometers offshore (cores C2-C5) and 6 m water depth (Fig. 3). A dry, hydraulic, rotary-pressure drilling technique was used and a borehole casing prevented infiltration. Depths of penetration are shown in Figure 3 and listed in Table 1, along with the state of the sediment as determined upon recovery. Recovered sediment material remained frozen during transport and storage.

Sediment temperature was measured using calibrated thermistors. Measurements were made from 1 to 11 days after drilling at the depths shown in Figure 4 (Junker et al. accepted). The dry drilling technique allowed temperature equilibration within 3 days at the bottom of C2. A thermistor string was permanently installed at the onshore site (C1). Mean annual temperatures for C1 were calculated using hourly measurements for the time period June 1, 2005-June 1, 2006 (Fig. 4). The temperature profiles for C2, C3 and C4 were measured at least 96 hours after drilling, C5 was measured one day later.

Pore water salinity was measured by thawing the sediment and extracting pore water using small suction lysimeters with 0.2 µm pores. Thawing and extraction took up to three days, depending on sample grain-size. The extracted pore water salinity was measured to a reference temperature of 25°C. Uncertainty in salinity depended on the measurement range with an upper limit of ±0.1‰.

At low salinity, the ice content in cryotic sediment mostly depends on grain-size and temperature. At higher salinities, however, the salinity of the pore water is more important. For low-salinity samples (<5‰), we used the total water content of frozen samples as a proxy for volumetric ice content (θ_i). For high-salinity samples (≥5‰), volumetric ice content was estimated as the difference between total (θ_{tot}) and liquid water content (θ_l). Total volumetric water content (ice and water) was measured using the weight (w_{fr}) and water displacement (V_{tot}) of sealed frozen samples and the weight of the sample after freeze-drying (w_{dry}).

Uncertainties were ±5 x 10^{-5} kg in weight and ±5 x 10^{-5} m^3 in volume. The error introduced by ignoring liquid water content in fresh water samples is small for these sediments (<5%) relative to absolute variations in ice content between samples, since grain sizes are not small and segregated ice is present in much of the profile.

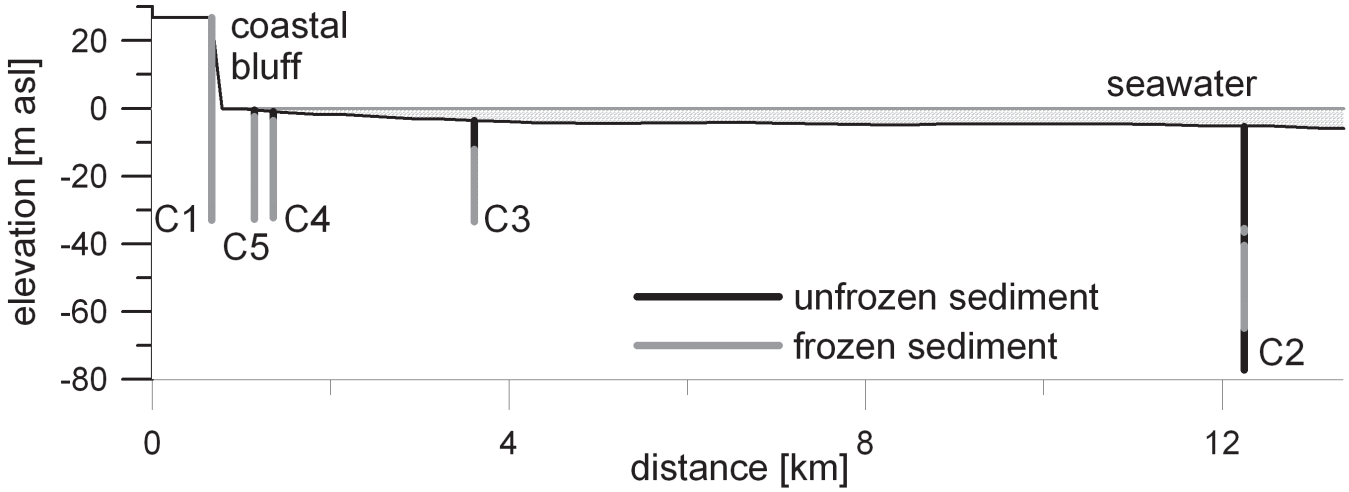

Figure 3. The locations and elevations (in meters relative to sea level) of cores along the transect are shown, along with the field-determined state (frozen/unfrozen) of the sediment (adapted from Overduin et al. 2007a).

Sediment liquid water content lay between 4 and -25°C in the laboratory using 7 cm time domain reflectometry (TDR) sensors in a 100 mL cell, which had been calibrated in air and deionized water. A Campbell Scientific TDR100 was used to generate waveforms, which were analyzed for bulk relative dielectric permittivity. Liquid water content was estimated using a mixing model for the relative dielectric permittivity of a porous medium. We assume that the sediment may be represented as a rigid three-component medium (ice, soil, water). The mixing model gives the composite relative dielectric permittivity (ε_c) based on the volumetric fractions and dielectric permittivities of the components:

$$\varepsilon_c = \left[(1-\eta)\varepsilon_s^{\alpha} + (\eta-\theta_l)\varepsilon_i^{\alpha} + (\theta_l)\varepsilon_l^{\alpha}\right]^{1/\alpha} \quad (1)$$

where η is the porosity, and the subscripts, *i*, *s* and *l* refer to ice, soil and liquid, respectively (Roth et al. 1990). The exponent, α, is related to the geometry of the components in the mixture. Soil and ice relative dielectric permittivities are assumed to be similar at the frequency of measurement ($\varepsilon_m = \varepsilon_s \approx \varepsilon_i$), leading to an expression for the liquid water content that is equivalent to a two-component model:

$$\theta_l = \left[\varepsilon_{comp}^{\alpha} - \varepsilon_m^{\alpha}\right]\left[\varepsilon_l(T)^{\alpha} - \varepsilon_m^{\alpha}\right]^{-1} \quad (2)$$

Changes in pore solution dielectric permittivity as a result of changes in solute concentration are ignored, as are temperature dependencies of the soil and ice dielectric permittivity. Temperature was varied using an external cooling bath and a pump, which circulated the cooling fluid around the sample cell. Liquid water content was measured during multiple warming and cooling cycles. Temperature was monitored in the sediment sample using PT100s with an accuracy of better than ±0.1°C.

Table 1. Borehole and sediment characteristics for each drill site.

	C2	C3	C4	C5	C1
Distance to coast [km]	11.5	3	1	0.5	0.1
Water depth [m]	6.0	4.4	2.2	1.5	--
Ice thickness [m]	1.35	1.85	2.1	1.5	--
Core depths	to	to	to	to	+26.2
[m relative to sea level]	-77	-31	-32	-31	to
					-34
Bottom water salinity [‰]	29.2	30.0	32.2	>100	--
Bottom water temp. [°C]	-1.5	-1.6	-1.7	-6	--
Frost table depth [m]	35	12	3.9	2.8	--

Results

The exposed coastal profile is described in Schirrmeister et al. (submitted), and consists of silty sand, organic-rich ice complex deposits overlying silty sand to fine sand deposits. The subsea sediment is composed of silty sands to fine sands. Based on available analyses, we cannot distinguish between unfrozen sediment that has been redeposited and sediment that has thawed in place. The upper thawed subsea sediment shows weakly layered structure, and has probably been reworked in its upper portion by redeposition and wave action. Below the frozen-unfrozen interface, the presence of freshwater ice, ice wedges, composite ice wedges, ataxitic layers indicating the presence of an active layer with seasonal thawing and layers of organic debris and twigs suggest terrestrial and shallow water environments. These features were found in C1 (25.5-12.8 m r.s.l.), C5 (2.8-14.5 m r.s.l.), C4 (3.9-14 m r.s.l.) and C2 (40.3-64.7 m r.s.l.), roughly corresponding to the upper portion of the frozen sediments for the subsea cores in Figure 3. In each core, these sediments are underlain by sandier, cryotic sediments without significant segregated ice.

Water depth decreased gradually with distance from the shore (1.5, 2.2, 4.4, 6.0 m at C5, C4, C3 and C2, resp.). C5

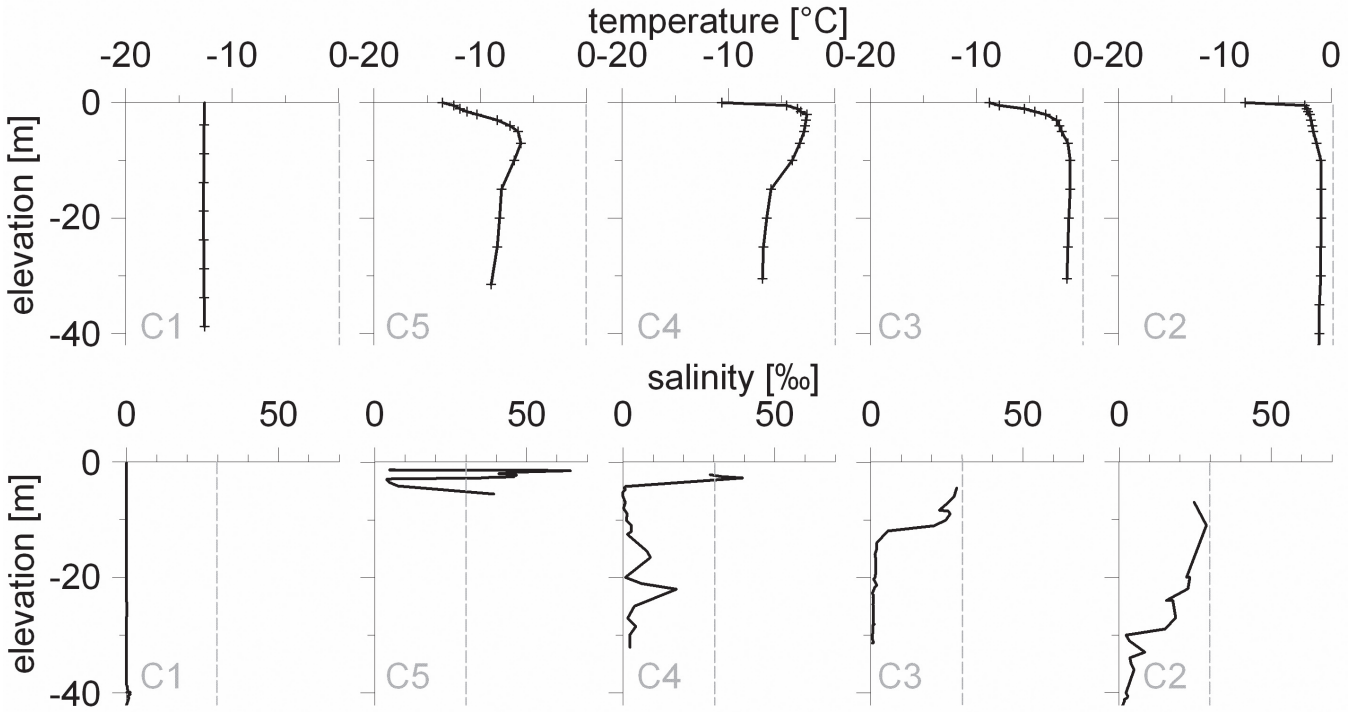

Figure 4. Profiles of sediment temperature (top) and pore water salinity (bottom) from onshore (at left) to furthest offshore (at right; some data taken from Rachold et al. 2007). Available data for the depths from 0 to 42 m below sea level are presented for all cores.

was therefore located in the bottom-fast ice zone. Bottom water salinities decreased with distance from shore, while temperatures increased (Table 1). The interface between unfrozen and frozen sediment was located at successively lower depths within the sediment column with increasing distance from the coastline (2.8, 3.9, 12 and 36 m at C5, C4, C3 and C2, respectively). Sediment temperatures at 20 m below sea level increased from an almost constant mean

Annual value of -13°C onshore (C1), to -8°C, -6°C, -1.5°C and -1°C with increasing distance from the coast (Fig. 4). The temperature gradient over depth in C2 was almost flat over the upper 40 m of the sediment profile. The temperatures at the frozen/unfrozen interface were -8.4, -2.8, -1.2 and -1.1 in C5, C4, C3 and C2, respectively. The salinity of pore water extracted from the sediment varied between 0 and 65‰ (Fig. 4). Salinities exceeding that of bottom water measured in August 2003 (17.3‰ to 20.7‰) and below the ice in April 2005 (29.2‰ to over 100‰) were found in C5 and C4. In C3 and C2, a saline pore water front was observed at depths of about 12 and 36 m, respectively. Frozen sediment generally had pore water salinity less than 5‰. Higher salinity found below the uppermost salt water front in C4 (around 16 and 22 m), and the variability in C5 salinity, suggest irregular brine production or migration.

Figure 5 shows the ice content as a function of temperature for four sediment samples. The sediment samples vary in terms of grain-size, sediment composition, and pore-water salinity. Differences in salinity are large enough (12, 25, 45 and 65‰) to make grain-size differences negligible in determining volumetric liquid water content at temperatures less than about -2°C. Increasing salinity decreases the sediment volumetric ice content. Ice content is shown for both cooling and warming temperature histories of all four samples. Hysteresis is clearly visible for the two lower salinity samples, but results in no more than a 4% ice content difference between warming and cooling at 45‰, and negligible differences at 65‰. For the latter, warming and cooling curves are superimposed. For the lowest salinity sample, the rate of change of state with temperature is low at temperatures below -5°C. At higher salinities, any addition or removal of heat results in significant phase change (around 2% K^{-1}), rather than temperature change.

Measured total volumetric water contents in core C2 range from 14% to 100%. Ice content in C2 increased with depth from a low value of 3% (based on temperature and pore-water salinity) to a maximum of 20% in the unfrozen zone. In the frozen sediment, ice contents ranged from 17% to 100%. Values in excess of 40% (based on core volume and weight loss on drying) corresponded to depths which were identified as frozen in the field and contained segregated ice. Segregated ice occurred as ice lenses, injection ice, ice wedges, and composite ice wedges. Values determined by weighing dried samples match to within 15% of adjacent freshwater samples.

Discussion

Previous results from this campaign were based on field observations (Overduin et al. 2007a+b, Rachold et al. 2007). In this paper, we add laboratory analyses performed on pore water and sediment samples to describe the position and temperature of the frozen-unfrozen interface in the subsea

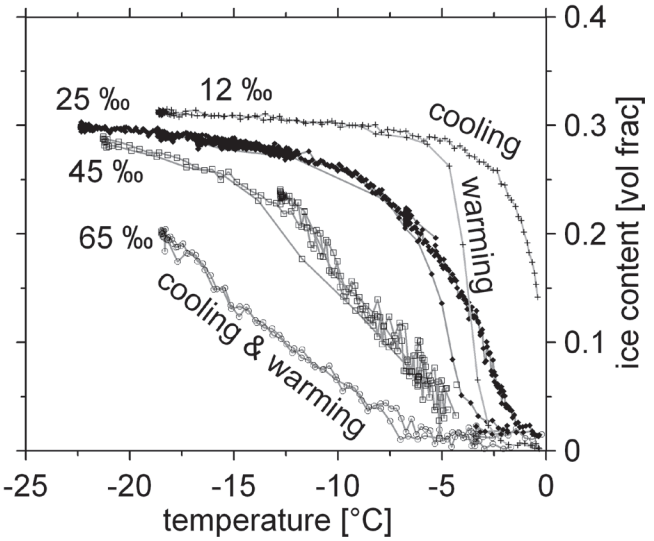

Figure 5. The volumetric ice content of four sediment samples (salinities: 12, 25, 45, and 65‰) as a function of temperature. Data were collected during cooling and warming for all four samples.

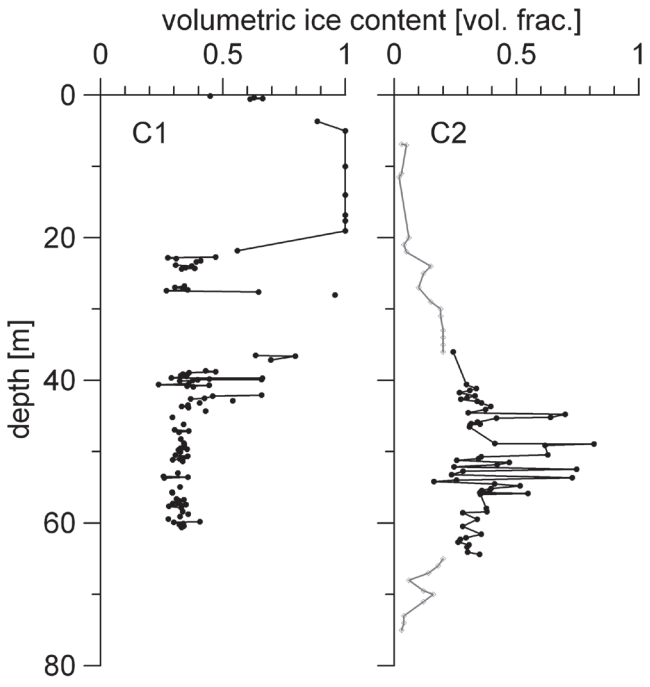

Figure 6. The volumetric ice content of the cores C1 and C2.

sediment. Coastal erosion and the subsequent inundation of the land at Cape Mamontov Klyk result in a large geomorphologic change in the upper permafrost, including thermoerosion, reworking of the eroded material, transport and redeposition offshore. These processes currently result in the thawing, removal, and redeposition of about the upper 25 m of permafrost. Redeposited and underlying unredeposited (in-situ) sediment is considered permafrost, as it remains cryotic. The boundary between the two is not yet clear, but must lie at or above the frozen/unfrozen interface. The actions of thermoerosion, thermokarst basin flooding, and wave action on the shallow sea bottom (Are et al. 2001), will have attenuated any topographic reflections of the previous thermokarst topography in the transition from terrestrial to marine.

The depth within the sediment of the frozen/unfrozen interface is difficult to determine. The classification of sediment as frozen or unfrozen in the field is highly subjective, since it rests upon a determination of plasticity. The determination is generally made by examining core sections at the surface, after they have been subjected to drilling and passage through the borehole. In some studies, the sea bottom was probed, akin to a permafrost probe, until sufficient resistance was encountered (Osterkamp et al. 1989). The temperatures at the interface observed here ranged from -1.1°C to -8.4°C, with inferred ice contents between 5% and over 25%, based on salinity and temperature. The transition from ice-free to ice-bearing to ice-bonded is likely to be gradual in most settings. Sediment ice and liquid water content depends strongly on pore water salinity over a wide temperature range (from 0°C to -20°C). As a consequence of this and the low temperature gradient, the phase boundary (the zone between ice-free sediment and sediment unaffected by saline solution) in C2 is almost 30 m thick, and covers a range of ice contents from 3% to over 20% by volume. Detection methods sensitive to step-like transitions in material properties over a short depth range, such as seismic or geoelectric methods, are thus confronted with a poor reflector.

The high salinities observed in the uppermost sediment at C5 (Fig. 4) strongly suggest that salt exclusion during sea ice formation results in brine formation. In this case, the brine formed was under positive pressure, and flooded and flowed out of the borehole 8-10 hours after drilling (Rachold et al. 2007). The salinity profile for C5 suggests the diffusion of at least one brine front down a strong concentration gradient into the sediment, which may be due to the formation of a seasonal active layer (Osterkamp et al. 1989). The progressive diffusion of the brine front into the sediment pore water is evident from the salinity graphs of Figure 4. Applying a mean ice thickness of 1.7 m, the bottom-fast ice (BFI) zone extends over 2 km from shore. Under current coastline retreat (4 to 4.5 m a^{-1}), this translates to seasonal brine production over a period of 440 to 500 years. The low inclination of the seabed in the western Laptev suggests that even longer periods are common, since coastal retreat for the Laptev Sea is 2 to 2.5 m a^{-1}. Both coastal retreat rates and the nearshore shore face profile will be important in determining the rate of descent of the salt front into the sediment, and differences may help to explain the variability observed in the position of the frozen/unfrozen interface. Provided that sediment could be removed from the shoreface effectively enough to account for increased erosion, increases to sea level rise will lower the rate of permafrost degradation by seawater penetration.

Conclusions

The saline-freshwater interface in the sediment column was identified in cores drilled off the coast of Mamontov Klyk in the Laptev Sea. Bottom-fast ice results in highly concentrated sea water being produced at the ice-sediment interface, and probably accelerates the degradation of subsea permafrost. Saltwater diffusion into the sea bottom results in the presence of ice-free sediment at sub-zero temperatures down to a depth of 40 m in subsea sediments, 12 km offshore. The transition from ice-free to ice-bonded sediment occurs over a depth range of about 30 m 2.6-6.0 ka after inundation. The energy requirements for the permafrost to become near-isothermal are reduced by the diffusion of salt water into the sediment. Changes in phase as a result of salt water intrusion and warming change the effective thermal properties of the sediment and affecting the rate of further degradation.

Acknowledgments

We gratefully acknowledge the help of all those involved in the field and lab work, including Alexander Derevyagin, Antje Eulenburg, Katja Hockun, Viktor Kunitsky, Franziska Merker, Gunter Stoof, and Maria Winterfeld. This work was supported by the German Ministry for Education and Research (BMBF). We thank Dmitry Melnichenko, director of the Tiksi Hydrobase, for providing logistic support. Improvements to the paper were suggested by two reviewers and William R. Bolton.

References

Arctic Coastal Dynamics Project Team, 2008. The Arctic Coastal Dynamics (ACD) Circumpolar Coastal Classification.

Are, F.E., Grigoriev, M.N., Rachold, V., Hubberten, H.-W., Rasumov, S.O. & Schneider, W. 2001. Shoreface profiles of the central and western Laptev Sea coast. *Reports on Polar Research* 388: 60-64.

Bauch, H.A., Mueller-Lupp, T., Taldenkova, E., Spielhagen, R.F., Hassens, H., Grootes, P.M., Thiede, J., Heinemeier, J. & Petryashov, V.V. 2001. Chronology of the Holocene transgression at the North Siberian margin. *Global and Planetary Change* 31: 125-139.

Brown, J., Ferrians Jr., O.J., Heginbottom, J.A. & Melnikov, E.S. 1998. Digital Circum-Arctic Map of Permafrost and Ground-Ice Conditions. In: International Permafrost Association, *Circumpolar Active-Layer Permafrost System (CAPS) version 1.0.*

Grigoriev, M.N. & Rachold, V. 2003. The degradation of coastal permafrost and the organic carbon balance of the Laptev and East Siberian Seas. In: M. Phillips (ed.), *Proceedings of the 8th International Conference on Permafrost, Zürich, Switzerland, 21-25 July 2003*, 319-324.

Grosse, G., Schirrmeister, L. & Malthus, T. 2006. Application of Landsat-7 satellite data and a DEM for the quntification of thermokarst-affected terrain types in the periglacial Lena-Anabar coastal lowland. *Polar Research* 25(1): 51-67.

Hutter, K. & Straughan, B. 1999. Models for convection in thawing porous media in support of the subsea permafrost equations. *Journal of Geophysical Research* 104(B12): 29 249-29 260.

Junker R., Grigoriev, M.N. & Kaul, N. Non-contact infrared temperature measurement in dry permafrost boreholes, accepted for publication in the *Journal of Geophysical Research*.

Osterkamp, T.E., Baker, G.C., Harrison, W.D. & Matava, T. 1989. Characteristics of the active layer and shallow subsea permafrost. *Journal of Geophysical Research* 94(C11): 16227-16236.

Outcalt, S. 1985. A numerical model of subsea permafrost. In: D.M. Anderson & P.J. Williams (eds.), *Freezing and Thawing of Soil-Water Systems*. New York: American Society of Civil Engineers, 58-65.

Overduin, P.P., Grigoriev, M.N., Junker, R., Rachold, V., Kunitsky, V.V., Bolshiyanov, D.Yu. & Schirrmeister, L. 2007a. The Expedition COAST I: COAST Drilling Campaign 2005: Subea permafrost Studies in the near-shore zone of the Laptev Sea. *Reports on Polar Research* 550: 1-40.

Overduin, P.P., Hubberten, H.-W., Rachold, V., Romanovskii, N.N., Grigoriev, M.N. & Kasymskaya, M. 2007b. The evolution and degradation of coastal and offshore permafrost in the Laptev and East Siberian Seas during the last climatic cycle. In: J. Harff, W.W. Hay & D.M. Tetzlaff (eds.), *Coastline Changes: Interrelation of Climate and Geological Processes, Geological Society of America*, Special Paper 426, Boulder, USA.

Rachold, V., Bolshiyanov, D.Yu., Grigoriev, M.N., Hubberten, H.-W., Junker, R., Kunitsky, V.V., Merker, F., Overduin, P.P. & Schneider, W. 2007. Near-shore Arctic subsea permafrost in transition. *EOS: Transactions of the American Geophysical Union* 88(13): 149-156.

Romanovskii, N.N. 1993. Osnovy Kriogeneza Litosfery, Izdatelstvo Moscow State University, Moscow.

Romanovskii, N.N. & Hubberten, H.-W. 2001. Results of permafrost modeling of the lowlands and shelf of the Laptev Sea region, Russia. *Permafrost and Periglacial Processes* 12: 191-202.

Romanovskii, N.N., Hubberten, H.-W., Gavrilov, A.V., Tumskoy, V.E. & Kholodov, A.L. 2005. Permafrost of the east Siberian Arctic shelf and coastal lowlands. *Quaternary Science Reviews* 23: 1359-1369.

Roth, K., Schulin, R., Flühler, H. & Attinger, W. 1990. Calibration of time domain reflectometry for water content measurement using a composite dielectric approach. *Water Resources Research* 26(10): 2267-2273.

Schirrmeister, L., Grosse, G., Kunitsky, V.V., Magens, M., Meyer, H., Derivyagin, A.Yu., Kuznetsova, T., Andreev, A.A., Kienast, F., Grigoriev, M. & Preusser, F. submitted. Periglacial landscape evolution and environmental changes of Arctic lowland areas during the Late Quaternary (Western Laptev Sea coast, Cape Mamontov Klyk). submitted to *Polar Research.*

Swift, D.W. & Harrison, W.D. 1984. Convective transport of brine and thaw of subsea permafrost: Results of numerical simulations. *Journal of Geophysical Research* 89(C4): 2080-2086

Sources of Discrepancy Between CCSM Simulated and Gridded Observation-Based Soil Temperature Over Siberia: The Influence of Site Density and Distribution

Debasish PaiMazumder
University of Alaska Fairbanks, Geophysical Institute & College of Natural Science and Mathematics
Nicole Mölders
University of Alaska Fairbanks, Geophysical Institute & College of Natural Science and Mathematics

Abstract

Soil-temperature climatologies determined at different depths from simulations with the Community Climate System Model version 3 (CCSM), capture the annual phase of gridded soil-temperature climatologies based on observations for 1951–1980, 1961–1990, and 1971–2000, but not the amplitude; some of these discrepancies can be attributed to simulated forcing (PaiMazumder et al. 2007). By using soil-temperature data simulated by the Weather Research and Forecasting (WRF) model, it is shown that some of the discrepancies between CCSM-derived and gridded observed climatologies may result from the interpolation required for gridding and/or network design (density and distribution of sites).

Keywords: climate simulation; network design; soil-temperature evaluation; Siberia; uncertainty.

Introduction

Accurate simulation of soil temperature in Climate System and Earth System Models is essential because soil temperature influences high-latitude hydrology, biochemical processes, and ecosystems. Soil temperatures are mostly controlled by the surface water and energy balance, which explains the strong connection and feedback between soil and near-surface atmospheric conditions. In the Arctic and Subarctic, the onset, duration, thickness, density, and structure of seasonal snow cover strongly influence soil temperatures (e.g., Zhang et al. 1996, Mölders & Romanovsky 2006).

Soil temperatures simulated at different depths by the Community Climate System Model version 3 (CCSM) (Collins et al. 2006a) are evaluated over Siberia for three climatologies (1951–1980, 1961–1990, 1971–2000) by means of observational data (PaiMazumder et al. 2007) provided by the National Snow Ice Data Center (NSIDC) (Zhang et al. 2001). PaiMazumder et al. (2007) also evaluated CCSM-derived climatologies of near-surface temperature, cloud fraction, precipitation, and snow depth with those from ERA40 reanalysis, the International Satellite Cloud Climatology project (ISCCP), the Global Precipitation Climatology Center (GPCC), and the NSIDC, respectively, to examine the sources for discrepancies between simulated and observed soil-temperature climatology. Inaccurate simulation of near-surface temperature, cloud fraction, precipitation, and snow depth may have some influences on discrepancies between CCSM-derived and observed soil-temperature climatology, but do not explain all discrepancy found. Sensitivity studies with slightly altered plant functional types and percentage of sand attributed marginal discrepancies from incorrect percentages of sand and/or plant types (PaiMazumder et al. 2007).

Typically, climate models like CCSM provide soil temperatures that represent a volume average of several hundred square kilometers in horizontal extension of several centimeters in thickness. It is obvious that soil temperatures simulated for such a volume are difficult to compare to measurements at a site (point measurements). Therefore, it has become common practice to interpolate available measurements to the grid of the climate model (e.g., Li et al. 2007). It is obvious that such interpolation may introduce uncertainty into the grid-cell averages; hence, the evaluation. Since the gridded soil-temperature climatologies are based on measurements projected onto the CCSM3 grid by Cressman interpolation (PaiMazumder et al. 2007), some discrepancies between CCSM-derived and gridded observed climatologies may result from interpolation and/or network density and distribution. Observational networks are often designed with accessibility and ease of maintenance in mind. Most of the Siberian soil-temperature sites are long-term agricultural monitoring stations. Consequently, the observational network follows agricultural-used land along major haul ways and is not uniformly distributed. Hence, the density and/or design of network may bias the regional averages estimated therefrom. Mitchell et al. (2004) assessed accuracy and reliability of gridded data and concluded that observed gridded data (1901–2000) are not appropriate for climate change. They also describe the development of high resolution (0.5°) of gridded dataset (Climate Research Unit [e.g., CRU TS 2.0] data) for the globe derived from climatological observations and transient coupled atmosphere-ocean general-circulation-model (GCM) simulations. The gridded dataset depends on the applied interpolation algorithms, and always has to be associated with an assessment of the accuracy of the grid point values. Therefore, it is essential to assess the uncertainty in regional averages resulting from the density and/or design of an observational network. The aim of our case study is to exemplarily investigate this uncertainty to further assess the discrepancies between CCSM-derived and observed soil-temperature climatologies found by PaiMazumder et al.

(2007). In doing so, the Weather Research and Forecasting (WRF) (Skamarock et al. 2005) model is used to provide a dataset of soil temperatures that will be considered as "reference" for determination of regional averages to which data from a real network and artificial networks are compared to assess the accuracy of gridded datasets based on station data, and to develop recommendations for network design to optimize their use for model validation.

Experimental Design

Brief model description

The CCSM is a fully coupled climate model to simulate the Earth system over broad ranges of spatial and temporal resolutions. It consists of the Climate Atmospheric Model, version 3 (CAM3) (Collins et al. 2006b), the Community Land Model version 3 (CLM3) (Dai et al. 2003, Oleson et al. 2006), the Community Sea Ice Model version 5 (CSIM5) (Briegleb et al. 2004), and the Parallel Ocean Program version 1.4.3 (POP) (Smith et al. 1992). These four components exchange data via a coupler without flux correction.

CCSM is run with 26 vertical layers at a spectral truncation of T42 corresponding to a spatial resolution of ≈2.8° x 2.8°. CCSM is started with the ecliptic conditions of 1-1-1950 and CO_2 concentration of 355 ppmv. Each model component is spun up separately. Based on these simulations, we determine three climatologies, 1951–1980, 1961–1990, and 1971–2000.

The WRF is a mesoscale non-hydrostatic model. Out of the variety of physical options, we use the following model setup: Cloud formation and precipitation processes at the resolvable scale are considered by Thompson et al.'s (2004) five-water class (cloud-water, rainwater, ice, snow, graupel) mixed-phase bulk-microphysics parameterization. The Grell-Devenyi (2002) ensemble parameterization considers subgrid-scale convective clouds. The Goddard shortwave-radiation scheme and the Rapid Radiative Transfer Model (Mlawer et al. 1997) are applied. The Yonsei University scheme (Skamarock et al. 2005) is used for simulating atmospheric boundary layer processes. Monin-Obukhov similarity theory is applied for surface-layer physics. Soil temperature, volumetric ice and water content, snow temperature and density and the exchange of heat and moisture at the land-atmosphere interface are determined by a modified version of the Rapid Update Cycle land-surface model (Smirnova et al. 1997, 2000).

The WRF domain encompasses Siberia by 70 x 150 grid-points with a grid-increment of 50 km and 31 vertical layers from the surface to 50 hPa. Soil conditions are determined at six levels. In the presence of snow, five snow layers are considered. The time step is 200s. The National Centers for Environmental Prediction (NCEP) 1.0° x 1.0° and 6h-resolution global final analyses (FNL) serve as initial and boundary conditions. For our case study, we perform simulations for July and December 2005. They start daily at 1800 UT for 30 hours of integration. We discard the first six hours as spin-up time.

Analysis

To estimate uncertainty due to network density and design, WRF-simulated soil temperatures serve to represent data from an optimal, dense, and equally distributed observational network. Regional averages of soil temperatures determined from the WRF output for July and December 2005 are considered to be the "reference."

Regional averages of soil temperature are determined for the 411 sites of the actual historic observation network used in PaiMazumder et al.'s (2007) CCSM soil-temperature evaluation. Herein, the soil temperature simulated for a WRF grid cell wherein a site falls is taken as the soil temperature for that site. This procedure is common practice in mesoscale modeling (e.g., Narapusetty & Mölders 2005). Four artificial networks are assumed with 500, 400, 200, and 100 arbitrarily taken WRF grid cells as "sites." These networks are denoted 500-, 400-, 200-, and 100-site networks hereafter. Soil temperatures obtained from WRF simulations at the 500, 400, 200, and 100 sites are used to calculate the regional averages for these networks. These regional averages are compared with the reference regional averages to assess the contribution of network density and design to uncertainty in gridded data used for evaluation of climate model data.

Since systematic and nonsystematic errors can contribute to any simulation result, as well as to regional averages obtained from different networks, performance measures like bias, standard deviation of errors (SDE), root mean square errors (RMSE), and correlation coefficients (e.g., Anthes 1983, Anthes et al. 1989) are calculated at different spatial and temporal scales for the various networks. The performance measures and correlation coefficients are determined to evaluate the discrepancies between the regional averages obtained from the "reference" and those of a network. They are calculated for all networks for the daily and monthly course.

To estimate the uncertainties in regional averages resulting from the density and design of networks, we compare the regional averages of soil temperature obtained from the WRF simulation ("reference") and various site networks (500-, 400-, 200-, 100-site network and historic networks). In this case study, we consider the accuracy of soil temperature measurements to be within ±0.5 K for the reasons discussed in PaiMazumder et al. (2007). The regional averages of soil temperature estimated from the "reference" and the different networks will be considered to be in good agreement if regional averages obtained from the different networks lie within the above-mentioned uncertainty range to the "reference."

In a next step, we compare the uncertainty determined as described above with the discrepancies found between CCSM-derived and gridded-observation-derived climatologies by PaiMazumder et al. (2007) to assess how much the network design may explain some of these discrepancies.

Results

Impact of network design on regional averages

Regional averages of soil temperature obtained from the artificial networks are highly correlated with those of the reference (>0.972) at all depths in both months. Regional averages of soil temperature obtained from the historic network are more highly correlated with the "reference" in December (R = 0.921) than in July (R = 0.732) at 00 UT, 06 UT, 12 UT, and 18 UT at all depths.

In both months, the daily spatial standard deviations of soil temperatures obtained from the historic network are higher than those of all other networks. The standard deviations of soil temperature obtained from the various networks are higher at all depths in December than in July. In December, in general, soil temperatures vary strongly in space due to the large horizontal differences in snow cover and/or thickness. Thus, taking measurement along the haul ways leads to larger standard deviations of the regional averages in winter than summer because of snow conditions and terrain height of the site. In July, for given insolation and soil type, soil heating/cooling varies less in space than in December, when differences in snow cover/thickness may strongly affect soil temperatures. Consequently, taking the measurement along a haul way has less impact on the regional average and its standard deviation for Siberia in summer than winter.

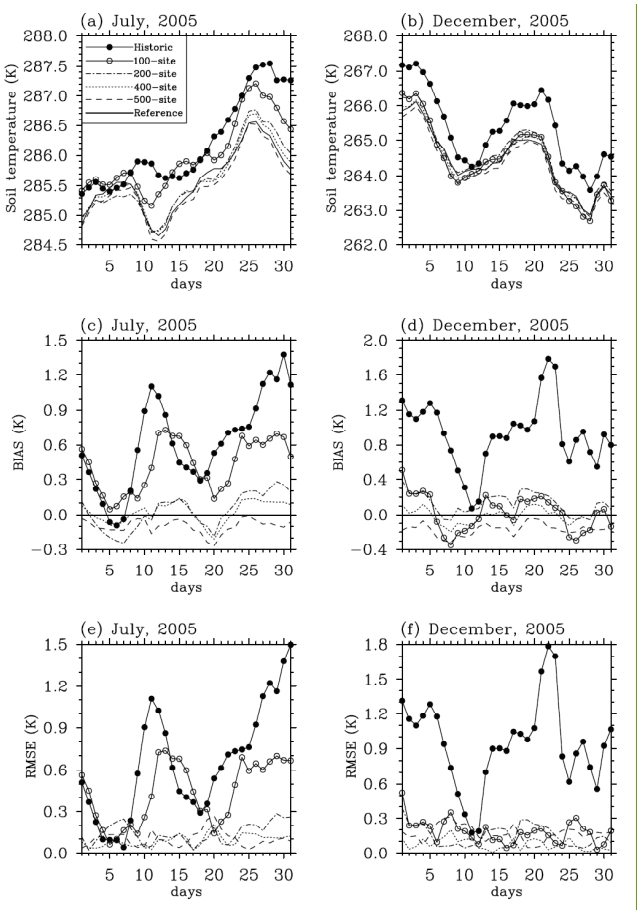

Figure 1. Temporal behavior of (a) regionally averaged soil temperature at 0.2-m depth obtained from the "reference," 500-, 400-, 200-, 100-site network and the historic network for July 2005 and (b) December 2005. Biases for (c) July and (d) December and RMSE for (e) July and (f) December between the "reference" and 500-, 400-, 200-, 100-site network and the historic network. Note that in (c) to (f), labels on the y-axis differ. In (c) and (d), the thick line serves to better visualize the positive and negative bias.

At 0.2-m depth, soil temperatures obtained from the historic network overestimate the reference average by up to 1.5 K and 1.8 K in July and December, respectively (Fig. 1). The historic network also fails to capture the timing of the soil-temperature maxima and minima represented in the reference average. For example, on July 11 and 26, upper soil temperatures from the historic network average do not reflect the warm periods seen in the reference average (Fig. 1). These differences in timing of extremes between the regional averages of the historic network and "reference" occur due to a frontal system passing Siberia. The non-equal distribution of sites of the historic network therefore gets "biased" to the time when the system passes the majority of the sites. In December, the high bias found for the historic network may partly be explained by the fact that the sites of the historic network may not well represent the regional differences in snow cover and/or thickness. The 100-site network also fails to capture the regional soil-temperature averages obtained from the "reference" with 0.8-K bias in July (Fig. 1), while in December, the 100-site network captures the reference average well. Obviously, a randomly distributed 100-site network represents soil conditions in winter well when the soil is partly insulated by snow. However, in summer, convection may lead to spatial differences in soil heating due to shading by clouds and/or heat input by precipitation that a 100-site network cannot capture appropriately. Regional averages of soil temperature obtained from 500-, 400-, and 200-site networks provide acceptable results in comparison to the reference average at all depths in both months. The historic network shows higher biases and RMSEs than all other networks in both months (Fig. 1, Table 1). This means that the historic network introduces some bias into regional averages and any evaluation study therewith.

Higher systematic bias may have occurred due to the difference in landscape and terrain elevations between the regional averages derived from the "reference" and historic network. At 0.2-m depth (0.4 m and 1.6 m), RMSEs for the historic network reach up to 1.5 K (1 K and 1.9 K) and 1.8 K (1.3 K and 1.1 K) in July and December, respectively (Fig. 1). Errors in regional soil-temperature averages based on the historic network are also high for the upper soil layer, and errors decrease at 0.4-m depth and increase again for deeper soil layers in both months. The high diurnal variability close

Table 1. Monthly averages of bias and RMSE for the historic and 200-site networks for upper and deeper soil.

Networks		Historic network		200-site network	
Month	Layer	bias	RMSE	bias	RMSE
July	Upper	0.6	0.7	0.02	0.1
	Deeper	1.7	1.9	0.3	0.3
December	Upper	1	1	0.1	0.2
	Deeper	1.2	1.2	0.2	0.3

to the surface may cause the high errors in the upper soil (Table 1). The increase found for deeper soil layers may be related to the constant lower boundary condition used in WRF. These soil-temperature values are from climatologies which differ notably in space. Thus, the historic network cannot represent the "reference" because the sites are not randomly distributed to capture the regional pattern.

Evaluation of CCSM by gridded data

As reported by PaiMazumder et al. (2007), CCSM captures well the phase of the 30-year average annual soil temperature curves at all depths, but not the amplitude. CCSM overestimates the 0.2-m soil temperature for the majority of the grid cells over Siberia from December to March for the first climatology (1951–1980) (Fig. 2). Similar is true for 0.4-m and 1.6-m depths, but with marginally decreasing frequency with increasing depth, whereas at 0.8 m and 3.2 m, CCSM overestimates soil temperature throughout the year (Fig. 2). In April, soil temperature will be overestimated for most of the grid cells at all depths if soil temperature is below freezing and underestimated otherwise, leading to overall overestimation. In May and June, the general pattern shifts towards underestimation at all depths except 3.2 m (Fig. 2). In July and August, CCSM tends to underestimate soil temperature by up to 1.2 K at 0.2 m, and overestimates them by up to 0.5 K at 0.4-m and 0.8-m depth. At 1.6 m, the tendency to overestimate soil temperature is obvious for the colder (<275 K), but less obvious for the warmer (>285 K) end of the temperature range. In September, soil temperatures are underestimated at 0.2-m and 0.4-m depth by up to 0.6 K and 0.4 K for most grid cells (Fig. 2). At 0.8 m and 1.6 m, CCSM overestimates soil temperatures by up to 0.4 K and 1.1 K, respectively, for most grid cells. In October, the general pattern again shifts towards overestimation by up to 2.5 K (Fig. 2). In November, simulated soil conditions are too warm for soil temperatures below the freezing point at all depths. PaiMazumder et al. (2007) also found that biases and RMSEs decrease with increasing depth because most variability occurs near the surface. RMSEs are higher in winter than in the other seasons for all three climatologies. Mean annual soil temperatures are over-estimated by 2.5 K, on average.

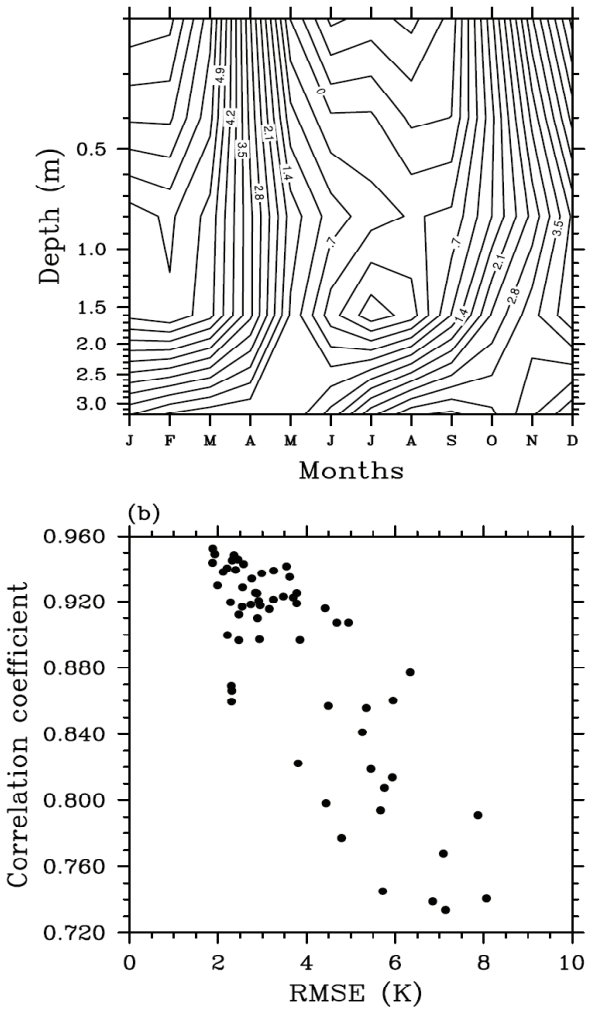

Figure 2. (a) Contour plot of temporal behavior of biases with depths for the first climatology (1951–1980). (b) RMSE vs. correlation coefficient for the first climatology for all 12 months at 0.2-m, 0.4-m, 0.8-m, 1.6-m, and 3.2-m depth.

Overall, CCSM simulates the annual average soil temperature reasonably well, though its performance is better in summer than in winter. Due to acceptable RMSEs and high correlations (cf. Fig. 2), PaiMazumder et al. (2007) concluded that the fully coupled CCSM acceptably simulates soil temperature. As pointed out by these authors, CCSM also has some difficulties in capturing near-surface temperature, cloud fraction, precipitation, and snow depth with biases (RMSEs) -1.0 K (3 K), 0.32% (0.52%), 7.6 mm/month (19.9 mm/month), and 0.04 m (0.09 m), respectively (for further details see Table 1 in PaiMazumder et al. 2007). Hence, the inaccurate simulation of near-surface temperature, cloud fraction, precipitation, and snow depth may contribute to the discrepancies between CCSM-derived and observed soil temperature climatology. Difference in plant functional types between model and real world and decreasing and increasing sand percentage in the model may marginally affect soil temperature. Thus, incorrect assumptions on the mineral soil type cannot explain the discrepancies found. Another source of these discrepancies may be that CCSM only considers mineral soils. However, large areas of Siberia have organic soils at least in the upper soil layers. The thermal and hydraulic properties of mineral and organic soils differ strongly and yield to appreciable differences in soil temperature and soil-water freezing behavior (cf. Mölders & Walsh 2004, Lawrence & Salter 2007). Nicolsky et al. (2007) showed that incorporating organic matter in CLM3 significantly changes the soil temperature simulation. Thus, providing gridded data of organic material distribution and consideration of organic material in CCSM are essential future steps for the scientific community to take.

Discussion and Conclusions

PaiMazumder et al. (2007) found that CCSM tends to overestimate soil temperature in winter and underestimate in summer, with better performance in summer than winter. In spring and fall, simulated and observed climatologies agree the best. Therefore, we performed a case study with WRF for December and July 2005 to further examine reasons for discrepancies in CCSM-derived and observed soil-temperature climatologies. In this case study, we assume the soil temperatures simulated by WRF as a reference dataset from which we determine the "reference" regional averages. These reference averages are compared to the regional averages determined from WRF data at the sites of the network used in PaiMazumder et al. (2007) and to four randomly but spatially even distributed artificial networks to assess exemplarily potential contribution of the historic network to the discrepancies found by these authors.

The high differences (1.8 K) between regional averages of soil temperature obtained from the historic network and "reference" in December suggest that the network design may affect gridded observational averages more in December than in July. This means that the high discrepancies between CCSM-derived and observation-based gridded soil-temperature climatologies can be explained by the network design in winter.

PaiMazumder et al. (2007) also showed that in December, biases between simulated and observed soil temperature reach up to 6 K at 0.2-m depth; about 2.5 K bias may result from incorrect simulation of observed forcing. Our study shows that about 2-K bias may be explained by uncertainties due to network density in winter. This means that about 1.5-K bias may result from measurement errors and/or model deficiencies.

In July, biases caused by the historic network are higher than biases in CCSM found by PaiMazumder et al. (2007). Hence, we have to conclude that in summer, CCSM performs well for simulating soil temperature. On the contrary, in winter, biases in CCSM can only partially be explained by uncertainties due to network density.

Similar results are found for RMSE and SDE in winter, whereas in summer, RMSEs for the historic network are lower than RMSEs in CCSM by 1 K on average. Hence, the discrepancies between CCSM-simulated and observation-based gridded soil-temperature climatologies in winter can be explained by incorrect simulation of atmospheric forcing as well as network design. Thus, improvement of soil-model physics is essential for better winter soil temperature simulation.

From this case study, it can also be concluded that the historic network always fails to capture the "reference" regional soil temperature averages with high biases, RMSEs, and SDEs in both months. On the contrary, the randomly distributed 500-, 400-, and 200-site networks capture the "reference" regional soil-temperature averages well at all layers. These networks also capture well the diurnal variation of soil temperature in the upper soil. Hence, our case study suggests that randomly distributed networks of 200 sites or more reliably reproduce acceptable regional averages of soil temperatures for Siberia. However, maintenance of such networks may be expensive because many of the sites would not be easily accessible in a remote area like Siberia. Future studies should examine the general robustness of the influence of the network density and design.

Acknowledgments

We thank U.S. Bhatt, M.E. Brown, G. Kramm, S.E. Porter, J.E. Walsh, and the anonymous reviewers for fruitful comments; C. Swingly for help with the ERA40 data; B. Rudolf for access to the precipitation data; T. Zhang, A. Etringer, and J. McCreight for providing the gridded soil-temperature and snow-depth data; and J. Miller for installing CCSM3 at ARSC. This research was supported by the International Arctic Research Center, UAF, under the auspices of the NSF cooperative agreement OPP-0327664, and from EPSCoR grant 0701898. ARSC and NCAR provided computational support.

References

Anthes, R.A. 1983. Regional models of the atmosphere in middle latitudes. *Mon. Wea. Rev.* 111: 1306-1335.

Anthes, R.A., Kuo, Y.H., Hsie, E.Y., Low-Nam, S. & Bettge, T.W. 1989. Estimation of skill and uncertainty in regional numerical models. *Quart. J. Roy. Meteorol. Soc.* 111: 763-806.

Briegleb, B.P., Bitz, C.M., Hunke, E.C., Lipscomb, W.H., Holland, M.M., Schramm, J.L. & Moritz, R.E., 2004. Scientific description of the sea ice component in the Community Climate System Model, version three. NCAR Technical Note NCAR/TN463-STR, 70 pp.

Collins, W.D., Bitz, C.M., Blackmon, M.L., Bonan, G.B., Bretherton, C.S., Carton, J.A., Chang, P., Doney, S.C., Hack, J.J., Henderson, T.B., Kiehl, J.T., Large, W.G., McKenna, D.S., Santer, B.D. & Smith, R.D. 2006a. The Community Climate System Model: CCSM3. *J. Climate* 19: 2122-2143.

Collins, W.D., Rasch, P.J., Boville, B.A., Hack, J.J., McCaa, J.R., Williamson, D.L., Briegleb, B.P., Bitz, C.M., Lin, S.J. & Zhang, M. 2006b. The formulation and atmospheric simulation of the Community Atmosphere Model: CAM3. *J. Climate* 19: 2144-2161.

Dai, Y., Zeng, X., Dickinson, R.E., Baker, I., Bonan, G., Bosilovich, M., Denning, S., Dirmeyer, P., Houser, P., Niu, G., Oleson, K., Schlosser, A. & Yang, Z.L. 2003. The Common Land Model (CLM). *Bull. Amer. Meteor. Soc.* 84: 1013-1023

Lawrence, D.M. & Slater, A.G. 2007. Incorporating organic soil into a global climate model. *Clim. Dyn.* doi: 10.1007/s00382-007-0278-1.

Li, Z., Bhatt, U.S. & Mölders, N. 2007. Impact of doubled CO_2 on the interaction between the regional and global water cycle in four study regions. *Clim. Dyn.* doi 10.1007/s00382-007-0283-4.

Mitchell, T.D., Carter, T.R., Jones, P.D., Hulme M. & New, M. 2004. A comprehensive set of high-resolution grids of the monthly climate for Europe and the globe: the observed record (1901-2000) and 16 scenarios (2002-2100). Tyndall Centre for Climate Change Research, 55 pp.

Mlawer, E.J., Taubman, S.J., Brown, P.D., Iacono, M.J. & Clough, S.A. 1997. Radiative transfer for inhomogeneous atmospheres: RRTM, a validated correlated-k model for the longwave. *J. Geophys. Res.* 102D: 16663-16682.

Mölders, N. & Walsh, J.E. 2004. Atmospheric response to soil-frost and snow in Alaska in March. *Theor. Appl. Climatol.* 77: 77-105.

Mölders, N. & Romanovsky, V.E. 2006. Long-term evaluation of the Hydro-Thermodynamic Soil-Vegetation Scheme's frozen ground/permafrost component using observations at Barrow, Alaska. *J. Geophys. Res.* 111: D04105, doi: 10.1029/2005JD005957.

Narapusetty, B. & Mölders, N. 2005. Evaluation of snow depth and soil temperature predicted by the Hydro-Thermodynamic Soil Vegetation Scheme (HTSVS) coupled with the PennState/NCAR Mesoscale Meteorological Model (MM5). *J. Appl. Meteor.* 44: 1827-1843.

Nicolsky, D.J. & Romanovsky, V.E. 2007. Improved modeling of permafrost dynamics in a GCM land-surface scheme. *Geophys. Res. Lett.* 34: L08501, doi:10.1029/2007GL029525.

Oleson, K.W., Dai, Y., Bonan, G.B., Bosilovich, M., Dickinson, R., Dirmeyer, P., Hoffman, F., Houser, P., Levis, S., Niu, G.Y., Thornton, P., Vertenstein, M., Yang, Z.L. & Zeng, X. 2004. Technical description of Community Land Model (CLM). Technical Report NCAR/TN-461+STR, National Center for Atmospheric Research, Boulder, CO. 80307-3000, 174 pp.

PaiMazumder D., Miller, J., Li, Z., Walsh, J.E., Etringer, A., McCreight, J., Zhang, T. & Mölders, N. 2007. Evaluation of Community Climate System Model soil temperatures using observations from Russia. *Theor. Appl. Climatol.* doi: 10.1007/s00704-007-0350-0.

Skamarock, W.C., Klemp, J.B., Dudhia, J., Gill, D.O., Baker, D.M., Wang, W. & Powers, J.G. 2005. A description of the advanced research WRF version 2. NCAR Technical Note, NCAR/TN-468+STR, 88 pp.

Smirnova T.G., Brown, J.M. & Benjamin, S.G. 1997. Performance of different soil model configurations in simulating ground surface temperature and surface fluxes. *Mon. Wea. Rev.* 125: 1870-1884.

Smirnova T.G., Brown, J.M., Benjamin, S.G. & Kim, D. 2000. Parameterization of cold season processes in the MAPS land-surface scheme. *J. Geophys. Res.* 105D: 4077-4086.

Thompson G., Rasmussen, R.M. & Manning, K. 2004. Explicit forecasts of winter precipitation using an improved bulk microphysics scheme. Part I: Description and sensitivity analysis. *Mon. Wea. Rev.* 132: 519-542.

Zhang, T., Osterkamp, T.E. & Stamnes, K. 1996. Influence of the depth hoar layer of the seasonal snow cover on the ground thermal regime. *Water Resour. Res.* 32: 2075-2086.

Zhang, T., Barry, R.G. & Gilichinsky D. 2001. Russian historical soil temperature data. National Snow and Ice Data Center, Boulder, CO, http://nsidc.org/arcss078.html/.

Remote Sensing-Based Study of Vegetation Distribution and Its Relation to Permafrost in and Around the George Lake Area, Central Alaska

Santosh K. Panda
Geophysical Institute, University of Alaska Fairbanks, Fairbanks, USA
Anupma Prakash
Geophysical Institute, University of Alaska Fairbanks, Fairbanks, USA
Diana N. Solie
Alaska Division of Geological & Geophysical Surveys, Department of Natural Resources, Fairbanks, USA

Abstract

We employed remote sensing techniques in combination with in situ measurements to investigate the presence/absence of permafrost in and around the George Lake area, central Alaska. The complex interrelationship between vegetation, topography, local geology, and permafrost in a discontinuous permafrost setting was examined. We used SPOT multispectral data to generate a land cover map for the study area. Eleven land cover classes were mapped including eight vegetation classes in a maximum likelihood classifier. Correlative relationship between surface parameters and permafrost was used to gain a preliminary understanding of permafrost distribution in the study area. In situ measurements in different vegetation and topographic settings disclosed that scattered short black spruce with thick moss layer is a potential indicator of permafrost with shallow active layer depth. Integrated analysis of vegetation map, equivalent latitude values, and field observations suggests that equivalent latitude greater than 63° is permissive of permafrost in the study area.

Keywords: Interior Alaska; mapping; permafrost; remote sensing.

Introduction

This study integrates remotely sensed (SPOT multispectral) data with field data for the area near George Lake, central Alaska, to understand the complex interrelationship between vegetation, topography, local geology, and permafrost in a discontinuous permafrost setting. It is a part of the Alaska Division of Geological & Geophysical Surveys (DGGS) project on the proposed Alaska gas pipeline corridor that aspires to identify the associated geohazards along the Alaska Highway corridor (such as areas underlain by permafrost, areas with highest potential for active faulting, liquefaction, landslides) (Solie & Burns 2007).

In order to make informed decisions regarding alignment and design of future infrastructure development, and assess the impact of climate change, a precise understanding of near-surface permafrost conditions is critical. Direct field investigation of permafrost or detection by indirect geophysical technique is limited to small areas due to the huge extent, extreme climate, and limited fieldwork time, and poor accessibility to most parts of arctic and sub-arctic Alaska. In such a situation, remote sensing techniques can be of great help. Many environmental factors that reflect the permafrost condition and indicate its presence/absence (like vegetation, topography, snow cover) can be mapped fairly from remote sensing data. The correlative relationship between these environmental factors and permafrost is exploited to get indirect information about subsurface permafrost (e.g., Etzelmuller et al. 2001, 2006, Frauenfelder et al. 1998, Jorgenson & Kreig 1988, Leverington & Duguay 1996, 1997, Morrissey et al. 1986, Peddle 1991, Peddle & Franklin 1993). Distribution of permafrost in discontinuous permafrost zones is strongly influenced by local climate, topography (elevation, slope, and aspect), local hydrology, vegetation cover, geology, and seasonal snow cover (e.g., Smith 1975, Goodrich 1982). Vegetation cover is one of the best indicators of spatial distribution of permafrost and relative thickness of active layer in discontinuous permafrost zones (Duguay et al. 2005). Hence, detailed vegetation mapping is critical in mapping near-surface permafrost.

Methods

Fieldwork was carried out during summer 2007 along the Alaska Highway between Lisa Lake and Dot Lake (Fig. 1). We visited different vegetation, topographic, and geologic settings, and collected data on active layer depth, soil type, moss layer thickness, and vegetation type. We sampled a total of 155 locations using a frost probe for active layer depth measurements and a soil auger to reveal the soil profile in the top 1.5 m.

The most widely accepted definition of permafrost is "any ground that remains frozen for at least two consecutive years" (French 2007). However, in this study, we adopted the permafrost definition by Brown (1967) and French (1976) that define "ground remaining frozen (at or below 0°C) throughout at least one summer" as permafrost. We also assume the depth to frozen ground measured using a frost probe in the field as active layer depth.

Absence of ice in well-drained sandy soil makes it impossible to measure active layer depth using a frost probe. In such situations, soil temperature is the only criteria

Table 1. Classification accuracy totals. For a brief description of classes (superscript 1-11), please refer to text.

Class Name	Reference totals	Classified totals	Number correct	Producer's accuracy (%)	Kappa statistics
[1]Thick spruce	15	15	15	100	1.00
[2]Spruce	64	63	62	96.88	0.98
[3]Spruce & Willow	43	41	35	81.4	0.82
[4]Birch & Spruce	34	31	31	91.18	1.00
[5]Deciduous	22	22	16	72.73	0.70
[6]Aspen	20	25	19	95	0.74
[7]Alpine Vegetation	5	6	5	100	0.83
[8]Grassland	16	11	10	62.5	0.90
[9]Turbid river water	13	13	13	100	1.00
[10]Lake	15	15	15	100	1.00
[11]Exposed surface	5	10	4	80	0.38
Totals	252	252	225	89.29	0.87

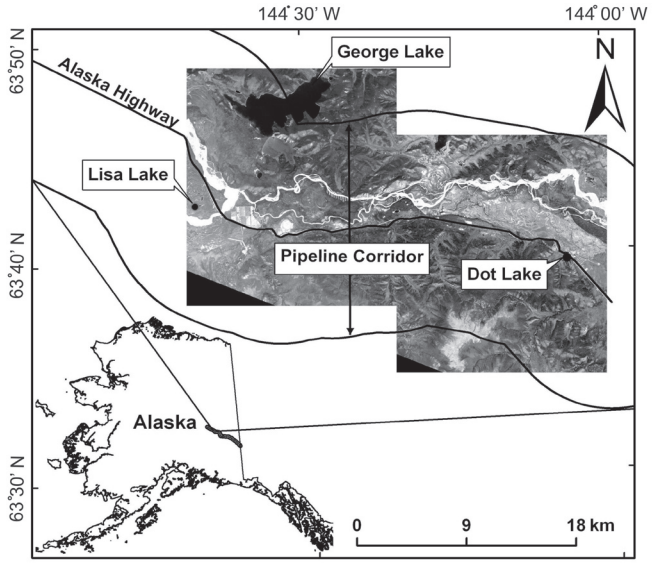

Figure 1. Study area extends from Lisa Lake to Dot Lake along the Alaska Highway. It is a small section of DGGS' proposed gas pipeline corridor study.

to define active layer depth. Hence, we installed Hobo temperature data loggers at 14 selected locations to record soil temperature. The temperature loggers are logging in their first year, and we have not used temperature data in the analysis. These temperature data will be used to estimate thetemperature at any depth and eventually to estimate the active layer depth (Williams & Smith 1989).

We used SPOT 5 multispectral data that has four spectral bands in visible and near infrared (IR) range (Green: 500–590 nm; Red: 610–680 nm; NearIR: 780–890 nm; SWIR: 1580–1750 nm) for land cover classification. Two rectangular scenes covering the study area were clipped from original SPOT scene (acquired on June 30, 2003) that was ortho-rectified and fused with the 2.5 m panchromatic band to improve the spatial resolution of multispectral data (Pohl & Van Genderen 1998). Classification was done using a combination of both unsupervised and supervised signature in a maximum likelihood classifier using ERDAS Imagine, a commercially available image processing software package (Schowengerdt 1983, ERDAS Imagine 2005). We classified the SPOT scenes into eleven land cover classes. These include 1) very dense stands of both black spruce and white spruce; 2) relatively less dense than thick spruce stands; 3) mostly observed in valleys, where spruce is widespread and willows generally grow near small water channel or creek; 4) mix of birch and spruce, generally observed in north facing slope, most prominent forest type in interior Alaska; 5) mix stands of deciduous trees including balsam poplar, willow, alder and birch; 6) stands of aspen vegetation only; 7) small alpine plants (e.g., mountain avens, dryas, sage, etc.); 8) open areas filled with grass; 9) flowing river water with heavy sediment loads; 10) standing water body; and 11) includes different types of bare surfaces (bed rock surfaces, bare surfaces on steep slopes, cut slopes surfaces on foot hills, soils, gravel quarry). Reference totals are the reference pixels selected randomly on the classified image for which actual classes are known. Classified totals are the pixels classified as a particular class by the classification process. Two hundred fifty-two randomly generated points were used to assess the classification accuracy. The superscripts 1–11 in Table 1 refer to the eleven land cover classes described above.

We generated an equivalent latitudes map of the study area from slope and aspect images using 60 m (pixel size) Digital Elevation Model (DEM). Equivalent latitude is an index of long-term potential solar beam irradiation on a surface (Lee 1962). A close relationship exists between equivalent latitude and presence or absence of permafrost, vegetation assemblages, and thaw depth (Dingman 1970, Koutz & Slaughter 1973).

We used the following equation to calculate equivalent latitude (Okanoue 1957):

$$\theta' = \sin^{-1}(\sin k \cdot \cos h \cdot \cos\theta + \cos k \cdot \sin\theta) \quad (1)$$

where k is the slope of the surface, h is the aspect of the surface, θ is the actual latitude of the area, and θ' is the equivalent latitude of the area.

Results and Discussion

The study area is classified into eleven land cover classes, including eight vegetation classes using a combination of both unsupervised and supervised signatures in a maximum likelihood classifier (Fig. 2). For classes 1, 2, 3, 4, 5, and 9, signatures obtained from unsupervised classification were used. For classes 6, 7, 8, 10, and 11, the following numbers of training areas were used in classification 120, 46, 214, 76, and 44, respectively (Table 1). We assessed the classification results using field records, field photographs and in consultation with DGGS scientists. A team of geologists from DGGS did a detailed geologic mapping of the study area as part of the "Alaska Gas Pipeline Corridor" project. Classification results yield an overall accuracy of 89.29% and overall Kappa statistics (Congalton 1991) of 0.87 (Table 1). Classification results of four land cover classes (thick spruce, alpine vegetation, turbid river water, and lake) show 100% accuracy whereas grassland class shows lowest accuracy (62.5%) owing to overlap of spectral signature of grassland and exposed surface classes in visible and near IR bands. Both the grassland and exposed surfaces classes have high digital number (DN) values in all the visible bands. High DN values for exposed surfaces in all the visible bands are obvious, but high DN values for grassland is most likely due to the summer timing of image acquisition (June 30, 2003). During field survey we found that grasslands are mostly dominant in open drained lake beds, and towards the middle of summer lot of grass stems became dry. At the same time the upper soil surface was also very dry. Therefore, the high digital values of grasslands in all the visible bands might be due to the combined effect of dry soil and dry grass stems.

Field sampling in different vegetation settings during summer 2007 revealed that tussocky areas with short, scattered black spruce were characterized by permafrost with shallow active layer depth (less than 50 cm); birch, tall black spruce, and white spruce were found in areas characterized by deeper active layer (greater than 50 cm); and aspen and mixed deciduous vegetation dominated where the upper 1.5 m was unfrozen.

Dividing the classified vegetation map into two elevation units reveals that valleys and floodplain deposits of the low elevation unit (<500 m a.s.l.) are dominated by spruce trees and tussocks. Analysis of the high elevation unit (>500 m a.s.l.) with respect to slope and aspect reveals the dominance of mixed birch and tall spruce on north- and west-facing slopes. Aspen and mixed deciduous trees are generally found in south- and east-facing slopes in well-drained conditions.

On the basis of equivalent latitude values, we classified the study area into three distinct zones. All south-facing slopes have equivalent latitudes less than 60°. Relatively flat floodplain, moraine, and eolian deposits have equivalent latitudes between 63–65°. All north-facing slopes are characterized by equivalent latitudes greater than 65°. The result of integrated analysis of vegetation map, equivalent latitude map and field observation is summarized in Table 2.

Table 2. Interpretation of integrated analysis of vegetation map, equivalent latitude map, and field observations.

Topography	Equivalent latitude (°)	Vegetation	Depth to frozen ground (Summer 2007)
Valleys and flood plain deposits (<500 m asl)	63 – 65	Scattered and/or drunken short black spruce	Less than 50 cm.
North facing slopes (>500 m asl)	Greater than 65	Tall black and white spruce, birch	Greater than 50 cm
South facing slopes (>500 m asl)	Less than 60	Deciduous (aspen, poplar, willow etc.)	None/deeper than 1.5 m

Our findings suggest that equivalent latitude greater than 63° is permissive of permafrost in the study area. This is in close agreement with the findings of Dingman (1970) and Koutz & Slaughter (1973). Dingman (1970) showed that in the elevation range of 256–494 m for Glenn Creek watershed, the permafrost/non-permafrost boundary lay between the 60° and 65° equivalent latitude isopleth lines. Koutz & Slaughter (1973) found a marked correspondence between soils with permafrost and the area above 65° equivalent latitude; and soils without permafrost with equivalent latitude isopleths below 60°.

In the prevailing climatic conditions the high variability of active layer depth

$$(\overline{X} \pm s = 65.61 \pm 19.72 \text{ cm};$$

where $\overline{X}$ is sample mean; s is standard deviation of sample is attributed to difference in soil types, moss layer thickness, and local geology. Thus, even though the equivalent latitude of north-facing slopes is more northerly than that of the valleys and flood plains, the active layer tends to be deeper due to soils which are generally less silt-rich and well drained.

Conclusions

The applied remote sensing technique in combination with *in situ* measurements has considerable potential for use as a tool in regional-scale permafrost mapping. We exploited the correlative relationship between surface parameters and permafrost to gain a preliminary understanding of permafrost distribution in the study area. Tussock land with scattered short black spruce tree and a thick moss layer is a potential indicator of permafrost with shallow active layer depth. At the higher elevation unit (>500 m a.s.l.) birch, tall black spruce and white spruce are dominant in north- and west-facing slopes characterized by a relatively deeper active layer. Broad-leaved, deep rooted deciduous vegetation in south- and east-facing slopes in well-drained soil condition

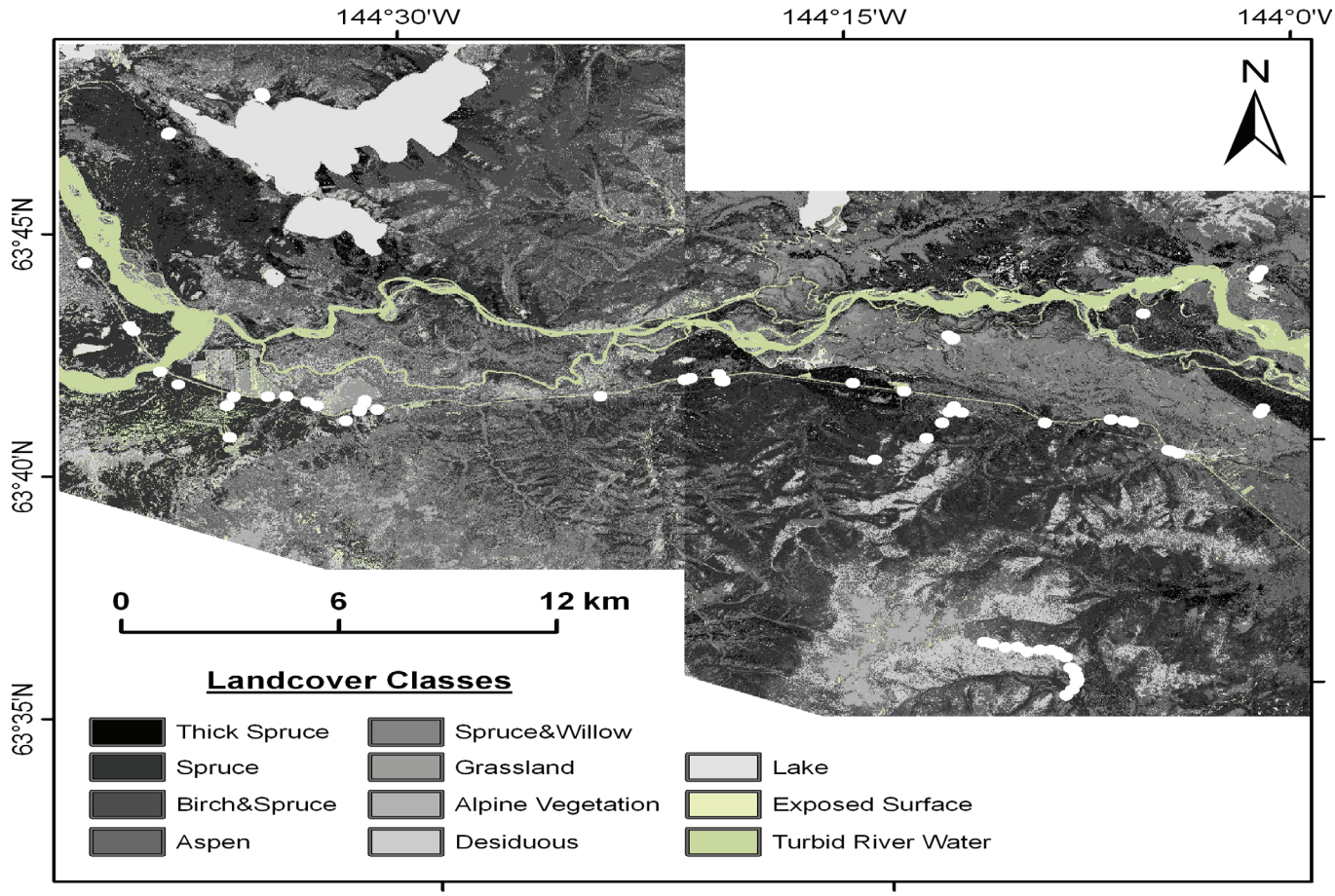

Figure 2. Land cover classification map of George Lake area. Eleven land cover classes including eight vegetation classes were mapped from SPOT multispectral data (acquired on June 30, 2003) in supervised maximum likelihood classifier. White dots represent the sampled locations for permafrost investigations, vegetation distribution, and field data collection.

indicates absence of near-surface permafrost. Equivalent latitude values for the permafrost and non-permafrost portion of the study area also supports the accepted generalization that near-surface permafrost is present under north-facing slopes and absent under south-facing slopes. However, we do not rule out the possibility of deeper permafrost in south-facing slopes. In the prevailing climate conditions, high variance of active layer depth is attributed to different soil types and moss layer thickness.

Acknowledgments

Field support and partial funding for this research was provided through DGGS as part of an on-going project to map bedrock and surficial geology and identify geohazards along the proposed natural gas pipeline corridor from Delta Junction, Alaska, to the Canadian border. We acknowledge additional support from the Alaska Space Grant Program. (ASGP). The authors acknowledge Dr. Richard D. Reger and De Anne Stevens for guidance and help in taking measurements in the field. Special thanks to Dr. Vladimir Romanovsky for advice regarding the various aspects of this study and providing temperature data loggers.

References

Brown, R.J.E. 1967. *Permafrost in Canada.* Canada Geological Survey Map 1246A. National Research Council publication NRC 9769.

Congalton, R. 1991. A review of assessing the accuracy of classifications of remotely sensed data. *Remote Sensing of Environment* 37: 35-46.

Dingman, S.L. 1970. *Hydrology of the Glenn Creek Watershed Tanana River Drainage, Central Alaska.* Ph.D thesis. Cambridge, Massachusetts: Harvard University, 122 pp.

Duguay, C.R., Zhang, T., Leverington, D.W. & Romanovsky, V.E. 2005. Satellite remote sensing of permafrost and seasonally frozen ground. In: C.R. Duguay & A. Pietroniro (eds.), *Remote Sensing in Northern Hydrology: Measuring Environmental Change.* Washington, DC: American Geophysical Union, 91-118.

ERDAS Imagine. 2005. Norcross, GA, USA: Leica Geosystem Geospatial Imaging, LLC.

Etzelmuller, B., Heggem, E.S.F., Sharkhuu, N., Frauenfelder, R., Kaab, A. & Goulden, C. 2006. Mountain permafrost distribution modeling using a multi-criteria approach in the Hovsgol area, Northern Mongolia. *Permafrost and Periglacial Processes* 17: 91-104.

Etzelmuller, B., Hoelzle, M., Heggem, E.S.F., Isaksen, K., Mittaz, C., Vonder Muhll, D., Odegard, R.S., Haeberli, W. & Sollid, J.L. 2001. Mapping and modeling the occurrence and distribution of mountain permafrost. *Norsk Geografisk Tidsskrift–Norwegian Journal of Geography* 55: 186-194.

Frauenfelder, R., Allgower, B., Haeberli, W. & Hoelzle, M. 1998. Permafrost investigations with GIS - A case study in the Fletschhorn area, Wallis, Swiss Alps. *Proceedings of the Seventh International Conference on Permafrost*, *Yellowknife, Canada*: 291-295.

French, H.M. 1976. *The Periglacial Environment* (First edition). London: Longman Group Limited, 309 pp.

French, H.M. 2007. *The Periglacial Environment* (Third edition). John Wiley and Sons, 458 pp.

Goodrich, L.E. 1982. The influence of snow cover on the ground thermal regime. *Canadian Journal of Earth Sciences* 19: 421-432.

Jorgenson, M.T. & Kreig, R. A. 1988. A model for mapping permafrost distribution based on landscape component maps and climatic variables. *Proceedings of the Fifth International Conference on Permafrost, Trondheim, Norway, August 2–5, 1988*: 176-182.

Koutz, F.R. & Slaughter, C.W. 1973. *Equivalent Latitude (Potential Insolation) and a Permafrost Environment: Caribou-Poker Creeks Research Watershed, Interior Alaska.* Unpublished report. U.S. Army Cold Region Research and Engineering Laboratory, 31 pp.

Lee, R. 1962. Theory of the "Equivalent Slope". *Monthly Weather Review* 90: 165-196.

Leverington, D.W. & Duguay, C.R. 1996. Evaluation of three supervised classifiers in mapping depth to late-summer frozen ground, central Yukon Territory. *Canadian Journal of Remote Sensing* 22(2): 163-174.

Leverington, D.W. & Duguay, C.R. 1997. A Neural network method to determine the presence or absence of Permafrost near Mayo, Yukon Territory, Canada. *Permafrost and Periglacial Processes* 8: 205-215.

Morrissey L.A., Strong, L. & Card, D.H. 1986. Mapping permafrost in the boreal forest with thematic mapper satellite data. *Photogrammetric Engineering and Remote Sensing* 52: 1513-1520.

Okanoue, M. 1957. A simple method to compute the amount of sunshine on a slope. *Journal of Japanese Forest Society* 39(11): 435-437.

Peddle, D.R. 1991. Evidential classification of land cover and permafrost from multisource remote sensing imagery in mountainous terrain, Yukon. Calgary: Department of Geography, University of Calgary, 178 pp.

Peddle, D.R. & Franklin, S.E. 1993. Classification of permafrost active layer from remote sensed and topographic evidence. *Remote Sensing of Environment* 44: 67-80.

Pohl, C. & Van Genderen, J.L. 1998. Multisensor image fusion in remote sensing: concept, methods and applications. *International Journal of Remote Sensing* 19(5): 823-854.

Schowengerdt, R.A. 1983. *Techniques for Image Processing and Classification in Remote Sensing*. Academic Press, 249 pp.

Smith, M.W. 1975. Microclimate influences on ground temperatures and permafrost distribution, Mackenzie Delta, Northwest Territories. *Canadian Journal of Earth Sciences* 12: 1421-1438.

Solie, D.N. & Burns, L.E. 2007. Alaska Highway corridor geology and geophysics. *Alaska GeoSurvey News* 10(1): 1-5.

Williams, P.J. & Smith, M.W. 1989. *The Frozen Earth: Fundamentals of Geocryology*. Cambridge: Cambridge University Press, 306 pp.

Electrical Freezing Potentials During Permafrost Aggradation at the Illisarvik Drained-Lake Experiment, Western Arctic Coast, Canada

V.R. (Sivan) Parameswaran
Department of Geography and Environmental Sciences, Carleton University, Ottawa, Canada, and Institute for Research in Construction, National Research Council Canada, Ottawa, Canada
C.R. Burn
Department of Geography and Environmental Studies, Carleton University, Ottawa, Canada

Abstract

A probe containing a series of electrodes spaced at regular intervals was used to monitor electrical potentials developed across the freezing front during permafrost aggradation at depth in the talik of the Illisarvik drained lake bed. Data were collected from 2000 to 2007. The electrode located at the freezing interface showed a peak electrical potential, commonly of tens of mV, when measured with respect to reference electrodes in the unfrozen or the completely frozen region. The location of the freezing front was consistent with temperature measurements using thermistors installed at these depths. This experiment suggests that, with proper electrode probes and frequent measurements, electrical freezing potentials can be used for monitoring the movement of the freezing front in permafrost areas.

Keywords: freezing potential; Illisarvik; permafrost aggradation.

Introduction

The development of electrical freezing potentials across freezing interfaces in aqueous solutions and moist soils has been studied for the past five decades (e.g., Workman & Reynolds 1950). The potentials arise due to charge separation during phase change of water and selective incorporation in the frozen and unfrozen regions of H^+ and OH^- ions in pure water and other cations and anions in solutions and soils. Early measurements of freezing potentials in water and dilute solutions, as well as in soils, have been reviewed by Parameswaran (1982) and Parameswaran et al. (2005). Field measurements of such potentials developed during permafrost aggradation were presented by Parameswaran & Mackay (1983, 1996), during thawing of the active layer by Parameswaran et al. (1985), and during freezing of lake water by Burn et al. (1998).

During freezing, liquid water migrates to the freezing interface, especially in fine-grained silty and clayey soils (Williams & Smith 1989). An electrical field developing at the freezing front will enhance the drift of unfrozen water, leading to accumulation of ice at the freezing interface (Hoekstra & Chamberlain 1963, Nersesova & Tsytovich 1966). Such geo-electrical potentials may also affect the cathodic protection of buried pipelines and other utilities. The purpose of this paper is to present recent measurements of electrical potentials made at depth during freezing of the talik at the Illisarvik drained-lake experiment, near the western Arctic coast of Canada (Figs. 1, 2).

Illisarvik

A field experiment to drain a lake and to study the aggradation of permafrost in a natural arctic environment was conceived by Professor J.R. Mackay in the 1960s

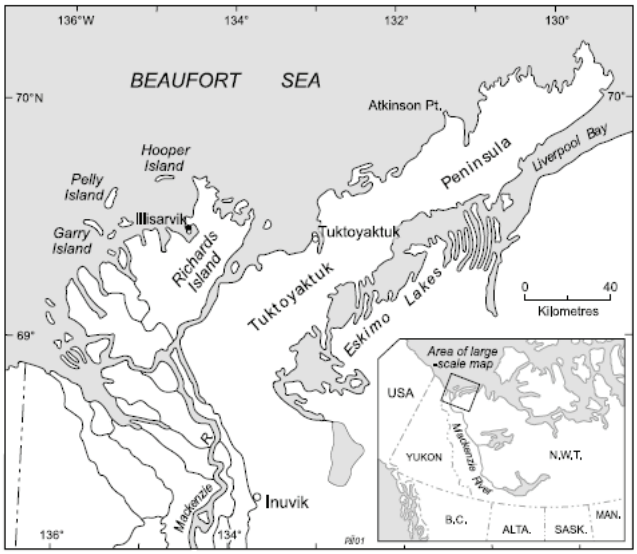

Figure 1. Location of Illisarvik (Mackay & Burn 2002a, Fig. 1, reproduced with permission of NRC Research Press).

(Mackay 1997). Illisarvik Lake, on the west coast of Richards Island, Northwest Territories, was 600 m long and 300 m wide, with a depth mostly between 2 and 3 m, and at the deepest point, over 5 m. Most of the lake bottom remained unfrozen throughout the year, and at the midpoint, the depth of the sublake talik was 32 m (Hunter et al. 1981). The lake was drained on 13 August 1978. After drainage, permafrost started to grow downwards and from the sides of the talik into the lake sediments, and since then, permafrost has been aggrading at the center of the lake by gradual freezing of the ground (Mackay 1997). Field studies have been conducted at the site on a continuing basis into several topics including growth of permafrost, development of ground ice, development of the active layer, pore-water

Figure 2. Aerial view of Illisarvik (Mackay & Burn 2002b, Fig. 2, reproduced with permission of NRC Research Press).

expulsion, electrical freezing potentials developed during permafrost growth, and other geophysical effects (see Burn & Burgess 2000).

By 1995 the talik was at -0.2°C or below, but surface evidence of pore-water expulsion, in the form of an annual ice dome on the residual pond near the center of the lake bed, has indicated that the talik is not frozen (Mackay 1997). The top of the ice dome has been up to about 1 m higher than the surrounding pond ice between 1995 and 2007. Water collected from beneath the ice dome in late winter 2000 may be indicative of the solute concentrations in the groundwater of the unfrozen talik. Measured concentrations of major ions were (mg/L): Na^+ 1000; Cl^- 2000; Ca^{++} 460; Mg^{++} 470; K^+ 51. The total dissolved solids were measured at 6700 mg/L. The conductivity of the water was 6 mS/cm. Similar data are presented by Mackay (1997).

Freezing Potentials at Illisarvik

The deposits in the lake bed consist of 2 to 4 m of fine-grained, organic-rich lake sediments over medium- to fine-grained sand. Permafrost was established in these deposits during the first winter following drainage, and by 1981 the ground had frozen to a depth of about 5.65 m. In June 1981, an electrode probe, about 10 m long, was installed at the center of the lake, with 21 ring electrodes placed around the bottom 3 m of the probe and spaced 150 mm apart. While the freezing front advanced downwards, a small electrical potential (a few hundred mV up to 1 V) developed at each electrode, as the freezing front crossed that location. These measurements, carried out over 15 months, were reported by Parameswaran & Mackay (1983).

The conclusion from this early field measurement, during relatively rapid ground freezing, was that progress of the freezing front could be monitored with suitable electrodes installed at regular intervals. Between March 1981 and August 1982, the freezing front advanced from electrode location 15 down to electrode location 11, about 0.6 m downwards. This was confirmed by temperature measurements near the electrode locations. It is important to note that at this stage of the field experiment, the temperature gradient in the frozen ground was relatively steep, and there was little temperature depression below 0°C within the talik (Mackay 1997). As a result, the freezing front was relatively well-defined in physical terms. The thermo-physical conditions were quite different by 1998 when the investigation reported here began (e.g., Mackay 1997).

Field Methods

Drilling in the center of Illisarvik in August 1998 indicated that the ground was at least partially frozen to a depth of 13.5 m. In August 1999, a hole was drilled by water jet in the center of the drained lake bed, and an electrode probe was inserted to a depth of 16 m. Water-jet drilling does not provide undisturbed samples from the hole, but it is possible to interpret a generalized stratigraphy from the soil materials returned uphole, the behavior of the pipe during drilling, and the resistance of the ground to the drill. A thermistor cable was placed in a second hole, approximately 3 m from the first. The cable was installed in a casing of 1-in steel pipe. We have found that near the ground surface the steel pipe is sufficiently robust to withstand environmental stresses in a field context, while PVC pipes we have installed have lasted only a few years before being damaged.

The stratigraphy at the site comprised the active layer, about 0.8 m thick, lying on top of hard frozen organic lake sediments. Below 4.3 m depth the ground was not as well bonded, and below 13.5 m the ground was unfrozen. Temperature profiles from August 2000 and 2005 for the upper 18 m at the lake center are presented in Figure 3.

Probe Design

Figure 4 presents a schematic diagram of the electrode probe. The top 2 segments of the probe consisted of 1-in steel pipe, each 2 m long. Below that were 6 schedule 80 PVC pipes, each also 2 m long. All the pipes were threaded at both ends to fit joining couplings. Below these 8 lengths was a 1-m long PVC pipe with a conical plug at the bottom.

Ten ring electrodes made of gold-plated copper strips, 12.5 mm wide and about 1 mm thick, were placed around the PVC tubes at various intervals. Most of the electrodes were located in the unfrozen zone below 13.5 m on the PVC pipe #6, but 1 electrode (E1) was located in the hard frozen zone (on PVC pipe #1), and 2 (E2 and E3) were in the partially frozen ground, E2 on PVC pipe #2 and E3 on pipe #4. Electrodes E4 to E10 were on pipe #6 (Fig. 4).

Coaxial cables of sufficient length were soldered to the ring electrodes and fed through the hollow center of the tube assembly. The ends were stored above ground in a pipe nipple connected to the top of the uppermost steel pipe.

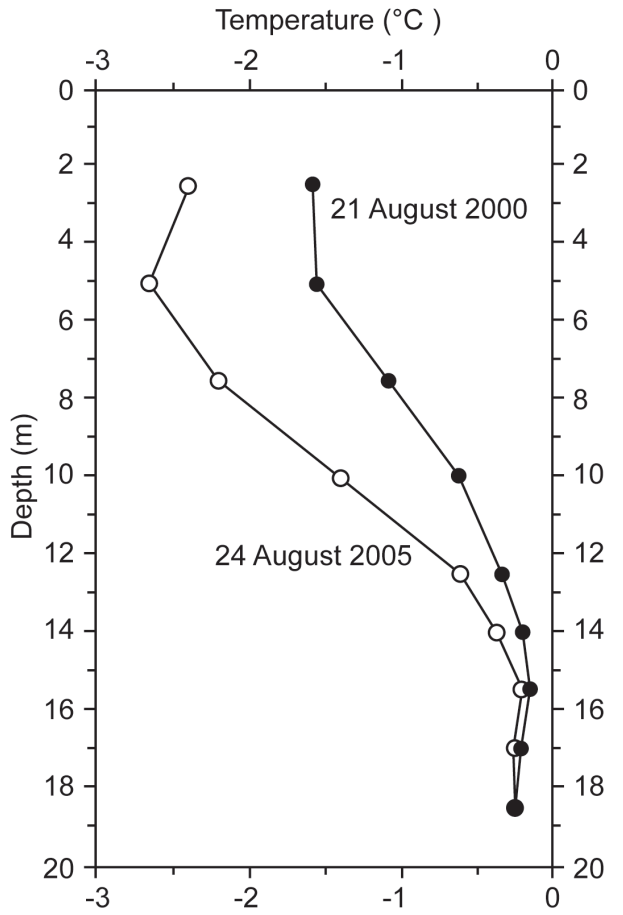

Figure 3. Ground temperature profiles at the center of Illisarvik, 21 August 2000 and 24 August 2005, showing evolution of the ground thermal regime during the study period.

During field visits throughout the year between 1999 and 2007, the electrical potentials developed at each electrode were measured with respect to the unfrozen ground at electrode E10 as well as the frozen ground at electrode E1. The potentials (in mV) were measured by multimeter with a sensitivity of 0.01 mV.

Results

Data collected up to March 2006 indicated a peak potential within the interval between E4 (13.5 m depth) and E10 (14.4 m depth). After this date, in August 2006 and April, June, and August 2007, the measurements provided no trend with depth, and the potentials at most electrodes tended to 0 mV shortly after connection.

Figure 5 presents data from 12 June 2001, showing a typical set of measurements for E4 to E10. In general, the potential at E1 was positive with respect to E10 throughout the period of measurement. The plot shows the potentials at each electrode as a function of depth.

A peak is observed at electrode E6, at a depth of 13.8 m below the ground surface, indicating the location of the freezing front. Both curves, with reference to E1 or E10, follow the same trend and show the peak at the same location. Figure 6 shows similar measurements from 20 August 2001,

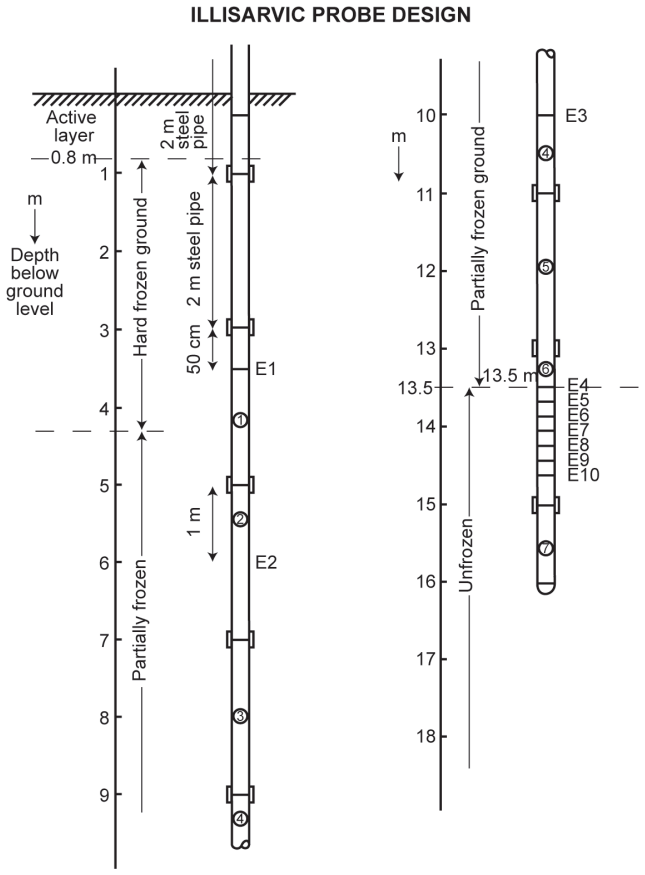

Figure 4. Probe design.

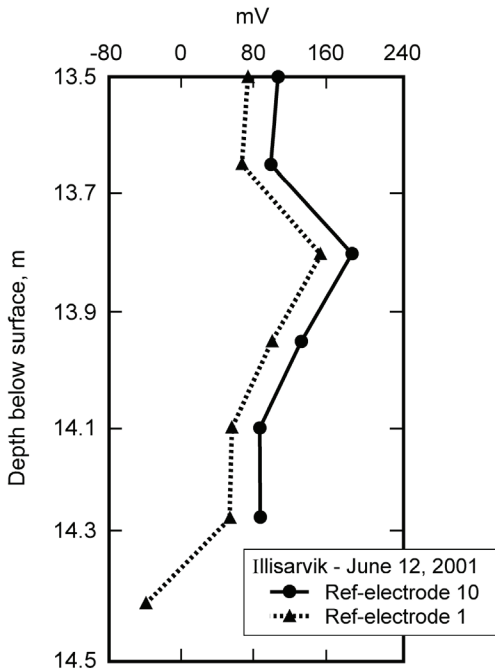

Figure 5. Electrical potential profiles from 12 June 2001.

when, again, the peak was recorded at electrode E6.

Figure 7 shows the readings taken on 14 April 2003. The peak potential had advanced to electrode E9, at a depth of 14.25 m below the ground surface. This suggests that between June 2001 and April 2003, the locus of electrical potential advanced downwards from 13.8 m to 14.25 m.

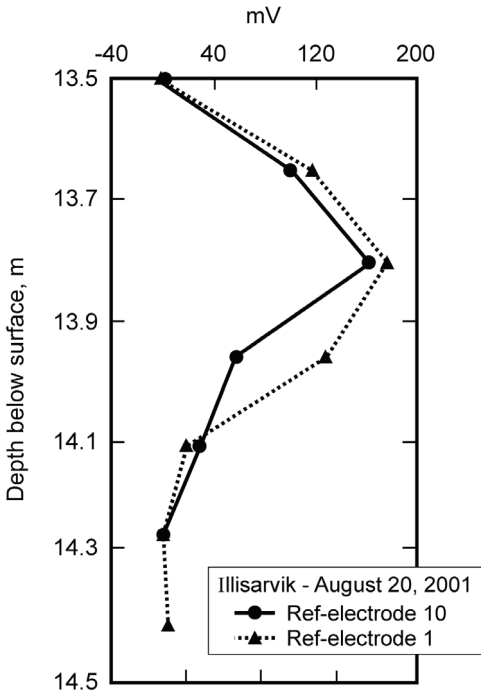

Figure 6. Electrical potential profiles from 20 August 2001.

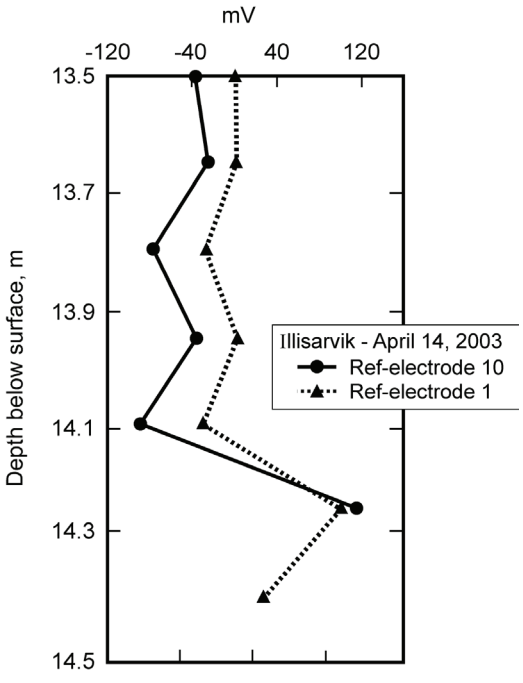

Figure 7. Electrical potential profiles from 14 April 2003.

However, measurements taken on 20 June 2004 showed considerable variation of potentials at the electrodes at different depths (Fig. 8), with the peak occurring at electrode E9 at a depth of 14.25 m below the ground surface. During the period of measurement, data similar to the profile in Figure 8 were collected on several occasions, but normally the profiles presented one distinct peak potential. The peak potential was measured at E8 or E9 between April 2002 and March 2006.

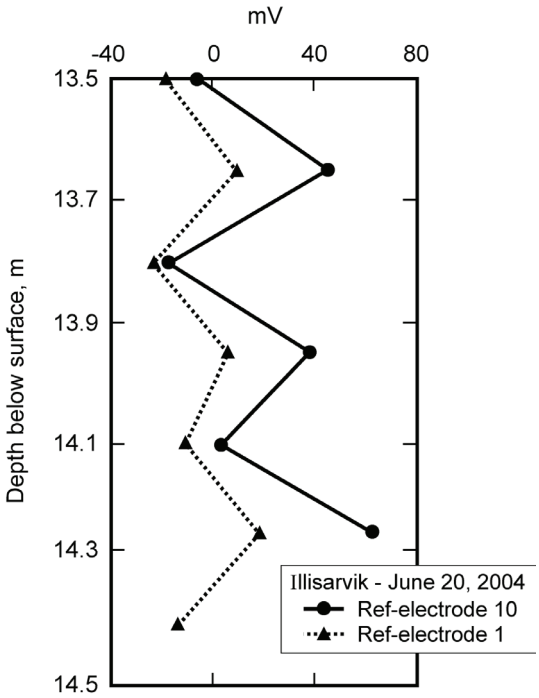

Figure 8. Electrical potential profiles from 20 June 2004.

Figure 9 is a plot of the location of the freezing front with time (as estimated from the peak electrical freezing potentials measured on the electrodes) and the variation of the temperature of the ground between 2000 and 2005. The lower curve shows the temperatures at a depth of 14.0 m and the upper one at 15.5 m. The peak potential in June and August 2001 was at electrode location E6, at a depth of 13.8 m. The temperatures measured by the thermistors installed in this region of the ground were -0.29°C to -0.30°C at a depth of 14 m and -0.20°C to -0.22°C at a depth of 15.5 m. In April 2002, the temperature at 14 m depth was -0.34°C and the peak potentials were observed on electrodes E8 and E9, at depths of 14.1 and 14.25 m, respectively. The temperature at the depth of 15.5 m was -0.18°C, in the unfrozen region of the ground. These data suggest that the peak potential developed at a temperature of about -0.3°C, for the temperature at 14 m, was between -0.3°C and -0.4°C when the peak was measured at depths between 14.1 m and 14.25 m. The pattern illustrated in Figure 8 and the persistence of potentials in the profile lower than the peak value, both above and below the location of the peak, indicate that the freezing front is not a distinct feature at the scale of these measurements (intervals of 15 cm). Instead, there is likely a freezing zone, with some temperature depression, within which the potentials develop. The stratigraphic interpretation from the drilling record indicated partially frozen ground from depths of 4.3 m to 13.5 m (Fig. 4). The measurements presented here suggest that there is a concentration of solutes close to the temperature of ice nucleation in the soil, leading to development of a potential by charge separation. In turn, this suggests that there is a relatively restricted area where solute effects are focused, in comparison with the 9 m of partially frozen ground.

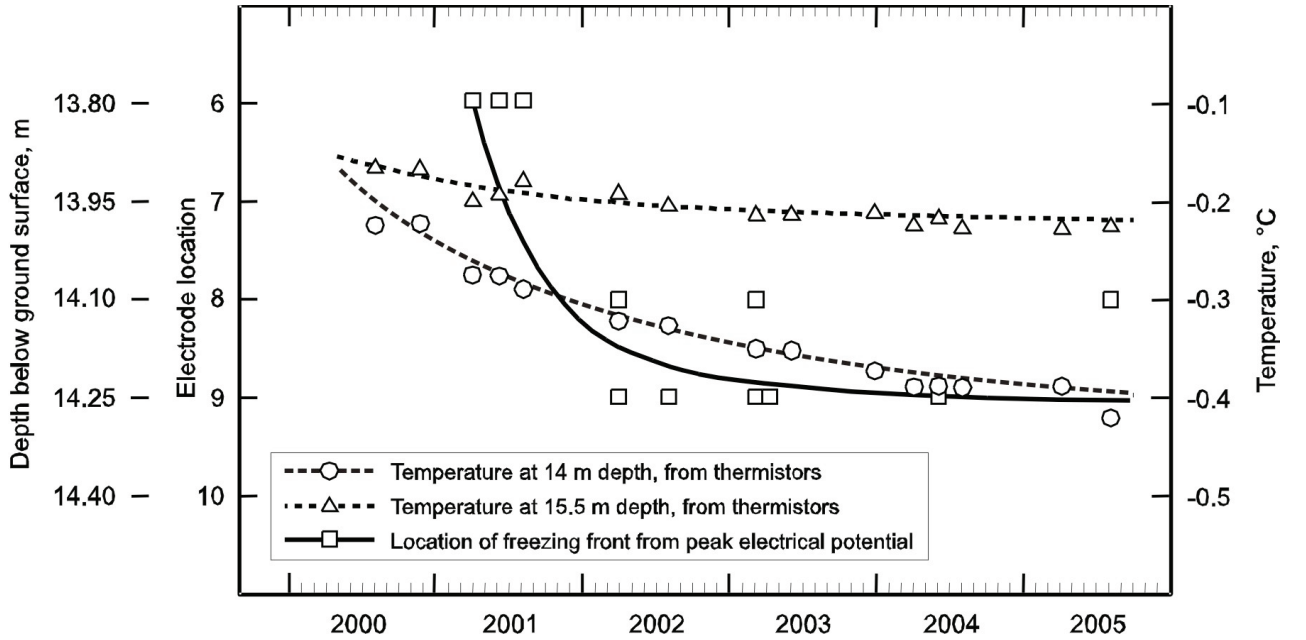

Figure 9. Location of the freezing front interpreted from peak potentials and proximal ground temperatures at depth in the talik at Illisarvik, 2000–2005.

Assuming a freezing point depression of about 0.2°C to 0.25°C due to the solutes present in the groundwater at these depths, we can assume electrode E8 is at the freezing front, and the electrode potential measurements indicate this. By January 2003, the temperature at 14 m depth was less than -0.35°C. The peak freezing potentials were observed on electrode E9, at a depth of 14.25 m. As shown by the upper curve in Figure 9, the temperature at the depth of 15.5 m was still around -0.2°C, the temperature measured after drilling, when it was determined to be unfrozen.

Measurements after March 2006 showed considerable oscillations in the profile, and very low absolute voltages, indicating probably that the freezing front had advanced below the lowest electrode in the assembly. Similar patterns in the measured profile were also observed in the measurements reported by Parameswaran & Mackay (1983), when all the electrodes were embedded in the frozen soil. This could be the effect of shorting the circuit, as the measuring electrode and the reference electrode were both embedded within the same frozen system. Laboratory observations of the shorting potentials were reported by Parameswaran et al. (2005).

Conclusions

Electrical freezing potentials were observed at electrodes positioned at the freezing interface in the talik of the Illisarvik drained lake. The location of the peak electrical potential indicated its development at a temperature of about -0.3°C. The principal results are:

(1) Electrical potentials can be measured during permafrost aggradation. The potential is permafrost positive.

(2) The potential is on the order of tens of mV.

(3) The potential may develop below 0°C, perhaps indicating the nucleation temperature of ice in groundwater.

With proper electrode probes and with more frequent measurements, electrical potential probes can be used for monitoring the movement of the freezing front in permafrost areas.

Acknowledgments

The research has been supported by the Natural Sciences and Engineering Research Council of Canada, the Polar Continental Shelf Project of Natural Resources Canada, and the Aurora Research Institute. We thank Larry Boyle for manufacturing the probe, and A. Burn, D. Riseborough, and J.R. Mackay for assistance during installation. D. Esagok and L. Kutny have provided assistance with measurements throughout the project. We also thank Don Hobbs, Peter Richards, and Michelle Gagnon of the Institute for Research in Construction, National Research Council Canada, for preparation of Figures 3 through 9. The National Research Council of Canada Research Press kindly gave permission to reproduce Figures 1 and 2. This paper is Polar Continental Shelf Project contribution number 00808.

References

Burn, C.R. & Burgess, M.M. 2000. The Illisarvik Bibliography. www.nwtresearch.com/illisarvik

Burn, C.R., Parameswaran, V.R., Kutny, L. & Boyle, L. 1998. Electrical potentials measured during growth of lake ice, Mackenzie Delta area, N.W.T. *Proceedings of the Seventh International Conference on Permafrost, Yellowknife, N.W.T., June 23-27, 1998*: 101-106.

Hoekstra, P. & Chamberlain, E. 1963. Electro-osmosis in frozen soils. *Nature* 203: 1406.

Hunter, J.A., MacAulay, H.A., Gagné, R.M., Burns, R.A., Harrison, T.E. & Hawkins, J.P. 1981. Drained lake experiment for investigation of growth of permafrost at Illisarvik, Northwest Territories – initial geophysical results. *In* Current research, part C. Geological Survey of Canada, Paper 81-1C, 67-76.

Mackay, J.R. 1997. A full-scale field experiment (1978-1995) on the growth of permafrost by means of lake drainage, western Arctic coast: a discussion of the method and some results. *Canadian Journal of Earth Sciences* 34: 17-33.

Mackay, J.R. & Burn, C.R. 2002a. The first 20 years (1978/79 to 1998/99) of ice-wedge growth at the Illisarvik experimental drained lake site, western Arctic coast, Canada. *Canadian Journal of Earth Sciences* 39: 95-111.

Mackay, J.R. & Burn, C.R. 2002b. The first 20 years (1978/79 to 1998/99) of active-layer development, Illisarvik experimental drained lake site, western Arctic coast, Canada. *Canadian Journal of Earth Sciences* 39: 1657-1674.

Nersesova, Z.A. & Tsytovich, N.A. 1966. Unfrozen water in frozen soils. *Permafrost, Proceedings of the First International Conference*, *Lafeyette, Indiana, November 11-15, 1963*: 230-234.

Parameswaran, V.R. 1982. Electrical freezing potentials in water and soils. *Proceedings of the Third International Symposium on Ground Freezing, Hanover, NH, June 22-24, 1982*: Vol. 2, 83-89.

Parameswaran, V.R. & Mackay, J.R. 1983. Field measurements of electrical freezing potentials in permafrost areas. *Proceedings of the Fourth International Conference on Permafrost, Fairbanks, Alaska*, *July 17-22, 1983*: Vol. 1, 962-967.

Parameswaran, V.R. & Mackay, J.R. 1996. Electrical freezing potentials measured in a pingo growing in Western Canadian Arctic. *Cold Regions Science and Technology* 24: 191-203.

Parameswaran, V.R., Johnston, G.H. & Mackay, J.R. 1985. Electrical potentials developed during thawing of frozen ground. *Proceedings of the Fourth International Symposium on Ground Freezing*, *Sapporo, Japan, August 5-7, 1985*. Vol. I, pp. 9-16.

Parameswaran, V.R., Burn, C.R., Profir, A. & Ngo, Q. 2005. A note on electrical freezing and shorting potentials. *Cold Regions Science and Technology* 41: 83-89.

Williams, P.J. & Smith, M.W. 1989. *The Frozen Earth: Fundamentals of Geocryology*. Cambridge: Cambridge University Press, 360 pp.

Workman, E.J. & Reynolds, S.E. 1950. Electrical phenomena occurring during the freezing of dilute aqueous solutions and their possible relationship to thunderstorm electricity. *Physical Review* 78: 254-259.

Managing Permafrost Data: Past Approaches and Future Directions

Mark A. Parsons
World Data Center for Glaciology, Boulder, USA
Sharon L. Smith
Geological Survey of Canada, Ottawa, Canada
Vladimir E. Romanovsky
University of Alaska Fairbanks, USA
Nikolai I. Shiklomanov
University of Delaware
Hanne H. Christiansen
The University Centre in Svalbard, UNIS, Norway
P. Paul Overduin,
Alfred Wegner Institute, Potsdam, Germany
Tingjun Zhang
National Snow and Ice Data Center, Boulder, USA
Megan R. Balks
University of Waikato, Private Bag 3105, Hamilton, New Zealand
Jerry Brown
International Permafrost Association, Woods Hole, USA

Abstract

The International Permafrost Association (IPA) has a long history of data management. Notable achievements include the establishment of a Global Geocryological Data (GGD) system and the publication of the Circumpolar Active-layer Permafrost System (CAPS) compilations. At the same time, the IPA has struggled to maintain continual stewardship of permafrost and related data with sustained support. Activities as part of the International Polar Year will significantly increase data holdings and will required renewed emphasis on data description, preservation, and integration with other disciplines.

Keywords: data management; frozen ground; GGD; IPA; IPY; permafrost.

Introduction

Permafrost and seasonally frozen ground data and information are critical for fundamental process understanding, environmental change detection, impact assessment, model validation, and engineering applications. The International Permafrost Association (IPA) has long emphasized the importance of these data and has encouraged ongoing data sharing and management through the Global Geocryological Data (GGD) system. The GGD is an internationally distributed system linking investigators and data centers around the world and was proposed by Barry et al. (1995). The World Data Center (WDC) for Glaciology at Boulder has historically acted as central node of the GGD and has published two compendiums of permafrost related data: *Circumpolar Active-Layer Permafrost System* (CAPS) Version 1 and the substantially updated Version 2 (IPA DIWG 1998, IPA SCDIC 2003).

Data advertised through the GGD and published on CAPS include information on borehole parameters, soil temperature, cryosols, and climatology as well as maps, metadata, and bibliographies. Data come from diverse international sources, but data produced by IPA projects have always been prominent in the collections. These products include benchmark maps such as the *Circum-Arctic Map of Permafrost and Ground-Ice Conditions* (Brown et al. 1998) as well as data and metadata from ongoing IPA programs such as the Global Terrestrial Network for Permafrost (GTN-P), the Arctic Coastal Dynamics (ACD) program, and the Antarctic Permafrost and Soils (ANTPAS) project. These IPA programs continue to produce important data with a burst of new activity in the International Polar Year (IPY). Another area of potential data growth is through satellite remote sensing.

While the GGD has succeeded in capturing and describing many important data resources, it has been an ad hoc activity without sustained support for ongoing data collection and stewardship. There is a critical need to sustain data stewardship activities throughout the entire data lifecycle. Note, data stewardship is a broader concept than data management. It can be defined as "all activities that preserve and improve the information content, accessibility, and usability of data and their associated metadata" (NRC 2008). Correspondingly, the concept of a data lifecycle reflects how data are continually evaluated, improved, and maintained for archiving until retired or discarded.

The GGD is linked to the broader IPY Data and Information Service (IPYDIS), which works with the Scientific Committee on Antarctic Research (SCAR) and International Arctic Science Committee (IASC) to establish a lasting polar data infrastructure. The IPA seeks to contribute to this international effort by capturing the burst of permafrost data collection during IPY, and ensuring the preservation of past data in a new CAPS Version 3 compilation. The IPA also seeks to develop a more sustainable data collection and stewardship strategy through linkages to other relevant international programs including the intergovernmental Group on Earth Observations (GEO).

Global Geocryological Data

The need for a consistent and comprehensive permafrost data management has long been recognized. In 1983, the U.S. National Research Council called for greater coordination and a specialized permafrost data clearinghouse (NRC 1983). In 1988, the WDC for Glaciology at Boulder organized a workshop in Trondheim, Norway in conjunction with the Fifth International Conference on Permafrost (Barry & Brennan 1989). This workshop, coupled with a paper presented by Roger Barry (1988), led to the establishment of a Data and Information Working Group within the IPA and established the overall IPA data strategy. The strategy was refined based on an international survey of permafrost data holdings (Barry & Brennan 1993) and culminated in the establishment of the GGD and the first CAPS compilation for the Seventh International Conference on Permafrost, SICOP, in 1998. Furthermore, delegates to the SICOP International Conference recognized the importance of continuity in data and information activities, and the existing Working Group was reestablished as a permanent Standing Committee on Data Information and Communication (SCDIC) during the Twelfth IPA Council Meeting at SICOP in Yellowknife, Canada.

The 1998 CAPS1 included 56 datasets and an additional 89 metadata descriptions for products held elsewhere around the world. In late 2002, the newly established Frozen Ground Data Center (FGDC) at the WDC for Glaciology at Boulder in collaboration with the International Arctic Research Center published the contents of CAPS online at the FGDC web site and began updating and adding to the CAPS collection to create CAPS Version 2. CAPS2 expanded the scope of CAPS by including data and information for seasonally frozen ground regions from in-situ measurements, satellite remote sensing, and model outputs and included data and metadata for more than 200 datasets. More comprehensive data documentation was also written.

Since the publication of CAPS2, the FGDC has published several other datasets. These additions include important historical data (Oberman & Kakunov 2004), maps (Sodnom & Yanshin 1990), and long-term, broad-scale time series of seasonally frozen soil parameters (Zhang et al. 2005). These products are available through the FGDC web site. Data will remain available until the next major media migration or system upgrade at the WDC, at which point the FGDC distribution will need to be retired, unless continued funding can be identified.

In many ways, the history of the GGD parallels the evolution of digital data management in general. Initial bibliographic efforts grew into data compilation and recording efforts. Standard metadata formats were created and implemented. Central catalogs describing distributed data were created. Media and distribution methods evolved.

In some ways the GGD was at the forefront of developments in data management. For example, CAPS1 included specific citations for all datasets and urged investigators to formally cite data use as they would any other publication. This practice is just now gaining wide spread acceptance as is evident in the IPY Data Policy and increasing acceptance of data citations by leading journals.

On the other hand, the GGD has been largely an ad hoc effort punctuated by intense activity around the CAPS compilations. This contrasts with the increasing recognition of the importance of continual data stewardship and full lifecycle data management (USGCRP 1999, NRC 2008). For example, part of the effort of updating CAPS was to try and contact the investigators and institutions holding the 89 GGD products described but not contained on CAPS1. Unfortunately, 45 of the 89 products were not readily accessible and may no longer be available. The potential loss of these data highlights the need for continued support of data management for the permafrost community.

The IPA through its SCDIC needs to evolve its data strategy and the general GGD system to more actively acquire current datasets, rescue data at risk of loss, ensure the planned migration of investigator held data to more permanent archives, and address the growth of data resulting from the burst of IPA activity as part of the IPY.

IPA Programs and the IPY

A summary of the major IPA activities since its formation in 1983 is presented in these proceedings (Brown et al. 2008). In addition to mapping, bibliographic, and terminology projects, the main IPA focus has been on broad, coordinated international field programs. Individual national sponsors fund each program, but the field efforts are unified through IPA coordination of site documentation, data collection methods, and metadata descriptions. Each program has its own data management structure that can be considered a node of the GGD, while metadata should be broadly shared to facilitate discovery across the GGD. IPA programs include:

- The Global Terrestrial Network for Permafrost (GTN-P), which includes both boreholes and active layer sampling protocols.
- The Arctic Coastal Dynamics (ACD) project.
- Northern Circumpolar Soil Carbon Database (NSCD) (Tarnocai et al. 2007).

• Each IPA program is linked to IPY approved and coordinated projects including "Permafrost Observatory Project: A Contribution to the Thermal State of Permafrost" (IPY project #50), "Arctic Circum-Polar Coastal Observatory Network (ACCO-Net)" (IPY 90), "Antarctic and sub-Antarctic Permafrost, Periglacial and Soil Environments" (IPY 33), "Carbon Pools in Permafrost Regions" (IPY 373), and the Russian project, "Response of Arctic and Subarctic soils in a changing Earth: dynamic and frontier studies" (IPY 262).

Global Terrestrial Network for Permafrost

The GTN-P consists of two components: the Thermal State of Permafrost (TSP) and the Circumpolar Active Layer Monitoring Network (CALM) (Burgess et al. 2000). Together they are contributing to the Global Earth Observation System of Systems and the UN Framework Convention on Climate Change through the Global Terrestrial Observing System.

The TSP component of GTN-P consists of a network of boreholes, in which permafrost temperatures are measured. The network currently consists of over 300 boreholes with many new sites to be established during IPY. This network is built on a number of regional networks. Boreholes range in depth from a few meters to greater than 100 m with record lengths of up to three decades. Data collected from this network has provided important information on the change in permafrost temperature over time and are important contributions to major regional and global assessments (ACIA 2004, IPCC 2007, UNEP 2007).

TSP borehole metadata (site descriptions) and summary permafrost temperature data are accessible through the GTN-P web site hosted by the Geological Survey of Canada (GSC). A major goal for IPY is to provide a "snapshot" that describes the thermal state of permafrost for a specific time period. This snapshot can serve as a baseline for the assessment of the rate of change of permafrost conditions and can be used to validate climate model scenarios and to support process research to improve our understanding of permafrost dynamics.

Two national programs within the TSP project illustrate the project scope and its data management challenges. The TSP Norway project plans to establish the North Scandinavia Permafrost Observatory around 70°N, covering a transect from maritime northern Norway into northwestern Sweden and Finland. The Svalbard Nordenskiöld Land Permafrost Observatory around 78°N is already being established. Both observatories deliver borehole temperatures, active layer thickness, meteorological, and periglacial process data from different permafrost landforms. All these data will be organized in the NORPERM database located at the Norwegian Geological Survey. The aim is to also include earlier permafrost and periglacial data from all of Norway and Svalbard in the database. Data from NORPERM shall also be available to others through the GTN-P.

The Canadian Permafrost Monitoring Network coordinated by the GSC consists of over 100 monitoring sites maintained by government agencies and universities. Sites are largely concentrated in the western Arctic (Mackenzie Valley and Delta), northern Quebec, with a few sites in the high Arctic. During IPY, scientists intend to establish new monitoring sites in northern Manitoba, Yukon and Nunavut Territories as part of the TSP project.

The Canadian network maintains a web site that links to the GTN-P web site and provides access to metadata for both active layer and permafrost thermal monitoring sites and summary data. Linkages with the Canadian cryospheric community are through the Canadian Cryospheric Information Network. Canada's contribution to the IPY will be a standardized set of permafrost temperatures collected during IPY that will be compiled into a digital database to be released through the web site and as a CD publication.

The other major component of GTN-P, CALM, monitors active layer thickness and shallow ground temperature, and coordinates field experiments. The CALM network currently consists of more than 150 sites distributed throughout the Arctic and several mountain ranges of the mid-latitudes. Efforts to expand the number and capabilities of sites in the Southern Hemisphere (CALM-S) are underway through ANTPAS. Instrumentation and data-acquisition methods include monitoring the soil thermal and moisture regimes with automatic data loggers, mechanical probing of the seasonally thawed layer at specified spatial and temporal intervals, frost/thaw tubes, and a variety of instruments for measuring frost heave and thaw subsidence.

Data are transferred to the CALM data repository at the University of Delaware for archive and distribution through the CALM web site, which is linked to the GTN-P site and FGDC (Shiklomanov et al. 2008).

Arctic Coastal Dynamics

The ACD project of IASC and the IPA was created in 1999 to improve understanding of circum-Arctic coastal dynamics under the influence of environmental changes and geologic controls. ACD's international and ongoing effort to segment and classify the entire circum-Arctic coastline has resulted in a scalable GIS database of coastal geomorphological characteristics evaluated by regional experts. This detailed evaluation has been compiled into a geographic information system (GIS), which contains data on coastal morphology, composition, dominant processes, ground ice, and environmental forcing parameters such as wind speed, storm counts, melt season, and wave energy.

This information is available for over 1300 segments, covering the coastline of all eight regional seas of the Arctic Ocean. The coasts of the Barents, Kara, Laptev, East Siberian, Chukchi, and Beaufort Seas have been segmented, as has the coastline of Svalbard. The length of individual segments varies (median length is 38 km), but the segmentation format is scalable, allowing the adoption of future digital coastlines and the integration of additional, higher-resolution data. The data are available via an Internet map server and as a downloadable geodatabase at the ACD web site. Others with complementary datasets are encouraged to contribute to this growing data resource. Future development will include the incorporation of remote sensing into the geodatabase.

ACD represents the coastal component of the ongoing international effort to integrate existing and planned Arctic observatories into a coherent Sustained Arctic Observatory Network (SAON). In addition, ACD's IPY activity, ACCO-Net, integrates 17 Arctic coastal observatory projects with 24 ACD key sites into an extended network.

Antarctic Permafrost and Soils

The overall objective of ANTPAS is to develop an internationally coordinated, web-accessible, database and monitoring system on Antarctic permafrost and soils. Specific objectives are to:

1. Develop a web-accessible repository for permafrost and soils data.
2. Prepare thematic maps on Antarctic permafrost and soils.
3. Develop a system of boreholes providing data on permafrost and soils properties, past environmental change, and responses to climate change.
4. Develop a monitoring system recording active layer and periglacial process responses to climate change along selected environmental gradients.

With no centralized funding, ANTPAS progress is restricted to member activity within existing research programs. ANTPAS has developed a web site for publications and links to relevant databases (Objective 1).

Progress has been made on developing soil and permafrost maps (Objective 2), particularly for the Antarctic Peninsula and the Trans-Antarctic Mountain regions. The soil and permafrost data are to be stored, and made available through the web sites of the individual investigators with links to each database from the ANTPAS web site. ANTPAS Objectives 3 and 4 compliment the TSP and CALM projects in the Northern Hemisphere.

Other Geocryological Data

Satellite remote sensing

Satellite remote sensing data are increasingly used for permafrost and seasonally frozen ground studies (Zhang et al. 2004, Duguay et al. 2005). Remote sensing of permafrost terrain and near-surface soil freeze/thaw cycles typically uses a combination of imaging in optical and thermal wavelengths, passive microwave remote sensing, and active microwave remote sensing using scatterometer and Synthetic Aperture Radar (SAR). Consequently, large amounts of valuable data can be generated.

Images and data from the orbiting visible and near-infrared sensors can be used to infer permafrost distribution (e.g., Anderson et al. 1984), active layer thickness, and various periglacial features (Leverington & Duguay 1996). LANDSAT data provide a high-resolution (15 m to 80 m), long (1972–present) time-series, useful to investigate changes in land surface morphology such as in rock glaciers, thaw lakes, and other periglacial phenomena. Land surface temperature is a key parameter for permafrost and seasonally frozen ground studies. The potential application of using land surface temperature products derived from visible and infrared sensors from 1980 to the present can be substantial (Zhang et al. 2004, Duguay et al. 2005). Remotely sensed land surface temperatures can be used to drive numerical models simulating the development of the active layer and thermal regime of permafrost or to estimate thawing index, which can be used to estimate active layer thickness.

SAR data has been used to map bottom fast ice that controls the preservation and development of subsea permafrost (Solomon et al. 2005). Data from passive microwave sensors dating from 1978 can be used to detect near-surface soil freeze-thaw status based on the spectral sensitivity of brightness temperatures to the state of water (liquid or solid) in soils. Zhang and Armstrong (2003) have provided the near-surface (<5 cm) soil freeze/thaw status derived from passive microwave satellite remote sensing data over the Arctic terrestrial drainage basin. Other near-surface soil freeze/thaw data products are also available but have not yet been archived.

Scatterometery can also be used to detect near-surface soil freeze/thaw status with relatively high spatial resolution. Attempts have been made to apply the differential interferometric synthetic aperture radar technique to monitor the surface deformation (frost heave and thaw settlement) due to the annual freeze/thaw cycle of the active layer over permafrost (Wang & Li 1999).

As satellite remote sensing techniques improve, more and better products will continue to be generated. It is essential to archive and distribute such data products.

Periglacial process data

Information on the movement and activity of different periglacial landforms derived from many different techniques including remote sensing, geophysical data such as resistivity and georadar, direct movement measurements, and snow distribution data are increasingly being collected; yet they are lacking coordinated data management arrangements. For example, the TSP Norway project is collecting significant periglacial process data. In another example, the FGDC at WDC for Glaciology at Boulder has received several offers of data on rock glaciers from independent investigators. Because these data are not part of a formal funded program at the WDC, it is difficult for the WDC to acquire the data.

Historical and other data

There are a variety of other important geocryological data sources. Various national programs continue to produce important data outside the bounds of formal IPA programs. While some of these data are well managed and readily available, others need to be better described through formal metadata protocols, converted to digital formats, or migrated to new media. Some data are at risk as investigators retire or research programs end. Some data even need to be "rediscovered", such as those datasets advertised on CAPS that are no longer readily available.

Models are also increasingly important in characterizing and predicting geocryological processes, especially in a changing climate regime (e.g., Marchenko et al. 2008).

Preservation and distribution of significant model outputs will be a growing concern.

Finally, the IPA has often produced specialized bibliographies and these have also been featured on CAPS. The Cold Regions Bibliography Project continues this work with the *Bibliography on Cold Regions Science and Technology* (Tahirkheli 2008).

Future Directions

The increased IPY field data collection, the increased application of remote sensing methods, and the growing need to integrate data across disciplines challenge the ad hoc nature of the GGD. To achieve the IPY goals of greater international collaboration and interdisciplinary research, it is insufficient to simply share basic metadata. Data must be provided in more consistent formats through more interoperable data exchange protocols. Open Geospatial Consortium (OGC) standards and technologies provide one approach to interoperable data sharing. Several information portals such as the Arctic Research Mapping Application and the Arctic Portal build off OGC technologies. Already, within the GGD, the ACD is providing its coastal segment database through an OGC map server, while the WDC for Glaciology provides the *Circum-Arctic Map of Permafrost* and other cryospheric data through several OGC protocols (WMS, WCS, WFS) (Maurer 2007). Users can then use these data and services to prepare their own maps, view regions and variables of interest, and compare data from different sources.

Another goal of IPY is to leave a legacy for future generations. This challenges the SCDIC and the GGD to develop a more continuous and sustainable data stewardship and preservation strategy. This applies not only to publicly available databases, but sufficient resources must also be committed for active data rescue activities. We should also recognize the value of the past CAPS compilations in providing data snapshots at periodic intervals. These snapshots can act as archival records that are, in essence, preserved simply through their broad and public distribution. IPY marks an important milestone for the IPA with a pulse of new data, and much of that data will be presented at the Ninth International Conference on Permafrost. The SCDIC hope to use this opportunity to create a new CAPS3 compilation. An excellent deadline and opportunity for broad distribution of CAPS3 is the large IPY closing conference in Oslo, Norway in June 2010. Table 1 summarizes some of the potential content.

As the SCDIC develops CAPS3, it must consider how CAPS can evolve as a preservation medium, as well as what data and information it will contain. Is it still appropriate to create physical media for public distribution (e.g., DVDs), or are other strategies such as the peer-to-peer based LOCKSS (Lots of Copies Keeps Stuff Safe) Program more appropriate? Documentation on CAPS3 should evolve to comply with the ISO standard Open Archival Information System Reference Model (CCSDS 2002, cf. Duerr et al. 2006). Finally, quality control procedures for the data compiled need to be determined. Historically, quality control was the responsibility of individual investigators and national programs, but CAPS3 compilers will want to ensure data are in suitably preserveable formats with adequate description of data uncertainties. CAPS3 can serve as benchmark in the development of a lasting polar data system.

Table 1. Initial CAPS3 data sources.

Source	Description or Activity
GTN-P TSP	Temperature data from 300 designated boreholes
GTN-P CALM	Active layer data from 150 sites
ACD	1331 coastal segments described in a geodatabase.
ANTPAS and TSP	Maps, thousands of soil profiles, and periglacial process data
NCSCD	Database of thousands of polygons with soil properties and carbon stocks
CAPS1 and CAPS2	Updates to key products Rescue of lost products
National programs	Identification, description, and acquisition of important products
Remote sensing & model output	Identification, description, and acquisition of important products
Other projects and investigators	Historical data and value added products such as maps, graphical presentations, analyses, etc.
Bibliographies	Monthly updates to the Cold Regions Bibliography

Acknowledgments

Work discussed in this paper is supported by the U.S. National Science Foundation Office of Polar Programs, the Canadian IPY programme, and the Norwegian Research Council's IPY programme.

References

ACIA (Arctic Climate Impacts Assessment). 2005. *Impacts of a Warming Arctic, Arctic Climate Impacts Assessment.* Cambridge University Press.

Anderson, D.M. et al. 1984. Applications of ERTS-1 imagery to terrestrial and marine environmental analysis in Alaska. *Proceedings of the 3rd Earth Resources Technology Satellite-1 Symposium, Washington, DC, V. 1: Technical Presentations, Section B*, *1984*: 1,575-1,606.

Barry, R.G. 1988. Permafrost data and information: Status and needs. In: K Senneset (ed.), *Proceedings of the Fifth International Conference on Permafrost,. Trondheim, Norway, 2–5 August 1988*. Tapir Publishers, 119-122.

Barry, R.G. & Brennan, A.M. (eds.) 1989. Workshop on Permafrost Data and Information, Trondheim, Norway, 2 August 1988. *Glaciological Data. GD-23*.

Barry, R.G. & Brennan, A.M. 1993. Towards a Permafrost Information and Data System. *Proceedings of the Sixth International Conference on Permafrost, Wushan, China, 5–9 July 1993*. South China University of Technology Press.

Barry, R.G., Heginbottom, J.A. & Brown, J. 1995. Workshop on Permafrost Data Rescue and Access. 3-5 November 1994, Oslo, Norway. *Glaciological Data. GD-28*.

Brown, J., Ferrians, O.J. Jr., Heginbottom, J.A. & Melnikov, E.S. 1998. revised February 2001. *Circum-Arctic Map of Permafrost and Ground-Ice Conditions.* Boulder, CO: National Snow and Ice Data Center/WDC for Glaciology. Digital Media.

Brown, J., French, H.M. & Guodong, C. 2008. History and Accomplishments of the International Permafrost Association on its 25th Anniversary. *Proceedings of the Ninth International Conference on Permafrost, Fairbanks, Alaska June 29–July 3, 2008* (this proceedings).

Burgess, M.M., Smith, S.L., Brown, J., Romanovsky, V. & Hinkel, K. 2000. Global Terrestrial Network for Permafrost (GTNet-P): permafrost monitoring contributing to global climate observations. *Geological Survey of Canada, Current Research.* 2000-E14: 8.

CCSDS (Consultative Committee for Space Data Systems). 2002. *Reference Model for an Open Archival Information System (OAIS) CCSDS 650.0-B-1 Issue 1* Washington, DC: CCSDS Secretariat.

Duerr, R., Weaver, R. & Parsons, M. 2006. A New approach to preservation metadata for scientific data: A real world example. *Geoscience and Remote Sensing Symposium, IGARSS 2006 IEEE International Conference,* 305-308.

Duguay, C.R., Zhang, T., Leverington, D.W. & Romanovsky, V.E. 2005. Satellite remote sensing of permafrost and seasonally frozen ground. In: C.R. Duguay & A. Pietroniro (eds.), *Remote Sensing in Northern Hydrology.* Geophyiscal Monograph 163, Washington, D.C.: American Geophysical Union, 91-118.

IPA DIWG (International Permafrost Association Data and Information Working Group) (comp.). 1998. *Circumpolar Active-Layer Permafrost System* Boulder, CO: National Snow and Ice Data Center/WDC for Glaciology. CD-ROM.

IPA SCDIC (International Permafrost Association Standing Committee on Data Information and Communication) (comp.). M.A. Parsons & T. Zhang (eds.) 2003. *Circumpolar Active-Layer Permafrost System Ver. 2.* Boulder, CO: National Snow and Ice Data Center/WDC for Glaciology. CD-ROM.

IPCC. 2007. *Climate Change 2007: The Physical Science Basis. Contribution of Working Group I to the Fourth Assessment Report of the Intergovernmental Panel on Climate Change. S.* Solomon et al. (eds.) Cambridge University Press, 996 pp.

Leverington, D.W. & Duguay, C.R. 1996. Evaluation of three supervised classifiers in mapping 'depth to late-summer frozen ground', central Yukon Territory. *Canadian J. of Remote Sensing* 22(2): 163-174.

Marchenko, S.S. et al. 2008. Numerical Modeling of Spatial Permafrost Dynamics in Alaska. *Proceedings of the Ninth International Conference on Permafrost, Fairbanks, Alaska June 29–July 3, 2008* (this proceedings).

Maurer, J. 2007. *Atlas of the Cryosphere* Boulder, CO: National Snow and Ice Data Center. Digital Media.

NRC (National Research Council). 1983. *Permafrost Research: An Assessment of Future Needs* Washington, DC: National Academy Press.

NRC (National Research Council). 2008. *Environmental Data Management at NOAA: Archiving, Stewardship, and Access*. Washington, DC: National Academies Press.

Oberman, N.G. & Kakunov, N.B. 2004. *Ground Temperatures from Deep Boreholes in the Ob River Valley, Russia (VK-1615 and Zs-124/124A).* Boulder, CO: National Snow and Ice Data Center/WDC for Glaciology. Digital Media.

Shiklomanov, N.I. et al. 2008. The Circumpolar Active Layer Monitoring (CALM) Program: Data Collection, Management, and Dissemination Strategies. *Proceedings of the Ninth International Conference on Permafrost, Fairbanks, Alaska June 29–July 3, 2008* (this proceedings).

Sodnom, N. & Yanshin A.L. (eds.) 1990. *Geocryology and Geocryological Zonation of Mongolia*. Digitized 2005 by M.A. Parsons. Boulder, CO: National Snow and Ice Data Center/WDC for Glaciology. Digital Media.

Solomon, S., Manson, G. & Fraser, P. 2005. Remote sensing of bottom-fast ice in the Mackenzie Delta region, Northwest Territories, Canada. *Report of the 5th International Arctic Coastal Dynamics workshop, Montreal, Canada, Oct. 13-16, 2004.*

Tahirkheli, S.N. 2008. Permafrost in the Bibliography on Cold Regions Science and Technology. *Proceedings of the Ninth International Conference on Permafrost, Fairbanks, Alaska June 29–July 3, 2008* (this proceedings).

Tarnocai, C., Swanson, D., Kimble, J. & Broll, G. 2007. *Northern Circumpolar Soil Carbon Database* Ottowa, Canada: Research Branch, Agriculture and Agri-Food Canada. Digital Media.

UNEP (United Nations Environment Program). 2007. *Global Outlook for Ice and Snow.* Birkeland, Norway: Birkeland Trykkeri A/S.

USGCRP. 1999. *Report of the USGCRP Workshop 28-30 Oct. 1998.* US Global Climate Research Program.

Wang, Z. & Li, S. 1999. Thaw deformation of permafrost active layer near Toolik Lake, Alaska, imaged by DINSAR technique during summer time. *Eos, Trans. of the American Geophysical Union* 80.

Zhang, T. & Armstrong, R. 2003 updated 2005. *Arctic Soil Freeze/Thaw Status from SMMR and SSM/I, Version 2*. Boulder, CO: National Snow and Ice Data Center/WDC for Glaciology. Digital Media

Zhang, T., Barry, R.G. & Armstrong, R.L. 2004. Application of satellite remote sensing techniques to frozen ground studies. *Polar Geog*. 28: 163-196.

Zhang, T., Frauenfeld, O.W., McCreight, J. & Barry, R.G. 2005. *Northern Hemisphere Ease-Grid Annual Freezing and Thawing Indices, 1901–2002.* Boulder, CO: National Snow and Ice Data Center/WDC for Glaciology. Digital Media.

Regional Geocryological Dangers Associated with Contemporary Climate Change

A.V. Pavlov
Earth Cryosphere Institute, Russian Academy of Sciences, Moscow, Russia
G.V. Malkova
Earth Cryosphere Institute, Russian Academy of Sciences, Moscow, Russia

Abstract

Contemporary climate plays an important role both in the evolution of frozen strata and in genesis of the cryogenic processes. The activation of seasonal thawing, thermokarst, and solifluction is specified by the perennial changeability of the climate characteristics during the warm period of the year. The activation of seasonal freezing, cryogenic cracking, frost heave, and partly of icing formation is specified by the winter ensemble of the climate factors. The small-scale map of the geocryological hazards in the north of Russia has been fulfilled. Western Siberia, the Taimyr Peninsula, southern Yakutia and the Trans-Amur territories are among the unstable regions. The most stable conditions have been registered in the European part of the Russian cryolithozone, in northeastern Siberia and on the Chukot. The climate warming has brought about the increase of the mean annual ground temperature, some displacement (towards north) of the boundary of the types of permafrost, and the 15% reduction of the area of the continuous permafrost.

Keywords: climate warming; cryogenic processes; geocryological hazards; permafrost temperature.

Introduction

During the last hundred years, the climate warming has become distinctly apparent and has been widely discussed in scientific literature and in press (Anisimov et al. 1999, Douchkov & Balobaev 2001, Izrael et al. 1999, 2002, Klimenko et al. 2001, Malevsky-Malevich et al. 2001, Obzor 2003, Pavlov & Ananieva 2005, Pavlov et al. 2002, Pavlov 2001, Fotiev 2000, Gavrilova 2005, Nelson et al. 1993, Osterkamp 2003, Zhang & Osterkamp, 1993).

The meteorological data revealed that the global climate warming which had begun in the 1960–1970s was most distinctly registered in subarctic and middle latitudes. For the end of the 20th Century, the rise in air temperature in the north of Russia made up on average 1.1–1.2°C whereas the rise in global temperature was about two times less (0.6°C). The greatest rate of global warming fell in the 1980s. The centers of contemporary warming in Russia were central Yakutia and Transbaikalia, where the air temperature increase amounted to 2–4°C during 1965–2000. In the arctic regions the increase made up not more than 0.5–0.7°C during the same period. Since the second half of the 1990s, the tendency towards the delay in climate warming has exhibited in some northern Russian regions (towns: Turukhansk, Olerkminsk, Aldan, and Yakutsk).

In 2001–2005 the air temperature rise all over the north of Russia has been estimated as very weak (about +0.1°C) (Pavlov et al. 2007). In northwestern Siberia the mean annual air temperature rise of 1/3 part has occurred due to the warm period, whereas in central Yakutia it has been less than of 1/3 part. Only since the middle of the 1990s the contribution of the warm period to the formation of the total climate warming has had a 15–16% increase in central Yakutia.

Methods

The researches are based on the accumulation, classification and analysis of data on the air temperature for more than 80 weather stations with the observation time up to 150–165 years. The data on each weather station have been presented in Excel format in order to make the carrying out of the computerized mode of the statistical assessment of the observation results easy to use. The data smoothing with 3, 5 and 10–year periods has been executed.

The correlation and regression analysis of the observational series have been used (Pavlov et al. 2007). The deviations of the moving mean 10–year air temperature values from climatic norm have been estimated as very weak, weak, moderate and strong. The spatial regularities of the contemporary changes in climate have been revealed by means of the small-scale electronic mapping (Pavlov & Malkova 2005).

The investigations have demonstrated the high performance of the electronic maps' application for regional assessments of the climate changes and for identification of the geocryological dangers under these changes. The electronic version of these maps allows the on-the-fly registration of the necessary refinements when new data are obtained.

Contemporary Increase in the Mean Annual Air Temperature during Warm and Cold Periods

In 2005–2007 the authors of this paper have worked out the maps of the contemporary increase in air temperature during the warm and the cold periods. In order to make the comparative assessment of the air temperature rise in the summer period, the coefficient n_s (relative thawing index) has been inserted. This coefficient is equal to the ratio of the summer air temperature sum in 1991–2000 to the climatic norm.

The regularities of this coefficient's change in the north of Russia are represented as isolines (Pavlov & Malkova 2005). For the most part in northern regions the rise in n_s makes up 1.05÷1.1 (Fig. 1). The north of central and eastern Siberia is remarkable for stable (in the perennial cycle) summer air temperatures (n_s is approximately 1.0). The air temperature rises in summer period are greater only for the Gydansky and Taimyr Peninsulas (1.1÷1.25). On the whole, the map characterizes the potential of seasonal thawing depth increase under the contemporary climate warming. The perennial decrease of n_s has been registered nowhere, and that's why the contemporary climate changes do not promote the thawing depth decrease in the north of Russia.

For the most part of the Russian cryolithozone we predict the weak increase of the ground seasonal thawing depth (up to 5%). The increases of seasonal thawing depth for 5–10% are to be expected only in western Siberia and in the Far East, and the greatest ones (10–20%) on the north of the Gydansky and Taimyr Peninsulas. In these regions, the massive and wedge ground ice beds are widely spread, and therefore the increase of seasonal thawing depth can contribute to activation of the thermokarst, thermodenudation and thermo-abrasion.

Our colleagues (Gravis & Konchenko 2007) also have executed in the short term a forecast of activization of cryogenic processes the nearest years, using other methods. By their estimations, significant activization of cryogenic processes of the Russian cryolithozone is expected on the arctic islands of the Kara Sea and on Taimyr. These researches have confirmed authentically our forecast estimations.

In order to make the comparative assessment of the air temperature change in the winter period, the coefficient n_w (relative freezing index) has been inserted. This coefficient is equal to the ratio of the winter air temperature sum in 1991–2000 to the climatic norm (Pavlov et al. 2007). The regularities of this coefficient's change in the north of Russia are represented as isolines. For the various regions of Russian cryolithozone the change of n_w makes up 0.85÷1.0 (Fig. 2). This fact testifies to the warming in the cold period of the year. According to the meteorological observation data all over the territory, the fall of temperature in the winter period has not been registered during the last decades. Thus, the existing climatic situation does not promote the increase of seasonal freezing and the activation of cryogenic cracking but contributes to the intensification of the cryogenic heave and of the icing formation, and sometimes to the kurum activation. The greatest dynamics of these processes is to be expected in Transbaikalia and in southern Siberia, where recently the East Siberia–Pacific Ocean trunk pipelining has been started.

Elaboration of the Small-Scale Map of the Geocryological Hazards under Contemporary Climate Warming

The elaboration of the map of geocryological hazards under contemporary climate warming is based on the maps of the contemporary air temperature increase during warm and cold periods. For that, the territories with the relative

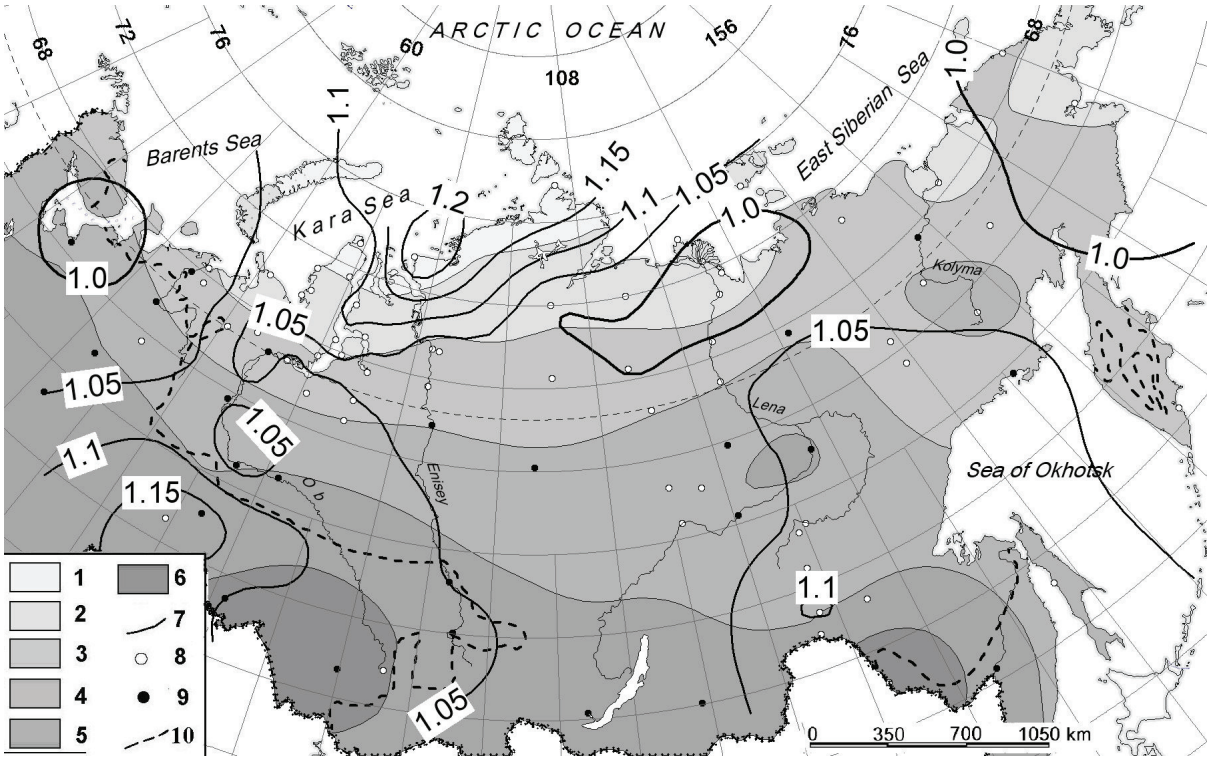

Figure 1. A map of the contemporary increase in air temperature during the warm period. The norm of sums of air temperature in warm season, °C•month: (1) less than 15, (2) 15 to 30, (3) 30 to 45, (4) 45 to 60, (5) 60 to 75, (6) >75, (7) isolines of the relative thawing index, (8) weather stations with observations made for <100 years, (9) weather stations with observations made for >100 years, and (10) the southern limit of permafrost.

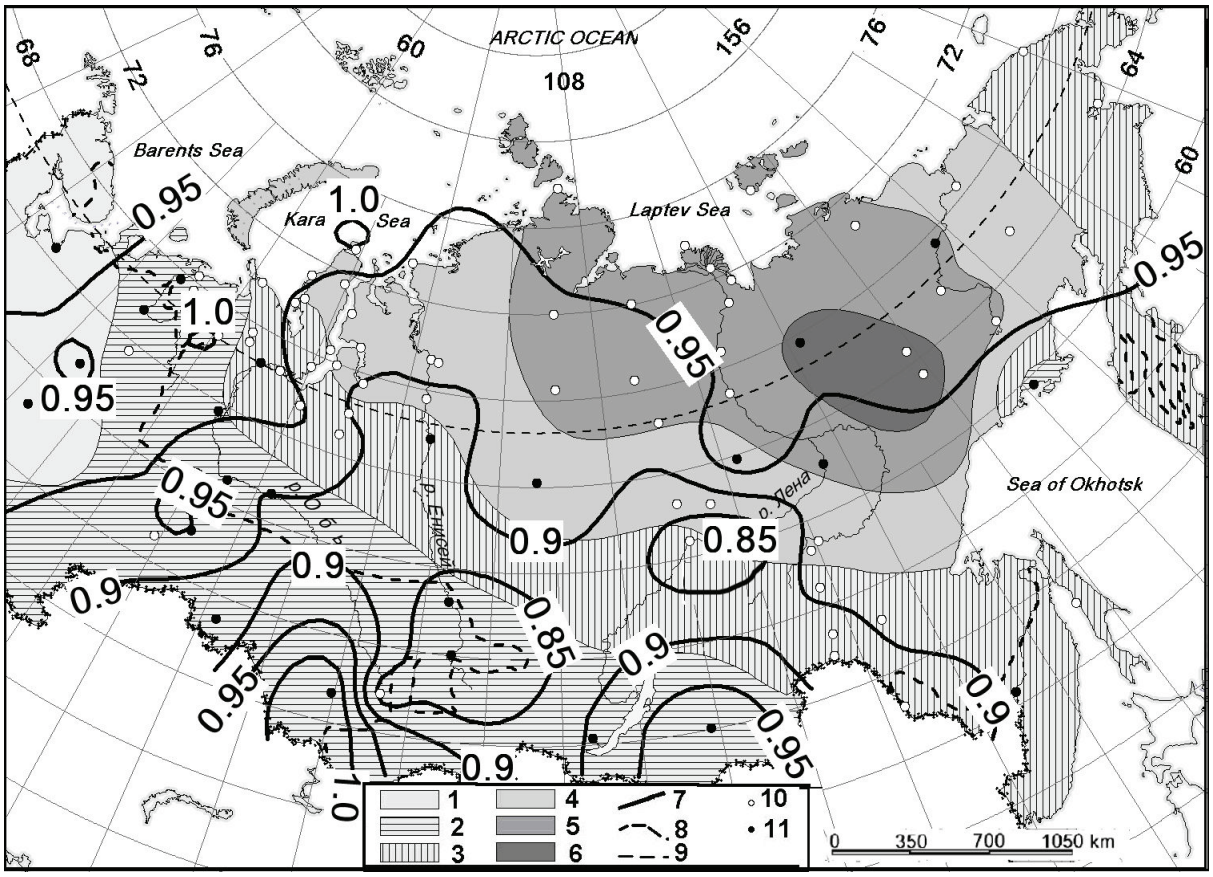

Figure 2. A map of the contemporary increase in air temperature during the cold period. The norm of sums of air temperature in cold season, °C•month: (1) > -60, (2) -60 to -100, (3) -100 to -140, (4) -140 to -180, (5) -180 to -220, (6) < -220, (7) isolines of the relative freezing index, (8) the southern limit of permafrost, (9) Arctic Circle, (10) weather stations with observations made for <100 years, and (11) weather stations with observations made for >100 years.

index n_s more than 1.1, within 1.1 and 1.05, and less 1.05 have been marked out on the map of the relative warming of summer period. The data of the territory are characteristic for strong, moderate and weak degree of the activation of cryogenic processes during summer period, respectively. The territories with the relative index n_w less than 0.9, from 0.9 to 0.95, and more than 1.05 have been marked out on the map of the relative warming of winter period. The singled-out territories characterize the degree of the potential activation of the cryogenic processes (strong, moderate and weak) during the summer period.

The superposition of the two transformed maps makes it possible to make up the map of the geocryological hazards under the climate warming (Fig. 3), depicting on the whole the extreme warming of the summer and winter periods.

The superposition of maps doesn't result in the coincidence of territories with strong activation of the cryogenic processes both in warm and in cold periods simultaneously. But there occurs the combination of strong activation of the processes in the warm period and the moderate one in the winter period (Taimyr Peninsula), as well as the strong activation in the winter period and the moderate one in the warm period (southern Siberia and the Trans-Amur territories). Besides, the intersection of the territories with moderate activation of the cryogenic processes both in warm and in cold periods has been noted (western Siberia, eastern Russia and Transbaikalia). During the perennial cycle the stable geocryological conditions have been registered on the most part of northern Europe, on northeastern Siberia and on the Chukot.

Within the ranges of the Russian cryolithozone, the stable climate conditions and hence the weak manifestation of the geocryological hazards are maintained for 1/4 of the area. The most unfavorable combination of the climate factors, and hence the greatest manifestation of the geocryological hazards, are characteristic for 10% of the territory. The moderate degree of the geocryological hazards is typical for the rest of the area.

Forecast of the Ground Temperature Change and Permafrost Extent

The predictive estimations of the increase of the temperature of the upper horizons of the permafrost on the territory of the Russian cryolithozone have been carried out taking into account the contemporary warming and change of air temperature during summer and winter periods (Malkova 2006). The approximate solutions of the Stephen's problem

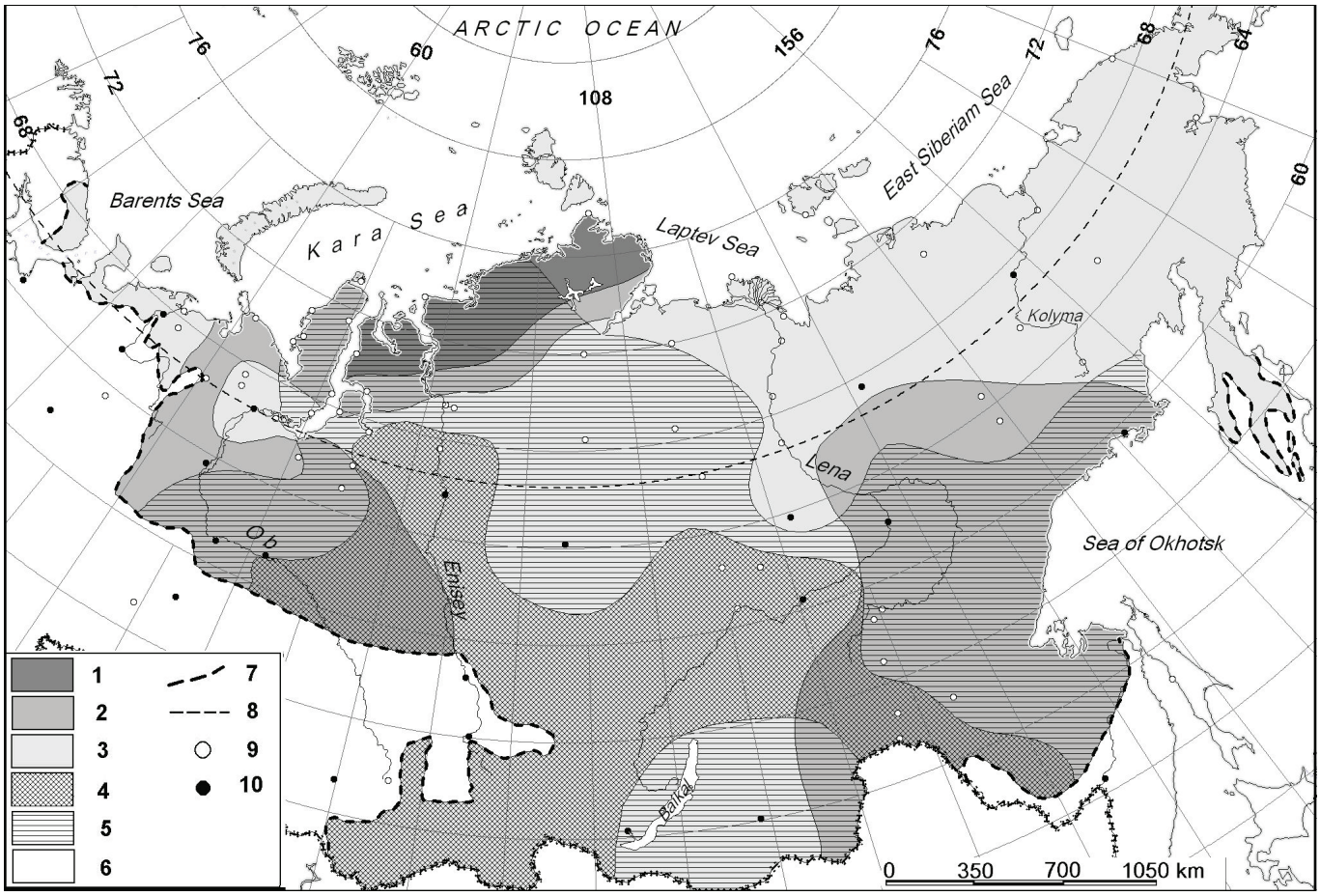

Figure 3. A map of geocryological hazards under the contemporary climate warming in the Russian cryolithozone. Potential activation of the cryogenic processes during the summer period: (1) strong, (2) moderate, (3) weak potential activation of the cryogenic processes during the cold period, (4) strong, (5) moderate, (6) weak, (7) the southern limit of permafrost, (8) Arctic Circle, (9) weather stations with observations made for <100 years, and (10) weather stations with observations made for >100 years.

and the on-line technique of calculation of the mean annual ground temperature have been used for the predictive estimates of the cryolithozone's evolution (*Recommendations*... 1989, *Geocryological forecast*... 1983).

According to the predictive estimates (during the last 30 years) the zone with the transient type of ground temperature (-1 to +1) under the influence of contemporary warming has moved towards north for 100–120 km in western Siberia, for 20–50 km in the European part, for 50–80 km in central Siberia and in eastern Russia. The adduced estimates of the changes of the mean annual temperature of the active layer are well agreed with the field data of the geocryological steady-state stations in the plains of western Siberia and northern Europe but are to be verified in the eastern regions of the country.

In the situation of the contemporary warming, the favorable conditions for permafrost thawing from the top and for replacement of seasonal thawing by seasonal freezing have occurred on the south of the Russian cryolithozone. The data of the recently drilled holes witness that the total thawing of the whole permafrost strata (both contemporary and relict) has not yet taken place. On the whole the area of the island permafrost has been reduced by a factor of 2 (for 1.3 million km^2) throughout Russia. As a result, the continuous and discontinuous permafrost limits have moved towards the north, and the area of the discontinuous permafrost extent has changed insignificantly whereas the area of the continuous permafrost diminished by 15% (for 1 million km^2).

Conclusions

During the last 30–40 years climate warming has been registered all over the territory of north of Russia due to the air temperature rise in summer and winter periods. The greatest increase of the mean annual air temperature is typical for subarctic and adjacent regions. The carried out researches demonstrate the possibility of using meteorological data for the assessment of the development of the dangerous cryogenic processes and the manifestation of the regional geocryological hazards. The conditions for some moving of the permafrost extent limits towards the north have been created due to the peculiarities of the contemporary warming. The tendency toward reduction of the island and continuous permafrost areas has been marked. The researches are proposed to be continued involving the fulfillment of verification of the results on data of the immediate observations on the development of the cryogenic geological processes and ground temperature.

Acknowledgments

This research was supported by RFBR grants 05-05-64215, 08-05-00421 and CALM II-project.

References

Anisimov, O.A., Nelson, F.E. & Pavlov, A.V. 1999. Predicting scenarios of the cryolithozone evolution under the global climate changes in XXI century. *Kriosfera Zemli* 3(4): 15-25.

Gavrilova, M.K. 2005. Climate change throughout the permafrost area in Eurasia during the XX century. *Materials of the Third Conference of the Russian Geocryologists* 2: 45-50 (in Russian).

Geocryological forecast for the West-Siberian gas-bearing province. 1983: 183. (in Russian).

Gravis, G.F. & Konchenco, L.A., 2007. Cryogenic geological processes: problems of the short–term forecast. *Cryogenic Resourses of Polar Region* 2: 131-133.

Douchkov, A.D.& Balobaev, V.T. 2001. Evolution of the thermal and phase state of the Siberian cryolithozone. *Global Changes of the Environment*: 79–104.

Izrael, Yu.A., Pavlov, A.V, & Anokhin, Yu.A. 2002. Cryolithozone's evolution under the contemporary changes of global climate *Meteorologiya i gidrologiya*, *2002, N*.1:10-18 (in Russian).

Klimenko, V.V., Mikushina, O.V. & Larin, D.A. 2001. Temperature trends of the Taimyr region in the conditions of the global climate change. *Geoecologiya: ingenernaya geologiya, gidrogeolgiya, geocryologiya* 1: 195-203 (in Russian).

Malevskii-Malevitch, S.P., Molkentin, E.K. & Nadiozhina, E.D. 2001. Modelling of contemporary and predicted distributions of ground temperature in the permafrost zone throughout the Russian territory. *Materials of the Second Conference of the Russian Geocryologists* 2: 189-196 (in Russian).

Malkova, G.V. 2006. An assessment of the geocryological changes in the upper permafrost horizons in the conditions of the varying climate and technogenesis. *Theory and practice of the assessment of the Earth cryosphere state and the forecast of its changes* 1: 82-86.

Nelson, F.E., Lachenbruch, A.H., Woo, M.-K., Koster, E.A., Osterkamp, T.E., Gavrilova, M.K.. & Cheng, G. 1993. Permafrost and Changing Climate. *Proceedings of the Sixth International Conference on Permafrost, Beijing, China.* Beijing: South China University of Technology Press, 987-1005.

Osterkamp, T.E. 2003.A thermal history of permafrost in Alaska. In: M. Phillips, S. Springman & L.U. Anderson (eds.), *Permafrost, Eighth International Conference Proceedings.* Lisse, Netherlands: Balkema, 863-868.

Pavlov, A.V. 2001. Response of the Permafrost to contemporary Climate Change. In: *Permafrost Response on Economic Development, Environmental Security and Natural Resources*. Kluver Academic Publishers, 277-292.

Pavlov, A.V. 2002. Secular anomalies of the air temperature in the Russian North. *Kriosfera Zemli*. *VI* 2: 75-81 (in Russian).

Pavlov, A.V. & Malkova, G.V. 2005. Contemporary changes of climate in northern Russia: Album of small-scale maps: 54 (in Russian).

Pavlov A.V., Malkova G.V. & Skachkov, Yu.B. 2007. Modern tendencies in the evolution of thermal state of cryolithozone under the climate changes. *Cryogenic Resources of the Polar Regions* 1: 34–38.

Recommendations on the forecast of the thermal state of the frozen ground. 1989: 73 (in Russian).

Zhang, T. & Osterkamp, T. 1993. Changing Climate and Permafrost Temperatures in the Alaskan Arctic. *Proceedings of the Sixth International Conference on Permafrost, Beijing, China*. Beijing: South China University of Technology Press, 783-788.

Wedge Structures in Southernmost Argentina (Rio Grande, Tierra del Fuego)

Augusto Perez-Alberti
Department of Geography, University of Santiago de Compostela, Spain
Andrea Coronato
CADIC. *Conicet., Argentine*
Manuela Costa Casais
Instituto Padre Sarmiento. CSIC. Santiago de Compostela, Spain
Marcos Valcarcel-Diaz
Department of Geography, University of Santiago de Compostela, Spain
Jorge Rabassa
CADIC. Conicet., Argentine

Abstract

Wedge-like structures occur in raised beach gravels near Rio Grande, eastern Tierra Del Fuego (latitude 53°50′S; longitude 67°5′W). They vary in dimension, being approximately 1.0–1.5 m deep and 0.3–0.8 m in apparent width. Some are closely spaced, while others are as much as 5.0–8.0 m apart. The infill is predominantly fine and coarse sand, together with silt, all of local provenance. There is little evidence of secondary infill. It is unclear whether these structures are soil wedges, sand wedges, or composite wedges. Their significance as regards the possible previous occurrence of perennially-frozen ground in the lowlands of Tierra del Fuego has yet to be determined.

Keywords: frozen ground; periglacial; soil wedges; Tierra de Fuego, Argentina.

Introduction

This paper documents the occurrence of wedge-like sedimentary structures in the lowlands of eastern Tierra del Fuego. The morphology of the wedges and the nature of the wedge infill are described.

The critical question is whether these structures are relict permafrost phenomena (i.e., ice wedge casts, sand wedges, or composite wedges), or whether they are simply soil (i.e., "ground") wedges and, as such, merely reflect deeper seasonal frost conditions than today. The recent literature that discusses the significance of these various phenomena includes Ghysels and Heyse (2006), Murton and Bateman (2007), and French (2007, 117–118, 127, 327).

Study Area

Tierra del Fuego is located between 52°40′S and 55°7′S and 65°05′W and 68°40′W. Its Atlantic coastline is about 330 km long and runs from northwest to southeast. The dominant feature is steep cliffs, in part formed on sediments, fronted by wide sedimentary intertidal surfaces developed under paraglacial conditions.

The study area near Cape Peñas (Fig. 1) is located at 53°50′S and 67°35′W. The present climatic conditions are temperate-cold, semi-arid, with a mean annual temperature of 5°C. The mean temperature during the coldest month, June, is 0°C while that of the warmest month, January, is 9°C. Rainfall is distributed throughout the year, diminishing between August and October. Total annual rainfall is 380 mm, and snow is generally scarce. The prevailing winds are westerly and to a lesser extent northwesterly and

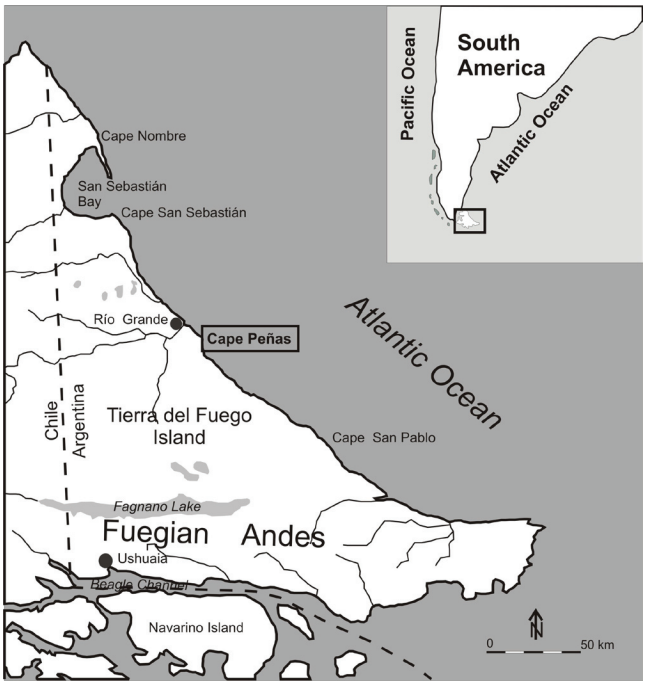

Figure 1. Location of Cape Peñas.

southwesterly. They reach their maximum intensity during the spring and summer months. The wedge-like sedimentary structures are developed on raised beach deposits and were first described by Coronato et al. (2004).

Codignoto (1983, 1984) obtained a radiocarbon age for the beach deposit that was older than 43 ky B.P., and amino-acid racemization on shells of *Pilar rostrata* gave a DL-aspartic acid ration of 0.36 (Rutter et al. 1989). The beach deposits

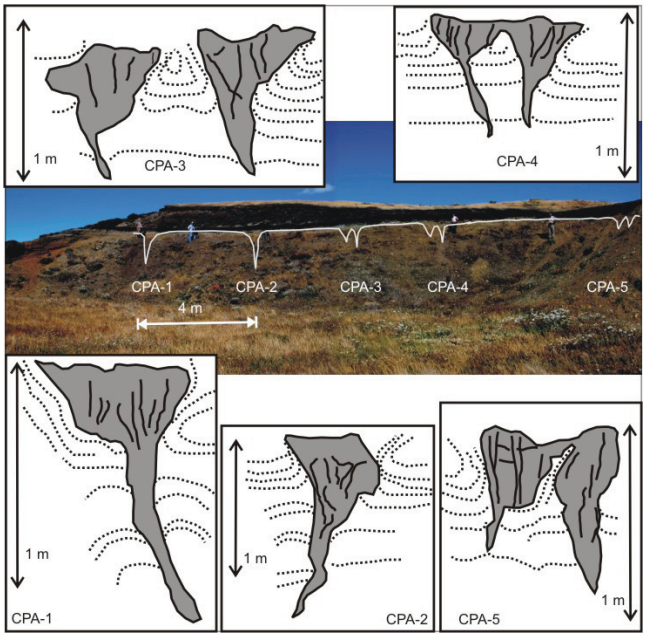

Figure 2. Morphological characterization of sector CPA.

were assigned therefore, to marine oxygen-isotope stage 5e (Meglioli 1992).

The depositional sequence consists from bottom to top of alternating layers about 12 cm in thickness, composed of gravel, pebbles, and sand. The pebbles are rarely more than 8 cm long. Near the coastline there are thick layers of gravels, while further inland there are alternating layers of gravel and sand. The gravel is covered by organic deposits rich in aeolian sand.

Wedge structures attributed to cold-climate conditions have been described previously from southern Argentina (Corte 1968, Auer 1970, Abrahan de Vazquez & Garleff 1984, Grosso & Corte 1989, Vogt & del Valle 1994).

The Permafrost Context

Several authors (e.g., Burn 1990, Murton & Kolstrup 2003, Lemcke & Nelson 2004) refer to the difficulty of determining the type of climatic environment that causes the formation of wedges. Polygonal networks may occur in temperate as well as cold (i.e., periglacial or permafrost) environments. Wedges that occur in non-periglacial environments rarely exceed a few meters in depth. In contrast, those formed in periglacial and permafrost environments are larger and may form polygons 10+ m in diameter. As a rule the polygons that develop in the absence of permafrost are smaller and usually measure between 0.5–2 m in diameter.

There appears to be little difference in the spacing of ice wedge and sand wedge networks. For example, in Siberia and Arctic North America ice and sand wedges are typically separated by distances of between 10–30 m. However, Gozdzik (1986) indicates that in Poland the distance between Pleistocene-age sand-wedge casts is usually much smaller, and the modal size of the dimensions of sand-wedge polygons is about 3.3 m.

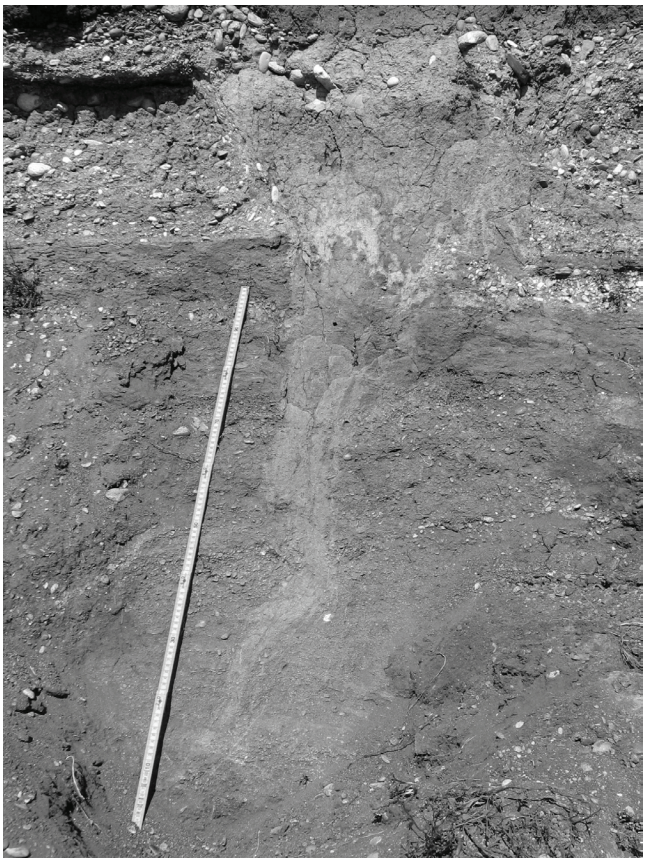

Figure 3. Wedge structure CPA-2.

It is increasingly understood that the mechanism underlying the formation of polygonal structures is related to fast and marked drops of temperature to below -15°C to -20°C. Also, the geometry and size of fissures is related to the type of material affected.

Another consideration is the material infill of the cracks and the thaw-modification that results as the permafrost degrades. Usually there is a slumping of the enclosing sediments and formation of sets of miniature faults. The fissure infill is regarded as secondary. In contrast sand wedges, even when thawed, constitute wedges of primary infill. Thus the resulting sedimentary structures are quite different between the two types of wedges.

The occurrence of cold-climate wedge structures always gives rise to the question of the climatic conditions under which they were formed.

Both sand and ice wedges form under conditions of continuous permafrost. Péwé (1966) indicated that ice wedges only exist where mean annual air temperature (MAAT) is in the -6°C to -8°C range, while Romanovskii (1985) pointed out that, on a substrate of sand or gravel, cracking commonly occurs at MAAT of around -7°C, but in silt the MAAT is slightly higher, -2.5°C.

Wedge Structures

At Cape Penas, a number of wedge structures are exposed in a gravel quarry. The wedges are elongate in shape, reaching

up to 1.50 meters in depth and 85cm in width, separated by distances ranging from 1.5 to 9m. One exposure (CPA) is parallel to the coast and nine well-defined forms were identified (Fig. 2).

Wedge structure CPA-1 is slightly inclined seawards and measures 120 cm in depth. The upper section is concave, funnel-shaped, and 85 cm deep and 40 cm wide. The wedge gradually narrows downwards. In the lower section of the wedge layers of sand and gravel dip toward the bottom. In the upper section rounded clasts are turned upwards. The wedge is covered by a level of pebbles and peaty-sandy materials.

CPA-2 (Fig. 3) is located 4m west of CPA-1 and is 140 cm deep. The upper section increases its width from 40 cm to 50 cm. The lower section narrows from 20 cm to 5 cm in width. Upturning of enclosing sediment is evident. CPA-3, located at a distance of 4 m from CPA-2, is smaller and more diffuse in shape. It has an open V-structure for a depth of 92 cm. It has a width of 32 cm in the upper section and 10 cm in the lower part. As in the previous wedge structures, pebbles in adjacent sediments are imbricated or tilted upwards.

CPA-4, located 4 m from CPA-3, shows a double wedge structure with a width of 58 cm and 73 cm. The smaller of the two structures is 47 cm wide at its head, while the bigger one (CPA-4a) is between 46 cm and 73 cm. The first narrows in depth whilst the second shows well differentiated segments: an upper one 25 cm deep and 13 cm wide, and a lower one of scarcely 5 cm.

Wedge structure CPA-4b shows the best example of adjacent pebbly strata being deformed upwards. The pebble layers trace perfect arches with clasts oriented in an upwards direction. Another double structure is found in CPA-5, about 9 m away from CPA-4. It is composed of two fissures measuring 80 cm and 68 cm in depth and 42 cm and 34 cm across their upper sections respectively. They also show evidence of upward deformation of enclosing beds.

CPA-6 is located about 3 m from CPA-5. It measures 70 cm in depth. Its width is 30 cm in the upper section and 19 cm in the middle. CPA-7 is 2.20 m away from CPA-6, and is 130 cm deep, with the top section being 80 cm wide. It also shows signs of upward thrusting of adjacent clasts. CPA-8 is at distance of 2.4 m from CPA-7. It is 140 cm deep and its upper section is 78 cm wide, decreasing to 18 cm in the middle part. The upper section shows some clast upturnings. CPA-9 is about 3.40 m from CPA-8. It is 90 cm long, 46 cm wide at the top, and 24 cm in the middle section. As in the previous cases, the infill is well defined with regard to the surrounding deposit.

Granulometry of Wedge Infill

In an attempt to understand the genesis of the wedge infill, samples of wedge infill material were taken from three wedges: CPA-2, CPA-4, and CPA-5. Samples were extracted from soil horizons that were common to each wedge: A, E, Bg_1, Bg_2, and BCg. Grain-size analysis was applied to the fine fraction (<2 mm) using the pipette method following

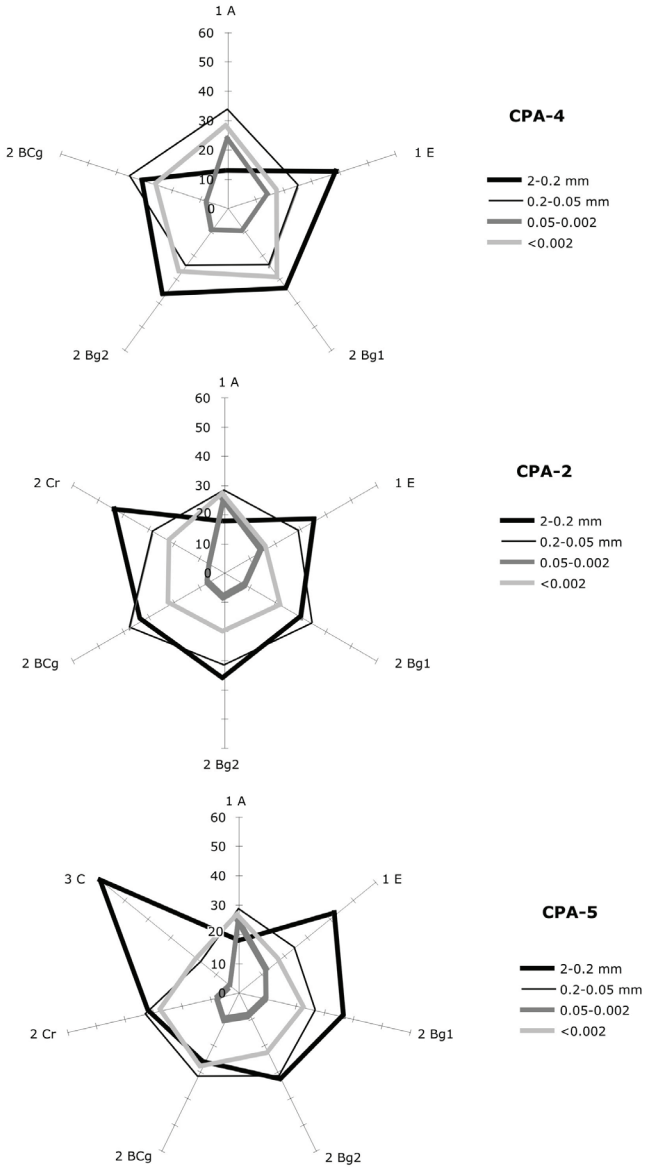

Figure 4. Granulometry of wedge infill.

dispersion with sodium hexametasulphate. The granulometric descriptions of the samples from each horizon are illustrated in Figure 4. The results for all wedges are similar except for the presence or absence of horizons Cr and C, the former being present in wedge CPA-2 and both in CPA-5.

Sand prevails in the three profiles analyzed, with mean values ranging from 46% to 77%. The lowest percentages of sand occur in horizons 1A (46%), while the highest values (between 64% and 77%) appear in 2Cr and 3C. These are in contact with the beach sediments. In horizon 2B, mean percentages ranges from 59% to 70%, increasing towards the lower subhorizon BCg with the exception of wedge CPA-5, which shows a tendency to decrease in this subhorizon.

In the three wedges analyzed there is a size-sorting reflected in the horizons. For example, in the 1A horizons the proportion of fine sands is greater (34% fine sands and 12% coarse in CPA-4), as it is in subhorizon BCg, although

the difference is not so marked (37% fine sands, 33% coarse sands in CPA-2). In the remaining 2B subhorizons the values of the fine and coarse fractions are very similar. This tendency changes towards the bottom of the wedges in horizons 2Cr and 3C. For example, the percentage of coarse sands tends to increase (with minimum values of 64% and maximum values of 77% in horizon 3C of CPA-5).

Clay is the second most important fraction. Maximum values occur in horizons A (28% in CPA-4), BCg (29% in CPA-5), and Cr (28% in CPA-5). This fraction decreases in horizons E (17% in CPA-2) and C, the latter at the base of the wedge (18%). The decrease is irregular.

The percentage of silt is never greater than 30%. The highest values are reached in horizon 1A (26%), diminishing progressively until horizon 3C (4%). Fractional analysis reveals a higher content in coarse silt than in fine sediment (9% fine silts as opposed to 17% coarse silts in horizon A of CPA-2).

Mineralogical Analyses

Study of the coarse and fine sand fraction was undertaken for the infill of wedge CPA-2 with the aim of describing the degree of weathering and roundness.

It was found that the mineral fragments are dominated by quartz and by rock fragments in which metamorphic rocks predominate. In general it is possible to classify the mineral fragments into three groups. The first group includes horizons 1A, 1E, and $2Bg_1$; the second group, the horizons $2Bg_2$ and 2BCg; and the third group includes the 2Cr and 3C horizons.

In the first group, rock fragments are predominant in the larger fraction, while monomineral particles prevail in the smaller one. There are rounded rock fragments, some of them spherical, with unpolished surfaces showing impact marks indicative of wind-dominated transportation. The quartz particles on the other hand generally show polished surfaces, with V-shaped impact pits that reveal that they were worked in a marine environment. The clearest marine features appear in the coarse sand, while the fine sand shows aeolian features.

The second group (from horizons $2Bg_2$, 2BCg) shows a smaller number of fragments of both rock and spherical minerals and a progressive increase in the number of sub-rounded and non-spherical fragments. The latter are highly polished and bear impact pits. There are some signs of contact with the upper horizon, evident in the existence of some unpolished, spherical, and rounded fragments in the fine fraction of subhorizon $2Bg_2$. The third group, composed of horizons 2Cr and 3C, reveals a more heterogeneous character. Rock fragments predominate in the coarse sand, and monomineral particles in the fine sand. The quartz particles are polished, ranging from rounded to subrounded, and show impact pits on their surface. There are traces of oxidization on the external faces of all grains, producing a highly characteristic shiny dark-brown patina.

X-ray diffraction analysis of the clay present in the wedge infill revealed the presence of illite and smectite, and the total absence of kaolinite.

Discussion and Conclusions

The origin of these wedge-like structures is not clear. They may or may not reflect cryogenic processes. If they are cold-climate phenomena, it is uncertain whether they formed in seasonally or perennially frozen ground.

Several generalizations can be made. First, it is clear that the wedge structures are not isolated phenomena but occur at regular intervals throughout the section studied. Second, the adjacent enclosing sediments frequently show upward deformation adjacent to the wedge. Third, fine or very fine sand is the predominant infill material, although other size fractions are also present. Fourth, the reworking of the sand-size material suggests an autochthonous contribution. Fifth, the surface characteristics shown by the majority of the sand particles indicate that they were modeled in a marine environment. However, some sand in horizons A, E, Bg_1 possess aeolian features that suggest transport into the wedge by wind.

If the wedges are cryogenic in origin, they appear to have been generated in two phases. In the first phase, thermal-contraction cracking would have occurred in a cold and arid environment marked by an intense temperature drop during the winter months. Such climatic conditions do not exist today on the coast of Tierra del Fuego. In the second phase, more humid conditions would have seen the incorporation of coarse sand and fine gravel into the wedge, presumably during episodes of deep seasonal frost.

The heterogeneous nature of the infill suggests the wedges are of a composite origin However, the possibility that they are soil or ground wedges and formed under conditions of deep seasonal frost rather than permafrost cannot be eliminated. Their age has yet to be determined.

Acknowledgments

Research in Tierra del Fuego is being supported by Spanish International Polar Year Program (POL2006-PC091) and the Spanish Ministerio de Educacion y Ciencia research project CGL2004-03380/BOS. The authors wish to acknowledge the constructive comments of two anonymous reviewers. They also wish to thank Professor Hugh French for help with the original manuscript and for his editorial assistance in rewriting the paper following review.

References

Abraham de Vazquez, E.M. & Garleff, K. 1985. Fossil phenomena in the central and southern part of the Piedmont of Mendoza Province, Argentina. *Zbl. Geol. Paläont.* Teil I, H. 11-12: 1709-1719, Stuttgart.

Auer, V. 1970. The Pleistocene of Fuego-Patagonia. Part. V: Quaternary problems of southern South America. *Ann. Acad. Sci. Fennicae* A. III: 100: 194.

Burn, C.R. 1990. Implications for palaeoenvironmental reconstruction of recent ice-wedge developement at Mayo, Yukon Territory. *Permafrost and Periglacial Processes* 1: 3-4.

Codignoto, J. 1983. Depósitos elevados y/o acreción del Pleistoceno-Holoceno en la costa fueguino-patagónica. *Simposio Oscilaciones del nivel del mar durante el último hemiciclo deglacial en la Argentina*. 12-16. Mar del Plata.

Codignoto, J. 1984. Estratigrafía y geomorfología del Pleistoceno-Holoceno costanero entre los paralelos 52º30′S y 42º00′S, Argentina. *IX Congreso Geológico Argentino*. Actas III: 513-519. San Carlos de Bariloche.

Coronato, A., Bujalesky, G., Pérez Alberti, A. & Rabassa, J. 2004. Evidencias criogénicas fósiles en depósitos marinos interglaciarios de Tierra del Fuego, Argentina. *X Reunión Argentina de Sedimentología, San Luis, September 2004*, Abstracts: 48-49.

Corte, A. 1968. Informe preliminar del progreso efectuado en el estudio d elas estructuras de crioturbación pleistocenicas fosiles en la provincia de Santa Cruz. *Terceras Jornadas Geologicas Argentinas*. Tomo II: 9-19.

French, H. 2007. *The Periglacial Environment. Third Edition.* Chichester: J. Wiley & Sons, Ltd., 458 pp.

Ghysels, G. & Heyse, I. 2006. Composite-wedge pseudomorphs in Flanders, Belgium. *Permafrost and Periglacial Processes* 17 : 145-162.

Gozdzik, J.S. 1986. Structures de fentes de remplissage primaire sableaux du Vistulien en Pologne et leur importance paléogéographique. *Biuletyn Peryglacjalny* 31: 71-105.

Grosso, S.A. & Corte, A.E. 1989. Pleistocene Ice Wedge Cast at 34 degrees S Eastern Andes Piedmont, South America. *Geografiska Annaler* 71A: 125-136.

Lemcke, M.D. & Nelson, F.E. 2004. Cryogenic Sediment-Filled Wedges, Northen Delaware, USA. *Permafrost and Periglacial Processes* 15: 319-326.

Meglioli, A. 1992. *Glacial Geology of Southernmost Patagonia, the Strait of Magellan and Northern Tierra del Fuego.* Ph.D. Dissertation. Bethlehem, USA: Lehigh University.

Murton, J.B. & Kolstrup, E. 2003. Ice-wedge casts as indicators of palaeotemperatures: precise proxy or wishful thinking? *Progress in Physical Geography* 27: 155-170.

Murton, J.B. & Bateman, M.D. 2007. Syngenetic sand veins and anti-syngenetic sand wedges, Tuktoyaktuk Coastlands, Western Arctic Canada. *Permafrost and Periglacial Processes* 18*:* 33-47.

Péwé, T. 1966. Paleoclimatic significance of fosil ice wedges. *Biuletyn Peryglajalny.* 15: 65-73.

Rutter, N., Schnack, E, del Río, J., Fasano, J., Isla, F. & Radke, U. 1989. Correlation and dating of Quaternary littoral ones along the Patagonian coast, Argentina. *Quaternary Science Review* 8: 213-234.

Romanovskii, N.N. 1985. Distribution of recently active ice and soil wedges in the USSR. In: Church, M. Slaymaker, O. eds., *Field and Theory: Lectures in geocryology.* Vancouver: University of British Columbia Press, 154-165.

Vogt, T. & del Valle, H. F. 1994. Calcretes and Cryogenic Structures in the Area of Puerto Madryb (Chubut, Patagonia, Argentina). *Geografiska Annaler* 76A: 57-75.

Modeling Interaction Between Filterable Solutions and Frozen Ground

G.Z. Perlshtein
Institute of Environmental Geoscience, Russian Academy of Sciences, Moscow, Russia
G.S. Tipenko
Institute of Environmental Geoscience, Russian Academy of Sciences, Moscow, Russia

Abstract

Research of interactions between filterable solutions and frozen ground are very important for many problems of contemporary basic and applied geocryology. In thaw zones, heat and salt transport by groundwater often proves to be more significant than transport by means of a molecular-diffusion mechanism. For the case of water movement in permeable frozen ground, quantitative description of convective heat and mass transfer is insufficiently devised. The presented model consists of the conventional equations set for convective heat and salt transfer. It is supplemented by an ice melting equation. Phase equilibrium ice-solution is expressed by dependency of the crystallization temperature upon concentration. The heat sink is prescribed in direct proportion to the difference between solution temperature and the eutectic point. Modeling results accord entirely to the modern view on the physical essence of the processes under consideration. The obtained method is planned for practical use, in particular, diamond mining in Yakutia.

Keywords: eutectic point; groundwater flow; ice melting; mathematical modeling; permeable frozen ground.

Introduction

The interaction between salts and frozen ground has increasingly drawn the attention of permafrost scientists and engineers. Salt and heat transfer with groundwater flow plays a significant role in forming the frozen massif structure, thermal regime, and ground characteristics in the cryolithozone. Solution appearance in ice-containing ground changes the phase equilibrium conditions: the temperature derived at the point of contact with the frozen zone corresponds to the eutectic point at a given concentration. For that reason, the temperature field dynamics of saline ground is highly dependent on the solute diffusion.

Understanding the essence and quantitative regularities of the process is very important for solving such problems as contemporary basic and applied geocryology : as an evaluation of salted ground state,; palaeoreconstructions and prediction of coastal and offshore permafrost behavior,; cryopeg dynamics,; thawing frozen ground by the use of salts, etc. A number of works (Ershov 1990, Komarov 2003, Permyakov & Romanov 2000, and others) are devoted to theseis problems. These works consider heat and salt transport only by means of a molecular-diffusive mechanism.

Quantitative research of heat and mass transfer induced by groundwater movement is of great interest. In the case of forced convection, energy and substance fluxes often prove to be much more intensive than those conditioned by molecular-diffusive forces.

It should be noted that the theory of convective diffusion started to develop rapidly about the middle of the last century (Bear 1961, Veriguin 1962, and others). In many respects, it was associated with leaching and other geotechnological method problems. (Kalabin 1981).

Existing quantitative theories of the interaction between groundwater flow and frozen ground have been developed in connection with solving practical problems such as hydraulic thawing of frozen ground and hydraulic engineering in permafrost regions (Bogoslovsky 1959, Goldtman et al. 1970, and others). These works consider movement of fresh water only, in the thaw zone.

However, it is not uncommon in nature that, when pores and fissures of frozen soils and rocks are only partially filled with ice, they keep an essential permeability and can not be considered as aquifuges. The movement of saliferous water in such a medium has some important features. Knowledge of them is important for general theory as well as for solving practical problems of drainage waters burial (in particular, at diamond mining in Yakutiya) and other technological challenges.

Short Review of Existing Models

There are two approaches to quantitative description of interrelated processes of heat and salt transfer: (1) the model of phase change on the mobile interphase surface that is well known as Stefan's problem, and (2) models of phase change in some temperature range. In the case of a classical (front) approach to the problem, diffusion occurs only in a thawed zone. The models with unfrozen water also take into account the salt transport in the frozen zone through the films of unfrozen water. In either case, the equations of heat transfer and diffusion use the dependency of the solution thermodynamic potential from its solute concentration (for instance, functional dependency of solution concentration on eutectic point).

As a rule, both approaches are realized in the frames of one-dimensional calculating schemes.

In equations, a heat-mass transfer with moving water is factored in through an additional item summand that is proportionate to the water flow velocity. The latter is found through solving groundwater dynamics equations.

Methods for calculating thaw rate are well-developed

for the cases of water moving in thawed zones along an impermeable boundary with frozen ground. They were used widely, for example, for designing mining works at the permafrost placers of northeastern Russia.

When deriving an equation, the assumption is used that the temperatures of matrix solid material and moving water are equal. Owing to that, the temperature fields of the ground components are described by one common equation.

It should be noted that coarse-grained ground and fissured rocks could have a significant permeability in the frozen state. It is obvious that this assumption noticeably conflicts with studied processes when water moves in permeable frozen ground that has some amount of ice in it. The simplest case of heat transfer during fresh water movement through permeable frozen zone has been analyzed by one of the authors (Perlshtein & Jiltsov 1984) and was distinguished into a special type of convective heat transfer in thawing ground. To date, however, the processes of joint convective transfer of heat and salts in permeable frozen rocks are very poorly explored and studied.

Main Assumptions and Mathematical Statement of the Problem

This paper offers a quantitative description of heat-mass transfer during solution movements, not only in the thaw zone, but also in permeable frozen massif. This model reflects the following features of the process:

1. salt diffusion occurs in the part of a fissured-pored space that is not filled with ice;

2. when solution gets in contact with frozen rocks, the temperature on the contact instantly settles to the crystallization temperature at a given concentration;

3. in every elementary volume of the area of study, moving solution and matrix solid material with ice inclusions can have different temperatures (at least, until the ice completely melts).

The source, brought into equations of convective heat and salt transfer, is defined by heat flux density from solution into solid phase for temperature fields, and by the water influx due to ice melting for concentration fields. The value for this source is included in a boundary condition for ice and matrix solid material temperature fields. In the first approximation, it is assumed that in both solid and liquid phases, the heat fluxes normal to solution flow are negligible in comparison to energy absorption on a melting front, and that right after ice melt-out, temperatures of medium components equalize.

The stated assumptions lead to the following system of heat-mass transfer equations:

$$\rho_w c \frac{\partial T}{\partial t} = \nabla(\lambda \nabla T + c\rho_w T k_f \nabla \varphi) + n\rho_i L \frac{\partial \theta}{\partial t}, \quad (1)$$

$$\frac{\partial \theta}{\partial t} = W_\theta(T, \theta, M), \quad (2)$$

$$\frac{\partial M}{\partial t} = \nabla(D\nabla M + M k_f \nabla \varphi) + W_M(T, \theta, M) \quad (3)$$

$$\nabla(k_f \nabla \varphi) + n W_\theta = 0 \quad (4)$$

where $W_\theta(T, \theta, M)$ – rate of ice saturation changes, units:

$$W_\theta(T, \theta, M) = \frac{\beta(V, \theta)}{n}\left(T^*(M) - T\right) \quad (5)$$

and $W_M(T, \theta, M)$ –rate of dissolution due to ice melting:

$$W_M(T, \theta, M) = \frac{M}{(1-\theta)} W_\theta(T, \theta, M); \quad (6)$$

T = temperature, K; M = concentration, kg/kg; t = time, s; ρ_w, ρ_i = water and ice density, kg/m^3; c = specific heat, J/(kg ·K); λ= heat conductivity, W/(m ·K); L = specific latent heat of ice melting, J/kg; k_f = hydraulic conductivity, m/s; V = water flow velocity**,** m/s; D = diffusion coefficient, m^2/s; φ = hydraulic pressure head, m; β = the volumetric coefficient of convective heat transfer, 1/s ·K; T* = eutectic point, K; θ = ice saturation in pores, m^3/ m^3; n = porosity.

Modeling Results

A modeling objective was to study ice melt-out processes with $CaCl_2$ solution being injected into the layer of permeable highly fissured frozen rocks. Temperature and concentration fields had an axial symmetry. The characteristics of permeable zone and country rocks are given in Table 1.

Surface rock temperature was equal to -4° with 0.01 K/m gradient. The brine injected in the borehole had constant temperature (7°C) and concentration (6 and 20% in two model runs).

Main calculation results are presented on the graphs. It shows that energy and material flow has a high propagation rate around the borehole. It is explained by the very high permeability of rocks that was specially set in calculations for evaluating an extreme impact of convective heat-mass transfer to frozen rocks.

Just as was expected, in the first model run (M_0 = 6%) salt concentration is monotonously increasing in the whole area studied and quickly approaches the concentration of injected solution. In the distance from the borehole, temperatures and concentrations very quickly equalize with eutectics of injected solution.

The temperature pattern of change is somewhat more complicated (Fig.1).

It is interesting to note that, in the second model run, the temperature is even decreasing in the beginning. The reason for it is the fast brine propagation, when the eutectic

Table 1. Characteristic of massif under consideration.

№ of layer	Depth	n	k_f	θ	λ	c
1	0–250	0	0	0	3.0	836
2	250–300	0.1	$3 \cdot 10^{-5}$	0.5	3.0	836
3	300–1000	0	0	0	3.0	836

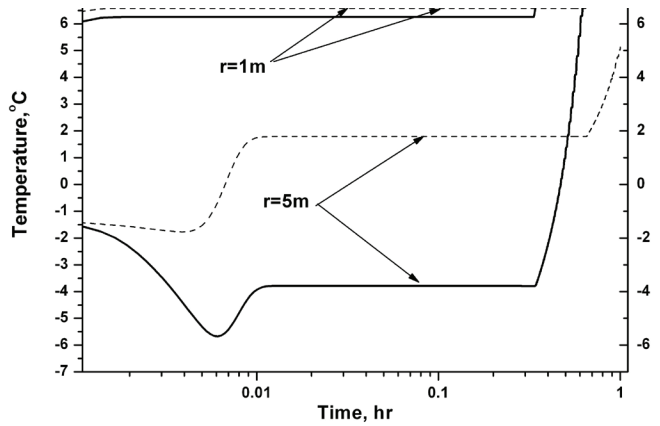

Figure 1. The temperature changes at different distance from borehole with mass transfer (solid line) and with initial concentration (dash line).

point of the brine is lower than the beginning temperature of the area studied. Its growth is obviously suppressed by heat consumption for melting the ice.

Quite interesting are the peculiarities of ice content dynamics in different parts of area studied (Fig.2)

High and constant thawing speed is registered close to the injection well because of a significant solution influx that has practically an initial temperature. A clearly defined jump in an ice-melting rate is traced on some distance from the borehole, and the value of this "step" does not change with the further distance increase. It indicates that thawing at this point happens at the expense of heat released due to rock cooling, provided that the solution temperature does not change much at all. It is to be recalled that the initial temperature in the permeable zone was significantly higher than the eutectic point. After that, the process happens with increasing speed due to the solution temperature that increases in time, arriving at every point.

Spatial variation of studied parameters is presented in Figure 3.

Conclusions

The most interesting of all the obtained results is the pattern of ice content change in space and time. For the first time ever, this paper gives a mathematical statement of a problem for temperature and concentration fields,

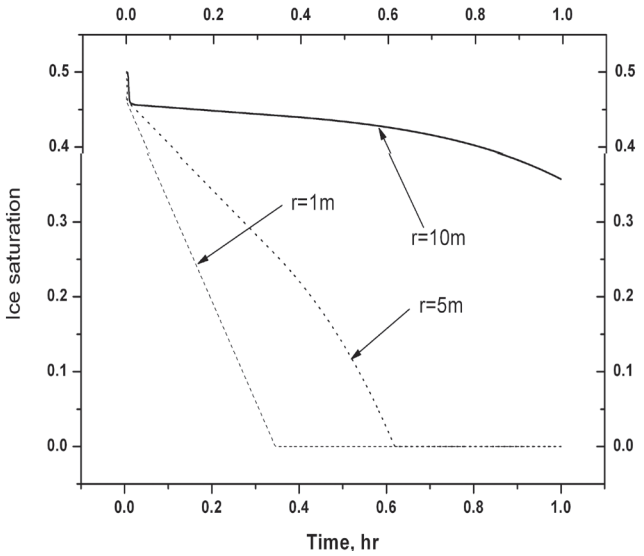

Figure 2. Ice content dynamics at different distances from the borehole.

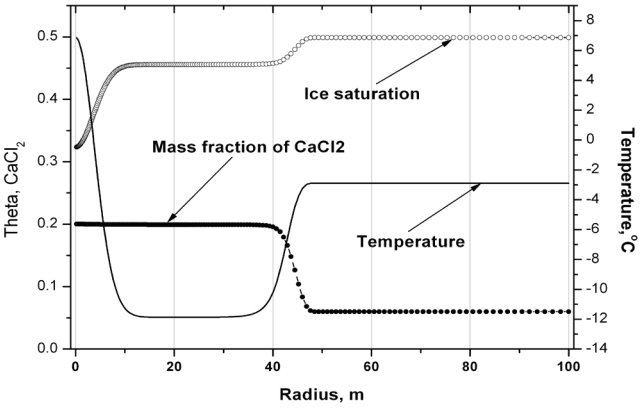

Figure 3. Spatial variation of the ice content, salt mass fraction, and temperature (time: 6 minutes).

which is determined by high rates of solution flow in permeable frozen massif. Model calculations are in good agreement with a general concept about the physics of studied processes of convective diffusion and heat transfer. It proves that it is a working model. It seems likely that the described calculation method could be used for solving practical problems associated with burial of drainage brines in permafrost. This is an acute problem for commercial development of diamond mining in Yakutia. The authors see the main object of further research in conducting laboratory and field experiments to verify the model and to develop methodology for experimental determination of volumetric (intra-pore) heat transfer coefficient. This coefficient needs to be determined for rocks of different composition, porosity (fissuring), and level of ice saturation.

Acknowledgments

The authors thank their colleagues F.G. Atrotschenko, A.N. Vlasov, V.P. Merzlyakov, and Marina Tishkova for participation in discussions regarding this research. This work has been supported by the RFBR (the Russian Foundation for Basic Research).

References

Bear, J. 1961. Some experiments on dispersion. *J. Geophys. Res*. 66(8): 2455-2467.

Bogoslovsky, P.A. 1959. On thermal calculation of filtering earth dams. *Proceedings of Gorky Building Engineer Institute.* Gorky: 86-112 (in Russian).

Chizhov, A.B., Buldovich, S.N. & Chizhova, N.I. 1975. Hydrogeological condition of Chulman Depression. In: *Southern Yakutia*, MGU Publ.: 291-311 (in Russian).

Ershov, E.D. 1990. *General Geocryology.* Moscow: Nedra, 119-157 (in Russian).

Goldtman, V.G., Znamensky, V.V. & Chistopolsky, S.D. 1970. *Hydraulic Thawing Frozen Ground.* Magadan: 450 pp. (in Russian).

Kalabin A.I. 1981. *Minerals Extraction by Underground Leaching and Other Geotechnical Methods*. Moscow: Atomizdat, 303 pp. (in Russian).

Komarov, I.A. 2003. *Thermodynamics and Heat-Mass Transfer in Dispersed Frozen Ground.* Moscow: Publishing Scientific World, 406-428.

Perlshtein, G.Z. & Jiltsov, V.D. 1984. Approximate formulae for calculating Hydraulic Thawing Duration of Permeable Frozen Ground. *Proceedings of VNII-1 Institut,* Magadan: 99-104 (in Russian).

Permyakov, P.P. & Romanov, P.G. 2000. *Heat and Salt Transport in Frozen Unsaturated Ground*. Yakutsk: 126 pp. (in Russian).

Veriguin, N.I. 1962. Foundations of salts dilution theory at water movement in ground. In: *Engineering Geological Properties of Ground and Methods of Their Study.* Moscow: AS USSR, 89-117.

—Plenary Paper—

Russian Approaches to Permafrost Engineering

Georgy Perlshtein
Institute of Environmental Geoscience, Russian Academy of Sciences, Moscow, Russia

Abstract

The basic goals and problems that permafrost engineers and scientists are facing presently remain almost the same as they were 20 years ago. Nevertheless, the contemporary stage of cold regions development has specific features. One of the most important is permafrost response to global climate changes. In this report, some new technical solutions are described concerning construction, mineral mining, and development of oil and gas fields, environmental protection, surveys, and other related activities. Among them, a foundation on sandy back-filled ground in Yakutsk is exemplified. Most erected buildings here have not undergone any dangerous deformations over a 20-year period of operational experience. The methods of roadbed operation were improved for the railroad lines Obskaya-Bovanenkovo, Chara-Cheena, and others. Some new features of thermokarst, frost heave and other dangerous cryogenic processes have been revealed in connection with pipeline construction. This has induced the development of permafrost monitoring. In any event, the main principle of Russian specialists is to apply such scientific-technical decisions that utilize the site's natural conditions. This helps alleviate the negative influence of permafrost and uses favorable features of the territory

Keywords: discontinuous permafrost; frozen ground; monitoring of cryogenic processes; permafrost engineering; pipeline; oil and gas field development.

Introduction

During long years of exploring and developing the large territories of Siberia, the Far East and the European North, Russians have gained considerable experience on living and working with permafrost conditions. At the end of the last century, the old system of scientific-technical maintenance of the economy proved to be obsolete, and the new one is in the process of being developed. The problems of development within the permafrost regions that engineers and scientists presently face remain the same as they were 20 years ago.

In the last few years, because of some positive shifts in the economic and political atmosphere, the demand for scientific and technical support of human activities in the permafrost zone has increased. New approaches for implementing innovative engineering solutions and improving survey and monitoring systems of permafrost terrains are important in relation to the economy.

Methodological approaches for operating on frozen ground state formed the basis of the natural-technical systems concept (Epishin 1985).

Permafrost response to climate change has received much attention. Research follows such directions as observations at permafrost stations and using specially equipped geothermal wells; improving methods for long-term geocryological forecast and modeling the permafrost thermal regime for different scenarios of climate changes; and comparative analysis of geocryological maps prepared at different times.

In spite of all obvious difficulties in the economic transitional period, the potential of Russian geocryology has remained high. Thus the modern approaches used by Russian specialists for solving permafrost engineering problems are of value.

Construction

Stability of construction in frozen ground is one of the most responsible and important goals in permafrost engineering. Existing federal construction norms and regulations (SNIP 2.02.04-88) specify two construction methods for permafrost territories: 1) preserving the ground in the frozen state, and 2) keeping the ground under foundations in a thawed state. The choice of method and particular technological scheme occurs at the design stage and depends on the engineering-geocryological conditions of a given construction site. However, in the area of continuous permafrost, the first methodology is usually preferred.

For example, in Central Yakutia (Yakutsk, Mirny), pile foundations are used widely, usually with a ventilated crawl space. The preference is for cast-in-place piles. Unfortunately, this method is expensive. Costs related to foundations can amount to 3 to 5 times as much as foundations outside of the permafrost zone and can be 40% of the total cost of building. Such construction does not prevent the subsidence of ground caused by water leakages, departure from recommended maintenance programs, and other factors. In the near future, these problems may increase due to global warming.

In conditions of discontinuous, warm permafrost, construction is usually carried out according to the second method, with the preliminary thawing of frozen ground to a depth no less than the thaw bulb. Most engineering constructions in the Central Transbaikalia, close to the southern limit of the permafrost zone, were built in the 1950s using the first method, and since then have undergone catastrophic deformation. Recommendations for foundation reconstruction have been developed, taking into consideration the fact that the major part of thaw settlement has already occurred. These recommendations suggested

Figure 1. Housing estate erected in Yakutsk on back-filled ground.

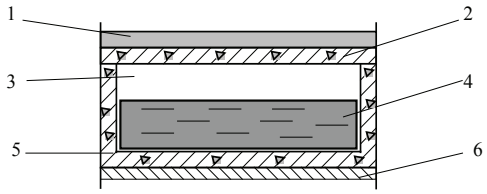

Figure 2. Scheme of foundation equipped with the cold accumulator: 1 – insulation; 2 – ceiling slab; 3 – ventilated channel; 4 – cold accumulator filled with water; 5 – concrete case; 6 – ground surface.

allowing thawing of ground (Recommendations… 1988). The resulting economic impact exceeded 100 million rubles (Institute of Natural Resources, Ecology and Cryology SB RAS).

A particularly interesting form of construction employed in Yakutsk has been to utilize sandy back-filled ground (Fig. 1).

Both permafrost construction methodologies were used in this case. Buildings with pile foundations were erected using the first methodology with ventilated crawl space. Meanwhile, the placement of sandy ground up to the design reference level was carried out after installing bearing posts of 4 m in height. Ground freezing occurred during the preparation of construction, construction itself, and at exploitation stages. The buildings have remained in satisfactory condition except for the kindergarten, which was dangerously deformed because of hot-water leakage under the building. A substantial number of the buildings are constructed on raft foundations without taking any special measures to regulate the foundations' temperature regime. Twenty years of operational experience have shown that none of these buildings has undergone any dangerous deformations, and they have sustained structural stability (Tseeva & Egorov 2005, Polishchuk et al. 2008).

The new method for assessment of foundation reliability is beginning to be applied. It is based upon statistical analysis of meteorological factors that change randomly (Khrustalyov & Pustovoit 1988). A characteristic feature of modern construction on permafrost is increased attention to maintaining a predetermined temperature regime, or ground thermal stabilization. There are active and passive stabilization methods. Active thermal stabilization involves refrigerating ground to a given depth by means of special equipment and technology. The most popular are seasonal refrigerating devices, especially two-phase thermosyphons (Dolgikh et al. 2005). In recent years, devices working year-round have become more and more common. During the summer period, their above-ground condensers are chilled by special devices that work using the Peltier effect (Bayasan et al. 2005).

Building reliability analysis using probabilistic methods brought us to the conclusion that, in many cases, use of thermal stabilizers drastically decreases the influence of chance meteorological factors on ground temperature. This approach gives the opportunity to determine the safety factor correctly, thereby preventing the damages caused by construction breakdown.

The original type of surface foundation on frozen ground deserves attention (Fig. 2). Here, the crawl space is equipped with a special device that acts as zero curtain (Khrustalev 2005).

Heat pump applications in permafrost engineering are important. New research on this subject has been carried out since the late 1980s (Goodrich & Plunkett 1990, Guly & Perlshtein 1998, Instanes 2000). Unfortunately, in Russia, research on the subject did not go beyond purely theoretical studies. Nevertheless techno-economic evaluations were accomplished, assisted by computer modeling for the temperature fields of foundations. They indicate that the cost of installing a heat pump to cool the foundation can be compensated for by using the heat produced by the building itself (Perlshtein et al. 1998). Heat pumps also can be successfully used in other engineering applications in cold regions; for example, in frozen food depots as conceived and constructed by Krylov (1951), which received wide recognition. To increase the storage life of perishables, it is necessary to maintain a low interior storage temperature, which in warm seasons requires artificial cooling. Heat pump cooling may frequently be the most economic way to achieve the necessary thermal regime. The design concept of such refrigerated ice storage, combined with a heated greenhouse, was worked out by the Northeastern Permafrost station for the native company Oyary. The results of this work were reported at the Seventh International Conference on Permafrost (Guly & Perlshtein 1998).

It should be noted that the considered examples do not exhaust all possibilities of heat pump usage in northern engineering. It is of great interest to study combinations such as warm and cold food depots; underground mine and surface domestic complexes; and a tailings impoundment and ore-dressing plant. Heat collection from solar heating in summer is considered to be especially prospective. Heat pump usage combined with the simplest solar collectors (synthetic hose) will allow for the reduction of 90% of hot water cost in the period June through August. Finally, in the global warming context, applying heat pumps is a unique technical solution which may make it possible to prevent catastrophic thawing of ground under foundations, practically without additional expense. Investments are needed to develop further research in this new direction of applied geocryology.

Valuable experience on the design, construction, and management of railroads on permafrost was accumulated in Russia during the twentieth century, and continues to increase. Measures are systematized that include control

Figure 3. Impoundment of the road surroundings, northwestern Siberia.

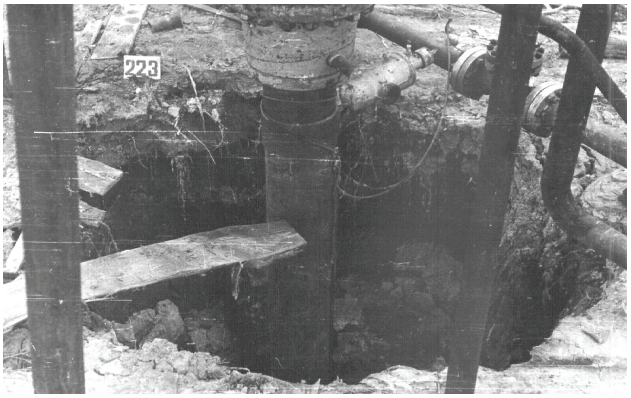

Figure 4. The thermokarst funnel around production wellhead.

of the ground surface heat exchange, combined usage of thermosyphons and heat insulation for stabilizing frozen foundations, and roadbed monitoring (Kondratiev 2005).

Rock fills have wide application in roadbed construction (Minailov 1979, Goering 1998). The physical effect consists in ground cooling at the expense of air convection. Rock fills are employed not only for road construction, but also in other branches of industry; for example, in pipeline installation.

The monitoring system of the railway on permafrost soils is based on the allotment of potentially hazardous sections with establishing the control on their deformation (Ashpiz 2005).

The methodology of roadbed operation was developed for projects of the railroad lines Obskaya-Bovanenkovo, Chara-Cheena, and others. Full-scale experiments and theoretical studies (Passek et al. 2005) were conducted on the temperature regime of the road foundations under conditions of flooded lands (Fig. 3). The impoundment depth was found that induces permafrost degradation in different climatic conditions.

A new algorithm and programs for numerical modeling have been developed at St. Petersburg State University of Means of Communication (Kudryavtsev 2004). These allow the calculation of 3-dimensional temperature and moisture fields of the ground in the roadbed base. The procedure for correct assignment of the bottom boundary condition was worked out (Danielyan & Tkachenko 2005).

Oil and Gas Field Development

In the last few decades, oil and gas field development has become more active in northwestern Siberia, especially on the Yamal Peninsula. Yamal is a unique place in regard to its natural wealth of resources and the difficulty of their development, which is caused by the complexity of natural geocryological conditions and by a particular vulnerability of this territory to technogenic pressure. As a result, there was a need to strengthen the geocryological service and organize monitoring of territories under development.

"Nadymgazprom" specialists, in collaboration with leading Russian scientific, design, and exploration organizations, conducted a geoecological evaluation of the territory and obtained several important results from the scientific point of view (Remizov et al. 2001). For the first time, the connection between cryogenic processes, not only related to climatic changes but also to tectonic sensitivity of the region, was documented. Also, the influence of surface subsidence as a result of hydrocarbon extraction at significant depths has been analyzed. These data are interesting for future statistical analysis of established quantitative characteristics of thermokarst and landslides-earthflow for understanding these cryogenic processes.

Local standards and environmental protection measures have been developed taking into account the prognosis of cryolithozone reaction to modern climate changes.

The stability of producing wells is one of serious technical-ecological difficulty to an oil and gas complex (Fig. 4). Heat exchange in the ground around an operational well has been modeled for the Bovanenkovo field. A new system of preventing "wellhead funnel" formation has been developed on the basis of this model. It includes radially positioned thermosyphons and thermal insulation (Bereznyakov et al. 1997).

The expansion of pipeline construction in the cryolithozone is due to Russia's increasing demands on hydrocarbon fuel for domestic and foreign markets. Unfortunately, an accelerated rate of construction negatively influences the quality of surveying and design solutions. Thermokarst subsidence and frost heave uplift of above-ground pipe foundations are among the common cryogenic processes (Fig. 5). Extremely intensive frost heave uplift of the tube support was recorded during Urengoy pipeline operation—up to 1.5 m in one year (Pazinyak 2001). Quite an attractive option is to install underground pipes; However, for safe operation, a proactive geotechnical monitoring service that can anticipate dangerous situations is a necessity.

Difficulties in the development of Yamal natural resources are induced not only by building and operating industrial structures. Conventional permafrost regions problems are connected with activity of the all local infrastructure.

Institute Fundamentprojekt (Institute of Foundation Design) has devised the main engineering solutions on foundations for the facilities of the Bovanenkovo and Harasavey gas fields (Yamal Peninsula) and also for the gas pipeline from Yamal to the central regions of Russia. These include frozen ground stabilizing with heat shields and thermosyphons, reinforcing ground surface on the slopes with geogrids and geocells (Grechichshev et al. 2005).

Figure 5. Deformations of the pipes due to thermokarst subsidence and frost heave processes.

Figure 6. Fissured rocks of the cryogenic weathering zone (gold-bearing ore deposit Troitskoje, Transbaikalia).

Mineral Mining

In many sites of eastern Siberia and the Far East that are located within the permafrost zone, mining plays an important part in the regional economy.

Open-pit mining of ore deposits has special features in most sites. It is known that the cryogenic weathering zone usually has significant thickness (Slagoda 2005). The fissured rocks of this zone have low ice content (as a rule, no more than 30–50 kg/m^3); however, it predetermines a loss of strength when thawing (Fig. 6).

That is the reason why, in the summer, miners thaw rocks layer by layer using natural heat. This minimizes and sometimes completely avoids the more expensive and dangerous drill-and-blasting operations. The calculation of the open-pit slope takes into account that the warm-season thawing penetrates several meters into rock massif. The placer mining with open-pit method occurs in the warm season, and earth is moved primarily with bulldozers. To make sense of using them, it is necessary to thaw frozen ground. The heat required to melt the ice consumes the main part of the overall energy spent on thawing the ground. Hence, the main goal of an engineering survey is to detect and show the borders of the frozen ground and determine its ice content. As for the ground temperature regime, there is no need to study it carefully.

One of the constant difficulties in placer mining is flushing out frozen sands from open-pit and underground mining. Deposits of the productive horizon, extracted by explosives and deposited in piles at the beginning of the summer, do not have enough time to thaw. And at the end of the flushing season, the ground quickly freezes. This leads to a tremendous loss of metal. This problem, however, is easily solved by using sprinkling thawing. The approximate analytic formulas for it were derived 25 years ago (Perlshtein & Giltsov 1984). The numerical model is described in a paper submitted for this conference.

The simplest methods of thermal melioration of frozen soils are applied to permafrost placers (for example, removal of plant-moss-peat cover). However, under new economic conditions, it is often necessary to use powerful excavators and prolong the season for overburden removal. This brings about hydraulic thawing and deposits drainage. In turn, this requires studying the permeability and other mass transfer properties.

Underground mining of gold placers is used when the burial depth is more than 20 m. It requires breaking gold-bearing deposits during the winter and processing them on the surface during the summer. In this case, the primary goal of the survey is to study permafrost thickness and its temperature. Also sub-permafrost waters must be detected to prevent their ingress into the mine. If the frozen massif temperature is warm (minus 1–2ºC), that predetermines reduced strength of the ground, and mining work is usually conducted in the winter. It is possible to harden the ground significantly at the expense of ventilation with cold air. This should be thoroughly examined in the course of underground-mine planning. Also a hard winter in the permafrost zone allows for the use of ice filling of underground workings. It provides stability when excavating the pillars (bearing blocks).

Hazards and Environmental Protection

For abatement against impact of dangerous cryogenic processes, Russian specialists try to take advantage of the local natural features (severe climate, specific properties of the frozen ground, etc.).

For example, burial of mining toxic waste poses a serious threat to the vulnerable environment. In any tailings disposal method, the seepage-control measures must be designed in such a way to exclude contaminating surface and ground water within the adjacent areas. It is possible to install dams with an impervious frozen core, as used widely in the permafrost zones of Canada, Russia, and Alaska. A new method of tailings management is planned for use at some ore deposits. Its essence consists in dividing the entire area of the tailings disposal facility into several cells. The winter ones (at the periphery of the tailings facility) are filled with successive layers of tailings each of them being permitted to freeze under natural cold conditions prior to

the placement of the next layer. The winter regime of slurry discharge must provide for tailings settlement, mill-water return, and complete freezing of sediments. This method makes it possible to turn the inclement climate into a helpful factor for mining in permafrost regions. Storage of the mine wastes in the frozen state reduces the risk of seepage losses of the toxic solutions. As a result, the construction cost of the tailings disposal facility considerably decreases, and the level of the environmental safety rises.

The method of keeping nuclear waste underground in artificially frozen ground was considered (Khrustalev et al. 2004; 2005). A facility for underground water storage also uses impermeability of frozen soils and ice walls (Kuzmin 2005).

Important data was collected by analyzing catastrophic shifts on the Kolka Glacier, where a huge ice block collapsed on September 20, 2002. The resulting giant ice-water-rock stream was 18 km in length and 80–100 m in height, and flowed at a speed of 150 km/hour. Over 120 lives were lost, the Verkhny Kardamon settlement was buried, the Verkhnaya Saniba village was flooded, and all communication systems were destroyed. After studying the consequences of the Kolka Glacier collapse, it has been determined that this catastrophe as a natural event most resembles a snow-rock-ice avalanche. Based on field research and satellite image analysis, the ice volume involved in this catastrophic shift was 80 ±15 million m^3. Part of the glacier could still remain in its bed. New data made it possible to refine the prognosis of how events could develop in the catastrophe zone. In the next 10–20 years, new catastrophic processes in the Kolka Glacier cirque are unlikely to occur. The main part of the ice body in the Karmadonskaya depression will melt in 2–3 years, but its full degradation will take not less than 10 years [include a reference].

Surveying, Mapping, and Monitoring

The Russian school of engineering-geological survey is traditionally based upon complex geosciences assessment of explored territories involving a wide range of information. Heightened attention is given to methods of mapping. Thus Fundamentprojekt has investigated natural conditions for major industrial facilities on the Barentz Sea coast. Maps at different scale and functions have been prepared and reflect frozen-ground properties (temperature, salinity, strength) and also the results of geocryologic prognosis.

The team at the Earth Cryosphere Institute SB RAS (ECI SB RAS) has drawn up a series of medium-scale GIS maps for permafrost territories with intensive economic activity, such as northwestern Siberia, central Yakutia, the northern variant of pipeline eastern Siberia-Pacific Ocean, and others. These maps present the clearest available information on permafrost conditions in these regions (Drozdov et al. 2007).

Geophysical methods of prospecting are widely practiced. The ECI SB RAS has developed an original methodology of high performance seismic prospecting on lateral SH waves.

Figure 7. Deformations of the railroad bed (Chara-Cheena).

Among the most significant practical implementations are surveying for the third traffic-ring road for Moscow, and research on the factory MFFR-R site to utilize weapon-grade plutonium in the Tomsk region, which was conducted in 2004 within the framework of the Intergovernmental Russian-American Agreement.

Monitoring of cryogenic processes was conducted for the Novaya Chara-Cheena Railroad (northern Transbaikalia). It has been determined that anthropogenic impact, along with climate change, in the foothills of the Udokan Ridge has caused thawing massive ice and ice-wedges as well as catastrophic subsidence of the railroad base (Fig. 7). Under the influence of earthquakes and cryogenic destruction, catastrophic landslides and flow slides occurred in the mid-elevation mountain zone. In the areas of rock streams (kurums) development, these processes led to a railroad slide (Institute of Natural Resources, Ecology and Cryology SB RAS).

Data from integrated monitoring was used to study the natural dynamics of vegetation and its changes under the influence of oil and gas development for northwestern Siberia. It is interesting to note that according to a second grading of peat-mineral hummocks, which took place 30 years after laying the pipeline, the surface had undergone subsidence, heave, and stabilization, but had never returned to its original position, remaining 8–80 cm lower. The intensity of subsidence decreases, moving further away from the pipeline (Institute of the Earth Cryosphere SB RAS).

Conclusions

Permafrost influences the development of northern territories (oil and gas production, mining placers and ore deposits, open-pit and underground operations, etc.). Applied technological methods must use advanced scientific-technical solutions according to the natural conditions of the site. This allows alleviation of the negative influence of permafrost and also uses favorable features of the territory. Accordingly, engineering services must determine necessary and sufficient

volume of geocryological information to provide for the success of prospecting, design, and operational activities.

Exchange of experience and analysis of design errors are very helpful in solution of such problems. Round-table discussions on permafrost engineering problems take place at the annual Russian permafrost conferences.

I think that, presently, the main tasks for Russian applied geocryology are:

- Arrange monitoring of cryolithozone for the most economically important regions;
- Enhance the theoretical basis and determine unified methods of quantitative geocryological prognosis;
- Develop a complex of quantitative models of permafrost-geological processes on the basis of combining deterministic and probabilistic approaches;
- Develop further explorative-investigational work around the use of nontraditional resources of natural heat and cold of the cryolithozone;
- Actively participate in and closely coordinate research within the framework of the International Polar Year;
- Equip laboratory, stationary and fieldwork with modern control and measurement instrumentation.

Acknowledgments

The author thanks S.E. Grechishchev, L.N. Khrustalev, V.P. Melnikov, M.A. Minkin, L.T.Roman, V.N. Zaitsev and R.V. Zhan for their proposals on selecting initial materials for the report. I appreciate the participation of my colleagues D. Sergueev and M. Tishkova in discussing and preparing this text. Especially I would like to express my thanks to IPA President Dr Jerry Brown, who reviewed and suggested revisions to this paper.

References

Ashpiz, E.S. 2005. The monitoring system of the railway bed situated on the permafrost soils. *Proceeding of III Conference of Geocryologists of Russia*, *June 1-3, 2005*. Moscow State University Publishing, vol. 4: 12-19 (in Russian).

Bayasan, R.M., Korotchenko, A.G., Lobanov, A.D. & Pustovoit, G.P. 2005. Technique for thermal stabilization of soils at bases of structures in permafrost regions. *Journ. of Glaciology and Geocryology* 26: 27-32.

Bereznyakov, A.I., Griva, G.I., Osokin, A.B., Popov, A.P., Salikhov, Z.S., Smolov, G.K. & Chugunov, L.S. 1997. *The Problems of Production Wells' Stability within the Gas-Condensate Fields of Yamal Peninsula.* Moscow: IRC Gazprom, 159 pp. (in Russian).

Danielyan, Yu.S. & Tkachenko, E.I. 2005. Resolution of the engineering geocryology problems in the limited areas. *Proceeding of III Conference of Geocryologists of Russia*, *June 1-3, 2005*. Moscow State University Publishing, vol. 4: 94-100 (in Russian).

Dolgikh, G.M., Okunev, S.N., Osokin, A.B., Popov, A.P., Smolov, G.K. & Galaktionov, E.Y. 2005. *Proceeding of III Conference of Geocryologists of Russia, June 1-3, 2005*. Moscow State University Publishing, vol. 4: 100-104 (in Russian).

Drozdov D.S., Korostelev Yu.V., Malkova G.V., Melnikov E.S., Soromotin A.V., Ukraintseva E.A. & Chekrygina, S.N. 2007. Preliminary geocryological and environmental mapping of the areas of perspective economic activity. *Cryogenic Resources of Polar Regions: International Conference, Vol. II, Salekhard, June, 2007*: 264-266.

Epishin, V.K. 1985. Natural-technical systems. In: *Theoretical Basis of Engineering Geology. Social and Economic Aspects.* Moscow: Nedra: 36-45 (in Russian).

Goering, D.J. 1998. Experimental investigation of air convection embankments for permafrost-resistant roadway design. *Proceeding of the Seventh International Conference on Permafrost*, *Yellowknife, NWT, Canada*: 319-326.

Goodrich, L.E. & Plunkett, J.C. 1990. Performance of heat pump chilled foundations. *Proceeding of the Fifth Canadian Permafrost Conference*. Centre d'Etudes Nordiques, Universite Laval: 409-418.

Grechichshev, S.E., Korobkov, N.F., Pavlov, Ark,V. & Sheshin, Yu.B. 2005. The optimum two-layered insulation composition in the embankment structure. *Proceeding of III Conference of Geocryologists of Russia*, *June 1-3, 2005*. Moscow State University Publishing, vol. 4: 72-79 (in Russian).

Guly, S.A. & Perlshtein, G.Z. 1998. Ice food depot cooled with the heat pump: Pre-feasibility study. *Proceedings of the Seventh International Conference on Permafrost*, *Yellowknife, Canada:* 383-390.

Instanes, B. 2000. Permafrost engineering on Svalbard. *International Workshop on Permafrost Engineering, Longyearbyen, Svalbard, Norway*: 1-23.

Khrustalev, L.N. 2005. *Geotechnical Fundamentals for Permafrost Regions.* Moscow: MSU, 82-97 (in Russian).

Khrustalev, L.N., Erchov, E.D., Parmuzin, S.Yu., Vorotyntseva, T.V., Barinov, A.S., Prosorov, L.B. & Tkachenko, A.V. 2005. Underground keeping of the nuclear waste in the artificially creating permafrost soil. *Proceeding of III Conference of Geocryologists of Russia*, *June 1-3, 2005*. Moscow State University Publishing, vol. 4: 214-218 (in Russian).

Khrustalyov, L.N. Erchov, E.D., Parmuzin, S.Y. & Dmitriyev S.A. 2004. Reinforced concrete depot of radioactive waste. *Patent of Russia* No. 242813, Bulletin No. 35, 2004 (in Russian).

Khrustalyov, L.N. & Pustovoyt, G.P. 1988. Probabilistic-statistical calculations of the building basements in cryolithozone. Novosibirsk: Nauka, 253 pp. (in Russian).

Krylov, M.M. 1951. *Isothermal Ice Storages.* Academy of Sciences of the USSR, 101 pp. (in Russian).

Kudryavtsev, S.A. 2004. Numerical modeling the processes of freezing, frost heave and thawing ground. *Basements, Foundations & Soil Mechanics* 4: 21-26 (in Russian).

Kondratiyev, V.G. Problems and ways of stabilization of railway and highway embankment on the icy permafrost. *Proceeding of the Third Conference of Geocryologists of Russia*, vol.4. Moscow: MSU: 144-149 (in Russian).

Kuzmin, G.P. 2005. Estimation of thawing-freezing dynamics in the walls of underground water storages. *Proceeding of III Conference of Geocryologists of Russia*, *June 1-3, 2005*. Moscow State University Publishing, vol. 4: 177-183 (in Russian).

Minailov, G.P. 1979. Experimental study of rock fill cooling impact on the underlying ground temperature. *Workshop "Improvement of Design and Construction Methods for Railroads in Siberia," November 20-22, Moscow,* Proceeding: 129-130 (in Russian).

Passek, V.V., Jusupov, S.N. & Nevmerghitskaya, L.I. 2005. Variation of permafrost ground temperature conditions as partial flooding of area located near earth bed. *Third Conference of Geocryologists of Russia*, vol.4. Moscow: MSU, 209-214 (in Russian).

Pazinyak, V.V. 2001. Frost heave as a destabilization factor of oil-and-gas industry objects. *Proceedings of International Conference: Conservation and Transformation of the Matter and Energy in Earth Cryosphere*. Pushino: 171-172 (in Russian).

Perlshtein, G.Z. & Giltsov, V.D. 1984. Approximate formulas for calculating the duration of hydraulic thawing permeable frozen ground. *Technique and Technology for Permafrost Placers Mining*, Magadan: VNII-1, 99-104 (in Russian).

Perlshtein, G.Z., Buiskih, A.A., & Guly, S.A. 1998. Some prospects for heat pump applications in permafrost engineering. *Proceedings of the International Workshop "Permafrost Response on Economic Development, Environmental Security and Natural Resources."* Novosibirsk: Kluwer Academic Publishers, Netherlands, 425-435.

Polishchuk V.L., Roman L.T., Tseeva A.N., Tsernant A.A. & Livanov, N.I. 2008. Construction on back-filled ground in cryolithozone. Moscow, "Economika, stroitel'stvo, transport," 350 pp. (in Russian).

Recommendations on the control of structures stability on the thawing ground. 1988. Yakutsk, Permafrost Institute SB RAS, 32 pp. (in Russian).

Remizov, V.V., Kononov, V.I., Bereznyakov, A.I., Glukhenkiy, A.G., Dyomin, V.M., Mikhaylov, N.V., Osokin, A.B., Popov, A.P., Rechetnikov, L.N. & Smolov, G.K. 2001. *Nadymgzprom: Geotechnical Monitoring in Cryolithozone*. Moscow: IRC Gazprom, 149 pp. (in Russian).

Slagoda, E.A. 2005. The reconstruction of the cryolithozone with using the micro-morphological traces of cryogenesis in the Upper Neozoic deposits. *Abstract of the doctor thesis,* Tyumen, 48 pp. (in Russian)

SNIP 2.02.04-88.1988. Basements and foundations on the permafrost. Gosstroy USSR (in Russian).

Tseeva, A.N. & Egorov, G.E. 2005. Experience of the use of surface slab foundations in Yakutsk. *Proceeding of III Conference of Geocryologists of Russia, June 1-3, 2005*. Moscow State University Publishing, vol. 4: 219-228 (in Russian).

Numerical Modeling of Differential Frost Heave

Rorik A. Peterson
Mechanical Engineering, College of Engineering and Mines, University of Alaska Fairbanks, Fairbanks AK, USA

Abstract

Differential frost heave (DFH) is laterally non-uniform heave. DFH occurs near buried chilled pipelines, leads to roadway and foundation damage, and also causes some types of patterned ground. Several recent advances in numerically modeling multi-dimensional frost heave at two different spatial scales are discussed. Coupled heat and liquid water transport in a partially frozen saturated soil is modeled at the millimeter scale. Individual ice lens formation is shown to occur when the effective interparticle pressure becomes zero at a finite distance below the nearest existing lens. Liquid water velocity is time dependent, and initially increases quickly and then decreases more gradually until subsequent lens initiation. Velocity also appears to be temporally unstable, occurring in pulses balanced by heat flux. DFH is also spatially unstable on the meter-scale and strongly dependent on the frozen soil mechanical properties. A three dimensional model on the meter-scale shows pattern ground development that depends on soil modulus.

Keywords: frost heave; ice lens; numerical modeling; patterned ground.

Introduction

Differential frost heave (DFH) is laterally non-uniform (i.e., multi-dimensional) heave. The spatial irregularity of DFH causes out-of-plane stresses that result in bending, compaction, dilation, and failure of both the frozen and unfrozen soil. DFH occurs at buried chilled pipelines, leads to roadway and foundation damage, and also causes some types of patterned ground. Analytic and numerical frost heave modeling has progressed significantly as our fundamental understanding of its origins has improved and computational techniques and resources continue to advance. The problem remains complex, however, due to the wide range of length scales from micron-scale unfrozen water films, to the millimeter-scale frozen fringe, to meter-scale soil deformation.

Some of the early numerical models of frost heave that attempted to account for individual ice lens formation are due to O'Neill and Miller (1985) and Gilpin (1980). These models were one-dimensional, which made them both more numerically tractable at the time and also directly applicable to laboratory frost heave experiments. Over the next few decade several numerical variations were developed for the one-dimensional solution, but the underlying physics remained essentially the same.

More recently, Rempel (2007) has shown that an assumption in the previous models concerning local ice pressure is unnecessary and probably incorrect, and provided both an analytical and numerical solution to the one-dimensional frost heave problem. Quantitatively, this solution is not drastically different than those previous when reproducing laboratory frost heave scale experiments. However, it may have more profound implications when describing frost heave with greater overburden pressure as would occur below glaciers and ice sheets.

Multi-dimensional solutions of frost heave are less prevalent, perhaps due to the complicating factor of describing the unfrozen and frozen soil deformation that one-dimensional solutions need not address. Michalowski and Zhu (2006) have recently addressed this issue numerically by introducing a "porosity rate function". The effect of frozen soil elastic modulus on the spontaneous initiation of DFH has been demonstrated analytically by Peterson and Krantz (2003) using a linear stability analysis.

Several recent advances in numerically modeling DFH at two different spatial scales are discussed here. The formation of discrete ice lenses occurs on a roughly millimeter scale in a region of partially frozen soil. The coupled heat and liquid water transport is modeled in two dimensions. The formation of a new ice lens at a discrete location below the nearest existing lens is shown, and its dependence on a spatially variable overburden pressure is demonstrated. The flux of liquid water to the growing ice lens is shown to vary in time. Flux initially increases rapidly as the frost heave pressure increases, but then quickly subsides due to decreasing permeability as pore ice increases. Additionally, the velocity appears to be temporally unstable when the heat flux from the lens is held constant. Pulses of water on an approximately one-second scale occur, and are balanced by the constant heat flux and slowing decreasing temperature at the lens boundary.

During freeze up of a natural soil such as the active layer in permafrost regions, hundreds of individual ice lens can form, and modeling at the millimeter scale rapidly becomes complex due to discontinuities in water flux as each new lens forms and the liquid water pressure adjusts nearly instantaneously. Scaling analysis (Fowler & Krantz 1994) indicates that the process can be recast into a more continuous problem by applying jump boundary conditions at the frozen fringe. This reduced model still accounts for discrete lens formation but does not directly solve for the temporally evolving temperature, pressure and liquid water profile within the frozen fringe. Analytic solutions to this reduced model are currently known only in one dimension. A multi-dimensional numerical solution can be used to investigate the effects of surface variability in temperature

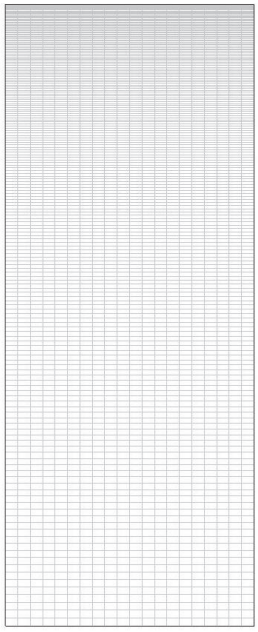

Figure 1. The finite element grid with a logarithmic vertical element size distribution.

and pressure, due to ground vegetation cover or engineering infrastructure, for example.

Here a three-dimensional solution demonstrates that patterned ground can form due to a positive feedback mechanism when small perturbations in the ground surface are randomly distributed as an initial condition. The elastic modulus of the frozen soil provides a stabilizing mechanism once perturbations reach a moderate size, resulting in larger patterns in more stiff soils. This may have implications for changes in natural patterned ground size when soil properties and/or ice content are spatially variable. The soil elastic modulus is only one of several properties than may be spatially and temporally variable, and conclusive model predictions will likely have to consider the combined effect of them all.

Model Description

The two-dimensional model of the partially frozen, saturated soil beneath an ice lens includes transient heat and liquid water transport. The transient energy balance equation is

$$\rho_{eff} C_{eff} \frac{\partial T}{\partial t} = \nabla \bullet \left(k_{eff} \nabla T \right) \tag{1}$$

where T is temperature, C is heat capacity, ρ is density, and k is thermal conductivity. The subscript *eff* denotes effective properties that are volume averages of the three phases: liquid water, ice, and soil. The soil volume fraction is assumed constant. The water transport equation is Darcy's Law for a saturated soil

$$\nabla \bullet \left(\frac{\rho_w \kappa}{\eta} \nabla p_w \right) = 0 \tag{2}$$

where κ is permeability, η is viscosity, and p_w is water pressure. The permeability is a non-linear function of the ice content, W, which is also a non-linear function of the temperature

$$\kappa = \kappa_0 W^{\gamma} \tag{3}$$

where the exponent γ=8 and κ_0 is the unfrozen permeability. Here an exponential function is also used to describe the unfrozen water content.

$$W = \exp[\alpha T] \tag{4}$$

where α = 5 and T is in °C. The exponent depends on the soil type and is usually in the range of 2–10. The results discussed here are general for any value of the exponent, although the exact numerical values will vary.

A two-dimensional finite element mesh consisting of quadrilateral elements was created in a 1-cm wide by 2.5 cm tall domain. The third dimension is not modeled a this scale. The temperature, pressure, and their dependent properties are highly non-linear just below the top boundary. Therefore, element size follows a log space distribution in the vertical direction with evenly spaced elements in the horizontal. The resulting 20 by 200 element grid is shown in Figure 1. The smallest element at top is 2.9 microns by 0.5 millimeters.

Frost susceptible soils are usually silty clays, with relatively wide particle size distributions spanning 1.0 to several hundred microns. This model makes a continuum assumption that material properties are continuous throughout each numerical element, and therefore mass transport can be modeled using Darcy's flow equation. Although the smallest elements in this analysis are of the order of some particle dimensions, it is assumed that micron-scale heterogeneities will average out and the continuum assumption is valid. An attractive alternative would be to use a Discrete Element (DEM) or Material Point Method (MPM), but they are not investigated here.

Initial and Boundary Conditions

The initial conditions are 0°C for temperature and zero gage pressure throughout the domain. The pressure boundary conditions are zero gage pressure at the bottom and $P_{load}(x)$ at the top. Gravitational effects on the pressure distribution are negligible at this scale compared to flow resistance and thermomolecular pressure. The functional form of P_{load} is discussed below. The thermal boundary conditions are 0°C at the bottom and constant heat flux at the top; the flux value is discussed below. The side boundaries have a no-energy-flux condition for the thermal problem, and no mass flux for pressure.

The numerical problem is solved using Comsol Multiphysics version 3.2, a commercial finite element package that is tailored to coupled physical problems. The non-linear solver uses an adjustable time step based on the temporal dynamics of the transient solution.

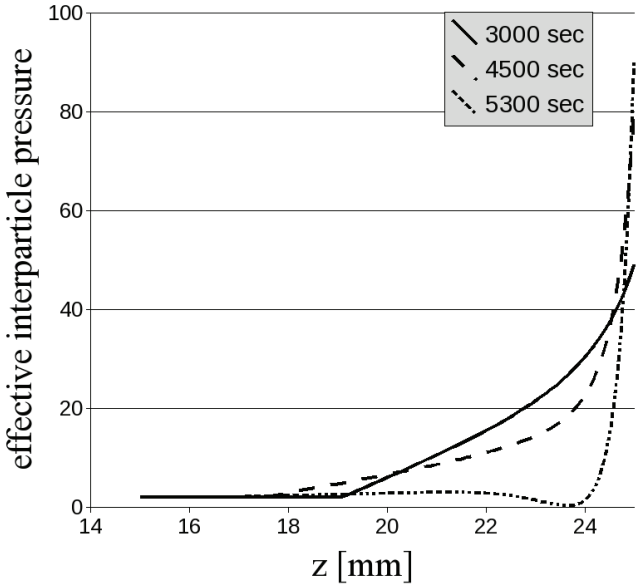

Figure 2. Interparticle pressure in kPa as a function of the vertical location below the existing ice lens.

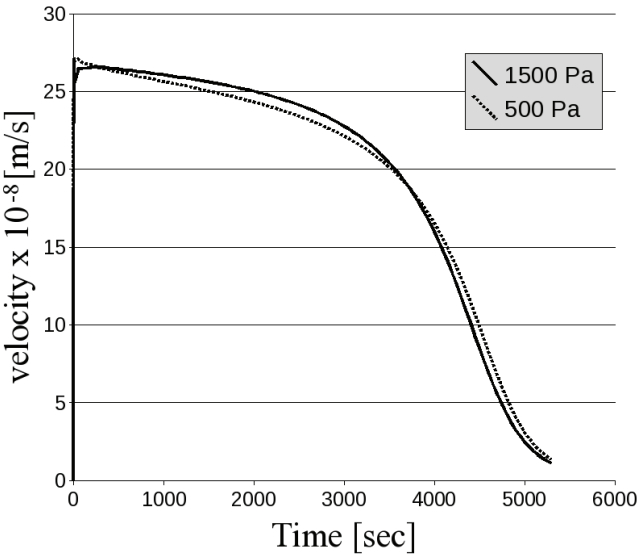

Figure 3. Water flux to the upper boundary for two extremes of the overburden pressure. Len initiation occurs at about 5300 seconds.

Small-Scale Fringe Behavior

All results discussed here used a constant heat flux from the top surface of 100 watts (W) per square meter. During natural soil freezing in autumn when snow depth is relatively thin, the rate of heat flux would be on the order of 10-–100 W/m^2. This estimate assumes a snow thermal conductivity of 0.1 W/m·K (Sturm et al., 2002) a snow depth of 1-–10 cm, and an air temperature of negative 10°C. The higher range of this flux estimate is used to expedite the numerical solution, and a preliminary sensitivity investigation indicates that the overall trends discussed here are general for the entire range of heat flux values.

The energy flux is balanced by thermal conduction to the boundary and latent heat of fusion for the water flux advecting to the boundary and freezing. The interparticle effective pressure is calculated at each time step within the domain and initiation of a new lens begins whenever this function reaches zero. Using a sinusoidal varying surface pressure on the top boundary, p_{load}=1000+500[cos(πx/0.01] Pa, the effective pressure is less on the right hand side and a new lens will initiate on that side first. Figure 2 shows the computed interparticle effective pressure at three different times on the right-hand side of the domain.

The *x*-axis of Figure 2 only shows the upper 1 cm of the domain where the effective pressure is changing most dramatically. Note that the major pressure variation is occurring on the scale of 1 mm, which is one to two orders of magnitude larger than the smallest particle dimensions, and lends support to the continuum assumption when using the Darcy flow equation. Initially the effective pressure increases from the base value because of cryostatic suction. In an unconsolidated soil, compaction may occur during this time with a loss of porosity. These effects are not considered at this point and the porosity is held constant. The suction region extends further downward as time progresses and the ice content increases.

As time nears 5300 seconds, the effective pressure begins to decrease below its base value as the thermomolecular force increases and begins to accommodate a larger fraction of the overburden pressure. As the ice content increases at a particular depth, the unfrozen water film thickness decreases and the dispersion force will increase. Eventually, this force is great enough to push between the soil particles and the effective pressure becomes zero. At this point, a new ice lens will form at this location. This is shown in Figure 2 at about 1-mm below the previous ice lens.

The flux of liquid water to the top boundary freezes and causes the existing ice lens to thicken. The velocity is a function of the cryostatic suction and is therefore spatially varying due to the pressure boundary condition at the top surface. The velocity as a function of time is shown in Figure 3 at the left and right sides of the domain where the pressure is largest and smallest, respectively. The *y*-axis is shown in m/s and scaled by 10^{-8}, so the maximum velocity is 0.25 microns per second. There is an initial rapid rise in the velocity followed by a more gradual decrease until subsequent lens initiation. The initial rise occurs as the ice content initially becomes non-zero and the thermomolecular force is greater than the overburden pressure. The decline is due to increasing ice content that decreases the permeability. The magnitude of velocity throughout the domain is similar, and the two curves span the entire range. From about 200 to 3700 seconds, the larger overburden results in greater water flux by about 3%. At times greater than 2700 seconds, the lower pressure results in a greater velocity. This can be seen where the lines cross in Figure 3 near 3700 seconds. The total increase in lens thickness is spatially varying, and can be determined by integrating the velocity with time and is equal to the area underneath the curves. For the data shown

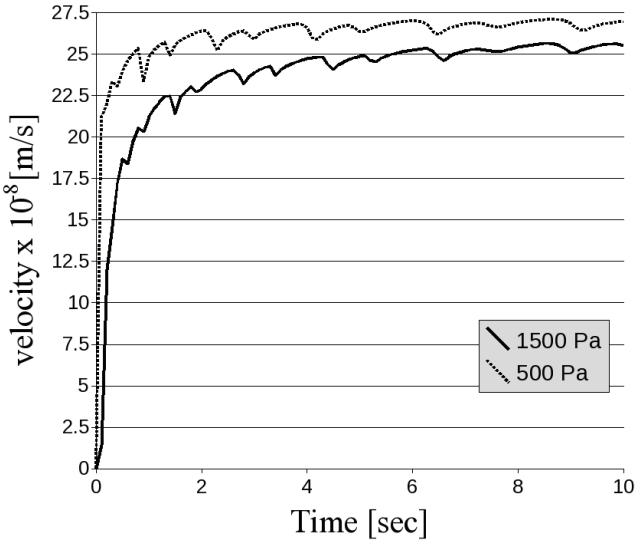

Figure 4. Water flux to the upper boundary during the initial 10 seconds. Pulses occur on a scale of one second.

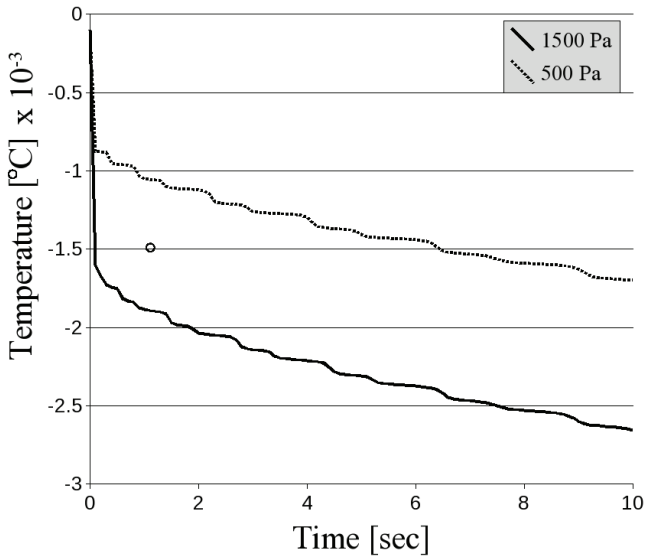

Figure 5. Temperature of the upper lens boundary during the initial 10 seconds. Fluctuations correspond to pulses in the liquid water velocity.

in Figure 3, this results in a thickness of 1.047 mm when P=1500 Pa, and 1.043 mm when P=500 Pa.

The rapid increase in velocity occurs during the first 10 seconds and is shown in Figure 4. There is a slight delay for the greater pressure on the left-hand side because it takes longer for the thermomolecular pressure to balance the greater overburden. A larger ice content is required for water flux to begin and is controlled by the finite energy flux at the top surface. Because the overburden pressures in this simulation are relatively small at only 0.5–1.5 kPa, the delay is less than 1 second. The velocity reaches its maximum value by 5 seconds, and already begins to decline around 10 seconds.

There are obvious fluctuations in the velocity that occur with a periodicity on the order of 1 second. These fluctuations

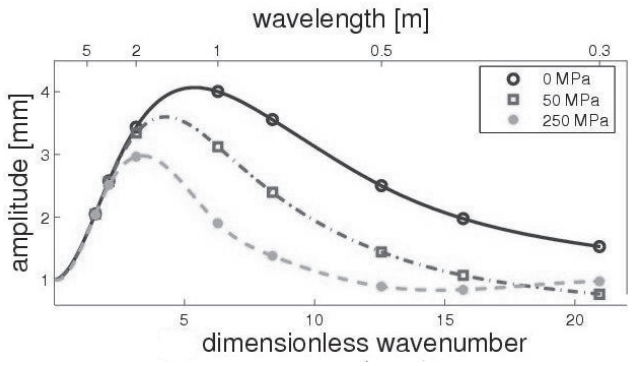

Figure 6. Amplitude of the surface perturbations after one freeze cycle to a depth of 1 meter.

are not due to numerical time stepping and are reproducible with changes in the time stepping protocol. For the results shown in Figure 4, the time step was adaptive and on the order of 0.001 seconds during the first 10 seconds. The fluctuations appear to be due to a temporal instability where a small increase in water flux temporarily slows the rate of ice formation below. Because the heat flux from the top boundary is fixed at 100 W/m^2, it is balanced by the combination of thermal conduction and latent heat of fusion for the liquid water. An increase in velocity means that more lens ice is formed, and therefore less pore ice is formed below the lens. It is the increase in pore ice that eventually slows the liquid water flux. There is a corresponding negative feedback when the water flux decreases slightly. The combination of these two effects results in pulses of water reaching the growing ice lens.

The temperature at the top boundary also shows fluctuations on the 1-second time scale, corresponding to these pulses of liquid water. Figure 5 shows the temperature at the upper boundary for the high and low pressure sides. Overall, the temperature slowly decreases, but there are periods of quick decline that correspond directly with when the liquid water flux is at a minimum. During these short periods more pore ice is formed. When the temperature decline is nearly flat, the corresponding water flux is at a maximum and lens ice formation is at a maximum. These short-term fluctuations become damped as time progresses, and are not readily apparent at times greater than a few hundred seconds.

Large-Scale Pattern Formation

The larger scale frost heave problem is solved using the generalized model equations of Fowler and Krantz (1994). An additional description of how the frozen soil deforms must be added to their model, and here it is assumed to behave as a thin plate with Young's Modulus E. The bending of a thin plate of thickness h can be described by

$$P_b = \frac{Eh^3}{12\left(1-\nu^2\right)}w \tag{5}$$

where P_b is the additional pressure (force per area) required (or resulting from) the bending on the plate, w is the deflection of the plate mid-plane, and ν is Poisson's ratio. A

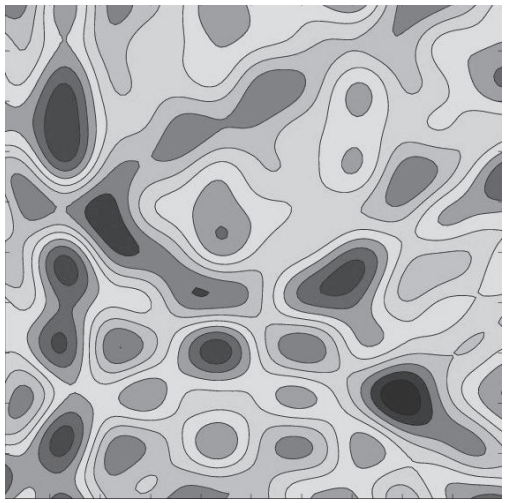

Figure 7. Initial random ground surface perturbations with a maximum amplitude of 1 millimeter.

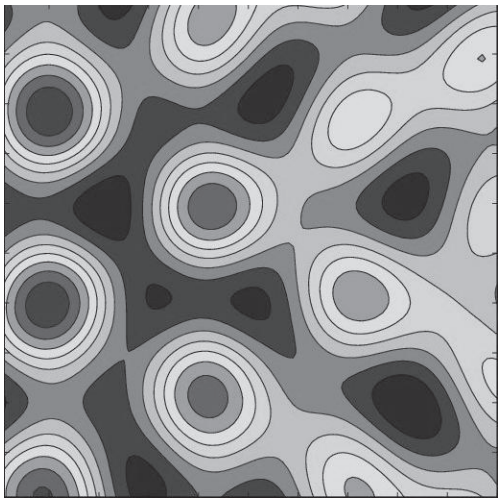

Figure 9. Final ground surface topography after 16 freeze cycles to one meter. Young's modulus is 50 MPa.

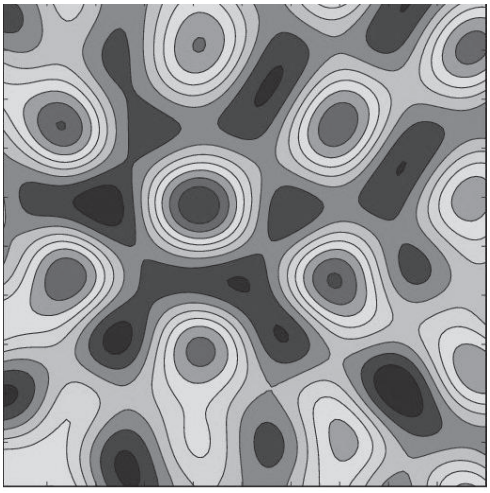

Figure 8. Final ground surface topography after 16 freeze cycles to one meter. Young's Modulus is zero.

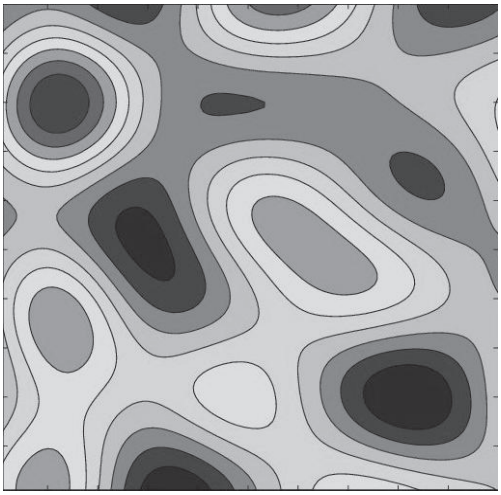

Figure 10. Final ground surface topography after 16 freeze cycles to one meter. Young's modulus is 250 MPa.

two dimensional model for freezing with a constant surface temperature of -10°C was solved using small, sinusoidal varying ground surface perturbations of 1-millimeter amplitude. Because of a singularity when the thickness of frozen soil is zero, an initial frozen thickness of 10 cm was used. The model was run until the depth of freezing reached 100 cm, which is typical of the active layer in permafrost regions.

The final amplitude of the surface perturbations is shown in Figure 6. The top *x*-axis shows the dimensional wavelength of the perturbations, and each curve represents three different values of the Young's Modulus. The symbols show the numerical results of different simulations and the curves are a cubic spline fit to the results. There is a maximum in each curve which indicates the wavelength pattern that is most likely to evolve in the long term from an otherwise homogeneous system that experiences only random perturbations. Even when the modulus is zero, short wavelength patterns do not tend to grow significantly.

Each of the simulations that generated the results shown in Figure 6 involved a perturbation with only a single wavelength. The development of a pattern with a characteristic wavelength can be demonstrated by solving the frost heave model in three dimensions. Random perturbations are once again imposed on the top surface with maximum amplitude of 1 millimeter. In order to approximate the "white noise" of naturally occurring perturbations in nature, a linear superposition of 25 randomly chosen three-dimensional patterns with varying frequencies and spatial offsets was generated. A contour plot of this initial condition is shown in Figure 7, where eight equally-spaced contours represent the range from 0 to 1 millimeter.

Using the same initial conditions, the three-dimensional model was solved for 16 sequential freeze cycles. At the end of each freeze cycle, the final surface topography was used as the initial surface topology for the subsequent year. In this way, the thaw process is not explicitly modeled, and it is assumed that any topography changes due to differential ice formation are maintained. This likely leads to an overestimation of the final pattern amplitude, and probably

favors patterns of a shorter wavelength that would otherwise be mitigated by solifluction or other melt-related processes.

Figures 8, 9, and 10 show contour plots of the final surface topology when the modulus is 0 MPa, 50 MPa, and 250 MPa, respectively. Eight equally-spaced contours are shown, and the lateral dimension is $2\pi = 6.28$ meters. Because of the simplifying assumptions concerning the thaw process, the final magnitude of the pattern is of less consequence than the spatial characteristics. It is readily apparent that when the modulus of the frozen soil increases (Figs. 8–10), the dominant pattern that evolves has a characteristically larger size. All other conditions are identical including the initially perturbed surface. This general conclusion has been postulated before based on linear stability analysis (Peterson & Krantz 1994) and a numerical model for stone circle development (Kessler et al. 2001). However, this model solves for the time-dependent evolution of the pattern, and also explicitly accounts for differential soil movement that depends on the mechanical properties of the frozen soil.

Conclusions

Differential frost heave is a complicated process to model due to important processes that occur over a wide range of spatial scales, ranging from micron-scale liquid water films, to millimeter-scale partially frozen fringe, and to meter-scale soil deformation. Results from numerical modeling of differential frost heave in multiple dimensions at the two larger spatial scales have been discussed. Discrete ice lens formation is predicted to occur on the scale of 1-millimeter below an existing lens, which is in agreement with laboratory measurements and field observations of freezing soils under similar conditions. Spatial variability in the time and location of new ice lens formation is shown by solving for when the interparticle effective pressure becomes zero.

The velocity of liquid water to a thickening ice lens is shown to vary in time, with an initially rapid increase followed by a more gradual decrease as the pore ice content increases. The total amount of lens ice that forms is the time integral of this velocity, and is shown to spatially vary with variations in the overburden pressure. Similar behavior would be expected with a spatially varying surface temperature or thermal flux due to variations in surface ground cover. The liquid water velocity also appears to be temporally unstable, resulting in pulses on a scale of one second. The lens temperature also fluctuates on a similar scale because the total heat flux is balanced by the rate of heat conduction from below and the latent heat of fusion of liquid water. These fluctuations eventually dampen long after the liquid water velocity has reached a maximum and are not apparent at the time of subsequent lens initiation.

The larger scale frost heave problem is solved to demonstrate pattern growth that is dependent on the frozen soil mechanical properties. Patterns of a different characteristic wavelength will develop depending on the elastic modulus, with more still soils resulting in patterns of a larger size. The characteristic pattern size is on the order of 1–2 meters, which is in the range of naturally occurring patterns. A more complete model of pattern generation and evolution must more properly account for the dynamics of thawing soil, which will likely lead to favoring of larger patterns.

References

Fowler, A.C. & Krantz, W.B. 1994. A generalized secondary frost heave model. SIAM *J. Appl. Math.* 54: 1650-1675.

Gilpin, R.R. 1980. A model for the prediction of ice lensing and frost heave in soils. *Water Resour. Res.* 16(5): 918-930.

Kessler, M.A., Murray, A.B. & Werner, B.T. 2001. A model for sorted circles as self-organized patterns. *J. Geophys. Res.* 106(B7): 13287-13306.

Michalowski, R.L. & Zhu, M. 2006. Frost heave modeling using porosity rate function. *Int. J. Num. and Anal. Methods in Geomechanics* 30(8): 703-722.

O'Neill, K. & Miller, R.D. 1985. Exploration of a rigid ice model of frost heave. *Water Resour. Res.* 21: 281-296.

Peterson, R.A. & Krantz, W.B. 2003. A mechanism for differential frost heave and its implications for patterned-ground formation. *J. Glaciology* 49(164): 69-80.

Rempel, A. 2007. Formation of ice lenses and frost heave. *J. Geophys. Res.* 112: F02S21, doi: 10.1029/2006JF000525.

Sturm, M., Perovich, D. K. & Holmgren, J. 2002. Thermal conductivity and heat transfer through the snow on the ice of the Beaufort Sea. *J. Geophys. Res.* 107: (8043,) doi: 10.1029/2000JC000409.

Energy Balance Response of a Shallow Subarctic Lake to Atmospheric Temperature and Advective Persistence

Richard M. Petrone
Cold Regions Research Centre, Wilfrid Laurier University, Waterloo, Ontario, Canada
Wayne R. Rouse
School of Geography & Geology, McMaster University, Hamilton, Ontario, Canada
L. Dale Boudreau
National Archives & Data Management, Environment Canada, Downsview, Ontario, Canada

Abstract

This paper examines two hypotheses that apply to the energy balance of shallow subarctic lakes. These are other factors remaining constant, evaporation and sensible heat fluxes will increase with increasing air temperature, and the influence of mesoscale advection on latent and sensible heat fluxes decreases with increasing wind directional frequency. The data used to examine these hypotheses are derived from a shallow subarctic lake in the Hudson Bay Lowland coastal area near Churchill, Manitoba. They represent two separate years with differing weather and wind directional frequencies. Directional frequencies are divided into onshore (from Hudson Bay) and offshore (from the continental interior). For the former, the air masses are generally cool and moist, and for the latter, they are relatively warm and dry. Analysis of these data indicates that both hypotheses are valid within the framework of this study.

Keywords: advective persistence; Hudson Bay.

Introduction

There are a plethora of small, shallow freshwater lakes and ponds in the North American subarctic. Rouse (1973) estimates that small lakes cover ~3% of the Hudson Bay Lowlands in Ontario, while Dredge (1986) estimates lakes to cover 50% of the Hudson Bay Lowlands in Manitoba. These subarctic freshwater systems, which are dominated by low energy environments and cold region processes, play important hydrological and biogeochemical roles (Pienitz 1995). Hydrologically, these lakes are an important link between the regional hydrology and climate via their evaporative processes, while biogeochemically they can be significant from a nutrient cycling and biological perspective (Schertzer et al. 2003, Nagarajan et al. 2004, Boudreau & Rouse 1995, Macrae et al. 2004). Thus, lakes are an important component of the landscape in this environment and are worthy of consideration in hydrologic and climatologic studies. However, the pronounced warming predicted by global climate models may alter the surface energy balance of these lakes, thereby directly and indirectly altering their hydrological and/or biogeochemical function. Thus, an understanding of the energy regimes of these lakes, and how they are influenced by their regional climate, is required. The goal of this paper is to compare the surface energy fluxes of a shallow tundra lake between a normal wet and warm wet year to gain a better understanding of the potential interactions of these systems with their surrounding environments.

Shallow water bodies have been shown to be especially sensitive to warmer temperatures depending on the amount and timing of regional precipitation (Hondzo & Stefan 1991, Smol et al. 1991, Hondzo & Stefan 1993, Douglas et al. 1994, Nagarajan et al. 2004, Binyamin et al. 2006). Due to their distinctively small size, northern lakes are generally thoroughly mixed with a uniform temperature distribution and may become ephemeral (Bello & Smith 1990). Thus, if global climate models are accurate in their predictions of pronounced warming in high latitudes, the susceptibility of these lakes to ephemeral behaviour, or complete disappearance, is increased. The surface energy fluxes of these shallow tundra lakes have also been shown to be very responsive to advective effects, especially in the Churchill, Manitoba region, where Hudson Bay is seen to have a strong influence on the surface energy balance of the adjacent land up to 65 km inland (Rouse & Bello 1985). In order to investigate this influence on the region's abundant lakes, measurements were taken during the snow free period over Golf Lake, located east of the town of Churchill, Manitoba.

Churchill, a high subarctic wetland region in northern Manitoba, is an area that has been studied in detail. Many shallow lakes and ponds are dispersed throughout this region, most of which are less than 0.5 m deep, and less than 200 m in diameter (Bello & Smith 1990). The smaller ponds are generally poorly defined, very shallow, and frequently flood and dry up. Like most lakes in the subarctic tundra, Golf Lake is shallow (average depth of ~0.88 m) promoting thorough mixing and a uniform temperature distribution >95% of the time (Stewart & Rouse 1976, Binyamin et al. 2006).

The specific objectives of this paper are to study the atmospheric influence on Golf Lake from the surrounding land and adjacent bay, and to examine how the partitioning of the lake energy balance responds to changing mesoscale climatic conditions.

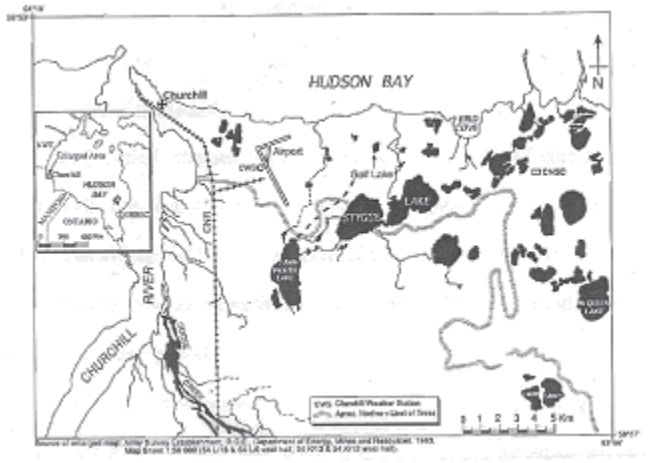

Figure 1. Study map illustrating the location of the town of Churchill, Manitoba and position of Golf Lake relative to the town and Hudson Bay.

Methods

Study area

Golf Lake is located in a wetland-dominated area, 11 km east of Churchill, Manitoba (58°46′N, 94°09′W) (Fig. 1). This region is classified as a high subarctic wetland region (N.W.W.G., Wetland Regions of Canada 1987). Hudson Bay exerts a strong influence on the climate of the area, causing Churchill to have high subarctic conditions, such as long, cold winters, short, cool summers, and low annual precipitation. This strong regional influence of Hudson Bay has been shown to extend at least 65 km inland, enhancing the flux of sensible heat and suppressing the fluxes of both latent and ground heating when winds originate offshore over Hudson Bay (Rouse 1991). This suppression of temperatures by the bay in the Churchill region causes the treeline and region of continuous permafrost to extend relatively far south in the Hudson Bay Lowland when compared to the rest of northern Canada.

Golf Lake is oval in shape with its long axis oriented approximately northeast–southwest (Fig. 1). The lake is approximately 550 m long by 350 m wide, 0.88 m deep on average, and is 1.2 m at its deepest point (Boudreau & Rouse 1995). The lake is surrounded by treeless upland heath to the east and sedge fens to the south, north, and west, with only a few larch (*Larix larcina*) and white spruce trees (*Picea glauca*) two to three meters in height. The immediate perimeter of the lake is dominated by various *Carex* species.

Measurements

An instrumented meteorological tower was located in the centre of the lake in 1.2 m of water. Air temperature, vapor pressure, and wind speed were measured at heights of 0.55, 1.05 and 1.55 m above the water surface. Lake temperatures were taken at the water surface, and at seven depths within the water column, with the bottom two sensors located within the loose organic bottom sediment. The heat flux through the bottom of the lake was measured using a Middleton heat flux plate.

Table 1. Mean precipitation (P), incident solar radiation (K↓) and air temperature (TAir) for Golf Lake, Churchill, Manitoba, 1991 and 1995.

	P (mm)	K↓ (W m^{-2})	T_{Air} (°C)
1995	224	182	10.4
1995	224	182	10.4

Table 2. Mean precipitation (P), incident solar radiation (K↓), air temperature (Ta), water temperature (Tw) Bowen ratio (β), the frequency of temperature inversion and lapse conditions (T-Inv. and T-Lapse, respectively), and the frequency of vapour pressure inversion and lapse conditions (e-Inv. and e-Lapse, respectively) for on and offshore winds, Golf Lake, Churchill, Manitoba, Canada, 1991 and 1995. n denotes the number of days with ON and OFF shore wind directions.

	1991		1995		COMBINED	
	ON	OFF	ON	OFF	ON	OFF
P(mm)	10	24	74	72	84	96
K↓(W/m^2)	209	226	198	164	203	195
Ta (°C)	9.7	15.7	10.1	14.9	9.9	15.3
Tw (°C)	14.9	16.1	12.9	16.4	13.9	16.3
β	0.5	0.1	0.7	-0.5	0.6	-0.2
T-Inv.	7	40	3	23	5	31.5
T-Lapse	93	60	97	77	95	68.5
e-Inv.	0	0	0	0	0	0
e-Lapse	100	100	100	100	100	100
n	10	12	26	14	36	26

Measurements yielded all components of the lake's energy balance via,

$$Q^* = Q_W + Q_E + Q_H \quad (1)$$

where Q^* (W m^{-2}) is the net radiation, Q_W is the lake heat storage and Q_E and Q_H are the fluxes of latent and sensible heat, respectively.

The partitioning of the available energy between the sensible and latent heat fluxes is described by the Bowen ratio (β),

$$\beta = \frac{Q_H}{Q_E} \quad (2)$$

Substitution of the flux equations for sensible and latent heat into equation (2) yields the following expression for the Bowen ratio,

$$\beta = \gamma \frac{\Delta T}{\Delta e} \quad (3)$$

where γ is the psychrometric constant (0.0662 kPa °C^{-1}), ΔT is the vertical change in air temperature, and e is the vertical change in vapor pressure (kPa). β is a useful term to examine the relative importance of the sensible and latent heat fluxes, and the importance of cold air advection.

The heat storage within the lake (Q_W) is calculated from the sum of the series of lake layers, using the mean temperature and thickness of each layer giving,

$$Q_W = \sum C_W \left(\frac{\Delta T_W}{\Delta t} \right) \Delta z \quad (4)$$

where C_W is the volumetric heat capacity, ($\Delta T_W / \Delta t$) is the water temperature change over time, and Δz is the depth increment of the volume of water in question, usually from the surface to the lake bottom.

The latent heat flux Q_E is derived using the energy balance approach in which,

$$Q_E = \frac{(Q^* - Q_W)}{1 + \gamma \frac{\Delta T_a}{\Delta e}} \quad (5)$$

where $\gamma(\Delta T_a/\Delta e)$ is the Bowen ratio. After determining Q_E, the sensible heat flux Q_H is derived as a residual in equation (1). Measurements are then grouped according to wind direction (with 360° representing true north) according to the following criteria: 315°–45° are referred to as *Onshore winds* (originating over Hudson Bay); 225°–315°and 45°–135° are referred to as *Along shore winds*, and 135°–225° are referred to as *Offshore winds* (originating over the interior tundra). The surface energy balance terms are then normalized as a ratio of the net radiation.

Results and Discussion

The two study seasons differed significantly in their seasonal weather. 1991 was on average about 5°C warmer than 1995, and was wetter and sunnier (Table 1). The air temperature and precipitation for 1991 and 1995 were greater than the observed normals for the region (9.7°C and 112 mm, respectively, Rouse et al. 1987), with 1991 being notably warmer and wetter than normal. The impact of differences in the summer weather on the energy balance of Golf Lake for these two seasons was substantial (Fig. 2). In both years, Q_H followed the same trend as Q*, reaching maximum in late June or early July and decreasing subsequently. Q_E reached maximum values around the first week of July, but remaining high through the measurement periods. There was little lake net heat storage (Q_w) in either year.

Lake and air temperature trends help to understand observed trends in the surface energy balance. In both years, onshore winds were associated with cooler temperatures and offshore winds with warmer temperatures (Table 2). In 1991, onshore winds were less frequent, and also less frequently associated with increased precipitation than in 1995. Inversion periods with negative sensible heat flux were frequent in 1991 (Fig. 2). In contrast, 1995 experienced lapse conditions (air temperature less than lake temperature) for the bulk of the season, with a resulting enhanced sensible heat flux (Table 2). Onshore winds always corresponded with lapse conditions in both years. $\beta = Q_H/Q_E$ generally showed large fluctuations from day to day, but over the season averaged out near zero (Table 3). β was higher for onshore than for offshore winds in both years.

Since the surface fluxes are strongly coupled with the net

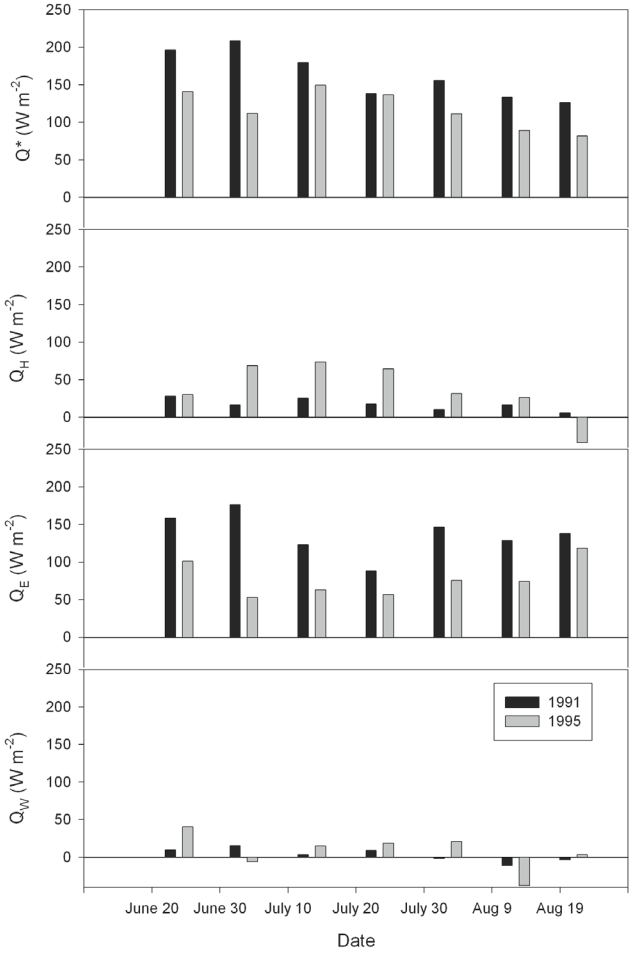

Figure 2. Surface energy balance for Golf Lake, Churchill, Manitoba, 1991 and 1995. Net radiation (Q*), sensible heat flux (Q_H), latent heat flux (Q_E) and lake heat storage (Q_W) data are expressed as 10-day running averages.

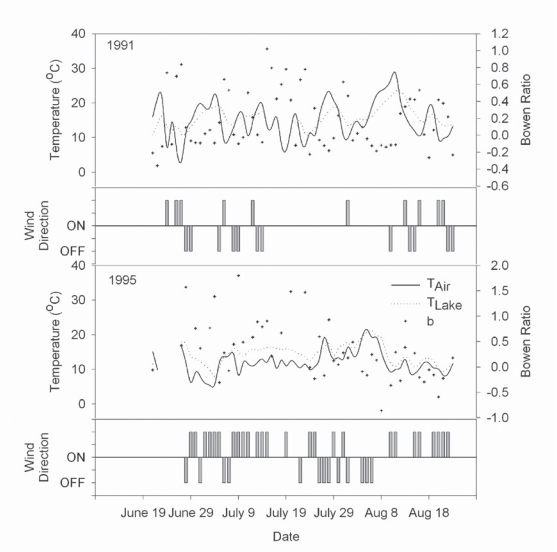

Figure 3. Air and lake temperatures (T_a and T_W, respectively), and Bowen ratio (β) for onshore and offshore winds, Golf Lake, Churchill, Manitoba, 1991 and 1995. All variables are expressed as daily averages.

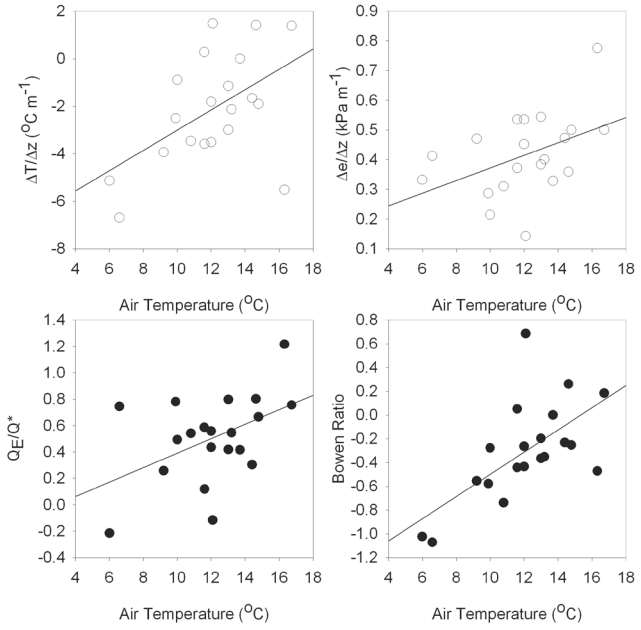

Figure 4. Relationship of vertical temperature ($\Delta T/\Delta z$) and vapour ($\Delta e/\Delta z$) gradients, relative latent heat (Q_E/Q^*) flux, and Bowen ratio (β) to air temperature. Data are plotted for both On and Offshore winds for both 1991 and 1995, for $Q^* = 200 \pm 40$ W m^{-2}. The lines are best-fit regression lines.

Table 3. Seasonal averages of the relative sensible (Q_H/Q^*) and latent heat (Q_E/Q^*) fluxes, relative lake heat storage (Q_W/Q^*), lake (T_W) and air (T_a) temperatures, and air temperature gradient (dT/dz). Golf Lake, Churchill, Manitoba, Canada, 1991 and 1995. Values are for Onshore and Offshore winds and standardized for $Q^* = 200 \pm 40$ Wm^{-2}.

		Q_H/Q^*	Q_E/Q^*	Q_W/Q^*	T_a (°C)	T_w (°C)	dT/dz (°C/m)
1991	ON	0.35	0.85	-0.30	11.5	15.8	2.2
	OFF	0.03	0.75	0.23	16.9	16.1	0.4
1995	ON	0.29	0.63	0.10	9.9	13.5	-1.8
	OFF	0.42	0.79	0.01	15.3	16.2	-0.4

radiation, to better understand their dynamics, it is useful to normalize them as a ratio of the net radiation, to give relative latent and sensible heat fluxes (Table 3). This brings out yearly contrasts. In 1995, all offshore flows produced large relative evaporation, and most onshore flows produced large relative sensible heat fluxes (Table 3). In 1991, onshore winds frequently resulted in larger relative evaporation than offshore winds (Table 3). By eliminating Q* as a variable, it is evident that $\Delta T/\Delta z$, $\Delta e/\Delta z$, Q_E/Q^* and β all increase with increasing atmospheric temperatures (Fig. 4). The rapid increase in β with increasing Ta arises because the rate of increase in Q_H substantially exceeds that in Q_E.

Many of the differences seen in the 1991 and 1995 data are due to differences in the directional persistence of winds. These have a substantial impact on $\Delta T/\Delta z$ and $\Delta e/\Delta z$. $\Delta e/\Delta z$ over the lake resulting from the differing response of lake and air temperatures. Even a shallow lake's response to changing atmospheric conditions requires periods of time

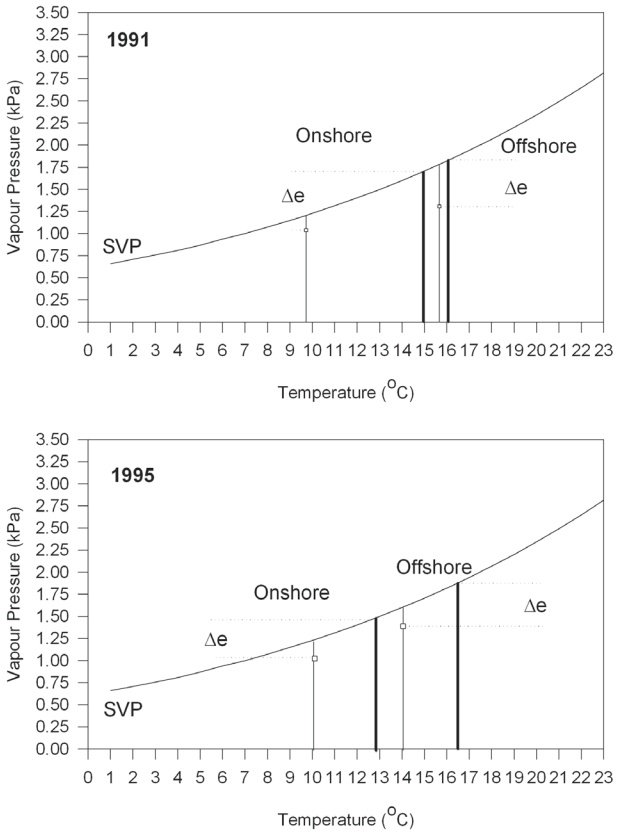

Figure 5. Vapour pressure-temperature relationships, during On and Offshore conditions, Golf Lake, Churchill, Manitoba, 1991 and 1995. Squares represent seasonal vapour pressures; thick lines represent seasonal lake temperatures; and fine lines represent seasonal air temperatures.

ranging from several hours to days, due to its relatively large heat capacity compared with the atmosphere. The large increases in $\Delta e/\Delta z$ and Q_E for onshore conditions in 1991 were due both to the increased temperatures and lesser persistence of onshore winds, which never persisted for longer than two days. (Fig. 3, Table 3). In 1995, there was substantially greater persistence in wind direction (Fig. 3). In 1991, lake temperatures were very close for both onshore and offshore winds, due to the much lower frequency and persistence of onshore winds compared with 1995 (Fig. 3). During offshore winds, larger differences between air and lake temperature generated large vapor pressure gradients. The relationship became stronger as lake temperature increased, due to physical principles dictated by the slope of the saturated vapor pressure-mean temperature curve (Fig. 5). The warmer conditions in 1991 stimulated greater vapor pressure gradients over the lake (Fig. 4), which resulted in greater Q_E. This is similar to the results in Rouse et al. (1987) who reported on a similar increase in evaporation with increasing air temperature for a sedge fen in the Churchill region. The enhancement of the latent heat flux for warmer conditions could also be due to the greater suppression of the sensible heat flux during the frequent inversion conditions of 1991 (Strub & Powell 1987).

Conclusions

Within the context of this study, our evidence indicates that both hypotheses appear valid. With a control on interacting variables, the vertical temperature and vapor pressure gradients increase with increasing air temperatures which, in turn, results in increased sensible and latent heat fluxes. With increasing atmospheric temperatures, sensible heat fluxes increase more rapidly than latent heat fluxes. Thus, shallow lakes respond fairly rapidly to atmospheric temperature changes, especially in the direct heating of the atmosphere. However, this response in advective situations depends on wind directional frequencies. Where wind directions change frequently, the response is greater than when they change less frequently.

Acknowledgments

The authors wish to thank M. Macrae and the staff of the Churchill Northern Studies Centre for their assistance in the field. Funding was provided by the Natural Science and Engineering Research Council of Canada, and the Northern Science Training Program.

References

Bello, R.L. & Smith, J.D. 1990. The effect of weather variability on the energy balance of a lake in the Hudson Bay Lowlands, Canada. *Arctic and Alpine Research* 22(1): 98-107.

Binyamin, J., Rouse, W.R., Davies, J.A., Oswald, C.J. & Schertzer, W.M. 2006. Surface energy balance calculations for small northern lakes. *International Journal of Climatology* 26: 2261-2273.

Boudreau, L.D. & Rouse, W.R. 1995. The role of individual terrain units in the water balance of wetland tundra. *Climate Research* 5: 31-47.

Douglas, M.S.V., Smol, J.P. & Blake Jr., W. 1994. Marked post-18th Century environmental change in high Arctic ecosystems. *Science* 266: 416-419.

Dredge, L.A. 1986. *Surficial Geology, Northeastern Manitoba*. Geological Survey of Canada, Map 1517A. 1:500,000.

Hondzo, M. & Stefan, H.G. 1993. Regional water temperature characteristics of lakes subjected to climate change. *Climatic Change* 24: 187-211.

Hondzo, M. & Stefan, H.G. 1991. Three case studies of lake temperature and stratification response to warmer climate. *Water Resources Research* 27(8): 1837-1846.

Macrae, M., Bello, R.L. & Molot, L. 2004. Intermittent Hydrologic Pathways in Tundra Ponds and Implications for Carbon Dynamics in the Hudson Bay Lowland. *Hydrological Processes* 18(11): 2051-2069.

Nagarajan, B., Yau, M.K. & Schuepp, P.H. 2004. The effects of small water bodies on the atmospheric heat and water budgets over the MacKenzie River Basin. *Hydrological Processes* 18: 913-938.

N.W.W.G., The Canadian Wetland Classification System, National Wetlands Working Group of the Canada Committee on Ecological Land Classification, 1987: *Ecological Land Classification Series*, No. 21, Lands Conservation Branch, Canadian Wildlife Service, Environment Canada, Ottawa, Ontario, 18 pp.

Pienitz, R., Smol, J.P. & Birks, H.J.B. 1995. Assessment of freshwater diatoms as quantitative indicators of past climatic change in the Yukon and Northwest Territories, Canada. *Journal of Paleolimnology* 13: 21-49.

Rouse, W.R. 1991. Impacts of Hudson Bay on the terrestrial climate of the Hudson Bay Lowlands. *Arctic and Alpine Research* 23: 24-30.

Rouse, W.R. 1973. The microclimate of different terrain units in the Hudson Bay Lowlands. In B.D. Kay (ed.), *Proceedings: Symposium of the Physical Environment of the Hudson Bay Lowlands: March 30-31, 1973*. University of Guelph, pp. 69-82.

Rouse, W.R., Hardill, S.G. & Lafleur, P.M. 1987. The energy balance in the coastal environment of James Bay and Hudson Bay during the growing season. *Journal of Climatology* 7: 165-179.

Rouse, W.R. & Bello, R.L. 1985. Impact of Hudson Bay on the energy balance in the Hudson Bay Lowlands and the potential for climatic modification. *Atmosphere-Ocean* 23(4): 375-392.

Schertzer W.M., Rouse, W.R., Blanken, P. & Walker, A. 2003. Over-lake meteorology and estimated bulk heat exchange of Great Slave Lake in 1998 and 1999. *Journal of Hydrometeorology* 4: 649-659.

Smol, J.P., Walker, I.R. & Leavitt, P.R. 1991. Paleolimnology and hindcasting climatic trends. *Verh. Internat. Verein. Limnol.* 24: 1240-1246.

Stewart, R.B. & Rouse, W.R. 1976. A simple method for determining evaporation from shallow lakes and ponds. *Water Resources Research* 12: 623-628.

Strub, P.T. & Powell, T.M. 1987. The exchange coefficients for latent and sensible heat flux over lakes: dependence upon atmospheric stability. *Boundary-Layer Meteorology* 40: 349-361.

Numerical Analysis of Forced and Natural Convection in Waste-Rock Piles in Permafrost Environments

Hoang-Nam Pham
Department of Civil and Environmental Engineering – University of Alberta, Edmonton, AB, Canada
Lukas U. Arenson
BGC Engineering Inc., Vancouver, BC, Canada
David C. Sego
Department of Civil and Environmental Engineering – University of Alberta, Edmonton, AB, Canada

Abstract

Mine waste-rock material is often a highly porous medium and it is an ideal environment to analyze the effect of natural and forced air convections on the waste-rock pile temperatures in permafrost regions. Two-dimensional finite element method is utilized to examine the behavior of different waste-rock piles. Forced convection as a function of air velocity is solved by applying the Navier-Stokes momentum equation and the continuity equation. Coupled thermal and air flow modeling of waste-rock piles is carried out for a period of 10 years. The cooling effect of the closed waste-rock piles mainly relies on gravity driven natural convection within the porous waste-rock layer, which is controlled by the thermal boundary condition. The cooling effect of the open waste-rock piles, on the other hand, is controlled by the cold temperature air flow that penetrates the pile. Preliminary results indicate that the center of the waste-rock piles will form a frozen core and an active layer of about 5 meters in approximately 2.2 years.

Keywords: convective heat transfer; natural convection; numerical simulation; waste-rock piles.

Introduction

Natural convection in fluid saturated porous media plays a key role in a wide range of technical applications, such as fluid flow in geothermal reservoirs, insulations, dispersion of chemical contaminants and migration of moisture in grain storage system. A comprehensive literature survey focusing on this subject is given by Nield & Bejan (1998).

Research on natural convection in permafrost regions has seen increasing attention by many researchers. Goering & Kumar (1996) investigated the characteristics of natural convection in porous rock embankments and showed significantly enhanced cooling effects in winter beneath these porous rock embankments. A large number of numerical models showed that natural convection during winter time can lower the foundation soil temperature by as much as 5°C on an annual average basis in comparison with standard sand or gravel embankments. In addition, researchers at the State Key Laboratory of Frozen Soil Engineering at the Chinese Academy of Sciences in Lanzhou have performed numerical and experimental studies on natural convection for the railway project on the Qinghai-Tibetan Plateau. Yu et al. (2003) investigated the cooling effect of coarse rock layers and fine rock layers under open-top and windy boundary in a laboratory investigation. Lai et. al. (2003) proposed the ripped-rock embankment structure on the Qinghai-Tibet railway under climatic warming by numerical simulation. Arenson et al. (2007) presented the results of numerical simulation of natural convection of waste-rock material, where the temperature at the base decreased from -4°C (conduction only) to -6°C due to convection.

In this work, numerical simulation of convection in waste-rock pile will be performed to evaluate the parameters that affect the convective heat transfer in coarse materials, namely wind, snow cover (boundary conditions), and internal intrinsic permeability of the waste-rock.

Governing Equations and Material Properties

Governing equations

Consider a fluid-saturated porous media with constant physical properties except for the density in the buoyancy force term, which is satisfied by the Boussinesq's approximation, thermal conductivity and volumetric heat capacity which are variation with temperature. Local thermal equilibrium is taken into consideration; e.g., the temperature of the fluid phase is equal to the temperature of the solid phase. The porous media is homogenous and isotropic. The flow of fluid within the porous media is governed by Darcy's law and the flow of fluid over the waste-rock pile is controlled by Navier-Stockes law with a Darcy term account

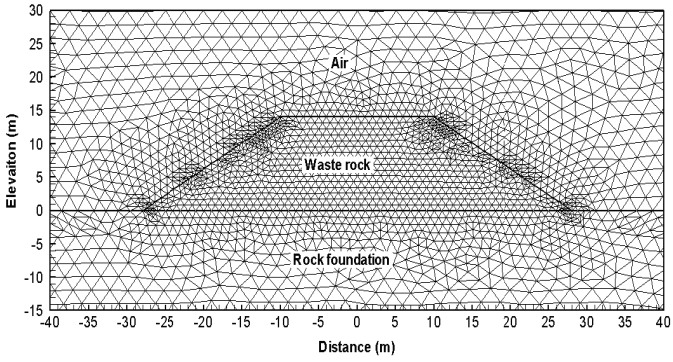

Figure 1. Finite element mesh and general geometry of the simulation.

for the effects of forced convection into the pile. Figure 1 shows the computational domain and mesh.

Conservation of mass:

$$\frac{\partial u}{\partial x}+\frac{\partial v}{\partial y}=0 \tag{1}$$

Conservation of momentum

- Fluid in porous media

Darcy's law

$$u=-\frac{K}{\mu}\frac{\partial P}{\partial x} \tag{2a}$$

$$v=-\frac{K}{\mu}\left[\frac{\partial P}{\partial y}-\rho_o g\beta(T-T_o)\right] \tag{2b}$$

- Free fluid flow

Navier-Stokes equation with Darcy's term

$$\rho\left(u\frac{\partial u}{\partial x}+v\frac{\partial u}{\partial y}\right)=-\frac{\partial P}{\partial x}+\mu\left(\frac{\partial^2 u}{\partial x^2}+\frac{\partial^2 u}{\partial y^2}\right)-\frac{\mu}{K}u \tag{3a}$$

$$\rho\left(u\frac{\partial v}{\partial x}+v\frac{\partial v}{\partial y}\right)=-\frac{\partial P}{\partial y}+\mu\left(\frac{\partial^2 v}{\partial x^2}+\frac{\partial^2 v}{\partial y^2}\right)-\frac{\mu}{K}v+\rho g\beta(T-T_o) \tag{3b}$$

Conservation of energy

$$\left(C_S+L\frac{\partial W_u}{\partial T}\right)\frac{\partial T}{\partial t}+C_a\left(u\frac{\partial T}{\partial x}+v\frac{\partial T}{\partial y}\right)=\frac{\partial}{\partial x}\left(\lambda_x\frac{\partial T}{\partial x}\right)+\frac{\partial}{\partial y}\left(\lambda_y\frac{\partial T}{\partial y}\right) \tag{4}$$

where u and v are velocity in x, y direction; K is the intrinsic permeability; μ: dynamic viscosity; P: air pressure; ρ_O: air density; C_S: volumetric heat capacity of the waste-rock; C_a: volumetric heat capacity of air; L: latent heat of water; W_u: unfrozen water content; λ_x, λ_y: thermal conductivity in x, y direction; β: thermal expansion of air; T is temperature of solid and fluid.

We introduce the stream function ψ, expressed as:

$$u=\frac{\partial \psi}{\partial y} \tag{5a}$$

$$v=-\frac{\partial \psi}{\partial x} \tag{5b}$$

By substituting Equations (5a, 5b) into Equations (2a, 2b), and eliminating the pressure term, we obtain:

$$\frac{\partial}{\partial x}\left(\frac{\mu}{K}\frac{\partial \psi}{\partial x}\right)+\frac{\partial}{\partial y}\left(\frac{\mu}{K}\frac{\partial \psi}{\partial y}\right)=\rho_o\beta g\frac{\partial T}{\partial x} \tag{6}$$

By introducing the stream function, the conservation of mass in the porous media is automatically satisfied.

One of common methods to solve Equations (3a, 3b) is to eliminate the pressure terms through the penalty parameter γ. The method is called the penalty finite element method (Reddy & Gartling 2000).

$$P=-\gamma\left(\frac{\partial u}{\partial x}+\frac{\partial v}{\partial y}\right) \tag{7}$$

where $\gamma = 10^4 Re$ to $10^{12} Re$; Re is the Reynolds number.

To determine the effects of heat transfer, the local Nusselt number and Rayleigh number are defined as following:

The local Nusselt number on the base of the waste-rock

$$Nu_b=\frac{1}{L_b}\int_0^{L_b}\frac{\partial T}{\partial y}dx \tag{8}$$

The Rayleigh number of waste-rock

$$Ra=\frac{\rho_o g\beta C_a K H\Delta T}{\mu\lambda} \tag{9}$$

where L_b is the length of the base of the waste-rock pile; H is the height of the waste-rock pile.

The average Nusselt number on the base is defined as.

$$\overline{Nu}=\frac{\left(\frac{1}{L_b}\int_0^{L_b}\frac{\partial T}{\partial y}dx\right)_{convection}}{\left(\frac{1}{L_b}\int_0^{L_b}\frac{\partial T}{\partial y}dx\right)_{conduction}} \tag{10}$$

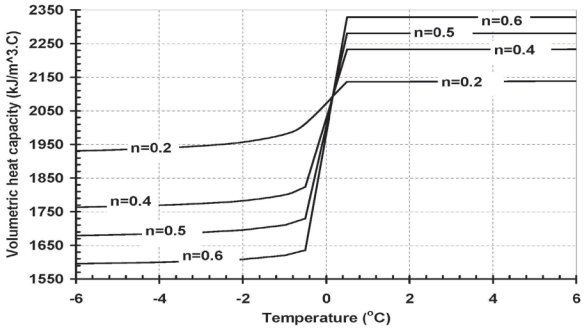

Figure 2. Relation between volumetric heat capacity and temperature with degree of saturation S = 0.6 and porosity n of the waste-rock material at the Diavik mine.

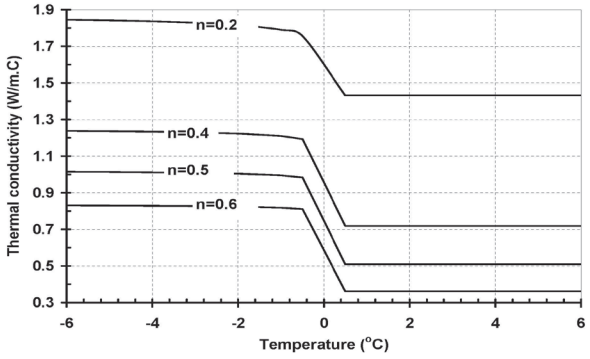

Figure 3. Relation between thermal conductivity and temperature with degree of the saturation S = 0.6 and porosity n of waste-rock material at the Diavik mine.

Material properties

The intrinsic permeability of the waste-rock material varies from 10^{-8} to $3x10^{-7}m^2$, based on calculation from grain size distribution resulting porosity between 0.3 and 0.5 and the degree of saturation is 0.6. A porosity $n = 0.4$ was chosen for this study.

Figure 2 shows a sharp change in volumetric heat capacity around the freezing point due to phase change of pore water. Similarly, the thermal conductivity changes with temperature as shown in Figure 3.

Additional parameters used are air density $\rho_o = 1.293kg/m^3$, dynamic viscosity $\mu = 1.49kg/mday$, thermal expansion of air $\beta = 3.6710^{-3}(C^{-1})$, and volumetric heat capacity of air $C_a = 1.3$ kJ/m^{3}C.

Temperature variation with time is governed by the following equation with a mean average surface temperature of -4.8°C.

Ground temperature:

$$T = -4.8 + 17\sin\left(\frac{-2\pi t}{365} + \frac{17\pi}{180}\right) \quad (11)$$

Air temperature:

$$T = -9.5 + 28\sin\left(\frac{-2\pi t}{365} + \frac{17\pi}{180}\right) \quad (12)$$

Figure 4 shows that the wind velocity varies from 3m/s to 10m/s. Thus, this range was used to analyze the influence of forced convection on heat transfer in the waste-rock piles.

Numerical Results and Discussions

The strength and pattern of the convective heat transfer within a waste-rock depends mainly on geometry, intrinsic permeability of the waste-rock and the ambient temperature on the ground surfaces (Nield & Bejan 1999).

With impermeable surfaces (snow cover during winter), the influence of wind velocity is negligible and the motion of air is governed by natural convection.

With permeable surfaces during summer, the magnitude of the air velocity inside a waste-rock due to wind blow (forced convection) is mainly controlled by the intrinsic permeability of the waste material.

Table 1 and 2 show how the air velocity at the center axis of a waste-rock pile is strongly influenced by the intrinsic permeability based on the modeling in this study.

Results for impermeable surfaces of waste-rock piles

Figure 5a, b, c, and d show temperature distributions 10 years after construction. Figure 5a and b give similar temperature contours and the lowest temperature is -5.5°C. This can be explained by the fact that, under small intrinsic permeabilities ($1x10^{-8}$ and $3x10^{-8}$), heat transfer in waste-rock material is dominated by conduction; e.g., only dependent on the thermal conductivity of the material with small Rayleigh and Nusselt number. Furthermore, a 5-m active layer is formed normal to surface of the waste-rock and ground. In Figure 5c, temperatures at the base of the waste-rock pile are colder than in Figure 5a and 5b. This indicates an increase in the Rayleigh numbers and heat transfer via convection is developing. Figure 5d shows a significant change in temperature at the base in comparison with those shown in Figure 5a, b, and c. Temperatures drop from -5.5°C down to -8°C. This results from the increasing permeability. Furthermore, the unfrozen zone at the toe of the waste-rock decreases substantially.

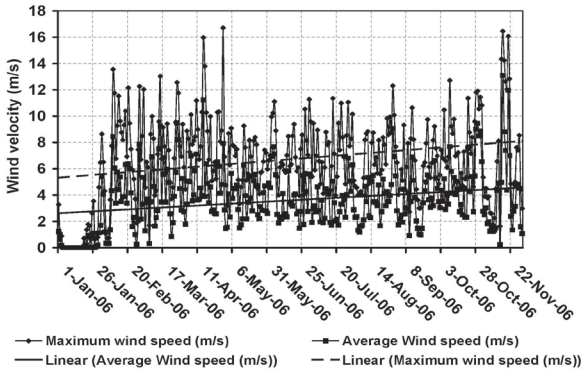

Figure 4. Wind velocity measured at the Diavik mine site.

Table 1. Air velocity inside waste-rock with $K = 1x10^{-8}m^2$.

Wind velocity (m/s)	Range of air velocity (m/s)
4	$3.13x10^{-5} – 3.59x10^{-5}$
5	$3.88x10^{-5} – 4.40x10^{-5}$
6	$4.51x10^{-5} – 5.21x10^{-5}$
8	$6.25x10^{-5} – 6.94x10^{-5}$
10	$7.75x10^{-5} – 8.68x10^{-5}$

Table 2. Air velocity inside waste-rock with $K = 3x10^{-7}m^2$.

Wind velocity (m/s)	Range of air velocity (m/s)
4	$9.38x10^{-4} – 1.05x10^{-3}$
5	$1.16x10^{-3} – 1.31x10^{-3}$
6	$1.40x10^{-3} – 1.57x10^{-3}$
8	$1.88x10^{-3} – 2.11x10^{-3}$
10	$2.31x10^{-3} – 2.60x10^{-3}$

Figure 6a, b, c, and d indicate the variation in temperature with time for selected points within the pile. Those points are used to determine when a 5-m active layer forms.

With $K = 1x10^{-8}$ and $3x10^{-8}$, there is no difference in time as conduction dominates the heat transfer and this process is controlled by thermal conductivity. A frozen core forms after 800 *days* following construction as shown in Figure 6a and b. In addition, heat transfer approaches nearly steady state after around 2000 *days*.

In Figure 6c, the time required to form a frozen core is about 780 *days;* i.e., 20 *days* earlier than shown in Figure 6a, 6b. These 20 *days* reduction are due to convective heat transfer, however, conduction still dominates the heat transfer in the waste-rock with $K = 1x10^{-7}$.

Four hundred and fifty *days* is the time required to form this frozen core as with $K = 3x10^{-7}m^2$ (Fig. 6d). Note that the temperature at the base drops rapidly, and after about 200 *days*, it is below the freezing point (0°C). Convective heat transfer dominates with high Rayleigh and Nusselt numbers.

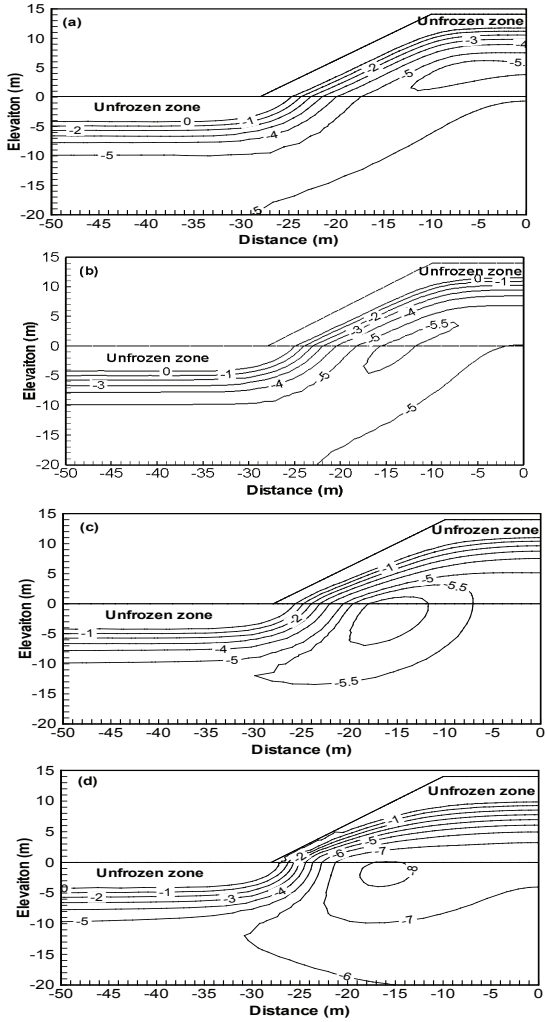

Figure 5. Temperature distribution after 10 *years*, impermeable boundary surfaces with (a) K = 1x10^{-8}, (b) K = 3x10^{-8}, (c) K = 1x10^{-7}, (d) K = 3x10^{-7}.

Just a small change in permeability K = 1x10^{-7} to 3x10^{-7} changes the temperature at point H from -4°C to -6°C after 1.5 *years* (Fig. 7). This establishes the importance of the Rayleigh being greater than a critical value; the convective heat transfer accelerates changing the temperatures. In Figure 7, measured temperatures from the Diavik mine site match the temperature for K = 3x10^{-7}.

The measured temperature from the site shows that the heat transfer in the waste-rock is dominated by convection and the selected intrinsic permeability, thermal conductivity and volumetric capacity are close to the in situ values. However, long-term measurements at the base and inside of the waste-rock pile are needed to confirm these.

They are small at low values of K = 1x10^{-8} – 3x10^{-8}, thus conduction dominates the heat transfer (Fig. 8). The amount of heat extracted from the base is small, and temperatures at the base change slowly. There is a "jump" in the Nusselt number by changing K from 1x10^{-7} to 3x10^{-7}. Therefore, it can be concluded that a small variation in K, assuming the corresponding Rayleigh number is larger than a critical value, will produce significant changes in Nusselt number which controls the heat transfer rate.

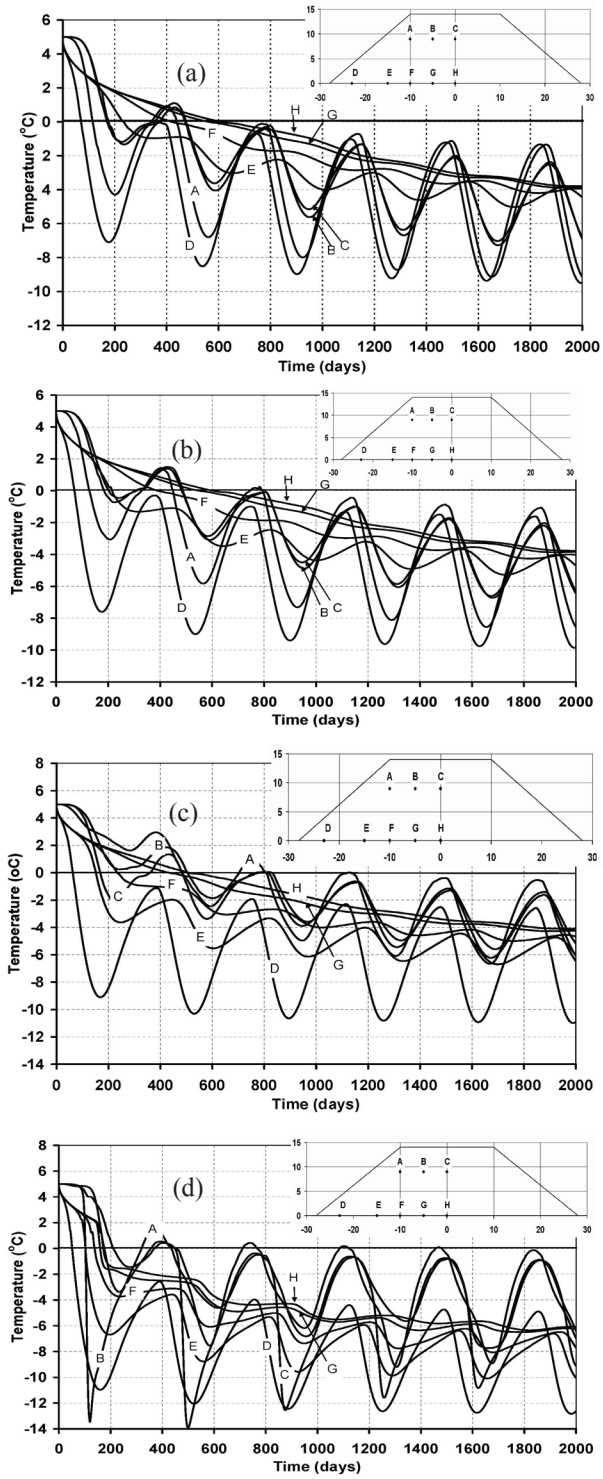

Figure 6. Temperature with time at particular points for K = 1x10^{-8} (a), 3x10^{-8} (b), 1x10^{-7} (c), 3x10^{-7} (c), respectively.

There is a significant change in Rayleigh number when K varies from 1x10^{-7} to 3x10^{-7} and thus the heat transfer rate as indicated in Figure 9. However, there is no significant change in Rayleigh numbers when K changes from 1x10^{-8} to 3x10^{-8} because these values produce a Rayleigh number smaller than the critical value. Zero values of Rayleigh number with K = 1x10^{-7} and 3x10^{-7}m^2 happen during summer when conduction dominates. Critical Rayleigh number is

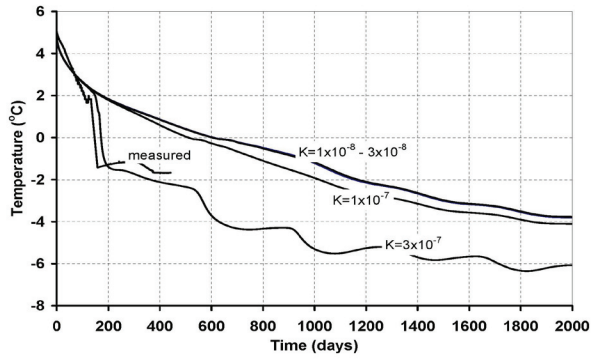

Figure 7. Temperature variation at point H (central point waste-rock pile).

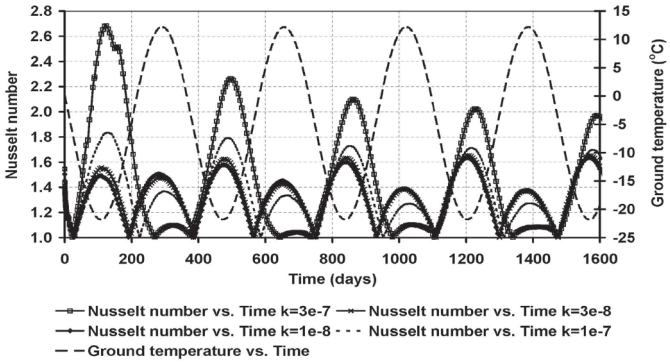

Figure 8. Variation of local Nusselt number (Eq. 8) versus time with K = 1x10^{-8}, 3x10^{-8}, 1x10^{-7} and 3x10^{-7}.

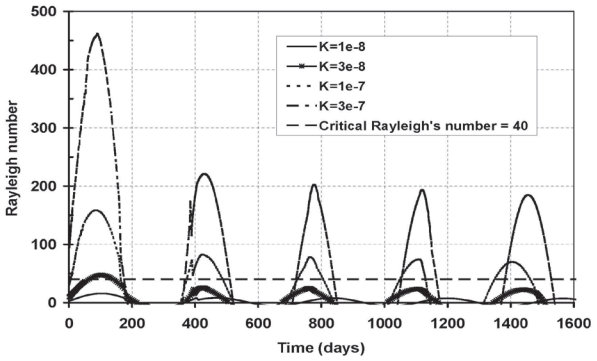

Figure 9. Variation of Rayleigh number with time.

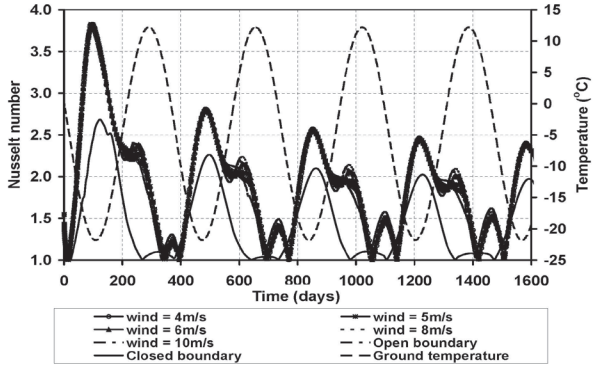

Figure 10. Variation of local Nusselt number with time in the case of open boundary with K = 3x10^{-7}.

defined as $Ra_{cr} = 4\pi^2$ when the conduction state is unstable or an average Nusselt number larger than 1 (Nield & Bejan 1999).

Results for permeable surfaces of waste-rock pile

With permeable surfaces, the heat transfer rate, which is represented by the Nusselt number, does not change for wind velocity up to 10m/s with K = 3x10^{-7}m^2 (Fig. 10). However, there is a large change in the Nusselt number when moving from a closed to an open boundary. Thus, with open surfaces, heat transfer rate into the waste-rock pile does not change due to change in wind velocity of the environment with K up to 3x10^{-7}.

With a small value of K = 1x10^{-8}m^2, there is only a very small change in the local Nusselt number when the wind velocity changes up to 10 m/s in the case of an open boundary condition or a closed boundary condition. Because with small values of K, the air velocity due to forced convection and natural convection is very small, and thus, convective heat transfer is not significant compared to conductive heat transfer.

Conclusions

Heat transfers in the waste-rock pile are investigated using numerical modeling for two-dimensional momentum, continuity, and energy equations. The results are compared to measured temperatures at the Diavik mine site.

The following conclusions can be drawn from the analysis presented:

- The value of intrinsic permeability has a large impact on the heat transfer in waste-rock materials with Rayleigh's number larger than a critical value. However, with small Rayleigh numbers (conduction dominates), heat transfer does not depend on the intrinsic permeability. With K = 3x10^{-7}m^2 (convection dominates), temperature at the base of a 14-m-high waste-rock pile is about -6°C instead of -4°C for K below 1x10^{-8} to 1x10^{-7}m^2.
- When the Rayleigh number is larger than a critical value, a small increase in K results in a significant increase in the Nusselt and Rayleigh number and thus, heat transfer rates due to convection also increase rapidly.
- Heat transfer becomes steady after 6 years for these studies independent on K. A frozen core with a 5-m active layer is formed after 800 days with K = 1x10^{-8} to 1x10^{-7}m^2 and 450 *days* with K = 3x10^{-7}m^2.
- The influence of the wind velocity on the heat transfer in waste-rock piles with open boundary conditions is not significant when the value of K is below 3x10^{-7} m^2. However, there is a rapid change in the heat transfer due to the conditions of the surface of a waste-rock pile (open or closed boundary) at high values of K.
- A comparison with measurements from the Diavik mine site confirmed the convection within the waste-rock pile, and good agreement was achieved by using an intrinsic permeability of 3x10-7 m^2. However, more data are required to confirm this initial comparison.

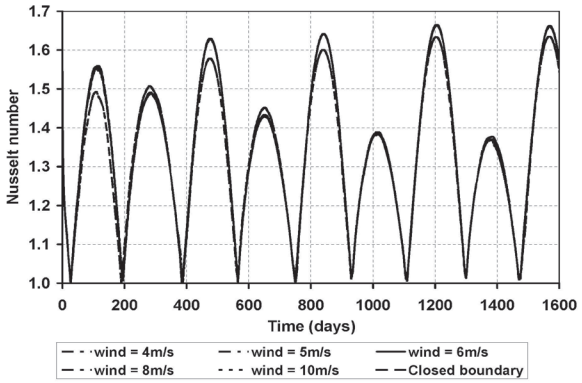

Figure 11. Variation of local Nusselt number with time in the case of open boundary with $K = 1x10^{-8}$.

The results presented clearly confirm reports on convective heat transfer made for arctic waste-rock piles, where temperatures measured within these coarse piles cannot be explained by conduction alone. Numerical modeling showed that once a critical Rayleigh number is reached, significant cooling at the base occurs. However, additional modeling and field data are required to study the combination in parameters and boundary conditions necessary to further convection in waste-rock piles.

Acknowledgments

This research is made possible through funding provided by Diavik Diamond Mines Inc. (DDMI), the Canada Foundation for Innovation (CFI), the Natural Science and Engineering Research Council of Canada (NSERC), the International Network for Acid Prevention (INAP), and the Mine Environment Neutral Drainage (MEND) program. In-kind support provided by Environment Canada is greatly appreciated. We thank Carol Ptacek (Environment Canada), and FDA Engineering for their technical support and patience during the construction phase.

References

Arenson, L.U., Pham, H.N., Klassen, R. & Sego, D.C. 2007. Heat convection in coarse waste-rock piles. *Canadian GeotechnicalCconference, Ottawa, Ontario, Canada. October –21-24, 2007.* In press

Arenson, L.U., Chen, J.F., Pham, H.N. & Sego, D.C. Laboratory investigations on air convection in porous media. Canadian *Geotechnical Conference, Ottawa, Ontario, Canada. October 21 - 24, 2007*. In press

Goering, D.J. & Kumar, P. 1996. Winter-time convection in open-graded embankments. *Cold Regions Science and Technology* 24(1): 57-74.

Lai, Y.M., Li, J.J., Niu, F.J. & Yu, W.B. 2003. Nonlinear thermal analysis for Qing-Tibet railway embankments in cold regions. *Journal of Cold Regions Engineering* 17(4): 171-184.

Lai, Y.M., Zhang, S.J., Zhang, L.X. & Xiao, J.Z. 2004. Adjusting temperature distribution under the south and north slopes of embankment in permafrost regions by the ripped-rock revetment. *Cold Regions Science and Technology* 39(1): 67-79.

Nield, D.A. & Bejan, A. 1999. *Convection in Porous Media.* New York: Springer.

Reddy, J.N. & Gartling, D.K. 2000. *The Finite Element Method in Heat Transfer and Fluid Dynamics*. New York: CRC press.

Effects of Ground Temperature and Slope Deformation on the Service Life of Snow-Supporting Structures in Mountain Permafrost: Wisse Schijen, Randa, Swiss Alps

Marcia Phillips
Swiss Federal Institute for Snow and Avalanche Research WSL-SLF
Stefan Margreth
Swiss Federal Institute for Snow and Avalanche Research WSL-SLF

Abstract

Modifications of ground temperature are of special interest in alpine permafrost regions, as the thermal properties of the permafrost influence the geotechnical characteristics of the ground and thus the stability and service life of mountain infrastructure. Air temperatures have been particularly warm in the past decade in the Swiss Alps, leading to various occurrences of slope and structure instability. The case of snow-supporting structures (snow nets) located on a steep slope in alpine permafrost is presented. Some of the structures have undergone such strong deformation that they must be replaced after only 17 years, as opposed to a service life of ~80 years under normal conditions. Borehole temperature and deformation measurements and surveys of the positions of the snow nets show that creep is particularly pronounced during hot summers in steep slope sectors. Technical solutions include the use of floating foundations and of construction techniques specially adapted to permafrost conditions.

Keywords: creep; floating foundations; mountain permafrost; service life; snow nets; technical solutions.

Introduction

Modifications of permafrost conditions and in particular warming and thawing of near-surface ground ice and active layer thickening can have devastating effects on the stability and service life of infrastructure in mountain permafrost regions (Haeberli 1992, Harris et al. 2001). Thaw subsidence, differential settlement, or heave and enhanced creep rates are particularly problematic for alpine infrastructure that is partly or completely anchored in sediments or bedrock containing ice (Phillips et al. 2007), especially in steep terrain. Alpine infrastructure typically includes structures such as cable-car stations, pylons, water pipes, shelters, and snow-supporting structures—many with high safety requirements. The service life of snow-supporting structures in creeping permafrost is the focus of this paper.

The past decade was characterized by a number of abnormal climatic events in the Swiss Alps. Seven of the last 10 years were among the 10 warmest registered since 1900. The warming was generally more pronounced in summer than in winter. The most extreme event was summer 2003, which was 4–5.5°C warmer than average and was the hottest measured since 1753 (MeteoSchweiz (annual reports), North et al. 2007). Mean annual snow depths varied strongly, with some very snow-rich winters (e.g., 1998/1999, 2000/2001) or winters with very little snow (e.g., 2001/2002, 2004/2005). It is not yet possible to determine trends in snow depth at altitudes where permafrost occurs (Marty et al. 2007).

In parallel to observations of slope and rock wall instability (Gruber et al. 2004, Gruber & Haeberli 2007, Springman et al. 2003), reports of structure instability in permafrost in the Alps during this warm decade have increased (e.g., Personal communications P. Feuz, C. Danioth, M. Walser, H.-R. Keusen). Alongside direct monitoring of the structures themselves (Phillips et al. 2003, Steiner et al. 1996, Vonder Mühll & Keusen 1995), the long-term monitoring of ground temperatures and deformation rates is essential to understand the current and future nature of these developments and the influence of factors such as climate fluctuations, construction activity, or the very presence of infrastructure. Improvements of design and service life are consequently the aim of such observations.

This paper presents borehole data (temperatures and deformation) and displacement data for snow-supporting structures (snow nets) that have undergone such strong creep-induced deformation that partial reconstruction is planned for 2008, only 17 years after their construction.

Site Description

The study site Wisse Schijen is a steep east-northeast-oriented slope located between 3010 and 3140 m a.s.l. in the Mattertal, above Randa (Canton Valais, Switzerland). Permafrost occurs in almost the entire slope (Keller 1995, Phillips et al. 2003). Slope angles range between 37 and 42°. The blocky scree is 2.5 m thick (gneiss, quartzite and marble), underlain by approximately 0.5 m of ice-rich sediments and finally by bedrock. There are narrow bands of bedrock visible in places and these are subject to flexular toppling, causing rockfall.

Wisse Schijen is an avalanche-starting zone, equipped with snow nets to protect Randa. There are several rows of snow bridges (rigid avalanche defense structures) below the area protected with snow nets, which would be destroyed if the latter were damaged or removed, and consequently, avalanches would break loose (Fig. 1).

Eight horizontal rows of snow nets between 24.5 and 45.5 m long and with a structure height of 4.0 m were built at Wisse Schijen in 1990 (upper rows 1–4) and 1991 (lower rows 5–8). The snow nets consist of triangular wire rope

Figure 1. The study site Wisse Schijen with 8 rows of snow nets is located in the upper part of the slope (outlined). Row 2 is shown inset. Several rows of snow bridges are visible in the slope sector below.

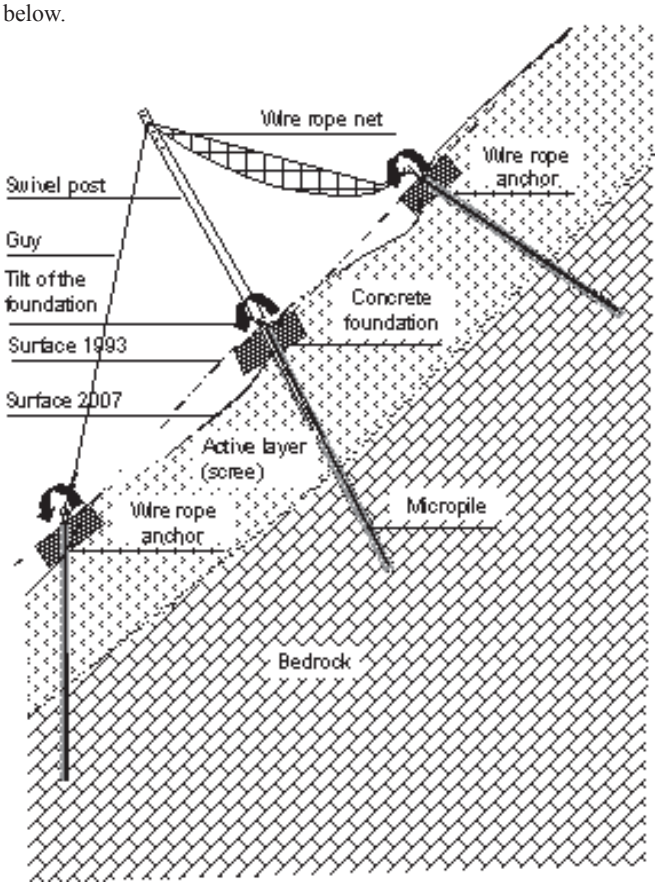

Figure 2 Configuration of the snow nets used. The location of the ground surface in 1993 and 2007 and the direction of tilt of the foundations are shown.

nets, which are attached to swivel supports with a ball joint at the contact to the base plate (Fig. 2).

The support and anchor spacing distance is 3.5 m. The structures are anchored with micropiles consisting of steel tubes (Ø 76 mm, length 1.5 m) and anchor bars (Ø 32 mm) under the supports and with wire rope anchors for the up- and downslope anchors. Concrete foundations were built to facilitate drilling and to stabilize the anchor heads. The anchor boreholes (Ø 100 mm) were drilled through these foundations rather than directly into the unstable scree.

Anchor lengths are 5 m and the anchors penetrate the bedrock. Large amounts of anchor grout were used (up to 30 kg m^{-1} (Personal communication, R. Bumann)) due to the large voids in the scree.

Snow nets were chosen for this sector of the slope (as opposed to snow bridges) because they are better adapted to rockfall. No specific construction methods were applied for permafrost conditions (e.g., the preheating of anchor grout to prevent freezing during the curing process as recommended by Margreth (2007)) or creep.

Two boreholes (B1 and B2) were drilled in 1998 when it became obvious that there were permafrost-related stability problems on the site. B1 is between net rows 5 and 6 (3046 m a.s.l.), B2 is between rows 7 and 8 (3019 m). A third, B3 is located between the top two rows of snow bridges (2953 m a.s.l.), where there is no occurrence of permafrost. All three boreholes are equipped with inclinometer tubes and borehole temperatures are measured in B1 and B2. The boreholes are shallow (6 m) due to various technical problems that arose during drilling.

Methods

Air temperatures and snow depth

Air temperatures and snow depth were measured by an automatic weather station (STN 2, Oberer Stelligletscher) located at 2910 m a.s.l., above St. Niklaus, 8 km away from the study site, on the same side of the valley. There is no weather station on the site itself. The snow data in particular therefore only gives a rough indication of the conditions in the area (e.g., if a winter was snow-rich or not).

Ground temperatures

Universal Temperature Loggers (UTL/Hobo) were used to measure borehole temperatures at five depths (0.5, 1, 2, 3, 4 m) in B1 and B2 (precision 0.25°C). Measurements were carried out hourly and were started in 2001.

Borehole deformations

The boreholes are equipped with inclinometer tubes, and measurements are effected using a Sinco Digitilt inclinometer (precision ±0.15 mm m^{-1}). The measurements were made at 1-m intervals and were carried out once a year (summer 1999–2007), which implies that data covers the second half of the previous summer period and the first half of the current one. Permanent borehole deformation measurements effected at a similar site in the eastern Swiss Alps (Rist 2007, in press) have shown that no deformation whatsoever occurs in winter; all movement ceases when the active layer freezes and only recommences when the latter thaws due to snowmelt infiltration in spring.

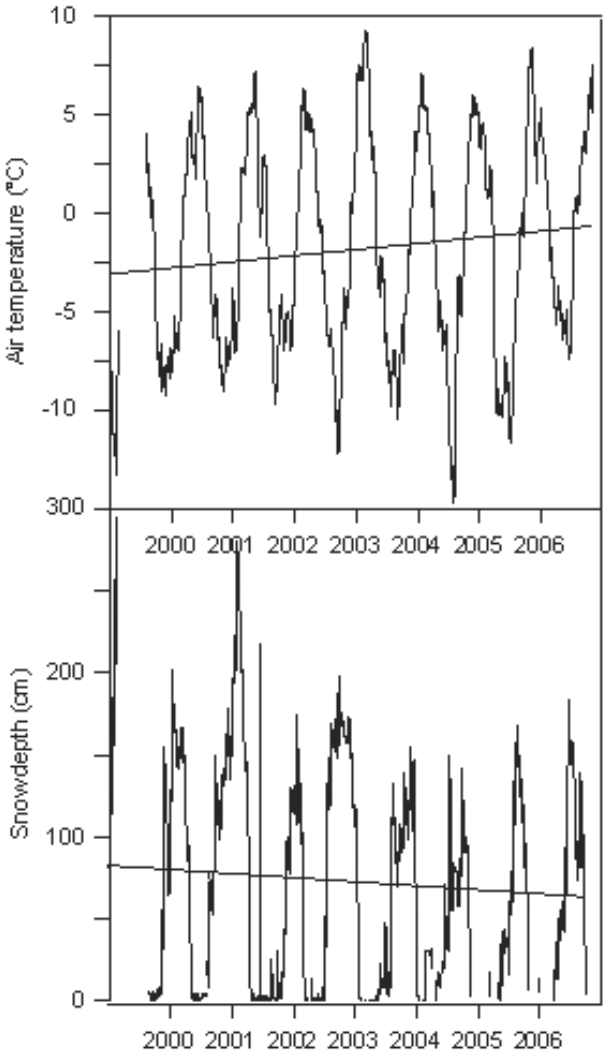

Figure 3. Air temperature (30-day running means) (top) and snow depth measured (bottom) by the automatic weather station STN2 (Stelligletscher, 2910 m, 1999–2007). Trends are shown.

Structure stability

The position of 48 anchor heads was surveyed (1999–2007) using a Wild TC 1610 theodolite (precision ±2 mm). Both horizontal and vertical displacements were measured. The measurements were carried out once a year (summer), which implies that data covers the second half of the previous summer period and the first half of the current one and that the influence of the previous winter (e.g., particularly large snow loads on snow nets, meltwater in spring) must be taken into account.

Visual inspection

The 8 rows of nets were systematically inspected and photographed every summer, and problems recorded and reported. The visual observations include the inspection of row geometry, of the state of the foundations and of the superstructure. Any damage induced by differential creep or settlement, rockfall and surface erosion is assessed according to Margreth (2007).

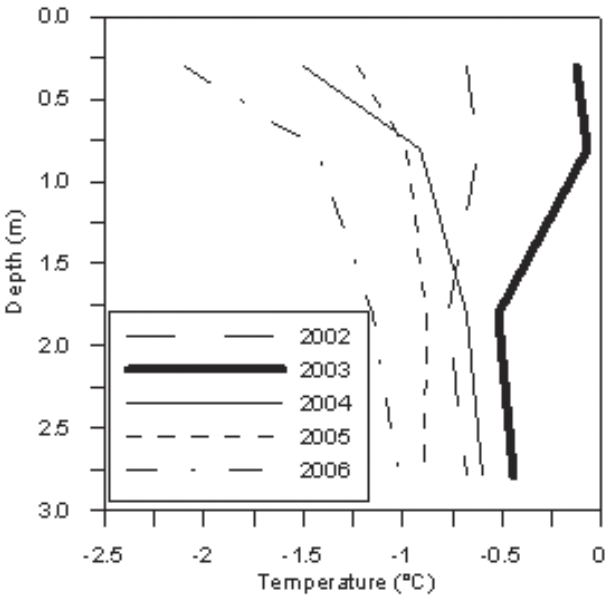

Figure 4a. Mean annual vertical temperature distribution in borehole B1.

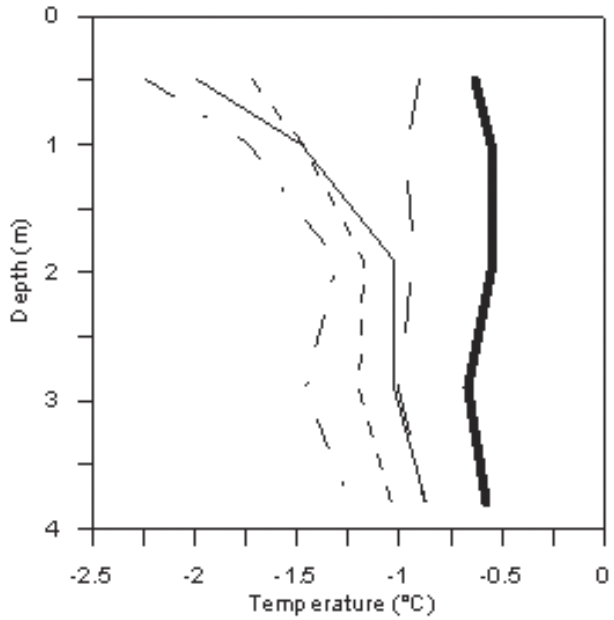

Figure 4b. Mean annual vertical temperature distribution in borehole B2 (same legend as Fig. 4a).

Results

Air temperature and snow depth

Mean annual air temperature measured by the automatic weather station STN2 during the period 1999–2006 was -1.9°C. Figure 3 (top) shows the 30-day running means for air temperature. Summers 2003 and 2006 were particularly warm, with high thawing degree-days during the snow-free period (744 and 654, respectively, as opposed to a mean of 428 for all other years, see Fig. 5).

Mean snow depth during the period 1999–2006 was 70 cm. Winter 2000–2001 was snow-rich, with snow depths up to 270 cm. In contrast, shallow snow covers characterized winters 2004–2005 and 2005–2006 (Fig. 3, bottom).

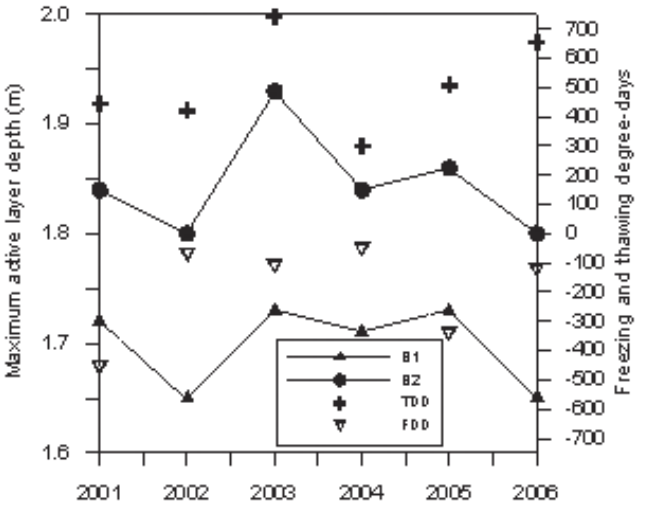

Figure 5. Maximum annual active layer depths measured in B1 and B2 (2001–2006) and thawing- (TDD) and freezing degree-days (FDD) during the annual snow-free period (right y axis).

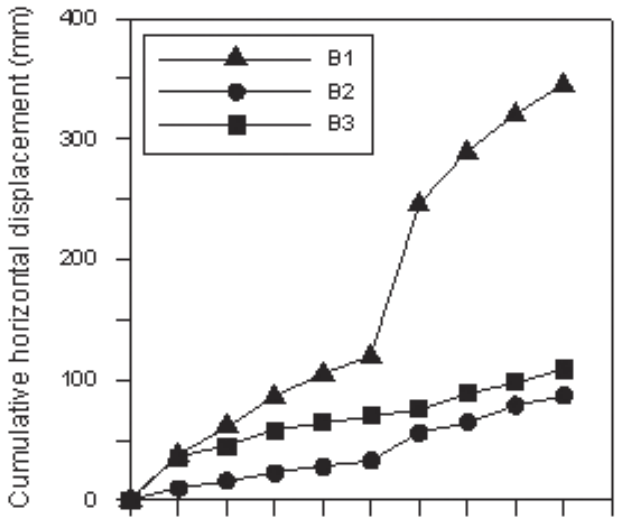

Figure 6. Cumulative displacement (mm) at 1 m depth in boreholes B1, B2, and B3 (1998–2007).

Ground temperatures

Borehole temperatures measured in B1 and B2 indicate that B1 is slightly warmer, despite being at a higher altitude. The mean annual temperature was warmest in 2003 in both boreholes (Figs. 4a, b). Shallow snow covers probably cause the slight cooling trend after 2003.

Maximum annual active layer depths are shown in Figure 5. The base of the active layer is defined here as being the depth of maximum seasonal penetration of the 0°C isotherm into the ground (Burn 1998). Mean active layer depth in B1 is 1.70 m and 1.85 m in B2. Active layer depths remained fairly constant throughout the measurement period, with a slight deepening in B2 (9 cm deeper than average) in summer 2003.

Borehole deformations

The cumulative horizontal displacements measured at 1 m depth (Fig. 6) indicate that the yearly displacements were

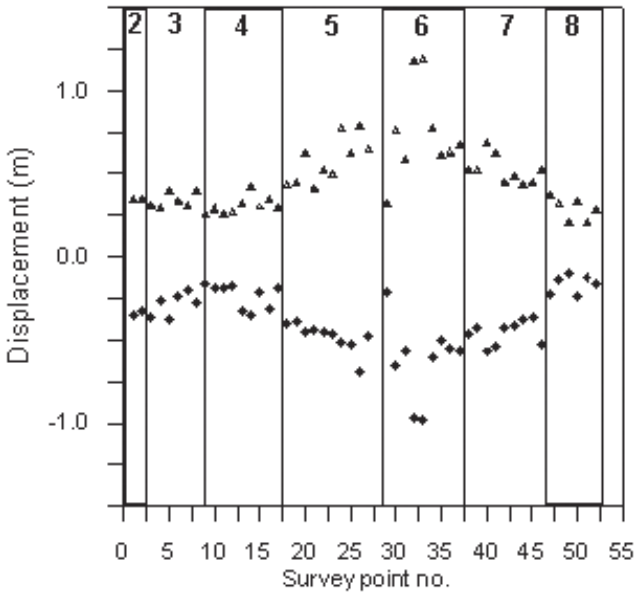

Figure 7. Mean horizontal (triangles) and vertical (diamonds) displacements of 52 anchor heads between 1999 and 2007. The snow net row numbers are indicated in bold.

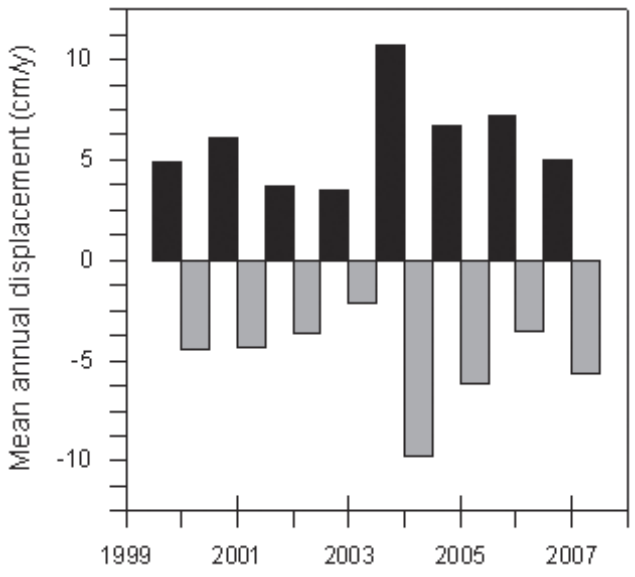

Figure 8. Mean annual horizontal (black) and vertical (grey) displacement of the anchor heads.

quite regular, with the exception of the measurement period 2003–2004, during which a pronounced deformation of 126 mm occurred in B1 and a slight increase is also visible in B2. It should be noted that B1 is located between the damaged snow net rows 5 and 6. From 2005 onwards, it was no longer possible to measure deeper than 1.8 m in B1, as the inclinometer tube was too strongly deformed.

Structure stability

During the measurement period 1999–2007, the horizontal displacements of the anchor heads varied between 0.2 and 1.2 m (average 0.47 m) and the vertical displacements between -0.1 and -0.97 m (average -0.38 m). Displacements exceeding 0.5 m occurred in the net rows 5, 6 and 7 (Fig. 7). Mean

Figure 9a. Dislocated swivel support (left). Fig. 9b. Tipped concrete foundation (right) in the damaged snow net rows 5 and 6.

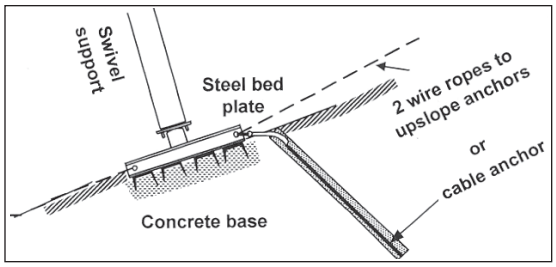

Figure 10. Floating foundation for snow nets in creeping permafrost conditions: steel bed plate on a base of lean concrete.

annual displacement velocities of the anchor heads varied from year to year. In the measurement period 2003–2004, they were particularly pronounced with mean displacements of 10.7 cm and -9.7 cm, respectively (Fig. 8).

Visual inspection

The problems observed at the study site include:

- Disturbed geometry of entire rows of nets, which can lead to uneven snow loading and to elevated constraints in the superstructure.
- Tipping of the base plates, leading to a blockage of the ball joint and to dislocation of swivel supports (Fig. 9a).
- Downslope tipping of the concrete foundations (Fig. 9b).
- Surface erosion and settlement of several decimeters causing anchor tendon exposure, which can lead to buckling or failure.
- Rockfall into the nets.

It is not known whether the anchor tendons are deformed or have undergone failure.

The assessment of the state of the snow nets has shown that all rows with the exception of rows 5 and 6 are in Condition Class 2 ("Damaged"). This implies that repairs are moderately urgent (within 1–3 years), and there is no immediate impairment for the serviceability of the structures. Rows 5 and 6 are, however, in Condition Class 3 ("Poor") (Margreth 2007) and repairs are very urgent, as there is a danger of collapse and their supporting function is no longer warranted.

Discussion

State of the permafrost, slope, and structure stability

As the deformation and displacement measurements occur in mid-summer, it is difficult to attribute movements to a particular cause. However, borehole deformations (in B1) and structure movements were significantly higher in the measurement period 2003–2004. They cannot be attributed to a significant deepening of the active layer or to a snow-rich winter. The mean annual borehole temperatures (January 1 to December 31) show that 2003 was the warmest year at all depths (Figs. 4a, b), and this seems to have influenced the creep rates. Creep rates remained constant in B3 where creep is not temperature-dependant (non-permafrost).

Not only the thickness of the active layer can vary, but also its position relative to the underlying stratigraphy (e.g., downward extension of the active layer into finer, ice-rich sediments due to warming or to settlement), which can augment the potential for slope instability (Rist 2007, in press). The degree of exposure of the micropiles and foundations (up to 0.4 m) indicates that settlement has occurred in places due to loss of permafrost ice. The exact amount and rate of settlement is difficult to quantify however, because scree is constantly eroded and replaced from upslope.

The presence of 300 foundations in the slope may have a slight stabilizing effect at a very local scale, as is shown by the accumulation of material directly above the foundations. However, this may be countered by the fact that there is more snowmelt water in spring due to the artificial retention of snow on the slope. The slope, therefore, cannot be characterized as being more stable due to the presence of the snow nets.

Technical solutions

The anchor heads have undergone substantial displacement from the start—in the first year after construction-isolated damages were visible (Stoffel 1995). Two rows of snow nets (5 and 6, located in the steepest sector) have now been subjected to such intense creep-induced deformation that their replacement is planned for 2008.

Under normal conditions snow nets have an expected service life of 80 years. The mid- and long-term service life of the structures are however not assured with creep rates exceeding 5 cm/year (Margreth 2007). The data presented above helps to explain the remarkably short service life of the snow nets at the study site. Whereas various problems are visible in the superstructure, the current state of the anchors is unknown. It is possible that deformation or failure of the micropiles and wire rope anchors has occurred in places and that collapse may be imminent. In order to ensure protection against avalanches, it is therefore necessary to replace the most badly damaged rows of nets (5 and 6) as soon as possible and to monitor the remaining rows carefully.

In order to improve the service life of the new structures in this highly unstable terrain, floating foundations will be used under the swivel posts, rather than fixed ones (Fig. 10). Steel bed plates on a base of lean concrete have been tested in similar terrain and proved to be well-adapted (Phillips 2006). If necessary, they can be readjusted relatively easily, whereas the replacement of fixed anchors is hardly possible. In addition, specially adapted construction techniques will

be used, as recommended for permafrost terrain (Margreth 2007).

As a result of the experience gained with the snow nets in the Wisse Schijen sector, the neighboring avalanche slopes are triggered artificially. Special reinforcement measures against snow avalanches will be met for potentially affected infrastructure in the valley.

Conclusions

Wisse Schijen is a site with particularly difficult conditions for snow-supporting structures. The creep rates in the steep permafrost slope can exceed 5 cm/year, particularly in hot summers, implying that mid- and long-term service life is not ensured. In such cases the construction of snow-supporting structures is only advisable if no alternatives are available (Margreth 2007). In this particular case, it is not possible to build an avalanche retention dam to protect the village due to lack of space at the base of the avalanche slope. In addition, there are snow bridges below that must be protected. It is necessary, therefore, to replace the most strongly damaged structures (rows 5 and 6) as soon as possible and to use floating foundations rather than fixed ones under the supports. In addition, permafrost-specific construction methods must be used (Margreth 2007). It is advisable to continue monitoring ground temperature, slope deformation and the position of the snow nets in order to determine the effects of short- and long-term climate fluctuations on the stability and service life of the structures. The state of the snow nets on the study site is surprisingly good in view of the difficult conditions; rigid steel snow bridges would probably have had much more severe damages and an even shorter service life.

Acknowledgments

The authors would like to thank the Swiss Canton Valais for the financial support of the project and in particular Charly Wuilloud, Head of Natural Hazards in Valais and Leo Jörger, mayor of Randa. Klaus Aufdenblatten and his team carried out the surveys of the snow nets, and Herman Rovina and Damian Gitz carried out the borehole inclinometer measurements—all under difficult terrain conditions, for which they are sincerely thanked. Christian Bommer and two anonymous reviewers provided useful comments.

References

Burn, C.R. 1998. The active layer: two contrasting definitions. *Permafrost and Periglacial Processes* 9: 411-416.

Gruber, S., Hoelzle, M. & Haeberli, W. 2004. Permafrost thaw and destabilization of Alpine rock walls in the hot summer of 2003. *Geophys. Res. Lett*. 31 (L13504): 1-4.

Gruber, S. & Haeberli, W. 2007. Permafrost in steep bedrock slopes and its temperature-related destabilization following climate change. *Journal of Geophysical Research* 112, F02S18, doi:10.1029/2006JF000547.

Haeberli, W. 1992. Construction, environmental problems and natural hazards in periglacial mountain belts. *Permafrost and Periglacial Processes* 3: 111-124.

Harris, C., Davies, M. & Etzelmüller, B. 2001. The assessment of potential geotechnical hazards associated with mountain permafrost in a warming global climate. *Permafrost and Periglacial Processes* 12: 145-156.

Keller, F. 1995. *Permafrost in Lawinenanrisszonen. Bericht über BTS-Messungen zur Kartierung von Permafrost in Lawinenanrisszonen*, Report 500.7.

Margreth, S. 2007. *Defense structures in avalanche starting zones*. Technical Guideline as an aid to enforcement. FOEN, SLF, Bern and Davos.

Marty, C., Phillips, M. & Lehning, M. 2007. Klimaänderung und Naturgefahren. *Bündner Wald* 60(3): 35-42.

MeteoSchweiz (annual reports). *Witterungsberichte*.

North, N., Kljun, N., Kasser, F., Heldstab, J., Maibach, M., Reutimann, J. & Guyer, M. 2007. *Klimaänderung in der Schweiz. Indikatoren zu Ursachen, Auswirkungen, Massnahmen*. Report Umwelt Zustand Nr. 0728, Bern.

Phillips, M., Margreth, S. & Ammann, W. 2003. Creep of snow-supporting structures in alpine permafrost. *Proceedings of the Eighth International Conference on Permafrost, Balkema July 21-25*: 891-896.

Phillips, M. 2006. Avalanche defence strategies and monitoring of two sites in mountain permafrost terrain, Pontresina, Eastern Swiss Alps. *Natural Hazards* 39: 353-379.

Phillips, M., Ladner, F., Muller, M., Sambeth, U., Sorg, J. & Teysseire, P. 2007. Monitoring and reconstruction of a chairlift midway station in creeping permafrost terrain, Grachen, Swiss Alps. *Cold Regions Science and Technology*.

A Selection of papers presented at the International Snow Science Workshop, Jackson Hole, Wyoming, September 19-24, 2004, 47(1-2): 32-42.

Rist, A. 2007 (in press). *Hydrothermal processes within the active layer above alpine permafrost in steep scree slopes and their influence on slope stability*. PhD Thesis, Swiss Federal Institute for Snow and Avalanche Research SLF and University of Zurich.

Springman, S.M., Jommi, C. & Teysseire, P. 2003. Instabilities on moraine slopes induced by loss of suction: a case history. *Geotechnique* 53: 3-10.

Steiner, W., Graber, U. & Keusen, H.-R. 1996. Construction in rock at 3550 meters elevation (Jungfraujoch, Switzerland), In: G. Barla (ed.), *Eurock 96*. Torino, Italy: A.A. Balkema, 543-550.

Stoffel, L. 1995. *Bautechnische Grundlagen für das Erstellen von Lawinenverbauungen im alpinen Permafrost*. SLF, Davos.

Vonder Mühll, D. & Keusen, H.-R. 1995. Bauen auf kriechendem Eis. *Schweizerische Technische Zeitschrift* 10: 45-48.

Classification of Arctic Tundra Soils Along the Beaufort Sea Coast, Alaska

C.L Ping, L.A. Lynn, G.J. Michaelson
Palmer Research Center, Agricultural & Forestry Experiment Station, University of Alaska Fairbanks, Palmer, AK
M.T. Jorgenson
Alaska Biological Research, Inc., Fairbanks, AK
Y.L. Shur, M. Kanevskiy
Department of Civil & Environmental Engineering, University of Alaska Fairbanks, Fairbanks, AK

Abstract

The Study of Northern Alaska Coastal Systems project provided the opportunity to examine cryogenic soils and permafrost features using exposed bluffs along the coastline. More than 50 study sites were selected along the 1,957 km coastline of the Beaufort Sea. The soil exposures that were sampled represent the soils and permafrost in similar landforms with similar microtopography and permafrost features 20–50 miles inland. Nearly all the soil profiles described along the exposed bluffs and drilled cores from deltas were classified in the Histel, Turbel, and Orthel suborders of the Gelisol order. The presence and depth of ice wedges, cryturbation features, gleyed horizons, and the abundance of organic matter differentiated the soils into great groups and subgroups. Soil morphological features suggest the multigenic origin of soil carbon. Classification of soils associated with different microtopography will facilitate soil mapping on the Arctic Coastal Plain.

Keywords: arctic tundra; coastal erosion; Gelisols; soil classification.

Introduction

A soils map is an important tool needed for land resource management. A detailed soils map is greatly needed for ecosystem/land management, land-based research, and most recently, accurate estimation of terrestrial carbon stock and other major and minor nutrients levels. The currently existing soils map of arctic Alaska was based on an exploratory survey (Reiger 1979) and was mapped at a scale of 1:1,000,000, much too crude for site-specific resource management. Thus, the National Cooperative Soil Survey in Alaska is planning a soil project for arctic Alaska which involves the cooperation and partnership of federal and state, the University of Alaska Fairbanks and all other interested parties. Most soils in the arctic tundra are cryoturbated. To correctly describe and classify the soils it is necessary to observe the soil profile under the whole cycle of patterned ground (Agriculture Canada Expert Committee on Soil Survey 1998, Kimble et al. 1993). However, based on past experience (Ping et al. 1998), soil inventory in the permafrost regions is time consuming and usually limited to shallow depths due to logistical limitations. Because of the nearly flat or very gentle slopes of the Arctic Coastal Plain (Brown & Kreig 1983), the landforms at different segments of the coast extend inland for 10s of km. Thus, the soils information gained from the coastal bluffs can be extrapolated to similar landforms inland.

The study of arctic coastal erosion and the fate and transformation of soil carbon, which is a component of the Study of Northern Alaska Coastal Systems (Jorgenson et al. 2005), provided pedologists with the opportunity to study the soils on wide and deep coastal exposures along the Beaufort Sea coast. The project was designed to study the carbon flux and transformation and material transfer across the land-sea boundary across 1,957 km of coastline of the Beaufort Sea (Jorgenson & Brown 2005, Jorgenson et al. 2005).

Along the Beaufort Sea coast, there are five types of coastal exposure identified by Jorgenson & Brown (2005): deep bays and inlets, deltas, exposed bluffs, lagoons, and tapped basins. Deep bay and inlets are composed of ice-rich marine silt and are most common in the western portion of the coast. The landforms resulted from coalescence of large lakes and subsequent flooding during sea level rise in mid-late Holocene. The bluff heights are 2–3 m. Large and small deltas are found across the Beaufort Sea coast. Exposed bluffs occur primarily along the western and eastern portion of the study area. Bluff heights range from 2–4 m. The reworked marine silt of early Holocene to late Pleistocene on the western part is ice-rich, about 20% ice wedges by volume. The late Pleistocene sand deposit in the middle part is ice-poor. Lagoons are bordered seaward by barrier islands, thus the erosion rates are lowest among the above-mentioned coastal types. The lagoons have the same exposures as that of the exposed bluffs. Tapped basins occur in ice-rich marine silt in the western portion of the coast. This type is characterized by large thaw lakes with raised ridges between them. Ice wedge contents increase with age up to 20% in older surfaces.

Methods

A total of 50 extensive study sites were systematically distributed along the 1,957 km of Beaufort Sea mainland coast. The sites included all five coastal types. At each site, geomorphic characteristics, surface cryogenic features, shoreline morphology, and land cover types were recorded. A vertical face along the coastal bluffs was cleaned to expose the soil profile and the ground ice stratigraphy. At

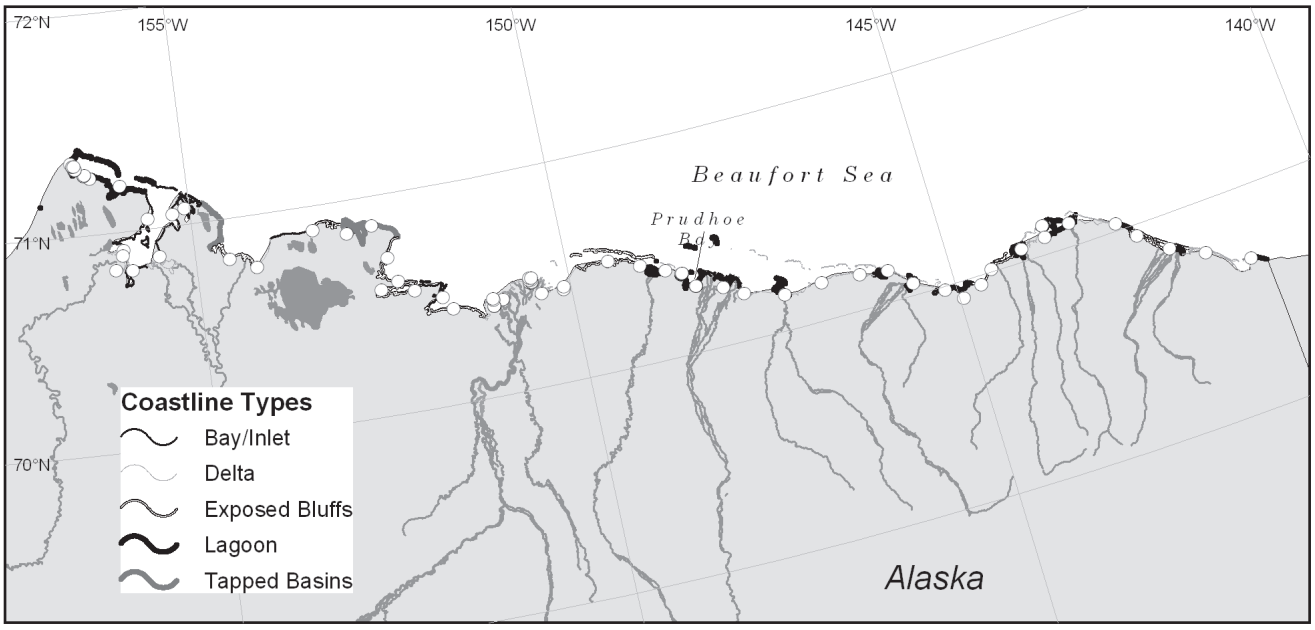

Figure 1. Five types of coastal exposure along the Beaufort Sea Coast.

sites along the thawed lake sequence, which were nearly all sea-level deltas, soil pits were excavated to the top of seasonal frost then a 7.5 cm diameter SIPRE core was used to drill the frozen cores, usually to 2 m. Geomorphic units were classified according to standard engineering geology terminology developed for Alaska. Soil morphological properties were described according to Schoeneberger et al. (1988) and soil classification according to Soil Survey Staff (2006). Ground ice structure and cryogenic features were described based on Shur & Jorgenson (1998).

Result and Discussion

Morphology and classification

The patterned ground type, cryogenic process involved, and soil classification of the study sites were summarized in Table 1. The deep bay/inlet coast type has mixed surface morphology of tapped basin and lagoon, but with fewer ice wedges (<20%). Thus there are both low- and high-centered polygons and thaw lake sequences. Ruptic Histoturbels and Typic Aquiturbels dominate the high-centered polygons with frost boils, Typic Histoturbels and Histic Aquiturbels dominate the low-centered polygons, whereas Fibric Glacistels and Glacic Historthels dominate the very poorly drained troughs between polygons.

In newly formed river deltas, the permafrost table is generally below 1 m and there are no diagnostic horizons with little or no cryoturbated features. Since these soils were frequently inundated by tidal or flooding waters, they were classified in the Aquic suborder of Entisols, i.e., Aquents. The mean annual soil temperature (MAST) at 50 cm was estimated to be below freezing; thus all soils found in recently formed deltas are Typic Gelaquents. However, where the deltas were vegetated with mostly sedges, and the deltas become estuaries, the repeated inundation and deposition of fine textured minerals on the vegetation mat caused repeated burial of thin vegetation layers. In addition, there were large areas of deltas and estuaries with sulfur-rich fluvial deposits. The surface had patches of bare ground with a thin crust of rusty red color over black mud, indicative of quick oxidation of ferrous Fe. These soils had subsurface horizons rich in iron sulfite (pyrite), which has a characteristic color of 4/N according to the Munsell Color Chart. They keyed out as Sulfuric Aquorthels. Those soils had stratified organic and reduced mineral horizons, a combined thickness of organic horizons generally greater then 6 cm within the top 50 cm, a permafrost table within 1 m, lacked cryoturbation, and were keyed out as Fluvaquentic Historthel. Both the Sulfuric and the Fluvaquentic Historthels had strong H_2S odor when the pits were opened.

Exposed bluffs and lagoon coastal types have similar morphology except the prevalence to the open ocean. In the eastern and western portions of the coast, high bluffs contained massive ice wedges occupying more than 20% of the exposed face. The surface of these coastal types is characterized by flat polygons and high-centered polygons dotted with frost boils. The troughs between the polygons were wide, generally 3–4 m due to deterioration of the underlying ice wedges. The ice wedges were usually within 1 m of the surface; thus the soils were classified as Sapric Glacistels and Glacic Histoturbels. Soils formed in the high-centered polygons were highly cryoturbated, and the continuity of the surface organic horizons were interrupted by frost boils; Ruptic-Histic Aquiturbels become the dominant soil type. In the flat polygons, Typic Histoturbels were the dominant soil type. In the ice-poor sand sheet in the mid-coastal zone, there was less cryoturbation, existing only at the margin of the polygons. The drainage in this area was moderately well to somewhat poor and the soils contained dark organic-rich mineral surface horizons; thus the dominant soil types were Aquic Molliorthels.

Table 1. Coastal type, patterned ground, cryogenesis, and soil classification of selected studied sites along the Beaufort Sea coast.

Coast type/ Site #	Patterned ground	Thcickness OM in top 50 cm	Cryogenic processes	Glacic (Wf) horizon , cm	Degree of cryoturbation	Thaw depth, cm	Soil classification
Bay/Inlet							
BSC-2	High-center polygon/ frost boils	9	Small ice wedge, Ojj, O/Bgjj	not present	High	38	Histic Aquiturbels
BSC-4	flat polygon/ polygon rim	19	Ice lens, ataxitic structure, Ojj, O/Bgjj	not present	high	44	Ruptic Histoturbels
Delta							
BSC -	River delta	0	not present	none	none	>100	Typic Gelaquents
BSC-37	Coastal marsh	24	not present	none	minimal	71	Typic Historthels
CAHA-T1-02	Estuary	12	ice lens, ice wedge, microataxitic	39-182 cm	medium	39	Glacic Aquorthels
Exposed bluff							
BSC-22	Flat polygon, deep trough	23	Ice lens, reticulate structure, Oe/Bgjj,Oajj	not present	high	42	Typic Histoturbels
BSC-36	Low-center polygon	90	Ice wedge, ice lens	76	low	43	Fibric Glacistels
Lagoon							
BSC-25	high-center polygon	8	hummocky surface, frsot cracks	Not present	low	49	Aquic Molliturbels
BSC-40	flat polygon/frsot boil	6 - 26	Oe/Bgjj, Oejj, Oa/Cgjj	not present	high	45	Ruptic Histoturbels
			highly cryoturbated	60	medium	50	Glacic Histoturbels
ELS-3	flat polygon	7	horizon, Oa/Bgjj Ice lens,	not present	minimal	28	Typic Historthels
Taped Basin							
CAHA-T1-05	Flat basin floor	14	Cryogenic fabrics, Oa/Bg	not present	high	26	Typic Histoturbels
CAHA-T1-06	low-center polygon	47	Ice belt, reticulate fabric	39-44, 47-49	low	34	Typic Sapristels
CAHA-T1-08	flat sedge meadow	6	Ice lens, ice belt	Not present	minimal	55	Typic Aquorthels
CAHA-T1-09	high-center polygon/ frost boil	27	Ice wedge, Oa/Bgjj, Oejj	90	high	51	Glacic Histoturbels
CAHA-T1-E4	high-center polygon polygon trough	40	Ice wedge, Bgjj, Oa/Bgjj	40	high	38	Hemic Glacistels

In the tapped basin/thaw lake basins, a microtoposequence formed following the lake draining. In the recently drained lake beds, there was a continuous organic horizon under sedge vegetation that was generally more than 14 cm thick over stratified reduced mineral and organic horizons. They lacked cryoturbation. Most of these soils have ice wedges or ground ice within 1 m and thus keyed out as Glacic Historthels. Soils without a glacic horizon within 1 m keyed out as Typic Historthels. Where the surface-organic layer was thin the soils keyed out as Ruptic-Histic Aquorthels and Glacic Aquorthels. Toward the slightly elevated edge of the drained-lake basin flat-polygons formed which have observable cryoturbation around 20–40 cm. These soils had thin organic horizons and some have ice wedges within 1 m, and thus keyed out as Typic Aquiturbels and Glacic Aquiturbels, respectively. Between the drained lakes there were raised broad ridges with high-centered polygons formed from ice wedge deterioration in the troughs. There was a high degree of cryoturbation under the polygon center in that the surface organic layers were broken and the underlying reduced mineral horizons were mixed with cryoturbated organics (Bg/Ojj or Ojj/Bg). Thus, these soils keyed out as Ruptic-Histic Aquiturbels. Glacic Aquiturbels appear as a minor component in this microtopography. In the troughs, the thick organic horizon sits on top of ice wedges, and thus the soils keyed out as Fibric Glacistels.

Mode of carbon accumulation

The arctic tundra soils are known to accumulate and sequester organic carbon (Michaelson et al. 1996). In most soils examined in the five coastal types, cryturbation was prevalent throughout most landform types except deltas. In the deltas, organic carbon accumulated through burial by fluvial sedimentation by the rivers. Organic horizons only formed after the establishment of sedge marsh vegetation.

In the tapped basins, organic carbon accumulated when marsh vegetation grows in the drained-lake basins, followed by mixing and burial from bank erosion/collapsing and flooding. Once the lakes were drained and the land surface was raised due to ice wedge formation, there was increased cryoturbation evident that churned the surface organic matter down into the lower active layer and upper permafrost. Carbon sequestration reached the maximum in the high-center polygons formed in between the drained lakes due the increased surface age and cryoturbation. In the exposed bluffs and lagoons, carbon accumulated and was sequestered through two main mechanisms. First, through the commonly known near-surface cryoturbation associated with patterned-ground formation that churns surface organic matter generally within the top 1 m. (Bockheim et al. 1998, Ping et al. 1998, 2008). Second, this field investigation found that ice wedge formation also plays an important role in carbon sequestration because the pressure from the expanding ice wedge deforms the surface organic matter down as far as 3 m deep, as seen in both sites 2 and 40.

Summary

In landforms dominated by high-centered polygons, Ruptic Histoturbels and Typic Histoturbels are the main soil types with Histic Aquiturbels and Glacic Histoturbels as minor components. In landforms dominated by flat and low-centered polygons, Typic Histoturbels and Typic Historthels are the main soil types with Glacic Historthels as minor components. In landforms dominated by thaw lake basins, Typic Historthels and Glacic Aquorthels are the main soil types and Ruptic Histurbels and Glacistels are minor components. In deltas, Typic Aquorthels and Typic Historthels are the dominant soil types with Glacic and Sulfuric Historthels as minor components. As found in this study, soil types were more related to microtopography rather than the physiographic classification of the coastal types, with the exception of delta. Also found in this study, organic-carbon accumulation and sequestration in arctic Alaska as examined from the exposed Beaufort Sea coast are multigenic and not just the result of cryoturbation.

Acknowledgments

This study was supported by National Science Foundation Arctic System Science Program, Collaborative Research: Flux and transformation of organic carbon across the eroding coastline of northern Alaska (NSF-0436179).

References

Agriculture Canada Expert Committee on Soil Survey. 1998. *The Canadian System of Soil Classification, Third Edition.* Ottawa: NRC Research Press.

Bockheim, J.G., Walker, D.A., Everett, L.R., Nelson, F.E. & Shiklomanov, N.I. 1998. Soils and cryoturbation in moist nonacidic and acidic tundra in the Kuparuk River Basin, arctic Alaska, U.S.A. *Arc. Alp. Res*. 30: 166-174.

Brown, J. & Kreig, R.A. 1983. Elliott and Dalton Highway, Fox to Prudhoe Bay, Alaska. In: *Guidebook 4: Guidebook to Permafrost and Related Features.* Fairbanks: Alaska Div. of Geol. and Geophys. Surv., 230pp.

Jorgenson, M.T. & Brown, J. 2005. Classification of the Alaskan Beaufort Sea coast and estimation of carbon and sediment inputs from coastal erosion. *Geo-Mar Lett.* 25: 69-80.

Jorgenson, M. T., Ping, C.L., Guo, L., Shur Y. & Brown, J. 2005. A multi-scale approach to assessing the flux and transformation of organic carbon across the eroding coastline of northern Alaska. *Berichte Zur Polarund Meeresforschung* 506: 65-68.

Kimble, J.M., Tarnocai, C., Ping, C.L., Ahrens, R., Smith, C.A.S., Moore, J. & Lynn, W. 1993. Determination of the amount of carbon in highly cryoturbated soils. In: D.A. Gilichinsky (ed.), *Post-Seminar Proceedings of the Joint Russian-American Seminar on Cryopedology and Global Change, Pushchino, Russia, 15-16 Nov. 1992.* Pushchino, Russia: Russian Academy of Science.

Michaelson, G.J., Ping, C.L. & Kimble, J.M. 1996. Carbon storage and distribution in tundra soils of arctic Alaska, U.S.A. *Arctic and Alpine Research* 28(4): 414-424.

Ping, C.L., Bockheim, J.G., Kimble, J.M., Michaelson, G.J. &. Walker, D.A. 1998. Characteristics of cryogenic soils along a latitudinal transect in arctic Alaska. *Journal of Geophysical Research* 103(D22): 28,917-28,928.

Ping, C.L., Michaelson, G.J., Jorgenson, M.T., Kimble, J.M., Epstein, H., Romanovsky, V.E. & Walker, D.A. 2008. High stocks of organic carbon in North American arctic region. *Nature Geoscience* (in review).

Rieger, S., Schoephorster, D.B. & Furbush, C.E. 1979. *Exploratory Soil Survey of Alaska.* Washington, D.C.: U.S. Dept. of Agriculture, Soil Conservation Service, U.S. Government Printing Office.

Schoeneberger, P.J., Wysocki, D.A., Benham, E.C. & Broderson, W.D. 1998. *Field Book for Describing and Sampling Soils*. Lincoln, Nebraska: Natural Resources Conservation Service, USDA, National Soil Survey Center.

Shur, Y. & Jorgenson, M.T. 1998. Cryostructure development on the floodplain of the Colville River delta, northern Alaska. In: A.G. Lewkowicz & M. Allard (eds.), *Proceedings Seventh International Conference on Permafrost, Yellowknife, Canada*. Universite Laval. Nordicana 57: 993-999.

Soil Survey Staff 2006. *Keys to Soil Taxonomy, 10th edition.* Washington, D.C.: USDA Natural Resources Conservation Service.

Thermal Diffusivity Variability in Alpine Permafrost Rock Walls

P. Pogliotti
GEOSITLAB, Department of Earth Sciences, University of Turin, Italy
ARPA Valle d'Aosta, Climate Change Div., Aosta, Italy
E. Cremonese
ARPA Valle d'Aosta, Climate Change Div., Aosta, Italy
U. Morra di Cella
ARPA Valle d'Aosta, Climate Change Div., Aosta, Italy
S. Gruber
Glaciology and Geomorphodynamics Group, Department of Geography, University of Zurich, Switzerland
M. Giardino
GEOSITLAB, Department of Earth Sciences, University of Turin, Italy

Abstract

Permafrost degradation has been hypothesized as being one of the main causes of rockfalls and rock wall instability in the recent past in high mountain areas. Ongoing rock wall permafrost evolution remains poorly understood because of the lack of systematic measurements; models are often validated and driven by few existing instrumented sites. In rock wall subsurface temperature modeling, thermal diffusivity (κ) is one of the main parameters to be considered. In this study, thermal diffusivity data series were inferred from rock temperature data in order to understand their annual variation, their distribution in different temperature ranges, and their relation to atmospheric conditions. A harmonic analysis was performed to define amplitude and phase of the daily temperature waves at different depths by means of a least square minimizing optimization procedure. The analysis conducted shows that changes in κ values are influenced by different factors such as depth, season, rock temperature, aspect, and snowfall.

Keywords: rock wall temperature; thermal diffusivity.

Introduction

Steep bedrock slopes in high mountain areas are subjected to permafrost action. During the very hot summer of 2003, many rockfalls occurred in the European Alps, and sometimes massive ice was visible in the exposed detachment zone (Gruber et al. 2004b). These observations suggest that permafrost degradation may be one of the main causes of rock wall instability observed in recent years in high mountain areas (Dramis et al. 1995, Noetzli et al. 2003, Gruber et al. 2004a).

Thawing and degradation of rock wall permafrost is very fast if compared to permafrost in gentle morphology because of the lesser amount of ice content and the absence of a debris insulation layer (Gruber et al. 2004b); moreover, steep bedrock morphologies are abundant in many cold mountain regions and contain a significant proportion of permafrost (Gruber & Haeberli 2007).

Present and future global warming (IPCC 2007) will likely lead to a significant increase in frequency and intensity of rockfall events caused by variations in rock wall thermal regimes (Davies et al. 2001). Consequently, its degradation is spatially a widespread problem (Gruber & Haeberli 2007) which causes an increment in risks for people and infrastructures in high mountain areas (Harris et al. 2001).

In order to obtain a better understanding of rockfall trigger mechanisms and processes linking slopes warming and their local destabilization, an increase in knowledge on rock wall temperature regimes and their evolution is very important (Gruber & Haeberli 2007). Quantitative understanding and models of surface temperature distribution within steep rock faces in complex topography exist and have been validated with near-surface measurements (Gruber & Hoelzle 2001, Gruber 2005). However, many questions about active layer and sub-surface rock wall permafrost evolution remains poorly understood because of the lack of deeper systematic measurements and models.

In purely diffusive and stationary state models, thermal diffusivity is considered the only petrophysical parameter of importance (Yershov 1998), and in permafrost modeling, it is often considered as constant. Nevertheless, the continuous variability of water content linked to environmental conditions (Saas 2005), together with the latent heat effect associated with thawing and freezing (Mottaghy & Rath 2006), may cause great variability in thermal diffusivity in the active layer. These mechanisms may affect deeper temperature regimes and cause a probable "thermal offset" (Gruber & Haeberli 2007) between the rock surface and the top of permafrost.

The main purpose of this work is to evaluate the annual course of thermal diffusivity on some alpine permafrost rock walls and its variability related to environmental conditions. Using rock wall temperature data series measured at different depths of the active layer, a harmonic analysis was used to define amplitude and phase of daily temperature waves by means of a least square minimization procedure. Optimized amplitude values at each depth were used to obtain hourly

data of rock thermal diffusivity κ. These data series were analysed in order to understand their annual variation, their distribution in different temperature ranges, and their relation to atmospheric conditions inferred from in situ meteorological collected data.

Research Strategy

Field measurements

All data series were collected within the international project PERMAdataROC started in March 2006, during which several measurement sites were equipped on high steep slopes in six different areas in the western European Alps. For this study, two of the six areas were selected because they are characterized by long data series and by a higher number of measured variables. One is the SW ridge of the Matterhorn, and the other is the peak of the Aiguille du Midì in the Mont Blanc massif (Fig. 1).

In each area the measured variables are: rock wall temperature at depths of 3, 30, and 55 cm; air temperature and relative humidity (10 cm from the rock surface); and solar radiation, wind speed, and wind direction, measured by means of an automatic weather station (MAWS), installed on the rock wall with sensors parallel to the rock surface (Table 1).

Measurements started in November 2005 at the Matterhorn site, and at the end of December 2006 at the Aiguille du Midì site. For this study, a total of eight data series were used; data series characteristics are shown in Table 2.

In order to identify snow events, daily albedo values were calculated from radiation data, and a snow index (S_i) was defined as the ratio between daily and mean albedo: snow index values greater than 1.25 are caused by snow events. Since some problems in snow index definition may occur, mainly in winter due to snow deposition on MAWS's sensors during snowfalls events, sonic anemometer, air temperature, and humidity data series were also used as further confirmation of snow events.

Thermal diffusivity evaluation

Rock temperature data were used for thermal diffusivity evaluation. Signal detrending using running-mean was performed on rock temperature data series in order to remove low frequency oscillations as seasonal and annual ones. Assuming that temperature variation at any depth is sinusoidal, the thermal diffusivity of rock, κ ($m^2\ s^{-1}$), can be calculated with the following equation (1) (Matsuoka 1993):

$$\kappa = \frac{\pi}{P}\left[\frac{Z_1 - Z_2}{\ln(A_1 / A_2)}\right]^2 \quad (1)$$

where P is the period of one complete harmonic oscillation (24 hours) given in seconds, A_1 and A_2 are the amplitude of temperature waves (°C) at depth Z_1 (i.e., 0.03 m) and Z_2 (i.e., 0.3 m).

A harmonic analysis of rock temperature data was performed to define amplitude A_1 and A_2 of daily temperature waves at different depths using the following equation which describes a general harmonic oscillation:

$$T_{(z,t)} = A_{(z)} \sin(\omega t + \phi) \quad (2)$$

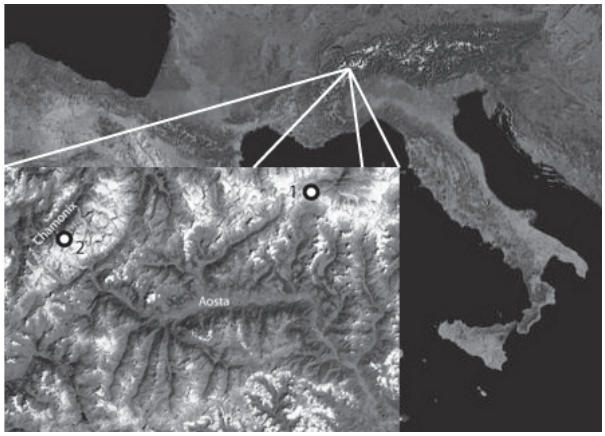

Figure 1. Research site localization. 1: Matterhorn. 2: Aiguille du Midì.

Table 1. Instrumentation

Parameter	Instrument	Log. interval
Rock temp.	Geoprecision - M-Log 6	60 min
Air temp. & hum.	Geoprecision - M-Log 5	60 min
Radiation	Kipp&Zonen - CNR-1	10 min
Wind	Vaisala - WMT50	10 min

Table 2. Data series characteristics

Site	Series name	Aspect	Elevation (m a.s.l.)	Length (days)	Season	Mean rock temp. (°C) -55cm	-30cm	-3cm
Matterhorn	CCS_Tr	N158-90	3820	126	sum	3.12	3.70	4.14
	CCS_Ta	N158-90	3820	126	sum			
	CCS_Rad	N158-90	3820	370	sum			
	CHEM_Tr	N180-90	3750	744	win-sum	0.58	0.90	1.28
Aig. du Midì	ADMS_Tr	N160-85	3820	209	win-sum	0.56	0.98	1.05
	ADMN_Tr	N335-80	3825	209	win-sum	-7.20	-7.16	-7.03
	ADMS_Ta	N160-85	3820	209	win-sum			
	ADMS_Rad	N160-85	3820	209	win-sum			

Abbreviations: Tr: rock temperature; Ta: air temperature and relative humidity; Rad: solar radiation.
Lithology: Matterhorn, gneiss; Aiguille du Midì, granite.

Table 3. Mean values and standard deviations of κ data series at Cheminèe site (Matterhorn).

Depth interval	Entire series		Warm Period		Cold Period	
	κ mean	standard deviation	κ mean	standard deviation	κ mean	standard deviation
(cm)	x10^{-6} (m^2 s^{-1})	x10^{-6} (m^2 s^{-1})	x10^{-6} (m^2 s^{-1})	x10^{-6} (m^2 s^{-1})	x10^{-6} (m^2 s^{-1})	x10^{-6} (m^2 s^{-1})
3 - 30	2.401	0.175	2.505	0.189	2.298	0.065
30 - 55	1.524	0.041	1.517	0.029	1.530	0.050
3 - 55	1.898	0.072	1.932	0.077	1.865	0.048

Warm period: summary of all springs and summers; cold period: summary of all autumns and winters.

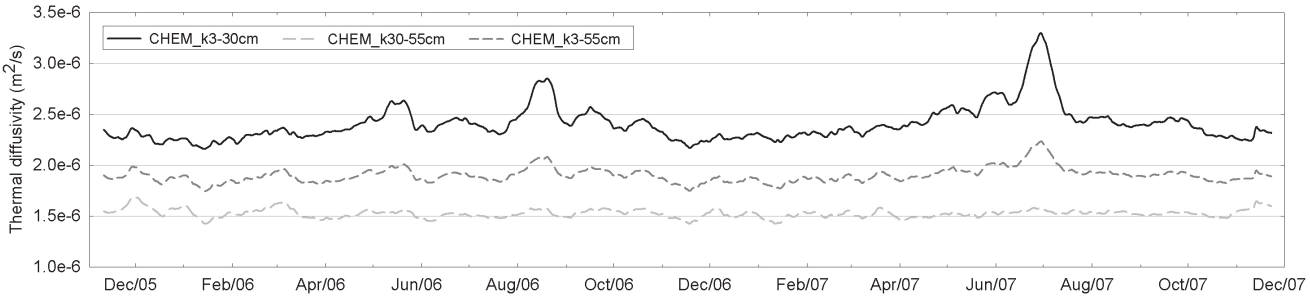

Figure 2. Annual course of computed thermal diffusivity at the Cheminèe site (Matterhorn) smoothed over 15 days.

where ω is the angular frequency of the oscillation (i.e, for daily cycles $\omega=(2\pi/24)$ h^{-1}), $A_{(z)}$ is the amplitude of temperature oscillation at depth z, and Φ is the phase angle.

A least-square minimization procedure was applied using equation 2 in order to obtain estimates of unknown parameters A(z) and Φ. A(z) is the parameter chosen for thermal diffusivity evaluation. Amplitude values at different depths were used in equation 1 to obtain hourly data of rock thermal diffusivity κ. As rock temperature data at three different depths were available, three different couples of amplitude data series were used: 3÷30cm, 30÷55cm, and 3÷55cm. The fitting procedure was computed on every series using a three-day running-window, moving with an hourly step. The standard error of computed thermal diffusivity values was evaluated using a bootstrap resampling technique. In the bootstrap procedure, the original dataset is randomly resampled N times (in this study N=500); in this way, for each hourly step, 500 synthetic thermal diffusivity datasets were generated. Instead, as described in Efron and Tbshirani (1993), the standard deviation of the distribution of these 500 values is a good measure of the parameter's standard error. The parameter standard error was used as an indicator of the reliability of amplitude values. Finally, the resulting thermal diffusivity data series was smoothed with a median filter of three hour's width, to avoid rapid fluctuations.

Results and Discussion

Annual course of thermal diffusivity

In order to show the annual variations in thermal diffusivity at each depth, the longer available data series (CHEM) is considered in Figure 2. Table 3 shows mean values of κ and standard errors of the whole data series and for cold (autumn plus winter) and warm (spring plus summer) periods.

The first 30 cm of rock show a mean value of about 2.4×10^{-6} m^{2}s^{-1} and great annual variability, with values generally below the mean during the cold season, and above the mean during the warm season. This observed variability decreases with depth: oscillations of deeper thermal conductivity data series are strongly reduced, and the seasonal behaviour underlined for the shallower rock layer cannot be seen. These differences are probably due to the different variability in water content during the year: greater in the first centimetres of rock and lesser at depth. Moreover, mean κ values of 30–55cm depth interval are significantly reduced, probably because of the different degree of saturation in comparison to the shallower rock layer.

To gain an understanding of the reliability of the diffusivity values presented, laboratory measurements of thermal conductivity were performed on gneiss samples collected at the Matterhorn study site. The results give a mean value of thermal conductivity equal to 2.7 Wm^{-1}K^{-1}. Using a mean tabled value of volumetric heat capacity for granitic rock equal to 1.75×10^6 Jm^{-3}K^{-1} (Yershov 1998), the resulting value of thermal diffusivity is 1.54×10^{-6} m^2 s^{-1}, a value which is very similar to the mean of the whole series calculated for the 30–55cm depth interval (1.52×10^{-6} m^2 s^{-1}).

These results seem to suggest that significant differences in thermal diffusivity values can be obtained by considering the first centimetres rather than the deeper rock layers. This matter should be taken into account when thermal diffusivity values are applied to heat conduction models for the projection in depth of rock wall temperature.

Distribution of κ values in different rock temperature ranges

Figure 3 show the distribution of 3–55cm thermal diffusivity values above and below 0°C both at the north and south Aiguille du Midì sites.

The 30 cm depth data series was used as the rock temperature reference at each site. In the period considered, on the northern site only 10% of rock temperature data were

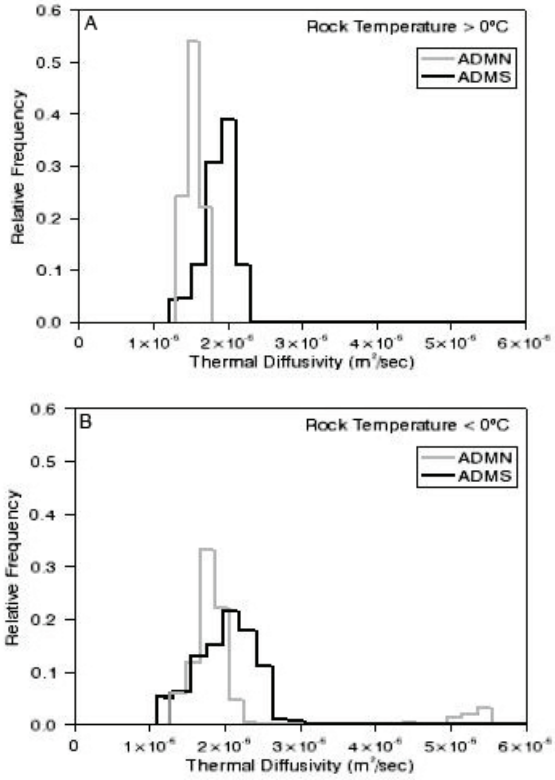

Figure 3. Distribution of thermal diffusivity values (3–55cm depth interval) below and above 0°C at ADM northern and southern sites.

above 0°C, whereas in the south, this proportion was around 50%. Moreover, minimum north and south values were -17.97°C and -14.06°C respectively, while the maxima were 3.97°C and 16.4°C, respectively.

The histograms in Figure 3 show the effect of rock wall aspect and different conditions on thermal diffusivity.

Regarding aspect, the northern site showed values lower than the southern one and less dispersed around the mean. Lower values suggest that northern exposures may be more saturated than southern exposures, as indicated in previous studies (Saas 2005). On both aspects, κ values are generally greater below 0°C; this is probably due to the substitution of water by ice in the pore space and fractures of frozen rock (Williams & Smith 1989).

Thermal diffusivity variations caused by snow events and rock wall temperature

Evaluation of the effect of snow events on thermal diffusivity was conducted by choosing some meaningful summer and winter events in the Matterhorn and Aiguille du Midì data series. Using a smoothed (24-hour) thermal diffusivity normalized deviation index κ_{di} (defined as κ/κ_{mean}), the temporal evolution of the CCS and ADM thermal diffusivity data series was analysed, considering 3–55cm depths.

In the CCS data series, an intense summer snow event (2nd half of August 2006) was considered. As shown in Figure 4, when the snow index increases, κ_{di} decreases (maximum

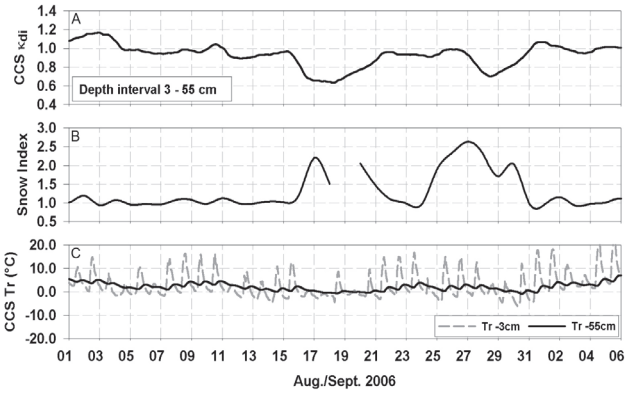

Figure 4. Comparison between CCS thermal diffusivity deviation index, snow index, and rock temperature.

reduction of about 40% of the mean value) and vice-versa: as the S_i starts decreasing κ_{di} rises closer to the mean value. During snowy days, shallower rock (-3 cm) temperature crosses above and below 0°C several times, while the deeper one (-55 cm) is closer to zero. In such a condition, phase changes may occur in the active layer: thus the consumption and release of latent heat due to thawing and freezing of percolating water cause the variation in apparent heat capacity. This variation affects κ which is inversely proportional to apparent heat capacity (Mottaghy & Rath 2006). The decrease in thermal diffusivity shown in Figure 4a during snow events is probably linked to water phase changes.

Similar considerations can arise from the observations of thermal diffusivity data series at ADM northern and southern sites (Fig. 5). During the spring-summer period κ_{di} temporal evolution, and the magnitude of its variation during snow events, are similar to what is observed in CCS data series. The southern face shows thermal diffusivity reduction related to snow events starting from the end of March (Fig. 5c); the same behaviour is observed on the northern side (Fig. 5a) only at the end of spring, when rock temperature rises toward 0°C (Fig. 5b), suggesting a possible role played by rock temperature on water availability.

On the other hand, during winter, κ_{di} variations related to snow events show an opposite behaviour: a strong increase in κ_{di} is observed on both faces, with a general higher intensity on the northern one, where a doubling of thermal diffusivity value occurred.

On the southern face, a strong increase of κ_{di} values, comparable to those in the north, occurred at the end of February. During this event, the southern face rock temperature showed values of about -10°C at the depth of 55 cm: a value closer to annual minima and similar to northern face rock temperature in the same period (-13°C). This means that the thermal conditions of the south wall were very similar to those experienced by a northern wall, suggesting, once again, that rock temperature may influence thermal diffusivity variability. However, further investigations are needed in order to understand the reliability of these winter increases.

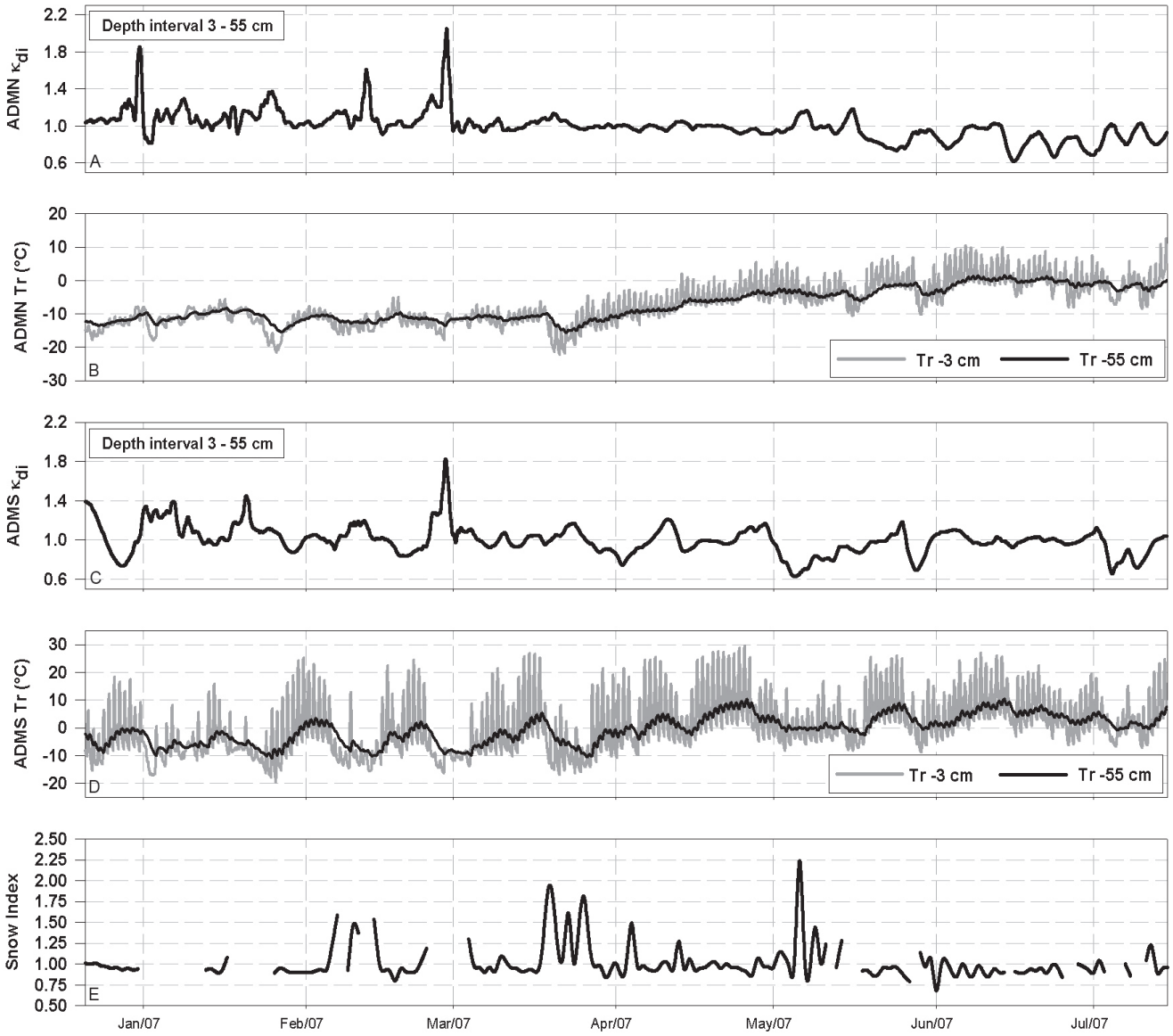

Figure 5. Temporal variation of thermal diffusivity deviation index at Aiguille du Midì northern (A) and southern (C) face. Rock temperature data at Aiguille du Midì north (B) and south (D) at depths of 3 and 55 cm. Snow Index value (S_i) used to identify snow events (E). All data series are smoothed with a 24-hour moving average, with the exception of the Snow Index (daily data).

As outlined in Figure 5d, periods of strong rock wall warming can be followed by thermal diffusivity reductions: κ_{di} variations observed at the end of April on the ADM southern face may have been caused by the previous 10 days of rock temperature above 0°C.

This reduction is more likely related to this rock warming period, rather than to the snow event which occurred during the first days of May, when the κ_{di} reduction had already reached its maximum value. A similar situation can be observed at the end of May. Moreover, on the northern face, a late May κ_{di} reduction occurred when rock temperature was above 0°C (Fig. 5b).

These observations suggest that thermal diffusivity variability may be influenced both by snow events and rock temperature and their interactions. Summer κ_{di} reductions can be explained by an increase in water circulating in the rock heap resulting from snow melting, and from ice-filled discontinuities melting due to warming periods. Winter thermal diffusivity increases, which occur during snow events, appear to be related to cooling intensity rather than to water supply as discussed in Williams & Smith (1989).

Conclusions and Outlook

The analysis conducted in this study leads to the following conclusions:

The estimation of thermal diffusivity variability, from rock temperature data measured at different depths, is possible, and the applied methodology gives reliable values. Changes in thermal diffusivity values are influenced by different factors such as depth, season, rock temperature, aspect, and snowfall. Thermal diffusivity variability decreases with

depth, and its mean values in deeper layers are significantly reduced with respect to shallower ones. This should be taken into account when using heat conduction models on the whole rocky heap.

Mean northern κ values are lower than southern ones: this difference may be related to the higher degree of saturation experienced by northern exposures. κ values are greater below 0°C because of the substitution of water by ice in the pore space and fractures of frozen rock.

Reductions in thermal diffusivity related to snow events were observed both on southern and northern faces during warm periods and are probably linked to water phase changes. Winter thermal diffusivity increases, which occur during snow events, appear to be related to cooling intensity rather than to water supply. Thermal diffusivity variations seem to be related to rock temperature, as well: warming periods may result in strong reductions in κ values, likely due to an increase in water circulating in the rock wall.

Such behaviours were observed on both monitoring sites: they, therefore, appear to be independent of system variables such as lithotype, degree of fracturing, and aspect.

In order to test the reliability of these first observations, it is necessary to wait for the results of the PERMAdataROC project: longer data series are needed in order to better understand the behaviour of thermal diffusivity variability.

A first application of computed thermal diffusivity values can be found in energy balance estimation. k values. and rock temperature data at different depths allow calculation of heat conduction which, coupled with net radiation measurements, may allow estimation of the ratio of available energy dissipated through turbulent fluxes. This information may be useful in heat conduction modeling.

References

Davies, M.C.R. Hamza, O. & Harris, C. 2001. The effect of rise in mean annual temperature on the stability of rock slope containing ice-filled discontinuities. *Permafrost Periglac. Process.* 12: 137-144.

Dramis, F. Govi, M. Guglielmin, M. & Mortara, G. 1995. Mountain permafrost and slope instability in the Italian Alps: the Val Pola landslide. *Permafrost Periglac. Process*. 6: 73-82.

Efron, B.B. & Tbshirani, R.J. 1993. *An Introduction of the Bootstrap*. New York: Chapman & Hall.

Gruber, S. & Hoelzle, M. 2001. Statistical modelling of mountain permafrost distribution—local calibration and incorporation of remotely sensed data. *Permafrost and Periglac. Process*. 12: 69-77.

Gruber, S., Hoelzle, M. & Haeberli, W. 2004a. Rock-wall temperature in the Alps: modelling their topographic distribution and regional differences. *Permafrost and Periglac. Process*. 15: 299-307.

Gruber, S., Hoelzle, M. & Haeberli, W. 2004b. Permafrost thaw and destabilization of Alpine rock walls in the hot summer of 2003. *Geophysical Research Letters* 3 1:L13504,doi:10.1029/2004GL020051.

Gruber, S. 2005. *Mountain permafrost: transient spatial modelling , model verification and use of remote sensing*. Ph.D. Thesis. Zurich, Switzerland: University of Zurich, 121 pp.

Gruber, S. & Haeberli, W. 2007. Permafrost in steep bedrock slopes and its temperature-related destabilization following climate change. *J. Geophys. Res*. 112:F02S18, doi:10.1029/2006JF000547.

Harris, C., Davies, M.C.R. & Etzelmüller, B. 2001. The assessment of potential geotechnical hazards associated with mountain permafrost in a warming global climate. *Permafrost and Periglac. Process*. 12(1):145-156.

IPCC. 2007. Summary for Policymakers. In*: Climate Change 2007: The Physical Science Basis. Contribution of Working Group I to the Fourth Assessment Report of the Intergovernmental Panel on Climate Change*. Cambridge, U.K. & N.Y., N.Y.: Cambridge University Press, 18pp.

Matsuoka, N. 1994. Diurnal freeze-thaw depth in rock walls: field measurements and theoretical considerations. *Earth Surf. Process. Landforms* 19: 423-435.

Monteith, J.L. & Unsworth, M. 1990. *Principles of Environmental Physics* (2nd ed). London: Edward Arnold, 307pp.

Mottaghy, D. & Rath, V. 2006. Latent heat effect in subsurface heat transport modeling and their impact on palaeotemperature reconstructions. *Geophys. J. Int.* 164: 236-245.

Noetzli, J., Hoelzle, M. & Haeberli, W. 2003. Mountain permafrost and recent alpine rock-fall events: a GIS-based approach to determine critical factors. *Proceedings of the 8th International Conference on Permafrost, Zurich, Switzerland*: 827-832.

Saas, O. 2005. Rock moisture measurements: techniques, results and implications for weathering. *Earth Surf. Process. Landforms* 30: 359-374.

Williams, P.J. & Smith, M.W. 1989. *Frozen Earth: fundamentals of geocryology*. Cambridge, U.K.: Cambridge University Press, 306 pp.

Yershov, E.D. 1998. *General Geocryology.* Cambridge: Cambridge University Press, 604 pp.

Massive Ground Ice in the Eureka Sound Lowlands, Canadian High Arctic

Wayne H. Pollard, Nicole Couture
Department of Geography, McGill University

Abstract

This paper documents the nature and significance of massive ground ice and thermokarst in the Eureka Sound lowlands in central Ellesmere and Axel Heiberg Islands in the Canadian High Arctic. We characterize the stratigraphic, ice content, and distribution patterns of ground ice, estimate potential thaw, and document recent trends in the rate and pattern of thermokarst. The Eureka area (~80°N) is characterized by cold polar desert conditions (mean air temperature of -19.7ºC) and permafrost up to 600 m thick. A total of 189 natural exposures of massive ice were mapped between 1991 and 2007, including 91 that were active in 2007. Most of these exposures are in the headwall of retrogressive thaw slumps. Repeated surveys of headwall positions have provided both short- and long-term retreat rates. Since 2004 there has been a detectable increase in thermokarst activity, including retrogressive thaw slumps, development of new thaw ponds, and degraded ice wedges.

Keywords: cryostratigraphy; ground ice; High Arctic; polar desert; thermokarst.

Introduction

Ground ice plays a major role in the evolution of landscapes underlain by continuous permafrost. Thawing permafrost, widespread terrain instability and resulting infrastructure problems are often cited as serious problems facing polar regions in response to global warming (ACIA 2005, IPCC 2001). Information about ice content and distribution is extremely variable across the Arctic. For example, there is considerable detailed information about the nature and distribution of ground ice for parts of Siberia (Astakov 1986, Astakov & Isayeva 1988, Streletskaya & Leibman 2003), the Alaskan coastal plain (Lawson 1986), and the western Canadian Arctic (Mackay 1971, 1989, Mackay & Dallimore 1992, Murton & French 1994), but by comparison, ground ice occurrence in the High Arctic has received limited attention (Robinson 1993, 2000, Pollard 1991, 2000a, 200b, Pollard & Bell 1998). Several studies have alluded to increased thermokarst as an outcome of climate change (Lawrence & Slater 2005, Nelson et al. 2001, Zimov et al. 2006). However, little is known about its anticipated pattern or the potential magnitude of thermokarst because it is entirely dependent on information about near-surface ground ice. Detailed information about the active layer is also needed before a realistic prediction about thaw subsidence can be made. Areas where the active layer is relatively thin, like the High Arctic, are more vulnerable to even small increases in summer temperature and the duration of the thaw season because the buffering capacity of the active layer is limited.

This paper documents massive ground ice, ice-rich sediments and thermokarst for the Eureka area in central Ellesmere and Axel Heiberg Islands in the Canadian High Arctic (Fig. 1). Recent data on the nature and distribution of ground ice conditions, ice content, and potential thaw are presented along with observations on the rate and pattern of thermokarst. The objectives of this paper are (i) to describe the nature and distribution of ground ice in the Eureka Sound Lowlands; (ii) to describe permafrost stratigraphy and ice contents, and (iii) to describe current patterns in thermokarst activity in this area. Preliminary findings on massive ice in the Eureka area were presented in Pollard & Bell (1998) and Couture & Pollard (1998), the current paper presents new findings, is based on new data and focuses more on thermokarst.

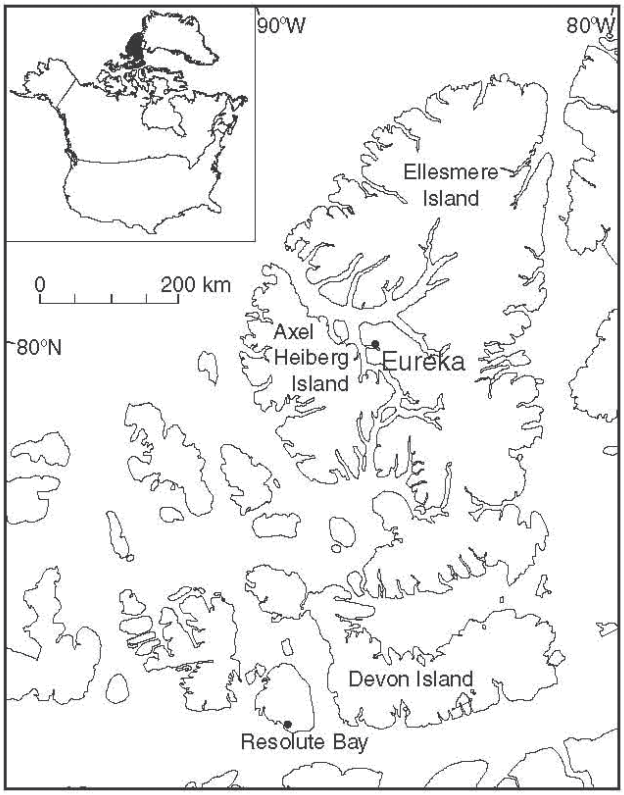

Figure 1. Map showing the location of Eureka in the Eureka Sound lowlands.

Ground ice remains one of the most problematic aspects of permafrost and a major obstacle to development in arctic regions. Knowledge about ground ice, particularly massive ice and ice-rich sediments, is necessary not only to understand the Late Quaternary landscape evolution of this

region, but also to assess the potential geomorphic response of the landscape to natural and anthropogenic disturbances of permafrost regimes. Thermokarst and erosion associated with the Eureka weather station and the Panarctic Gemini E-10 well site reflect the sensitive nature of surficial sediments and icy permafrost in this part of the Arctic (Couture & Pollard 2007). Concern that global warming will not only cause a shift in the pattern of permafrost distribution but will also induce widespread thermokarst (Lawrence et al. 2005) in areas underlain by ice-rich sediments provides additional impetus for ground ice investigation. Ground ice studies may also provide useful proxy information on paleoclimates and paleogeomorphology.

Study Area

This study focuses on massive ground ice located in the Eureka Sound lowlands on west-central Ellesmere Island and east-central Axel Heiberg Island (Fig. 2). Eureka Sound is bordered by gently rolling lowlands surrounded by glacierized mountains rising to elevations of more than 500 m a.s.l.

The landscape is incised by several short river channels and dotted by numerous tundra ponds. Ice wedge polygons are ubiquitous over most of the area and active layer detachment and retrogressive thaw slump scars are common. This area is underlain by poorly lithified Mesozoic and Cenozoic clastic rocks of the Savik, Awingak, Deer Bay, Isachsen, Christopher, Hassel, Kangkuk and Eureka Sound Formations (oldest to youngest). Outcrops of weathered bedrock are widespread at elevations above marine limit and resistant sandstones of the Heiberg Formation form steep ridges in excess of 500 m a.s.l. Fosheim Peninsula lies east of (beyond) a glacial drift belt that marks the Late Pleistocene glacial limit (Bell 1996). Approximately 30% of the peninsula lies below the Holocene marine limit, which is approximately 140–150 m a.s.l. (Bell 1996). Below this elevation a blanket of thinly laminated sandy silt and silty clay from <1 to ~15 m thick covers most surfaces.

Pollard & Bell (1998) developed an emergence history for the Fosheim Peninsula (from dates for articulated bivalves of marine origin) that constrain the age of ground ice deposits for different elevations. A fine-grained till and diamicton overlying bedrock is described by Hodgson (1985) for the northern part of Fosheim Peninsula. The Quaternary history and the extent of Pleistocene glaciation in this area are still poorly understood (Bell 1996, Pollard & Bell 1998) and could have a strong bearing on the interpretation of massive ground ice origin, in particular its age and the possible preservation of buried glacier ice. Thus, a particular concern of field mapping and section description is the identification of fine till or diamicton units and their association with massive ice.

The study area is characterized by cold polar desert conditions (the Eureka weather station has a mean air temperature of -19.7°C based on a 50-year record) and permafrost up to 600 m thick (Pollard 2000b). Preliminary studies indicate that the marine sediments are extremely ice-rich (Pollard 1991, 2000a). Of particular interest is the widespread occurrence of massive ice in the lowlands surrounding Eureka Sound, Slidre Fiord and the Slidre River Valley, where it frequently occurs as extensive bodies of massive tabular ice (Couture & Pollard 1998, Robinson 1993, Pollard 1991, Pollard & Bell 1998, Pollard 2000a).

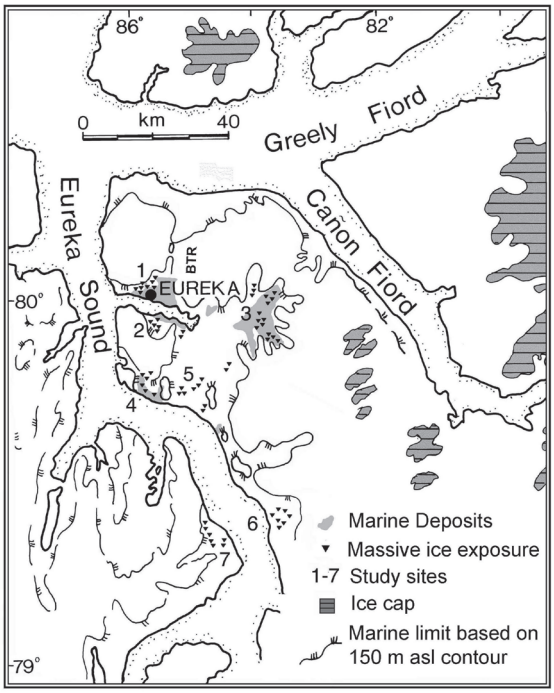

Figure 2. Map of the Eureka Sound Lowlands showing the location of ice-rich permafrost, massive ground ice exposures and study sites 1–7 (see text for details). BTR refers to Black Top Ridge.

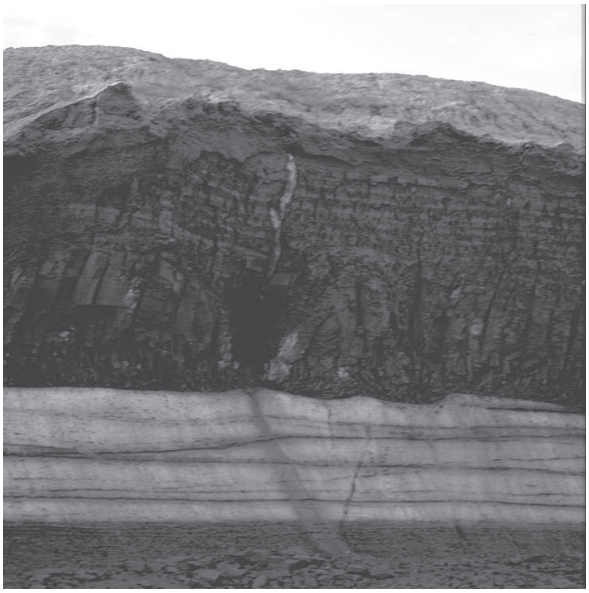

Figure 3. Massive ground ice (~3 m thick) conformably overlain by 5+ m of laminated marine sediments containing reticulate ice veins.

Ground Ice Conditions

Ground ice conditions

Fieldwork on massive ground ice in this area began in 1991 by examining natural exposures (retrogressive thaw slumps, river banks and block failures), but since 2001 has included coring (~40 cores <5 m and 5 cores between 5–17 m) and geophysical investigations (GPR and resistivity).

Ground ice distribution

Seven ice-rich areas characterized by numerous ground ice exposures with massive ice as well as both active and inactive thermokarst features and tundra ponds have been identified (Fig. 2). Study sites include: (1) Eureka, (80°00′N, 85°57′W); (2) South Slidre Fiord (79°56′N, 86°05′W & 79°54′N, 85°30′W), (3) Slidre River, (79°55′N, 84°14′W) including Hot Weather Creek (79°59 & 84°28′W) and Gemini (79°58′N, 84°10′W) (4) Blue Man Cape, (79°44′N, 85°57′W) (5) Eureka Sound (79°43′N, 84°30′W) (6) South Fosheim (79°28′N, 84°20′W) and (7) May Point (79°25′N, 84°29′W). The Romulus Lake (79°52′N, 84°55′W) and the Depot Point (79°22′N, 86°24′W & 79°24′N, 86°00′W) areas also display widespread thermokarst, but only a few exposures of massive ice. A number of isolated massive ice exposures and retrogressive thaw slumps have also been mapped. Retrogressive thaw slumps frequently contain relatively large bodies of massive ice and ice-rich permafrost (excess ice). The distribution of massive ice corresponds closely with the distribution of fine-grained marine sediments identified by Bell (1996), in fact 181 exposures (96%) occurred in marine sediments. The nature of the ice is also stratigraphically controlled by these and other surficial materials. The most significant ice exposures occur where marine deposits >7 m thick form flat to gently dipping plateaus.

Of the 189 natural exposures containing massive ice and ice-rich sediments 88% are retrogressive thaw slump head walls, 8% river cuts and 4% block failures. These data are supplemented by 20 core holes.

Cryostratigraphy

Most exposures include horizontally layered massive ice several meters thick conformably overlain by 1–7 m of massive to weakly laminated marine sediment (Fig. 3). The ground surface is often littered with cobble to boulder-sized clasts and a fine gravel lag deposit in areas of wind erosion. A typical section includes a thin surface layer 5–20 cm thick of massive fine sand with a few large sub-rounded clasts (gravel to cobble sized) that grades into a massive fine silty sand. The fine sand unit varies in thickness between 1–3 m. This unit grades into a finely laminated silt and silty sand. Layers (laminae) 1–1.5 cm thick of well sorted silt and fine sand are interpreted as rythmites associated with episodic glacial melt water deposition into a shallow marine (brackish) system (Bell 1996). Soil salinities range between 0.2%–0.5%. The active layer is typically 30–70 cm deep.

Ice contents are initially high immediately below the base of the active layer. This unit grades into 0.5–2.0 m of faintly laminated to massive silty clay. It is extremely ice-rich, ice occurs in a regular to irregular reticulate cryotextures with vertical fissures initially predominating. Salinities are between 0.4%–0.6%. Ice content tends to increase with depth forming a network of vertical and horizontal segregated ice lenses which grades into massive ice with angular blocks of silty clay 2–5 cm in diameter. The contact between the silty clay unit and the massive ice is abrupt but conformable. Sediments in the ice are similar to the sediments in the overlying silty clay unit. There is also chemical continuity in the major ions and environmental isotopes.

The massive ice unit ranges from 2–10 m plus in thickness. Given that basal contacts are rarely observed in natural exposures the total thickness is inferred from geophysical surveys and a few deep core holes. Massive ice displays horizontal to gently dipping bands of sediment and sediment-rich ice. Ice color varies between white (bubble rich) and clear (appears black). Ice petrofabrics range from strong preferred vertical c-axes with large (1–3 cm long) euhedral crystals in the middle of the unit to random c-axis orientations and small anhedral crystals near sediment bands and at the upper contact. The basal contact is observed in 3 core holes from the Eureka area. In all 3 cases the ice grades into ice-rich bedrock (poorly lithfied sandstone). Technically this is an unconformity however there is chemical continuity between the massive ice and ice retrieved from 10 cm into the bedrock.

In the Eureka Sound Lowlands the pattern in ground ice content is closely linked to the thickness of marine sediments, and although considerable variation exists both locally and regionally, the presence of terraced marine deposits has proven to be an extremely good indicator of massive ice. Several sections at each massive ice site were analyzed for ice content. For convenience, ice content values are expressed as percent volume although most of the measurements

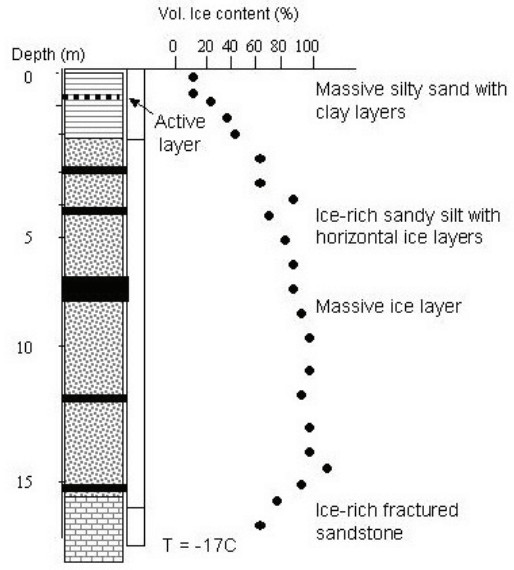

Figure 4. Typical cryostratigraphic profile through a massive ice body, based on a 17 m core taken near Eureka obtained using a modified seismic drill.

were done gravimetrically. Gravimetric ice contents were converted to volumetric ice contents following a procedure outlined in Pollard & French (1980). The base of the active layer formed the top of most measured profiles. Active layer depths display considerable variation ranging from 60–70 cm for dry south-facing surfaces to 30–40 cm for damp north facing or shaded locations. For much of Fosheim Peninsula, particularly above marine limit where surficial materials are coarse, the permafrost is quite dry and ice contents average between 3–10% by volume.

Ice content profiles

In the ice-rich areas below marine limit three patterns in ice content profile occur (Fig. 5). The first is marked by moderately high ice contents (20%–30%), occurring as pore ice and thin discontinuous ice lenses and layers near the base of the active layer. Beneath the active layer, ice contents increase sharply so that at depths of roughly 1.0–1.3 m they reach 60%–99% where layers of pure ice and muddy ice predominate; the sediment in the ice is mainly silt or clay sized. In this pattern, high ice contents extend between 2–7 m to depths of up to 8–9 m. In only a few instances is it possible to obtain data below the base of the massive ice zone, and in such cases the ice contents drop dramatically (10%–30%).

Pore and lens ice occur where the lithology changes to coarse sandy material or weathered bedrock. The second pattern includes a layer of weakly laminated sandy silt 5–7 m thick with ice contents ranging from 8%–15% near the base of the active layer, to 12%–17% at depths of 2–3 m. Near the base of this unit, ice contents increase to 30%–40% as the clay and silt contents increase. Pore and lens ice grade into more regular vertical and reticulate patterns of ice veins. At depths ranging from 7–10 m, faintly laminated silty clay materials abruptly change to massive ice with fragments or layers of silty clay (60%–70% ice) to pure horizontally foliated massive ice (90%–100% ice). The third pattern is intermediate between the first and second patterns. In this case, ice contents increase gradually (15%–30%) with depth usually reflecting a rise in silt content. At a depth of roughly 4–5 m, interbedded layers of silty ice and icy silt with ice

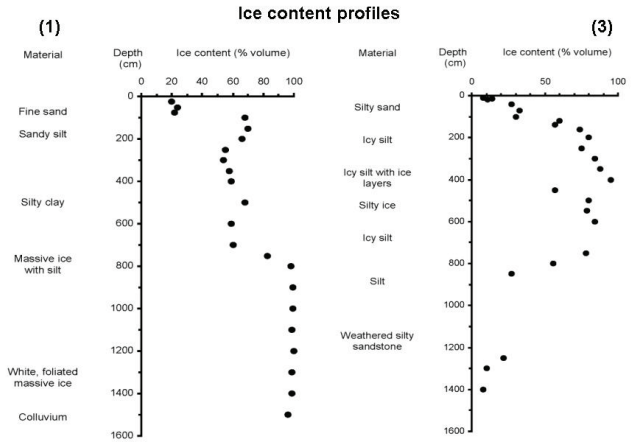

Figure 5. Ice content profiles, patterns 1 & 3.

contents of 65%–78% (sometimes higher) predominate for up to 5 m. At a depth of 9–10 m ice contents decrease to 50%–60% and below this depth, they drop off dramatically (5%–10%) as materials grade into a weathered bedrock substrate.

Various forms of ground ice occur in the surficial materials in the Eureka Sound Lowlands. Pore ice occurs in virtually all perennially frozen unconsolidated sediments and in places is a source of excess ice. Similarly, ice-wedge polygons occur on most surfaces except resistant bedrock outcrops and ridges (e.g., Black Top Ridge). High centered polygons are most common and polygon dimensions are highly variable, ranging from 7–20 m in diameter depending on setting and materials. In low-lying areas ice-wedge troughs are usually well developed, but at higher elevations and in coarse-grained materials they are poorly defined. Ice wedge dimensions are also highly variable and depend on a combination of setting, age and water supply. In the Eureka area, for example, ice wedges range from small fissures 10–30 cm wide and 100–200 cm deep, to classic V-shaped wedges 100–200 cm wide and 350 cm deep. The average ice wedge trough width based on the measurement of 350 wedges in 5 different areas (70 x 5) is 130 cm. Following the method described in Pollard & French (1980, Equation 8), it is estimated that ice-wedge ice comprises approximately 10%–12% of the upper 5 m of permafrost; this is comparable with estimates from the Mackenzie Delta and Yukon Coast. Segregated ice ranges through a full spectrum of forms from thin discontinuous ice lenses, to fully developed reticulate textures, to thick tabular bodies of massive ice (Fig. 3). It is particularly significant in fine-grained marine silts, silty clays and sandy silts that were deposited during the late Quaternary and have subsequently been exposed to cold subaerial permafrost conditions (Bell 1996). Roughly 25%–30% (~4000 km^2) of the Eureka Sound lowlands lie below the Holocene marine limit (150 m a.s.l.). Above this elevation, dry, weathered coarse-grained Tertiary deposits are widespread. Apart from large, widely spaced ice wedges (Lewkowicz 1994), areas above marine limit do not seem to contain significant amounts of ground ice. Elevated, more resistant bedrock surfaces display no evidence of ground ice, but at Hot Weather Creek thick layers of pure ice were observed at depth in consolidated rock strata of the Eureka Sound Formation. Buried ice is present in relatively small quantities as buried snow bank deposits in the stabilized headwalls of retrogressive thaw slumps. Buried glacier ice could be present in various till deposits but to date has not been observed. These studies have shown that pore ice and wedge ice form a significant contribution to the total volume of ground ice in the upper 10 m of permafrost (Couture & Pollard 1998). Buried snow bank ice is present in small amounts in areas of active thermokarst and buried glacier ice occurs in association with moraines formed by modern ice caps and glaciers.

Following a methodology presented in Pollard & French (1980) and modified in Couture and Pollard (1998) we attempt a first approximation of ground ice in the top 7 m of

permafrost in the Eureka Sound Lowlands, an area of roughly 12,000 km^2. The total volume of ground ice is calculated by estimating the areal extent of various types of ice-rich terrain in the study area. We establish percentages of ice content by volume for each type of terrain unit. This study considers the top 7.5 m of soil because this was the lower limit of most of our sample data, and because the immediate effects of surface disturbance are unlikely to penetrate to much greater depths. Our estimates concern only the volume of permafrost, or frozen materials, so we subtract the average active layer thickness of 0.6 m, so that the thickness of materials actually used in calculations is 6.9 m. Ice content profiles were used to calculate the average volumetric ice content associated with pore ice and massive ice based on terrain type. A combination of air photo analysis and field data were used to estimate the volume of ice associated with ice wedges. The highest ice volumes (65%) were associated with marine terraces. Below marine limit, pore ice segregated ice comprise 45% by volume of frozen sediment while in areas underlain by bedrock they account for 9.5%. Ice wedges comprise only 5% of the volume of frozen sediments. This low value reflects the relatively small size of ice wedges. Ground ice in all forms makes up approximately 30% of the upper 6.9 m of permafrost.

Thermokarst

Thermokarst is an important erosional process unique to areas underlain by ice-rich permafrost and refers to landforms resulting from the thawing of ground ice. The importance of thermokarst is often discussed in terms of its potential occurrence as an impact on human activity (e.g., as a response to construction of pipelines and highways) or global warming; however, it should not be forgotten that thermokarst is a naturally occurring erosional process. The nature and magnitude of thermokarst is directly related to two important variables, (i) the thermal stability of the upper part of permafrost, including the depth of the active layer, and (ii) ground ice contents. Retrogressive thaw slumps (also called retrogressive thaw flow slides) are one of the more spectacular forms of backwearing thermokarst and also involve thermal erosion (Fig. 6). Preliminary observation on thermokarst in the Eureka area are presented in Robinson (2000).

Most of the 189 natural massive ice exposures were in retrogressive thaw slumps. In comparison with similar landforms in the Mackenzie Delta-Yukon Coastal Plain area the retrogressive thaw slumps in the Eureka Sound Lowlands are relatively small. The average length of exposed headwall was <80 m (the largest was 158 m) and average headwall height was 5–7 m. The highest head wall was 12 m but heights around 4–5 m were common. Through the course of this study the headwall position of 3–4 slumps in each of the study areas was monitored by a combination of DGPS, total station surveys and tape surveys. In addition late July thaw depths (active layer) were also monitored in the vicinity of the headwall. Climate data from the Eureka weather station and an automatic weather station in the Eureka area allowed us to compare retreat rates with air temperature. The average mean daily temperature for July (the warmest month) was +5.7°C and the average number of thawing degree-days for July was 176.7.

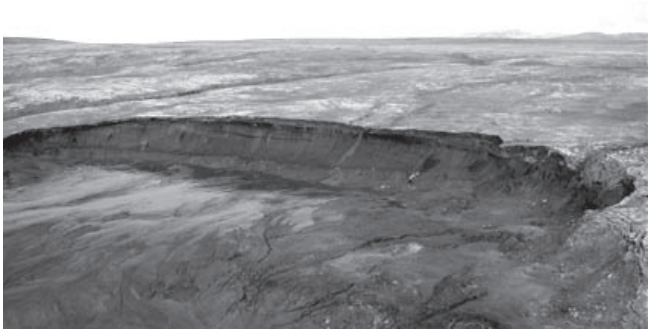

Figure 6. A retrogressive thaw slump near Depot Point. The exposed headwall is approximately 80 m long.

July 1998 and 2003 were the two warmest Julys during this study. Through the course of this study 30 slumps were surveyed. In some cases sites were measured annually, but most were surveyed every second or third year. With the exception of two slumps that remained active through the entire study (one at South Slidre and one at Blue Man Cape—sites 2 and 4 respectively) most (70%) stabilized after 7–8 years, (20%) after 10 years and (4%) stabilized only 2–3 years after their initiation. Slumps stabilized very quickly following 1–2 years with of rapid retreat. Stabilization occurs when the sediment from the active layer is not removed (by viscous flow) fast enough and buries the head wall. Retreat rate varies across the headwall of every slump; maximum retreat at a point along the headwall can be misleading so we took the average of the most active 10 m section. Over 17 years of observation the average retreat for all sites is 6.9 m/yr, the highest annual retreat was 21 m. A comparison between average annual retreat based on all the slumps and mean July temperature does not show a particularly strong relationship although the highest single retreat rates occurred in years with warmer than average July temperatures. The number of active slumps seems to correspond with years with warm mean July temperatures. Between 1990 and 1995, there were 85–90 active slumps, from 1995–2000 the number dropped to 67–70, from 2000–2005 the number of slumps went back up to 75–77, but since 2005 the number has risen to 91–93. There is a close relationship between July thaw depth and mean July temperature. In 1998, 2003 and 2006 mean July temperatures were 3°C–4°C warmer than average and July thaw depths we 10% higher than average. Since 2000 many of the ice wedge polygons in the vicinity of the monitoring sites exhibited significant thaw degradation and deepening of ice wedge troughs. Numerous new thaw ponds have formed with ice wedge troughs and intersections.

Conclusions

This paper summarizes 15 years of observations on massive ice in the Eureka Sound Lowlands. Three main conclusions can be drawn from this research. First, massive

ground ice is a significant component of surficial sediments in the Eureka Sound Lowlands, which represents one of the more ice-rich regions in the Canadian Arctic. Second, the nature and distribution of massive ice is closely linked to the presence of marine sediments and sea level history. And thirdly, shallow massive ice and ice wedges are highly vulnerable to thermokarst. Prior to 2005 there appeared to be little relationship between warmer-than-normal July temperatures and thermokarst, but from 2005–2007 the number of thermokarst features and the amount of thermokarst has been increasing.

Acknowledgments

The authors wish to acknowledge the following sources of funding NSERC Discovery Grant (W. Pollard), ArcticNet NCE, and DIAND's NSTP Program (Couture). Logistical support from NRCan's Polar Continental Shelf Project and the Eureka Weather Station (EC) are gratefully acknowledged. The authors also wish to acknowledge the useful comments of two anonymous reviewers.

References

Arctic Climate Impact Assessment (ACIA). 2005. Arctic Climate Impact Assessment. Cambridge University Press. 1042 pp.

Astakhov, V.I. 1986. Geological conditions for the burial of Pleistocene glacier ice on the Yenisey. *Polar Geography and Geology* 10: 286-295.

Astakhov, V.I. & Isayeva, L.L. 1988. The Ice Hill: an example of retarded deglaciation in Siberia. *Quaternary Science Reviews 7*: 29-40.

Bell, T. 1996. Later Quaternary glacial and sea level history of Fosheim Peninsula, Ellesmere Island, Canadian High Arctic. *Canadian Journal of Earth Sciences* 33: 1075-1086.

Couture, N.J. & Pollard, W.H., 2007 Modelling geomorphic response of a high Arctic polar desert to climatic change. *Climatic Change,* doi: 10.1007/s10584-007-9309-5.

Couture, N. & Pollard, W. 1998. An assessment of ground ice volume near Eureka, Northwest Territories. In: *Proceedings, Seventh International Permafrost Conference,* Centre d' études nordiques, Collection Nordicana, No 57: 195-200.

International Panel on Climate Change (IPCC). 2001a. Climate Change 2001: impacts, adaptation, and vulnerability. Third Assessment Report, Cambridge University Press, Cambridge, UK. 1032 pp.

Lawrence, D.M. & Slater, A.G., 2005. A projection of severe near surface permafrost degradation during the 21st century. *Geophysical Research Letters* 32, L22401, doi:10.1029/2005GL025080.

Lawson, D. 1986. Ground ice in perennially frozen sediments, northern Alaska. *Proceedings of the Fourth International Conference on Permafrost.* Washington, DC: National Academy Press, 695-700.

Lewkowicz, A. 1994. Ice wedge rejuvenation, Fosheim Peninsula, Ellesmere Island, Canada. *Permafrost and Periglacial Processes* 5: 251-268.

Mackay, J.R. 1971. The origin of massive icy beds in permafrost, western Arctic, Canada; *Canadian Journal of Earth Sciences* 8: 397-422.

Mackay, J.R. 1989. Massive ice some field criteria for the identification of ice types. *in Current Research, Part G;* Geological Survey of Canada, Paper 89-1G, 5-11.

Mackay, J.R. & Dallimore, S.R. 1992. Massive ice of the Tuktoyaktuk area, western Arctic coast, *Canada. Canadian Journal of Earth Sciences* 29: 1235-1249.

Murton, J.B. & French, H.M. 1994. Cryostructures in permafrost, Tuktoyaktuk coastlands, western Arctic *Canadian Journal of Earth Sciences* 31: 737-747.

Nelson, F., Anisimov, O. & Shiklomonov, N. 2001 Subsidence risk from thawing permafrost. *Nature* 410: 889-890.

Pollard, W.H. & French, H.M. 1980. A first approximation of the volume of ground ice, Richard Island, Pleistocene Mackenzie Delta, NWT *Canadian Geotechnical Journal* 17: 509-516.

Pollard, W. & Bell, T. 1998. Massive ice formation in the Eureka Sound Lowlands: A landscape model. In: *Proceedings, Seventh International Permafrost Conference*, Université Laval, Centre d'etudes nordiques, Collection Nordicana, No 57: 903-908.

Pollard, W.H. 1991. Observations on massive ground ice on Fosheim Peninsula, Ellesmere Island, Northwest Territories; *in Current Research, Part E, Geological Survey of Canada, Paper 91-1E*, 223-231.

Pollard, W.H. 2000. Distribution and characterization of ground ice on Fosheim Peninsula, Ellesmere Island, Nunavut, *in Environmental Response to Climate Change in the Canadian High Arctic,* Geological Survey of Canada, Bulletin 529: 207-233

Pollard, W.H. 2000. Ground ice aggradation on Fosheim Peninsula, Ellesmere Island, Nunavut, *in Environmental Response to Climate Change in the Canadian High Arctic, Geological Survey of Canada, Bulletin* 529: 325-333.

Robinson, S.D. 1993. Geophysical and Geomorphological Investigations of Massive Ground Ice, Fosheim Peninsula, Ellesmere Island, Northwest Territories. M.Sc. thesis, Queen's University, Kingston, Ontario, 171 pp.

Robinson, S.D. 2000. Thaw-slump-derived thermokarst near Hot Weather Creek, Ellesmere Island, Nunavut. *Geological Survey of Canada* 529: 335-345.

Streletskaya, I.D. & Leibman, M.O. 2003 Cryogeochemical model of tabular ground ice and cryopegs, Yamal Peninsula, Russia. *Proceedings of the Eighth International Conference on Permafrost*, *Zurich, Switzerland, 21-25 July 2003*: 1111-1115.

Zimov, S., Schur, E. & Chaplin, F. 2006. Permafrost and global carbon budget. *Science* 5780: 1612-1613.

Long-Term Monitoring of Frost Heave and Thaw Settlement in the Northern Taiga of West Siberia

Olga Ponomareva
Earth Cryosphere Institute, Russian Academy of Sciences, Siberian Branch, Moscow, Russian Federation
Yuri Shur
University of Alaska Fairbanks, Department of Civil and Environmental Engineering, Fairbanks, Alaska USA

Abstract

Monitoring of frost heave and thaw settlement has been carried out for 37 years in the discontinuous permafrost zone of West Siberia. Long-term frost heave is a modern process in the natural condition of the discontinuous permafrost zone. The rise of old frost mounds and the formation of new ones has been observed. Old mound development occurs non-uniformly in time and is associated with cold winters. The rate of frost heave is maximum in the central part of frost mounds and minimal at the margins. Long-term frost heave in flat peatland has also been observed; it occurs at about the same rate but is more spatially uniform. The exception is represented at peripheral sites in flat peatland with a lowered permafrost table. Contemporary thermokarst is inactive in natural conditions. Thaw settlement is very intensive after the removal of a vegetative cover and part of the soil layer. The subsidence rate decreases substantially after 2–3 years. The maximum observed thermokarst subsidence reached 1 m during the period of monitoring.

Keywords: climate; human-induced disturbances; long-term frost heave; thermokarst.

Introduction

Frost heave and thermokarst-related features occur widely in the northern taiga of Western Siberia (Melnikov et al. 1983) where permafrost is discontinuous. Frost heave forms are represented by individual mounds, ridges (with length many time greater then width and height), and vast flat elevated areas. Heights vary from 0.5 to 10 m (Veisman et al. 1976). These forms develop both in natural and disturbed areas (Fig. 1)

Contemporary forms related to thermal subsidence occur primarily in disturbed areas along the Nadym-Punga gas pipeline. Their depth reaches 1 m. There are different opinions on the contemporary activity of these cryogenic processes. According to Evseyev (1976), frost mounds in the region are relic and degrading forms. Nevecherja (1980) described modern frost mounds and has evaluated the growth rate in the northern taiga of Western Siberia. However, he believed that the majority of frost mounds, ridges, and frost-heaved areas were formed long ago, and do not currently grow, and some mounds degrade in the contemporary environment. According to Nevecherja (1980), frost mound growth stops after the frozen nucleus reaches about 10 m. Recently, changes in vegetation on old frost mounds associated with their rise was described by Moskalenko & Ponomareva (2004).

Study Site

A long-term monitoring program was established by N. Moskalenko, V. Nevecherja, and Y. Shur in 1971 to study the impact of pipeline construction on permafrost stability, and on the development of permafrost-related processes in the pipeline right-of-way and surrounding terrain. In this paper, we present data from the Nadym site to demonstrate contemporary dynamics of frost heave and thermokarst in natural areas and those impacted by pipeline construction.

Figure 1. Disturbed frost mounds.

The Nadym monitoring station is located 30 km to the south from the city of Nadym (Fig. 2), in a subzone of northern taiga. It encompasses three geomorphological levels: the third lacustrine-fluvial plain, the flood plain of the Hejgi-Jaha River, and the second fluvial terrace of the Nadym River. The relief is nearly flat with numerous lakes and mires.

The studied region is characterized by two layers of permafrost, which can be defined as surface permafrost and deep permafrost. The surface permafrost is discontinuous and sporadic on the lacustrine-fluvial plain and the flood plain of the Hejgi-Jaha River. Patches of permafrost are confined to peatlands, tundra, and frost mounds. On the terrace of the Nadim River, the permafrost table is lowered and does not merge with the bottom of the active layer.

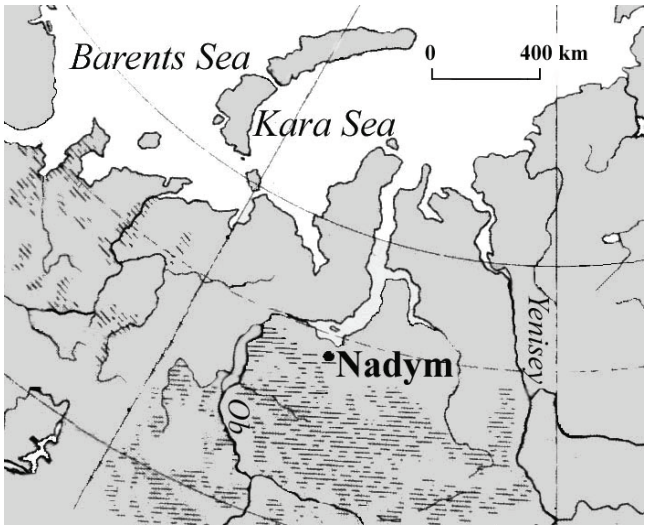

Figure 2. Study site near Nadym.

Depending on terrain conditions, mean annual permafrost temperature varies from 0 to -2°C. The warmer permafrost temperature is typical for dry forest-covered sandy soils. Extensive peatlands have the coldest permafrost temperature. The active layer varies from 0.5–0.7 m on peatlands, and up to 4 m on blowout sand.

The depth of seasonal freezing varies from 0.3 to 0.8 m in peatland, and from 1.5 to 2.5 m in forest with well-drained sandy soil. Recently the permafrost temperature and seasonal thaw depth has increased in both natural and disturbed settings, which is reflected in the dynamics of natural processes (Moskalenko 1998)

Research Objectives and Methods

The analysis of climatic conditions is based on long-term observations at the Nadym weather station.

Observations of long-term frost heave and thaw subsidence were conducted along four transects that cross the gas pipeline right-of-way, the surrounding disturbed zone, and the terrain unaffected by construction that has remained in a natural state. Measurements of frost heave and thaw settlement were made relative to deeply anchored reference bench marks. Elevation surveys and vegetation descriptions were carried out yearly at the end of August. The active layer thickness and permafrost temperature were measured in September.

Analysis of Results

The analysis of the climatic data

According to long-term data, air temperatures and the precipitation amount in in the study region vary markedly from year to year (Fig. 3). The long-term mean annual air temperature is -5.6°C; the difference between annual mean temperatures of the coldest and warmest years reached 5.69° during last 40 years. Despite such fluctuations, a 10-year moving average of annual mean air temperature shows an increase in the period from 1966 to 1997, and small variations

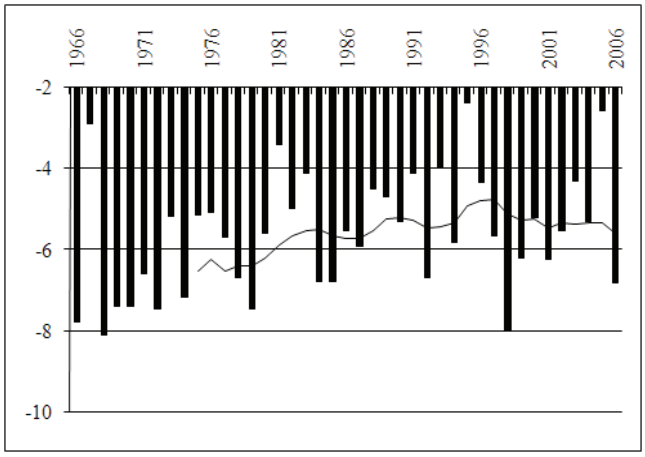

Figure 3. Annual mean temperatures with a 10-year moving average, °C.

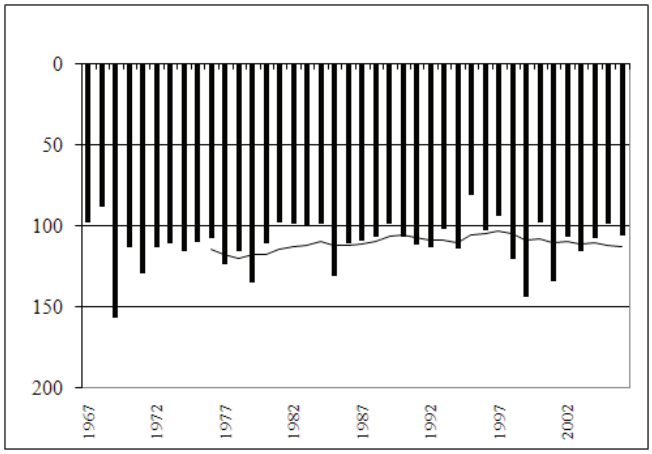

Figure 4. Freezing indices (in °C months) with a 10-year moving average. One degree-month is equal to 30 degree-days.

from 1998 to 2006 (Fig. 3).

Figure 4 shows the freezing Iindices and Figure 5, the thawing indices for the same period. The winter of 1995 had the smallest freezing index for the entire observation period. It was equal to 80.5°C-month, and occurred at the end of the period of warming. The most severe winters occurred in 1999 and 2001 following the warm period, with freezing indices of 144 and 134° C-months. An exception was the cold winter of 1985. Freezing and thawing indices in this paper are presented in °C-months because they were evaluated from available information on monthly mean air temperatures. Their presentation as °C-days would create the wrong impression about the data, but can be estimated by multiplying °C-months by 30.

Thawing indices (Fig. 5) show continuous increase; with time, this will lead to a steady deepening of the active layer and thawing of the ice-rich upper layer of permafrost. However, thermokarst activation under natural conditions has not been detected so far.

The annual mean precipitation is shown in Figure 6. Winter and summer precipitation for the same period is shown in Figure 7 and Figure 8.

It was expected that the abundance of precipitation during

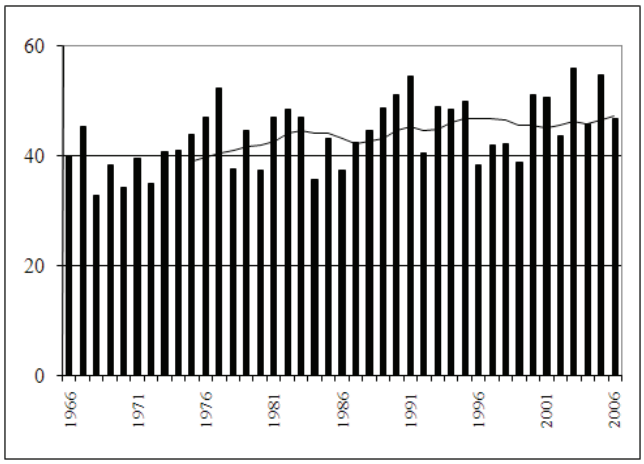

Figure 5. Thawing indices (in °C-months) with a 10-year moving average. One degree month is equal to 30 degree-days.

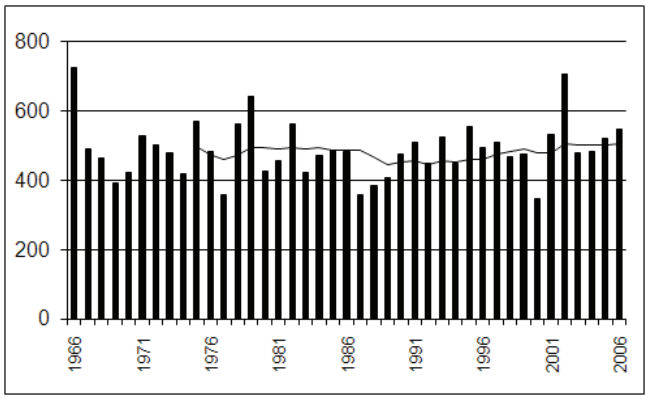

Figure 6. Annual mean precipitation (mm) with a 10-year moving average.

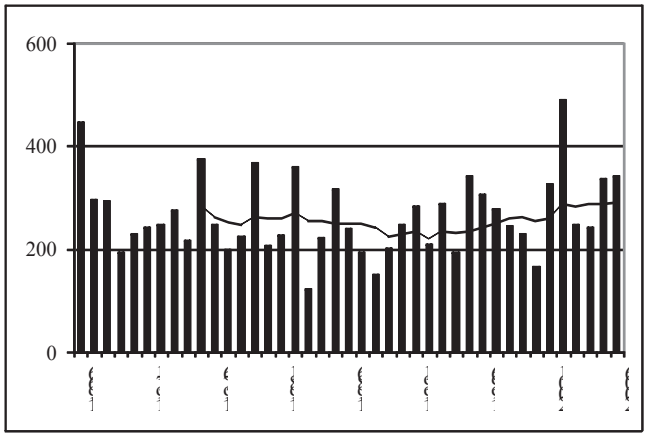

Figure 7. Summer precipitation (mm) with a 10-year moving average.

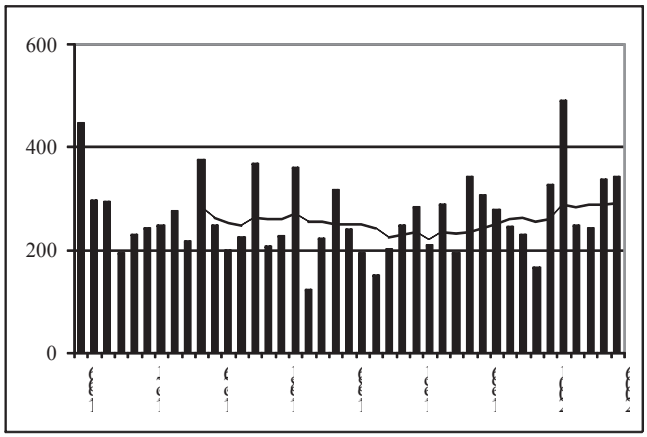

Figure 8. Winter precipitation (mm) with a 10-year moving average.

the period with negative air temperatures would lead to a decrease in the intensity of frost heave, and the amount of precipitation for the period with positive temperatures would impact bog development. According to the data presented in Figure 6, the total amount of yearly precipitation increases after 1987, as did the summer precipitation (Fig. 7). The increase in summer precipitation after 1987 has caused an expansion of the bog and lake area, as revealed by 1989 and 2004 satellite images. There is no visible trend in winter precipitation (Fig. 8).

Long-term frost heave of soils of third lacustrine-fluvial plain

Frost heave of soils in the third lacustrine-fluvial plain was studied at 327 points along four transects. Transects were located across various landscapes. The survey of surface elevation was conducted once a year, at the end of August or beginning of September, when seasonal thaw depth had reached its maximum and surface elevation reflected the effects of long-term frost heave processes with minimum seasonal effects. The survey was performed with reference to deep permanent benchmarks.

Transect I-I (Fig. 9) crosses a series of peat-mineral and mineral frost mounds that are surrounded by mires. A survey of frost mounds surfaces shows that frost heave is not uniform; there is a steady rise of mound tops and sporadic rise of slopes which is intermittent with subsidence. They rise in the coldest winters;. dDuring the monitoring period, maximal rise occurred in the most severe winter of 1999. During the last 26 years, the central part of one peat-mineral frost mound rose 70 cm, while a mineral frost mound rose 30 cm. For the analysis of frost heave intensity, it is important to note that a thin snow cover occurred nine9 times, including 1985, 1995, 2000, and 2001, during which intensive frost heave took place. The winters of 1985 and 2001 were especially severe. The snow thickness impact on frost heave was obvious in the warm winter of 1995 with low snow thickness. The rise of frost mounds tops with subsidence of their slopes was observed in 2005.

Maintenance work along the gas pipeline in 2004 initiated new surface disturbances and changes in the drainage conditions, which led to the formation of small lakes and widespread flooding (Fig. 10). It decreased the growth of frost mound tops and led to subsidence of their slopes in 2005 and 2006.

Transect II-II was established on the flat peatland and bogs of the third lacustrine-fluvial plain (Fig. 11). The thickness of peat along transect II-II varies from several centimeters to 1.75 m. To a depth of 5 m, peat is underlain by fine and

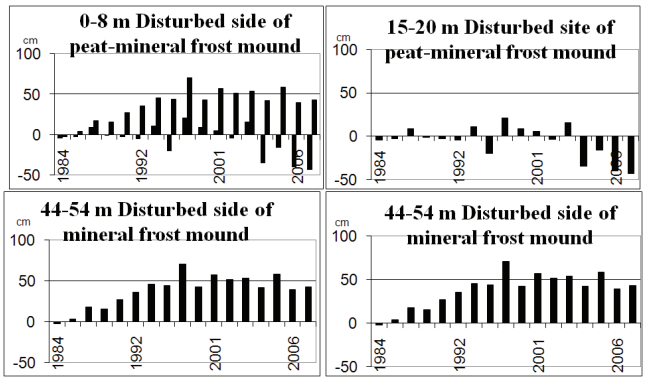

Figure 9. Changes in surface elevation (cm) along transect I-I relative to surface elevation in 1980. Annual values represent averages for that segment of the transect.

Figure 10. Flooding of the area adjacent to the pipeline in the vicinity of transect I-I. View from the gas pipeline.

silty sands and seams of sandy loam with some gravel and pebbles. The layer of sandy loam continues to a depth of 7 to 8 m, where it is underlain by sand. The layer of surface permafrost associates with flat peatlands here.

It was found that the surface along transect II-II experienced a rise in the severe winters of 1985 and 1999 , and in 32 years has became higher by 67 cm than it was in 1980. Frost heave of the flat peatland is uniform in the study area. After 1999, surface rise has slowed down. (Fig. 12).

Transect III-III includes flat peatland and hummocky tundra. Peat, which varies in thickness from several to 80 cm, is underlain by loamy sand to a depth of 3 to 8 m, with loam below. The permafrost table here is lowered to a depth of 3.5 to 4 m. Pereletoks are formed in some years above it. (aA pereletok is a layer of frozen ground which formed as a part of seasonally frozen ground and remained frozen for several summers ([van Everdingen 1998)]). Frost heave on transect III-III (Fig. 13) in one year is intermittent with thermal settlement in another, and the accumulated surface rise for the monitoring period is only 12 cm. The maximal rise of the surface occurred in the cold winter of 2001, with a thin snow cover in the previous winter.

Transect IV-IV is located on a peat-mineral frost ridge, disturbed in 1971 during construction of the gas pipeline. Removal of the vegetation cover triggered thermokarst, an increase in permafrost temperature, and a lowering of the permafrost table (Shur 1981). Vegetation recovery reverses these processes and

Figure 11. Flat peatland along transect II-II.

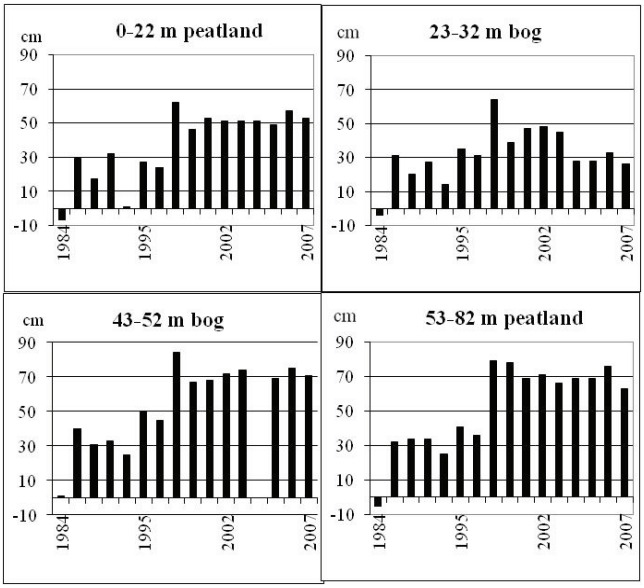

Figure 12. Deviation of surface elevation (cm) along transect II-II from elevation in 1980. Annual values represent averages for labeled segments of the transect.

is favorable to frost heave, although its intensity is very low. It is possible to identify two periods in the direction of processes on the soil surface. The period 1972–1977 is characterized by surface subsidence following construction, and the period which began in 1978 is the period of slow rise of the surface (Fig. 13). During the first period, the surface subsidence was 104 cm on average. The slow rise of the surface (by 50 cm on average) during the second period did not compensate for the earlier subsidence.

Thaw subsidence

In natural conditions, inactive thermokarst forms associated with thawing ice-wedges are typical for peatlands (Fig. 14). Ice-wedge pseudomorphs are also widespread in the region (Fig. 15). Distinguishing forms which could be attributed to contemporary thermokarst in natural conditions are rare, local, and occur on the margins of flat peatlands mainly in association with thermal erosion. Observation show that,

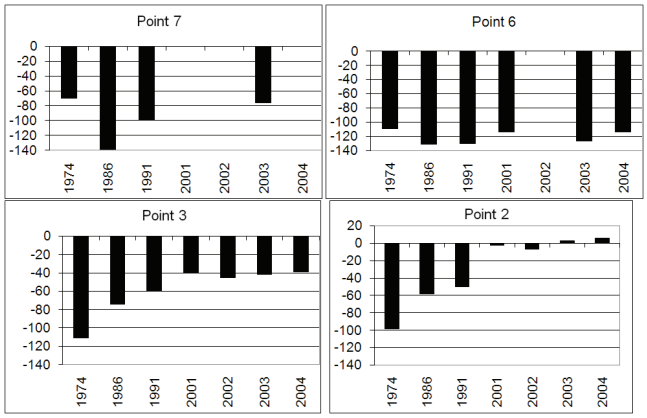

Figure 13. Deviation of surface elevation (cm) along transect IV-IV from elevation in 1972. Annual values represent deviations for every point along the transect.

despite the lack of notable thermokarst forms, uniform thermal settlement takes place. From 2000 to 2005, the rise of frost mounds and peatlands slowed down, and thermal settlement increased. It reached 31 cm on a peat-mineral frost mound, 47 cm on a mineral frost mound, and up to 64 cm on flat peatland. However, settlement has not led to formation of prominent thermokarst features. Our observations confirm Vejsmana's (1976) conclusion about weak development of modern thermokarst features under natural conditions. This conclusion is correct for natural, undisturbed terrestrial complexes. Presumably, thermokarst will develop at the margins of lakes as their area increases. We expect that our ongoing studies will reveal this.

Conclusions

1. The formation of frost mounds in the discontinuous permafrost zone of West Siberia is a contemporary process on lacustrine-fluvial plain and flood plains in the northern taiga of West Siberia. During the last 30 years, their height has increased from 30 to 70 cm, with a maximal rise occurring in the coldest winters of 1999 and 2001.
2. In areas disturbed during pipeline construction, peat frost mounds occur in three stages: thaw settlement, surface stabilization, and frost heave. The last two stages largely depend on vegetation recovery.
3. Thermokarst is not active under natural conditions. It is triggered by construction work, and is very active in the first several years. The total thaw settlement in the study area reached 100 cm during the period of observation.

Acknowledgments

This research was partly funded by the Polar Earth Science Program, Office of Polar Programs, National Science Foundation (ARC-0632400 and ARC-0520578). Natalia Moskalenko has been our long-term companion in the field and our mentor on terrain analysis. Comments by reviewers and their advice were very helpful. Ken Hinkel provided valuable suggestions that improved the manuscript.

Figure 14. Inactive thermokarst forms in the vicinity of transect III-III.

Figure 15. Ice-wedge pseudomorphs in the vicinity of transect I-I

References

Evseev, V.P. 1976. Migration pingos in the northeast of the European part of the U.S.S.R. and in Western Siberia. *Problems of cryolitology*, Vol. V. MGU: 95-160 (in Russian).

Melnikov, E.S., Veisman, L.I., Moskalenko, N.G., Tagunova, L.N., Ukraintzeva, N.G., Chekrigina, S.N., Ananieva, G.V., Goralchuk, M.I., Krizuk, L.N., Lazareva, N.A., Merkushenkova, R.I., Slavin-Borovsky, V.B. & Shirshikova, A.S. 1983. *Terrain Units of Permafrost Region of the West Siberian Gas Province*. Novosibirsk: Nauka, 164 pp. (in Russian).

Moskalenko, N.G. 1998. Impact of vegetation removal and its recovery after disturbance on permafrost. *Proceedings of the Seventh International Conference on Permafrost*, *Yellowknife:* 763-769.

Moskalenko, N.G. & Ponomareva, O.E. 2004. Changes of frost mounds, disturbed by construction work in northern taiga of West Siberia. *Earth Cryosphere* II(8): 10-16 (in Russian).

Nevecherya, V.L. 1980. Cryogenic heave at long-term freezing of grounds in the north of Western Siberia. *Geocryological Research*: M. VSEGINGEO: 45-49 (in Russian).

Shur, Y.L. 1981. The thermokarst forecast. In: *Methodical Recommendations Under the Forecast of Development Cryogenic Physical – Geological Processes in the Mastered Regions of the Far North)*. M. VSEGINGEO: 18-37 (in Russian).

van Everdingen, R. (ed.) 1998. Multi-language glossaryof permafrost and related ground-ice terms. International Permafrost Association

Veisman, L.I. et al. 1976. Contemporary geologocal processes and their occurrence in the middle course of Nadym r. and Pur-Taz einterfluve. *Abstract collection TSINIC*, Series II, RELEASE 2(43б), Moscow, 50-54 (in Russian).

The Permafrost of the Imuruk Lake Basaltic Field Area (Alaska) and Astrobiological Implications

O. Prieto-Ballesteros
D.C. Fernández-Remolar
J. Torres Redondo
M. Fernández-Sampedro
M.P. Martín Redondo
J.A. Rodriguez-Manfredi
J. Gómez-Elvira
Centro de Astrobiología-INTA-CSIC, 28850 Torrejón de Ardoz. Spain
D. Gómez-Ortiz
Rey Juan Carlos University, 28933 Móstoles, Spain
F. Gómez
Centro de Astrobiología-INTA-CSIC, 28850 Torrejón de Ardoz. Spain

Abstract

We have studied the permafrost in the Imuruk Lake volcanic field area (Alaska) from an astrobiological perspective. Our main goal was to test in terrestrial permafrost the type of instrumentation designed to search for biosignatures in this environment to obtain a performance baseline, should the instrument be used on a future space mission to explore Mars. Permafrost characterization was performed using geophysical sounding and drilling, and different levels of the rock cores were analyzed to determine the mineralogy, geochemistry, and microbiology. Thirteen lines of electric tomography from the Imuruk Lake coast up to the hill of the Imuruk formation were analyzed. Three perforations were made at strategic locations along the slope of the hill. Samples were collected at several depths in the three holes for mineralogical, geochemical, and biological analysis. Here we present the results of the subsurface mapping performed to locate the permafrost and of the analyses of the core samples.

Keywords: Alaska; astrobiology; electrical tomography; Imuruk Lake; permafrost.

Introduction

The study of terrestrial permafrost has become a priority for planetary missions focused on Mars. The main reason is that the martian permafrost likely represents the current main water reservoir of the planet (Clifford & Parker 2001). From an astrobiological perspective, permafrost is important not only because of the role of the water in the planet's hydrological cycle and the fact that it may hold a direct record of the planet's paleoclimatic record, but also because it may be a potential habitat for microorganisms (or preserve biomolecular tracers of past life) since it (a) acts as a thermally stable shelter, (b) is a source of moisture, and (c) is a shield against incoming radiation (Gomez et al. 2004). Consequently, robotic exploration of permafrost on Mars is being considered for future missions by the international suite of space agencies (Smith & McKay 2005, Shotwell 2005). At present, direct study of the martian permafrost has not been possible due to technical limitations and uncertainties. However, terrestrial analogues to Mars' permafrost are currently being investigated from novel perspectives that include space technology and astrobiology. The results are being used to develop instrumentation for future space missions focused on the search for life.

Some characteristics of martian permafrost have been modeled by using data from planetary exploration missions. At the present time, this dataset is continuous at circumpolar latitudes, where an active layer (the top layer of permafrost that seasonally thaws) is absent. At middle latitudes, permafrost is continuous although a thin active layer may exist, especially if salts are present to depress the melting point. In the tropical zone, ground temperatures exceed 273 K during the summer, and annual mean temperatures indicate that continuous permafrost exists, but ice is absent or patchy at best due to hyperaridity (Squyres et al. 1992). Recently, *Mars Odyssey* mission data have defined the periennial underground ice stability zone from latitudes higher than 60º (Feldman et al 2002, Mellon et al. 2004).

The Alaskan permafrost now serves as a martian analogue for the planetary science community. The permafrost of the Imuruk Lake area (Seward Peninsula, Alaska) offers a valuable and relatively accessible location for testing instruments for remote mapping and searching for life in the water underground. There are few studies about this area, though some report the general geology (Hopkins 1963) or different analyses of cores from several drill sites in the area, which were cored to constrain the climatic events that have occurred in the area (Colinvaux 1964, Colbaugh 1968, Marino 1977, Shackleton 1982, Hamilton 1991). None of the reports, however, covers permafrost mapping, mineralogy, geochemistry, and biology simultaneously. Nor do any reports consider the recent interest in the permafrost as an analogue environment of Mars. The permafrost on this

area is considered continuous (Péwé 1975), and it extends in some parts to more than 50 m thick (Hopkins 1963). Ice wedges and polygons are frequent in the Imuruk Lake area. It has been suggested from analyses of the stratigraphy that certain ice wedges in frozen ground are at least from the early Wisconsinan glacial period.

We show here the results of a field campaign performed during the summer of 2005 in the Imuruk Lake area. With the intent to develop future instrumentation for remote life detection systems, we pursued three main objectives: (1) permafrost localization by geophysical techniques and drilling the permafrost, (2) microbial diversity analysis, with special interest on the deeper part of the cores given the older age of this permafrost (i.e., the preservation pattern of biosignatures in cold environments is of extraordinary astrobiological interest), and (3) understanding of the cold ecosystem for the purpose of detecting and mapping permafrost niches. Geophysical sounding for mapping the permafrost was made before we sampled it. Three cores in the mapped area were taken. Clean drilling techniques were used, following planetary protection rules. Geochemical and biological analyses were made in the laboratory, though they were previously prepared in situ.

Regional Setting

The Imuruk Lake area is on the Seward Peninsula, a few kilometers above the polar circle. It is north of the Bendeleben Mountains in a Cenozoic lava plain. Landscape heights of the surrounding area vary from 45 to 600 m, with the highest topography caused by Mesozoic granitoid intrusions and Paleozoic metamorphic rocks, which constitute the geological rock basement. The central part of the area is characterized by monogenetic volcanoes, active from the late Paleogene. Five volcanic formations have been distinguished in the Imuruk Lake area, among which mantles of windblown silt with different extent and thickness have been deposited (Hopkins 1963). Volcanism is basaltic to andesitic, mainly with pahoehoe lava flows, although locally there are some dome structures. Permafrost in these materials is especially interesting with regard to the interaction between rocks and ice, from which we derive analogies to important martian landforms and materials. Ice-rich permafrost is primarily continuous—tens of meters thick, except under and near the major lakes and rivers. In addition, parts of the lava flows interrupt the permafrost, thus allowing groundwater circulation.

The Imuruk Lake occupies a basin configured by a distorted northwest trending graben. Tectonics during the Cenozoic formed several fracture systems in three different stages. The lake area was uplifted to the northwest, as well as bent, as shown by the study of the terraces. Three levels of terraces have been identified: The low level is presently occupied by active beaches on the east shores of the lake; intermediate terraces are cover by peat and silt; and the higher terrace is a wave cut not associated with sediments.

Current climate in the Imuruk Lake area is cold, with a mean temperature of 266 K and minimum values during winter of 213 K. Annual precipitation is 20 cm, from which 50% is between July and September, and 25% is as snow.

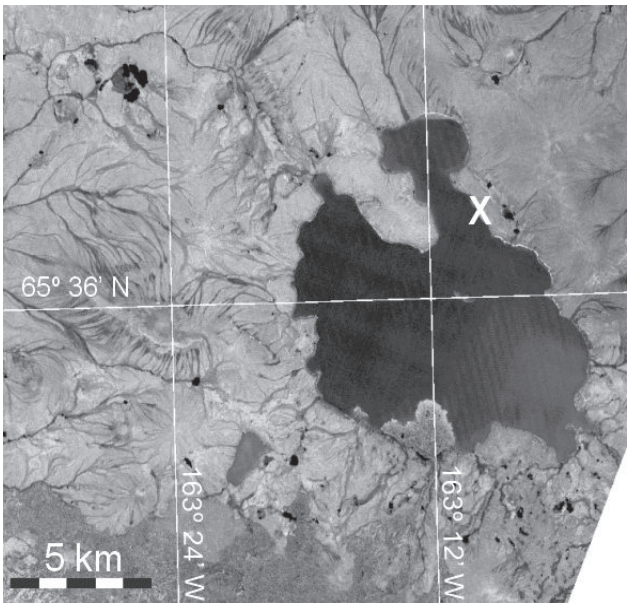

Figure 1. Imuruk lake area. Field work of 2005 campaign was made at the east shore of the lake (X).

Glaciations have affected the Imuruk area from lower Pleistocene: Nome River, Salmon Lake and Mount Osborn glaciations altered the successive volcanic rocks, which were erupted and produced eolic silts that covered them.

Considering the bad accessibility of the area, some analysis of ASTER images was performed in order to constrain the study area before the fieldwork campaign. The selection of the study area was made among the most ancient volcanic formations, where surface materials showed a low brightness temperature during summer and the topography is smooth enough to facilitate the drilling. Fieldwork performed during the 2005 expedition was made in the eastern part of the Imuruk Lake between Nimrod Hill and the lake itself (Fig. 1). This area was mapped by Hopkins (1963) as the named Imuruk volcanic formation, which is dominated by basalts and basaltic andesite lava flows overlain by 1–6 m of windblow silt. A cover of peat is present at the top. Surrounding the volcanic hill, some lake sediments, gravel, sand, silt, and peat of intermediate terraces have been mapped already (Hopkins 1963).

Geophysical Survey

To map the permafrost underground, electrical resistivity tomography (ERT) sounding was performed. ERT is a geophysical prospecting technique designed for the investigation of areas of complex geology. The principal applications of this technique are (Telford et al. 1990, Reynolds 1997, Hauck & Mühll 2003, Kneisel 2004; Šumanovac 2006) mapping stratigraphy and aquifer boundary units, such as aquitards, bedrock, faults and fractures, delineation of voids in karstic regions, mapping saltwater intrusion into coastal aquifers, identification of contaminated groundwater plumes, mapping of mineralization zones, exploration of

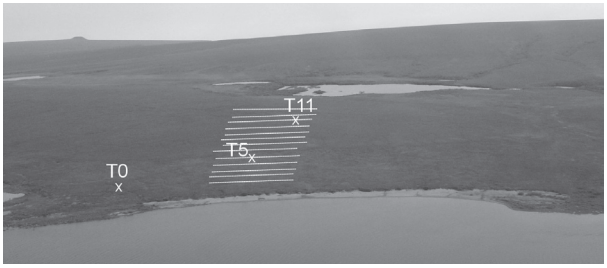

Figure 2. Image of the area where the 13 ERT lines were done. T0, T5, and T11 are the locations of the drill sites.

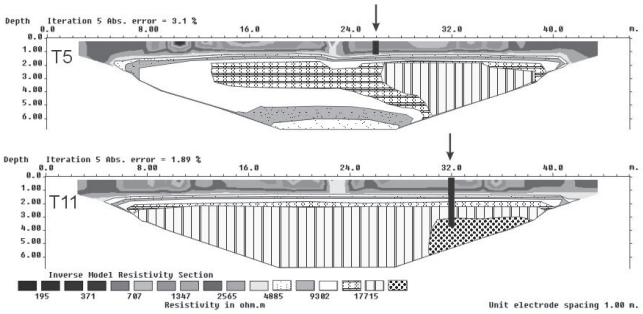

Figure 3. Tomographic profiles 5 and 11. Black arrows indicate the drilling sites.

sand and gravel deposits, as well as mapping permafrost in mountainous regions, among others.

Several standard electrode arrays are available, such as Wenner, dipole-dipole, and pole-dipole arrays, with different horizontal and vertical resolution, penetration depth, and signal-to-noise ratio. The Wenner array provides good vertical resolution, though it also gives reasonable horizontal resolution (Sasaki 1992). This method has a greater signal-to-noise ratio than others (e.g., the dipole-dipole method) because the potential electrodes are placed between the two current electrodes. These features provide greater depth of investigation.

Syscal KID Swich-24 equipment was used for taking the measurements. Thirteen parallel lines from the Imuruk lake coast up to the hill of Imuruk formation were accomplished (Fig. 2). Each ERT line was 48 m long, with 2 m between each pair of electrodes. The space between lines was around 15 m, depending on the difficulty of the topography for settling the electrical lines.

The resistivity field dataset comprises resistance measurements between various electrodes and related geometry information. An apparent resistivity value is calculated, which depends only on the resistance measurements and the array geometry. These data are plotted as a pseudosection, which is a plot of the apparent resistivity values based on the geometry of the electrodes. These pseudosections, which are difficult to work with, are then converted into sections with true resistivity values and depths via a data inversion procedure that helps in the interpretation process. An inversion of the data produces a plot that shows a resistivity value for each horizontal and vertical node. This resistivity inversion section is then used to interpret the subsurface lithology. The data are inverted with RES2DINV software. Data processing steps include removing bad data points, selecting the inversion method, and then interpreting the data.

The resulting ERT data for our study indicated that permafrost in the region analyzed is at a mean depth of 0.50 m under the surface, sometimes even shallower. The presence of peat materials at the top of the stratigraphic column acts as an insulator layer, maintaining very effectively the low temperature below.

From the analysis of the 13 ERT profiles, 2 clearly distinctive units were identified (Fig. 3): an upper unit that extended from the surface to 0.5–1 m depth, characterized by resistivity values ranging from 130 to 680 ohm·m, and a lower unit that reached 6 m depth (the maximum depth of investigation), defined by a resistivity that ranged from 12,400 to 30,000 ohm·m. Taking into account the in situ drilling observations, the study area was comprised by silt overlain by a thin level of peat.

Typical resistivity values for silt and peat are 10–200 ohm·m (Telford et al. 1990, Reynolds 1997, Comas et al. 2004), a value that depends mainly on the water content and ionic concentration. Permafrost resistivity values are typically greater than 10^3–10^4 ohm·m (Reynolds 1997, Hauck & Mühll 2003, Kneisel 2004) due to the strong resistance of the ice. Bearing this in mind, the upper low-resistivity unit could be related to the presence of peat and silt material with unfrozen water, whereas the lower high-resistivity unit represents the permafrost developed in silt materials. Vertical heterogeneities in electrical resistivity were observed in the upper part of all the profiles, which have been interpreted as the edges of the polygonal terrains (Fig. 3). Thus, the lower resistivity values in the upper unit correspond to finer grained and higher water content materials of the polygonal terrains, whereas higher resistivity values are associated with the coarser materials (i.e., at the edges of the polygonal terrains).

The high resistivity in the lower unit represents the permafrost developed in silt materials, which reached a thickness of at least 5–5.5 m in all the profiles. At first glance, this unit is much more homogeneous than the upper unit, although some spatial variations were measured. ERT profiles 1 to 8 exhibited resistivity values for permafrost that ranged from 12,500 to 21,000 ohm·m, with higher values at the end of the profiles than at the center. In addition to this, ERT profiles 6 and 7 showed resistivity values at 6 m depth (about 5,000 ohm·m), similar to the ones that defined the top of the permafrost at 0.5–1 m depth. This fact makes evident that the base of the permafrost in these profiles is located near the maximum depth of investigation. The resistivity values for the permafrost in ERT profiles 9 to 13 ranged from 24,000 to 30,000 ohm·m, being much more homogeneous than in profiles 1 to 8. The resistivity did not decrease in depth, so the lower boundary of the permafrost must be below 6 m depth. Only profiles 12 and 13 showed a spatial variation in the resistivity of the permafrost, with higher values to the western end.

Drilling Survey

A Cardi E-400 driller—small, portable, and fuel-operated—was employed in this expedition. By connecting 0.5 m bits, a maximum 5 m long drill was obtained. The diameters of the bit and the recovered core were 50 mm and 40 mm, respectively. No refrigerant substances were applied to preserve the area from contamination.

Drilling points were selected on the basis of the permafrost depth known from the ERT data analysis. Three perforations were done along the hill (Fig. 2). The first core obtained, which was placed in the ERT line 5 (T5), was about 1 m long. It consisted of peat and brown silt with abundant organic matter. The permafrost started at 0.3 m underneath the surface. The second core, drilled at ERT line 11 (T11), reached 3.6 m depth. Permafrost was found at 0.55 m. The peat cover above it was smaller. Below it, brown silt with organic matter was observed to a depth of 3.0 m. The sand fraction of the silt was composed of quartz and plagioclases (albite and anorthite), while the fine fraction was composed of clinochlore, montmorionite, illite, and vermiculite. From this point to the core bottom, the materials were green-yellowish silt, almost free of organic material (Fig. 4). The third core was drilled out of the study area by tomographic lines closer to the lake, and penetrated a 2 m depth (T0). Permafrost was at 0.50 m, at the same depth as the peat cover. Below that level, we found the green-yellowish silt with transversal lenses of both clean ice and organic silt. The silt found in this core was free of quartz. The sand fraction was made by anorthite, labradorite, and microcline as plagioclases, with diopside, augite, and acmite as pyroxenes. From 1.5 m down, the materials are basaltic-andesitic pebbles inlayed in a silt matrix (Fig. 5).

Samples were collected at several depths in the three holes for mineralogical, geochemical, and biological analysis. They were fixed in situ with formaldehyde to maintain them until biological laboratory analyses were developed. Several types of fresh growth media were inoculated with samples from different depths in the field for microbial enrichment. The mineralogy of the core samples was analyzed by XRD, FTIR, petrographic microscope, and SEM.

Laboratory Analysis

Core sampling for further laboratory analyses was performed in all 3 cores, starting at 50 cm from the surface. Geochemical analysis of selected samples of the melted ice and sediment along the cores was run by ICP- MS Perkin Elmer Elan 9000 and an elemental analyzer LECO CHNS-932. Mineralogical studies were performed with XRD and microscope thin sections analysis.

Dating and correlation with other cores

Samples from cores 11 and 5 were taken for age analysis. The C^{14} dating analyses were done in the Angström Laboratory of Uppsala University (Sweden). Measurements were performed on the sediments after the roots and carbonates were removed. Our analysis indicated that the age of the silt sediment at 2.0 m in the T11 drill site is 11155±75 BP, and 12705±90 BP at the bottom of the core (3.6 m). We found that the T0 core ages are 13450±100 at 1.5 m and 20250±225 years BP at 2 m depth.

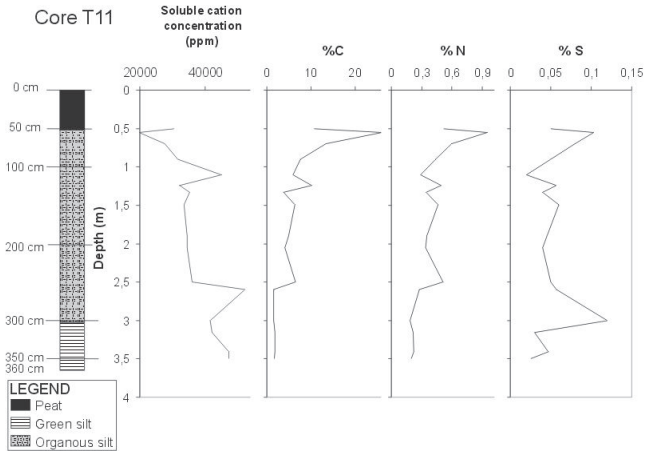

Figure 4. Lithology and distribution of soluble cation concentration, %C, %N, and %S in core T11.

Some other drilling studies, which included C^{14} dating analysis, are available in the bibliography. All of the cores in our study were obtained from the lake floor. Colinvaux (1964) reported the results from some cores, named cores I and V, made in Imuruk Lake between the east shore and the Gull Islands. Core I is the more relevant and longest one (8 m long). It consists of layers of mud from the weathering of the volcanic rocks, as well as sand layers that were transported from the beach in low-water-level episodes of the lake. The mud layers are enriched with montmorillonite and kaolinite. Dating of this core was problematic because: (a) two of the youngest dates were measured near the core base (probably due to tectonics), and (b) there are some gaps in the sediment record (possible erosion occurred during the lower-water-level episodes). Later revisions of the core data were done by Colbaugh (1968), Shackleton (1982), and Hamilton (1991) to constrain the climatic events that occurred in the area. Marino (1977) studied the paleomagnetism of the cores. It is worth noting that no detailed petrologic descriptions of the core sections are published, so we are unable to correlate the cores we collected with any others.

Geochemistry.

In cold areas, the mineralogy of the sediment is made up of many chemical elements, though some soluble ions are commonly removed or concentrated, depending on the availability of liquid water (Chegue-Goff & Fyfe 1997, Kokelj & Burn 2003, 2005). These soluble elements can indicate the depth of the active layer of the permafrost. CHNS elemental analysis is useful for delimiting the peat and organic-rich layers in the sediment cores. The entire core T5 is peat, with a carbon content that ranged from 34.7 to 40.9 %. In core T11, the concentration of carbon had a maximum peak of 26% at 0.55 m, though it decreased with depth. The peat should end at 0.6 m. The silt from 0.6 to 2.5 had an average of 7% C, and from 2.5 to 3.6 m, the green silt had an average of 1.6% C (Fig. 4). Samples taken from below the T0 core (Fig. 5) had a very low carbon concentration, except

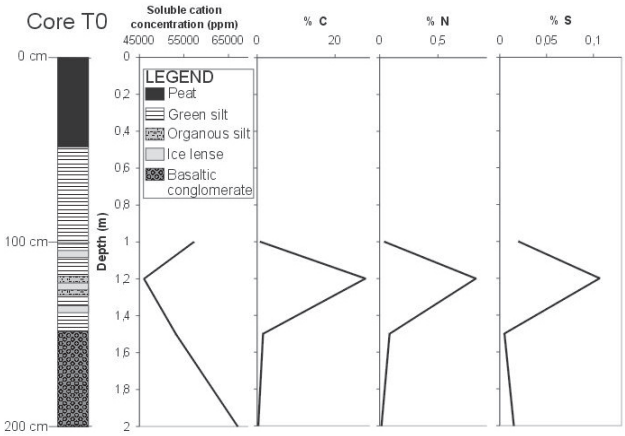

Figure 5. Lithology and distribution of soluble cation concentration, %C, %N, and %S in Core T0.

in a thin layer at 1.2 m. In the three cores, the trend of H, N, and S are well correlated to C, except for S in core T11, where there was a positive anomaly at 3 m.

Soluble cations (Na, Mg, Ca, K) are good indicators of permafrost active layer fluctuation. These elements are mobilized when liquid water is present and they are concentrated above the ice table (Fig. 4 and 5). Note the lack of data from the upper centimeters of the T11 and T0 cores. The T11 core data showed a positive anomaly at 1.1 m and 2.6 m. The anomaly at 1.1 m is mostly due to Na and K, which are probably related to an enrichment of feldspars in the sediment. In the 2.6 m anomaly, the presence of all four cations in the mineralogy of the silt contributed to the change. The T0 core was found to be enriched in Ca and Mg in the upper part, and there was a negative anomaly at 1.2 m due to the organic rich and clean ice water layers at this level. The total content of cations increased at the bottom of the core as a result of the presence of K and Na in the feldspars and clays.

Biology

In situ hybridization techniques were used to document the distribution of targeted microorganisms in the study area. Samples were fixed in the field with formaldehyde (4% v/v) and refrigerated for 2 h. After incubation, samples were washed twice with PBS and filtered. Filters were stored under frozen conditions in PBS-ethanol (1:1). Samples from several depths were chosen for further study with different DNA-specific probes. Cell counts were measured using the optical microscope.

The abundance of cells per mg of sample was analyzed in the first 60–70 cm of the column (the permafrost active layer). Elemental chemical analyses determined an active layer of 50–70 cm (according to the microbiological studies; see Gomez et al. 2008).

Hybridization with DNA-specific probes determined a high presence of bacteria in the upper part of the T11 column. In contrast, lower concentrations of active cells of bacteria were found deeper in the sample. From 2.1 m to 3.6 m depth, we found that the Archaea were the most abundant cell types in the samples.

Discussion

Our ERT survey in the Imuruk Lake area revealed the occurrence of two units: an upper low-resistivity unit that consists of peat and silt with unfrozen water, which was vertically heterogeneous due to the structure of the polygonal terrains; and a lower unit of higher resistivity, which was found associated with the development of permafrost in silt materials. Variations in resistivity in this lower unit revealed that permafrost in the southern part has a higher content of liquid water that decreased in thickness towards the central part of the study area, where the base could be located at around 6 m depth. In contrast, we found that permafrost in the northern zone contains a lesser volume of liquid water and/or reaches a greater thickness. Geophysical sounding by ERT or GPR (Corbel et al. 2006) could be useful in a planetary mission for mapping the stratigraphy, structure, and position of ice-rich permafrost on Mars before deploying the complex instrumentation needed to drill on Mars.

When ice-rich permafrost is drilled on Mars, in situ analyses should (a) confirm the presence of the liquid phase and its movements, for example, by following the salts; (b) characterize the environment, for example, by recording the temperature and pH; and (c) search for biosignatures. Mineral analysis would reveal elements that might be used by some microorganisms. The changes in the oxidation state of the elements and the pH of the liquid phase would affect the state of the organic matter (Vogt & Larqué 2002). The secondary mineralogy that would result from this type of interaction could be detected by space missions, and might indicate the presence of life. Microbial activity may be traced by direct or indirect fingerprints on the minerals. Mineral biosignatures may be distinguished by textural and chemical changes due to dissolution and the growing kinetics variation shifted by metabolism, such as the formation of nanometric particles of iron oxyhydroxides during the iron-oxidizing bacterial enzymatic catalysis, or the reorganization of mineral paragenesis when equilibrium is perturbed biologically.

Given the thermal stability of permafrost (at temperatures less than 0ºC), such a deposit could harbor extinct organisms. Living organisms could thrive if they are able to extend the adaptation processes because of the slower metabolism at low temperatures. However, sudden changes of activity due to the seasonal melting of ice could occur inside the active layer of the permafrost. The metabolic state and the biochemistry of permafrost organisms have not been well studied to date. Microorganisms living in the permafrost could survive frozen during long periods of time (Gilichinsky et al. 2007) and could be activated instantaneously as indicated by some biogeochemical manifestations (for instance, enzymes suddenly working, presence of metastable iron sulfides and nitrates, or lipids, protein, and ADN synthesis) (Rivkina et al. 2004, Vorobyova et al. 1997). Moreover, the study of biosignature preservation in permafrost environments will reveal whether they might be useful places to search for evidence of life in future missions to Mars.

Conclusions

We are studying the permafrost in the Imuruk Lake volcanic field area (Alaska) from an astrobiological perspective. Terrestrial permafrost is an essential reference for potential habitable environments on Mars.

Studies like this will help guide future planetary explorations and guide the interpretation of their data by providing directions on how to (1) develop new instrumentation for detecting and mapping the permafrost on Mars; the current or ancient (but now frozen) active layer could be search with geophysical methods such as the ERT used in this study, though more fieldwork is needed to be capable of interpreting data from Mars; (2) define preservation patterns of biosignatures in cold environments that may be used in future missions; and (3) develop new instrumentation for detecting life, in situ and remotely. The extreme environment in which this kind of work was accomplished entails a suitable testbed for developing robust and effective techniques that warranty the success of the mission.

Acknowledgments

We would like to thank to Jeffrey S. Kargel, the U.S. National Park Bering Land Preserve, Rosalyn Grimes, NASA-JPL, Juan Perez-Mercader, and INTA for the support.

References

Chegue-Goff, C. & Fyfe, W.S. 1997. Effect of the permafrost on geochemistry in a Canadian peat plateau bog. *Applied Geochem*. 12: 465-472.

Colbaugh, P.R. 1968. *The environment of the Imuruk Lake area, Seward Peninsula, Alaska during Wisconsin time.* Masters thesis. Dept. of Zoology, Ohio State University, Columbus.

Colinvaux, P.A. 1964. Environment of Bering land bridge. *Ecological Monographs* 34: 297-329.

Comas, X. & Slater, L. 2004. Low-frequency electrical properties of peat. *Water Resources Res.* 40: W12414.

Corbel, C. et al. 2006. WISDOM: An UHF GPR on the Exomars Mission. *Eos Trans. AGU* 87(52): P51D-1218.

Clifford, S.M. & Parker, T.J. 2001. The evolution of the Martian hydrosphere: Implications for the fate of a primordial ocean and the current state of the northern plains. *Icarus* 154: 40-79.

Feldman, W.C. et al. 2002. Global distribution of neutrons from Mars: Results from Mars Odyssey. *Science* 297: 75-78.

Gilichinsky, D.A. et al. 2007 Microbial Populations in Antarctic Permafrost: Biodiversity, State, Age, and Implication for Astrobiology. *Astrobiol.* 7*:* 275-311.

Gomez et al. 2004. UV radiation effects over microorganisms and study of protective agents. *ESA SP*-545: 21-25.

Gomez, F. et al. 2008. Microbial diversity in a permafrost environment of a volcanic-sedimentary Mars analog: Imuruk Lake, Alaska *Proceedings of the Ninth International Conference on Permafrost, Fairbanks, Alaska, June 29–July 3, 2008* (this proceedings).

Hamilton, T.D. & Brigham-Grette, J. 1991. The last interglaciacion in Alaska: Stratigraphy and paleoecology of potential sites. *Quat. Int*. 10–12: 49-71.

Hauck, C. & Mühll, V.D. 2003. Inversion and interpretation of two-dimensional geoelectrical measurements for detecting permafrost in mountainous regions. *Permafrost and Periglac. Process*. 14: 305-318.

Hopkins, D.M. 1963. Geology of Imuruk Lake area, Seaward Peninsula, Alaska. *USGS Bulletin 1141*-C, 98 pp.

Kneisel, C. 2004. New insights into mountain permafrost occurrence and characteristics in glacier forefields at high altitude through the application of 2D resistivity imaging. *Permafrost and Periglac. Process.* 15: 221-227.

Kokelj, S.V. & Burn, C.R. 2003 Ground ice and soluble cations in near-surface permafrost, Inuvik, Northwest Territories, Canada. *Permafrost and Periglac. Process.* 14: 275-289.

Kokelj, S.V. & Burn, C.R. 2005. Geochemistry of the active layer and near-surface permafrost, Mackenzie delta region, Northwest Territories, Canada. *Canadian J. of Earth Sci*. 42: 37-48.

Marino, R.J. 1977. *Paleomagnetism of two lake sediment cores from Seaward Peninsula, Alaska.* M.S. Thesis, Ohio State Univ., 183 pp.

Mellon, M.T. et al. 2004. The presence and stability of ground ice in the southern hemisphere of Mars. *Icarus* 169(2): 324-340.

Péwé, T.L. 1975. Quaternary geology of Alaska. *Geological Survey Prof. Paper* 835.

Reynolds, J.M. 1997. *An Introduction to Applied and Environmental Geophysics.* John Wiley and Sons, 796 pp.

Rivkina et al. 2004. Microbial life in permafrost. Space life sciences: Search for signatures of life, and space flight environmental effects on the nervous system. *Advances in Space Research* 33(8): 1215-1221.

Sasaki, Y. 1992. Resolution of resistivity tomography inferred from numerical-simulation. *Geophys. Prospecting* 40: 453-463.

Smith, H.D. & McKay, C.P. 2005. Drilling in ancient permafrost on Mars for evidence of a second genesis of life. *Planet. and Space science* 53(12): 1302-1308.

Shotwell, R. 2005. Phoenix –the first Mars Scout mission. *Acta Astronautica* 57: 121-134.

Squyres, S.W. et al. 1992. In: H.H. Kieffer (ed.), *Mars*. University of Arizona Press.

Šumanovac, F. 2006. Mapping of thin sandy aquifers by using high resolution reflection seismics and 2D electrical tomography. *J. Appl. Geophys.* 58: 144-157.

Shackleton, J. 1982. Paleoenvironmental histories from Whitefish and Imuruk lakes, Seaward Peninsula, Alaska. *Inst. Polar Studies Report* 76.

Vogt, T. & Larqué, P. 2002. Clays and secondary minerals as permafrost indicators: examples from the circum-Baikal region. *Quaternary Internat.* 95-6: 175-187.

Vorobyova, E. et al. 1997. The deep cold biosphere: facts and hypothesis. *FEMS Microbiol. Rev.* 20: 277-290.

Telford, W.M. et al. 1990. *Applied Geophysics*. Cambridge University Press, 770 pp.

What Dictates the Occurrence of Zero Curtain Effect?

Jaakko Putkonen
Department of Earth and Space Sciences, University of Washington, Seattle, WA 98195, USA.

Abstract

Zero curtain effect refers to the persistence of ground temperatures at or close to 0°C during annual ground freezing or thawing. This phenomenon is related to both active layer underlain by permafrost and seasonally frozen ground. Zero curtain effect in the permafrost areas is traditionally contributed to the ground water freezing in the fall and resulting release of the latent heat. If the phase change of water to ice or vice versa is the primary reason then the zero curtain should be found in the fall and spring in both the active layer and seasonally frozen soils, which is not the case. Through thermal modeling it is shown that the annual evolution of the subsurface thermal field leads into the establishment of isothermal soil near 0°C between two phase change fronts only in special cases. The modeled occurrence and timing of zero curtain effect corresponds well with the observations.

Keywords: active layer; ground ice; permafrost; thermal modeling; unfrozen water; zero curtain.

Introduction

Zero curtain is defined in the *Glossary of Permafrost and Related Ground-ice Terms* as the persistence of a nearly constant temperature, very close to the freezing point, during annual freezing (and occasionally during thawing) of the active layer (van Everdingen 2005). Outcalt et al. (1990) provide a good history of the definition and related research, and a suggestion of the correct usage of the term which is followed here.

Figure 1A shows prominently the modeled zero curtain in the fall that is a characteristic feature of active layer annual thermal regime and has important implications to water migration in soil and related ice lensing and frost heave (e.g., Hallet et al. 2004). For good examples of zero curtain in natural soils see Washburn (1979, Figure 3.34) and French (1996, Figure 4.5). This phenomenon is explained to result of the latent heat that is released through the phase change of water into ice (Washburn 1979, Williams & Smith 1991, French 1996, Osterkamp & Romanovsky 1997, van Everdingen 2005). A careful examination of the evolution and maintenance of the zero curtain has revealed mass and heat fluxes in the forms of water and vapor in some cases (Hinkel et al. 1990, Outcalt et al. 1990, Hinkel & Outcalt 1994) and only heat conduction and phase change in others (e.g., Osterkamp & Romanovsky 1997).

The release of latent heat through freezing of water is generally found to be the primary explanation for the occurrence of the zero curtain effect that is often seen in the fall in the thermal record of active layer underlain by permafrost. Therefore it is intriguing that those same thermal records often show no zero curtain in the spring, when the same amount of soil ice melts. Simplistically one would expect to see approximately similar zero curtain in the spring as is seen in the fall at a given field site. Yet, typical field observations show active layer temperatures at any given level in the soil to cross 0°C in the spring at a steady rate. This is also well represented in Figure 1B.

No clear explanation has been given in the literature for the intriguing lack of the zero curtain in the spring in the permafrost areas or the intriguing reversal of zero curtain effect occurring in the spring and no zero curtain effect in the fall in seasonally frozen ground.

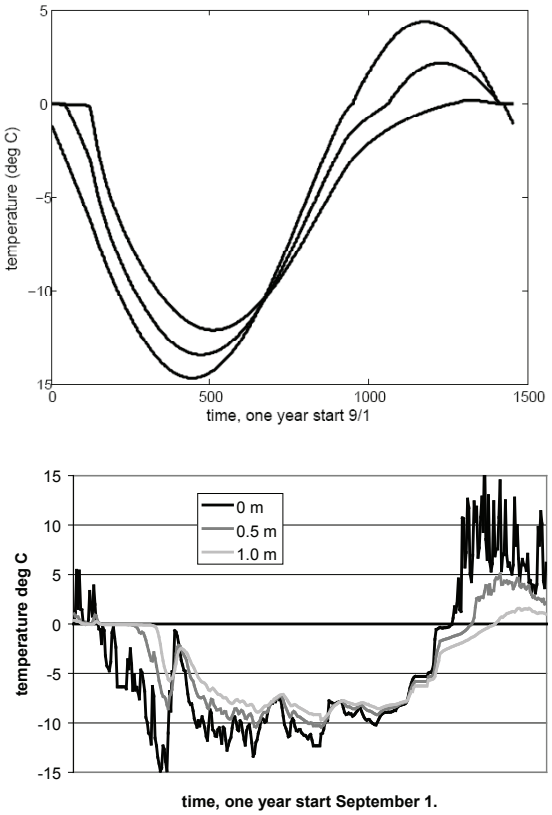

Figure 1. A. Modeled soil temperatures over one year at 0.1 (largest amplitude), 0.5, and 1.0 m (smallest amplitude) below ground surface. Mean annual temperature of the surface forcing is -5°C. B. Measured soil temperatures over one year at a field site in Spistbergen (Putkonen, 1997). Note prominent zero curtain in the fall in both model and observations and the lack of zero curtain in the spring.

This apparent contradiction between observations and the simplistic phase change governed explanation motivated the analyses that are presented here.

The purpose of this paper is not to model or explain all the possible soil thermal processes such as non-conductive heat transfer that potentially contribute to the maintenance and longevity of the zero degree curtain. However, the objective of this analysis is to provide a clear explanation for the characteristic occurrence (fall or spring) of the zero curtain effect and the intriguing contrast in timing of zero curtain effect between permafrost and seasonally frozen soils.

It is suggested here that the occurrence of zero curtain is primarily controlled by the soil thermal regime rather than just the existence of the water or ice and related phase change at or near 0°C. In the case of the soil that is underlain by permafrost where the mean annual soil temperature is below 0°C, the time lag in the penetration of the annual thermal wave into the soil will make the soil almost isothermal close to 0°C at the beginning of the fall freeze up regardless of the water content. Because of the almost vanishing thermal gradient at shallow subsurface (~0.5 m), and the presence of water in the soil, the temperatures are changing only near the surface and at depth. This explains why the soil is retained for a prolonged period at the 0°C. On the other hand, in the spring the time lag in the penetration of the annual surface thermal wave enhances the steepness of the thermal gradient near 0°C, the isothermal soil domain is too cold to be affected by phase change of ice to water, and therefore the energy is effectively transferred through the whole soil column. This results in slow but steady temperature increase at all levels in the soil. Therefore the soil temperatures increase at a steady rate through the spring at all levels without any significant slowing in the warming rate at or near 0°C.

In some instances the soil surface temperature may be held at 0°C for weeks due to the melting of the snow and resulting ice/water bath at soil surface. However, this will only modify the driving temperature and potentially slow the overall warming of the soil, but it will not result in zero curtain effect.

The above suggestion that the occurrence of zero curtain effect is dictated by the annual evolution of the soil thermal profile leads to three robust and testable predictions: 1) in soils that are underlain by permafrost and where mean annual soil temperature is <0°C, the zero curtain effect occurs in the fall and there is no significant zero curtain effect in the spring, 2) in areas of seasonally frozen ground (mean annual soil temperature >0°C) the zero curtain effect occurs in the spring rather than in the fall and remarkably there should be no significant zero curtain effect in the fall, and 3) in the areas where the mean annual soil surface temperature is close to 0°C, there should be a short and weak zero curtain effect at both fall and spring.

To study the annual evolution of the thermal regime of soil that contains ice and water, a soil thermal model is used. Finally the model results are qualitatively compared to representative soil temperatures from three field sites that correspond to the above mentioned three soil thermal regimes.

Soil Thermal Model

A one-dimensional thermal model (Putkonen 1998, Putkonen et al. 2003, Putkonen & Roe 2003) is used where soil heat flux (Eq. 1), q is given as

$$q = k\frac{dT}{dx} \tag{1}$$

where k is thermal conductivity [W/m K], and dT is the temperature difference [K] at two points separated by dx, the distance in x direction [m]. When the soil heat flux (Eq. 1) is combined with an expression for the conservation of energy, they lead to the differential equation that describes the time dependent soil thermal evolution (Eq. 2)

$$\frac{dT}{dt} = \frac{dq}{dx} \tag{2}$$

where dt is time difference [s]. This leads to the general formulation of thermal diffusion (Eq. 3):

$$\frac{dT}{dt} = K\left(\frac{d^2T}{dx^2}\right) - dT \cdot LE\left(V_{ufwater}\left(T_{t=t-1}\right) - V_{ufwater}\left(T_{t=t}\right)\right) \tag{3}$$

where $V_{ufwater}(T_{t=t-1})$ is the volume of unfrozen water [kg/m^3] at the temperature $T_{t=t-1}$ [K] at the time step t = t − 1, and K (Greek Kappa) is the thermal diffusivity [m^2/s].

In the model the phase change of water is distributed over a wide temperature range rather than occurring sharply at 0°C. This formulation is based on direct determination of unfrozen water content of a representative frozen soil sample at varying temperatures (Putkonen 1997). The initial soil water content is 295 kg/m^3.

To achieve maximum clarity in the model results the soil surface temperature is forced by a simple sinusoidal thermal wave with annual amplitude of 20°C. The initial soil thermal state is generated by running the model with five consecutively repeated annual cycles that carry over the soil moisture and temperatures from the end of previous year to the beginning of the following. After this initializing sequence the maximum difference between soil temperatures at the end of model years 4 and 5 is less than 0.02°C.

The lower boundary condition in the model is adiabatic (no flux across the boundary) at 20 m below ground surface where the initial temperature is the mean of the annual surface forcing (-5°C, 5°C, or 0°C depending on the case).

Soil thermal properties and surface thermal forcing that are used in the model are representative of general permafrost soils and are inspired by actual measurements at a field site in Spitsbergen (Putkonen 1997). However, these model runs do not attempt to reproduce any actual observations. The

mean annual temperature of the forcing corresponds to the three climatic cases.

Soil thermal conductivity of a frozen soil with all water frozen is 3.0 W/m K; thawed soil thermal conductivity is 2.6 W/m K. The frozen soil thermal conductivity that contains unfrozen water scales between the completely frozen and completely thawed stages with the unfrozen water content. The thermal conductivity of the bedrock is 5.0 W/m K. The heat capacity of the soil mineral matter is 1.7×10^6 J/m^3 K. The heat capacities of water and ice are 4.18×10^6 J/m^3 K and 1.92×10^6 J/m^3 K respectively. The soil bulk heat capacity is a sum of the constituent heat capacities and therefore varies continuously as the water is freezing or thawing in the soil.

The internal consistency of the thermal model was tested by contrasting the modeled soil surface heat flow over a given time period (W/m^2) against the energy involved in the water phase change and soil temperature change. These two independent calculations of the soil energy were within 2% of one and other. This is probably as close as a finite difference formulation can be expected to be.

Results

As shown in Figure 1A, the model reproduces the zero curtain effect in the fall and does not reproduce a zero curtain effect in the spring exactly as reported for typical active layer underlain by permafrost (Washburn 1979, Williams & Smith 1991, French 1996). This same pattern is also seen in the field data obtained in Spitsbergen (Putkonen 1997) and shown for comparison in Figure 1B.

When the same model is run for the seasonally frozen ground (mean annual soil temperatures >0°C) a zero curtain effect is seen only in the spring (Figure 2A), which is also seen in the field data. And finally when the model is run for the case where mean annual soil temperature is exactly 0°C, short and weak zero curtain effect is seen both in the spring and fall (Figure 3A).

Discussion

It is counterintuitive that the soil temperatures from a given field site show a distinct zero curtain in the fall (Fig. 1, mean annual soil temperature is -5°C) and no zero curtain in the spring, although same amount of water is freezing in the fall as ice is melting in the spring. To illustrate the reasons for this phenomenon it is useful to consider the soil thermal gradient and the annual evolution of the soil vertical thermal profile (temperature vs. depth below surface).

It is well known that the original amplitude of the thermal wave at the soil surface decreases as it penetrates into the soil and that there is a time lag that increases with depth for a thermal perturbation to travel into the soil (e.g., Turcotte & Schubert 1982). For those reasons the soil thermal gradient in the spring when the surface starts to thaw is almost constant, which makes the soil temperatures at all levels to increase slowly but at steady rate (Fig. 4). Even though the ice is melting in the soil no sections of the soil profile remain persistently at or near 0°C.

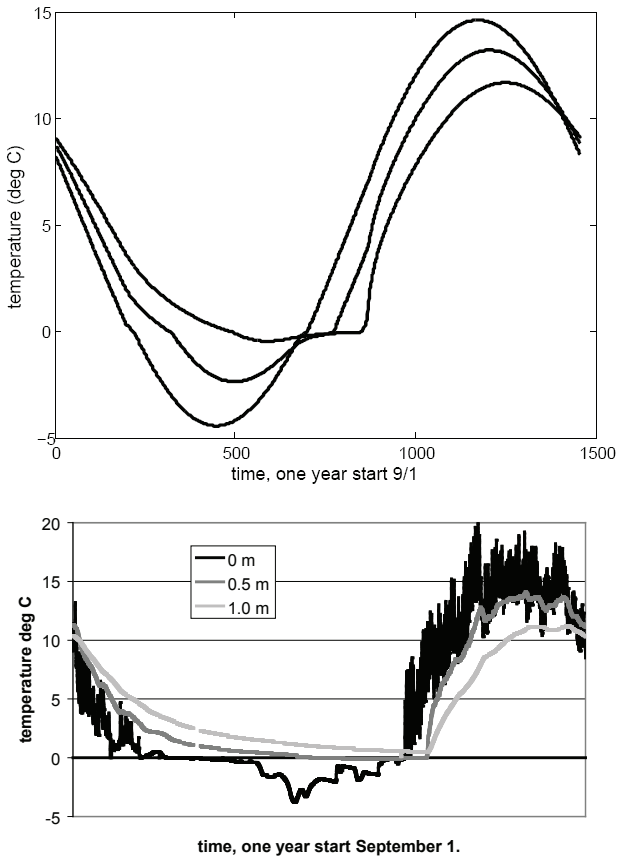

Figure 2. A. Modeled soil temperatures over one year at 0.1, (largest amplitude) 0.5, and 1.0 m (smallest amplitude) below ground surface. Mean annual temperature of the surface forcing is 5°C. B. Measured soil temperatures over one year at the Bonanza Creek Experimental Forest's primary upland weather station LTER1 (Hollingsworth et al. 2005). Note prominent zero curtain in the spring in both model and observations and the lack of zero curtain in the fall.

In the fall the soil temperatures between about 0.5–1.0 m below surface are above freezing but already close to 0°C. A moderate amount of cooling at the surface and at the depth below 1.0 m suffices to bring the soil temperatures to freezing point in the layer 0.5–1.0 m below surface. At that point the thermal gradient in this middle layer approaches 0°C/m and consequently the temperature in that domain do not change until a thermal gradient is re-established.

For these reasons it is clear that two conditions have to be met for the zero curtain to develop in the soil: 1) the active layer has to contain ice or water, and 2) the thermal gradient in the soil has to become 0°C/m at or near 0°C.

Since water and ice are common in the natural soils the soil thermal gradient near 0°C appears to dictate the timing and presence of zero curtain effect.

Although present at some field areas, the non-conductive heat transfer processes (Outcalt et al. 1990) do not appear to be necessary for the zero curtain effect to develop because the zero curtain effect is seen both at the sites without non-conductive heat transfer and it is also well developed in the model without non-conductive heat transfer.

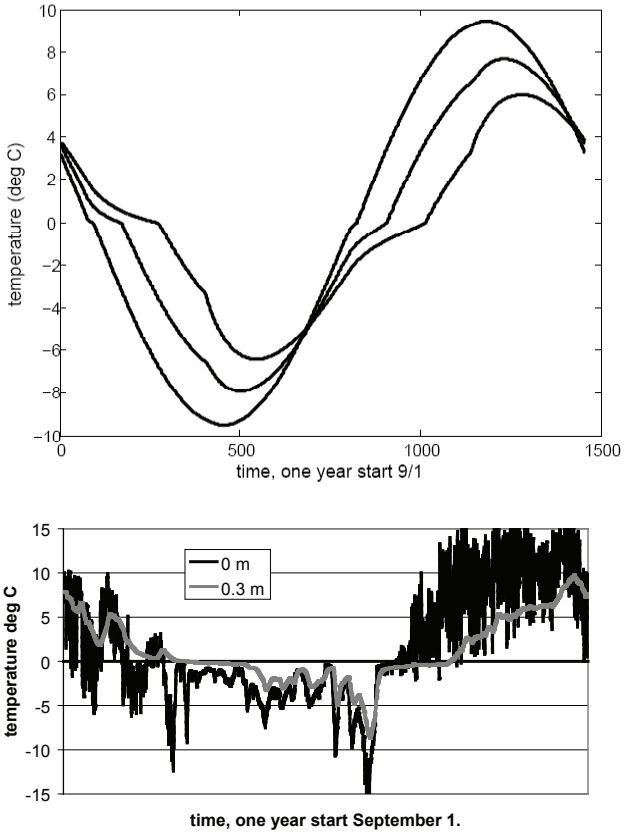

Figure 3. A. Modeled soil temperatures over one year at 0.1, (largest amplitude) 0.5, and 1.0 m (smallest amplitude) below ground surface. Mean annual temperature of the surface forcing is 0°C. B. Measured soil temperatures over one year at the USDA SCAN site #2065, Aniak, AK, USA (USDA, 2007). Note the absence of the zero curtain in the fall and spring in both model and observations.

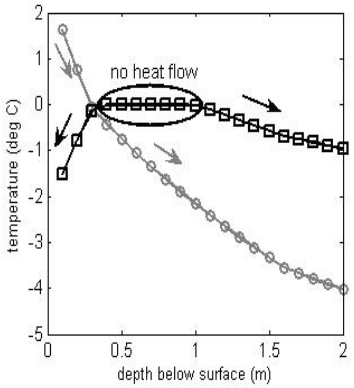

Figure 4. Modeled soil vertical thermal profiles for spring (gray) and fall (black) for a soil with mean annual thermal forcing of -5°C. The segment of the profile marked with black oval represents the zero curtain. As is illustrated by the spring (gray) profile the presence of significant thermal gradient at this time ensures that all levels of the soil are warming in concert and zero curtain can not develop. In the fall the soil at 0.5–1.0 m below surface quickly reaches freezing point and the thermal gradient vanishes. Therefore no heat flows through this segment of soil and the temperatures remain at or near 0°C until all the water has frozen. The black and gray arrows show the direction of heat flow during fall and spring respectively.

Two phase change boundaries in close proximity bracket the domain of the soil where zero curtain effect is seen (Osterkamp & Romanovsky 1997). However, as shown in this paper the first order explanation for both the presence of the two phase change boundaries, and the zero curtain effect is the annual evolution of the soil thermal profile which clearly predicts the timing (fall and/or spring) of the zero curtain effect.

When soil temperatures from real field sites are studied it is important to keep in mind that seasonal snow cover may affect the soil thermal forcing and render the annual soil surface temperature cycle significantly different from the modeled sinusoidal annual thermal wave.

Conclusions

If zero curtain effect was caused only by release or consumption of the latent heat in the soil then there should be symmetrically a zero curtain both in the fall and spring. Or at the least there should be a zero curtain effect present in the fall in both permafrost underlain and seasonally frozen soil which is not the case.

For the clear conceptual description of the occurrence of the zero curtain effect let's assume that the soil surface thermal forcing follows a simple sinusoidal pattern that repeats itself in the annual time scale. When the forcing temperature at the soil surface crosses 0°C and approaches the mean annual soil temperature, the near surface soil thermal profile becomes inverted and a section of the soil just below it becomes nearly isothermal near 0°C. Two separate phase change fronts develop in the soil as pointed out by Osterkamp & Romanovsky (1997). The soil domain in between of the two phase change fronts quickly approaches 0°C and the zero curtain effect develops. However, when the forcing temperature at the soil surface crosses 0°C again approximately six months later in the following transitional season (either spring or fall depending on the case) and diverges further from the mean annual soil temperature, the near surface soil temperature inversion underlain by a nearly isothermal soil domain develop again, but at this time the isothermal soil is thermally far from 0°C and no phase change is present. Without phase change the isothermal soil quickly develops a monotonic thermal gradient and consequently only one phase change front develops. Therefore no zero curtain effect is present.

The above explanation highlights the importance of the soil thermal regime and annual thermal evolution in determining the timing and occurrence of the zero curtain effect. The phase change of water to ice or vice versa is necessary as well but it fails to explain the timing and the lack of zero curtain effect in fall in seasonally frozen soil.

It is also important to notice that the zero curtain is not only limited to condition where water is freezing (fall). In the case of seasonally frozen ground (mean annual soil temperature >0°C), the zero curtain appears in the spring when the soil ice is melting.

Acknowledgments

The author is grateful to the dynamic group of colleagues in the Quaternary Research Center, University of Washington, who have stimulated innovative research over the years. The manuscript was improved by the comments of two anonymous reviewers and an associate editor.

References

French, H.M. 1996. *The periglacial environment.* Harlow: Addison Wesley Longman Limited, 341 pp.

Hallet, B., Putkonen, J., Sletten, R. & Potter, N., Jr. 2004. Permafrost process research in the United States since 1960. In: A.R. Gillespie, S.C. Porter & B.F. Atwater (eds.), *The Quaternary period in the United States.* San Francisco: Elsevier, 584 pp.

Hinkel, K.M. & Outcalt, S.I. 1994. Identification of heat-transfer processes during soil cooling, freezing, and thaw in Central Alaska. *Permafrost and Periglacial Processes* 5: 217-235.

Hinkel, K.M., Outcalt, S.I. & Nelson, F.E. 1990. Temperature variation and apparent thermal diffusivity in the refreezing active layer, Toolik Lake, Alaska. *Permafrost and Periglacial Processes* 1: 265-274.

Hollingsworth, J., Downing, J. & Charlton, B. 2005. *BNZ-LTER Data Catalog, Bonanza Creek Experimental Forest: Hourly Soil Temperature at varying depths from 1988 to Present.* http://www.lter.uaf.edu/.

Osterkamp, T. & Romanovsky, V. 1997. Freezing of the Active Layer on the Coastal Plain of the Alaskan Arctic. *Permafrost and Periglacial Processes* 8: 23-44.

Outcalt, S.I., Nelson, F.E. & Hinkel, K.M. 1990. The Zero-curtain effect: Heat and mass transfer across an isothermal region in freezing soil. *Water Resources Research* 26(7): 1509-1516.

Putkonen, J. 1997. *Climatic control of the thermal regime of permafrost, northwest Spitsbergen*. Ph.D Dissertation Thesis. Seattle: University of Washington, 121 pp.

Putkonen, J., Sletten, R.S. & Hallet, B. 2003. Atmosphere/ice energy exchange through thin debris cover in Beacon Valley, Antarctica. In: M. Phillips, S.M. Springman & L.U. Arenson (eds.), *Eighth International Conference on Permafrost, Zurich, Switzerland, July 21–25, 2003*. Zurich, Switzerland: Swiss Federal Institute for Snow and Avalanche Research, Davos, Switzerland (CHE), 913-915.

Putkonen, J.K. 1998. Soil thermal properties and heat transfer processes near Ny Alesund, Northwestern Spitsbergen, Svalbard. *Polar Research* 17: 165-179.

Putkonen, J.K. & Roe, G. 2003. Rain on snow events impact soil temperatures and affect ungulate survival. *Geophysical Research Letters* 30(4): 200-204.

Turcotte, D.L. & Schubert, G. 1982. *Geodynamics, Applications of Continuum Physics to Geological Problems.* New York: John Wiley & Sons, 450 pp.

USDA, 2007. USDA, Soil Climate Analysis Network (SCAN) web page. http://www.wcc.nrcs.usda.gov/scan/.

van Everdingen, R. (ed.), 2005. *Multi-language glossary of permafrost and related ground-ice terms.* Boulder, CO: National Snow and Ice Data Center/World Data Center for Glaciology.

Washburn, A.L. 1979. *Geocryology: A survey of periglacial processes and environments.* Norwich: Fletcher & Sons Ltd, 406 pp.

Williams, P.J. & Smith, M.W. 1991. *The Frozen Earth: Fundamentals of Geocryology*. Oxford: Alden Press, 306 pp.

Definition of Warm Permafrost Based on Mechanical Properties of Frozen Soil

Jilin Qi
State Key Laboratory of Frozen Soil Engineering, Cold and Arid Regions Environmental and Engineering Research Institute, Chinese Academy of Sciences, 320 Donggang West Road, Lanzhou 730000, China
Jianming Zhang
State Key Laboratory of Frozen Soil Engineering, Cold and Arid Regions Environmental and Engineering Research Institute, Chinese Academy of Sciences, 320 Donggang West Road, Lanzhou 730000, China

Abstract

This paper attempts to give a definition of "warm frozen soil" according to the mechanical behavior of frozen soils with K_0 compression. K_0 compression tests were carried out on ice-rich frozen silty clay to investigate its straining properties. Three groups of samples were tested, with ice contents of 40%, 80% and 120%, respectively. The samples were compressed under a constant load and with stepped temperature rising from about -1.5°C to -0.3°C. Strain rates at different temperatures were examined. It was found that the strain rate at around -0.6°C increased abruptly. At the same time, strain rates under temperatures higher than -0.6°C were not as temperature-sensitive as was generally understood. Analysis of compressive coefficients was made on the data both from our own testing program and from the literature, which showed that at about -1°C was a turning point in the compressive coefficient against temperature. Based on both our work and taking into account the unfrozen water content vs. temperature, the range of -1°C to -0.5°C seems to be the temperature where the mechanical properties change greatly. For convenience, -1.0°C can be defined as the boundary for warm frozen soils.

Keywords: compressive coefficient; K_0 compression; strain rate; warm frozen soil.

Introduction

The mechanical properties of soils have been extensively studied in the last century. For unfrozen soils, various strength criteria and constitutive models have been proposed and applied to practice in geotechnical engineering. On the other hand, due to their sensitivity to temperature and ice content, the mechanical properties of frozen soils are more complicated, and many investigations have been carried out to study these properties (Jessberger 1980, Landanyi 1981, Morgenstern 1981, Sayles 1988). However, many of these studies were carried out on frozen soils at relatively low temperatures. When the temperature of frozen soil is close to 0°C, its plastic deformation must also be taken into consideration (Landanyi 1999), especially with high ice contents (Phukan 1983). Monitored temperatures of the soil layers underneath the embankments of the newly built Qinghai-Tibet railway on the Tibetan Plateau show that a warmer frozen zone formed after a certain period of time (Fig. 1). In this case, neither the theories for unfrozen soils nor those for cold frozen soils are suitable for describing the soils' mechanical properties. This kind of frozen soil can be named *warm frozen soil*.

In the literature, the term *warm frozen soil* is often used to describe a frozen soil at a relatively high temperature. However, what "warm" really means has not been clearly and logically defined. It is generally accepted that a warm frozen soil has higher unfrozen water content and therefore has less ability to resist loads and is more temperature-sensitive (Tsytovich, 1975). For these materials, the mechanical properties should be used to define the temperature boundary between "warm" or "cold" frozen soils. Tsytovich (1975) defined temperature boundaries for stiff and plastic frozen soils for different soil classifications according to their failure characteristics, for instance, -0.3, -0.6, -1.0 and -1.5°C for fine sand, silty sand, silty clay, and clay. This is reasonable because the fine grains lower the freezing temperature to a certain degree. However, these definitions are difficult to apply to engineering practice. On the one hand, failure is only the ultimate stage of loading for the safety of engineering constructions. On the other hand, from the point of view of engineering practice, a simple boundary may be convenient for engineers to follow, as long as it is reasonably accepted.

During construction of the Qinghai-Tibet railway on the Qinghai-Tibetan Plateau, a preliminary rule was made where *warm permafrost zone* was defined as the region with a mean annual ground temperature higher than -1°C. This was mainly based on the investigation of damage to embankments of the Qinghai-Tibetan highway. It is a rather geographical definition (Preliminary Regulations for Design of the Qinghai-Tibet Railway in Permafrost Regions, 2002). Where the frozen soil is concerned, it would be more rational to take into account the mechanical properties to define what a warm frozen soil really is. In this field, much confusion can be found from previous studies. For instance, Shields et al. (1985) studied the creep behavior of sand at a temperature between -2.5°C and -3.0°C, and called that warm permafrost. Foster et al. (1991) studied permafrost with a temperature of about -1°C which was regarded as warm permafrost. It is recognized that the term *warm* is a rather relative definition without a clear and reasonable basis.

In this paper, silty clay obtained from the Qinghai-Tibetan plateau along the newly constructed railway was

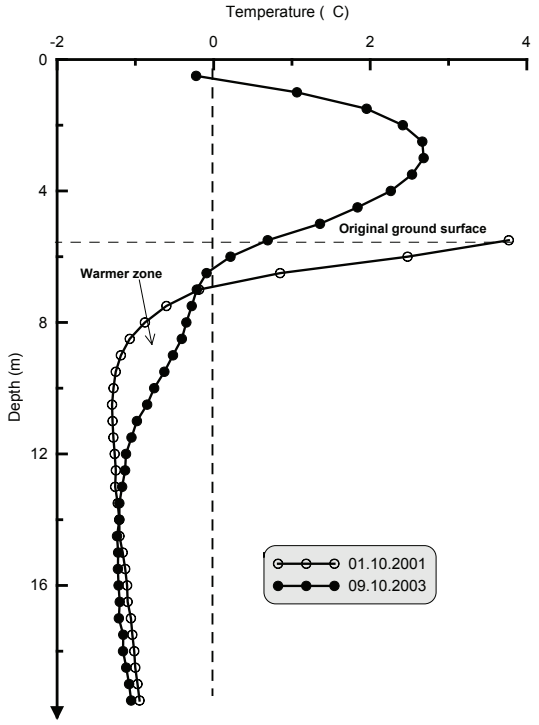

Figure 1. A warmer frozen zone formed in the layers underneath the embankment of the Qinghai-Tibet railway.

studied using K_0 compression under constant load and stepped temperature. The strain rate at each temperature step was studied. Data from the literature on the relationship between the compressive coefficient and temperature were re-analyzed. Based on these two testing programs, the temperature boundary for warm frozen soils as a material will be defined.

Description of the Testing Program

In the study of the mechanical properties of warm frozen soils, the temperature must be controlled precisely. To meet this demand, a new apparatus was designed, where a refrigerator was combined with a fan to control the temperature. An oedometer was placed in the box of the refrigerator for K_0 compression tests, as is shown in Figure 2. From the results, it can be seen that the temperatures could be controlled very well, and temperatures showed only small variations as will be seen in the next section of this paper.

The soil obtained along the Qinghai-Tibet Railway has a plastic limit and liquid limit of 18.8% and 36.5%, respectively. Its grain size distribution is shown in Figure 3. The freezing temperature of the soil is -0.2°C. Soil samples were prepared with ice contents of 40%, 80% and 120%. The dimensions of the samples were 61.8 mm in diameter and 40 mm in height. Loads of 0.1, 0.2 and 0.3 MPa were applied. Altogether 9 tests were carried out on samples with different ice contents and different loads.

The samples were installed in the oedometer and then placed in the refrigerator box. The desired temperature of about -1.5°C in the box was kept constant for 24 h, then

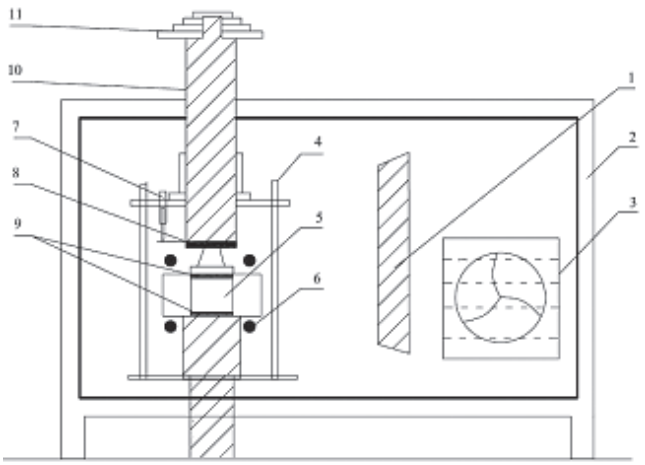

Figure 2. Sketch of the apparatus for precise temperature controlled K_0 testing.

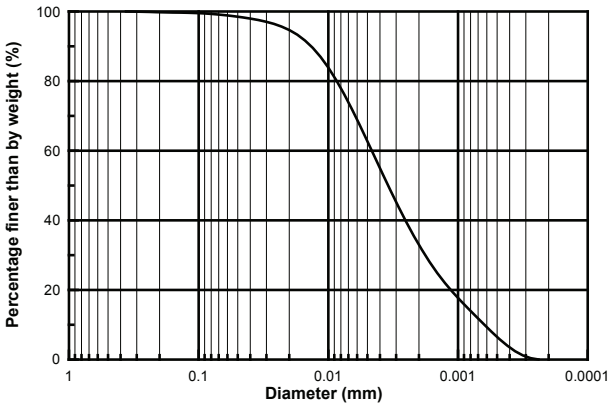

Figure 3. Grain size distribution of the tested soil.

a load was applied to the sample. When the strain became constant, the next higher temperature was adjusted and new strain occurred. In all, 5 temperature steps were applied in each test, approximately -1.5, -1.0, -0.6, -0.5 and -0.3°C.

Test Results and Discussion

Strain rate vs. temperature in this testing program

Figure 4 shows the development of strain against time with change in temperature for the soil with an ice content of 40%. It can be seen that at every step the temperature was controlled quite well, even at higher than -0.5°C. From the three tests shown in Figure 4, it seems that when the temperature rose above a certain value, the strain developed more quickly. This phenomenon was also found in the other 6 tests. In this paper, the strain rate at each temperature step was used for analysis. The strain rate is defined as the inclination of the tangent line at the starting point of the new strain-time curve when the temperature rose to a new step, as is shown in Figure 4 (a).

Five strain rates corresponding to the five temperature steps were obtained from each test, allowing a curve of strain rate against temperature to be plotted. Nine curves were obtained from the 9 tests in the whole program. These are all shown in Figure 5. It can be seen in Figure 5 that the strain rate increased with the increase in temperature up to about -0.6°C, then decreased dramatically. In previous studies it was thought that, with a small increase in temperature, the mechanical properties for the warm frozen soils would change greatly. However, this is not found (see Fig. 4). The strain rates increased again when the temperature rose to about -0.2°C, which was very close to the freezing point of the soil.

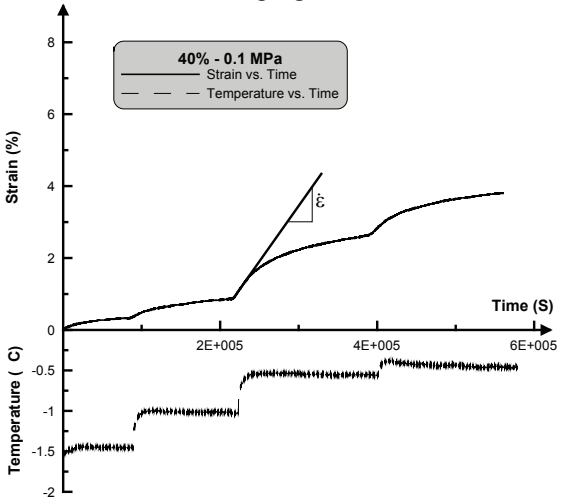

a. Ice content 40% and load of 0.1 MPa.

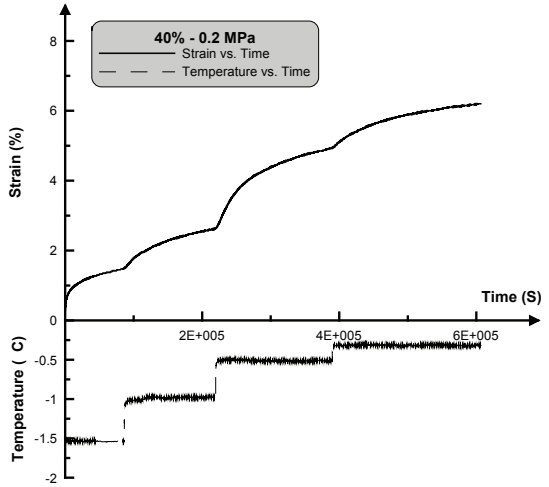

b. Ice content 40% and load of 0.2 MPa.

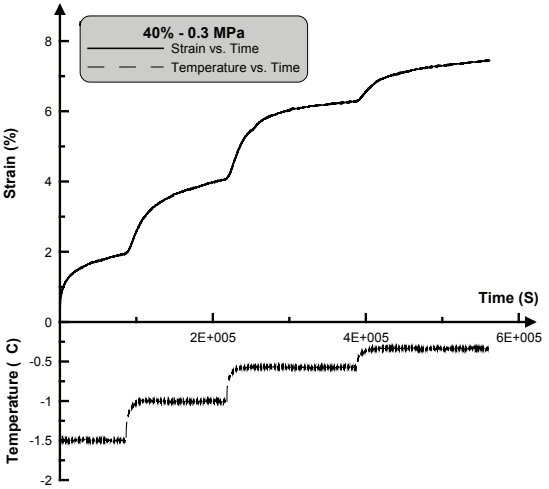

c. Ice content 40% and load of 0.3 MPa.

Figure 4. Temperature change with time and the corresponding strain development for the soil with water content of 40% and loads of 0.1, 0.2, and 0.3 MPa.

It should be pointed out that the data corresponding to the first temperature step (about -1.5°C) were excluded in order to get rid of the influence induced by the experiment setup.

Compressive coefficient

Another mechanical property, the compressive coefficient (C), was examined in this work. This parameter was defined as the ratio of the strain to the corresponding load range by the following formula:

$$C = \frac{\Delta\varepsilon}{\sigma_2 - \sigma_1} \tag{1}$$

In this paper, C is the change in strain when stress increases from 0 to 0.2 MPa. Figure 6 shows that for the soil used in this testing program, C decreases with the decrease in temperature, and -0.6°C seems to be the turning point.

Confined compression of frozen soils was also studied by Zhu et al. (1982). In their testing program, a silty clay from the Qinghai-Tibet plateau and a medium-grained sand from Lanzhou were tested under different temperatures with stepped load. For the silty clay, different water content ranges were also investigated The temperatures investigated were in a relatively wide range from -0.5°C to -7.0°C, and the applied load was up to 0.8 MPa.

The relationship between the compressive coefficient of the silty clay and temperature at different water content range is shown in Figure 7. It can be seen that with the decrease in temperature, the compressive coefficient decreases. The turning points are all near a temperature of about -1°C. The frozen Lanzhou sand showed similar results.

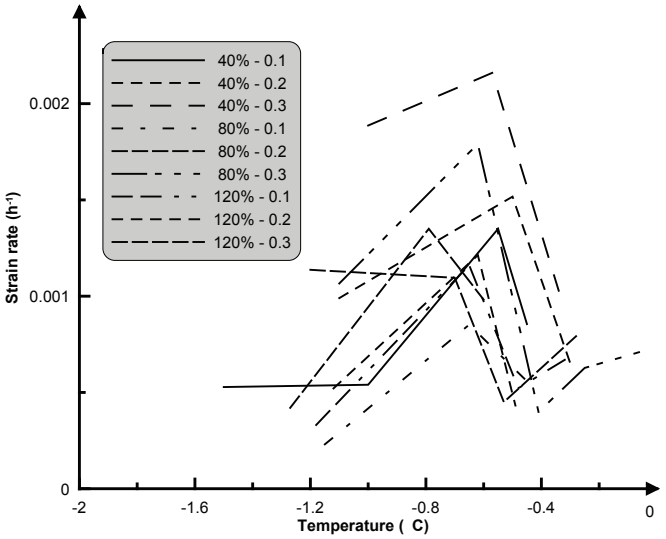

Figure 5. Strain rate against temperature (40% – 0.1: 40% refers to the water content, and 0.1 in MPa is the applied load).

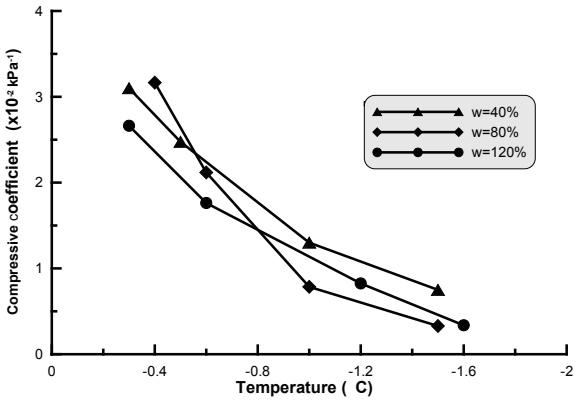

Figure 6. Compressive coefficient against temperature for silty clay in own testing program.

Unfrozen water content vs. temperature

It is widely accepted that changes in mechanical properties of frozen soils are due to changes in unfrozen water content with temperature. Loads also lower the freezing point of water in frozen soils, but this is only noticeable under loads of tens of MPa (Chamberlain et al. 1972). In the loading range discussed in this paper, this effect can be ignored.

The unfrozen water content of the soil in the tests carried out for this investigation was measured using Nuclear Magnetic Resonance (NMR) in a separate testing program. Figure 8 shows the relationship between unfrozen water content and temperature of the soils in these tests and in the work by Zhu et al. (1982). Both soils show that the unfrozen water content increases with an increase in temperature. For both soils, the most rapid change of unfrozen water content occurs within the temperature range of about 0～-1.0 °C. Considering that both testing programs showed that the mechanical properties changed more rapidly at temperatures between -0.6°C and -1.0°C, it seems reasonable that the temperature boundary for warm frozen soils should be -1.0°C. This is also in accordance with the temperature boundary for the warm permafrost zone in permafrost engineering.

This temperature boundary is based on testing data on sand and silty clay which are often encountered in engineering practice in permafrost regions on the Qinghai-Tibet plateau. On rare occasions variations can be expected. For instance, Tsytovich (1975) pointed out that for clayey soils with montmorillonite minerals, the temperature boundary for stiff and plastic frozen soil could be as low as -5.0°C.

Conclusions

As a material, the temperature boundary of warm frozen soils should be defined by mechanical properties. According to the tests carried out and the testing program in the literature on sand and silty clay, it can be concluded that -1.0°C should be defined as the temperature boundary for warm frozen soils. This seems reasonable taking into consideration the relationship between unfrozen water content and temperature. It is also convenient for the engineers because it coincides with the temperature boundary for the "warm permafrost

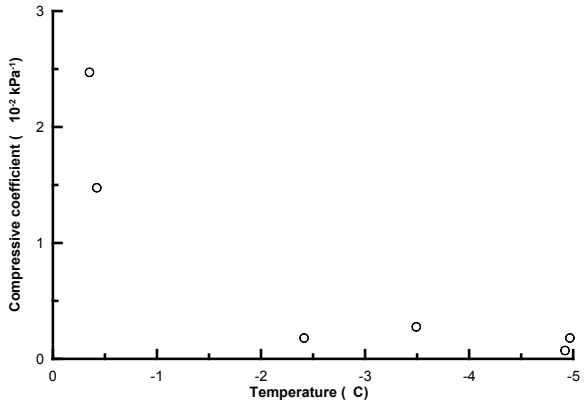

a. Water content of less than 17%.

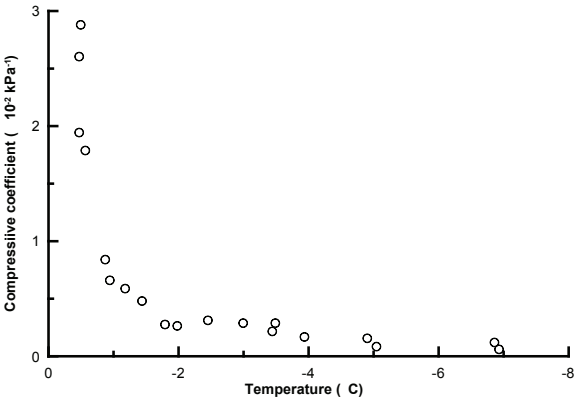

b. Water content of 18%-28%.

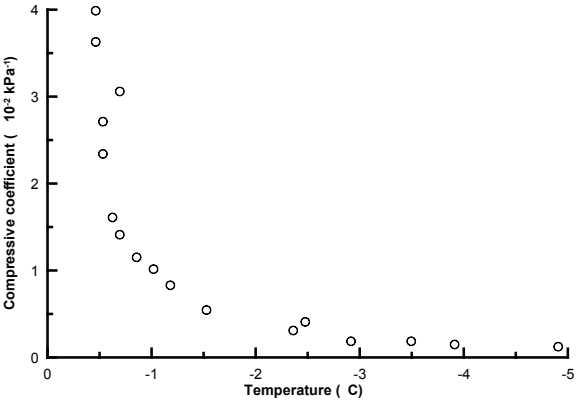

c. Water content of 30%-40%.

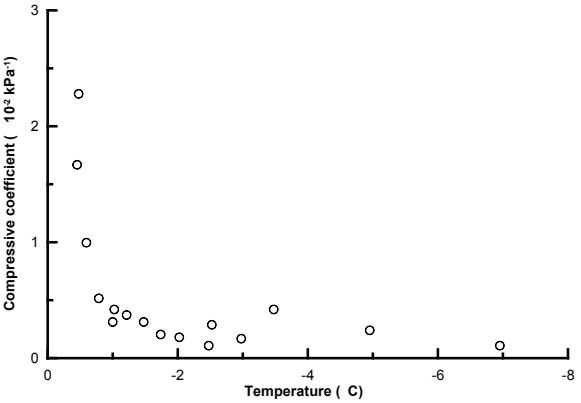

d. Water content of 50%-90%.

Figure 7. Compressive coefficient vs. temperature for the silty clay at different water content range (after Zhu et al. 1982)

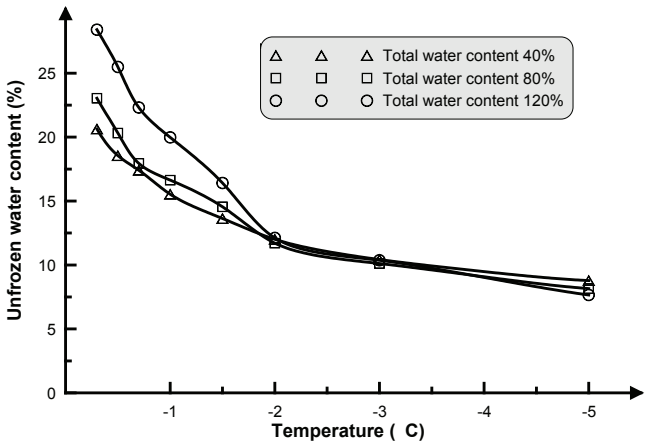

a. Soil tested in this program.

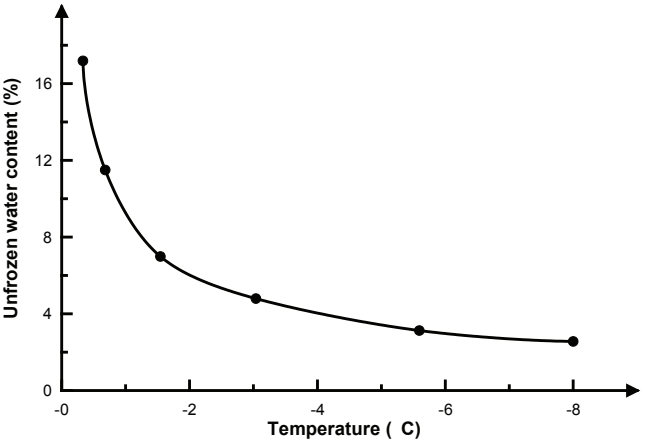

b. Soil tested by Zhu et al. (1982).

Figure 8. Unfrozen water content against temperature.

zone." Previous ideas that the mechanical properties of frozen soils would change dramatically with any small change in temperature was not found in the relationship between the strain rate and temperature.

Acknowledgments

This work was supported by the Hundred Young Talented Scientists Program of the Chinese Academy of Sciences granted to Dr. Jilin Qi. The authors thank Mr. Bo Zheng for his great efforts in performing the testing program.

References

Chamberlain E, Groves C. & Perham J. 1972. The mechanical behavior of frozen earth materials under high pressure triaxial test conditions. *Geotechnique* 22(3): 469-483.

First Survey and Design Institute of the Chinese Railway Ministry. 2001. Preliminary Regulations for Design of the Qinghai-Tibet Railway in Permafrost Regions. (unpublished).

Foster, M.L., Washburn, D.S. & Foote, D.S. 1991. OTH-backscatter power plant foundation design for warm, ice-rich permafrost soils. *Proceedings of the International Arctic Technology Conference. Anchorage, AK, USA, May 29–31, 1991*: 471-480.

Jessberger, H.L. 1980. State-of-the-art report - Ground freezing, mechanical properties, processes and design. *Engineering Geology* 18(1-4): 5-30.

Ladanyi, B. 1999. Creep behaviour of frozen and unfrozen soils: A comparison. *Proceedings of the Tenth International Conference, Lincoln, NH, USA, August 16-19, 1999*: 173-185.

Landanyi, B. 1981. Mechanical behavior of frozen soils (A). *Proceedings of the International Symposium on the Mechanics Behavior of Structure Media. Ottawa, Canada, May 18–21, 1981*: 205-245.

Morgenstern, N.R. 1981. Geotechnical engineering and frontier resource development. *Geotechnique* 31(3): 305-365.

Phukan, A. 1983. Long-Term creep deformation of roadway embankment on ice-rich permafrost. *Proceedings of the Fourth International Conference on Permafrost*, *Fairbanks, AK, USA, July 17–22, 1983*: 369-373.

Sayles, F.H. 1988. State of the art: Mechanical properties of frozen soil, mechanical properties of frozen soil. *Proceedings of the Fifth International Symposium on Ground Freezing, Nottingham, England, July 26-28, 1988* (1): 143-165.

Shields, D.H., Domaschuk, L., Man, C-S. & Kenyon, R.M. 1985. Deformation properties of warm permafrost. *Strength Testing of Marine Sediments: Laboratory and In-Situ Measurements*. San Diego, CA, January 26–27, 1984: 473-486.

Tsytovich, N.A. 1975. *The Mechanics of Frozen Ground.* Washington, DC: McGraw-Hill, Scripta Book Company, 426 pp.

Zhu, Y.L., Zhang, J.Y. & Wu, Z. W. 1982. Elastic and compressive deformation of frozen soils. *Proceedings of the Third International Symposium on Ground Freezing*. U.S. Army Corps of Engineers Cold Regions Research and Engineering Laboratory, Hanover, NH, USA, June 22–24, 1982: 65-77.

Active Layer Temperature Monitoring in Two Boreholes in Livingston Island, Maritime Antarctic: First Results for 2000–2006

M. Ramos
Department of Physics, University of Alcalá, Spain
G. Vieira
Centre for Geographical Studies, University of Lisbon, Portugal
J.J. Blanco
Department of Physics, University of Alcalá, Spain
S. Gruber
Glaciology and Geomorphodynamics Group, Department of Geography, University of Zurich, Switzerland
C. Hauck
Institute for Meteorology and Climate Research, Forschungszentrum Karlsruhe/University of Karlsruhe, Germany
M.A. Hidalgo and D. Tomé
Department of Physics, University of Alcalá, Spain

Abstract

This paper describes the active layer thermal regimes in two shallow boreholes, Sofía 275 m a.s.l. and Incinerador 35 m a.s.l., for which the ground temperature series has been recorded continuously from 2000 to 2006. The monitoring sites are located in Livingston Island, South Shetland Archipelago, Antarctica. This is one of the most sensitive regions of Earth to climate change, with a major warming trend over the last 50 years, of ca. +2.5ºC in the Mean Annual Air Temperatures (MAAT). This region is located near the climatic limit of permafrost, since MAAT at sea level is close to -2ºC. Lineal fits of the ground temperatures series for the study period at different depths in these boreholes show positive slopes. An outcome from the analysis of freezing and thawing indexes is that most of the ground warming seems to concentrate in the summer.

Keywords: active layer; freezing index; shallow boreholes; ground temperatures.

Introduction

The climate of the Antarctic Peninsula region has experienced a major warming trend over the last 50 years with annual mean air temperatures at Faraday/Vernadsky station having increased at a rate of 0.56ºC/decade and 1.09ºC/decade during the winter (King 1994, Turner et al. 2005).

Several factors contributing to the anomalous warming in the Antarctic Peninsula and the Weddell Sea region have been proposed, some of them related to the increase in westerlies observed over the last 30 years (Marshall 2002).

Increasing air temperatures and precipitation may cause the degradation or even the disappearance of permafrost in the sporadic permafrost zone, where current climatic conditions produce near-zero annual air temperatures, like in the South Shetlands Islands, north of the Antarctic Peninsula.

The energy exchange between the ground surface and the atmosphere depends on the radiation balance, ground heat fluxes and turbulent heat fluxes at the ground and snow surfaces. These are especially complex in the alpine or polar maritime areas, where the relief is mountainous and snow cover influence is particularly strong (Van Lipzig et al. 2004, King & Turner 1997, King et al. 2003). The seasonal snow cover, which presents a barrier to ground heat loss in winter, is a leading factor in the ground thermal regime and active layer depth (Romanosky & Osterkamp 2000, Ling & Zhang 2004). Snow has a high surface albedo and high emissivity, inducing cooling of the snow surface, while its low thermal conductivity makes it a good insulator. The ground heat flux is another important magnitude in the energy balance and the main factors that control it in permafrost terrain are: (i) moisture content in the active layer, (ii) thaw effects at the free boundary, and (iii) non-conductive heat transfer effects (variable thermal diffusivity).

The active layer thickness and dynamics are extremely important factors in polar ecology. Since most exchanges of energy, moisture, and gases between the atmospheric and terrestrial systems occur through the active layer, its thickening has important effects on physical, geomorphic, hydrologic and biological processes (Nelson & Anisimov 1993). Furthermore, the issue of active layer response to climate change is of increasing concern, particularly in what respects to its degradation and consequent physico-chemical influences on the biogeochemical cycle of carbon and on global change modeling (Anisimov et al. 1997, Osterkamp 2003).

Compared to the Arctic, very little is known about Antarctic permafrost (Bockheim 1995). In 2004 only 4 active layer boreholes were being monitored in the Antarctic Peninsula Region and a number as small as 21 in the whole Antarctic region (Bockheim & Hall 2004). Complex logistical and maintenance problems and the remoteness of the Antarctic are the main causes for this scarcity. The limited knowledge

of the ground temperature conditions led to a recent effort in order to increase active layer and permafrost research in the Antarctic under the framework of international programs. Two core projects of the International Polar Year 2007–08 where Antarctic permafrost plays a central role are under way: ANTPAS – Antarctic and Sub-Antarctic Permafrost, Soils and Periglacial Environments and TSP – Permafrost Observatory Project - Thermal State of Permafrost (Guglielmin 2006, Bockheim & Hall 2004). The present research is integrated in these projects and intends to monitor and model the active layer temperature regime in two shallow boreholes in Livingston Island (South Shetland Islands, Antarctic Peninsula) (Ramos & Vieira 2003, Ramos et al. 2007).

The study's ultimate aim is to document the influence of climate change on permafrost degradation in this area which has a very strong influence on the regional climate warming.

Study Area

Livingston Island is located in the South Shetlands Archipelago at (62º39′S, 60º21′W) (Fig. 1). The climate at sea level is cold oceanic, with frequent summer rainfall in the low areas and a moderate annual temperature range. The climate reflects the strong influence of the circum-Antarctic low-pressure system. Meteorological conditions in summer are dominated by the continuous influence of polar frontal systems (Simonov 1977, Styszynska 2004). Relative humidity is very high, with average values ranging from 80 to 90%.

Data from different stations in King George Island (South Shetlands Archipelago) show a mean annual air temperature of -1.6ºC near sea level and an annual precipitation of about 500 mm. Data that we collected in Livingston Island at 15 m a.s.l. show a MAAT from -3.2ºC to -1.5ºC. From April to November, average daily temperatures at sea level generally stay below 0ºC and from December to March they are generally positive. The MAAT (2003 to 2006) at 275 m a.s.l. in Reina Sofia Hill, near the Sofía borehole, was -4.2ºC. This corresponds to a lapse rate of -0.8ºC/hm and to an air freezing season about 1 month longer than at sea level.

Figure 1. Location of the study area in Livingston Island. Black areas represent glacier free terrain (SAS – Spanish Antarctic Station).

Table 1. Freezing season length (in days) in Incinerador and Sofía boreholes from 2000 to 2006. Temperatures at 15 cm depth at 30 min intervals.

Year	INC	SOFIA	Sofia-INC
1999		273	
2000	197	238	41
2001	211	294	83
2002	201	294	93
2003	225	332	107
2004	211	290	79
2005	176	246	71
2006	197	262	65
Mean	203	279	76

Permafrost in the South Shetland Islands is widespread above the Holocene raised-beaches (ca. 30 m a.s.l.) (Serrano & López-Martinez 2000). Meteorological and geophysical data indicate that environmental conditions close to sea-level are marginal for the maintenance of permafrost (Hauck et al. 2007).

Methodology

Shallow boreholes

Borehole sites are in the vicinity of the Spanish Antarctic Station Juan Carlos I in Livingston Island. One of them is located at Reina Sofia hill (275 m a.s.l., 0.9 m active layer thickness) in a diamicton with a water content of 22.1% in saturation conditions. The other borehole is located at Incinerador point (35 m a.s.l., 2.4 m of seasonal frost, with possible permafrost below) in quartzite bedrock with negligible interstitial water content. Both boreholes were drilled in 2000, providing a 7-year series of active layer temperatures.

Thermal diffusivity, calculated by analyzing cuasi-stationary sinusoidal temperature signals using inverse modeling (Blanco et al. 2007), has a mean winter value in the Incinerador borehole of 1.5 10^{-6} ms^{-2}. In Sofía borehole, in winter the value is 0.55 10^{-6} ms^{-2} (Ramos & Vieira 2003).

In the Incinerador borehole a chain composed of six data loggers measures temperatures at 5, 15, 40, 90, 150, and 230 cm depth. At Sofia borehole, four temperature dataloggers are installed at 5, 15, 40, and 90 cm. The logging interval is 30 min and the accuracy of the data loggers (Tiny Talk Gemini Co.) is 0.2ºC. Due to data logger limitations during the first years the series present a short period with lack of data for the thawing season in both boreholes.

At the monitoring sites there is no vegetation and in the islands, mosses and grasses are very sparsely distributed.

Following the Berggren equation, active layer thickness is a square root function of the freezing index (Andersland & Ladany 1994). Freezing and thawing indexes have been calculated for different depths in Sofía and Incinerador boreholes and these are used to estimate the evolution of the active layer thickness.

Results and Discussion

The analysis of the ground temperatures is based on the comparison of the temperatures at 15 and 90 cm depths in both boreholes. Temperatures at 230 cm from the Incinerador borehole complement the analysis. In the Sofía borehole the mean ground temperatures at 15 and 90 cm, from 2000 to

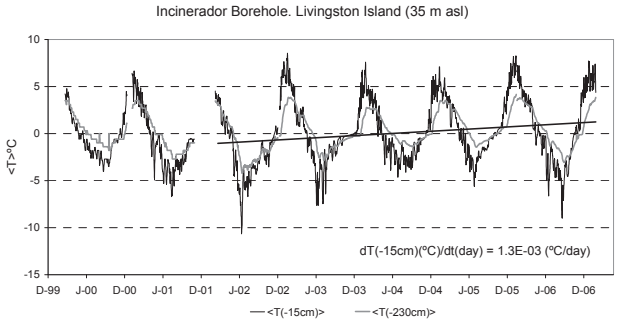

Figure 2. Temperatures at the Incinerador borehole from 2000 to 2006 at 15 and 230 cm depth. The lineal fit corresponds to the 15 cm sensor for the period of 2002–2006.

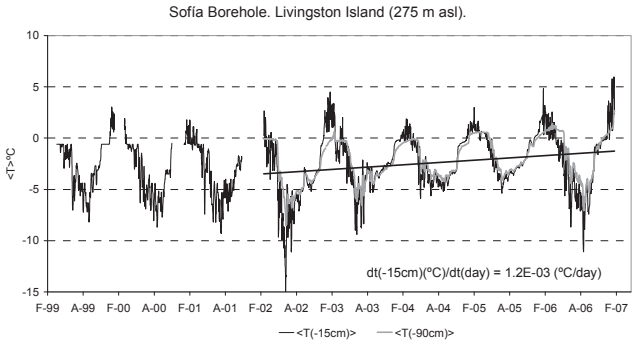

Figure 3. Temperature series at the Sofia borehole from 1999 to 2006 at 15 and 90 cm depth. The lineal fit corresponds to the 15 cm position sensor for the period of 2002–06.

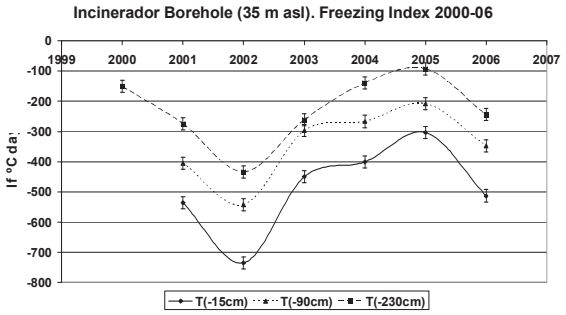

Figure 4. Incinerador freezing index evolution in the periods 2000 to 2006 at 15, 90, and 230 cm depth.

2006, were -2.6ºC and -2.1ºC respectively. In the Incinerador borehole (35 m a.s.l.) at the same depths, values of -0.1ºC and 0.2ºC were recorded for the same period. The differences between both places are close to the regional atmospheric lapse rate that has a value of -0.8ºC/hm (Ramos & Vieira 2003). The mean length of the freezing season in the Sofia site is 279 days per year, which is roughly two months longer than at the Incinerador site (see Table 1).

During the 7-year period the thermal regime in the Incinerador borehole showed the behavior of a typical annual period wave within a dry homogeneous material. Figure 2 shows the temperature oscillations around 0ºC at 15 and 230 cm. Signals at 15 and 230 cm are delayed more or less 5 days as a function of the ground thermal inertia.

Table 2. Lineal best-fit slopes (dT/dt x 10^{-3} ºC/day) of the daily ground temperatures in Sofia and Incinerador boreholes from 2002 to 2006.

depth (cm)	15	90	230
Incinerador	1.3	0.8	0.8
Sofia	1.2	1.2	--

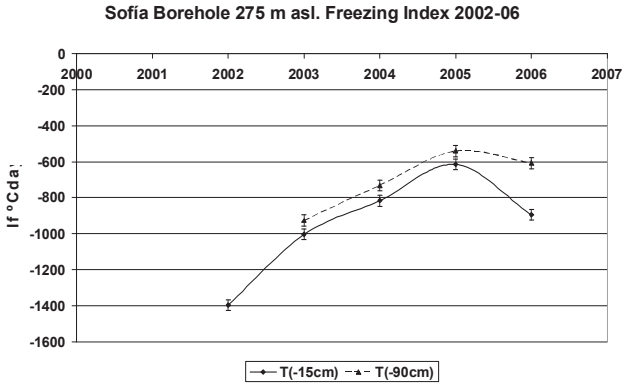

Figure 5. Sofía freezing index evolution in the periods 2002 to 2006 at 15 and 90 depth.

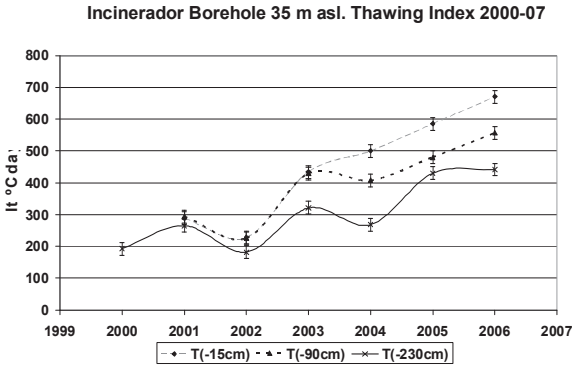

Figure 6. Incinerador thawing index evolution during the periods 2000 to 2006 at 15, 90, and 230 cm depth.

The lineal fit for the period with a complete data series for both boreholes (2002 to 2006) shows a warming trend at all depths, with similar values in both of them (see Table 2).

Direct observations in pits and temperature data show that from 1999 to 2002 the top of the permafrost table in Sofía borehole was at 90 cm, but since 2003 its depth increased.

Figure 4 shows the freezing index evolution in Incinerador borehole at 15, 90, and 230 cm depth. The curve shows a wave shape with a 5-year period and amplitude of more or less 300ºC-day. The mean at 15 cm depth for the period of 2002 to 2006 is -480ºC-day. In Sofía borehole (Fig. 5) the value for the same period, at the same depth is -945ºC-day.

Figure 6 shows the thawing index evolution from 2000 to 2006 at 15, 90, and 230 cm in the Incinerador borehole. In this period a very significant warming trend is observed at all depths, with, almost, a doubling of the thawing index. It changes from 300ºC-day at 15 cm depth in the summer of 2001, to more than 600ºC-day in the summer of 2006. Despite the short time-series, this trend seems to support a significant warming during the summer.

Conclusions

The scarcity of ground temperature data in the Maritime Antarctic has driven us to install shallow boreholes in Livingston Island. Theses are used for monitoring the impact of climate change on the active layer temperatures and on permafrost.

Lineal fits of the ground temperatures at different depths in Sofía (275 m a.s.l.) and Incinerador (35 m a.s.l.) boreholes show positive slopes. This confirms that the climate warming trend identified by other authors is contributing to ground warming. The similar positive slopes in both boreholes indicate that they are probably more influenced by a regional signal, than by local site-specific influences. The increase in active layer thickness at Sofia borehole has been confirmed by the direct observations of permafrost thaw at 90 cm depth. The short period of the data series limits the conclusions and therefore no absolute trends in the climate signal are presented here. An outcome from the analysis of freezing and thawing indexes is that most of the ground warming seems to concentrate in the summer. This is in agreement with climatological data for the Antarctic Peninsula region published by various authors.

Acknowledgments

We acknowledge the support from the MEC, Office of Spanish Polar Programs through the grant: CGL2005-25112-E/ANT. We thank the field support of the staff from UTM and Spanish Army in the Spanish Antarctic Station Juan Carlos I. This paper is integrated in IPY projects ANTPAS (ID. 33) and TSP (ID.50).

References

Andersland, O.B. & Ladany, B. 1994. *Frozen Ground Engineering.* Chapman & Hall, 352 pp.

Anisimov, O.A., Shiklomanov, N.I. & Nelson, F.E. 1997. Global warming and active layer thickness: results from transient general circulation models. *Global and Planetary Chang.* 15: 61-67.

Blanco, J.J. Tomé, D. Ramos, M. Vieira, G. Gruber, S. Hauck, C. & Hidalgo, M.A. 2007. *Active layer apparent thermal diffusivity and its dependence on atmospheric temperature (Livingston Island, Maritime Antarctic)*. U.S. Geological Survey and the National Academies, USGS OFR-2007, Extended Abstract, 1-4.

Bockheim, J. 1995. Permafrost distribution in Southern circumpolar region and its relation to the environment: a review and recommendations for further research. *Permafrost and Periglacial Processes* 6: 27-45.

Bockheim, J.G. & Hall, K.J. 2004. Permafrost, active layer dynamics and periglacial environments of continental Antarctica. *South Afr. J. Sci.* 98: 82-90.

Guglielmin, M. 2006. Ground surface temperature (GST), active layer, and permafrost monitoring in continental Antarctica. *Permafrost and Periglacial Processes* 17(2): 133-143.

Hauck, C., Vieira, G., Gruber, S. Blanco, J. & Ramos, M. 2007. Geophysical identification of permafrost in Livingston Island, maritime Antarctica. *J. Geophys. Res.* 112, (F02S19) doi:10.1029/2006JF000544.

King, J.C. 1994. Recent climate variability in the vicinity of Antarctic Peninsula. *Int. J. Climatol*. 14(4): 357-369.

King, J.C. & Turner, J. 1997. *Antarctic Meteorology and Climatology.* Cambridge: Cambridge University Press: 114-120.

King, J.C., Turner, J., Marchall, G.J., Connolley, W.M. & Lachlan-Cope, T.A. 2003. Antarctic Peninsula variability and its causes as revealed by analysis of instrumental records. In: E. Domack et al., *Antarctic Peninsula Climate Variability.* Antarctic research series, AGU, 79: 17-30.

Ling, F. & Zhang, T. 2004. A numerical model for surface energy balance and thermal regime of the active layer and permafrost containing unfrozen water. *Cold Regions Science and Technology* 38: 1- 15.

Marshall, G.J. 2002. Analysis of recent circulation and thermal advection change in the northern Antarctic Peninsula. *Int. J. Climatol.* 22(12): 1557-1567.

Nelson, F.E. & Anisimov, O.A. 1993. Permafrost zonation in Russia under anthropogenic climate change. *Permafrost and Periglacial Processes* 4(2): 137-148.

Osterkamp, T.E. 2003. Establishing long-term permafrost observatories for active-layer and permafrost investigations in Alaska: 1977-2002. *Permafrost and Periglacial Processes* 14: 331-342.

Ramos, M. & Vieira, G. 2003. Active layer and permafrost monitoring in Livingston Island, Antarctic. First results from 2000 to 2001. *Proceedings of the Eighth International Conference on Permafrost, Lisse, Zurich*: 929-933.

Ramos, M., Vieira, G., Gruber, S., Blanco, J.J., Hauck, C., Hidalgo, M.A., Tomé, D., Neves, M., & Trindade, A 2007. *Permafrost and active layer monitoring in the Maritime Antarctic: Preliminary results from CALM sites on Livingston and Deception Islands*. U.S. Geological Survey and the National Academies, USGS OF-2007-1047, Short Research Paper 070, doi:10.3133/of2007-1047.srp070.

Romanovsky, V.E. & Osterkamp, T.E. 2000. Effects of unfrozen water on heat and mass transport processes in the active layer and permafrost. *Permafrost and Periglacial Processes* 11: 219-239.

Serrano, E. & López-Martínez, J. 2000. Rock glaciers in the South Shetland Islands, Western Antarctica. *Geomorphology* 35: 145-162.

Simonov, I.M. 1977. Physical geographic description of Fildes Peninsula (South Shetland Islands). *Polar Geography* 1: 223-242.

Styszynska, A. 2004. The origin of coreless winters in the South Shetlands area (Antarctica). *Polish Polar Research* 25: 45-66.

Turner, J., Colwell, S.R., Marshall, G.J., Lachlan-Cope, T. A., Carleton, A.M., Jones, P.D., Phil, V.L., Reid, A. & Iagovkina S. 2005. Antarctic climate change during the last 50 years. *Int. J. Climatol.* 25: 279-294.

Van Lipzig., N.P.M., King J.C. & Lachlan-Cope. T.A. 2004. Precipitation, sublimation, and snow drift in the Antarctic Peninsula region from a regional atmospheric model. *J. Geophys. Res.* 109: 24106-24132.

Circumpolar Relationships Between Permafrost Characteristics, NDVI, and Arctic Vegetation Types

Martha K. Raynolds and Donald A. Walker
University of Alaska Fairbanks

Abstract

An understanding of the distribution and characteristics of vegetation found on different types of permafrost is necessary input for modeling permafrost response to climate change. Interactions between climate and soil thermal regime are modified where vegetation exists, and >75% of permafrost on land in the Arctic is covered by non-barren vegetation types. A circumpolar spatial analysis was conducted to compare mapped permafrost characteristics with the Normalized Difference Vegetation Index (NDVI), mapped vegetation types, and environmental characteristics. A General Linear Model (GLM) analysis found that, when added to a model that included climate and lake cover, permafrost characteristics accounted for an additional 11% of the variation in NDVI. High ice content in permafrost had the strongest effect, lowering NDVI. Over 65% of areas with thin overburden is vegetated by low-stature, low-cover, low-biomass vegetation types that have little impact on thermal regimes. This climbs to >82% for areas that also have high ice content permafrost. Over 83% of areas with thick overburden have vegetation types with denser, taller vegetation, which alters the interaction between climate and permafrost. Including vegetation characteristics in permafrost models will be particularly important in areas with thick overburden and medium or high ice content.

Keywords: arctic vegetation; Circum-Arctic Map of Permafrost and Ground Ice Conditions; Circumpolar Arctic Vegetation Map; NDVI; permafrost.

Introduction

Permafrost, its characteristics, and its vulnerability to change are increasingly in the public eye as a result of attention focused on climate change and the Arctic. Climate change is occurring at a faster rate in the Arctic than other biomes and is resulting in an increase in temperatures in almost all parts of the Arctic (Comiso 2006, Hassol 2004). The effects on the Arctic Ocean have resulted in dramatic loss of summer sea ice, especially in the summer of 2007 (Comiso et al. 2008). The effects on land, both to permafrost and vegetation, are a focus of on going research, particularly during the 2008 International Polar Year.

Most permafrost, even in the Arctic, is covered with vegetation, and the interactions between the permafrost and the vegetation affect both the growing environment for arctic plants and the thermal environment of the permafrost. Permafrost strongly affects vegetation by affecting landscape and soil characteristics. Permafrost underlying the annually-thawed active layer limits soil drainage and results in cryogenic features such as polygons, gelifluction lobes, circles, and mounds (Washburn 1980). Permafrost ice content can raise surface elevations through aggradation or lower it due to degradation (Jorgenson et al. 2001). Permafrost affects the characteristics of the active layer, such as its depth, soil temperatures, and soil moisture (Schuur et al. 2007).

Vegetation affects permafrost by changing the thermal characteristics of the soil. Vegetation shades and insulates the soil, reducing the transfer of summer warmth (Kade et al. 2006, Shur & Jorgenson 2007). Vegetation also cools the surface through evapotranspiration. Vegetation has the opposite effect in winter; well-vegetated areas are insulated by the plants and the snow they trap, while unvegetated soils are more exposed to winter temperatures (Kade et al. 2006). The types and strength of the effect of vegetation on the climate-soil interactions vary with vegetation type and depend on the amount of total plant biomass, plant lifeforms, and continuity of plant cover (Kade et al. 2006, Walker et al. 2003).

In order to understand the effects of climate change on permafrost, it is important to understand the distribution of vegetation types in permafrost areas and the characteristics of those vegetation types that affect the thermal regime of the soil. This study compares vegetation distribution in the Arctic, the area north of the treeline, with permafrost characteristics. The vegetation was characterized using both a vector vegetation map and satellite raster data of the normalized difference vegetation index (NDVI). This spatial comparison of arctic vegetation types and NDVI with permafrost distribution help define areas where vegetation has the strongest influence on permafrost, with implications for the possible effects of climate change.

Methods

The permafrost map

The extent and ground ice content of permafrost and depth of overburden in the Northern Hemisphere (20°N to 90°N), were mapped on the Circum-Arctic Map of Permafrost and Ground-Ice Conditions (Brown et al. 1997, http://nsidc.org/data/ggd318.html), and summarized by Zhang et al. (1999). The map was printed at 1:10,000,000 scale, and the digital format at 12.5-km pixel resolution was used for this study. Permafrost extent was mapped as continuous (94% of Arctic land area), discontinuous (3%), sporadic (2%), or isolated (1%). Ground-ice content was divided into low

Table 1. Vegetation types of the Circumpolar Arctic Vegetation Map (CAVM Team 2003).

Code	Vegetation Type
B1	Cryptogam, herb barren
B2	Cryptogam barren complex (bedrock)
B3	Noncarbonate mountain complex
B4	Carbonate mountain complex
G1	Rush/grass, forb, cryptogam tundra
G2	Graminoid, prostrate dwarf-shrub, forb tundra
G3	Nontussock sedge, dwarf-shrub moss tundra
G4	Tussock-sedge, dwarf-shrub, moss tundra
P1	Prostrate dwarf-shrub, herb tundra
P2	Prostrate/Hemiprostrate dwarf-shrub tundra
S1	Erect dwarf-shrub tundra
S2	Low-shrub tundra
W1	Sedge/grass, moss wetland
W2	Sedge, moss, dwarf-shrub wetland
W3	Sedge, moss, low-shrub wetland

(54%), medium (15%), and high (31%) categories, referring to the volume of visible ice in the upper 10–20 m. Two landscape categories were mapped. Lowlands, highlands, and intra- and inter-montane depressions characterized by thick (>5–10 m) overburden (any soil or other material that lies above the bedrock horizon in a given area) cover 36% of Arctic land areas. Mountains, highlands, ridges, and plateaus characterized by thin (<5–10 m) overburden cover and exposed bedrock cover 64% of the Arctic.

Satellite data (AVHRR NDVI)

The normalized difference vegetation index (NDVI) is a measure of relative greenness calculated as: NDVI = (NIR -R) / (NIR + R*),* where NIR is the spectral reflectance in the near-infrared where reflectance from the plant canopy is dominant, and R is the reflectance in the red portion of the spectrum where chlorophyll absorbs maximally. NDVI has a theoretical maximum of 1 and its relationship to vegetation characteristics such as biomass, productivity, percent cover, and leaf area index is asymptotically nonlinear as it approaches 1. As a result, NDVI is less sensitive to ground characteristics at higher values and essentially saturates when leaf area index >1 (van Wijk & Williams 2005). This is not a severe problem in the Arctic where vegetation is often sparse and patchy; the mean NDVI for arctic land areas in the data set used in this study was 0.32, well below the saturation point (Raynolds et al. 2006).

NDVI values in the Arctic increase with the amount of vegetation as measured by leaf area index (LAI), phytomass, and productivity (Riedel et al. 2005, Shippert et al. 1995). NDVI values correlate well with ground characteristics of arctic vegetation and can be used to distinguish between vegetation types (Hope et al. 1993, Stow et al. 2004).

A 1-km-resolution maximum-NDVI data set was used for this study. These data were derived from the U.S. Geological Survey EROS AVHRR polar composite of NDVI data for 1993 and 1995 (CAVM Team 2003, Markon et al. 1995). Daily data were collected by AVHRR sensors onboard NOAA satellites for channel 1, red (0.5 to 0.68 μm) and channel 2, near-infrared (0.725–1.1 μm). Satellite measurement of NDVI is affected by a variety of conditions, especially cloud cover, viewing angle and seasonal variation, that can be compensated for by compositing data over time (Goward et al. 1991, Riedel et al. 2005). Daily NDVI values were composited into 10-day maxima. The maximum values of these composited data during two relatively cloud-free summers (11 July–31 August in 1993 and 1995) were used to create an almost cloud-free data set of maximum NDVI for the circumpolar Arctic in the early 1990s.

The vegetation map

The third data set used in this analysis was the Circumpolar Arctic Vegetation Map (CAVM Team 2003, http://www.arcticatlas.org/atlas/cavm). The map extent includes all land areas north of the northern limit of trees. The map was created at 1:7,500,000 scale with minimum polygon diameter of 8 km and is available digitally as a vector map. The integrated vegetation mapping approach used to create the vegetation map was based on the principle that a combination of environmental characteristics controls the distribution of vegetation. Vegetation-type boundaries were based on existing ground data and vegetation maps, bioclimate (Tundra Subzones A–E), floristic regions, landscape categories, elevation, percent lake cover, substrate chemistry, and surficial and bedrock geology, drawn on an AVHRR false-color infrared base map. The distribution of 15 arctic vegetation types (Table 1) was mapped and described on the CAVM, using a unifying circumpolar legend which enables analysis of the entire Arctic (CAVM Team 2003, Walker et al. 2005).

Analysis

In each of the permafrost categories the area of different vegetation types and average NDVI values were tabulated. Spatial-distribution characteristics were analyzed using GIS software. The CAVM was mapped at finer resolution than the permafrost map, so the most common permafrost category for each CAVM polygon was determined. Results of the analysis were summarized graphically, showing vegetation types occurring on different types of permafrost, using symbols proportional to area. The NDVI raster data were analyzed by calculating the average NDVI value for different categories within the permafrost map and summarizing these results using bar graphs. This analysis of over 7 million 1-km^2 pixels represents the true mean of the classes, so comparative statistical tests based on sampling were not appropriate.

General linear models (GLM) (R Development Core Team 2006) were run to determine the importance of permafrost variables in accounting for variation in NDVI in the Arctic. Attributes mapped as characteristics of the CAVM polygons, weighted by area, were used as input data. A basic model

including variables known to be important in controlling NDVI (Raynolds et al. 2006) was run first, using the CAVM classes for bioclimate zone and percent lake cover. These variables accounted for the latitudinal variation in NDVI due to climate, and for the reduction in NDVI due to cover of water (NDVI of water is essentially zero). Variables from the permafrost map: extent, ice content, overburden, and the combined code (a unique number for each combination of extent, ice content, and overburden) were added to the model one at a time to evaluate their effect on the model. The amount of variation accounted for by the different variables in each model and the significance of the variable in the model were tabulated.

Interdependence of data sets

Climate and landscape characteristics including slope, elevation, geologic and glacial history have important effects on all three variables: NDVI, permafrost and vegetation. In some cases these characteristics will vary together, especially in extreme conditions. For example, steep, high elevation mountains will generally have low NDVI, continuous, low ice-content permafrost with little overburden, and barren vegetation types. In more moderate terrain the type of vegetation which will grow on a given type of permafrost varies. In these areas the vegetation map and the NDVI data provide valuable information about the distribution of vegetation on different types of permafrost.

Results

Most of the Arctic has continuous permafrost underlying 4.68 million km^2 of land surface (excluding ice and water). Arctic areas without continuous permafrost include southern Greenland, European Arctic Russia, and in Alaska the Seward Peninsula and southern parts of the Kuskokwim River Delta. Continuous permafrost in the Arctic supports a mix of vegetation types. Over 83% of areas with thick overburden commonly is vegetated by erect shrub tundras (S1, S2), graminoid-shrub tundra (G3, G4), or low-shrub wetlands (W3) (Fig. 1). All of these vegetation types have relatively high stature, high biomass, and complete cover (Walker et al. 2005). Over 65% of areas with thin overburden have barren vegetation types (B1-B4), sparse graminoid (G1, G2), or prostrate dwarf-shrub (P1, P2) vegetation types with low stature, low biomass, and partial ground cover (Walker et al. 2005). Areas with thin overburden and high ice content are likely to be vegetated with either cryptogam, herb barrens (B1), graminoid, prostrate dwarf-shrub (G2), or prostrate dwarf-shrub herb tundra (P1), with >82% of these areas vegetated by vegetation types that have low-stature, low cover, and low biomass.

In areas of discontinuous permafrost, tussock tundra (G4) and erect-shrub (S1, S2) vegetation types are common. Areas with sporadic permafrost support mostly low-shrub vegetation (S2) and sedge, moss, low-shrub wetland (W3). Areas with isolated permafrost are dominated by non-carbonate mountain vegetation complexes (B3).

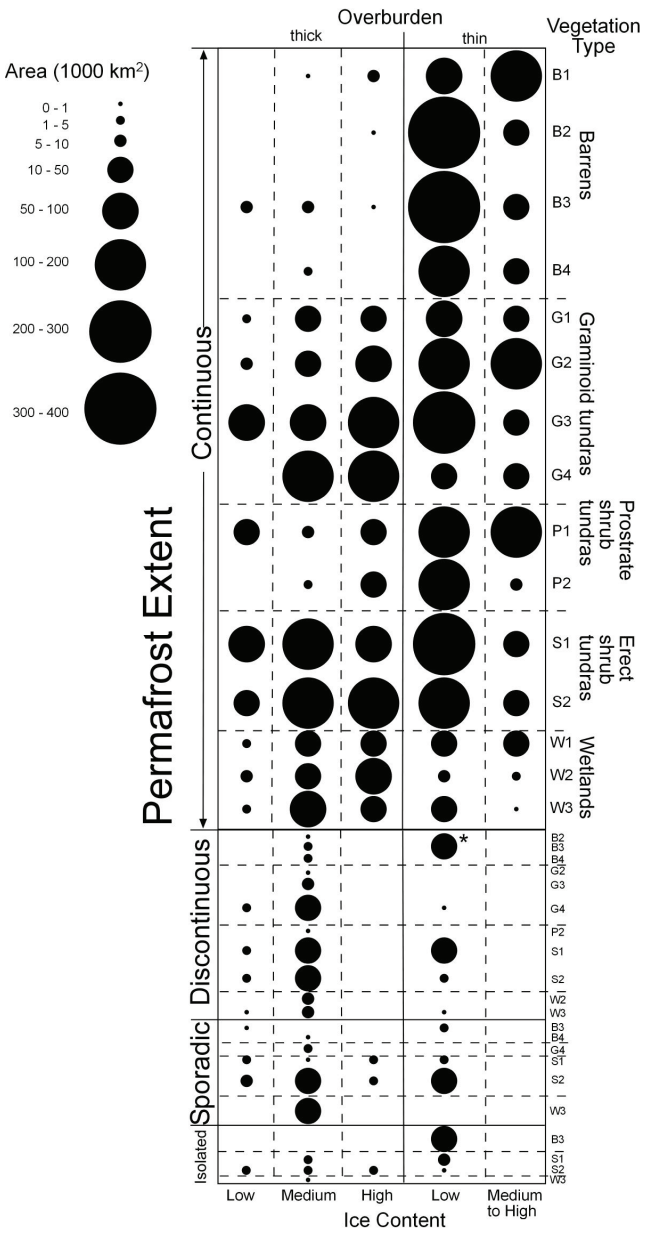

Figure 1. Area of Arctic in different types of permafrost categories (Brown et al. 1997) and different vegetation types (CAVM Team 2003). * The area represented by this symbol was all vegetation type B3.

Low ice-content permafrost is characterized by barren types (B2, B3) and shrub types (S1, S2). Medium ice-content permafrost supports graminoid- (G4) and shrub-dominated (S1, S2) vegetation, as well as wetlands (W3). High ice-content permafrost is most commonly vegetated by graminoid-dominated vegetation types (G2, G3, G4), prostrate dwarf-shrub (P1), or cryptogam barrens (B1).

Examination of the types of permafrost that characterize vegetation types reveals that only three vegetation types have <90% continuous permafrost: non-carbonate mountain complex (B3); low shrub tundra (S2); and sedge, moss, low-shrub wetland (W3). Vegetation types that occur mostly on low ice content permafrost include the barren types (B2,

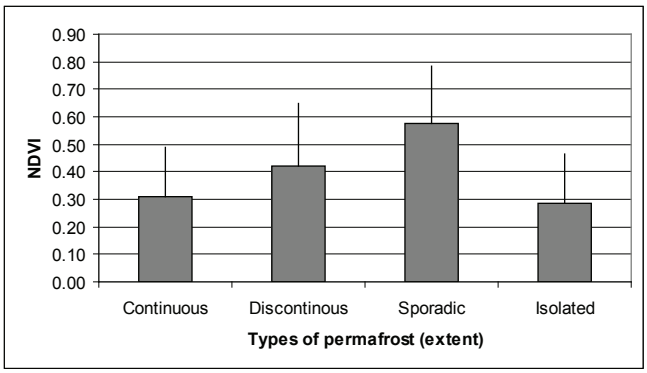

Figure 2. Average NDVI of Arctic areas with differing extent of permafrost (lines = s.d.).

B3, B4) and types common on the Canadian Shield (P2, S1). Cryptogam herb barrens (B1) characteristic of the High Arctic and wetland vegetation types (W1, W2, W3) occur mostly on medium or high ice content permafrost. Tussock sedge, dwarf-shrub, moss tundra (G4) occurs mostly on areas with thick overburden and medium or high ice content.

NDVI varied inversely with permafrost extent, increasing from continuous to discontinuous to sporadic (Fig. 2), as would be expected, following the climate gradient from colder to warmer (Raynolds et al. 2006). NDVI was lowest for isolated permafrost, which occurred mostly in the mountainous areas of southern Greenland, where steep slopes and exposed bedrock limit plant cover.

The largest differences in NDVI values occurred between overburden categories; NDVI was much greater in areas with thick overburden than with thin (Fig. 3). Thin overburden occurs in glaciated areas such as the Canadian Shield, on mountains, ridges, and plateaus. Thick overburden is less common in the Arctic and occurs at lower elevations and in depressions where sediments can accumulate. Areas with thick overburden are more commonly vegetated by graminoid (G3, G4) or erect-shrub (S1, S2) vegetation types with high NDVI values, while areas with thin overburden often have sparse vegetation with low NDVI values (B1, B2, B3, Fig. 1).

NDVI values varied less by ice content within overburden types (Fig. 3). High and medium-to-high ice-content permafrost had lower NDVI than average. Areas with thick overburden and high ice-content permafrost are largely covered with graminoid vegetation types, while medium ice-content permafrost areas are more commonly vegetated by shrub-dominated types (Fig. 1). Areas with thin overburden and medium-to-high ice-content permafrost mostly occur in high-latitude areas (such as the Canadian Arctic Islands), and have barren or sparse, prostrate vegetation (B1, P1, G2).

Permafrost characteristics accounted for 11.9% of the variation in arctic NDVI in a general linear model that included bioclimate zone, percent lake cover, and permafrost characteristics (Table 2). The CAVM variables accounted for 54.9% of the variation, with bioclimate zone responsible for 38.6% and percent lake cover for 16.3%. Permafrost ice content accounted for more of the remaining variation than either extent or depth of overburden.

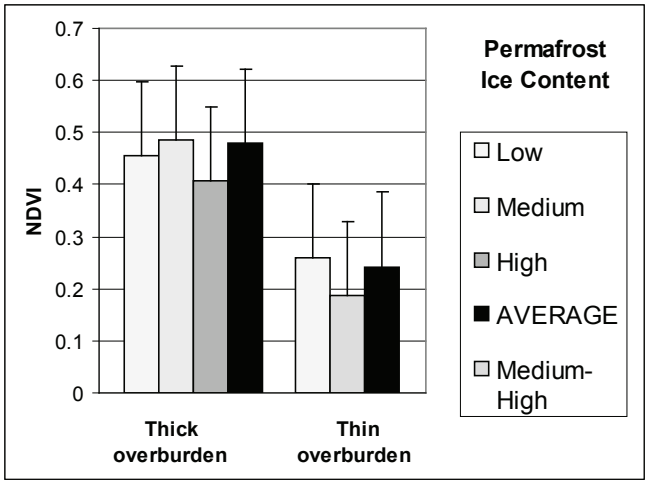

Figure 3. Average NDVI of Arctic areas with shallow vs. deep overburden over bedrock, and different levels of ice content (lines = s.d.).

Discussion

The comparison of the Circum-arctic Map of Permafrost and Ground Ice Conditions, the Circumpolar Arctic Vegetation Map, and satellite NDVI values emphasized the importance of the difference between areas with thick overburden (>5–10 m) and thin overburden (<5–10 m). The thick overburden areas had NDVI values almost twice as high as those of the thin overburden areas, indicating a much greater amount of vegetation cover (Shippert et al. 1995). NDVI would be expected to be lower in areas with thin soils, but the distinction between overburden <5 m and >5 m occurs far below the rooting depth of arctic plants. GLM models showed that once climate and percent lake cover were accounted for, overburden depth was much less important. Areas with thin overburden had more lake cover (especially on the Canadian Shield) and a more northerly distribution than areas with thick overburden, both effects reducing the average NDVI.

The model results showed that ice content correlated with variation in NDVI, and the map summaries showed that medium-high ice-content permafrost with thin overburden has especially low NDVI values. These conditions occurred mainly in the northern areas of the Arctic: the Canadian Arctic Islands and Novaya Zemlya.

About one quarter of the Arctic land area is covered by barren vegetation types. In these areas the vegetation plays a minimal role in the soil thermal regime, and the permafrost is climate-driven. The rest of the continuous permafrost in the Arctic would be considered climate–driven, ecosystem-modified permafrost, according to Shur & Jorgenson (2007). The effect of the vegetation modification is to reduce soil temperatures in summer and to increase them in winter (Kade et al. 2006). Vegetation types that have the most plant cover, thickest moss layers, and deepest organic soils insulate the soil most from summer warming (Kade et al. 2006). Types with the tallest vegetation trap the most snow in winter and

Table 2. Results of GLM analysis of variation in NDVI. Models included 3 variables, bioclimate subzone and percent lake cover plus one of the other variables. Results are from the Type 1 sums of squares, with terms added sequentially.

Model variables	% of variation in NDVI accounted for by variables	Significance (p)
Bioclimate zone	38.6	$< 2 \times 10^{-16}$
Percent lake cover	16.3	$< 2 \times 10^{-16}$
+ Permafrost ice content	6.1	$< 2 \times 10^{-16}$
+ Permafrost extent	4.2	$< 2 \times 10^{-16}$
+ Overburden	1.4	$< 2 \times 10^{-16}$
+ Permafrost combination	11.9	$< 2 \times 10^{-16}$

insulate the soils from winter cooling (Sturm et al. 2001).

The net effect of vegetation on soil thermal regimes depends largely on the thickness of the moss/peat layer and the height of the vegetation. For example, tussock tundra (G4) at Happy Valley on the North Slope of Alaska has a thick peat layer (12 cm) developed from dead tussocks and mosses, a relatively thick layer of live moss (5 cm), and also a dwarf-shrub layer (25 cm tall) (Walker et al. in press). The vegetative factors in tussock tundra decreasing absorption of summer warmth by the soil outweigh the factors warming the soil in winter, resulting in thinning of the active layer and aggradation of ice at the top of the permafrost (Shur & Jorgenson 2007). This process had been recognized by arctic researchers as paludification, a process whereby soils become progressively wetter and more acidic as reduced thaw depth restricts soil drainage (Mann et al. 2002, Walker et al. 2003). The shallower thaw and saturated soils in turn favor peat-producing species like sphagnum mosses and tussock sedges in a positively reinforcing cycle.

The vegetation types with characteristics resulting in the greatest effect on the soil thermal regime are graminoid-erect dwarf-shrub (G3, G4, W3) and erect-shrub (S1, S2) types (Walker et al. in press). These vegetation types are common in areas with thick overburden and medium or high ice-content permafrost, which occur mostly in the foothills and coastal plains of the southern Arctic. These vegetation types are also common in areas with thin overburden and low ice-content permafrost, which occur mostly on the Canadian Shield and mountainous areas.

Areas with thin overburden and low-ice content permafrost are shown as having mostly low to medium risk of subsidence due to climate change in a study that modeled IPCC climate predictions, soils, and permafrost data (Nelson et al. 2001). Risk of subsidence increases with ice-content, and areas with medium and high ice content permafrost on deep overburden are more commonly mapped as having medium or high risk of subsidence (Nelson et al. 2001).

Medium ice-content permafrost extends into discontinuous and sporadic permafrost where the permafrost is preserved by the effects of the vegetation (climate-driven, ecosystem-protected, Shur & Jorgenson 2007). Although researchers have recognized the importance of predicting the effects of climate change on permafrost in these areas because of the high risk of subsidence (Nelson et al. 2001), the complex interactions between the climate, the vegetation, and the soil are difficult to quantify. Vegetation cover varies from shrub- (42% S2, 13% S1) to graminoid-dominated (14% G4, 5% G3), and 20% of the area is wetlands (W3), in a mosaic of vegetation types with differing thermal attributes. Not surprisingly, different models project either thawing or persistence of this permafrost (Anisimov & Reneva 2006). Spatially detailed models that include vegetation data will be required to understand the effects of climate change on permafrost in these areas.

An additional complicating factor is that vegetation is not a static characteristic but will in many cases change in response to changes in permafrost. Changes in surface elevation and stability due to subsidence and erosion will change vegetation, usually to wetter types (Jorgenson et al. 2006). Increases in active layer depths in southern tundra are likely to increase shrubbiness (Schuur et al. 2007). Complete thawing of permafrost that allows previously saturated soils to drain will improve conditions for tree-line advance (Lloyd et al. 2003).

Conclusions

This study highlights both the effects of permafrost on vegetation, and conversely, the effects of vegetation on permafrost. A GLM analysis found that when added to a model that included climate and lake cover, permafrost characteristics accounted for an additional 11% of the variation in NDVI. High ice-content permafrost with shallow overburden was most strongly correlated with lower NDVI.

Over 75% of permafrost on land in the Arctic is covered by non-barren vegetation types, resulting in some degree of ecosystem-modification of the permafrost. Vegetation insulates the soil from both summer warmth and winter cold, with the net effect depending on vegetation characteristics. Thick moss layers and erect shrubs have the greatest effects on soil thermal regimes, and vegetation types with both occur in areas with medium to high ice-content permafrost and in areas of non-continuous permafrost. Including thermal characteristics of vegetation and the spatial distribution of different vegetation types, though complex, will be important for predicting the effects of climate change on permafrost in these areas.

Acknowledgments

Research for this publication was supported in part by a Univ. of Alaska International Polar Year (IPY) graduate fellowship through the Cooperative Institute for Arctic Research (CIFAR) with funds from NOAA under cooperative agreement NA17RJ1224, and NSF grants ARC-0531180 and ARC-0425517. Comments from three anonymous reviewers were very helpful in revising and focusing the paper.

References

Anisimov, O.A. & Reneva, S. 2006. Permafrost and changing climate: the Russian perspective. *Ambio.* 35(4): 169-175.

CAVM Team. 2003. *Circumpolar Arctic Vegetation Map*, scale 1:7,500,000, Conservation of Arctic Flora and Fauna (CAFF) Map No. 1. U.S. Fish and Wildlife Service, Anchorage, Alaska.

Comiso, J.C. 2006. Arctic warming signals from satellite observations. *Weather* 61(3): 70-76.

Comiso, J.C., Parkinson, C.L., Gersten, R. & Stock, L. 2008. Accelerated decline in the Arctic sea ice cover. *Geophysical Research Letters* 35: L01703.

Goward, S.N., Markham, B., Dye, D.G., Dulaney, W. & Yang, J. 1991. Normalized Difference Vegetation Index measurements from the Advanced Very High Resolution Radiometer. *Remote Sensing of Environment* 35: 257-277.

Hassol, S.J. (ed.) 2004. *Impacts of a Warming Arctic, Arctic Climate Impact Assessment*. Cambridge, UK: Cambridge University Press, 146 pp.

Hope, A.S., Kimball, J.S. & Stow, D.A. 1993. The relationship between tussock tundra spectral reflectance properties, and biomass and vegetation composition. *International Journal of Remote Sensing* 14(10): 1861-1874.

Jorgenson, M.T., Racine, C.H., Walters, J.C. & Osterkakmp, T.E. 2001. Permafrost degradation and ecological changes associated with a warming climate in Central Alaska. *Clim. Change* 48: 551-579.

Jorgenson, M.T., Shur, Y.L. & Pullman, E.R. 2006. Abrupt increase in permafrost degradation in Arctic Alaska. *Geophysical Research Letters* 33: L02503.

Kade, A.N., Romanovsky, V.E. & Walker, D.A. 2006. The *n*-factor of nonsorted circles along a climate gradient in arctic Alaska. *Permafrost and Periglacial Processes* 17: 279-289.

Lloyd, A.H., Yoshikawa, K., Fastie, C.L., Hinzman, L. & Fraver, M. 2003. Effects of permafrost degradation on woody vegetation at arctic treeline on the Seward Peninsula, Alaska. *Permafrost and Periglacial Processes* 14: 93-101.

Mann, D.H., Peteet, D.M., Reanier, R.E., & Kunz, M.L. 2002. Responses of an arctic landscape to Late Glacial and Early Holocene climatic changes: the importance of moisture. *Quaternary Science Reviews* 21: 997-1021.

Markon, C.J., Fleming, M.D. & Binnian, E.F. 1995. Characteristics of vegetation phenology over the Alaskan landscape using AVHRR time-series data. *Polar Record* 31(177): 179-190.

Nelson, F.E., Anisimov, O.A. & Shiklomanov, N.I. 2001. Subsidence risk from thawing permafrost. *Nature* 410: 889-890.

R Development Core Team 2006. *R: A language and environment for statistical computing*. R Foundation for Statistical Computing, Vienna, Austria.

Raynolds, M.K., Walker, D.A. & Maier, H.A. 2006. NDVI patterns and phytomass distribution in the circumpolar Arctic. *Remote Sensing of Environment* 102(2006): 271-281.

Riedel, S.M., Epstein, H.E., Walker, D.A., Richardson, D.L., Calef, M.P., Edwards, E.J. & Moody, A. 2005. Spatial and temporal heterogeneity of vegetation properties among four tundra plant communities at Ivotuk, Alaska, U.S.A. *Arctic, Antarctic and Alpine Research* 37(1): 25-33.

Schuur, E.A.G., Crummer, K.G., Vogel, J.G. & Mack, M.C. 2007. Plant species composition and productivity following permafrost thaw and thermokarst in Alaskan tundra. *Ecosyst.* 10:280-292.

Shippert, M.M., Walker, D.A., Auerbach, N.A. & Lewis, B.E. 1995. Biomass and leaf-area index maps derived from SPOT images for Toolik Lake and Imnavait Creek areas, Alaska. *Polar Record* 31: 147-154.

Shur, Y. & Jorgenson, M.T. 2007. Patterns of permafrost formation and degradation in relation to climate and ecosystems. *Permafrost & Periglac. Proc.* 18: 7-19.

Stow, D.A., Hope, A., McGuire, D., Verbyla, D., Gamon, J., Huemmrich, F., Houston, S., Racine, C., Sturm, M., Tape, K., Hinzman, L., Yoshikawa, K., Tweedie, C., Noyle, B., Silapaswan, C., Douglas, D., Griffith, B., Jia, G., Epstein, H., Walker, D., Daeschner, S., Petersen, A., Zhou, L. & Myneni, R. 2004. Remote sensing of vegetation and land-cover change in arctic tundra ecosystems. *Remote Sensing of Environment* 89(3): 281-308.

van Wijk, M.T. & Williams, M. 2005. Optical instruments for measuring leaf area index in low vegetation: application in arctic ecosystems. *Ecological Applications* 15(4): 1462-1470.

Walker, D.A., Epstein, H.E., Gould, W.A., Ping, C.-L., Romanovsky, V.E., Shur, Y., Tarnocai, C.T., Daanen, R.P., Gonzalez, G., Kade, A.N., Kelley, A.M., Krantz, W.B., Kuss, H.P., Matveeva, N.V., Michaelsen, G.J., Munger, C.A., Nicolsky, D.J., Peterson, R.A., Raynolds, M.K. & Vonlanthen, C.M. 2007 (in press). Arctic patterned-ground ecosystems: a synthesis of studies along a North American Arctic Transect. *Journal of Geophysical Research - Biogeosciences.*

Walker, D.A., Jia, G.J., Epstein, H.E., Chapin, F.S., Copass, C., Hinzman, L.D., Knudson, J.A., Maier, H.A., Michaelson, G.J., Nelson, F.E., Ping, C.L., Romanovsky, V.E. & Shiklomanov, N. 2003. Vegetation-soil-thaw-depth relationships along a low-arctic bioclimate gradient, Alaska: synthesis of information from the ATLAS studies. *Permafrost and Periglacial Processes* 14: 103-123.

Walker, D.A., Raynolds, M.K., Daniels, F.J.A., Einarsson, E., Elvebakk, A., Gould, W.A., Katenin, A.E., Kholod, S.S., Markon, C.J., Melnikov, E.S., Moskalenko, N.G., Talbot, S.S., & Yurtsev, B.A. 2005. The Circumpolar Arctic Vegetation Map. *Journal of Vegetation Science* 16: 267-282.

Washburn, A.L. 1980. *Geocryology*. New York: John Wiley & Sons, 406 pp.

Zhang, T., Barry, R.G., Knowles, K., Heginbottom, J.A. & Brown, J. 1999. Statistics and characteristics of permafrost and ground-ice distribution in the northern hemisphere. *Polar Geogr.* 23(2): 132-154.

Rock Glacier Distribution and the Lower Limit of Discontinuous Mountain Permafrost in the Nepal Himalaya

Dhananjay Regmi
Central Department of Geography, Tribhuvan University, Kathmandu, Nepal

Abstract

This study, by dealing with the distribution of rock glaciers as an indicator landform for mountain permafrost occurrence, estimated the existence of permafrost in five different study areas of the Nepal Himalaya (from east to west): Kangchenjunga, Khumbu, Langtang, Annapurna, and Sisne). Rock glaciers were identified by aerial photographs at all five sites, and they were checked in the field at the three sites Kangchenjunga, Khumbu, and Langtang. First, periglacial as well as glacial rock glaciers were mapped. Glacial rock glaciers were observed only in eastern Nepal, which may be attributed to the high amount of precipitation. In a second step, only periglacial rock glaciers were extracted and analyzed within a GIS by considering area, altitude, and aspect. The results show that: (1) the size of the rock glaciers tends to decrease from east to west, (2) the mean altitude of rock glaciers decreases towards the west, and (3) the aspects of the rock glaciers are variable, but southerly aspects are most common.

Keywords: glacial rock glaciers; Nepal Himalaya; periglacial rock glaciers; permafrost; rock glaciers.

Introduction

Rock glaciers, known and studied in high altitudes as well as high latitude regions, are considered to be one of the indicators of the presence of permafrost (Haeberli 1985, Barsch 1996). The spatial distribution of rock glaciers reflects climatic conditions, particularly the mean annual air temperature (MAAT) and mean annual precipitation (MAP) (Humlum 1998). The calculated critical conditions for the presence of active rock glaciers in the Central European Alps are MAAT of less than -1/-2°C and MAP of less than 2000 mm. These landforms are typical of regions with a cold, dry continental climate (Barsch 1996, King 1986).

Mountain permafrost in low and mid latitudes is considered to be sensitive to climate changes due to the fact that its temperature is close to the melting point (e.g., Haeberli 1985). Warming and degradation of permafrost have been reported in many mid latitude mountains: air and borehole temperatures have shown apparent warming trends in recent years in European mountains (Vonder Mühll et al. 1998, Harris et al. 2001, Isaksen et al. 2001, Harris et al. 2003). This may lead to an increase of natural hazards in high alpine environments. Slope failures, rockfalls, landslides and debris flows, all of which are assumed to be influenced by changes in the permafrost conditions, are known from numerous locations in high mountains, especially in the Alps (Haeberli et al. 1999, Harris et al. 2001). Therefore, proper knowledge of the permafrost distribution becomes highly significant.

Permafrost in Nepal has received very little scientific attention, despite the fact that Nepal is a country known for the Himalaya. The number of studies in the Nepal Himalaya is comparatively few and the knowledge of permafrost distribution is very limited. The distribution of permafrost was evaluated in the Nepal Himalaya initially by Fujii and Higuchi (1976) using ground temperatures. They indicated the possibility of permafrost occurrence above 4900 m in the Khumbu valley and above 5000 m in the Hidden valley. Since then, the zonation of mountain permafrost has been attempted based on the distribution of rock glaciers (Jacob 1992, Ishikawa et al. 2001), and the lower limit of discontinuous mountain permafrost zone was predicted to be at around 4800 to 5500 m.

This study examines the distribution of rock glaciers in the Nepal Himalaya in terms of size, altitude and slope orientation by focusing on five study areas. Furthermore, on the basis of active and inactive rock glaciers in these five areas of the Nepal Himalaya, the study describes the distribution of discontinuous permafrost. The relationship between the altitudinal distribution of rock glaciers and precipitation is also discussed.

Study Area

This study focuses on five study areas of the Nepal Himalaya: Kangchenjunga, Khumbu, Langtang, Annapurna, and Sisne Himal (Fig. 1). The easternmost area, Kangchenjunga, is located around 700 km from the Bay of Bengal, whereas the westernmost area, Sisne Himal, lies approximately 1100 km from Kangchenjunga. The climate in the east is strongly influenced by the southwest monsoon of the Indian sub-continent, whereas the one in the west is dominantly influenced by the mid-latitude westerlies (Asahi 2004). Hence, a substantial decrease in the MAP occurs across the Himalaya from the east to the west (Fig. 1). The selected study areas described here provide an opportunity to examine rock glaciers within different climatic and geomorphological settings. A brief description of all five study areas is given below and summarized in Table 1.

Kangchenjunga Himal (size of study area: 260 km²)

Kangchenjunga Himal, which includes peaks higher than 8000 m in altitude including the third highest peak in the world (Mount Kangchenjunga, 8586 m a.s.l.), lies in

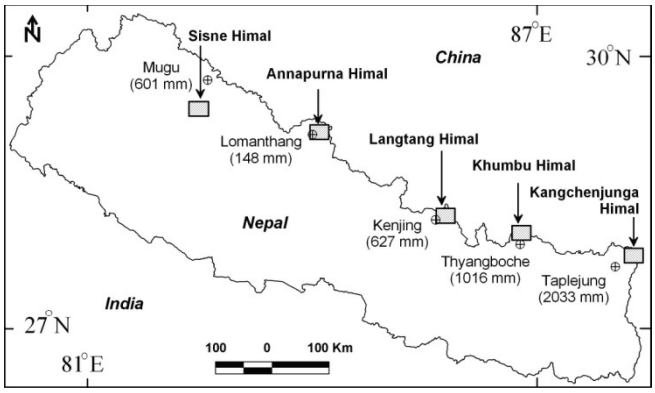

Figure 1. Location of the study area (shaded rectangles) and mean annual Precipitation (MAP) at relevant meteorological stations.

Table 1. Name and location of the five study areas, its coverage by aerial photograph interpretation and number of used aerial photographs at each site.

Name	Lat.	Long.	Area (km²)	Number of aerial phot.
Kangchenjunga Himal	27°45	88°05	260	41
Khumbu Himal	27°55	86°50	345	55
Langtang Himal	28°10	85°35	396	63
Annapurna Himal				
(a) Damodar Himal	*29°10*	*83°50*	*199*	*32*
(b) Mustang Himal	*29°10*	*84°10*	*161*	*24*
Sisne Himal	29°25	82°20	293	46
Total			1654	261

the easternmost part of the Nepal Himalaya (Fig. 1). The climate of this area is strongly influenced by maritime air masses (Ishikawa et al. 2001). The recorded MAP between 1987 and 1998, at the nearest permanent meteorological station (Taplejung: 1732 m a.s.l., about 60 km southwest of the study area), was 2033.4 mm, approximately 70% of which occurred during the summer monsoon period between June and September (DHM 1991, 1997, 2000). The study area receives less rainfall than the Taplejung area due to its leeward location further inland.

Khumbu Himal (size of study area: 345 km²)

Khumbu Himal is located in the eastern part of the Nepal Himalaya and includes Mount Everest and other peaks higher than 8000 m a.s.l. The climate in Khumbu is dominated by strong seasonality. A rainy season occurs between June and September; similar to the Kangchenjunga study area. Precipitation generally falls as snow above 5600 m a.s.l. The recorded MAP between 1967 and 1979 at the nearest permanent meteorological station (Thyangboche: 3867 m a.s.l., about 10 km southwest of the study area), was 1016 mm (DHM 1976, 1980).

Langtang Himal (size of study area: 396 km²)

Langtang Himal is located about 60 km north of Kathmandu (Fig. 1). The Langtang valley is surrounded by the high mountain ranges of Langtang Himal and Jugal Himal. Langtang Himal, with summit altitudes of about 6500 to 7200 m a.s.l., makes the northern and eastern divides, bordering Nepal and Tibet (China). Jugal Himal, with the peak altitudes of about 6800 m a.s.l., makes the southern divide. The MAP in the period 1987 to 1997 at the nearest permanent meteorological station (Kenjing: 3920 m a.s.l.) was 626 mm (DHM 1991, 1997, 2000).

Annapurna Himal - Upper Mustang area (size of study area: 360 km²)

Upper Mustang lies in the northern part of Mustang. It borders Tibet to the northeast, Dolpa District to the west. The highest peaks to the south exceed 6000 m in elevation. In 1992, Upper Mustang was included as one of the seven sectors of the Annapurna Conservation Area, the largest protected area in Nepal. The study area is subdivided into Damodar Himal to the south-east, and the Mustang Himal to the south-west of Lo Manthang, the largest settlement of Upper Mustang. The climate of Upper Mustang can be characterized as a rain shadow desert, desiccated by strong winds and high solar radiation. The region falls under the Dhaulagiri–Annapurna mountain rain-shadow zone (Asahi 2004). The recorded MAP for the neighboring station Lomanthang: 3705 m a.s.l. in the period 1976 to 1996 was only 148 mm (DHM 1980, 1986, 1991, 1997). Rainfall varies within Mustang with southern areas receiving slightly more rain than the north (Kunwar 2002).

Sisne Himal (size of study area: 293 km²)

Sisne Himal lies in the central southern part of western Nepal, with its highest peak of 5582 m a.s.l. The major parts of the mountain ridges do not exceed 5000 m in elevation and only some small glaciers exist. The recorded MAP between 1973 and 1996 at the nearest permanent meteorological station (Mugu: 3803 m a.s.l.) was 601 mm (DHM 1976, 1980, 1986, 1991, 1997).

Methodology

Permafrost, usually a subsurface phenomenon, and its presence is difficult to identify on the surface. Therefore, rock glaciers were used as a landform indicating permafrost by applying aerial photograph interpretation in all five study areas. Vertical aerial photographs of each study area in its entirety were interpreted using a stereoscope. The 1:50,000 scale aerial photographs were taken by the Survey Department, Government of Nepal in 1992 for eastern Nepal (Kangchenjunga, Khumbu, Langtang) and in 1996 for western Nepal (Annapurna and Sisne). More than 250 photographs were investigated for this study. Rock glaciers were carefully delineated on the aerial photographs and drawn onto analog topographic maps of 1:50,000 scale published by Survey Department, Government of Nepal.

Prior to the interpretation of aerial photographs, field observations were made to check the distribution of rock glaciers in three areas of Kangchenjunga, Khumbu, and

Langtang. The field observations allowed for accurate and more detailed interpretation of the aerial photographs.

The front and side slopes of rock glaciers appear "lighter" than their upper surface on aerial photographs, reflecting the exposure of "fresh" (unweathered) materials and the lack of lichen cover. Such characteristics enabled identification of the location of active and inactive rock glaciers using aerial photographs. Inactive rock glaciers having darker frontal and marginal slopes are observed and mapped in the field.

In order to delineate the discontinuous mountain permafrost zone based on rock glacier distribution, it is important to distinguish the type and origin of rock glaciers (Barsch 1978). Based on origin and geographical locations, rock glaciers are divided into two categories: glacial-origin and periglacial-origin rock glaciers (Humlum 1996). However, the terms glacier rock glacier and periglacial rock glacier are used in this study following Benn and Evans (1998). The origin of rock glaciers was identified on the basis of the rock glacier initiation line altitude (RILA) as suggested by Humlum (1988).

Based on these approaches, periglacial and glacial rock glaciers were mapped by aerial photograph interpretation with field verification. The analog maps with detail field and aerial photograph interpretation results were scanned and digitized in ArcView 3.2. After that, size, altitude, and aspect of each of the periglacial rock glaciers were analyzed using the ArcView Spatial Analyst.

Results

Distribution of periglacial and glacial rock glaciers in the five study areas

A total of 140 rock glaciers were identified by interpretation of aerial photographs in the five study areas of Nepal, covering a total area of 1654 km². Glacial rock glaciers were only found in the eastern Nepal Himalaya, i.e., Kangchenjunga and Khumbu Himal (Table 2).

A total of 22 rock glaciers were identified above 4800 m a.s.l. in Kangchenjunga Himal (Fig. 2a), covering an area of 259.6 km². Eight were recognized as glacial and 14 were periglacial rock glacier.

A total of 58 rock glaciers were identified in Khumbu Himal (Fig. 2b), covering an area of 345.4 km². Four rock glaciers were recognized as glacial and 54 were periglacial rock glacier.

Table 2. Summarized results at each of the five study areas.

Name	r.g. gla. (n)	r.g. perigl. (n)	r.g. all (n)	Total r.g. area	Mean r.g. area
Kangchenjunga Himal	8	14	22	2.45	0.11
Khumbu Himal	4	54	58	5.56	0.09
Langtang Himal	0	13	13	0.89	0.07
Annapurna Himal	0	18	18	1.32	0.07
(a) Damodar Himal	*0*	*9*	*9*	*0.63*	*0.07*
(b) Mustang Himal	*0*	*9*	*9*	*0.09*	*0.07*
Sisne Himal	0	29	29	1.35	0.04
Total	12	128	140		

In Langtang, Annapurna, and Sisne Himal with the examined area of 396.2, 359.7, and 293.1 km², a total of 13, 18, and 29 rock glaciers were identified, respectively (Figs. 2c; 2d; 2e). All rock glaciers in Langtang, Annapurna and Sisne Himal were identified to be of periglacial rock glacier.

The mean size of the rock glaciers (including glacier rock glaciers) is 0.11, 0.09, 0.07, 0.07, and 0.04 km² in Kangchenjunga, Khumbu, Langtang, Annapurna, and Sisne Himal, respectively.

Difference in the size of the periglacial rock glaciers in the Nepal Himalaya

The size comparisons show that the periglacial rock glaciers become smaller from eastern Nepal towards western Nepal although the size of the rock glaciers substantially varies among the study areas (Fig. 3).

In Kanchenjunga Himal, the size of the rock glaciers ranges between 0.03 km² and 0.19 km² with the average of 0.09 km². It ranges between 0.01 km² and 0.29 km² with the average of 0.09 km² in Khumbu Himal. Similarly, in Langtang, the size of rock glaciers ranges between 0.009 km² and 0.028 km², with the average of 0.07 km². In Annapurna, the size of the rock glaciers ranges between 0.04 km² and 0.14 km², with the average of 0.07 km² (Fig. 3). The size of the rock glaciers is substantially decreased in the western Nepal and it ranges between 0.009 km² and 0.107 km², with the average of 0.046 km² in Sisne Himal (Table 3).

Altitudinal variations in periglacial rock glacier distribution from east to west of Nepal

The mean lower limit of periglacial rock glaciers shows a decreasing trend from eastern Nepal (5239 m a.s.l) to western Nepal (4513 m a.s.l.) although the altitude of the rock glaciers significantly varies (Fig. 3). The lowest altitude of all 128 mapped periglacial rock glaciers is 5300 m a.s.l. on the south- to east-facing slopes, and 4800 m a.s.l. on the north to west-facing slopes (Fig. 2a; 3). Rock glaciers are located at the altitude ranging from 4800 m to 5640 m Kangchenjunga Himal. They are located at altitudes ranging from 4440 m to 5400 m, with the mean altitude of 4996 m in Khumbu. Similarly, in Langtang Himal they are located at altitudes ranging from 4600 m to 4920 m, with the mean altitude of 4722 m (Fig. 3). In Annapurna Himal they are

Table 3. Summarized result of altitudinal distribution and mean area of periglacial rock glaciers in five study areas.

Name	Altitudinal range (m a.s.l)	Mean altitude (m a.s.l)	Mean r.g. area
Kangchenjunga Himal	4800-5640	5239	0.09
Khumbu Himal	4440-5400	4996	0.09
Langtang Himal	4600-4920	4722	0.07
Annapurna Himal	4450-5120	4746	0.07
(a) Damodar Himal	*4480-4960*	*4681*	*0.07*
(b) Mustang Himal	*4450-5120*	*4810*	*0.07*
Sisne Himal	4200-4800	4513	0.04

located at altitudes ranging from 4450 m to 5120 m, with the mean altitude of 4746 m, whereas in Sisne Himal they are located at altitudes ranging from 4200 m to 4800 m (Table 3).

Orientational variations in periglacial rock glacier distribution from east to west of Nepal

The aspects of the periglacial rock glaciers from all Nepal Himalaya are shown in Figure 4. The rock glaciers are orientated toward the different directions, but they are mostly found on the south-, southeast-, and southwest-facing slopes.

In Kanchenjunga Himal, aspectual distribution suggests that most rock glaciers are oriented toward the east, south, and southwest directions (Fig. 2a). In Khumbu, rock glaciers are mostly found to be oriented toward the southeast, south and west directions (Fig. 2b). Similarly, rock glaciers are mostly found to be oriented toward the southwest directions in Langtang Himal (Fig. 2c). In Annapurna Himal, rock glaciers are mostly found to be oriented toward the southeast and south directions (Fig. 2d). Likewise, rock glaciers are mostly found to be oriented towards the southeast in Sisne Himal (Fig. 2e).

Discussion

King (1986) and Haeberli et al. (1993) indicated that the total amount of annual precipitation plays an important role in determining a mountain permafrost zone. The altitudinal range of the mountain permafrost zone in general decreases

(a) Kanchenjunga Himal

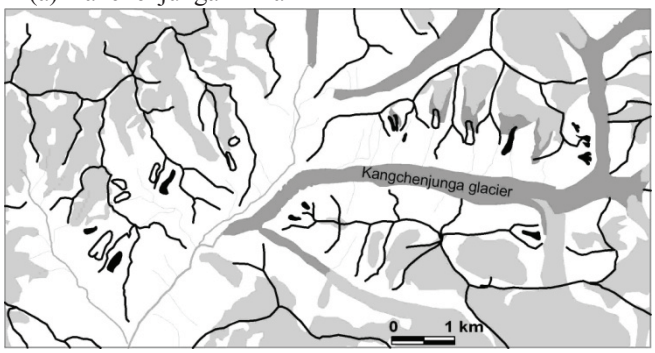

(b) Khumbu Himal

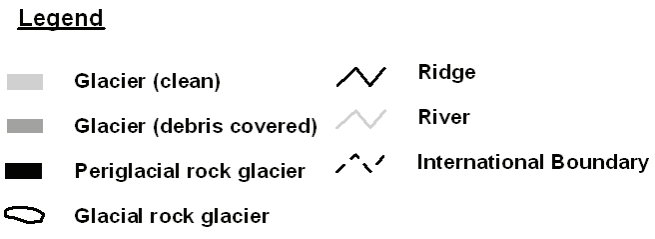

(c) Langtang Himal

(d) Annapurna Himal

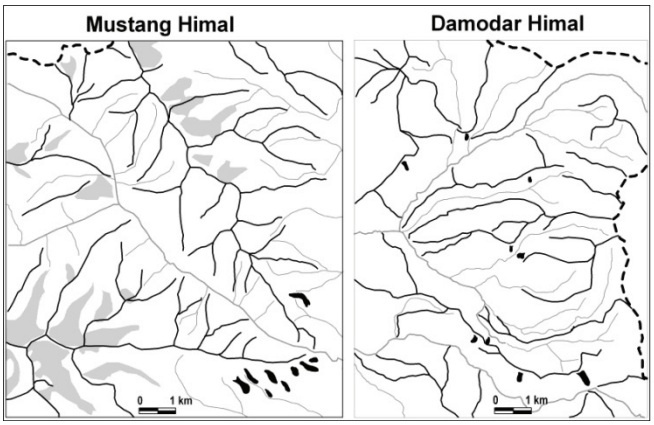

(e) Sisne Himal

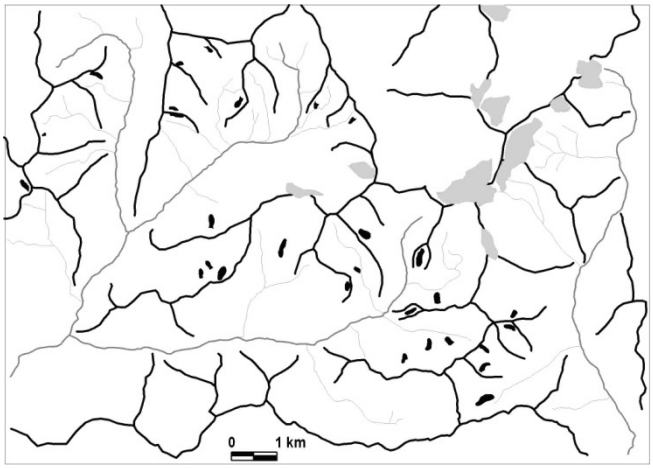

Figure 2. Rock glacier distribution and other landforms in the five study sites (a, b, c, d, and e) in the Nepal Himalaya.

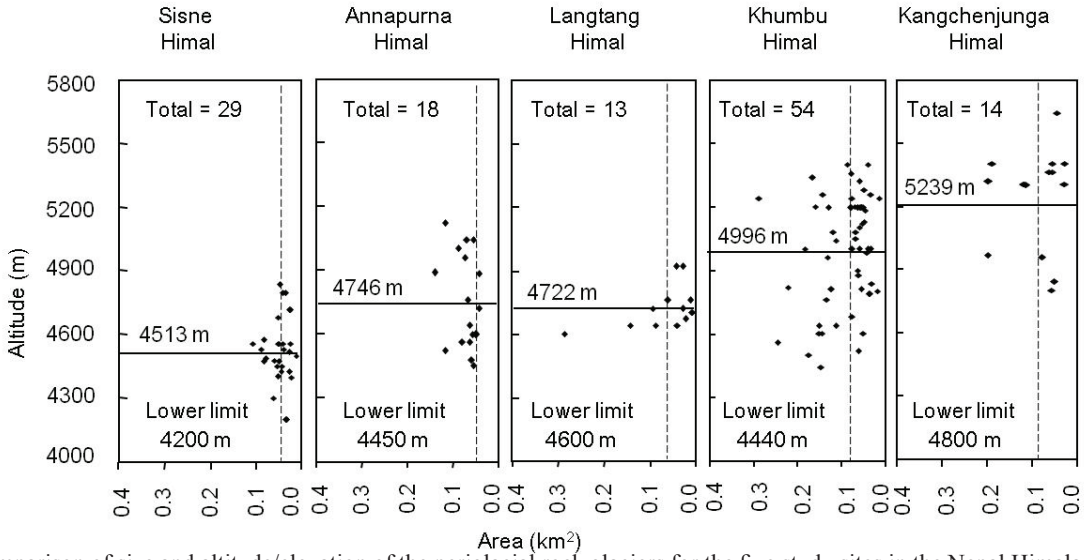

Figure 3. Comparison of size and altitude/elevation of the periglacial rock glaciers for the five study sites in the Nepal Himalaya. Horizontal line indicates the mean altitude of the rock glacier front of all rock glaciers of the given study area. Vertical dotted line indicates the mean area of each region.

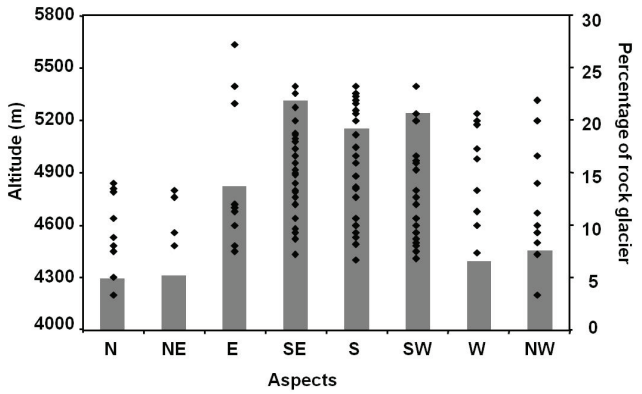

Figure 4. Altitudes and aspects of the periglacial rock glaciers in the Nepal Himalaya (n=128). Each dot shows the altitude of a rock glacier by slope aspect. The bar shows the percentage of the rock glaciers in a given aspect class.

with increasing annual precipitation. MAP substantially decreases from east to west in the Nepal Himalaya. Discussion focuses mainly on the effect of the decrease in precipitation from east to west Nepal Himalaya.

Due to its location in the easternmost part of the Nepal Himalaya, Kangchenjunga Himal is strongly influenced by monsoon winds coming from the Bay of Bengal, which provides high precipitation. MAP at the nearest meteorological station (Taplejung, 1732 m) in the Kangchenjunga region is approximately 2400 mm. Dhar and Nandargi (2000) reported a MAP of 1167 mm at Kambachen (4100 m altitude). This indicates that the permafrost in Kangchenjunga Himal belongs to an oceanic type of mountain permafrost. In contrast, the small amount of MAP in western Nepal (472 mm, in Sisne) indicates that the permafrost in Sisne belongs to a continental type.

The mean lower limit of periglacial rock glacier occurrence is 5239 m a.s.l. in Kangchenjunga Himal and 4996 m in Khumbu Himal (Fig. 3). These altitudes are considerably higher than those in the western Himalaya, which are under dry continental climatic conditions, e.g., 4513 m for Sisne Himal. Owen and England (1998) indicated that rock glaciers in the Pakistan Himalaya are restricted to regions with an MAP of less than 1000 mm and altitudes above 4000 m a.s.l. The decrease in the lower limit of rock glaciers from east to west coincides with the decrease in annual precipitation. This suggests that the MAP may cause the altitudinal difference in the lower limit of discontinuous mountain permafrost zone within the Nepal Himalaya.

Conclusions

The distribution of rock glaciers in five selected study areas in the Nepal Himalaya was mapped by applying aerial photograph interpretation and field observations. Based on this, the distribution of mountain permafrost was assessed. The following conclusions can be drawn from this study.

1. High amount of precipitation in eastern Nepal is most likely to lead to the development of glacial rock glaciers. However, further investigations are recommended considering temperature, snow cover, weathering rates, bedrock type and topography.
2. Periglacial rock glaciers in the eastern Nepal Himalaya tend to be larger than those of the western Nepal Himalaya.
3. The mean altitude of the periglacial rock glaciers decreases towards the western Nepal Himalaya.
4. Aspect of the periglacial rock glaciers is inhomogeneous, but they are mostly found in southern aspects.

Acknowledgments

I would like to thank Dr. Teiji Watanabe for his valuable comments on this manuscript. Special thanks are due to Dr. Yuki Sawada for his suggestions. The Japan Science Society is gratefully acknowledged for the Sasagawa Scientific Research Grant which partly supported this research.

References

Asahi, K. 2004. *Late Pleistocene and Holocene glaciations in the Nepal Himalaya and their implications for reconstruction of paleoclimate*. Ph.D. Thesis. Japan: Graduate School of Environmental Earth Science, Hokkaido University.

Barsch, D. 1978. Rock glaciers as indicators of discontinuous Alpine permafrost. An example from the Swiss Alps. In: *Proceedings, Third International Conference on Permafrost*. Ottawa: National Research Council, 349-352.

Barsch, D. 1996. *Rockglaciers. Indicators for the Permafrost and Former Geoecology in High Mountain Environments.* Berlin: Springer, 331 pp.

Benn, D.I. & Evans, D.J.A. 1998: *Glaciers and Glaciation*. London: Arnold, 734 pp.

Dhar, O.N. & Nandargi, S. 2000. An appraisal of precipitation distribution around the Everest and Kanchenjunga peaks in the Himalayas. *Weather* 55: 223-234.

DHM 1976. *Precipitation Records of Nepal,* 1971-1975. Department of Hydrology and Meteorology (DHM), Ministry of Science and Technology, HMG Nepal, Kathmandu.

DHM 1980. *Precipitation Records of Nepal,* 1976-1979. Department of Hydrology and Meteorology (DHM), Ministry of Science and Technology, HMG Nepal, Kathmandu.

DHM 1986. *Climatological Records of Nepal,* 1980-1985. Department of Hydrology and Meteorology (DHM), Ministry of Water Resources, HMG Nepal, Kathmandu.

DHM 1991. *Precipitation Records of Nepal,* 1987-1990. Department of Hydrology and Meteorology (DHM), Ministry of Science and Technology, HMG Nepal, Kathmandu.

DHM 1997. *Precipitation Records of Nepal,* 1991-1994. Department of Hydrology and Meteorology (DHM), Ministry of Science and Technology, HMG Nepal, Kathmandu.

DHM 2000. *Precipitation Records of Nepal,* 1994-1998. Department of Hydrology and Meteorology (DHM), Ministry of Science and Technology, HMG Nepal, Kathmandu.

Fujii, Y. & Higuchi, K. 1976. Ground temperature and its relation to permafrost occurrences in the Khumbu Himal and Hidden Valley. *Seppyo* Special Issue 38: 125-128.

Haeberli, W. 1985. Creep of mountain permafrost: internal structure and flow of Alpine rock glaciers. *Mitteilungen der Versuchsanstalt fur Wasserbau, Hydrologie und Glaziologie.* Eidgenossische Technische Hochschule, Zurich 77: 142 pp.

Haeberli, W., Guodong, C.H., Gorbunov, A.P. & Harris, S.A. 1993. Mountain permafrost and climatic change. *Permafrost and Periglacial Processes* 4: 165-174.

Haeberli, W., Kääb, A., Hoelzle, M., Bösch H., Funk, M., Vonder Mühll, D. & Keller, F. 1999. Eisschwund und Naturkatastrophen im Hochgebirge, *Schlussbericht*, NFP, Zürich 31.

Harris, C., Davies, M.C.R. & Etzel Müller, B. 2001. The assessment of potential geotechnical hazards associated with mountain permafrost in a warming global climate. *Permafrost and Periglacial Processes* 12: 145-156.

Harris, C., Vonder Muhll, D., Isaksen, K., Haeberli, W., Sollid, J.L., King, L., Holmlund, P., Dramish, F., Guglielmin, M. & Palacios, D. 2003. Warming permafrost in European mountains. *Global and Planetary Change* 39: 215-225.

Humlum, O. 1988. Rock glacier appearance level and rock glacier initiation line altitude: a methodological approach to the study of rock glaciers. *Arctic and Alpine Research* 20: 160-178.

Humlum, O. 1996. Origin of rock glaciers: Observation from Mellemfjord Disko Island, Central West Greenland. *Permafrost and Periglacial Processes* 7: 361-380.

Humlum, O. 1998. The climatic significance of rock glaciers. *Permafrost and Periglacial Processes* 9: 375-395.

Isaksen, K., Holmlund, J., Solid, L. & Harris, C. 2001. Three deep alpine-permafrost boreholes in Svalbard and Scandinavia. *Permafrost and Periglacial Processes* 12: 13-25.

Ishikawa, M., Watanabe, T. & Nakamura, N. 2001. Genetic differences of rock glacier and the discontinuous mountain permafrost zone in Kanchenjunga Himal, eastern Nepal. *Permafrost and Periglacial Processes* 12: 243-253.

Jacob, M. 1992. Active rock glacier and the lower limit of discontinuous alpine permafrost, Khumbu Himalaya, Nepal. *Permafrost and Periglacial Processes* 3: 253-256.

King, L. 1986. Zonation and ecology of high mountain permafrost in Scandinavia. *Geografiska Annaler* 68: 131-139.

Kunwar, P.B. 2002. *Fuel Energy Research in Upper Mustang of Annapurna Conservation Area*. King Mahendra Trust for Nature Conservation/Annapurna Conservation Area Project. Upper Mustang Biodiversity Conservation Program NEP/99/G35 (GEF) & NEP/99/021(TRAC).

Owen, L.A. & England J. 1998. Observations on rock glaciers in the Himalayas and Karakoram Mountains of northern Pakistan and India. *Geomorphology* 26: 199-213.

Vonder Mühll, D., Stucki, T. & Haeberli, W. 1998. Borehole temperatures in alpine permafrost: a ten year series. In: A.G. Lewkowicz & M. Allard (eds.), *Proceedings of the Seventh International Conference on Permafrost.* Collection Nordicana, vol. 57. Quebec: Universite´ Laval: 1089-1095.

Frost-Protected Shallow Foundation Design Issues: A Case Study

Charles H. Riddle
R&M Consultants, Inc., Anchorage, Alaska, USA
James W. Rooney
J&F Rooney, LLC, Anchorage, Alaska, USA
Gregory W. Carpenter
U.S. Army Corps of Engineers, Anchorage, Alaska, USA

Abstract

As part of the Housing Privatization Project at Elmendorf Air Force Base, Alaska, a design/build contract was implemented for the construction of 372 housing units and all associated site improvements. Adverse weather conditions including heavy rainfall with early freezing temperatures and limited snow cover during the fall and early winter period produced conditions conducive to excessive ground frost heaving. The building appurtenances adjacent to the vertical insulation and above the horizontal insulation were exhibiting excessive and unacceptable upward movement. These adverse impacts included heaving stoops, patio slabs, driveways, and uplifting of the protective perimeter vertical insulation board. A plan to repair the damaged work product was developed and implemented. The repair efforts involved removal of all damaged items. Either excavation of the silt layer or placement of additional horizontal insulation board was determined on a site-specific basis. It is important to critically assess the potential for differential movement associated with building perimeter appurtenances.

Keywords: building appurtenances; foundation insulation; frost heave.

Introduction

As part of the Housing Privatization Project at Elmendorf Air Force Base, Alaska, a design/build contract was implemented for the construction of 372 housing units and all associated site improvements. Figure 1 provides an aerial photograph of the site and completed project. The housing units consisted of 93 four-plex buildings of two-story wood frame structure constructed on frost-protected, thickened-slab shallow foundations. The project is located near the Boniface gate entrance, east of Vandenberg Avenue and immediately north and south of Provider Drive. The project owner is Aurora Military Housing, LLC, and construction was completed by Osborne Construction Company and Davis Constructors and Engineers, Inc., in a joint effort with the Hunt Building Corporation.

During the spring of 2001, "fast track" construction was initiated on the Boniface Housing Project. It continued through the following winter period and into the next 2002 full season, with the intent of allowing early occupancy as each of the four phases were completed. The first phase was completed and occupied in early fall 2001 while work continued on the remaining three phases. Adverse weather conditions including heavy rainfall with early freezing temperatures and limited snow cover during the fall and early winter period produced conditions conducive to excessive ground frost heaving. Adverse impacts to building unit perimeter entrances became visually apparent through the winter months. These impacts included heaving stoops, patio slabs, driveways, and uplifting of the protective perimeter vertical insulation board with consequent distortion of cover flashing. The authors were retained to evaluate site conditions and assist in developing remedial solutions for the contractors.

Investigation of soil conditions and perimeter appurtenances revealed frost penetration to depths of 0.9 to 1.2 m and the presence of a saturated frozen silt layer, having a variable thickness ranging from 0.3 to 1.2 m, interspersed in a sandy gravel and gravelly sand outwash deposit. It was apparent that the buildings' shallow foundation perimeter insulation was limiting frost penetration below the slabs in accordance with design requirements; however, the building appurtenances adjacent to the vertical insulation and above the horizontal insulation were exhibiting excessive and unacceptable upward movement, up to as much as 75 to 100 mm. In many instances, the larger movement resulted from a "cantilevered" lifting of the frozen material overlying the horizontal insulation board.

After review of all the conditions, a plan to repair the damaged work product was developed and implemented. The repair efforts involved removal of all damaged items. Either excavation of the silt layer or placement of additional horizontal insulation board was determined on a site-specific basis. Additional efforts were made to control roof drainage and to improve drainage away from the building perimeter. The vertical insulation board was removed and reattached in a more positive manner in those areas where excessive movement had occurred. For the 192 housing units involved, the required repairs included 111 front entry stoops, 98 patios, 92 back stoops, 80 driveways, and 82 sidewalks.

As with most structures founded on soils that are subjected to frost heave effects, it is important to critically assess the

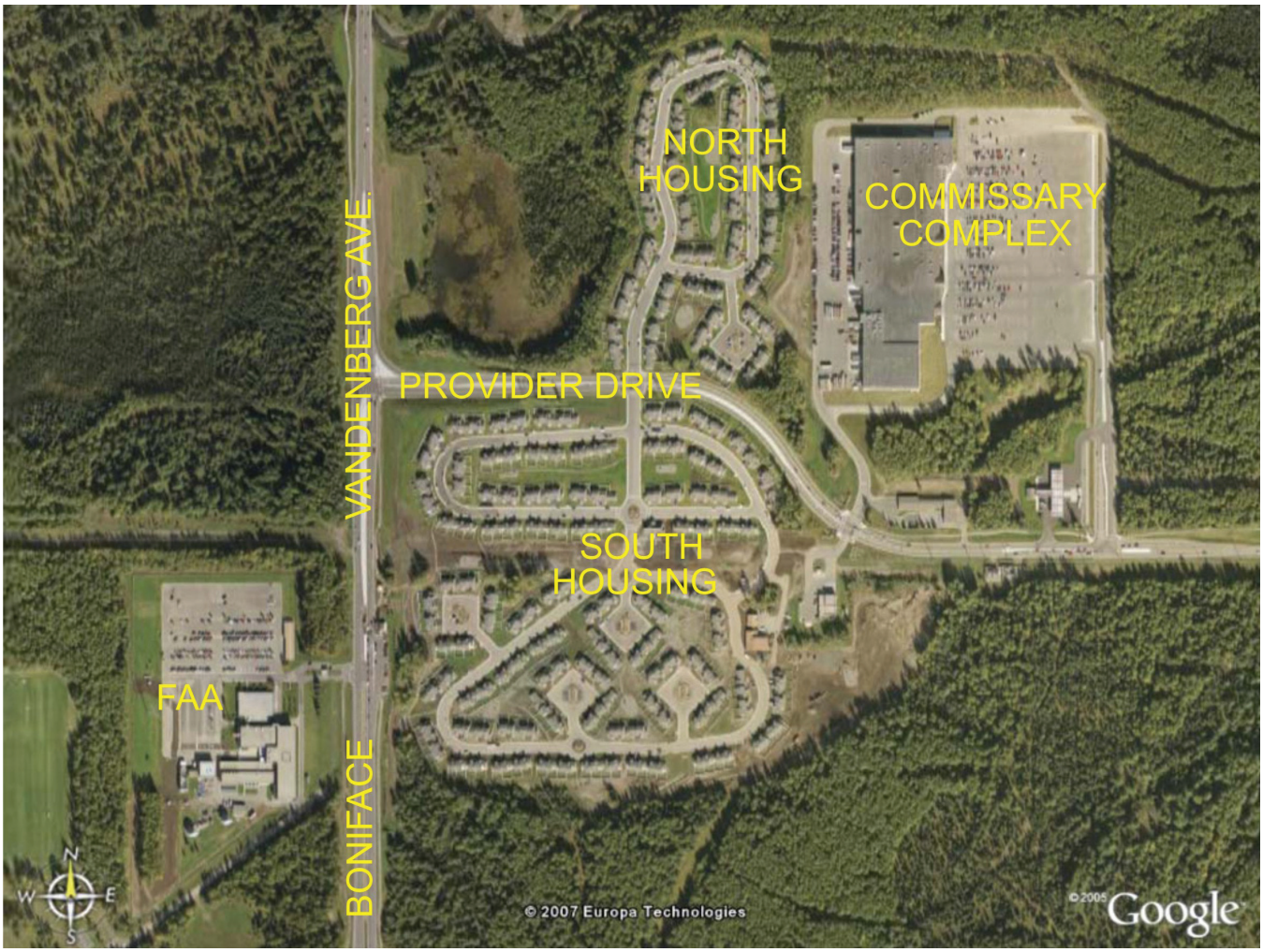

Figure 1. Aerial photograph showing Boniface Housing Project and adjacent commissary complex.

potential for differential movement associated with building perimeter appurtenances. In this case, a combination of circumstances created conditions that caused excessive differential frost heaving.

Historical Use of Frost-Protected Shallow Foundations

Some of the earliest reported work on the use of frost-protected foundations dates back to the late 1960s and early 1970s (Woodworth & Krzewinski 2002, Robinsky & Bespflug 1973, Thue 1974). Since that time, a number of technical papers have identified the effectiveness of this shallow foundation solution when appropriate design measures are implemented. It has also been utilized for remedial applications in repairing frost heave affected foundation systems such as documented in a prior case study (Woodworth & Krzewinski 2002). The Boniface Housing Project utilized the "Design Guide for Frost-Protected Shallow Foundations" (U.S. Dept. of Housing & Urban Dev. 1994). At this point in time, the principle guidelines provided in "Design of Frost-Protected Shallow Foundations" serve as an American Society of Civil Engineers (ASCE) practice standard in the United States.

While all of these documents fully address concerns with building structure foundation performance, little to no information is provided on the treatment of building perimeter appurtenances and the potential adverse effects of transitions at the outer edge of the horizontal insulation boards. This paper is presented for the purpose of identifying some of the adverse impacts that occurred when excess frost heave and unanticipated climate conditions developed during the Boniface Housing Project construction period.

Site Conditions

Elmendorf AFB is located within the Cook Inlet-Susitna Lowland physiographic province and is immediately adjacent to the northern boundary of Anchorage, Alaska. The area is characterized as a glaciated lowland containing areas of ground moraine and stagnant ice topography, drumlin fields, eskers, and outwash plains, with rugged mountains located immediately to the east. This region of Alaska is considered to be generally free of permafrost. One exception is where isolated masses of permafrost occur in lowland areas with high ground insulation, such as peat bogs and swamps. Soils

at the site are interpreted as generally coarse-grained alluvial deposits of well-bedded and well-sorted gravel and sand overlying glacio-marine clay deposits of the Bootlegger Cove formation. The alluvial material is commonly overlain by 0.3 to 1.5 m of silt (R&M Engineering Consultants 2001). Bedrock was encountered at a depth of approximately 136 m in a nearby water well.

Lying between Cook Inlet and the Chugach Mountains, Elmendorf AFB has a transitional climate which may be characterized as variable, with the influence of both maritime and continental climates. Elmendorf AFB receives about 398 mm of precipitation per year. The temperature ranges from extremes of about -36ºC to 29ºC with an annual mean of 2.2ºC. The mean monthly temperature ranges from about -11ºC in January to 14ºC in July.

The undeveloped site was relatively flat, having a gentle southward slope. Much of the site was wooded with spruce and birch trees. Soil conditions within the site were defined by 20 test borings drilled to a depth of about 8.2 m by the Corps of Engineers in September 1998. The surficial soils consisted of silts and silty sand extending to a depth of 0.9 to 1.2 m, overlying sand and gravel that continued to the bottom of the test borings. Groundwater was only encountered in three test holes and was at a depth of 6 m or greater. Moisture content of the silty soil varied from 8% to 33% and averaged about 18%. Average moisture content for the granular soil was less than 4%.

Foundation Design and Building Perimeter Insulation Details

The buildings were constructed with slab-on-grade floor systems and bearing foundations consisting of a thickened perimeter edge, as shown in Figure 2. An air freezing index of 1905ºC-days, corresponding to a 100-year return period, as identified in the "Design Guide for Frost-Protected Shallow Foundations" was utilized. The insulation requirements for preventing frost heave of the thickened edge and spread footings are presented in Table 1.

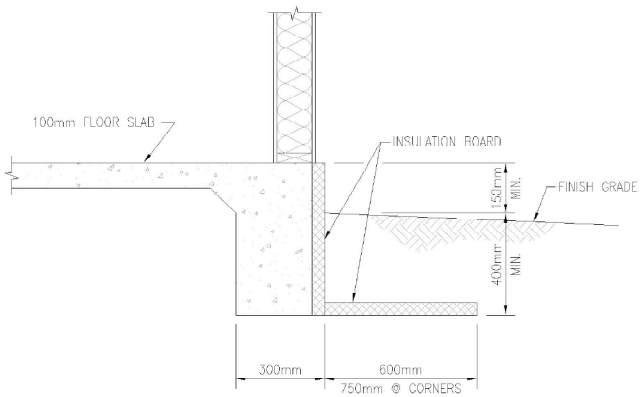

Figure 2. Thickened-slab edge foundation.

Table 1. Project insulation requirements.

Insulation	Thickness	R-Value	Required R-Value
Vertical	38 mm	1.1 k • m²/w	1.0 k • m²/w
Horiz. (walls)	76 mm	2.3 k • m²/w	1.4 k • m²/w
Horiz. (corners)	76 mm	2.3 k • m²/w	2.0 k • m²/w

Freezing temperatures were not observed below any of the foundation insulation board, and the building foundations have remained stable.

The design procedures were based on those required for heated buildings utilizing Anchorage, Alaska, climatic data, and assumed no insulating ground vegetation or snow cover. Since construction continued through the winter months without full building heat effects, it is likely that requirements for an unheated building would have been more appropriate. However, in either case, it seems that the adverse frost heave impacts on perimeter appurtenances would have been the same. With this in mind, an attempt has not been made to evaluate the climate and thermal conditions that actually occurred, but only to address the adverse building perimeter appurtenance impacts.

Frost Heave Impacts on Building Appurtenances

The adverse frost heave impacts resulted from both vertical and horizontal volumetric expansion of the soil, and also from a "cantilevered" lifting of the soil overlying the insulation board. Horizontal forces exerted against the vertical insulation board caused upward movement of the boards as the soil beyond the edge of horizontal board continued to heave. This resulted in sufficient vertical board movement that 1) displaced building perimeter flashing, 2) lifted stoop and patio slabs against door jambs, and 3) raised driveway pavement well above the garage door floor slab surfaces. Some of these conditions are shown in Figures 3a, 3b, 4, 5a, and 5b.

As can be seen in the test pit photograph (Fig. 6), an air gap of over 25 to 30 mm was found above the top of insulation board and the overlying soil cover. An interpretation of the forces and movements that occurred is shown in Figure 7.

When problems with the building perimeter appurtenances became visually apparent, the project contractors initiated efforts to evaluate the causes and to implement corrective

Figure 3a. Ponded water against building between driveway in insulated area that did not heave.

Figure 3b. Garage door and driveway entry with pavement fracture above outside edge of buried horizontal insulation board. Note temporary tapered wood spacer between uplifted asphalt pavement and garage door.

Figure 4. Uplifted concrete patio slab. Door sill and jambs were lifted by patio slab.

actions. Such factors as project schedules, costs, and disruption of occupied building units needed to be considered in developing appropriate corrective action. The project contractors, owner/developer, and involved governmental agencies all worked together to implement necessary corrective measures.

Many driveways that had been constructed experienced significant frost heaving during the period of sub-freezing temperatures. Surface heaving of up to 63 mm was measured between the driveway surface and top of garage floor slab. Heaving of the concrete door stoops and patio slabs was also experienced to the point where door sills and jambs were distorted and impacting door swings and closures. Heaving soil conditions on the outer side of the insulation were also blocking drainage from roof snowmelt during thawing periods and, thus, compounding soil moisture and icing conditions.

Corrective actions for driveways included the following efforts and are shown in Figure 8.

Figure 5a. Displaced vertical insulation board with flashing partially removed.

Figure 5b. View of perimeter base flashing covering vertical insulation board. Flashing has been slightly distorted by upward board movement.

• Removal of all asphalt and underlying silty soil down to gravelly soil or to a depth of 1.5 m.

• Extension of 76 mm horizontal insulation out to 1.8 m from the building edge within the driveway limits.

• Backfill excavation with F2 soil or better up to the insulation level and overlay with 450 mm of non-frost susceptible (NFS) material, 50 mm of crushed aggregate base course, and 50 mm of asphalt.

• Pave driveway to an elevation 12 mm below garage slab floor surface.

Corrective action for concrete stoops and patio slabs included the following efforts and are shown in Figure 9.

• Break up and remove concrete.

• Excavate and remove underlying soil down to the top of horizontal insulation board.

Figure 6. Test pit exposing horizontal insulation board. Air gap was found between insulation board and overlying frozen soil that was lifted by adjacent deeper frozen ground.

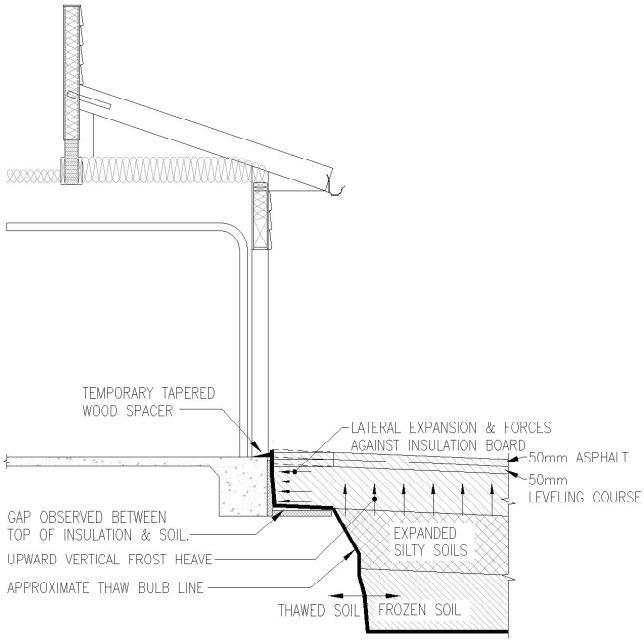

Figure 7. Interpreted ground heaving conditions and consequent expansion forces that caused vertical movement of pavement, stoops, patio slabs, and vertical insulation boards.

• Extend horizontal insulation coverage under entire slab area.

• Backfill with approximately 28 mm of NFS material.

• Remove and replace vertical base flashing using a modified flashing detail.

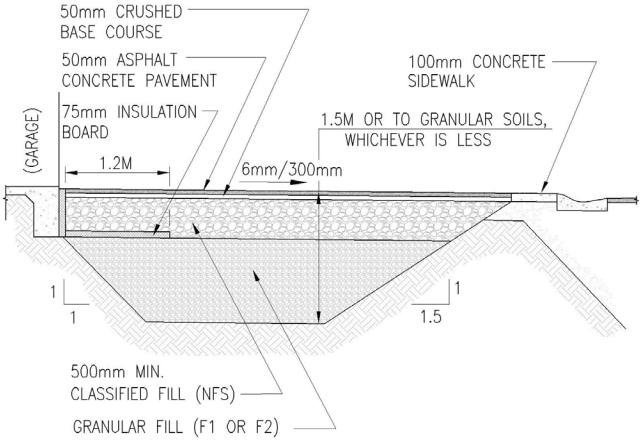

Figure 8. Profile of revised driveway improvement to reduce frost heave effects.

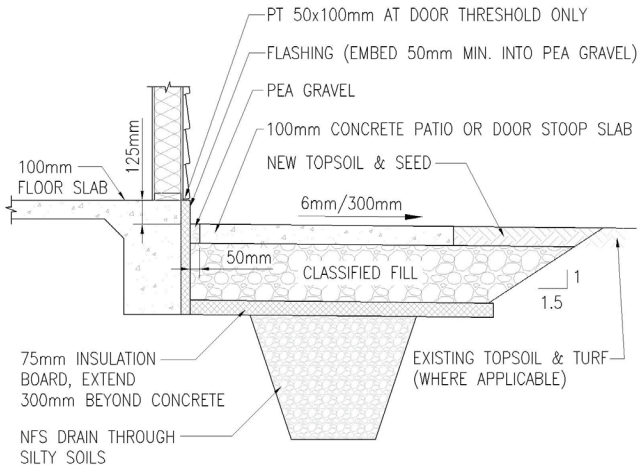

Figure 9. Profile of patio and stoop slab improvements to reduce frost heave effects.

• Re-pour new concrete patio/stoop 125 mm to 150 mm below finish floor elevation using a modified patio/stoop detail.

Corrective action for perimeter base flashing involved some limited total replacement of flashing, but in most cases consisted of cutting off existing flashing and installing new flashing using a two-piece flashing detail, as shown in Figure 10.

Roof drainage collection and disbursement modifications involved the following:

• Revising gutter location over garages to drain to center of driveways and install downspouts to improve drainage away from the building.

• Extension of gutters over front entries to reduce drainage and ice buildup on stoop.

Repairs and modifications for the project were completed by late 2002, and it is apparent that the contractor's efforts to address the frost heave-related problems were successful. Brief visual investigations have been made at those areas

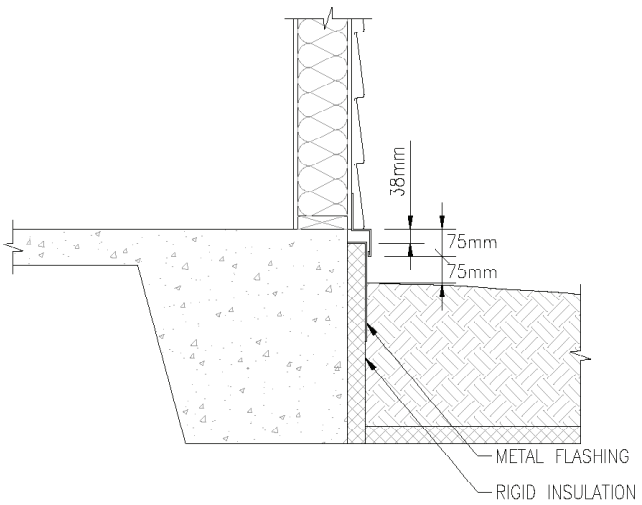

Figure 10. Foundation flashing detail modification to reduce frost jacking effects.

where the more significant frost heave impacts occurred. No evidence of adverse effects have been observed through the summer of 2007.

Closure

As with most structures founded on soils that are subjected to frost heave effects, it is important to critically assess the potential for differential movement associated with building perimeter appurtenances. In this case, a combination of circumstances created conditions that caused excessive differential frost heaving. Adverse weather conditions, including heavy rainfall with early freezing temperatures and limited snow cover during the fall and early winter period, produced conditions conducive to excessive ground frost heaving.

After review of all the conditions, a plan to repair the damaged work product was developed and implemented. The repair efforts involved removal of all damaged items. Either excavation of the silt layer or placement of additional horizontal insulation board was determined on a site-specific basis. Additional efforts were made to control roof drainage and to improve drainage away from the building perimeter.

Problems with building structure perimeter frost heave effects are not unique to just frost-protected shallow foundation structures. There are far too many examples of frost heave and jacking of driveways, decks, patios, and seasonally ponded drainage around buildings constructed on other foundation systems. This paper has been prepared for the purpose of identifying a condition that can occur with any foundation system that has the potential for vertical ground movement adjacent to the perimeter of a fixed structure. It is important for project designers to fully assess the potential for such movement and to develop details that can accommodate anticipated movements.

References

R&M Engineering Consultants. 2001. Soils and Foundation Evaluation, Boniface Gate Housing Development, Elmendorf AFB, Alaska.

Robinsky, E.I. & Bespflug, K.E. 1973. Design of Insulated Foundations, *ASCE Journal of the Soil Mechanics and Foundations Division* Sept.: 649-667.

Thue, J.V. 1974. Thermal Design of Shallow Foundations, *Frost I Jord (Frost Action in Soil)* 13: 5-21.

U.S. Department of Housing and Urban Development, Office of Policy Development Research. 1994. Design Guide for Frost-Protected Shallow Foundations.

Woodworth, J.R. and Krzewinski, T.G. 2002. Case Study: Townhouse Complex Failure Due to Frost Action: Investigation and Repair. *Proceedings of the 11th International Conference Cold Regions Engineering, ASCE.*

Estimating Active Layer and Talik Thickness from Temperature Data: Implications from Modeling Results

D. W. Riseborough
Geological Survey of Canada

Abstract

Projected permafrost warming and degradation due to climate change will make it difficult to continue with current monitoring protocols at some sites, as the top of permafrost descends to depths beyond the reach of active layer probes and thaw tubes. In this paper, thermal modeling results were used to evaluate the accuracy of active layer and talik depths estimates obtained using temperature cable data. The thermal regime of degrading permafrost was simulated using a fine-mesh 1-dimensional finite element model, while active layer and talik depths were estimated using model output at the coarse spacing typical of thermistor cable strings. Results show that estimates of annual active layer and talik depths obtained by extrapolation from above (the unfrozen side of the 0°C isotherm) were more accurate than those obtained by interpolation, or by extrapolation from below, especially where the soil thermal properties were significantly temperature-dependent. Estimates of active layer depth obtained using the annual temperature envelope were no more accurate than those obtained using individual temperature profiles, while estimates of talik depths were more accurate than estimates of active layer depth.

Keywords: active layer; ground temperature; models; talik; permafrost monitoring.

Introduction

Projected permafrost warming and degradation due to climate change will make it difficult to continue with current monitoring protocols at some sites, as the top of permafrost descends to depths beyond the reach of some methods for active layer monitoring. The standard methods for determining active layer thickness include probing, frost tubes, and estimation from soil temperature profiles (Nelson & Hinkel 2004). Probing is limited by field logistics to less than 1.5 m, while thaw tubes as currently designed are limited to about 2.4 m depth (Mark Nixon, personal communication). Estimating active layer and talik depth from temperature profiles is a common practice, but is subject to errors that are the subject of this paper.

Nelson & Hinkel (2004) suggest that the accuracy of the active layer thickness estimates from temperature profiles depends on the distance between measurement depths and the data-collection interval, and indicate that simple linear interpolation between measurements is used to determine calculate the position of the 0ºC isotherm.

Estimating the position of the 0ºC isotherm is also a problem in geothermal modeling, since most numerical models calculate changes in temperature at finite intervals along a profile, and do not calculate the position of the 0ºC isotherm directly. Calculating active layer depths by interpolation in a coarse grid usually produces a time series that follows a scalloped pattern, with slow descent before and rapid descent after the front passes points in the calculation mesh (Fig. 1). This effect depends on the interpolation method, and occurs here because linear interpolation does not account for the change in thermal properties as ice forms at 0ºC, causing an abrupt change in temperature gradient (Fig. 2). Estimating the position of the 0ºC isotherm in profiles such as in Figure 2 could be improved by using extrapolation from the grid temperatures above or below the frost front. The analysis presented in this paper is an attempt to determine whether this is generally true, by examining the magnitude of errors in 0ºC isotherm depth estimates from temperature profiles. Active layer thickness and depth of taliks were both examined, and depth estimates by extrapolation from above, by interpolation, and by extrapolation from below were compared. The effect of the distance between temperature points was also examined. This approach to error analysis could also be applied to other interpolation methods (such as cubic spline or other more sophisticated methods that account for the change in properties across the phase boundary), which are not considered here.

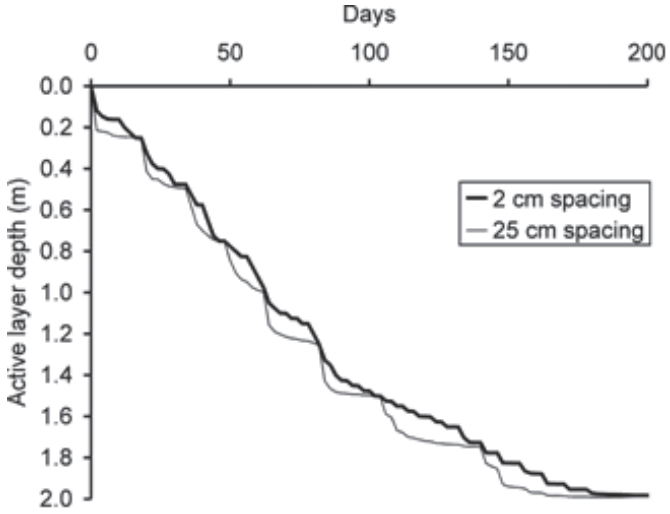

Figure 1. Example of active layer depth estimates from evenly-spaced node temperatures. Note the "scalloped" shape as node depths are approached.

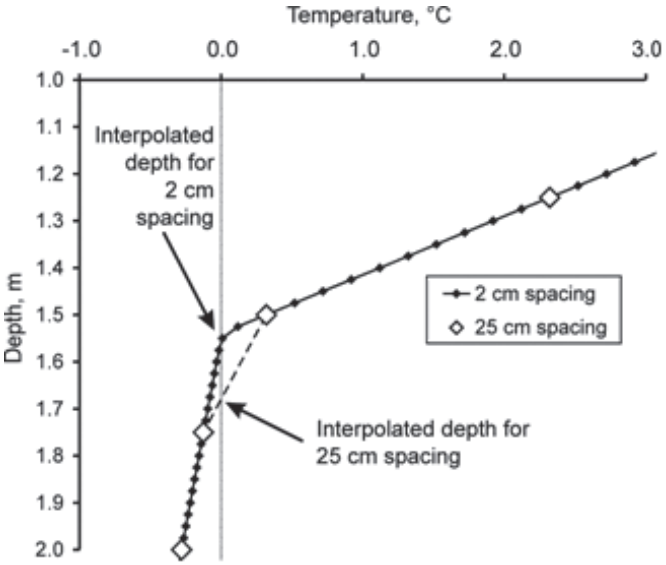

Figure 2. Typical temperature profile detail near the base of the active layer. The scalloping observed in Figure 1 is an effect of the interpolation method, as shown.

Method

Thermal modeling results were used to evaluate the accuracy of active layer and talik depth estimates obtained using temperature cable data. The multi-year thermal regime of degrading permafrost was simulated using a fine-mesh 1-dimensional finite element model, while active layer and talik depths were estimated using model output at the coarse spacing typical of thermistor cable strings. Using the fine-mesh output from the numerical model (spacings of 0.02 to 0.025 m for active layers, and 0.1 m for taliks), the "true" position of the 0ºC isotherm depth could be known to reasonable accuracy (within about 0.01m for active layers, and 0.05 m for taliks). Comparisons with active layer and talik depth estimates by extrapolation or interpolation from temperature data at coarser spacing allowed an evaluation of the relative accuracy of the estimation methods.

For active layer estimates, two different kinds of data were used. The *profile* method applied the estimation methods to instantaneous temperature profiles, allowing the tracking of seasonal progression of the active layer, as in Figure 1. The *envelope* method used annual temperature envelopes (depth profiles of the warmest and coldest ground temperatures experienced in a year) to estimate the annual maximum depth of thaw, applying the estimation methods to the profile of annual maximum temperature.

To evaluate the relationship between accuracy and sensor spacing, thermistor string data were simulated by selecting model output temperature corresponding to the depths appropriate for each spacing evaluated. For the analysis of active layer estimates, spacings of 0.1, 0.2, 0.3, 0.4, 0.5, 0.6, 0.75, and 1.0 m were used; for talik depth estimates, spacings of 0.2, 0.4, 0.6, 0.8, 1.0, 1.5, and 2.0 m were used.

This method was applied to simulations of similar climates, with two distinct substrates yielding somewhat different thermal regimes. The simulated surface climates included daily and inter-annual variability, with a long-term climate trend. Both simulation substrates included a 0.2-m thick saturated surface organic layer, overlying 20 m of saturated soil with 50% volumetric moisture content. For one substrate ("Bimodal"), all phase change was assumed to occur at 0ºC, with thermal properties having frozen and thawed values. The second ("Temperature dependent") substrate material had a substantial unfrozen water characteristic (using the freezing characteristic of Fairbanks silt), with phase change occurring over a broad range of freezing temperatures, resulting in temperature-dependent thermal properties at temperatures below freezing.

Model details

Simulations were made using Goodrich's discontinuous element model TONE (evaluated in Bouchard 1990 and Riseborough 2004). In each time step, the thermal conductivity and apparent heat capacity within each element were averaged based on the temperature profile, improving accounting for the total latent heat. This formulation should produce better results in soils that exhibit strong temperature dependence in thermal properties due to the freezing characteristic, as it accommodates the distribution of thermal properties across each element. Significant transitions over small temperature changes are not lost between points in the calculation mesh. However, this averaging results in a softer transition between frozen and thawed conditions in simulations where phase change is more abrupt.

Simulations

An initial 100-year simulation with a stationary climate was first performed for each substrate to establish an equilibrium initial temperature profile for subsequent simulations For each substrate, a 50-year active layer simulation and a 150-year talik simulation were performed with approximately the same surface climate (with initial mean annual temperature of -6.4, with a 1ºC per decade warming trend). Simulated climates included a 0.4-m deep annual snow cover with a parabolic accumulation function (Zhang 1993) and a density of 350 kg m^{-3}, inter-annual temperature variability (simulated by specifying standard deviations of 10% to the freezing and thawing indices, as described in Riseborough 2007), and daily variability with a standard deviation of 3ºC.

For both substrates, active layer simulations were performed with a fine mesh (0.02 and 0.025 cm spacing) in the upper 3 m (for analysis of active layer estimates) and 32 time steps per day, while talik simulations had a mesh of 0.1 m over the upper 15 m and 8 time steps per day. All simulations extended to 20 m, with a constant heat flux prescribed at the base of the mesh.

In bimodal simulations, talik depths reached 3 m depth after 68 years, and thawed to 15 m by year 118. In the simulations with temperature-dependent thermal properties, thaw depths reached 3 m by year 78, but the earliest were deep active layers, and a persistent talik did not form until year 89. Thaw depth extended to 15 m in year 137.

Analysis

Model outputs consisted of instantaneous temperature profiles at 10-day intervals and annual temperature envelopes, with results recorded for all nodes in the finite element mesh (node spacings of 0.02 and 0.025 m for active layer simulations, and 0.1 m for talik simulations). Once the simulations were complete, node temperatures (simulated "sensors") were used to construct coarser temperature profiles by sampling results at the appropriate depth intervals.

For all analyses, active layer depths were estimated in the same way, using temperature profile and temperature envelope results. Using either the instantaneous profiles or the profile of annual maximum temperature from the envelope, the node depths bounding the 0ºC isotherm were determined, and the appropriate node pairs were selected for the active layer estimate: for interpolation, the bounding nodes were used; for extrapolation, the first two nodes above or below the 0ºC position were used. Using the temperature gradients determined from these pairs, the position of the 0ºC isotherm was determined as the depth-intercept of the line defined by the sampled depth and temperature data.

Initial results showed that extrapolation methods were unreliable once freezeback had been initiated, due to the nearly isothermal conditions present between the freezing fronts bounding the unfrozen active layer. As a result, active layer estimates for instantaneous temperature profiles were not evaluated once freezeback had begun.

Talik depth estimates were obtained as for active layers, except that only one instantaneous temperature profile per year was evaluated. For the analysis of talik depths, only nodes between 3 m and 15 m were examined, in order to exclude active layers from the analysis, and to limit results to the part of the simulated profile with the smaller node spacing. For the cases with bimodal thermal properties, no active layers exceeded 3 m. In the cases with temperature dependent properties, deep active layers developed for several years before the establishment of a persistent talik.

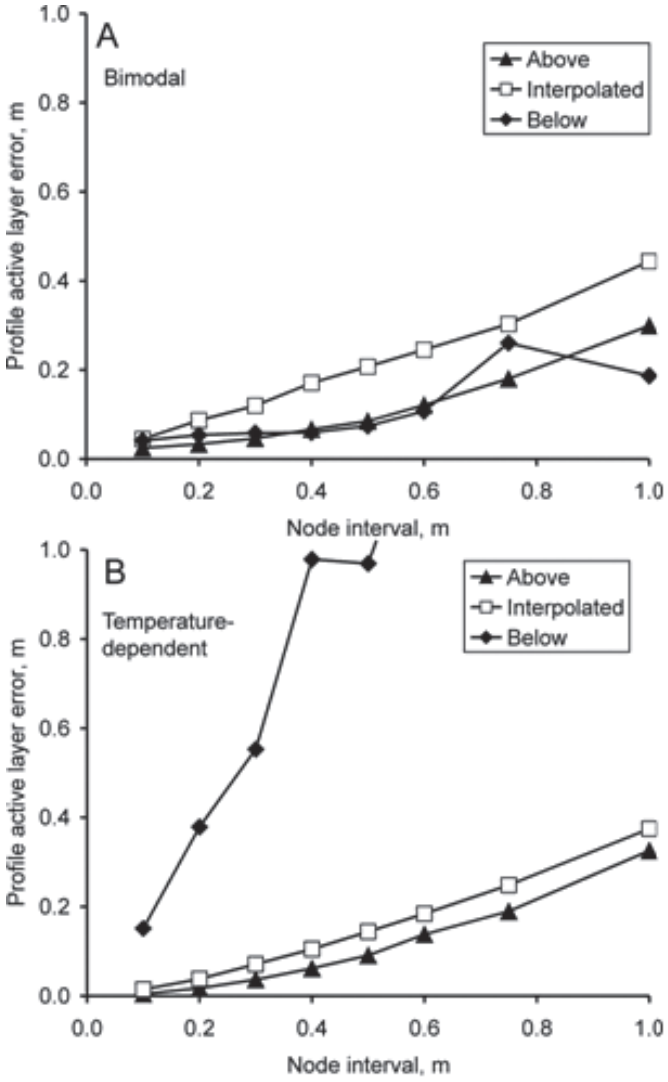

Figure 3. Average error in active layer depth estimated from instantaneous temperature profiles, as a function of selected node interval. A: simulations with bimodal (frozen/unfrozen) thermal properties and all phase change at 0ºC. B: simulations with temperature dependent thermal properties and unfrozen water.

Results and Discussion

Results for all interpolation methods were evaluated using the same procedure: for each profile or envelope, active layer or talik estimates with coarse temperature spacings were compared to estimates obtained with the fine mesh model output, and the average absolute value of all errors for each spacing calculated. Results are presented in Figures 3–5, and show that for all cases, errors increase as the node spacing increases, generally at a rate more than proportional to the increase in spacing. Errors in active layer estimates are not smooth functions of spacing, due to the variability imposed in the simulations.

Active layers from temperature profiles

Figure 3 shows the average error in active layer depth estimated from instantaneous temperature profiles. For the bimodal case, extrapolation yields more accurate active layer depth estimates, for all spacings. Up to a spacing of 0.6 m, the error in active layer depth with either extrapolation method is about half that of the error for interpolation. For the case with temperature dependent thermal properties, estimates based on extrapolation from below are very poor (exceeding the node spacing), while interpolation and extrapolation from above are better than for the bimodal case. The significant difference in errors when extrapolating from below is due to the effect of temperature dependent thermal properties on the temperature gradient, resulting in curvature in the temperature profiles that would make linear extrapolation through the frozen soil unreliable. This same effect is responsible for the improvement in the depth estimates using interpolation, as curvature in the frozen part of the temperature profiles reduces the rate of change of temperature gradient in the upper part of the frozen soil.

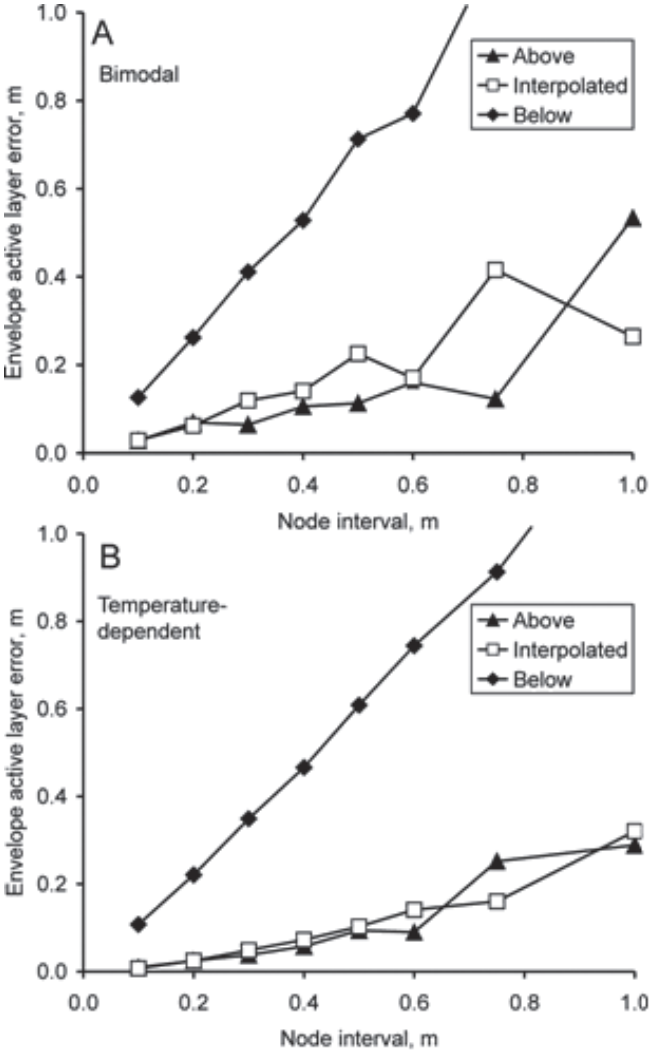

Figure 4. Average error in active layer depth estimated from annual temperature envelopes, as a function of selected node interval. A: simulations with bimodal (frozen/unfrozen) thermal properties and all phase change at 0ºC. B: simulations with temperature dependent thermal properties and unfrozen water.

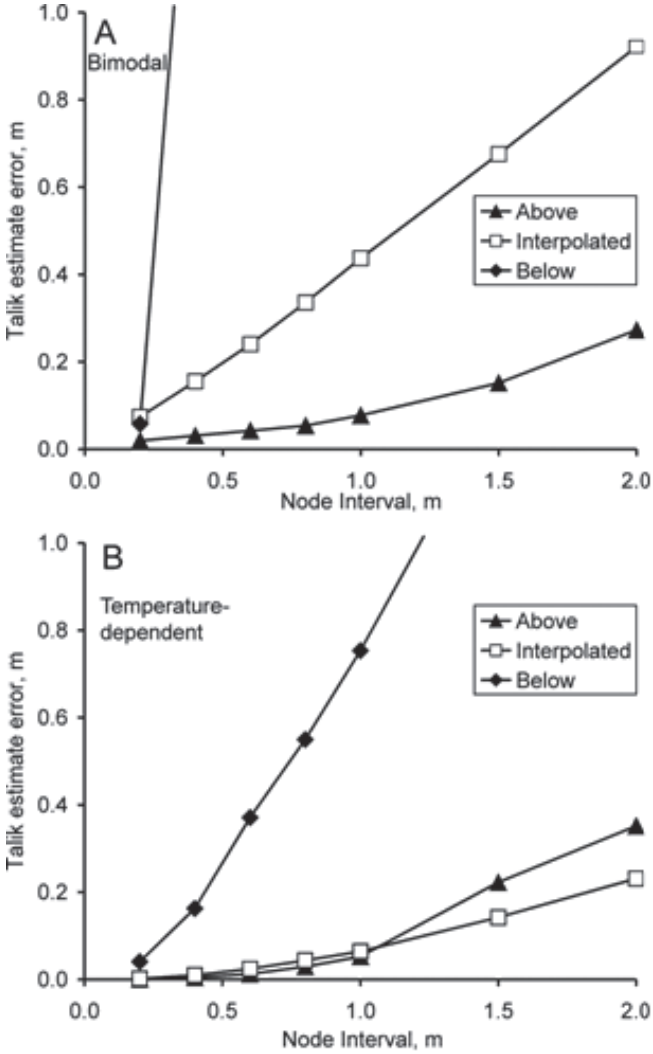

Figure 5. Average errors in estimated talik depth, as a function of selected node interval. A: simulations with bimodal (frozen/unfrozen) thermal properties and all phase change at 0ºC. B: simulations with temperature dependent thermal properties and unfrozen water.

Active layers from temperature envelopes

Figure 4 shows the average error in active layer depth estimated from annual temperature envelopes. These results represent the kinds of estimates that could be obtained using cable temperatures from a data acquisition system, from which a reliable temperature envelope could be derived. Results suggest that the errors in active layer estimates for extrapolation from above is similar to those for instantaneous profiles (Fig. 3), while estimates by extrapolation from below in soils is poor in both soil types (again exceeding the node spacing), and errors in estimates by interpolation are only slightly greater than with estimates by extrapolation from above.

Taliks

Figure 5 shows the average error in talik depth, estimated from instantaneous temperature profiles. Errors are a relatively smooth function of node spacing, due to the more steady thermal conditions within the talik compared to thermal conditions within the active layer. The accuracy of depth estimates by interpolation is similar to that for active layer estimates by instantaneous profiles (Fig. 3), while the error magnitudes when extrapolating from above are much smaller (less than half). For both soil types, extrapolation from below is unreliable, with estimation errors up to nine times the node spacing. This is due to the nearly isothermal conditions present in the permafrost degrading beneath the talik.

Conclusions

Results are summarized in Figure 6, in which the errors presented in Figures 3–5 are expressed as a proportion of the node spacing, shown as averages for all spacings:

1. Extrapolation from above is the most accurate method in all cases, and especially in cases with bimodal thermal properties.

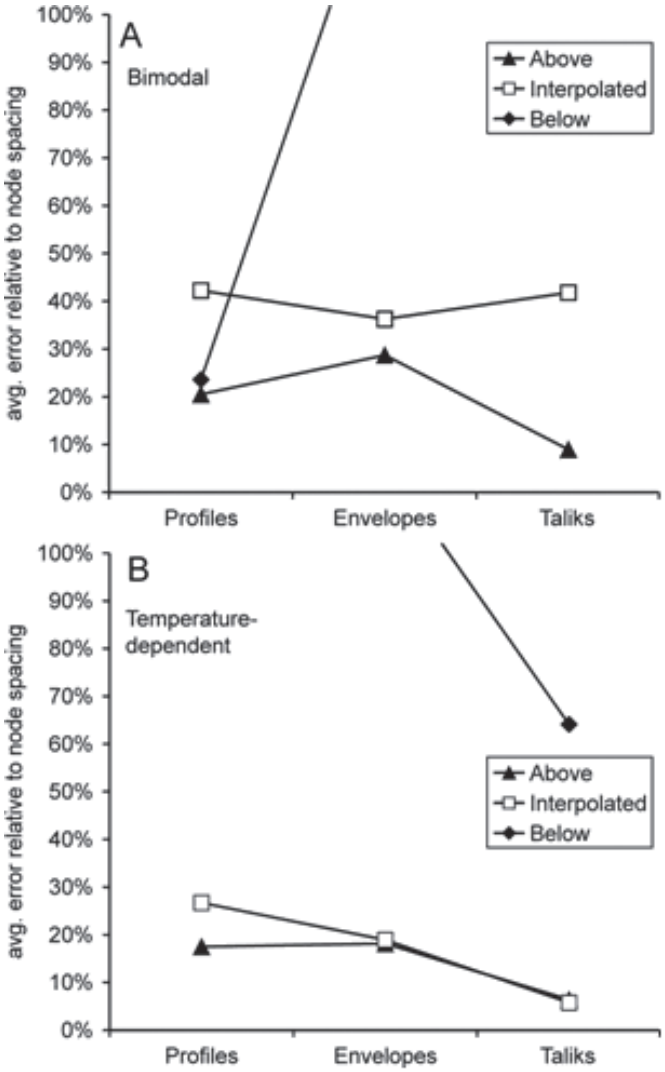

Figure 6. Average active layer/talik depth-estimate errors, expressed as a percentage of the node interval. A: simulations with bimodal (frozen/unfrozen) thermal properties and all phase change at 0ºC. B: simulations with temperature dependent thermal properties and unfrozen water. Results are truncated at 100%, as errors for extrapolation from below approached 900%.

2. For profiles, envelopes, and taliks, soils with bimodal thermal properties (and therefore an abrupt change in gradient at 0ºC), interpolation yields average errors of about 40% of the node spacing.

3. Estimation of active layer thickness from temperature envelopes is less accurate than estimates from profiles. This is likely due to the nature of the envelope data, which combines the effects of the phase transition and of diffusive extinction, yielding a profile that is not as simple to analyze as an instantaneous profile. Given that the average error for all methods exceed 25% of the node spacing when applied to envelope data in soils with bimodal thermal properties, estimates of active layer depth using temperature data from an acquisition system might be improved using sensor thawing indices (Riseborough 2003); alternately, the nearly continuous data would make it possible to select the best instantaneous profiles for estimating the active layer depth, although profiles may not capture the maximum active layer depth.

4. Except for active layer estimates from instantaneous temperature profiles in soils with bimodal thermal properties, extrapolation from below is not a reliable estimation method.

5. Talik depth can be estimated with greater relative precision than active layer depth, as deeper temperature profiles are less influenced by short term perturbations.

The extrapolation results presented here were used without a check to ensure that the 0ºC isotherm estimate was between the bounding sensors. The overall accuracy of active layer or talik estimates could be increased when used in an automated procedure by checking for this condition and reverting to estimation by interpolation where it is not met.

Results for the idealized conditions presented here may be considered a lower limit on the estimation errors investigated, since the precision of modeled temperatures exceeds that of most measurement and recording systems; Spatial and temporal variations in surface thermal conditions and in thermal properties along the soil profile will introduce additional variations not present in the smooth temperature profiles generated by the model.

While the results presented here may be applied to any temperature cable data, they also suggest a cable design strategy for optimizing 0°C isotherm depth estimates. Use of data acquisition systems typically limits the number of sensors to about 10.. Where talik depth or active layer depth is a key parameter in a monitoring program, an optimum cable design would concentrate sensors, with a relatively small spacing, close to the position of the front. A cable design with an extended lead would permit cable repositioning with the evolving thermal regime.

Acknowledgments

The ideas for the analysis presented in this paper developed from conversations with Caroline Duchesne. The comments of the anonymous reviewers were very helpful in improving the quality of the paper.

References

Burn, C.R. 1998. The active layer: two contrasting definitions. *Permafrost and Periglacial Processes* 9: 411-416

Bouchard, C. 1990. Simulation du régime thermique des sols pergélisolés: essai du modèle TONE. Université Laval, Département de Géographie, Mémoire de Maîtrise, 137 pp.

Nelson, F.E. & Hinkel, K.M. 2004. Methods for measuring active-layer thickness. In: Humlum, O. & Matsuoka, N. (eds.), *A Handbook on Periglacial Field Methods* Version 20040406. available on-line at: http://www.unis.no/RESEARCH/GEOLOGY/Geo_research/Ole/PeriglacialHandbook/HandbookMain.htm.

Riseborough, D.W. 2003. Thawing and freezing indices in the active layer. *Proceedings of the Eighth International Conference on Permafrost, Zurich, Switzerland*.

Riseborough, D.W. 2004. *Exploring the Parameters of a Simple Model of the Permafrost: Climate Relationship*. Unpublished PhD dissertation, Carleton University, Ottawa, Canada, 328 pp.

Riseborough, D.W. 2007. The effect of transient conditions on an equilibrium permafrost model. *Permafrost and Periglacial Processes* 18: 21-32.

Zhang, T.J. 1993. *Climate, Seasonal Snow Cover and Permafrost Temperatures in Alaska North of the Brooks Range.* PhD dissertation, University of Alaska, Fairbanks, 232 pp.

Mesoscale and Detailed Geocryological Mapping as a Basis for Carbon Budget Assessment (East European Russian Arctic, CARBO–North Project)

F.M. Rivkin, J.V. Vlasova, A.P. Popova
Fundamentprojekt Institute, Russia
G. Mazhitova
Komi Science Centre, Russian Academy of Sciences, Russia
P. Kuhry
Stockholm University, Sweden
I.S. Parmuzin, I.V. Chehina
Fundamentprojekt Institute, Russia

Abstract

A landscape-geocryological map is considered to be an important basic resource for comprehensive carbon budget studies under the international EU-funded CARBO-North project. The project is aimed at assessing the carbon balance at northern latitudes. The mesoscale and more detailed landscape-geocryological maps were produced for the intensive study sites using an integrated geosystem approach and landscape features indicative of permafrost conditions. The maps actually suggest a model showing spatial patterns of numerous landscape factors responsible for local and regional carbon budgets. The key issue of the mapping technique applied was the development of matrix legends arranged as tables. In general, the structure and content of such tables are variable and depend on study purposes, scale, and environmental conditions of particular areas. Under this study, a mesoscale landscape-geocryological map was produced for the Khoseda–Khard intensive site and a detailed map for the Seida intensive site, both sites located in the forest-tundra life zone.

Keywords: carbon budget; geocryological mapping; landscape; permafrost; zoning.

Introduction

Interannual climate dynamics and the ongoing rise of air temperature in the Arctic induce changes in geocryological conditions: increases in ground temperature and changes in its seasonal dynamics, increases in depth of seasonal thaw, partial degradation of thin permafrost, etc. As the permafrost is an enormous reservoir of organic matter, these changes in its upper layers bear the potential of producing a significant effect on the greenhouse gas balance at northern latitudes. Climate warming and the associated differential settlement of the soil surface can increase the thickness of the seasonally thawed (active) layer. This may substantially change conditions in the upper part of the geological section which, in turn, may lead to changes in drainage patterns and overall regional hydrology. The latter, meanwhile, is one of the major controls on regional carbon balance. In particular, the spatially differential settlement of soil surface may change the ratio of drained to wet areas. It is extremely difficult to forecast the dynamics and scope of such changes. Permafrost degradation is a complicated process associated with numerous feedbacks. Thus, it normally leads to enhancement of wet areas; however, such enhancement causes larger heat losses for the phase transition of water in a seasonal freeze-thaw cycle slowing down the progression of permafrost thaw, and, in some cases, even inducing the formation of new permafrost.

Permafrost is considered a "preserved greenhouse gases reservoir" (Samarkin et al. 1994), while the cryogenic landscapes are deemed a productive environment for this gas generation. The CARBO-North project includes as an important task the development of comprehensive landscape-geocryological maps to be used in the regional carbon budget studies for interpretation, upscaling, modeling, and forecast purposes. While developing the maps, we widely employed a technique related to the use of landscape indicators of permafrost conditions (Armand 1975). This insured common formatting of the maps of different intensive study sites and permitted the mapping of major controls on carbon budgets.

Study Area and Methods

Landscape-geocryological maps were produced for two sites, Khoseda-Khard and Seida (Fig.1).

The Khoseda-Khard site is located at 67°08′N, 59°30′E (center coordinates) and is considered in CARBO-North as a mesoscale intensive study site for assessment of the carbon budget. The site area is about 200 km^2.

Information available in achived databases, analysis of major environmental controls over geocryological conditions at the regional, landscape, and local levels, and results of a field survey we conducted earlier in this area were used for developing a map of the site.

The Seida site is located at 67°03′18″N, 62°56′06″E (center coordinates) and is considered a detailed intensive study site. The mapping area is around 4 km^2. Mapping was performed using satellite images and the results of the field surveys we conducted earlier in adjacent areas.

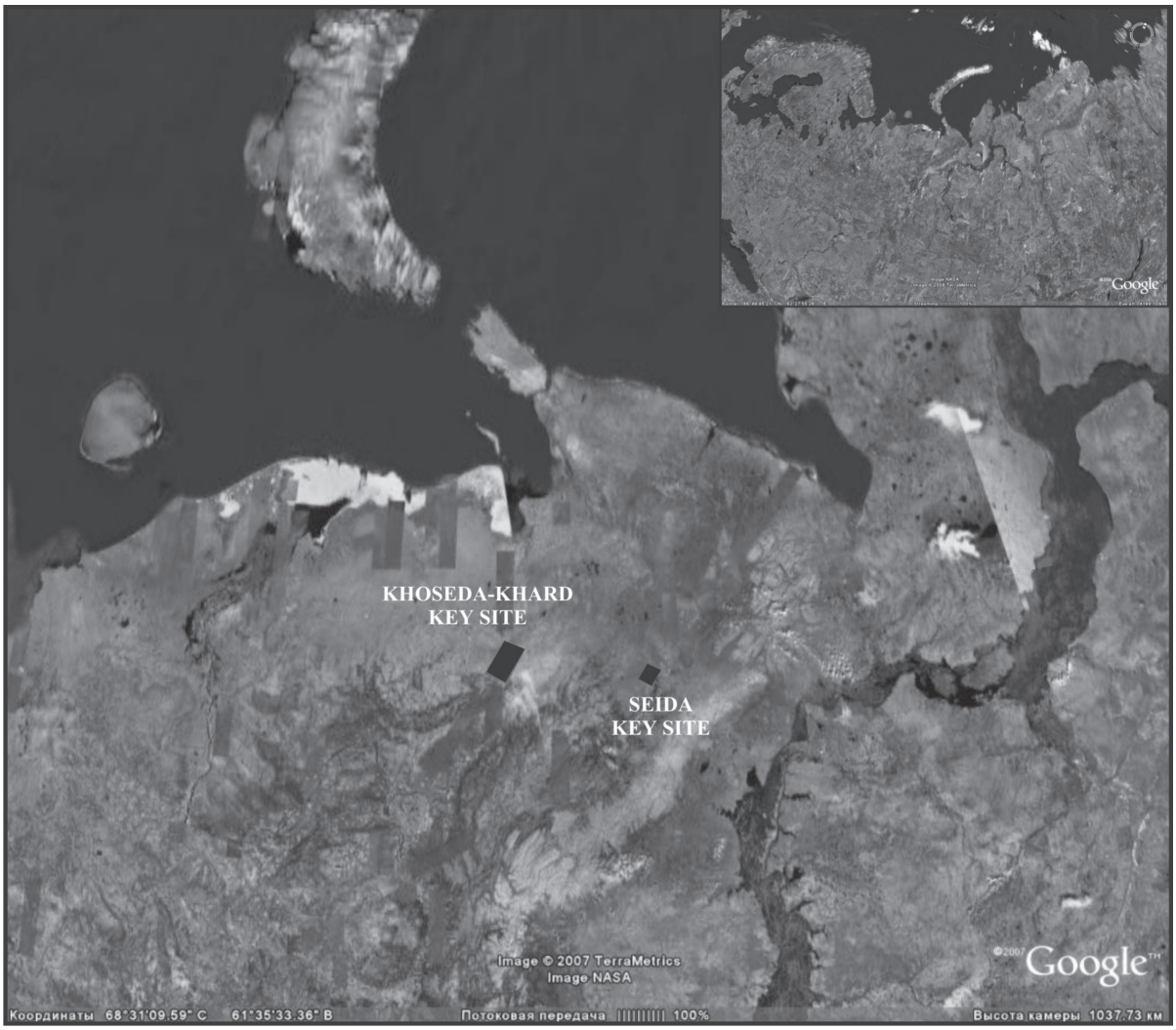

Figure 1. The location map of study sites**.**

The landscape-geocryological mapping technique we employed has been repeatedly used recently for compiling electronic atlases aimed at the assessment of the environment and human impacts upon it. The technique allows for mapping complex interrelations within the environment, in particular those between soil surface conditions and frozen ground distribution, or between ground lithological composition and temperature.

Accordingly, our landscape-geocryological mapping was based on revealing interrelations between the landscape features on the one hand, and the geological structure and geocryological conditions on the other. Information was summarized in matrix-format tables. Such tables are much more than just a form of data organization. They can serve for the purposes of system analysis, and at the same time they are the main component of map legends (Rivkin et al. 2004). Actually, the matrix schemes are regional geocryological classifications of an area, and accordingly, the GIS maps based on these schemes are spatial models of the classification. The combination of matrix schemes and GIS maps makes it possible to upscale rather accurately upscale point data on soil and vegetation carbon stocks and fluxes. Besides, various gradient and other spatial analyses become possible, as well as the assessment of partitioning of carbon between various landscape components, for example, active layer and permafrost, or permafrost-affected and permafrost-free soils. Moreover, the maps supplied with the matrix schemes are highly valuable for modeling changes in carbon budget induced by the climate change.

Results and Discussion

Mesoscale landscape-geocryological map of the Khoseda-Khard intensive study site

The Khoseda-Khard site is located in the southeastern part of the so-called Bolshezemelskaya Tundra and is stretched out along the Khoseda-Yu River. The vegetation represents a transition from the forest-tundra to the tundra life zone. The site altitudes vary from 60–70 m at the Khoseda-Yu water line to 130–175 m at the interfluve summits.

Most elevated parts of the interfluves represented by ridges and hills are composed of Middle Quaternary ice-marine deposits and dissected by numerous flow paths conveying surface water runoff. These flow paths are 5–100

meters wide and 0.5–3 meters deep. Away from the ridges and hills, the interfluve's surfaces are mostly represented by gentle slopes with altitudes of 90-120 m composed of Middle Quaternary lacustrine-alluvial deposits. This altitudinal level is characterized by large areas of peatlands and lakes.

The Khoseda-Yu River runs from south to north crossing the study site. The river is up to 50-60 m wide and 2–3 m deep with an average flow velocity of 0.8 m s^{-1}. The river valley is up to 30 m deep with steep (10°,-30°) slopes scarred by landslides and gullies. The I, II and III river terraces are clearly distinguishable above the flood plain. Smaller rivers are 5-20 m wide and up to 2 m deep. Their relative cut-in is 5-10 m. In the valleys of these rivers, the first and, less frequently, the second river terrace can be distinguished.

The site is rich in lakes. The lakes are mainly (except for the Neryta lake) shallow with depths of 1-3 m and small in size, less than 200 m across. They are of thermokarst origin and are located at peatlands. Many lakes are gradually draining.

The site location at the transition from tundra to forest-tundra provides for the diversity of plant associations. In a geocryological sense, the area is close to the southern boundary of the permafrost region. A characteristic feature of the area is that the permafrost distribution and temperatures are strongly controlled by landscape factors. Vegetation types and surface conditions are therefore reliable indicators of permafrost distribution. For example, in forest patches with tall understory and in shrub thickets the near-surface permafrost is typically absent, whereas in tundra it occurs at shallow depths. The high indicative value of landscape factors allowed for their use to map geocryological conditions.

The spatial analysis of environmental controls over present geocryological conditions was performed in a matrix format. The geomorphological and geological-genetic conditions of the terrain were plotted against the horizontal axis of the matrix. Identified were 8 successive geomorphological levels, within which 11 more geological-genetic complexes of deposits were distinguished, and within these complexes another 12 typical cryolithological sections were identified (Table 1). This subdivision was performed using the hierarchical approach. First of all, we identified the large geomorphological elements: interfluves and river valleys. After that we considered meso- and micro-relief, drainage, and vegetation type. Finally, the major types of cryological sections as well as exogenetic processes and associated landforms were identified.

The Middle Pleistocene ice-marine deposits of the Rogovaya suite ($gmII^{2-4}$) consist of clay loam and dark gray clay interbedded with layers and lenses of sand and sandy loam with inclusion of pebbles, gravel, and boulders. The Middle Pleistocene lacustrine-alluvial deposits of the Dozmer age ($laII^{4}$) are made up of loam interbedded with layers and lenses of sand and loamy sand. The Upper Pleistocene deposits of the Kazantsev age ($laIII^{1}$) are mainly formed by sand interbedded with layers and lenses of loamy sand and loam. All of the above deposits are classified as deposits with low ice content.

The floodplain alluvial deposits (aIV) and the deposits of the first river terrace consist mainly of gravel and pebbles, sand, and loamy sand. The alluvial deposits of the second ($aIII^{3-4}$) and the third ($aIII^{2-3}$) river terraces are made up of loam, loamy sand, and sand.

In peatland areas the bog-lacustrine deposits (lbIII-IV) with a 0.5–5 m thick peat layer overlap the ice-marine and lacustrine-alluvial deposits. When in a frozen state, peat has a high ice content, while the underlying mineral ground, frequently rich in peat admixture, has a medium to high ice content. The bog-lacustrine deposits are distributed at different geomorphological levels. They are not thick (3–7 m), and at each level there are various types of ground underlying these deposits.

On the landscape-geocryological map and in the matrix legend a specific digital code and color are assigned to each of the identified geological-genetic types of deposits and their typical cross-sections.

The landscape and geocryological conditions of the terrain are plotted along the vertical axis of the matrix. With consideration for surface topography, patterned grounds, vegetation, drainage, and depth to ground water, a total of 12 landscape sub-regions were identified:

- Spruce/birch forests and thin forests with dense understory (willow, dwarf birch) on flat plain surfaces and gentle (up to 6°) slopes, irregularly drained.
- Spruce/birch forests and thin forests with dense understory (willow, dwarf birch) on slopes more than 6° steep, well drained.
- Spruce/birch thin and sparse forests with sparse understory on flat plain surfaces and gentle (up to 6°) slopes, well drained.
- Hummocky dwarf-shrub/lichen tundra with patches of spruce/birch thin forests and shrub thickets on slopes more than 6° steep, well drained.
- Dwarf-shrub/moss/lichen tundra with low and medium hummocks on flat plain surfaces and gentle (up to 6°) slopes, well drained.
- Shrub/- and shrub/moss/lichen tundra (willow, dwarf birch up to 1 m high) on flat plain surfaces and gentle (up to 6°) slopes, irregularly drained.
- Willow, rarely dwarf birch thickets (willow up to 2 m and dwarf birch up to 1 m high) with grass/moss/sedge ground cover on flat depressed surfaces, gentle (up to 6°) slopes and along water lines, irregularly or poorly drained.
- Polygonal peatlands with hummocky dwarf-shrub/moss/lichen communities at drained polygon centers and sedge/moss communities in waterlogged dips, thermokarst depressions and subsided sites along thawing ice wedges.
- Palsa peatlands (degrading) with dwarf-shrub/moss/lichen communities on drained palsas and sedge/moss communities in waterlogged thermokarst depressions.
- Sedge/moss fens on depressed flat surfaces.
- Sedge/grass/moss meadows, in places hummocky, on large rivers flood plains, moderately drained.
- Small river and creek valleys with sedge/grass/moss communities on moderately drained flood plains and shrub/-

or dwarf- shrub/grass/moss communities on well drained terrace risers.

The map of a given scale allowed for identifying six types of permafrost sub-regions according to the degrees of permafrost spatial discontinuity:

1. discontinuous (sporadic) permafrost (covering 50%–90% of the area, of which 10%–50% has a permafrost table at 2–10 m depth);
2. massive-island permafrost (covering 20%–50% of the area, of which 10%–50% has a permafrost table at 3–10 m depth);
3. sparse island permafrost (covering <10% of the area, whereas >90% of the area is thawed grounds);
4. thawed ground underlain by the permafrost table at a depth of 3–8 m;
5. thawed ground with pereletoks and new formations of permafrost 1–3 m thick;
6. thawed ground.
7. The mean annual ground temperatures range from >0°C in the forested areas in the south of the site under survey to –1.5°C in the mineral tundra soil and polygonal peatlands in the north of the site.

Table 1. Geological-genetic complexes and cryolithological sections of Quaternary deposits at the Khoseda-Khard intensive study site.

Geomorphological level	Geological-genetic complex of deposits			Cryolithological section
Rogovskaya ice-marine plain	Bog-lacustrine	Late Pleistocene-Holocene	lb III-IV	One-to-three meters of peat underlain by loamy sand and sand. Ground is either thawed, or permanently frozen. Ice content in the frozen ground is medium or high in the upper 2-4 m layer and low in the deeper layers.
		Middle Pleistocen	gm II $^{2-4}$	Loam with layers and lenses of sand and loamy sand. Ground is either thawed, or frozen with low ice content.
Dozmer lacustrine-alluvial plain	Ice-marine	Late Pleistocene-Holocene	lb III-IV	Two-to-four meters of peat underlain by the interbedded loam, sandy loam and sand. Ground is either thawed, or permanently frozen. Ice content in the frozen ground is medium or high in the upper 3-7 m layer and low in the deeper layers.
	Bog-lacustrine	Middle Pleistocene	la II ^{4}	Loam with layers and lenses of sand and loamy sand partly overlain by a peat layer up to 0.5 m. Ground is either thawed, or permanently frozen with medium or low ice content.
Kazantsev lacustrine-alluvial plain	Lacustrine-alluvial	Late Pleistocene-Holocene	lb III-IV	Three-to five meters of peat underlain by interbedded sand, loamy sand and loam. Ground is either thawed or permanently frozen. Ice content in the frozen ground is medium to high in the upper 3-7-m layer and low in the deeper layers.
	Bog-lacustrine	Late Pleistocene	la III ^{1}	Sand with layers and lenses of sandy loam and loam partly overlain by a peat layer up to 0.5 m thick. Ground is thawed or permanently frozen with low ice content.
III river terrace	Alluvial	Late Pleistocene	a III $^{2-2}$	One-meter thick peat layer underlain by interbedded sand, loamy sand and loam. Ground is either thawed, or permanently frozen. Ice content in the frozen ground is medium in the upper 1-2 m layer and low in the deeper layers.
II river terrace	Bog-lacustrine	Late Pleistocene-Holocene	lb III-IV	One-meter thick peat layer underlain by interbedded sand, loamy sand and loam. Ground is either thawed, or permanently frozen. Ice content in the frozen ground is medium in the upper 1-2 m layer and low in the deeper layers.
	Alluvial	Late Pleistocene	a III $^{3-4}$	Sand with layers and lenses of loamy sand and loam. Ground is either thawed, or permanently frozen with low ice content.
I river terrace		Pleistocene-Holocene	a III-IV	Loam underlain by sand. Ground is either thawed, or permanently frozen with low ice content.
Floodplain and I river terrace (non-denudative)				Loam underlain by sand. Ground is either thawed, or permanently frozen with low ice content.
Floodplain	Alluvial	Holocene	a IV	Thawed sand underlain by thawed loam.

On the produced map and in the attached matrix legend, alphanumeric codes are assigned to combinations of landscape features, permafrost sub-regions, and ground temperatures; combinations are hatched differently on the map.

Within the identified permafrost sub-regions there are thus unique combinations of geological and physiographic factors: climatic, edaphic, botanical, lithologic, geomorphologic, hydrologic, hydro-geologic, and others, i.e. the entire spectrum of factors responsible for geocryological conditions. By combining the identified landscape and geocryological sub-regions (the vertical axis of the matrix) and the typical geological-genetic complexes (the horizontal axis of the matrix) we succeeded in identifying 64 typological areas at the Khoseda-Khard site.

The fact that the site is located at the transition between the tundra and the forest-tundra provides for diversity and contrast of the surface conditions, which in its turn results in spatial and temporal instability of seasonal thaw and freezing depths. The shallowest thaw depths, those of 0.3–0.8 m, are characteristic for peatlands. In mineral grounds at well drained interfluves, depths of seasonal thaw vary from 0.6 to 2.0 m depending on a ground lithological composition. Depths of seasonal thaw in loamy soils rich in peat admixture are 0.4–1.0 m, and in the loamy sand and sand deposits 0.8–2.0 m.

Cryogenic processes and landforms are highly characteristic of the area; they differ depending on the geocryological conditions of particular sites: composition, structure, physical properties, and temperature range of frozen or thawed ground. The most common are frost mounds of various shapes and sizes formed as a result of multi-annual and seasonal freezing of the ground. The seasonally thawed layer in the northern part of the site is associated with the patterned ground: non-sorted circles and hummocks. Cryogenic (frost) cracking occurs both in peatlands and mineral soils and is associated with large-block surfaces and residual polygonal relief. Ancient thermokarst lakes are numerous in peatlands. Present-day thermokarst manifests itself in the form of melting of repeatedly-wedge ice. Erosion, including thermal erosion is of limited occurrence and is confined to river valleys and thawing ice wedges with erosive gullies developing along the latter. Landslide accumulation areas can be found at the foot of steep slopes of river valleys. The ongoing paludification is limited to peatlands and wet interfluve depressions.

Detailed landscape-geocryological map of the Seida intensive study site

The site is located on the left bank of the Sediakha River, 6 km west of the Seida village. The site is the floor of a large, drained, ancient lake currently occupied by a peatland and scarred with water runoff paths and creek valleys. The perimeter of the lake basin is framed by a glacier spur with altitudes of 120–130 m. The site has a block-polygonal relief; well drained elevated blocks with shrub/moss/lichen vegetation are separated by erosive gullies differing in depth and width and overgrown by shrubs. The near-surface permafrost at the site can be subdivided into two sub-regions: discontinuous (sporadic) and massive-island. In peatlands and in the relatively elevated areas occupied by tundra with frost boils or low hummocks, the permafrost table is located directly under the active layer. In wet depressions, erosive gullies, at footslopes, and on smooth shrubby hillslopes the permafrost table is located at depths of 5 or more meters. Over 10 m deep continuous thawed ground is located under the lakes and in the large wet depressions with open water bodies.

The Seida site map indicates comprehensive information on geocryological features of the upper ground layers (down to 10 m depth). Geocryological mapping was performed on the basis of landscape subdivision of the area with the use of high-resolution satellite images.

Similarly to the mesoscale mapping of the Khoseda-Khard site, the spatial analysis of the environmental factors responsible for present-day geocryological conditions was performed in the matrix format. The structure of the detailed mapping matrix is, to a great extent, similar to that developed for the mesoscale mapping. Such consistency allows one to better correlate different types of terrain when working with maps of various scales and detail. Besides, it provides for more accurate upscaling of gas fluxes determined and estimated at various scales.

The geomorphologic and geological-genetic conditions of the area are plotted along the horizontal axis of the matrix. The whole site is located within one (non-segmented) geomorphological level (glaciofluvial lowland and II river terrace), within which are distinguished 3 geological-genetic complexes of deposits, within which another 4 typical cryolithological sections are identified (Table 2).

The landscape and geocryological conditions of the area are plotted against the vertical axis of the matrix. With consideration for surface topography, vegetation, depth to ground water, permafrost temperature and other characteristics, and thickness of seasonally frozen or seasonally thawed layers a total of 7 landscape sub-regions were identified:

- Dwarf-shrub/moss/lichen tundra, moderately drained, with small hummocks, occasionally with frost boils, ground-water at a depth of 1–3 m, discontinuous permafrost (occurs at 50%–90% of the area, and at 10%–50% of the area the permafrost table is at a depth of 3–5 m);
- Shrub/moss/lichen tundra, shrubs up to 1 m high, medium and large hummocks, irregularly drained, ground water at 0–1 m, permafrost surface at a depth of 3–6 m;
- Peatland, irregularly drained, with dwarf-shrub/moss/lichen communities on mounds and moss/sedge in hollows, ground water at 0–0.5 m, discontinuous permafrost (occurs at 70%–90% of the area, and at 10%–30% of the area the permafrost table is at a depth of 2–5 m);
- Palsa peatland, strongly eroded, with dwarf-shrub/moss/lichen tundra on palsas and sedge/moss communities in inter-palsa depressions, ground water at 0–0.5 m, massive-island permafrost (covering 50% of the area and within 50% of that area the permafrost surface is at a depth of 2–10 m);
- Sedge/moss mire with residual palsas occupied with dwarf shrub/moss/lichen communities, ground water at 0–0.3

Table 2.Geological-genetic complex of deposits and cryolithological sections of Quaternary deposits at the Seida intensive study site.

Geomorphological level	Glaciofluvial lowland and II river terrace			
Geological-genetic complex of deposits and their age	alluvial, glaciofluvial	bog-lacustrine		alluvial deposits of river channels and small water channels
	late Pleistocene	late Pleistocene-Holocene		Holocene
	a,fg III²	lbIII-IV		alV
Cryolithological section	thawed or frozen sand and loamy sand with pebble interbeds and low ice content	peat layer up to 1 m thick underlain by interbedded sand, loamy sand, and loam, thawed grounds or frozen grounds with a low ice content below a depth of 1-3 m	peat later from 1 to 4 m thick underlain by interbedded sand and loamy sand, rarely loam, frozen with medium or high ice content below a depth of 4 m	peat layer up to 1 m thick underlain by interbedded sand, loamy sand, and pebble

m, island permafrost (covering 20%–30% of the area and within area 70%–80% the depth of the permafrost table is 5–10 m);

- Water lines and bogged depressions with herb/sedge/moss and shrubs of varying coverage up to 2 m high, poorly drained, ground water at 0–1 m, thawed ground with possible pereletoks and new formations of permafrost;
- Creek valleys, irregularly drained, herb/sedge/moss communities, occasionally willow thickets up to 2 m high, ground water at 0–1 m, thawed grounds.

By combining the identified landscape sub-regions and the typical sections of geological-genetic complexes (the horizontal axis of the matrix) we managed to identify 8 typological areas at the Seida site, which in its turn allows for mapping the whole spectrum of the existing geocryological and landscape conditions.

The landscape-geocryological maps of the two intensive sites differ in the degree of detail. Variability within map polygons in permafrost conditions, ground temperatures, soil, vegetation, and degree of drainage is much higher on the Khoseda-Khard than on the Seida map. Attribution of a polygon to the particular typological area on the Khoseda-Khard map is based on generalization, so that for the local-level carbon budget assessment further detailization of the map is needed. The latter, in a large degree, can be done using the typological units defined and deliniated on the mesoscale map. On the contrary, on the detailed map of the Seida site, characteristics of the ground including ground temperatures, as well as degrees of drainage, soil and plant communities defined in the legend precisely correspond to each polygon shown on the map. This makes it possible to accurately enough determine landscape-geocryological features necessary to estimate and interprete local carbon budgets.

It should be stressed once again that the landscape-geocryological units identified during the mesoscale mapping, if necessary for carbon studies, can be subjected to further sequential detailization in the course of detailed field mapping. From the technical viewpoint it can be done in a form of sequential detailization of the spatial analysis matrix. It is important to keep the detailed-scale matrix in compliance with the medium-scale matrix, so that the detailed-scale matrix r would suggest more detail within the mapping units and, correspondingly, map polygons which were defined on the medium-scale map.

Conclusions

The matrix schemes of landscape-geocryological subdivision developed under the CARBO-North project represent regional classifications of landscape and geocryological conditions. They reflect the system of environmental controls over the geocryological situation, as well as major controls over carbon budget components at the studied areas. On the one hand, sequential detailed geocryological mapping of an area allows for sequential detailed assessment of the carbon budget components and, on the other hand, makes it possible to integrate and upscale the detailed carbon data to assess a regional carbon budget using mesoscale cartographic models.

Acknowledgments

The authors of this paper would like to thank all their colleagues for advice and proofreading.

References

Armand, D.A. 1975. *Landscape Science (Theoretical Basics and Logical-Mathematical Methods)*. Moscow, 288 pp.

Rivkin, F.M., Kuznetsova, I.L., Ivanova, N.V. & Suhodolsky, S.E. 2004. Engineering-geocryological mapping for construction purposes in permafrost regions. In: *Engineering Geology for Infrastructure Planning in Europe.* Berlin Heidelberg: Springer-Verlag, 172-178.

Samarkin, V.A., Fedorov-Davydov, D.G., Vecherskaya, M.S. & Rivkina, E.M. 1994. CO_2 and CH_4 emission from cryosols and subsoil permafrost and possible global climate changes. In: *Soil Processes and Greenhouse Gas Emission.* US National Soil Survey Centr. Nebraska, V. 3: 55-71.

Permafrost Degradation and Influx of Biogeogases into the Atmosphere

E. Rivkina
Institute of Physicochemical and Biological Problems in Soil Science, Pushchino, Russia
G. Kraev
Institute of Physicochemical and Biological Problems in Soil Science, Pushchino, Russia

Abstract

The data on methane content and pattern of its distribution across permafrost of different age and origin on late Cenozoic permafrost of Northeastern Arctic are summarized. We have found that methane is present in the epycryogenic Holocene and early Pleistocene layers and is absent in the syncryogenic late Pleistocene ice complex. Incubation under anaerobic conditions triggered the process of methane formation in Holocene and early Pleistocene layers and did not initiate it in the ice complex sediments. Based on the analysis of microbial community, organic matter, and potential for methane formation in various genetic types of permafrost sediments, we concluded that ice complex sediments, and to a lesser extent than epycryogenic ones, have the potential to produce methane in consequence of permafrost degradation.

Keywords*:* permafrost; methane production; methanogenic arhaea; isotopic composition.

Introduction

In the framework of global change studies in the last decades, attention has been given to CO_2 and CH_4 emission from high-latitude ecosystems (Whalen & Reeburgh 1990, Christensen, 1993, Fyodorov-Davydov 1998, Reeburgh et al. 1998, Worthy et al. 2000, Zamolodchikov & Fyodorov-Davydov 2004, Wagner et al. 2003, van Huissteden et al. 2005). However, significant amounts of these greenhouse gases have been isolated from biogeochemical cycling and conserved in permafrost (Rivkina et al. 1992,) together with organic matter (Schirrmeister et al. 2002, Kholodov et al. 2004) and viable anaerobic microorganisms (Rivkina et al. 1998, Gilichinsky 2002). Thus, permafrost is a huge deposit and potentially, a large source of old organic carbon. It is important to assess the consequences of permafrost degradation because at least four pathways of carbon moblilization are influenced by permafrost thaw:

1. The reservoir of carbon dioxide and methane bound in upper permafrost horizons that, unlike the deep high-pressure gas hydrates, could be easily liberated in the case of thawing in the polar regions.

2. The paleomicrobial community of viable methanogens expected to retain activity and be anew involved in biogeochemical processes, including generation of greenhouse gases (Rivkina et al. 2006).

3. Labile organic matter conserved in permafrost will be consumed by these microorganisms as an energy source for greenhouse gas production.

4. Increased production of methane in the active zone. This is in fact observed on northeastern Arctic exposures under present conditions with associated release methane, which is of similar magnitude to the direct production in Arctic tundra (Rivkina et al. 2001).

Recent studies have provided a new impetus to such discussion, as they forecast high gas emission in response to permafrost degradation (Walter et al. 2006, Zimov et al. 2006). These papers, describing the flux of greenhouse gases from thermokarst ponds, have stimulated significant public and scientific interest. Quantification of methane release from thawing permafrost is of prime importance in climate research.

Our objective is to clearly recognize the concentration and features of distribution of carbon sources in permafrost, based on its history (Sher 1974, Schiermeister et al. 2002). The present paper, based on the analysis of microbial community, organic matter and content of CO_2 and CH_4, as well as on the possibility of methane formation and oxidation in various genetic types of permafrost sediments, will discuss the potential of greenhouse gases emission to the atmosphere in response to permafrost degradation and specifically, the late Pleistocene Icy Complex thawing upon which most activities are now focused.

Study Area and Object of Investigation

Investigations were carried out in continuous permafrost area in tundra and forest tundra zone landscapes on north-eastern Arctic coastal lowlands (125–162°E, 68–72°N), located between the Lena and Kolyma River deltas (Fig. 1). Sites were located outside the oil and gas basins, and were characterized by different Quaternary deposits (early Pleistocene to Holocene) and permafrost of both syn- and epicryogenic origin (Kaplina et al. 1984, Schirrmeister et al. 2002). Permafrost here had begun to form 3 million years ago and until now has not been deeply affected by global thawing.

Studies were carried out down to 100 m depths on fine dispersed late Cenozoic stratotypes, which have been well described by many authors (Kaplina et al. 1981, 1988, Sher et al. 2005) on the bases of radiocarbon, palynological, paleontological, paleomagnetic, cryolithological, and physicochemical data.

Distribution, thickness and area of the following strata

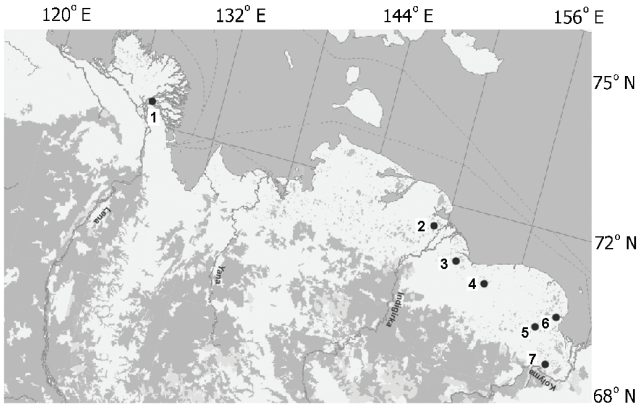

Figure 1. Arctic study sites: 1–Bykovskii Peninsula, Lena River; 2–Low basin of Indigirka River; 3– Khomus-Yuryakh River; 4–Alazeya River; 5–Chukochya River; 6– East Siberian Sea coast; 7–Khalarchinskaya tundra sandy plain.

were calculated, tested for microorganisms, organic matter, CO_2, and CH_4 presence:

- Thomus-Yar Suite, the lowermost (15–20 m below sea level) sediments in the middle Chukochya and Alazeya Rivers (Kolyma lowland) dated back to the second half of the Pliocene, 2–3 million years.
- Overlying Olerian Suite, the stratotype of late Pliocene.
- Early Pleistocene age (1.8–0.6 million years). The upper part of the suite is represented by epicryogenic horizons with pseudomorphoses, and the lower one, by syncryogenic layers.
- Middle Pleistocene syncryogenic sediments and ice wedges belong to buried Icy Complex, named as Jukagir Suite on Cape Svyatoy Nos (Laptev Sea coast), Allaikha Suite on the left channel inflow of Indigirka River, and Maastakh Suite on the right bank of the middle Chukochya River.
- Predominantly syncryogenic middle to upper Pleistocene cross-sections on Bolshoy Homus-Yuryah River (Kolyma lowland): three Ice Complex units with interbedded epicryogenic horizons. Age of deposits varied from >50 ka in the late Pleistocene Ice Complex to 200–600 ka in the middle Pleistocene.
- Marine sediments of Kon'kovaya Suite (East Siberian Sea coast), frozen after sea level dropped at the end of the middle Pleistocene 120 ka ago.
- Late Pleistocene (10–60 ka old) syncryogenic Ice Complex deposits known as Edoma Suite that compose the upper part of cross sections of remains of a late Pleistocene accumulative plane between Lena and Kolyma Rivers.
- Late Pleistocene epigenetically frozen river bed sands of Khalerchinskaya tundra region on the left bank of lower Kolyma River, overlain by Holocene eolian sands.
- Holocene (6–8 ka) syncryogenic alluvial deposits of water meadows on the modern flood-lands and epicryogenic alas horizon and "covering" layer on the top of the Icy Complex, formed by refreezing of the sediments that have melted and drained.

Methods

The data presented are based on 2000 tested samples. Thirty cm-long permafrost cores (diameter 68–107mm) were sampled from boreholes (step-interval 1 m). The strict protocols for drilling and the subsequent handling of cores are designed to ensure uncontaminated material. For microbiological studies the cores were split into c. 5-cm long segments, placed into sterile boxes or bags, stored in the field within a hole in the permafrost at a natural temperature of -10°C, and transported frozen to the laboratory.

Gas samples were collected in the field by degassing 50 g of frozen cores in a 150-mL syringe under a nitrogen atmosphere (Alperin & Reeburgh 1985). The gas mixture was then transferred through a needle to the rubber septa sealed vials filled with salt water. At that point, brine was substituted by gas with the excess water flowing out through the second needle. Gas samples were kept in the vials until further analysis in the lab. CH_4 and CO_2 concentrations were measured using KhPM gas chromatograph (Russia) equipped with katharometer (for carbon dioxide) and hydrogen-flame ionization detector (for methane). Hydrogen was used as a carrier gas in both cases. The same samples were analyzed for $\delta^{13}C$ methane and carbon dioxide using GC Combustion Thermo Finnigan interface and Delta XL mass spectrometer (Germany). To estimate methanogenesis, samples were incubated for 3 weeks at temperatures -16.5, -10, -5, -1.8, and 5°C as described by Rivkina et al. (2007). At the end of the incubation, newly formed radioactive CH_4 was removed from the experimental vials by an air flow (50 ml/min). It was passed through a drexel bottle with a solution of 200 g/l NaCl and 1N KOH and combusted to $^{14}CO_2$ at 700–800°C with cobalt oxide as a catalyst. At the final stage $^{14}CH_4$, oxidized to $^{14}CO_2$, was absorbed in the vial with a mixture of 2 ml β-phenylethylamine and 10 ml of Universal LSC cocktail (Sigma). Vials were counted on an LS 5000 TD liquid scintillation counter (Beckman). Archaea were cultivated according the Hungate anaerobic technique (1969).

The total organic matter was estimated by wet and dry incineration methods. Redox potential was measured in the field immediately after melting, using an "Ecotest-120" (Russia) potentiometer with a platinum electrode and a silver chloride electrode as reference.

Results

Methane and carbon dioxide content and distribution

Unlike CO_2, which is found in all layers below the permafrost table (in various concentrations up to 20 ml of gas per 1 kg of frozen ground), CH_4 shows a distinct and alternating pattern with depth. In a generalized geological cross-section, in which all the geological layers exist in chronological order, CH_4-containing layers would be sandwiched between layers free of methane (Fig. 2). The CH_4 concentration (0.4 to 30.0 ml/kg) does not appear to be correlated to any textural or chemical characteristics of the sediments, age, or the depth of burial. Methane is found

primarily on a present-day floodplain bog, in the "covering" layer, alas horizons, marine deposits, late Pliocene-early Pleistocene and Pliocene suites. The lowest concentrations of CH_4 (<0.01 ml/kg) are present in modern alluvial plains in virtually all the river valleys of the area, in Holocene eolian and late Pleistocene river-bed sands, and in the mid and late Pleistocene Icy Complexes in different locations in the region.

For at least several hundreds of thousands years, methane has not diffused from the methane-rich layers into adjacent layers, which are devoid of methane, which implies that there is negligible diffusion of methane in the permafrost under both present and past conditions. We can estimate an upper limit on the diffusion of methane by using the profile shown in Fig. 2 (sites 4 and 5). The methane profile in sediments that are 0.6 to 3 million years old retain structure over length scales of about 3 m. The relationship between time (T), and distance diffused (x), is given by $T = x^2/D$, where D is the diffusion coefficient. From this relationship we calculate that D must be less than 10^{-13} m^2/s; i.e., the upper limit on the diffusion of methane through permafrost is surprisingly low.

Evidence from the West Siberian natural gas fields and gas-hydrate bearing fields in Mackenzie Delta (Dallimore & Colett 1995) further supports the conclusion that methane is in a bound form and not able to diffuse through the near-surface fine dispersed frozen sediments with negligible lithostatic pressure. It suggests that the methane is held in a clathrate form within the sediments (Rivkina et al. 2001).

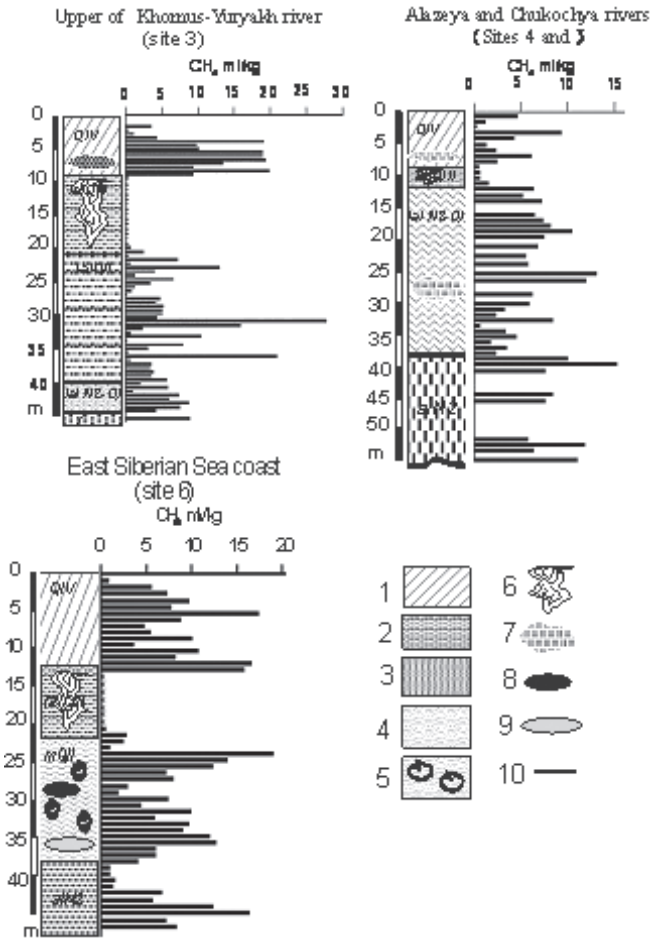

Figure 2. Methane content in permafrost: 1–loam, 2–sandy loam, 3–sand, 4–loamy sands, 5–marine sediments, 6–ice wedges, 7–peat, 8–methane hydrate, 9–lenses of cryopegs, and 10–methane concentration.

One possible way to reconcile the methane hydrate formation at low pressures with the theoretical requirement for stability only at high pressures is to assume that, within the pore spaces of the permafrost, high pressures are created by the freezing process and that it is within these zones of high pressure that the methane hydrate is located. The matrix formed by the sediment grains in permafrost may be crucial to the formation of these intrapore high-pressure zones. In the pore spaces, methane concentration is possibly much higher than it was measured in these samples. The possibility that methane-hydrate may exist in fine-grained sediments of the upper permafrost horizons was confirmed experimentally (Ershov et al. 1991, Chuvilin et al. 2005).

However, strong diffusion of methane from below was observed if the borehole crossed the fine dispersed sediments and reached the pebbles horizon (Fig. 3). Despite the fact that methane content in fine dispersed sands and sandy loams did not differ from typical value, the methane concentration in the borehole gas phase reached 90%. It means that methane in the borehole came from a different source (e.g., from a deeper strata). The same situation is often obtained if the borehole reached CH_4-lenses buried in near surface marine sediments (Fig. 2, site 6).

From the isotopic composition of C-CH_4 (Fig. 4) CH_4-containing layers can be separated into two groups: a main group containing horizons of different origin and age, late Pliocene to Holocene, with $\delta^{13}C$ values ranging -64 to -80 per mil and a minor group represented by mid Pleistocene epicryogenic soils with $\delta^{13}C$ value varying 90 to 100 per mil.

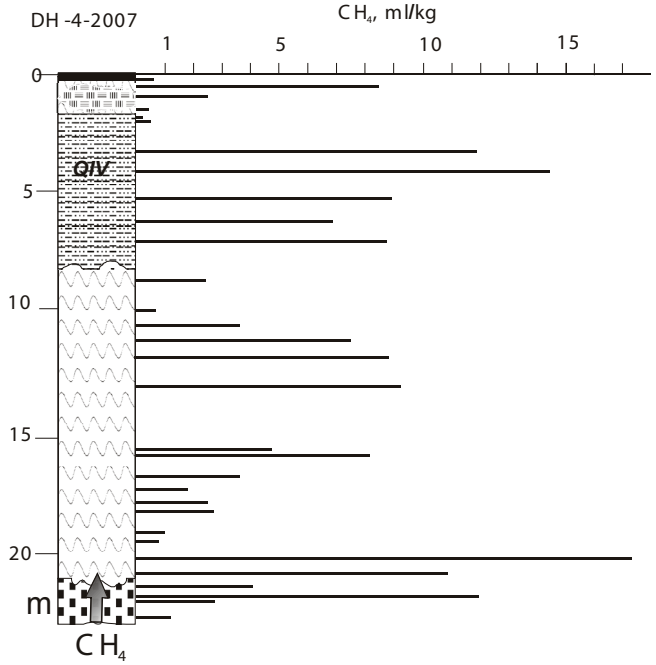

Figure 3. Methane entry in borehole from pebble horizon.

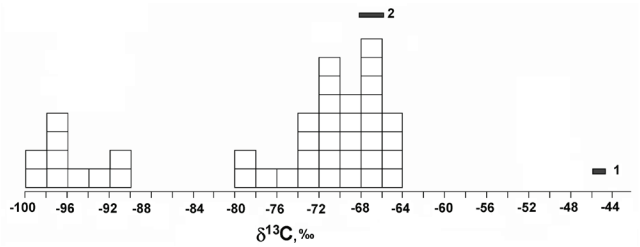

Figure 4. $\delta^{13}C$ of methane from permafrost. 1–atmospheric methane, 2–methane from gas fields, 3–methane hydrate from permafrost, Mackenzie River delta (Dallimore et al. 1995)

The isotopic composition of methane produced by methanogenic bacteria in natural ecosystems ranges from -50 to -70‰, while abiogenic methane is substantially more enriched in ^{13}C, with values ranging from -45 to -50‰ (Fig. 4). The isotopic composition of CH_4 carbon in permafrost ($\delta^{13}C$ -64 to -99‰) confirms its biological origin and, along with discrete bedding, suggests *in situ* formation of this biogenic gas. The extremely low value of $\delta^{13}C$ methane in some samples (-90 to -99‰) allows us to conclude that CH_4 mainly formed as a result of CO_2 reduction, and a portion of this methane could be formed at subzero temperatures, which was accompanied by significant fractionating of carbon isotopes.

Permafrost also contains viable methanogenic bacteria, but only in epigenetically frozen sediments, and not in the eastern Arctic sincryogenic Icy Complexes. In contrast, viable methanotrophic (methane-oxidizing) psychrophilic bacteria are present in both, epi- and syngenetically frozen layers (Khmelenina et al. 2002).

Incubation of thawed permafrost samples in anaerobic conditions with CO_2+ H_2 showed methanogenic activity in Holocene and late Pliocene-early Pleistocene epicryogenic sediments only. In the samples of Icy Complex this process was not observed (Fig. 5). At the same time, methanotrophic bacteria were able to oxidize and assimilate methane in samples from both, epi- and syncryogenic horizons with the maximum rate of methane oxidation was observed at permafrost table (Khmelenina et al. 2002).

The content of total organic carbon in epicryogenic layers and Icy Complex is similar and varied 1.5–2 to 5% (Fig. 6). But for all that the Icy Complex contains more labile organic matter than epicryogenic sediments: range of ulmification is 15 and 20%, respectively (Kholodov et al. 2006).

Discussion

Greenhouse gases of biological origin excluded during frozen state from biogeochemical turnover are a variety of geogases inherent to cryolithosphere only. Unlike the deep high-pressure gas hydrates, this reservoir of ancient biogeogases in the upper horizons of the cryolithosphere could be easily liberated into the atmosphere and reinvolved in the present-day turnover, should the permafrost degrade as a result of warming. However, this reservoir of organic carbon and methane has been very poorly quantified. Recent research has shown that considerable variation exists in the

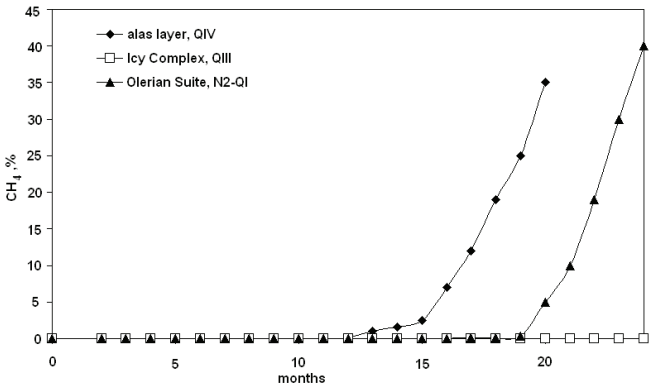

Figure 5. Increase of methane concentration (percentage by volume) in headspace of jars with different permafrost sediments incubated at 22°C in anaerobic condition

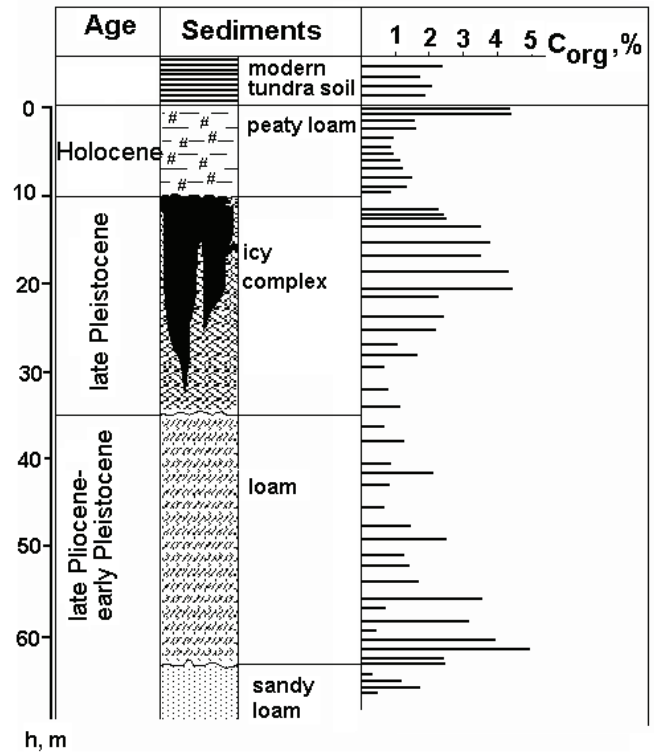

Figure 6. Content of organic carbon in late Cenozoic frozen suites (sites 4 and 5, Figs.1, 2).

amount of methane stored in frozen deposits (Rivkina et al. 2007). This strongly affects estimates of the amount of greenhouse gases that may be released from these deposits upon warming, and forecasting the contribution of these gases to atmosphere. To answer the question, does the release of bound methane and carbon dioxide and activation of CH_4 and CO_2 formation lead to dramatic effects on climate, it is necessary to understand the response of permafrost to climate warming in the past. The Holocene optimum, which was accompanied by widespread permafrost degradation, can be used as models of future warming.

Methane content in the Earth's atmosphere during the Pleistocene and Holocene was affected by the climate changes, varying between 0.35 to 0.7 ppm, reaching the

maximum concentrations during optima and minimum in cryochrones. This could be demonstrated by the high methane content in alas layers, formed during the Holocene optimum. Nevertheless, permafrost thawing during the Holocene optimum, which destroyed at least half of the Icy Complex in the eastern Arctic, did not lead to dramatic warming of air temperatures, probably because methane generation took place simultaneously with methane oxidation, and smoothly gave way to new cooling and refreezing of thawed sediments. Anthropogenic effects became more prominent during the last 270 years. During this time, atmospheric methane content has increased sharply to 1.8 ppm, independently of century cryo- and thermochrones.

Our data established several important findings:

1. Methane is present in the epicryogenic Holocene and late Pliocene-early Pleistocene sediments and is absent in the late Pleistocene Icy Complex.

2. Incubated under anaerobic conditions, Holocene and late Pliocene-early Pleistocene sediments, but not sediments of the Icy Complex, exhibited methane formation.

3. Permafrost contains viable paleomicroorganisms, including methane-producing archaea. Nevertheless, viable methanogenic bacteria were isolated from epicryogenic layers only, and never found in Icy Complexes.

4. The isotopic composition of CH_4 carbon in permafrost confirms its biological origin as a result of CO_2 reduction.

On the basis of these findings we can conclude that climate warming and, as a consequence, permafrost thawing, undoubtedly trigger biological activity, including the microorganisms of the carbon cycle. In this case the methane content, microbial community, organic matter, and methane production, show that Icy Complex have less potential as a methane producer than epicryogenic sediments. Thawing of the Icy Complex will not add methane to the atmosphere because 1) the Icy Complex does not contain bound methane, and 2) the Icy Complex does not contain methanogenic bacteria. An additional CH_4 flux is possible also in cases when the talik zone under thermokarst lakes penetrates through the Icy Complex and reaches the underlying methane-containing horizons (as shown on Fig. 3).

We calculated the possible additional greenhouse gases flux to atmosphere in the case of thawing 50-m thick CO_2 and CH_4-containing epicriogenic sediments under square 1 km^2. The sum of C (CO_2+CH_4) store in such volume is ~ 150 tons (without calculation of possible methane oxidation or production). Even the amount is not very significant; this flux of biogeogases bound in permafrost to atmosphere has to be taken into consideration even now. For example, the average abrasion rate of the Arctic coast consisting of frozen sediments is 3 m/year. Destruction of each kilometer of coast 25 m high is accompanied by the release of 3 tons of methane and carbon dioxide. Given the minimal length of the Arctic coastline, the total quantity of C (CO_2+CH_4) being annually released into the atmosphere today is 12 thousand tons. The same order of gases, likely due to the coastal abrasion, came from the river-banks and lakesides in the cryolithozone.

The other way is emission to atmosphere of the gases newly formed in thawed permafrost. In recent years, methanogenic archaea have been isolated from permanently cold lake and marine sediments (Franzmann et al. 1997; Von Klein et al. 2002; Kendall et al. 2007), as well as culture-independent methods, and have demonstrated that the active layer of arctic soils is a natural habitat of a diverse archaeal community (Ganzert et al. 2007). Even though there is limited data regarding microbial processes in thawed permafrost sediments, we can forecast that microbial activity in thawed layers and themokarst lakes is increasing, but not more than in the existing lakes and seasonally thawing soils.

Conclusion

One can expect that due to permafrost thawing and the accessibility of organic matter, the paleomicrobial community would become involved in the biogeochemical processes, including production of greenhouse gases. The ultimate goal of the current investigation is to estimate the sum effect of these processes, taking into account their outcomes in the past optima.

Acknowledgments

This research was supported by the Russian Fund for Basic Research (grants: 04-04-48257, 08-05-00268).

References

Alperin, M.J. & Reeburgh, W.S. 1985. Inhibition experiments on anaerobic methane oxidation. *Appl. Environ. Microbiol*. 50: 940-945.

Christensen, T. 1993. Seasonal emission of methane from the active layer of organic tundra soil scale and controlling factors. *Proc. of Joint Russia-American Seminar on Cryopedology and Global Change, Puschino, Russia*, pp. 325-341.

Chuvilin, E.M., Perlova, E.V. & Yakushev, V.S. 2005. Classification of gas compound in rocks of permafrost zone. *Kriosfera Zemli* 3: 73-76. (in Russian).

Dallimore, S.R. & Colett, T.S. 1995. Intrapermafrost gas hydrates from a deep core hole in the Mackenzie Delta, Northwest Territories, Canada. *Geology* 23(6): 527-530.

Ershov, E.D., Lebedenko, Yu.P, Chuvilin, E.M., Istomin, V.A. & Yakushev, V.S. 1991. Peculiarities of gas hydrates existence in cryolithozone. *Dokl. Akad. Nauk* 321:788-791.

Fedorov-Davydov, D.G. 1998, Respiration activity in tundra biocenoses and soils of the Kolyma Lowland. *Eurasian Soil Science* 31(3): 263-274.

Franzmann, P.D, Liu, Y, Balkwill, D.L., Aldrich, H.C., Conway de Macario, E. & Boone, D.R. 1997, Methanogenium frigidum sp. nov., a psychrophilic, H2-using methanogen from Ace Lake, Antarctica. *Int J Syst Bacteriol* 47(4): 1068-1072.

Ganzert, L, Jurgens, G, Munster, U. & Wagner, D. 2007. Methanogenic communities in permafrost-affected

soils of the Laptev Sea coast, Siberian Arctic, characterized by 16S rRNA gene fingerprints. *FEMS Microbiol Ecol*. 59: 476-488.

Gilichinsky, D. 2002. Permafrost as a microbial habitat. In : G. Bitton (ed.), *Encyclopedia of Environmental Microbiology*. New York: Wiley, 932-956.

Hungate, R.E. 1969. A roll tube method for cultivation of strict anaerobes. In: J.B. Norris & D.W. Ribbons (eds.), *Methods in Microbiology*. New York: Academic Press, 116-132.

Kaplina, T.N., Lakhtina, O.V. & Rybakova, N.O. 1981. Cainozoic sediments of Alazeya river midstream (Kolyma lowland) *Izves. of USSR Academy of Sciences, series geol*. 8: 51-63

Kaplina, T.N. & Lozhkin A.V. 1984. Age and history of accumulation of the "Ice Complex" of the Maritime Lowlands of Yakutia. In: A.A. Velichko, H.E. Wright Jr. & C.W. Barnosky (eds.), *Late Quaternary Environments of the Soviet Union*. The University of Minnesota Press. London: Longman, 147-151.

Khmelenina, V.N., Makutina, V.A., Kalyuzhnaya, M.G., Rivkina, E.M., Gilichinsky, D.A. & Trotsenko, Yu.A. 2002. Viable methanotrophic bacteria findings in permafrost sediments of North-Eastern Siberia. *Dokl. Biol. Sci.* 384: 235-237. Translated from Dokl. Akad. Nauk 384: 283–285.

Kholodov, A.L., Rivkina, E.M., Snytin, P.S., & Borisov, R.R. 2004. Quaternary deposits of Laptev Sea coast as a source of organic matter and biogenic gases. *Rep. on Polar Res*. 482: 117–124.

Kholodov, A.L. , Zolotareva, B.N. & Shirshova L.T. 2006. Organic matter in the main types of frozen quaternary deposits of the Bykovsky peninsula: Total content and group composition of the humus. *Earth Cryosphere*. X(4): 29-34.

Kendall, M.M., Wardlaw, G.D., Tang, C.F., Bonin, A.S., Liu, Y. & Valentine, D.L. 2007. Diversity of archaea in marine sediments from Skan Bay, Alaska, including cultivated methanogens and description of *Methanogenium boonei* sp. nov. *Appl Environ Microbiol*. 73: 407-414.

Rivkina, E.M., Samarkin, V.A. & Gilichinsky, D.A. 1992. Methane in the permafrost soils of Kolyma-Indigirka Lowland. *Dokl.Akad. Nauk* 323(3): 559-563. (in Russian).

Rivkina, E., Gilichinsky, D., Wagener, S., Tiedje, J. & McGrath, J. 1998. Biogeochemical activity of anaerobic microorganisms from buried permafrost sediments. *Geomicrobiol. Journ.* 15: 187-193.

Rivkina, E, Gilichinsky, D., McKay, C. & Dallimore, S. 2001. Methane distribution in permafrost: Evidence for an interpore pressure methane hydrate. In: R. Paepe & V. Melnikov (eds.), *Permafrost Response on Economic Development, Environmental Security and Natural Potential*, NATO series, Kluver Academic Publishers, 487-496.

Rivkina, E.M., Kraev, G.N., Krivushin, K.V., Laurinavichus, K.S., Fyodorov-Davydov, D.G., Kholodov, A.L., Shcherbakova, V.A. & Gilichinsky, D.A. 2006. Methane in permafrost of Northeastern Arctic. *Earth Cryosphere*. X(3): 23-41.

Rivkina, E., Shcherbakova, V., Laurinavichius, K., Petrovskaya, L., Krivushin, L., Kraev, G., Pecheritsina, S. & Gilichinsky, D. 2007. Biogeochemistry of methane and methanogenic archaea in permafrost. *FEMS Microbiol Ecol*, 61: 1-15.

Schirrmeister, L., Siegert, C., Kuznetsova, T., Kuzmina, S., Andreev, A., Kienast, F., Meyer, H. & Bobrov, A.A. 2002. Paleoenvironmental and paleoclimatic records from permafrost deposits in the Arctic region of Northern Siberia. *Quaternary International.* 89: 97-118.

Sher, AV. 1974. Pleistocene mammals and stratigraphy of the Far Northeast USSR and North America. *International Geology Review* 16(7-10): 1-282 (Book Section), American Geological Institute.

Sher, A.V., Kuzmina, S.A., Kuznetsova, T.V. & Sulerzhitsky, L.D. 2005. New insights into the Weichselian environment and climate of the East Siberian Arctic, derived from fossil insects, plants, and mammals. *Quaternary Science Reviews* 245: 533-569.

van Huissteden, J. 2004, Methane emission from northern wetlands in Europe during Oxygen Isotope Stage 3. *Quaternary Science Reviews* 23: 1989-2005.

van Huissteden, J., Maximov, T.C. & Dolman, A.J. 2005. High methane flux from an arctic floodplain (Indigirka lowlands, Eastern Siberia). *J. of Geophys. Res.* 110, G02002, doi:10.1029/2005JG000010.

Von Klein, D., Arab, H., Volker, H. & Thomm, M. 2002. Methanosarcina baltica sp. nov.: A novel methanogen isolated from the Gotland Deep of the Baltic Sea. *Extremophiles* 6: 103-110.

Wagner, D., Kobabe, S., Pfeiffer, E-M. & Hubberten, H-W. 2003. Microbial controls on methane fluxes from a polygonal tundra of the Lena Delta, Siberia. *Perm. Perigl. Proc.* 14: 173-185.

Walter, K.M., Zimov, S.A., Chanton, J.P., Verbyla, D. & Chapin III, F.S. 2006. Methane bubbling from Siberian thaw lakes as a positive feedback to climate warming. *Nature* 443: 71-75.

Whalen, S. & Reeburgh, W. 1990. Consumption of atmospheric methane by tundra soils. *Nature* 346: 160-162.

Zamolodchikov, D., Fyodorov-Davydov, D. 2004. The biological cycles in terrestrial Polar ecosystems and its influence on soil formation. In: J. Kimble (ed.), *Cryosols: Permafrost-Affected Soils,* Section 4, Chapter 2. Springer, 479-508.

Zimov, S.A., Schuur, E.A.G. & Chapin III, F.S. 2006 Permafrost and the global carbon budget. *Science* 312: 1612-1613

Observations and Considerations on Destabilizing Active Rock Glaciers in the European Alps

Isabelle Roer, Wilfried Haeberli
Glaciology, Geomorphodynamics & Geochronology; Geography Department, University of Zurich, Switzerland
Michael Avian, Viktor Kaufmann
Institute of Remote Sensing and Photogrammetry, Graz University of Technology, Austria
Reynald Delaloye
Department of Geosciences, Geography, University of Fribourg, Switzerland
Christophe Lambiel
Institute of Geography, University of Lausanne, Switzerland
Andreas Kääb
Department of Geosciences, University of Oslo, Norway

Abstract

In many high mountain regions, warming of perennially frozen ground in both coarse debris and rock walls has a major influence on slope stability. In this context, indications of destabilizing active rock glaciers, such as high horizontal velocities (up to 4 ma^{-1}), front advance rates of up to 4 ma^{-1}, and development of crevasse-like cracks (up to 14 m deep), have been documented and monitored in the Alps for a few years. Beside the limited knowledge of rock glacier dynamics, our principle hypothesis is that the primary factors controlling the development of cracks and the destabilization of rock glacier tongues are the rheological properties of warming ice. In addition, we postulate that hydrological effects of unfrozen water within the active layer, the permafrost body, or at its base may contribute to the initiation of the slide-like mass wasting.

Keywords: European Alps; kinematics; rock glacier; slope destabilization.

Introduction

In the context of recent climatic changes and their impact on the cryosphere, high-mountain environments play a key role due to their sensitivity to thermal changes. The indicative role of rock glaciers in these geosystems was emphasized only recently (e.g., Harris & Haeberli 2003, Haeberli et al. 2006), but was up to now mainly restricted to temperature variations within the permafrost body and variations in active layer thickness. Within the last decade, an increasing number of studies monitored and quantified the creep behavior of rock glaciers in the European Alps and observed increasing surface displacements since the 1990s (Schneider & Schneider 2001, Ikeda et al. 2003, Lambiel & Delaloye 2004, Kääb et al. 2007, Roer 2007). In this context it is described that the Alpine rock glaciers show a rather synchronous behavior and respond sensitively to recent temperature increase (Roer et al. 2005a, Roer et al. 2005b, Kääb et al. 2007, Delaloye et al. 2008). In 2003, Kääb et al. stated that the correlation between the velocity field (e.g., speed, creep direction, strain rates) and the present day three-dimensional geometry indicates that most active rock glaciers have not undergone significant dynamic changes in the past. But recently, distinct changes in surface topography are described for a number of active rock glaciers in the Alps, indicating the landslide-like behavior and destabilization of these landforms.

Based on these observations, the study aims at identifying primary factors controlling the development of cracks and causing the landslide-like behavior of the landforms. Furthermore, possible natural hazards due to rock glacier instabilities are discussed.

Observations

The destabilization of active rock glaciers is indicated by distinct changes in their kinematics, geometry and strongly modified topography. These phenomena are investigated qualitatively by field inspection and by interpretation of terrestrial and aerial photographs. In addition, horizontal velocities, advance rates of the rock glacier front, as well as the growth and depth of cracks, are measured and quantified by the use of digital othophotos and by differential GPS measurements in the field. Also, recently the remote sensing technique InSAR (Interferometric Synthetic Aperture Radar) has been applied to detect landform changes (Delaloye et al. in prep., Lambiel et al. 2008). Once indications for destabilizations are detected, the rock glaciers have been surveyed regularly and monitored in detail. Examples are provided from different regions of the European Alps:

(1) rock glacier Hinteres Langtalkar, Carinthia, Austria
(2) rock glacier Grueo1, Valais, Switzerland
(3) rock glacier Furggwanghorn, Valais, Switzerland
(4) rock glacier Petit-Vélan, Valais, Switzerland
(5) rock glacier Tsaté-Moiry, Valais, Switzerland

First, observations on variations in velocity fields accompanied by the development of transverse cracks were described for the rock glaciers Äusseres Hochebenkar and Hinteres Langtalkar, both situated in Austria (Kaufmann &

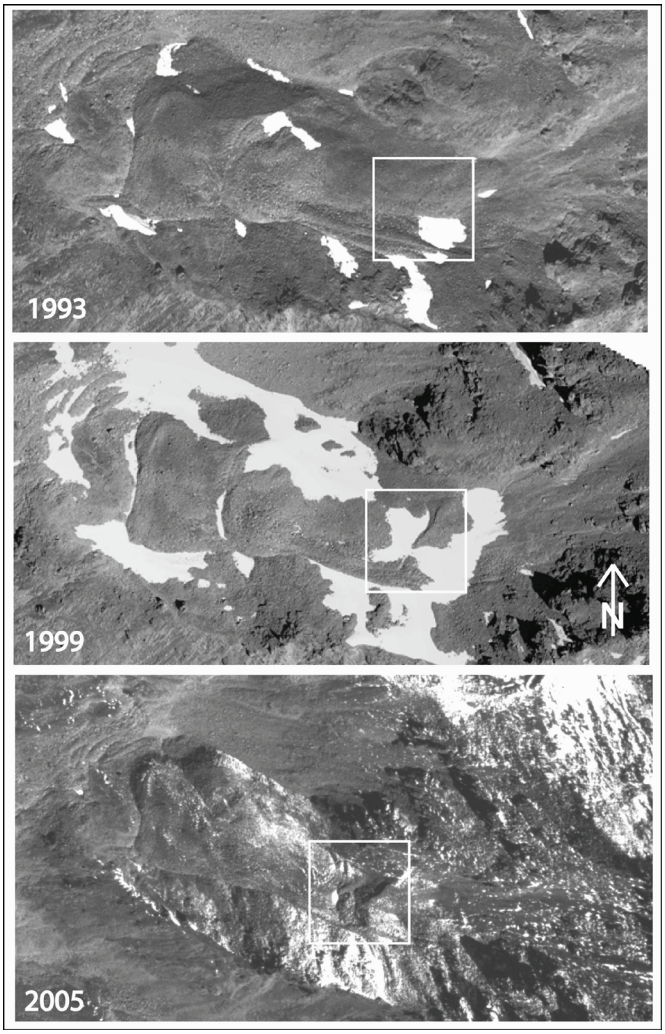

Figure 1. Development of cracks cracks phenologically similar to crevasses occurring on glaciers, in the rooting zone of rock glacier Furggwanghorn (Valais, Switzerland). A small crack started to grow between 1993 and 1999 and evolved into two 14 m deep cracks until 2005. In parallel, the former stable front of the rock glacier advanced about 1.55 ma^{-1} during this time. Orthoimages of 1993, 1999, and 2005 © Swiss Federal Office of Topography (Swisstopo).

Ladstädter 2003, Avian et al. 2005). The strong deformation of the lowest part of the rock glacier Hinteres Langtalkar was interpreted as expression of enhanced strain due to movement of the landform over a terrain ridge into steeper terrain. Thus, the sudden change in slope inclination seemed to cause this specific dynamic response. Later, further rock glaciers showing similar creep instabilities accompanied by the formation of surface ruptures were detected in the Valais, Switzerland.

Rock glacier topography

At the scale of an entire rock glacier, its typical topography is characterized by a relatively smooth and unstructured surface in the upper part (with sometimes longitudinal ridges) and a distinct pattern of ridges and furrows in the lower part, indicating compressive flow. Thus, the surface structure of a rock glacier depicts the complex strain history

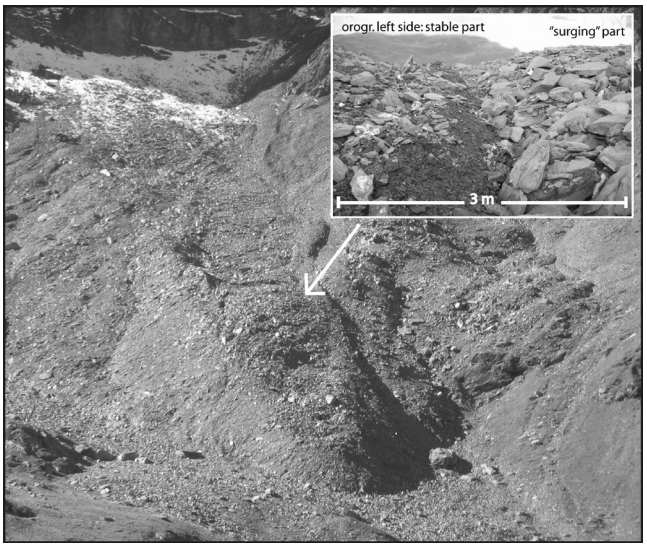

Figure 2. Rock glacier Tsaté-Moiry, Valais, Switzerland. Several scars, developing since the 1980s, are found all over the landform. Velocities at the front were about 7 ma^{-1} between 2006 and 2007. In the field, stable and surging parts can easily be differentiated due to stability (wedged or loose blocks) as well as sorting of the material at the rock glacier surface (Photos: C. Lambiel, 2007).

of the landform (Haeberli 1985, Kääb & Weber 2004). Normally, even if the horizontal velocities are high, the geometric change of the creeping permafrost body is very small (Kääb & Vollmer 2000, Roer 2007).

Most of the rock glaciers investigated here show a smooth morphology prior to the sliding behavior (e.g., rock glacier Furggwanghorn 1993, Fig. 1). In addition, those landforms featuring failures at the front in parallel, indicate smooth surfaces with continuous horizontal displacements in their rooting zones (Kaufmann & Ladstädter 2003, Roer 2007). In the case of rock glacier Tsaté-Moiry, indications for destabilization are not restricted to one part, but affect the whole landform (Fig. 2). Most of the rock glaciers show a collapse behavior in the lowermost part of their tongue. Such failures are indicated by the rugged topography due to the crack formation and by the strong advance of the tongue which is accompanied by a lowering of the surface.

Horizontal velocities and advance rates

As mentioned before, the morphological change of the rock glaciers studied here is caused by distinct high horizontal velocities over the entire landforms, between 1.00–3.76 ma^{-1} (Table 1). These velocities indicate strong spatial variations. In general, deformation rates of the investigated rock glaciers are very small in the rooting zone and at the margins of the landform; the highest movement rates are found in the central flow field. On most of the destabilizing rock glaciers, highest velocities are measured at the front, where most of the morphological changes occur (e.g., Fig. 3). For some of these rock glaciers, measurements of velocities were even inhibited on the destabilized parts of the tongue, due to a loss in corresponding features in the repeated orthophotos. In such cases, the surface is not slowly changing anymore,

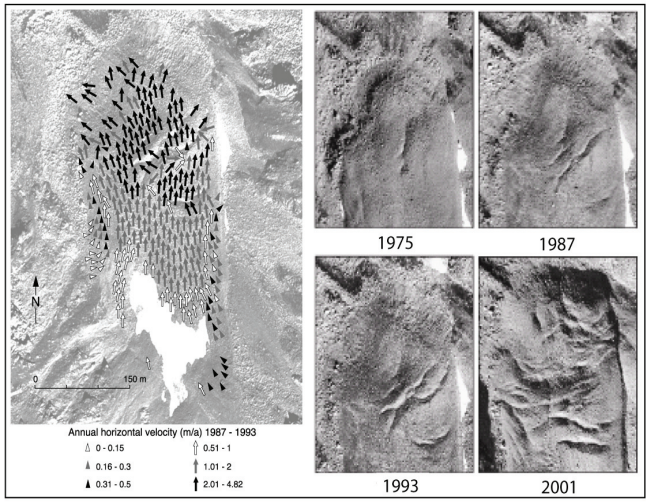

Figure 3. Collapsing tongue and development of deep cracks of rock glacier Grueo1 (Valais, Switzerland) between 1975 and 2001. The cracks started to develop on the orographic right side, while later (between 1993 and 2001) the landslide-like failure extended over the entire tongue. Between 1975 and 2001 the rock glacier advanced about 60 m (~ 2.3 ma^{-1}). (See also Roer 2007, Kääb et al. 2007). Orthoimages of 1975, 1987, and 1993 © Swiss Federal Office of Topography (Swisstopo). Orthoimage of 2001 © RTG 437, Department of Geography, University of Bonn.

but is rather characterized by tilting and toppling of blocks into the forming cracks.

In addition to the high displacement rates, all rock glaciers considered here indicate extraordinary changes at their fronts. Regarding typical rock glaciers, even if different advance mechanisms occur (Kääb & Reichmuth 2005), the annual rates are very small (0.1- 0.4 ma^{-1} in the Alps (Roer 2007)). In contrast, rock glaciers showing a landslide-like behavior, feature extraordinary advances of several meters per year (see Table 1, Fig. 5). Due to that fact, the shape of the terminal fronts changed significantly. Hence, they are not stable anymore, and often show a high rockfall frequency.

Formation of cracks

Caused by the high horizontal velocities and the pronounced advance of the fronts, cracks that are –phenologically similar to crevasses which occur on glaciers –developed on all rock glaciers in this study. These cracks are mostly found in the lower part of the tongues; rock glacier Furggwanghorn is the only one with cracks in the rooting zone after 1993 (Fig. 1). They are up to 14 m deep and feature lengths of 150 meters and more. An interesting fact is that, on most of the rock glaciers investigated, first indications of the existence and growth of cracks go back for over 20 years (Table 1). The formation of cracks on the rock glaciers Grueo1 (Fig. 3) and Hinteres Langtalkar (Fig. 4), expanded and accelerated in the 1990s. This is in accordance with observations on rock glacier Furggwanghorn, which show a more recent crack formation (between 1993 and 1999, Fig. 1). In the case of rock glacier Tsaté-Moiry, the phenomena is instead described by the occurrence of scars (which are less deep than cracks, and therefore seem to affect the active layer only) occurring all over the landform.

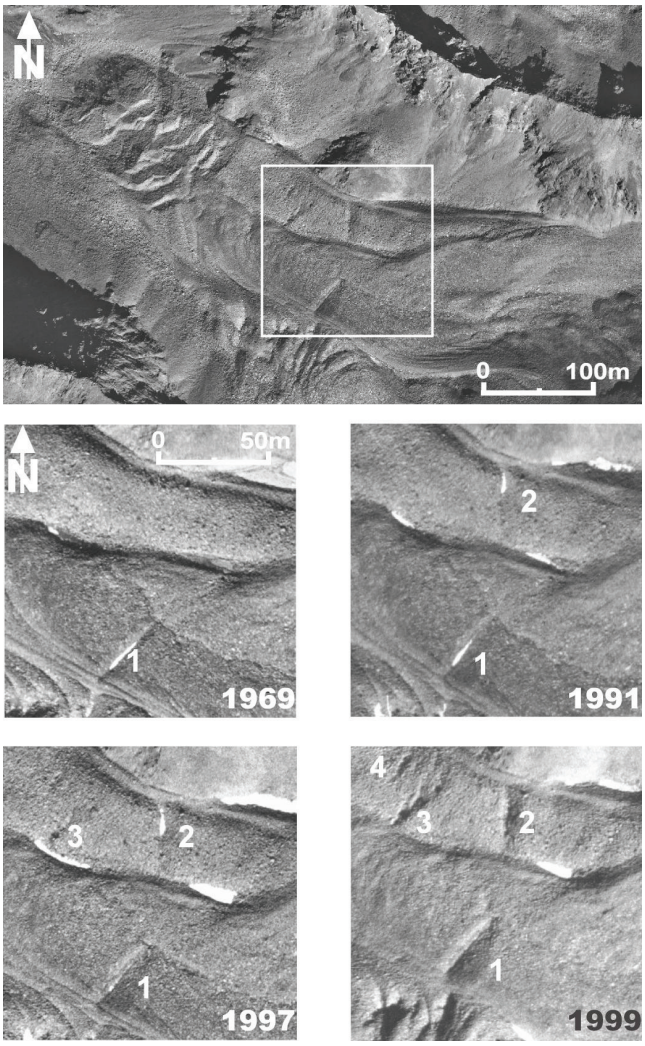

Figure 4. Rock glacier Hinteres Langtalkar (Carinthia, Austria): formation of cracks (1–4) between 1969 and 1999 in the middle part of the landform (square in uppermost image). Aerial photographs of rock glacier Hinteres Langtalkar for 1969, 1991, 1997, and 1999 © Austrian Federal Office of Metrology and Survey (BEV), Vienna, 2001.

Inspections and investigations of these cracks in the field offered more questions than answers. In most of the cracks, neither ice nor evidence of water was found during the summer months, hinting at a well-developed drainage through and/or underneath the creeping permafrost bodies. However, on rock glacier Hinteres Langtalkar (Fig. 4), two of the cracks were filled with water during summer.

Destabilization of rock glacier tongues

A destabilization of the rock glacier tongues happens in those cases where deep cracks form in the lower part of the landforms (i.e., rock glaciers Hinteres Langtalkar, Grueo1, and Tsaté-Moiry). The cracks indicate deep shear-zones similar to those known for rotational landslides (Dikau et al. 1996). Also, the movement of the tongue, which is characterized by a massive downslope displacement of the mass accompanied by a distinct lowering of the surface (see Fig. 5), is analagous to sliding processes. Hence, a change

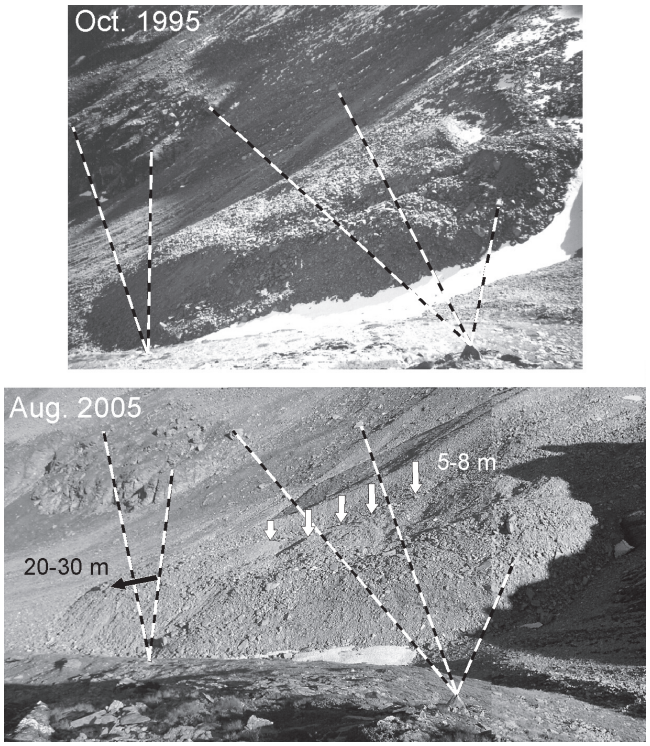

Figure 5. Instability of the tongue of rock glacier Petit-Vélan (Valais, Switzerland). The dashed lines connect the fixed points in stable terrain outside the rock glacier and provide the basis for the photo analysis. Between October 1995 and August 2005, this landform advanced about 20–30 m (approx. 2.5 m per year). Due to that shift of mass, vertical lowering of 5–8 m occurred (Photos: R. Delaloye)

in process regime is indicated. Related to the landslide-like mass wasting, the lowermost part of the tongues changed from a formerly convex to a more concave morphology.

Hazards

The changes described before can affect all parts of rock glaciers: the active layer, the permafrost body, the rooting zone, or the front. Arenson (2002) stated that instabilities within the active layer seem to be most probable due to the effect of unfrozen water during summer. The accelerated horizontal velocities, as well as the sliding processes, strongly influence the stability of the rock glacier front. Here, enhanced rockfall activity (frequency and magnitude) was recognized on several rock glaciers. In general, the position of the landform (especially the slope angle) is decisive for its hazard potential.

Considerations

The interpretation of the presented observations is, up to now, strongly limited due to the complexity of the phenomenon and the lack of information on the thermal state and internal structure of the rock glaciers considered here. Borehole data (internal deformation, temperatures) or data delivered by geophysical soundings from adjacent landforms can not be consulted, since the dynamics of individual rock glaciers cannot be readily compared. Therefore, only the given information on rock glacier kinematics can be analysed. Since these data provide a cumulative signal reflecting all components of the creep process (internal deformation, sliding in shear horizons, and deformation at the base), the processes below the surface can be considered to some degree. The key question is which of the creep components increased by certain changes, i.e., whether the internal deformation, the sliding in shear horizons, or the basal sliding increased significantly (Fig. 6).

Table 1. Summary of characteristics of the investigated rock glaciers. The numbers refer to the rock glaciers listed on page 1.

rockgl.	mean annual velocity (ma^{-1})	front advance (ma^{-1})	crevasses in lower part	crevasses in rooting zone	beginning of crevasse formation
1	2.80 (mean 1997 - 1998)	-	x	-	before 1954
2	2.79 (mean 1993 - 2001)	2.30 (1975-2001)	x	-	before 1975
3	1.46 (mean 1993 - 2001)	1.55 (1975-2001)	-	x	between 1993 and 1999
4	1.24 (mean 2005 - 2007)	2.50 (1995-2005)	x	-	between 1988 and 1995
5	1.50 (mean 2005 - 2007)	4.00 (1999-2005)	x	x	before 1988

Under constant temperatures, stresses, and strain rates, rock glaciers show long-term steady-state (secondary) creep behaviour (Haeberli 1985). The flow results from the plastic deformation of the ice inside the supersaturated permafrost body in response to gravity and is controlled mainly by its internal structure (Barsch 1992). Sliding in shear horizons, where reduction in viscosity enables higher deformations, plays an additional role (Wagner 1992, Arenson et al. 2002). Hence, different factors or a combination thereof, may lead to the observed geomorphic changes: changes in ice content or ice characteristics; changes in the shear horizons (e.g., number, position, frictional behaviour, occurrence of unfrozen water); or changes in the internal structure of the permafrost body leading to changes in deformation. Another creep component, which could have led to the observed changes, might be the deformation of subpermafrost sediments (Fig. 6).

All those effects may result from a change in ground temperature regime. The significance of a rise in air temperature for a change in the strength of ice-rock mixtures has been demonstrated by Davies et al. (2001) in laboratory tests. They proved that a rise in air–and consequently ground–temperature leads to a reduction in shear strength of ice-bonded discontinuities and thus may induce slope failures. In addition, Kääb et al. (2007) conclude from modeling and field investigations, that the creep of perennially frozen granular material close to 0°C is significantly more sensitive to climate forcing than the creep of colder material. Their modeling results also stress the importance of a deeper understanding of shear horizons in rock glaciers, since they appear to be the most sensitive parts in the response of the permafrost bodies to atmospheric and ground warming.

The analysis of the observed development of cracks indicates that strain rates increased significantly. It is not clear whether this formation is a gradual process (as indicated by the slow growth of most of the cracks, Figs. 3, 4) or sudden exceeding of a threshold (as given by the acceleration of crack formation in the 1990s). In addition, this development may differ between rock glaciers. The related changes at the rock glacier surface (e.g., thinning of the protecting debris cover) might enhance the process by positive

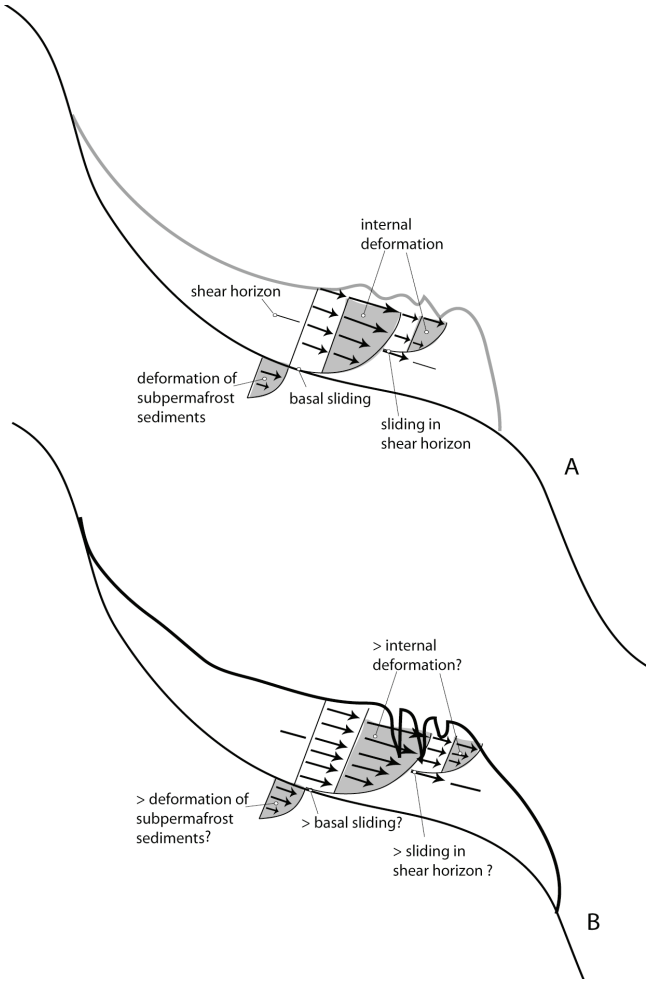

Figure 6. Schematic profile of a typical rock glacier for steady-state conditions (A), and a destabilized rock glacier with crack formation in the lower part of the tongue (B). A deformation profile showing the single creep components is depicted for both cases; it is not clear which component is decisive for the destabilization of the tongue

feedback mechanisms (Kääb et al. 2007). Due to the cracks, latent heat can easily penetrate into the permafrost body, and thus may lead to a warming of the ice (thermokarst phenomena).

The observed changes at the front of the rock glaciers' are probably not exclusively related to permafrost creep processes alone. The analysis of the morphological changes indicates a mass wasting similar to landslides.

Conclusions and Perspectives

Our principle hypotheses are that the primary factors controlling the development of cracks and the destabilization of rock glacier tongues are the rheological properties of warming ice and the resulting changes in the stress-strain relation. In addition, and related to the before mentioned, hydrological effects (unfrozen water) within the permafrost body or at its base may contribute to the initiation of rapid flow acceleration into tertiary creep. Unfrozen water ponding on the permafrost surface could lead to surface instabilities and trigger landslides (Arenson 2002). Another component in this context might be the deformation of subpermafrost sediments. In some cases, topographic influences due to movement onto steep slopes (>25-30°) and/or convex terrain can initiate the destabilization of the landform. Generally, the interpretation of those exceptional rock glaciers is limited, due to the little knowledge of rock glacier dynamics.

The challenge in the investigation of destabilized active rock glaciers lies in the ongoing monitoring of these landforms, for research purpose as well as for hazard assessments. In addition, more data related to internal characteristics are needed in order to develop a process model that couples creep and sliding mechanisms. The coupled analysis will allow for an assessment of how changes in subsurface characteristics will be translated into a rheological response. These goals fit into the key questions of future permafrost research addressing spatio-temporal changes of surface and subsurface processes in response to atmospheric forcing.

Acknowledgments

The photogrammetric analyses of Furggwanghorn rock glacier were conducted in collaboration with Patrick Thee, Swiss Federal Institute for Forest, Snow, and Landscape Research. We gratefully acknowledge the valuable comments of two anonymous reviewers.

References

Arenson, L.U. 2002. Unstable alpine permafrost: a potentially important natural hazard–variations of geotechnical behaviour with time and temperature. Doctoral thesis No. 14801, ETH Zurich.

Arenson, L.U., Hoelzle, M. & Springman, S. 2002. Borehole deformation measurements and internal structure of some rock glaciers in Switzerland. *Permafrost and Periglacial Processes* 13: 117-135.

Avian, M., Kaufmann, V. & Lieb, G.K. 2005. Recent and holocene dynamics of a rock glacier system: The example of Langtalkar (Central Alps, Austria). *Norwegian Journal of Geography* 59(2): 149-156.

Barsch, D. 1992. Permafrost creep and rockglaciers. *Permafrost and Periglacial Processes* 3: 175-188.

Davies, M.C.R., Hamza, O. & Harris, C. 2001. The effect of rise in mean annual temperature on the stability of rock slopes containing ice-filled discontinuities. *Permafrost and Periglacial Processes* 12: 137-144.

Delaloye, R., Perruchoud, E., Avian, M., Kaufmann, V., Bodin, X., Hausmann, H., Ikeda, A., Kääb, A., Kellerer-Pirklbauer, A., Krainer, K., Lambiel, C., Mihajlovic, D., Staub, B., Roer, I. & Thibert, E. 2008. The short-term response of rock glaciers creep to recent warm periods in the European Alps (2002–2007). *Proceedings of the Ninth International Conference on Permafrost, Fairbanks, Alaska, June 29–July 3, 2008* (this proceedings).

Delaloye, R., Strozzi, T., Lambiel, C. & Perruchoud, E. in prep. Landslide-like development of rockglaciers detected with ERS-1/2 SAR Interferometry. *Proceedings ESA FRINGE Symposium 2007*.

Dikau, R., Brunsden, D., Schrott, L. & Ibsen, M.L (eds.). 1996. *Landslide recognition. Identification, movement and causes.* Wiley. Chichester: 251.

Haeberli, W. 1985. Creep of mountain permafrost: internal structure and flow of alpine rock glaciers. *Mitteilungen der Versuchsanstalt für Wasserbau, Hydrologie und Glaziologie* 77: 139.

Haeberli, W., Hallet, B., Arenson, L., Elconin, R., Humlum, O., Kääb, A., Kaufmann, V., Ladanyi, B., Matusoka, N., Springman, S. & Vonder Mühll, D. 2006. Permafrost creep and rock glacier dynamics. *Permafrost and Periglacial Processes* 17: 189-214.

Harris, C. & Haeberli, W. 2003. Warming permafrost in the mountains of Europe. *Bulletin of the World Meteorological Organization* 52, 3: 1-6.

Ikeda, A., Maatsuoka, N. & Kääb, A. 2003. A rapidly moving small rock glacier at the lower limit of the mountain permafrost belt in the Swiss Alps. *Proceedings of the Eighth International Conference on Permafrost, Zürich, Switzerland, June, 2003*. Balkema, 1: 455-460.

Kääb, A. & Vollmer, M. 2000. Surface geometry, thickness changes and flow fields on creeping mountain permafrost: automatic extraction by digital image analysis. *Permafrost and Periglacial Processes* 11: 315-326.

Kääb, A., Kaufmann, V., Ladstädter, R. & Eiken, T. 2003. Rock glacier dynamics: implications from high-resolution measurements of surface velocity fields. *Proceedings of the Eighth International Conference on Permafrost, Zürich, Switzerland, June, 2003*. Balkema, 1: 501-506.

Kääb, A. & Weber, M. 2004. Development of transverse ridges on rock glaciers: field measurements and laboratory experiments. *Permafrost and Periglacial Processes* 15: 379-391.

Kääb, A. & Reichmuth, T. 2005. Advance mechanisms of rock glaciers. *Permafrost and Periglacial Processes* 16: 187-193.

Kääb, A., Frauenfelder, R. & Roer, I. 2007. On the response of rockglacier creep to surface temperature increase. *Global and Planetary Change* 56: 172-187.

Kaufmann, V. & Ladstädter, R. 2003. Quantitative analysis of rock glacier creep by means of digital photogrammetry using multi-temporal aerial photographs: two case studies in the Austrian Alps. *Proceedings of the Eighth International Conference on Permafrost, Zürich, Switzerland, June, 2003*. Balkema, 1: 525-530.

Lambiel, C. & Delaloye, R. 2004. Contribution of real-time kinematic GPS in the study of creeping mountain permafrost: Examples from the Western Swiss Alps. *Permafrost and Periglacial Processes* 15: 229-241.

Lambiel, C., Delaloye, R., Strozzi, T., Lugon, R. & Raetzo, H. 2008. ERS InSAR for assessing rock glacier activity. *Proceedings of the Ninth International Conference on Permafrost, Fairbanks, Alaska, June 29–July 3, 2008* (this proceedings).

Roer, I. 2007. Rockglacier kinematics in a high mounain geosystem. *Bonner Geographische Abhandlungen* 117: 217.

Roer, I., Kääb, A. & Dikau, R. 2005a. Rockglacier acceleration in the Turtmann valley (Swiss Alps) – probable controls. *Norwegian Journal of Geography* 59(2): 157-163.

Roer, I., Avian, M., Delaloye, R., Lambiel, C., Bodin, X., Thibert, E., Kääb, A., Kaufmann, V., Damm, B. & Langer, M. 2005b. Rockglacier "speed-up" throughout European Alps—a climatic signal? *Proceedings of the Second European Conference on Permafrost, Potsdam, Germany, June 2005*: 101-102.

Schneider, B. & Schneider, H. 2001. Zur 60jährigen Messreihe der kurzfristigen Geschwindigkeits-schwankungen am Blockgletscher im Äusseren Hochebenkar, Ötztaler Alpen, Tirol. *Zeitschrift für Gletscherkunde und Glazialgeologie* 37(1): 1-33.

Wagner, S. 1992. Creep of alpine permafrost from borehole deformation at Murtèl rock glacier, Grison (Swiss Alps). *Permafrost and Periglacial Processes* 3:157-162.

—Plenary Paper—

Thermal State and Fate of Permafrost in Russia: First Results of IPY

V.E. Romanovsky, A.L. Kholodov, S.S. Marchenko
Geophysical Institute, University of Alaska Fairbanks
N.G. Oberman
MIRECO Mining Company, Syktivkar, Russia
D.S. Drozdov, G.V. Malkova, N.G. Moskalenko, A.A. Vasiliev
Institute of Earth Cryosphere, Tyumen, Russia
D.O. Sergeev
Institute of Environmental Geoscience, Moscow, Russia
M.N. Zheleznyak
Melnikov Permafrost Institute, Yakutsk, Russia

Abstract

To characterize the thermal state of permafrost, the International Permafrost Association launched its International Polar Year Project #50, Thermal State of Permafrost (TSP). Ground temperatures are measured in existing and new boreholes within the global permafrost domain over a fixed time period in order to develop a snapshot of permafrost temperatures in both time and space. This data set will serve as a baseline against which to measure changes of near-surface permafrost temperatures and permafrost boundaries, to validate climate model scenarios, and for temperature reanalysis. The first results of the project based on data obtained from Russia are presented. Most of the observatories show a substantial warming during the last 20 to 30 years. The magnitude of warming varied with location, but was typically from 0.5 to 2°C at the depth of zero annual amplitude. Thawing of Little Ice Age permafrost is ongoing at many locations. There are some indications that Late Holocene permafrost has begun to thaw at some undisturbed locations in northeastern Europe and in northwest Siberia. Projections of future changes in permafrost suggest that by the end of the 21st century, Late Holocene permafrost in Russia may be actively thawing at all locations and some Late Pleistocene permafrost could start to thaw as well.

Keywords: dynamics of permafrost; long-term thaw; modeling; temperature regime.

Introduction

Permafrost has received much attention recently because surface temperatures are rising in most permafrost areas of the Earth, which may lead to permafrost thaw. Thawing of permafrost has been observed at the southern limits of the permafrost zone; thawing can lead to changes in ecosystems, in water and carbon cycles, and in infrastructure performance. If the current trends in climate continue, warming of permafrost will eventually lead to widespread permafrost thawing in the colder permafrost zones. There is, however, uncertainty concerning where this thawing will occur first, the rate of thaw, and the consequences for arctic, subarctic, and global natural systems. Hence, it is critically important to organize and sustain continuous observations of the thermal state of permafrost in various locations and for various natural settings within the entire Earth permafrost domain. To characterize the thermal state of permafrost, the International Permafrost Association launched its International Polar Year Project #50, Thermal State of Permafrost (TSP). Ground temperatures are measured in existing and new boreholes within the global permafrost domain over a fixed time period in order to develop a snapshot of permafrost temperatures in both time and space (Brown & Christiansen 2006). The resulting data set will serve as a baseline against which to measure changes of near-surface permafrost temperatures and permafrost boundaries, to validate climate model scenarios, and for temperature reanalysis.

More than half of Russia is occupied by permafrost, constituting a significant portion of the entire Northern Hemisphere permafrost area. Hence, without comprehensive understanding of permafrost dynamics in Russia it will be very difficult to draw any general conclusions about the state and fate of permafrost in the Northern Hemisphere. Permafrost research in Russia has a long, rich history. Many historically active institutions are still active in permafrost research today, though there is a strong need to develop an integrated network of permafrost research stations to improve the efficiency and sustainability of these efforts. The Russian-US TSP project funded by the US National Science Foundation (NSF) was established to initiate the process of collaborating and integrating US (mainly Alaskan) and Russian permafrost observing stations into an International Network of Permafrost Observatories (INPO) within the framework of the International Polar Year (IPY). Several institutions from the universities and the US Geological Survey and more than ten Russian institutions and organizations are involved in this project. This project is open to new participants, both individual and institutional. The first results of this project based on both currently measured and historical data from several permafrost regions in Russia (Fig. 1) are presented in this paper.

Examination of past trends in permafrost conditions and

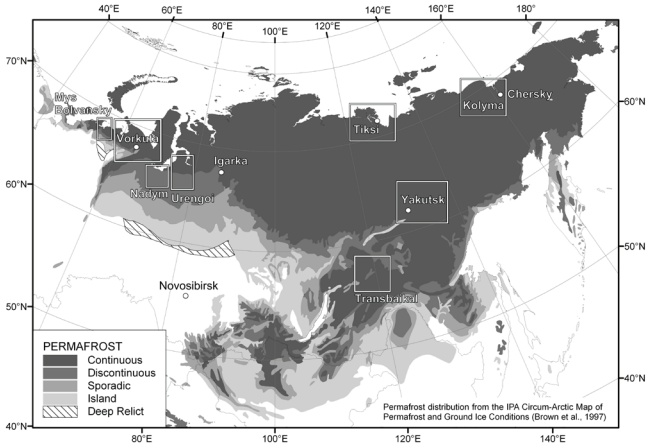

Figure 1. Location of selected Russian TSP research areas discussed in this paper.

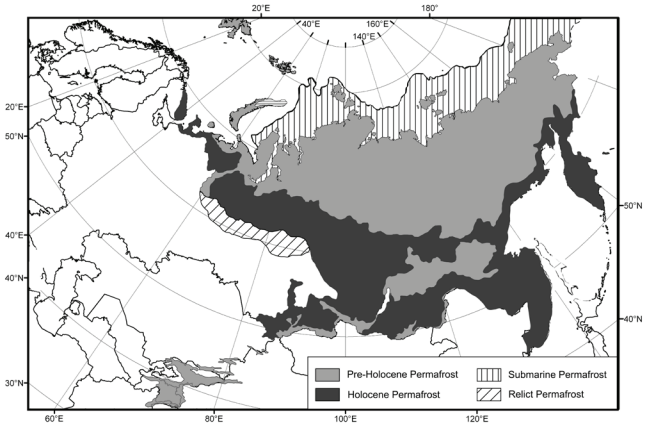

Figure 2. Present-day distribution of permafrost of different ages in Russia (after Lisitsyna & Romanovskii 1998).

distribution (especially during the last glacial-interglacial cycle) can also facilitate better understanding of the possible rates and pathways of permafrost degradation in the future. The primary reasons for this are: 1) many present-day features in permafrost distribution both vertically and laterally were formed during the last 100,000 years, and 2) we can expect that with persistent future climate warming, the first permafrost to thaw will be the youngest Little Ice Age permafrost, followed by Mid and Late Holocene permafrost, and last to thaw will be the Late Pleistocene permafrost. Thawing of the Little Ice Age permafrost is ongoing at many locations. There are some indications that Late Holocene permafrost has started to thaw at some specific undisturbed locations in northeastern Europe, in northwestern Siberia, and in Alaska. In this paper we will briefly describe our knowledge of permafrost development in Russia during the last glacial-interglacial cycle and provide currently available information about recent long-term permafrost thawing in this region.

Permafrost History in Russia During the Last Glacial-Interglacial Cycle

Permafrost distribution changed during the last glacial-interglacial cycle in response to changes in climate. During the last glacial maximum (ca. 20ky BP), permafrost underlay more land area than today. Significant portions of non-glaciated territory of Europe, northern Eurasia, and North America were affected by permafrost. With the termination of the last glacial epoch during the transition from glacial to interglacial climate, permafrost started to thaw rapidly both from the top and from the bottom at the southernmost limits of its Late Pleistocene maximum distribution. With climate warming in progress, more and more permafrost in this area became involved in rapid degradation. As a result, by the time of the Holocene Optimum (5-9 ky BP), permafrost had completely disappeared from most of the territory of deglaciated Europe, from northern Kazakhstan, and from a significant portion of West Siberia in northern Eurasia (Yershov 1998). In areas where the upper several hundred meters of permafrost was ice-rich, such as in the Pechora River basin and in the northern and central parts of West Siberia, permafrost had not disappeared completely; it is still present at greater depths (200 m and deeper). Permafrost on land was generally stable and did not experience any widespread thaw during the Holocene Optimum within the northern part of Central Siberia and within the entire continuous permafrost zone in East Siberia and in the Russian Far East (Fig. 2). However, numerous thermokarst lakes have rapidly developed during this period causing localized thawing of permafrost under lakes that were sufficiently deep.

Climate cooling during the Middle and Late Holocene resulted in a reappearance of permafrost in many areas of the present-day discontinuous permafrost zones (Fig. 2). In some areas, permafrost aggradation was accompanied by an accumulation of new sediments resulting in so-called syngenetic permafrost formation. More commonly, this new Holocene permafrost was formed by refreezing of already existing sediments and bedrock (termed epigenetic permafrost). In the areas where the Late Pleistocene permafrost was still in existence at some depth, two-layered permafrost was formed. The number of newly formed thermokarst lakes significantly declined within the continuous permafrost area.

Generally, Holocene climate has been much more stable than during the Late Pleistocene. However, several relatively warm and cold several-centuries-long intervals can be traced in the Middle and Late Holocene (Velichko & Nechaev 2005). During these intervals, new, fairly shallow, short-lived permafrost appeared and disappeared several times in some specific landscape types found within the sporadic and discontinuous permafrost zones near the southern boundary of present-day permafrost distribution. The last and probably the coldest of such intervals was the Little Ice Age, which dominated most of the Northern Hemisphere climate between ca. 1600 and 1850. During this period, shallow permafrost (15 to 25 m, e.g. Romanovsky et al. 1992) was established within the sediments that were predominantly unfrozen during most of the Holocene. Present-day warming initiated the Little Ice Age permafrost thawing that has been

documented for several regions in North America (Jorgensen et al. 2001, Payette et al. 2004).

A Short Description of Selected Research Areas and Methods of Measurements

A large number of borehole temperature measurements at different depths were obtained for the Eurasian permafrost regions starting in the 1960s. Only a small fraction of these data became available for analysis during the initial implementation stage of the Russian TSP project. Comparing retrospective data with results of modern observation allows estimation of the trends in thermal state of permafrost during the last few decades. During the first year of this project (2007), some data from the European North of Russia, north of the western Siberia and Yakutia regions were collected. New temperature monitoring instruments were installed in more than 100 already existing and newly drilled boreholes at various locations within the Russian permafrost domain. This instrumentation allows automatic continuous collection of temperature data with sub-daily time resolution.

The longest permafrost temperature time series from Russia in our records are from northeast European Russia and from northwest Siberia. Permafrost temperatures at various depths have been measured since the early 1970s in the Nadym and Urengoy research areas, since the late 1970s in the Vorkuta research area, and since the early 1980s near the Mys Bolvansky meteorological station located near the shore of the Barents Sea (Fig. 1). At each location the specially designed temperature-monitoring boreholes were established in different natural landscape settings within these research areas.

Permafrost temperatures in more than 200 boreholes were measured in the mid-1980s in the Transbaykal Chara research area (Romanovskiy et al. 1991). This area is characterized by extremely high variability in landscape and permafrost conditions. Temperature measurements were re-established in the 2000s in a very limited number of selected boreholes as a part of the Russian TSP activities.

Temperatures in permafrost boreholes have been measured in the Yakutsk research area (Fig. 1) since the 1960s; however, most collected data are not readily available. In this paper we present permafrost temperature data for 1990–2006 collected by scientists from the Melnikov Permafrost Institute at their long-term monitoring station in Yakutsk. A permafrost temperature time series similar in length was obtained from the Tiksi research station as a collaborative effort between the Melnikov Permafrost Institute and Hokkaido University, Japan (Prof M. Fukuda).

Since the 1970s, the researchers from the Institute of Physical-Chemical and Biological Problems of Soil Science (Russian Academy of Science, RAS) have obtained occasional temperature measurements within the network of boreholes on the Kolyma lowland (Fig. 1). However, many of these boreholes are abandoned now and only a few are still available for further observations. Recently, temperatures in four boreholes established in the 1990s were re-measured. During the 2007 field season, as a part of the Russian TSP project, three boreholes were reconstructed by drilling new boreholes next to the old ones for continuity of temperature measurements. The first results of these activities will be presented in this paper.

Most of the boreholes at the Russian permafrost research stations were equipped with permanently installed thermistor strings and temperatures were measured periodically. In some boreholes thermistor strings were inserted into the boreholes only for the short period during which measurements were performed (but long enough to equilibrate thermistor temperature with ambient borehole temperature). The accuracy of the measurements using calibrated thermistors was typically at or better than 0.1°C. In the Vorkuta region temperatures were monitored using mercury thermometers with a scale factor from 0.05 to 0.1°C. The thermometers were placed in cases filled with an inert material such as, for example, grease. The frequency of measurements varied at different locations from once per year to monthly measurements. Starting in 2006, boreholes are being equipped with HOBO U-12-008 temperature data loggers and TMC-HD temperature sensors (www.onsetcomp.com/products/data-loggers/u12-008). Ice bath testing of these sensors and loggers always shows an accuracy of 0.1°C or better. Time resolution of these measurements is typically at four-hour intervals.

The diversity of past measuring techniques could lead to uncertainty when comparing data obtained using these different sensors. Special field experiments were performed during the 2007 field season to address this concern. Temperatures were measured simultaneously with mercury thermometers and data loggers in a borehole within the Vorkuta research area (Oberman 2008). In the Urengoy research area, data logger and thermistor string measurements were performed simultaneously in the same borehole. Readings in both cases differed on average by 0.05°C. These experiments assure the comparability of all measurement techniques at an overall accuracy of 0.1°C. The high temporal resolution of data obtained by the newly installed sensors and data loggers also demonstrates that the depths of zero annual amplitude at the Urengoy, Nadym, Vorkuta, and Mys Bolvansky research areas are relatively shallow, not exceeding 7 to 8 m.

Long-Term Changes in Permafrost Temperatures

At the Urengoy research area in northwest Siberia (Fig. 1) permafrost temperature at the depth of zero seasonal amplitude increased during 1974–2007 in all landscape units (Fig. 3A). An increase of up to 2°C was measured at colder permafrost sites (e.g., borehole UR1503, Fig. 3A). Up to 1°C warming for the same period was observed in warmer permafrost. A 2°C warming was observed in warm permafrost in a borehole that was situated in deciduous forest (not shown). A similar increase was characteristic of marshes with standing water at the surface (borehole

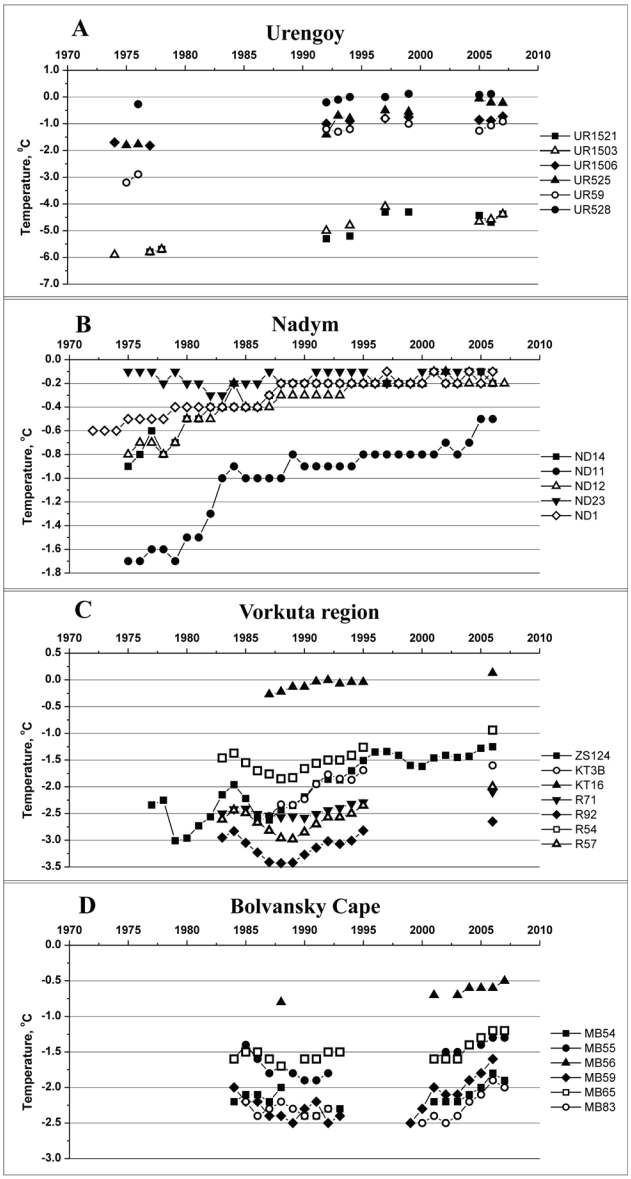

Figure 3. Decadal trends in permafrost temperatures at selected sites in Russia.

UR59, Fig. 3A) Generally, the most significant changes in permafrost were measured in the forested and shrubby areas; often the formation of taliks up to 10 m thick were observed. In undisturbed tundra, permafrost is still generally stable (Drozdov et al. 2008). It was also observed that most warming occurred between 1974 and 1997. At the majority of locations permafrost temperatures did not change, or even cooled between 1997 and 2005. A slight warming has occurred since then at sites characterized by temperatures colder than -0.5°C (Fig. 3A).

In the Nadym research area (Fig. 3B) the most significant permafrost warming occurred before 1990, by about 1°C at a colder site and by up to 0.5°C at the warmer sites (Moskalenko 2008). At the warmest site (borehole ND23) permafrost temperature was -0.1 to -0.2°C and did not change for the entire measurement period (1975–2007). Since the temperature reached the same values at the rest of the warm sites in the late-1980s or early-1990s, it appears

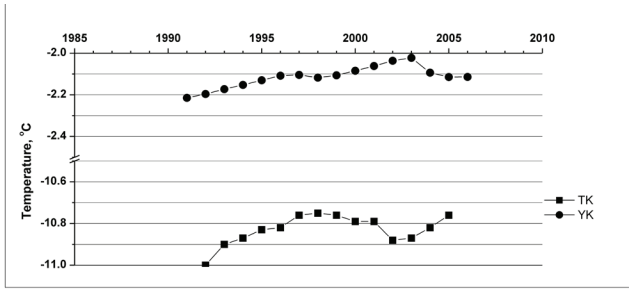

Figure 4. Time series of mean annual permafrost temperatures at 30 m depth at the Yakutsk (YK; circles) and Tiksi (TK; squares) sites.

that permafrost temperature has not changed at the depth of zero annual amplitude at these sites (boreholes ND14, ND 12, and ND1, Fig. 3B). High temporal resolution data obtained with new data loggers show that all annual variations in temperature have occurred in the upper 2 meters of soil, indicating that permafrost has already begun to thaw internally at these sites.

Relative cooling occurred in the Vorkuta region in the late 1970s, mid to late 1980s, and in the late 1990s (Fig. 3C). The most significant warming occurred between the late 1980s and late 1990s. The total warming since 1980 was almost 2°C at the Vorkuta site (Oberman 2008).

At the Bolvansky station in northwest Russia the warming trend in air temperature for the last 25 years is 0.04°C/yr; observed trends in mean annual permafrost temperatures vary from 0.003 to 0.02°C/yr in various natural landscapes (Malkova 2008). For the last 10 years, an increase in climatic variability and alternation of extremely cold and extremely warm years has been observed. These changes initially led to a considerable increase in permafrost temperature, followed in 2007 by a small decrease in temperature in most boreholes (Fig. 3D).

Continuous 15-year permafrost temperature time series were obtained in Tiksi and Yakutsk by researchers from the Melnikov Permafrost Institute in collaboration with scientists from Hokkaido University in Japan. Permafrost temperatures at 30 m depth show a slight positive trend for the 1990–2005 time period (Fig. 4). In contrast, permafrost temperatures apparently did not change significantly in the Kolyma research area (Fig. 1) in the eastern Siberian Arctic during the last 10 to 20 years (Kraev et al. 2008). However, further study is needed to test this conclusion, which was based on recent temperature measurements in or near the historical boreholes that were recently re-occupied as a part of the TSP program.

Permafrost temperatures obtained from the Transbaikal research area (Fig. 1) generally increased during the last 20 years. Borehole #6 was established in the mid-1980s by researchers from Moscow State University and is located in the upper belt of the Udokan Range; temperatures re-measured at this site show a 0.9°C increase between 1987 and 2005 at 20 m depth (Fig. 5). Since 2006, temperatures in this borehole have been recorded at 4-hour time intervals.

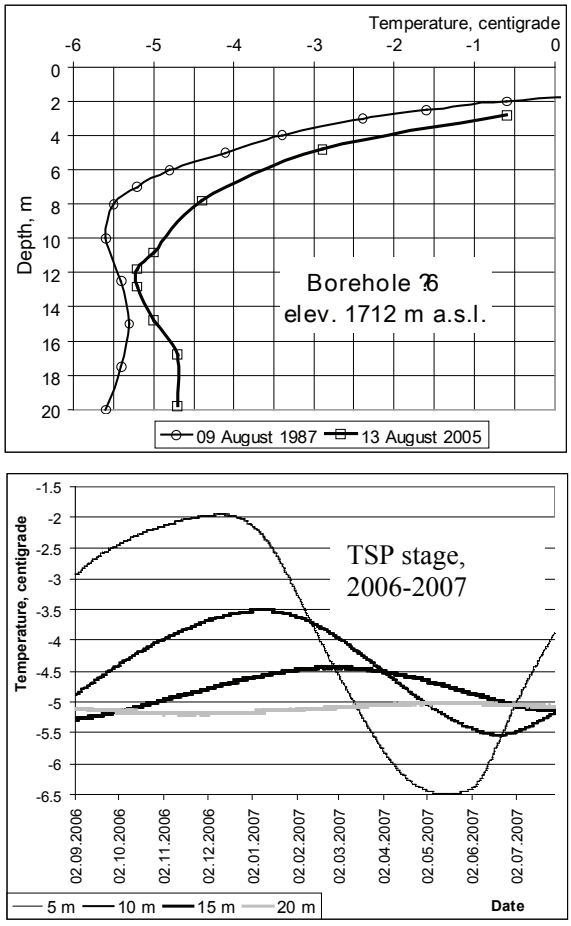

Figure 5. Upper graph: Temperature profiles from the Transbaikal research area obtained in 1987 and 2005. Lower graph: Continuous temperature records at four different depths.

Evidence of Long-Term Thawing of Permafrost

Recently observed warming in permafrost temperatures have resulted in thawing of natural, undisturbed permafrost in areas close to the southern boundary of the permafrost zone. Most observed thawing of long-term permafrost has occurred in the Vorkuta and Nadym research areas. At several locations in the Vorkuta area, long-term thawing of permafrost has led to the development of new closed taliks (Oberman 2008). At one of these locations, the permafrost table lowered to 8.6 m in 30 years. It lowered even more, to almost 16 m, in an area where a newly developed closed talik coalesced with an already existing lateral talik. Permafrost thawing during the last 30 years also resulted in the deepening of previously existing closed taliks. The total increase in depth of the closed taliks developed here ranged from 0.6 to 6.7 m depending on the geographical location, genetic type of a particular talik, ice content and lithological characteristics of the bearing sediments, hydrological, hydrogeological, and other factors.

As a result of recent climatic warming, permafrost patches 10 to 15 m thick thawed out completely in this area (Oberman 2008). In deposits perennially frozen to a depth of about 35 m, the permafrost base has been slowly rising. Comparing small-scale maps based on 1950–1960 data with maps based on 1970–1995 data shows a shift of the southern limit of permafrost by several tens of kilometers northwards (Oberman 2001). This also indicates that permafrost is mostly degrading in the southernmost part of the region.

Permafrost is also degrading in the Nadym and Urengoy research areas. Temperature records from five of a total of seven boreholes in the Nadym area show that cold winter temperatures do not penetrate deeper than 2 m into the ground and that permafrost became thermally disconnected from seasonal variations in air temperature. This also indicates that the constituent ice is already actively thawing in the upper permafrost although the permafrost table (based on the formal 0°C definition of permafrost) is still located just below the active layer. In Urengoy, permafrost is thawing in the forested and shrubby areas, developing closed taliks (Drozdov et al. 2008).

Permafrost degradation in natural undisturbed conditions not associated with surface water bodies has not been reported from the other research areas discussed in this paper. There are numerous occasions of long-term permafrost thawing in Central Yakutian areas around the city of Yakutsk, but all are directly related to natural (forest fire) or anthropogenic (agricultural activities, construction sites) disturbances (Fedorov 1996, Fedorov & Konstantinov 2003).

Permafrost Temperature Reanalysis and Modeling of Past and Future Changes in Permafrost Temperatures

Two levels of permafrost modeling are implemented in our research: a "permafrost temperature reanalysis" and spatially-distributed physically based permafrost modeling. The first level of modeling is the "permafrost temperature reanalysis" approach (Romanovsky et al. 2002). At this level, a sophisticated numerical model (Sergueev et al. 2003, Marchenko et al. 2008), which takes into account the temperature-dependent latent heat effects, is used to reproduce active layer and permafrost temperature field dynamics at the chosen sites. The input data are prescribed specifically for each site and include a detailed description of soil thermal properties and moisture for each distinct layer, surface vegetation, snow cover depth and density, and air temperature. In this modeling approach variations in air temperature and snow cover thickness and properties are the driving forces of permafrost temperature dynamics. The second level of permafrost modeling involves the application of a spatially distributed physically based model that was recently developed in the University of Alaska Fairbanks (UAF) Geophysical Institute Permafrost Lab (GIPL, Sazonova & Romanovsky 2003).

Permafrost temperature reanalysis was successfully applied to several locations within the Russian permafrost domain (Marchenko & Romanovsky 2007, Romanovsky et al. 2007). The model has been calibrated (Nicolsky et al. 2007) for each specific site using several years of measured

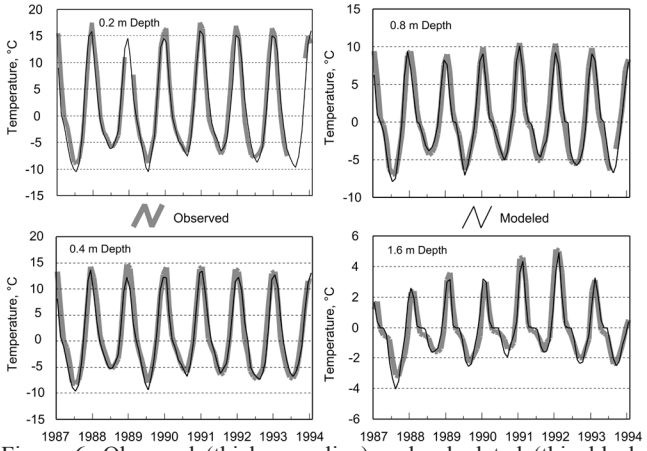

Figure 6. Observed (thick gray line) and calculated (thin black line) ground temperatures at the Yakutsk meteorological station at several depths.

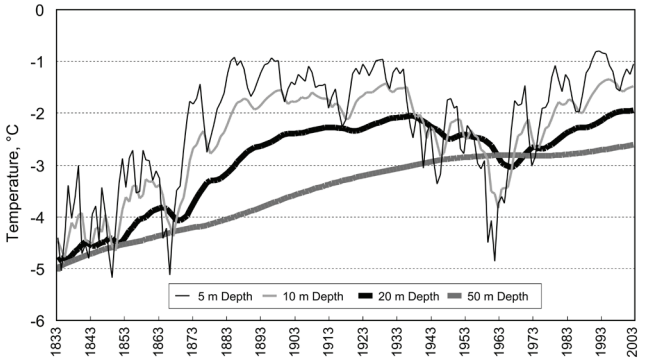

Figure 7. Calculated permafrost temperature time series at several depths for a specific location at the Yakutsk meteorological station.

permafrost and active layer temperature data and climatic data from the closest meteorological station for the same time interval. After validation on measured data that were not involved in the calibration process, the calibrated model can then be applied to the entire period of meteorological records at each station, producing a time series of permafrost temperature changes at various depths. Figure 6 shows the results of calibration of the permafrost model using climate and soil temperature data from the meteorological station in Yakutsk. The differences between measured and modeled temperatures are typically less than 0.5°C and rarely exceed 1°C. Deviation of modeled from measured temperatures decreases with depth (Fig. 6).

The calibrated model was then used to calculate the permafrost temperature dynamics during the transition period from the Little Ice Age up to the present (Fig. 7). Climate forcing includes the air temperature and snow cover dynamics for the period 1833–2003. Air temperature was reconstructed by using observed temperature records from 1834–1853 and 1887–2003 and a spectral analysis technique (Shender et al. 1999). It was also assumed that there were no long-term trends in the snow cover characteristics.

The initial (1833) temperature profile was derived from permafrost temperatures observed by Prof. Middendorf in 1844–1846 in the Shergin's mine in Yakutsk (Sumgin et al. 1939). All measurements were made in narrow horizontal holes in the walls of the mine. The length of each hole was about 2 m. Independent boreholes near Shergin's mine confirmed the characteristic permafrost temperature. Another independent method to test the choice of initial conditions is comparing calculated with measured temperatures for the time intervals when both are available. Such a comparison shows a satisfactory agreement (e.g., compare Figs. 4 and 7).

The results of calculations shown in Figure 7 indicate that the most rapid permafrost warming in the Yakutsk area occurred during the second half of the 19th century. Mean annual temperatures at the shallow depths (5 and 10 m) were already at the present-day level by the 1880s and 1890s, while deeper temperatures continued to increase up to the 1930s. A colder period in the 1940s and especially in the 1960s interrupted this warming trend. Only by the year 2000, permafrost temperatures at the 20 m depth had returned to the pre-cooling level. However, permafrost temperature at greater depths (e.g., 50 m in Fig. 7) continued to increase, although at a slower rate.

The spatially distributed permafrost model GIPL1 that was developed at the Permafrost Lab of the Geophysical Institute, UAF (Sazonova and Romanovsky 2003, Sazonova at al. 2004) was applied for the entire permafrost domain of northern Eurasia (Fig. 8). For present-day climatic conditions, the CRU2 data set with 0.5° x 0.5° latitude/longitude resolution (Mitchel & Jones 2005) was used. The future climate scenario was derived from the MIT 2D climate model output for the 21st century (Sokolov & Stone 1998).

Due to this model's spatial resolution (0.5 x 0.5 latitude/longitude) it is practically impossible to reflect the discontinuous character of permafrost in the southern permafrost zones. That is why we choose the ground surface and soil properties for each cell that will produce the coldest possible mean annual ground temperatures within the cell. This choice means that all results produced by this model reflect permafrost temperatures only in the coldest landscape types within this area. It also means that if our results show thawing permafrost somewhere within the domain, we should interpret this to mean that permafrost is thawing in practically all locations within the area. It also means that in the stable permafrost area identified in Figure 8, partial thawing of permafrost may occur at some specific locations.

According to this model, by the end of the 21st century permafrost that is presently discontinuous with temperatures between 0 and -2.5° C will have crossed the threshold and will be actively thawing. In Russia, the most severe permafrost degradation is projected for northwest Siberia and the European North. This model also shows that by the mid-21st century most of the Late Holocene permafrost will be actively thawing everywhere except for the south of East Siberia and the Far East of Russia.

By the end of 21st century, practically all Late Holocene permafrost will be thawing and some Late Pleistocene permafrost will begin to thaw in the European North and in Siberia (compare Figs. 2 and 8).

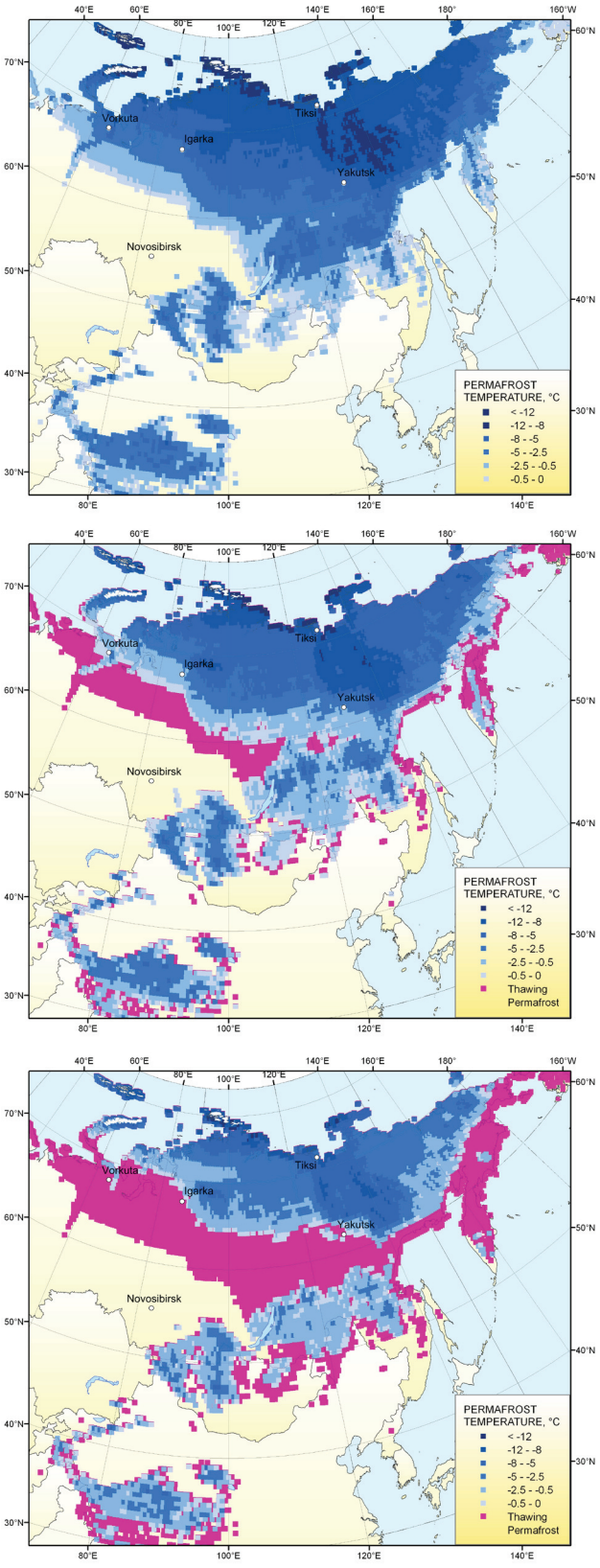

Figure 8. Calculated distribution of mean annual ground temperatures at the bottom of the active layer in Northern Eurasia averaged for three time intervals: 1990-2000 (upper graph), 2040-2050 (middle graph), and 2090-2100 (lower graph). The area with widespread permafrost thawing from the top down is shown in pink.

Conclusions

- Most of the permafrost observatories in Russia show substantial warming of permafrost during the last 20 to 30 years. The magnitude of warming varied with location, but was typically from 0.5 to 2°C at the depth of zero annual amplitude.
- This warming occurred predominantly between the 1970s and 1990s. There was no significant observed warming in permafrost temperatures in the 2000s in most of the research areas; some sites even show a slight cooling during the late-1990s and early-2000s. Warming has resumed during the last one to two years at some locations.
- Considerably less or no warming was observed during the same period in the north of East Siberia.
- Permafrost is already thawing in specific landscape settings within the southern part of the permafrost domain in the European North and in northwest Siberia. Formation of new closed taliks and an increase in depth of pre-existing taliks has been observed in this area during the last 20 to 30 years.
- Permafrost temperature reanalysis provides a valuable tool to study past changes in permafrost temperature, which helps to place recent changes into a long-term perspective.
- An implemented spatially-distributed permafrost model shows that if warming in air temperatures continues to occur, as predicted by most climate models, widespread thaw of Late Holocene permafrost may be in progress by the mid-21st century. If warming continues, some Late Pleistocene permafrost will begin to thaw by the end of the 21st century.

Acknowledgments

This research was funded by the Polar Earth Science Program, Office of Polar Programs, U.S. National Science Foundation (ARC-0632400, ARC-0520578), by the Russian Foundation for Basic Research, by the Russian Federal Agency for Mineral Resources Management (№АМ-18/35 pr, 30.01.2006), by a NASA Water and Energy Cycle grant, by the State of Alaska, and in cooperation with several earlier and on-going Russian activities. We would like to thank Drs. Jerry Brown, Kenneth Hinkel, and Candace O'Connor for their valuable suggestions, which improved the quality of this paper.

References

Brown, J. & Christiansen, H.H. 2006. Report of the International Permafrost Association. *Permafrost and Periglacial Processes* 17: 377-379.

Drozdov, D.S., Malkova, G.V. & Melnikov, V.P. 2008. Recent advances in Russian geocryological research: a contribution to the international polar year. *Proceedings of the Ninth International Conference on Permafrost*, Fairbanks, Alaska, June 29-July 3 (this proceedings).

Federov, A.N. 1996. Effects of recent climate change on permafrost landscapes in central Sakha. *Polar Geography* 20: 99-108.

Federov, A. & Konstantinov, P. 2003. Observations of surface dynamics with thermokarst initiation, Yukechi site, Central Yakutia. *Proceedings of the Eighth International Permafrost Conference*, Switzerland, July 21-25, pp. 239-243.

Jorgenson, M.T., Racine, C.H., Walters, J.C. & Osterkamp, T.E. 2001. Permafrost degradation and ecological changes associated with a warming climate in central Alaska. *Climatic Change*, 48(4): 551-571.

Kraev, G.A., Abramov, Bykhovets, S., Fyodorov-Davydov, D., Kholodov, A., Lupachev, A., Mamykin, V., Ostroumov, V., Sorokovikov, V., Gilichinsky, D., Zimova, G. & Zimov, S. 2008. Thermal state of permafrost in the eastern Arctic. *Proceedings of the Ninth International Conference on Permafrost*, Fairbanks, Alaska, June 29-July 3 (this proceedings).

Lisitsyna, O.M. & Romanovskii, N.N. 1998. Dynamics of permafrost in Northern Eurasia during the last 20,000 years. *Proceedings of the Seventh International Permafrost Conference*, Yellowknife, Canada, June 23-27, pp. 675-681.

Malkova, G.V. 2008. Last twenty-five years of changes in permafrost temperature of the European north of Russia. *Proceedings of the Ninth International Conference on Permafrost*, Fairbanks, Alaska, June 29-July 3 (this proceedings).

Marchenko, S.S. & Romanovsky, V.E. 2007. Modeling the effect of organic layer and water content on permafrost dynamics in the Northern Hemisphere. *Eos Trans. AGU*, 88(52): Fall Meet. Suppl., POSTER, Abstract GC23A-0985.

Marchenko, S.S, Romanovsky, V.E. & Tipenko, G.S. 2008. Numerical modeling of spatial permafrost dynamics in Alaska. *Proceedings of the Ninth International Conference on Permafrost*, Fairbanks, Alaska, June 29-July 3 (this proceedings).

Mitchell, T.D. & Jones, P.D. 2005. An improved method of constructing a database of monthly climate observations and associated high-resolution grids. *International Journal of Climatology* 25(6): 693-712.

Moskalenko, N.G. 2008. Vegetation and permafrost changes in West Siberia northern taiga. *Proceedings of the Ninth International Conference on Permafrost*, Fairbanks, Alaska, June 29-July 3 (this proceedings).

Nicolsky, D.J., Romanovsky, V.E. & Tipenko, G.S. 2007. Using in-situ temperature measurements to estimate saturated soil thermal properties by solving a sequence of optimization problems. *The Cryosphere* 1: 41-58.

Oberman, N.G. 2001. Intra-century dynamics of the permafrost zone in the European Northeast of Russia. *Proceedings of the 2nd Conference of Geocryologists of Russia*, Moscow, Russia, June 6-8, 2001 2: 212-217.

Oberman, N. 2008. Contemporary permafrost degradation of the European north of Russia. *Proceedings of the Ninth International Conference on Permafrost*, Fairbanks, Alaska, June 29-July 3 (this proceedings).

Payette, S., Delwaide, A., Caccianiga, M. & Beauchemin, M. 2004. Accelerated thawing of subarctic peatland permafrost over the last 50 years. *Geophysical Research Letters* 31: L18208, doi:10.1029/2004GL020358.

Romanovskiy, N.N., Zaitsev, V.N., Volchenkov, S.Yu., Zagryazkin, D.D. & Sergeyev, D.O. 1991. Alpine permafrost temperature zonality, northern Trans-Baikal region, USSR. *Permafrost and Periglacial Processes* 2: 187-195.

Romanovsky, V.E., Garagula, L.S. & Seregina, N.V. 1992. Freezing and thawing of soils under the influence of 300- and 90-year periods of temperature fluctuation. *Proceedings of the International Conference on the Role of Polar Regions in Global Change*, University of Alaska Fairbanks 2: 543-548.

Romanovsky, V.E., Burgess, M., Smith, S, Yoshikawa, K. & Brown, J. 2002. Permafrost temperature records: Indicator of climate change. *EOS* 83(50): 589-594.

Romanovsky, V.E., Sazonova, T.S., Balobaev, V.T., Shender N.I. & Sergueev, D.O. 2007. Past and recent changes in permafrost and air temperatures in Eastern Siberia. *Global and Planetary Change* 56: 399-413.

Sazonova, T.S. & Romanovsky, V.E. 2003. A model for regional-scale estimation of temporal and spatial variability of the active layer thickness and mean annual ground temperatures. *Permafrost and Periglacial Processes* 14(2): 125-139.

Sazonova, T.S., Romanovsky, V.E., Walsh, J.E. & Sergueev, D.O. 2004. Permafrost dynamics in 20th and 21st centuries along the East-Siberian Transect. *Journal of Geophysical Research* 109: D01108, doi:10.1029/2003JD003680.

Sergueev, D., Tipenko, G., Romanovsky, V. & Romanovskii, N. 2003. Mountain permafrost thickness evolution under influence of long-term climate fluctuations (results of numerical simulation). In: *Permafrost*, Phillips, M., S. Springman, and L.U. Arenson (eds.), Swets & Zeitlinger, Lisse, 1017-1021.

Shender, N.I., Romanovsky, V.E. & Tetelbaum, A.S. 1999. A forecast of the natural variability of climate in Yakutsk and Fairbanks (in Russian). *Science and Education* 2: 24-29.

Sokolov, A.P. & Stone, P.H. 1998. A flexible climate model for use in integrated assessments. *Climate Dynamics* 14: 291-303.

Sumgin, M.I., Kachurin, S.P., Tolstikhin, N.I. & Tumel, V.F. 1939. *General Geocryology* (in Russian), Soviet Academy of Science Publishing, 340 pp.

Velichko A.A. & Nechaev, V.P. (eds.). 2005. *Cenozoic climatic and environmental changes in Russia*, edited by H.E. Wright Jr., T.A. Blyakharchuk, A.A. Velichko & O. Borisova. Special Paper 382. *The Geological Society of America*, 226 pp.

Yershov, E. 1998. *General Geocryology*. Cambridge: Cambridge University Press, 580 pp.

Soil Climate and Frost Heave Along the Permafrost/Ecological North American Arctic Transect

V.E. Romanovsky, S.S. Marchenko, R. Daanen
Geophysical Institute, University of Alaska Fairbanks
D.O. Sergeev
Institute of Environmental Geoscience, Moscow, Russia
D.A. Walker
Institute of Arctic Biology, University of Alaska Fairbanks

Abstract

Soil climate data were collected during a recent biocomplexity study along a bioclimatic gradient in the North American Arctic tundra. The measurements were made from south to north at Happy Valley, Sagwon Hills, Franklin Bluffs, Deadhorse, West Dock, Howe Island, Green Cabin, Mould Bay, and Isachsen research sites. Mean annual air temperature changes from around -10°C at the Happy Valley and Sagwon Hills sites to -16°C at Mould Bay and Isachsen. Mean annual ground surface temperature has an even larger range, changing from -2°C to -15.5°C in the same direction. Mean annual ground temperature at the permafrost table changes from -3.5°C at Happy Valley to -15.5°C at Mould Bay and -14.7°C at Isachsen. Snow depth generally decreases from south to north, and snow density generally increases in the same direction. Measured maximal frost heave within the nonsorted circles in patterned ground vary between 18–20 cm at the Deadhorse and Franklin Bluffs sites and less than 1 cm at West Dock.

Keywords: active layer; frost heave; patterned ground; permafrost; snow cover; temperature regime; thermal offset.

Introduction

Recent warming in permafrost temperatures has been reported from many locations in the Circumpolar North (Harris & Haeberli 2003, Isaksen et al. 2000, Pavlov & Moskalenko 2002, Oberman & Mazhitova 2001, Osterkamp 2003a, Osterkamp & Romanovsky 1999, Romanovsky et al. 2002, Romanovsky et al. 2007b, Smith et al. 2005). At some of these locations that lay near the southern boundary of permafrost, this warming has already triggered long-term permafrost thawing. These changes in permafrost inevitably affect northern ecosystems, making them evolve rapidly. Some of these changes could be advantageous, but most of them have negative consequences for the natural and anthropogenic systems. Because of a wide variety in permafrost conditions in the Arctic and Subarctic, different regions experience different rates or even different directions of this change during the same time period. To document the temporal changes and spatial variability of permafrost in Alaska, a number of permafrost observatories were established in the late 1970s and early 1980s by the Geophysical Institute, University of Alaska Fairbanks, along the International Geosphere-Biosphere Program (IGBP) Alaska Transect, which spans the entire permafrost zone in Alaska (Osterkamp 1986, Osterkamp & Romanovsky 1999, Romanovsky & Osterkamp 2001, McGuire et al. 2002, Osterkamp 2003a, b, Romanovsky et al. 2003).

The recent Biocomplexity Project of the University of Alaska Fairbanks, which investigates small pattern-ground features that occur along a North American Arctic Transect (NAAT), has been funded by the National Science Foundation, USA, and is now in the final stage of its accomplishment (Walker et al. 2004, 2008). This project made it possible to extend the IGBP Alaska Transect into low- and high-Arctic regions in western Canada (Fig. 1). This extension was a valuable addition to the Transect because it adds sites where permafrost temperatures are some of the coldest in the Northern Hemisphere. Also, a reduced vegetative cover and high ice content make permafrost in this region extremely vulnerable to recently observed and projected changes in climate.

There are two types of natural gradients that will be discussed in this paper. One is the regional north to south gradient in air and soil temperatures, snow, and active layer thickness. Another is the local gradient in soil moisture and temperature, active layer thickness, and ground surface heave that is governed mostly by the surface vegetation distribution. The local gradients are the cause and, at the same time, affected by nonsorted circle formation and evolution. The regional gradients in the atmospheric climate, soil climate, and vegetation also modulate the formation and development of patterned ground and are responsible for the specific morphological features of the patterned ground in the arctic landscapes. The morphology and origination of these features have been discussed in the scientific literature for many years (e.g., Washburn 1980). Soil and permafrost climate data, together with air temperature, snow depth, and seasonal frost heave data collected at the sites along the Permafrost/Ecological North American Arctic Transect during the lifetime of the Biocomplexity Project, together with some previously collected temperature data, will be discussed in this paper. First, we will provide a brief description of natural settings at the research sites and provide some information on measuring technique and the equipment used. Further, using long-term data from several sites, we will show how relatively short records from the

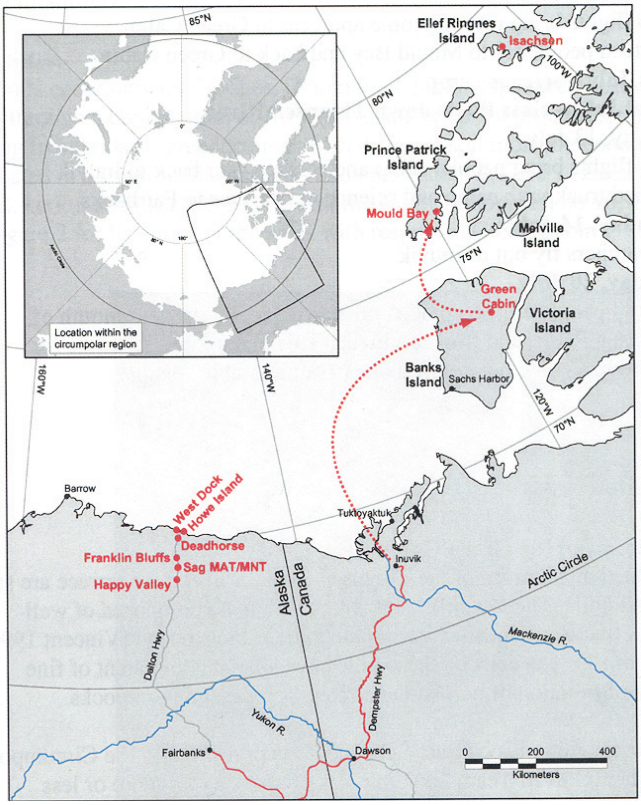

Figure 1. Location of research sites along the Permafrost/Ecological North American Arctic Transect.

biocomplexity project (2001–2006) fit a more general picture of temperature changes during the last 20 years. Then we will present data on soil climate and seasonal frost heave for the entire transect during the years of 2004–2006. Discussions based on these data lead to several important conclusions.

A Short Sites Description

Temperature, moisture, and snow measurement stations were installed from south to north at: Happy Valley, Sagwon Hills, Franklin Bluffs, Deadhorse, West Dock, Howe Island, Green Cabin (Banks Island), Mould Bay, and Isachsen (Fig. 1). All these sites are located in the continuous permafrost zone with a relatively cold climate. Climatic conditions determine type of vegetation along this transect. All sites are within the tundra biome and represent all types of tundra from subzone A (or arctic desert) at Isachsen to subzone E (or southern tundra) at Happy Valley. The specific locations were chosen as representative of zonal conditions within each of five Arctic bioclimate subzones (A through E) (Walker et al. 2005). All the studies were located on fine-grained sediments conducive to the formation of nonsorted patterned-ground features and zonal vegetation. The Sagwon MAT and Happy Valley locations had acidic soils (pH < 5.5), and all the others had nonacidic soils. Several sites (Howe Island, Green Cabin, Deadhorse, Franklin Bluffs) had soil pH values exceeding 8.0. The zonal vegetation varied from nearly barren surfaces with scattered mosses, lichens, and very small forbs in subzone A to knee-high shrub-dominated

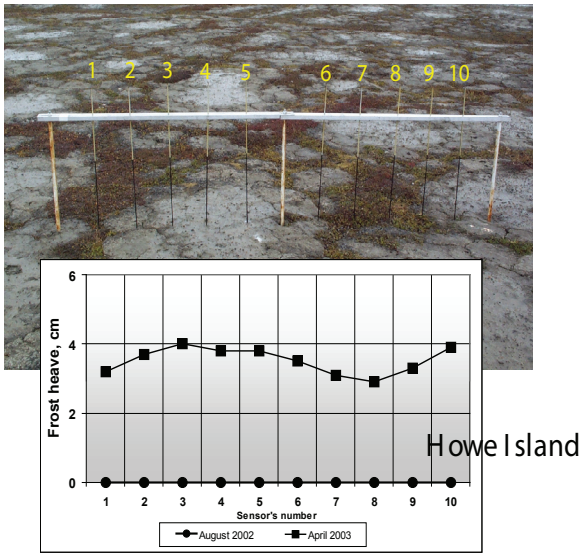

Figure 2. Frost heave measurements across a nonsorted circle at the Howe Island site.

tundra with thick moss carpets in subzone E. A more comprehensive description of natural settings at the study sites can be found in (Walker et al. 2008).

Methods of Measurements

Small climate stations were established at each location. The air and ground-surface temperatures at each location were recorded using standard Campbell Scientific L107 thermistors. Two ground surface thermistors and two 1-m long arrays of thermistors (with approximately 10 cm distance between thermistors) were located about six meters apart: one in an unsorted circle and the other between the circles. After pre-installation calibration, the precision of the sensors is better than 0.04°C. All measurements were made with one-hour time interval. The stations were operated and data were stored by Campbell Scientific CR10-X data loggers. A 20-watt regulated solar panel coupled with a 12-volt battery was used for power supply. The installations are also part of the Permafrost Observatory Network (Osterkamp 2003, Osterkamp & Romanovsky 1999, Romanovsky & Osterkamp 2001, Romanovsky et al. 2003). Snow depth was measured continuously with one-hour resolution at most of the sites using a Campbell Scientific SR50 Sonic Ranging Sensor that was connected to the Campbell data logger at the climate stations. Also, the maximum snow depth was measured every year manually at the Alaskan sites during spring (late April) field trips. At the Canadian sites, maximum snow depth was measured manually once in early May 2006. The ground moisture (including the unfrozen water content in winter) was measured at two depths within the unsorted circle and at two depths in the inter-circle space. SDI-12 volumetric water content sensors (http://www.stevenswater.com/catalog/stevensProduct.aspx?SKU=%2793640%27) were used. Each of the sensors was pared with an additional L107 temperature probe. Moisture content was recorded hourly during the entire year.

Frost heave was monitored on and off the unsorted circles at all sites using two types of specially designed heave meters. Along the Alaskan portion of the NAAT, a ten-pin heave instrument described in (Walker et al. 2004) was used (Fig. 2). In the High Arctic, heave scribers were used. Each of these instruments consisted of a 2-m x 1.5-cm solid copper grounding rod that was driven 1.5 m into the ground, anchoring it in the permafrost. A steel plate and sleeve with an attached sharp steel scriber was placed on the rod, with the plate resting on the ground. The steel plate and scriber slid freely on the rod, rising with the frost heave in the winter and allowing the scriber to scratch a line on the copper rod. The length of the scratched line above a reference scribe determined the amount of heave.

Long-Term Changes in the Air, Active Layer, and Permafrost Temperatures

When we describe atmosphere and soil climatic conditions for some period of time, it is always important to have information on how this period looks compared to longer-term patterns of these parameters. It is especially important now when the climate experiences significant changes within short time intervals. Fortunately, we have long-term (more than 20 years) continuous temperature records for three sites within the NAAT: West Dock, Deadhorse, and Franklin Bluffs. Data from the West Dock site are shown in Figure 3. This figure clearly shows a significant long-term warming trend in mean annual temperatures at all levels: air, ground surface, and permafrost at 20 m depth. A linear trend in air and ground surface temperatures was 3°C for the last 20 years, and an increase in permafrost temperature at 20 m depth was 2°C. This figure also shows that during the period of the Biocomplexity Project (2001–2006), soil climate was the warmest on average for the last 20 years. Also, during this period the soil climate was relatively stable except for an anomalously warm year, 2003.

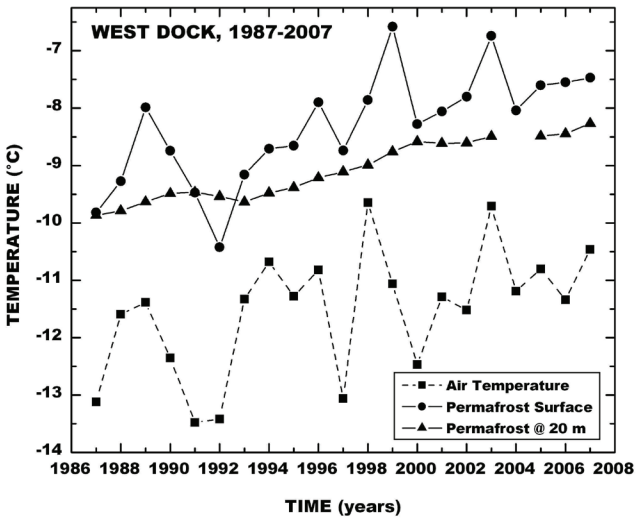

Figure 3. Time series of mean annual air (squares), permafrost surface (circles), and permafrost at 20 m depth (triangles) temperatures at the West Dock site.

Figure 3 also shows that the interannual variations in the surface temperature can differ significantly from the interannual changes in the air temperature. However, on a longer time scale (five years and longer), the match in these trends is very good. Similar results were obtained from the Deadhorse and Franklin Bluffs sites. We came to similar conclusion analyzing long-term data from the East Siberian Transect (Romanovsky et al. 2007b).

Snow Conditions and Air and Soil Temperatures Along the NAAT Transect

All our sites are within the continuous permafrost area. However, there is a significant range of air and soil temperatures along this transect. Mean annual air temperature (MAAT) changes from around -10°C at the Happy Valley and Sagwon Hills sites to -16°C at Mould Bay and Isachsen (Fig. 4), while mean July air temperatures vary in the range from 10°C at Happy Valley to 3°C at Isachsen (not shown). Elevated temperatures at Isachsen are an artifact, because only temperatures for 2005–2006 were available for this station (it was established in the summer of 2005) and the 2005–2006 year was substantially warmer in this region than 2004–2005. Data from the Mould Bay station show that MAAT in 2005–2006 was warmer by almost 2°C than in 2004–2005. Mean annual ground surface temperature (MAGST) was by more than 1°C warmer as well.

All Alaskan sites show very similar MAAT in the range between -9.7°C (Sagwon MNT) and -11.3°C (Franklin Bluffs). All Canadian sites are much colder with MAAT at or colder than -16°C. The spatial variability in MAGST is much more pronounced along NAAT. The warmest sites are all located in the inland part of the transect, with temperatures as warm as -2°C (Happy Valley) and just below -4°C (Deadhorse and Franklin Bluffs). Relatively colder temperatures were observed at Sagwon Hills (-5°C and -6°C). All coastal sites in Alaska have lower MAGST with -7.2°C at West Dock and -8.8°C at Howe Island. The coldest MAGST were observed in the Canadian Arctic with MAGST typically at or below -14°C. It was shown in previous publications (Kade et al. 2006, Walker et al. in review) that summer temperatures at the ground surface within the unsorted circles are significantly warmer than in inter-circle areas. As it can be seen from Figure 4, it is not true for the mean annual surface temperatures, which are generally very similar for both circle and inter-circle areas. A possible explanation is that differential frost heave within the circles decreases snow depth here and decreases surface temperatures during the winter. Colder winter temperatures compensate summer warmer temperatures within the circles with a net effect close to zero.

Snow cover is the major factor that determines the difference between MAGST and MAAT. Our data show that this difference is much larger at the inland sites than at the sites close to the Arctic coasts. Snow depth is generally decreasing from the south to the north, and snow density is generally increasing in the same direction. The maximum

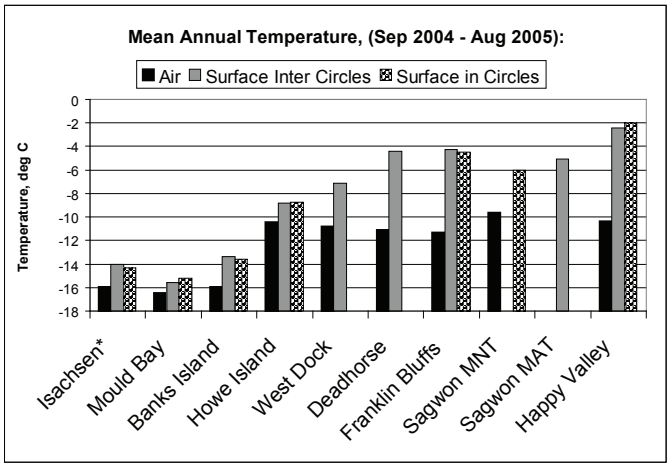

Figure 4. Mean annual temperatures (September 2004–August 2005, except for Isachsen where temperatures were measured in 2005–2006) in the air (black) and at the ground surface within inter-circles (gray) and circles (polka-dot) along NAAT.

snow thickness decreases from 60–70 cm at Happy Valley to 20 cm and less at the Banks Island and Mould Bay sites (Fig. 5). Accordingly, the warming effect of snow on MAGST is decreasing from 8°C at Happy Valley to only 1°C at the Mould Bay site (Fig. 4). Mean annual soil temperature near the permafrost table changes from -3.5°C at Happy Valley to -15.3°C at Mould Bay (Fig. 6). There is no noticeable difference in this parameter between circle and inter-circle areas.

Comparing Figures 4 and 6 we can see that the mean annual temperatures at the permafrost table are always colder than MAGST. This effect is very well-known as a "thermal offset" (Burn & Smith 1988, Romanovsky & Osterkamp 1995). Thermal offset for most of the sites along NAAT in 2004–2005 was less than -1°C, with the smallest number for Mold Bay (-0.1°C) and Banks Island (-0.15°C). For Isachsen, West Dock, Deadhorse, Franklin Bluffs, and Sagwon MNT, the thermal offset was in the range between -0.3 and -0.75°C. Significantly larger thermal offset was measured at the Howe Island site (-1°C), and for the acidic tundra sites Sagwon MAT (-1.3°C) and Happy Valley (-1.2°C). Increased thermal offset at the acidic tundra sites directly related to increased thickness of the organic soil layer that has a significantly larger ratio of the thermal conductivities in the frozen and thawed states. This ratio is the most important parameter responsible for thermal offset (Romanovsky & Osterkamp 1995).

Active Layer Depth

Active layer depth does not have a pronounced latitudinal trend and has a significant local variability, depending on the soil type and on the structure and density of the surface vegetation cover (Fig. 7). At the localities with dense vegetation, the active layer depth could be from 20 to 40% less than within the nonsorted circles with much less or no vegetation. For example, the mean depth of thaw at the end of August 2005 in the vegetated tundra between the nonsorted

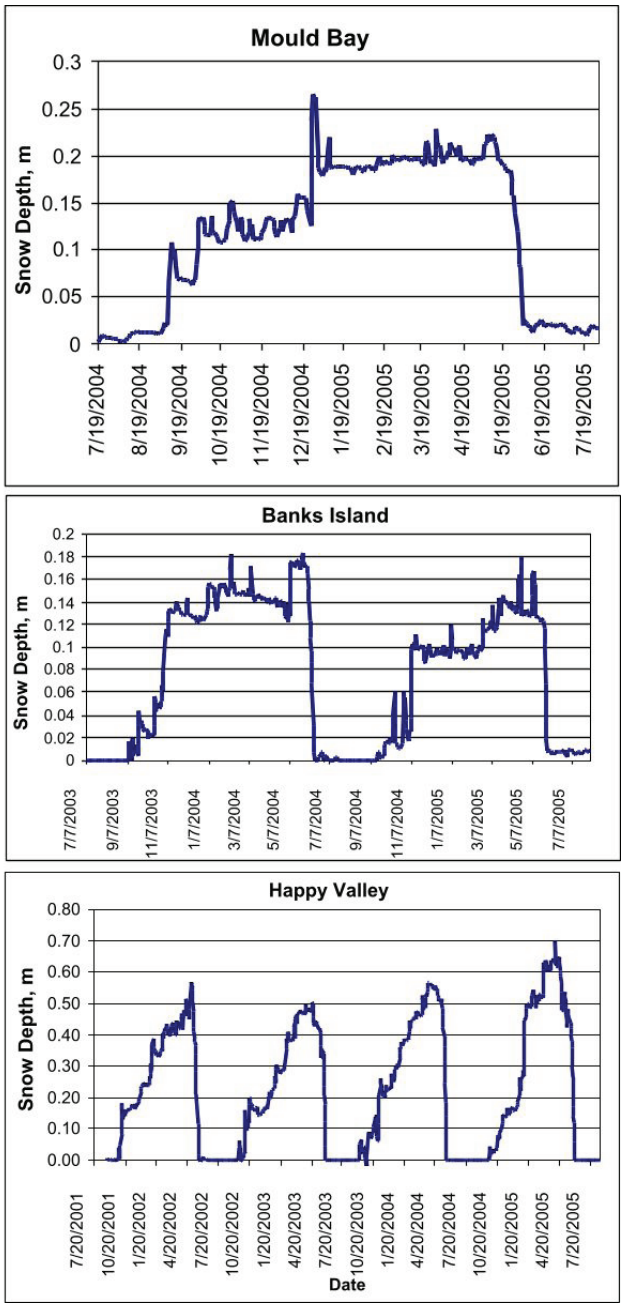

Figure 5. Hourly recorded snow cover depth at three sites: Mould Bay (A), Banks Island (B), and Happy Valley (C).

circle features was less at Happy Valley, the site with the warmest soil-surface temperatures (active layer = 30 cm), than it was at Isachsen, the coldest site (almost 50 cm). Maximum active layer thickness was observed in the middle part of the transect at the sites Franklin Bluffs, Deadhorse, Howe Island, and Banks Island.

A large difference in the active layer thickness between the nonsorted circles and inter-circle areas was observed in better vegetated sites Franklin Bluffs, Sagwon Hills, Happy Valley (Fig. 7), and Deadhorse (not shown). This difference was much less at the sites with less vegetation (Howe Island, Banks Island, Mould Bay, and Isachsen). Because of this local variability in the active layer thickness and because of

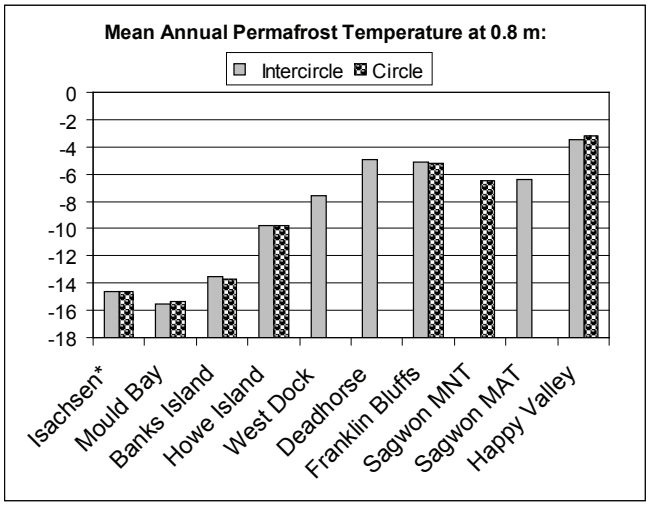

Figure 6. Mean annual soil temperatures (September 2004–August 2005, except for Isachsen, where temperatures were measured in 2005–2006) at 0.8 m depth at different sites along NAAT.

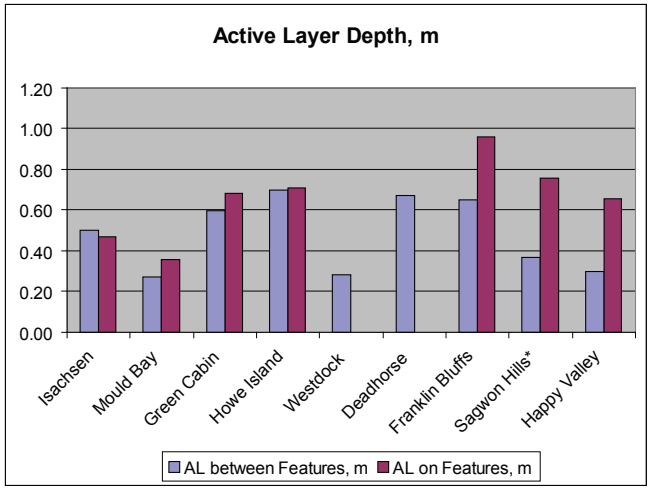

Figure 7. Maximum summer thaw (active layer depth) at the sites along NAAT.

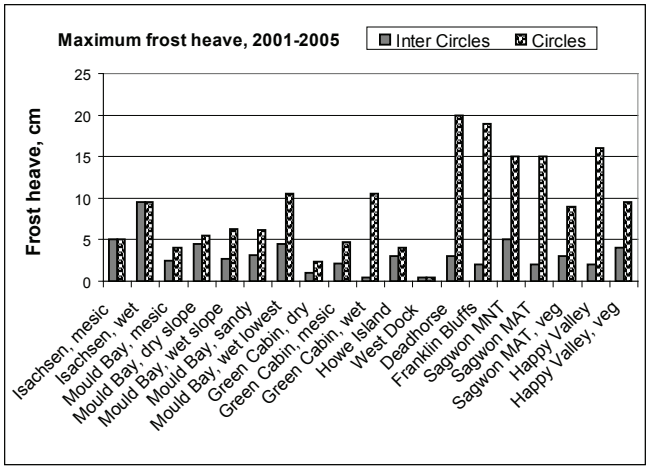

Figure 8. Maximum frost heave observed during period of measurements (2001–2005) at different sites along NAAT.

the differences in the timing of freezing, the ground surface experiences a significant differential frost heave, which is mostly responsible for nonsorted circle development.

Frost heave

Measured maximum frost heave within the circles vary between 18–20 cm at the Deadhorse and Franklin Bluffs sites and less than 3 cm at the Green Cabin site on Banks Island (Fig. 8). Frost heave in inter-circle areas was typically less than 3 cm and very seldom reached 5 cm. Frost heave was greatest in the centers of nonsorted circles on silty loess soils at Deadhorse, Franklin Bluffs, and Sagwon MNT (20, 19, and 15 cm, respectively) (Fig. 8). Intermediate amounts of heave occurred on the clay soils at Isachsen, and the acidic tundra sites at Sagwon MAT (9 cm) and Happy Valley (9.5 cm). Heave was least at West Dock (0.4 cm), where there was a thick organic soil layer and no patterned ground. Differential heave (difference in the heave on the circles and between circles) was also greatest at Deadhorse and Franklin Bluffs (17 cm), where there was strong contrast in the vegetation on and between the patterned ground features. Differential heave was least (0 cm) at Isachsen, where the zones between patterned ground features are very narrow. Generally low amounts of heave occurred in the sandier soils at Mould Bay, Howe Island (Fig. 2), and Green Cabin on Banks Island. Measured heave also varies significantly along the local topographical gradients illustrating the dependence of this process on local water availability. More information on governing physical processes responsible for frost heave and nonsorted circles formation and on numerical modeling of these processes can be found in (Nicolsky et al. 2008).

Conclusions

• A strong regional gradient exists in the air and soil temperatures along the North American Arctic Transect. Mean annual air temperature ranges between -10°C and -16°C, while the mean annual soil temperatures are in the range between -2°C and -14°C.

• Snow cover differs significantly between the inland sites (Happy Valley, Franklin Bluffs), where the maximum snow depth is typically at 45–65 cm, and the coastal sites (Howe and Banks Islands, Mould Bay, and Isachsen) with 15–25 cm.

• Local differences in surface conditions (vegetation and snow cover, and soil physical properties, etc.) are associated with the nonsorted circles, which produce significant local differences in the active layer depth, soil freezing rates, soil ice formation (Nicolsky et al. 2008) and, as a result, a significant differential frost heave.

• The amount of seasonal heave is governed by the degree of these differences and by the water availability that changes along the local topographic gradients. The measured differential frost heave ranges between a few cm at mesic and dry sites to almost 20 cm at wet sites on the Alaskan Arctic Plain.

Acknowledgments

This research was funded by ARCSS Program and by the Polar Earth Science Program, Office of Polar Programs, National Science Foundation (OPP-0120736, ARC-0632400, ARC-0520578, ARC-0612533, IARC-NSF CA: Project 3.1 Permafrost Research), by NASA Water and Energy Cycle grant, and by the State of Alaska.

References

Burn, C.R. & Smith, C.A.S. 1988. Observations of the "thermal offset" in near-surface mean annual ground temperatures at several sites near Mayo, Yukon Territory, Canada. *Arctic* 41(2): 99-104.

Harris, C. & Haeberli, W. 2003. Warming permafrost in European mountains. *World Meteorol. Org. Bull*. 52(3): 6 (see also *Global and Planetary Change* 39: 215–225).

Isaksen, K., Vonder Mühll, D., Gubler, H., Kohl, T. & Sollid, J.L. 2000. Ground surface temperature reconstruction based on data from a deep borehole in permafrost at Janssonhaugen, Svalbard. *Annals of Glaciology* 31: 287–294.

Kade, A., Romanovsky, V.E. & Walker, D.A. 2006. The N-factor of nonsorted circles along a climate gradient in Arctic Alaska. *Permafrost and Periglacial Processes* 17: 279-289.

McGuire, A.D. et al. 2002. Environmental variation, vegetation distribution, carbon dynamics, and water/energy exchange in high latitudes. *Journal of Vegetation Science* 13: 301-314.

Nicolsky, D.J., Tipenko, G.S., Romanovsky, V.E. and Walker, D.A. 2008. Modeling observed differential frost heave within nonsorted circles in Alaska. *Proceedings of the Ninth International Conference on Permafrost, June 29–July 3, 2008, Fairbanks, Alaska,* submitted.

Oberman, N.G. & Mazhitova, G.G. 2001. Permafrost dynamics in the northeast of European Russia at the end of the 20th century. *Norwegian Journal of Geography* 55: 241-244.

Osterkamp, T.E. 1986. Observations of shallow permafrost temperatures in Arctic Alaska. *EOS, Trans. AGU* 67(44).

Osterkamp, T.E. 2003a. A thermal history of permafrost in Alaska, *Proceedings of the Eighth International Conference on Permafrost, July 21-25, 2003, Zurich, Switzerland:* 863-868.

Osterkamp, T.E. 2003b. Establishing long-term permafrost observatories for active layer and permafrost investigations in Alaska: 1977-2002. *Permafrost and Periglacial Processes* 14: 331-342.

Osterkamp, T.E. & Romanovsky, V.E. 1999. Evidence for warming and thawing of discontinuous permafrost in Alaska. *Permafrost and Periglacial Processes* 10(1): 17-37.

Pavlov, A.V. & Moskalenko, N.G. 2002. The thermal regime of soils in the north of Western Siberia. *Permafrost and Periglacial Processes* 13: 43-51.

Romanovsky, V.E. & Osterkamp, T.E. 1995. Interannual variations of the thermal regime of the active layer and near-surface permafrost in Northern Alaska. *Permafrost and Periglacial Processes* 6(4): 313-335.

Romanovsky, V.E. & Osterkamp, T.E. 2001. Permafrost: changes and impacts. In: R. Paepe & V. Melnikov (Eds.), *Permafrost Response on Economic Development, Environmental Security and Natural Resources.* Kluwer Academic Publishers: 297-315.

Romanovsky, V.E., M. Burgess, Smith, S., Yoshikawa, K. & Brown, J. 2002. Permafrost temperature records: Indicator of climate change. *EOS* 83(50): 589, 593-594.

Romanovsky, V.E., Sergueev, D.O. & Osterkamp,T.E. 2003. Temporal variations in the active layer and near-surface permafrost temperatures at the long-term observatories in Northern Alaska. In: M. Phillips, S. Springman & L.U. Arenson (Eds.), *Permafrost.* Lisse: Swets & Zeitlinger: 989-994.

Romanovsky, V.E., Gruber, S., Instanes, A., Jin, H., Marchenko, S.S., Smith, S.L., Trombotto, D. & Walter, K.M 2007a. Frozen ground (Chapter 7). In: *Global Outlook for Ice and Snow, Earthprint*. UNEP/ GRID, Arendal, Norway: 181-200.

Romanovsky, V.E., Sazonova, T.S., Balobaev, V.T., Shender, N.I. & Sergueev, D.O. 2007b. Past and recent changes in permafrost and air temperatures in Eastern Siberia. *Global and Planetary Change* 56: 399-413.

Smith, S.L., Burgess, M.M., Riseborough, D. & Nixon, F.M. 2005. Recent trends from Canadian permafrost thermal monitoring network sites. *Permafrost and Periglacial Processes* 16: 19-30.

Walker, D.A. et al. 2004. Frost-boil ecosystems: Complex interactions between landforms, soils, vegetation, and climate. *Permafrost and Periglacial Processes* 15: 171-188.

Walker, D.A. et al. 2005. The circumpolar Arctic vegetation map. *Journal of Vegetation Science* 16: 267-282.

Walker, D.A. et al. 2008. Biocomplexity of small patterned-ground features along the North American Arctic Transect. *Journal of Geophysical Research* (accepted).

Washburn, A.L. 1980. *Geocryology: A Survey of Periglacial Processes and Environments*. New York: Halsted Press, John Wiley and Sons, 406 pp.

The Davidson Ditch – A Historical Review

James W. Rooney
J&F Rooney, LLC, Anchorage, Alaska, USA
Charles H. Riddle
R&M Consultants, Inc., Anchorage, Alaska, USA

Abstract

In the early 1920s, the Davidson Ditch project was initiated because of the need to develop an adequate water supply for placer mining properties on Cleary and Goldstream Creeks just north of Fairbanks, Alaska. The project, extending over a distance of 155 km along the Chatanika River drainage, was started in 1925 and completed in 1928. The water intake structure was located at the headwaters of the Chatanika River. Most of the project traversed permafrost terrain, and much of the ditch placement was located on sidehill terrain. There are still some remnants of the long-abandoned project some 80-plus years after construction. It is interesting that very little information has been provided through the years on the technical issues and facility performance, nor has any environmental assessment of the project's impact on terrain, vegetation, or regional infrastructure been addressed with regard to ground disturbance and continued climate-warming trends.

Keywords: Davidson Ditch; Fairbanks Exploration Company; global warming; permafrost; water supply.

Introduction

In the early 1920s, the Davidson Ditch project was initiated due to the need for developing an adequate water supply for the Fairbanks Exploration Company's (FE Company) placer mining properties on Cleary and Goldstream Creeks just north of Fairbanks, Alaska (Boswell 1979). James M. Davidson conceptually defined a plan and then surveyed a ditch route for collecting water along a major portion of the Chatanika drainage expected to supply water for development of the Fairbanks area dredge operations. Norman C. Stines, who believed in the application of cold water thawing of frozen gravels and who overcame considerable skepticism, with the support of the U.S. Smelting Refining and Mining Company (USSR&M), was the overall driving force that led to the Fairbanks area dredge mining activities. The Davidson Ditch was the key solution for attaining a sufficient water supply to support the planned development of the targeted placer mining areas (Stines 2006). In 1969, the senior author, while working on initial Trans Alaska Pipeline System (TAPS) route studies, had the opportunity to participate in a review of the Davidson Ditch project files at the FE Company's Fairbanks office and was impressed with the level of technical effort and some of the similarities between it and the proposed TAPS project.

Location and Concerns

The Davidson Ditch project, extending over a distance of 155 km along the Chatanika River drainage (as shown in Fig. 1), was started in 1925 and completed in 1928. The water intake structure, a small metal-faced dam, was located at the headwaters of the Chatanika River, just below the confluence of Faith and McManus Creeks. Most of the project traversed permafrost terrain. Because of the need to maintain a gradual flow gradient, much of the ditch placement was located on sidehill terrain facing south to reduce exposure to those soils having highly variable ice content. Even with the passage of more than 80 years following construction, there are still some remnants of the long-abandoned project. It is interesting that very little geotechnical and environmental information has been provided through the years on project issues and facility performance. Nor has much, if any, environmental assessment of the project's impact on terrain, vegetation, or regional infrastructure been assessed with regard to both current concerns and making future projections on manmade and climatic warming impacts. It seems apparent that both positive and negative impacts identified with this project could provide some relevant insight for our attempts to evaluate related climate-warming issues.

Project Infrastructure

This project involved construction of a 3.6 m wide main excavated ditch with a downslope fill berm. The main ditch had a gradient of 0.4 m/km and was 134 km in length. Two feeder ditches added another 9.7 km to the system. There were 15 valley-crossing siphons that had a total length of 9.8 km of steel lock-bar pipe with an inside diameter ranging from 1,168 to 1,422 mm. These siphons had a capacity to carry up to 212,340 liters of water at a maximum head pressure of 1,550 kPa. The length of the valley siphons extended from a minimum of 30 m to 1,128 m. Penstocks and flumes added an additional 0.6 km. Also, a 2.1 m square tunnel 1,128 m long was constructed between Vault and Fox Creeks.

Design Features

The project was designed by J.B. Lippincott, a consulting engineer from Los Angeles, California, who had prior experience on projects in areas with permafrost. His reports describe excavation of frozen muck containing pure ice

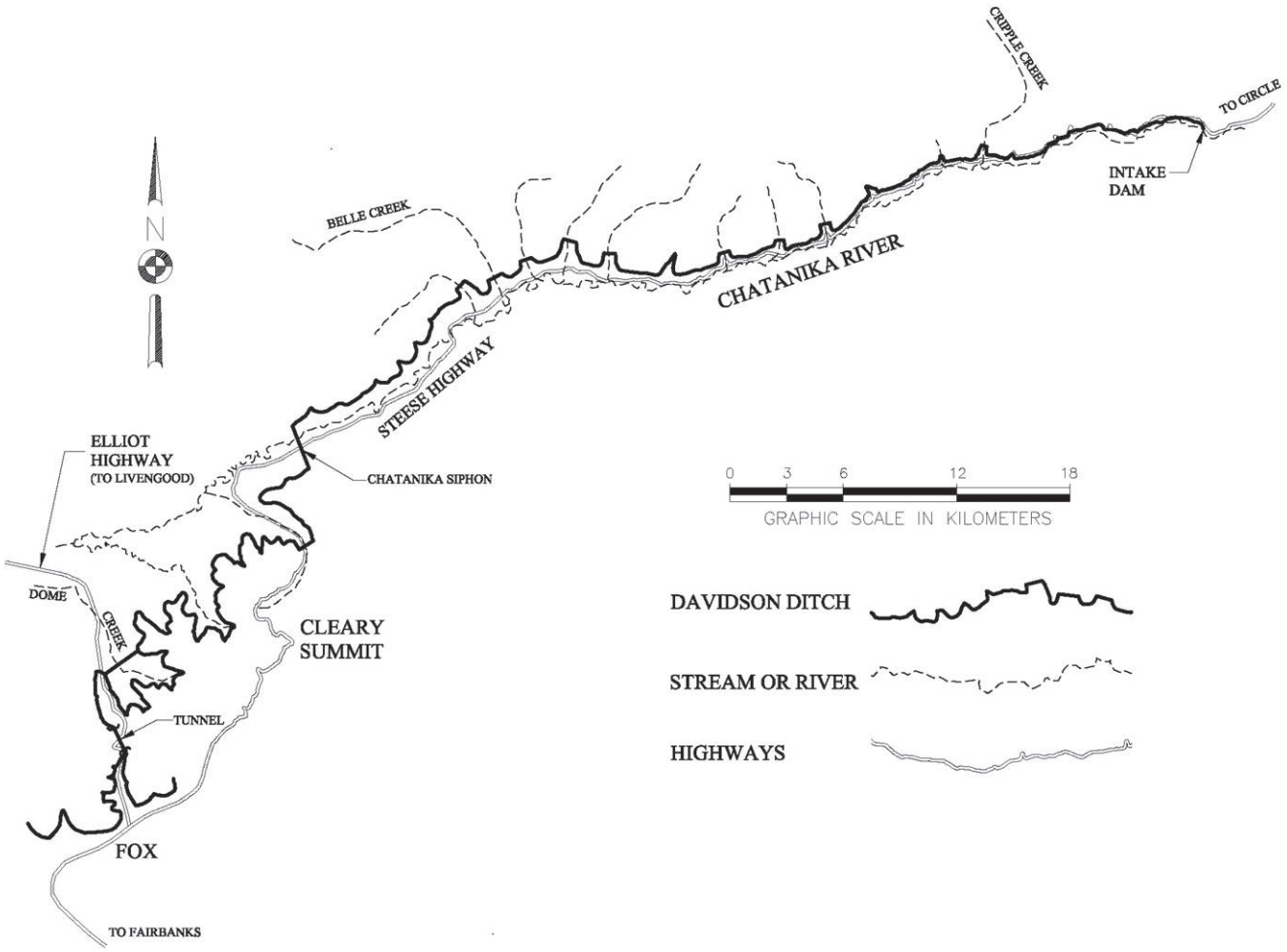

Figure 1. Davidson Ditch route map.

and silt soils having from 150 mm to 600 mm of organic mat overburden. The valley bottoms were described as containing soils with much higher ice content. Preference was given to the south-facing slopes to minimize exposure to the valley slopes that have higher ice content and face north. Concerns were also expressed with accomplishing the valley crossings on timber pile supported trestles with pile bents being spaced at 6 m. The timber piles were installed using steam jets and allowing pile freezeback, or were driven into competent soils to obtain pile support. Valley icing was a significant concern because of the possibility of pile flotation with spring breakup and flooding. The extreme effects of large temperature variation on the siphons were also considered. Temperature extremes of plus 37ºC to minus 57ºC and a full range of 94ºC were utilized to address expansion and contraction concerns along the siphons. Insulation of the pipe anchors to reduce ground warming was also addressed. Anchor systems were employed at the siphons to resist both anticipated vertical and horizontal forces associated with the potential for flotation, water flow, and temperature extremes. The anchors were installed midway between expansion joints.

A typical cross-section of the Davidson Ditch is shown in Figure 2. The construction zone width including the edge of clearing limits extended to over 15 m. Lippincott's evaluation of soil and permafrost conditions along the route, as quoted by Boswell (1979), in one of his reports follows:

> The material through which the ditch was excavated consisted of frozen muck, ranging from almost pure ice to almost solid silt, and covered with from six inches to two feet of moss; heavy slide rock, also covered with heavy moss; decomposed schist slide, usually covered with light moss; rock in place, but shattered so as not to require blasting; solid schist… The northern slopes of the hills are much more frozen than the southern ones… In this report, frozen ground is considered as distinct from the ancient glacial ice which contains but 20 to 30 percent of earth. Such ice is found usually in the valley flats.

The extent of earthwork involved in ditch construction, as summarized by Boswell, was:

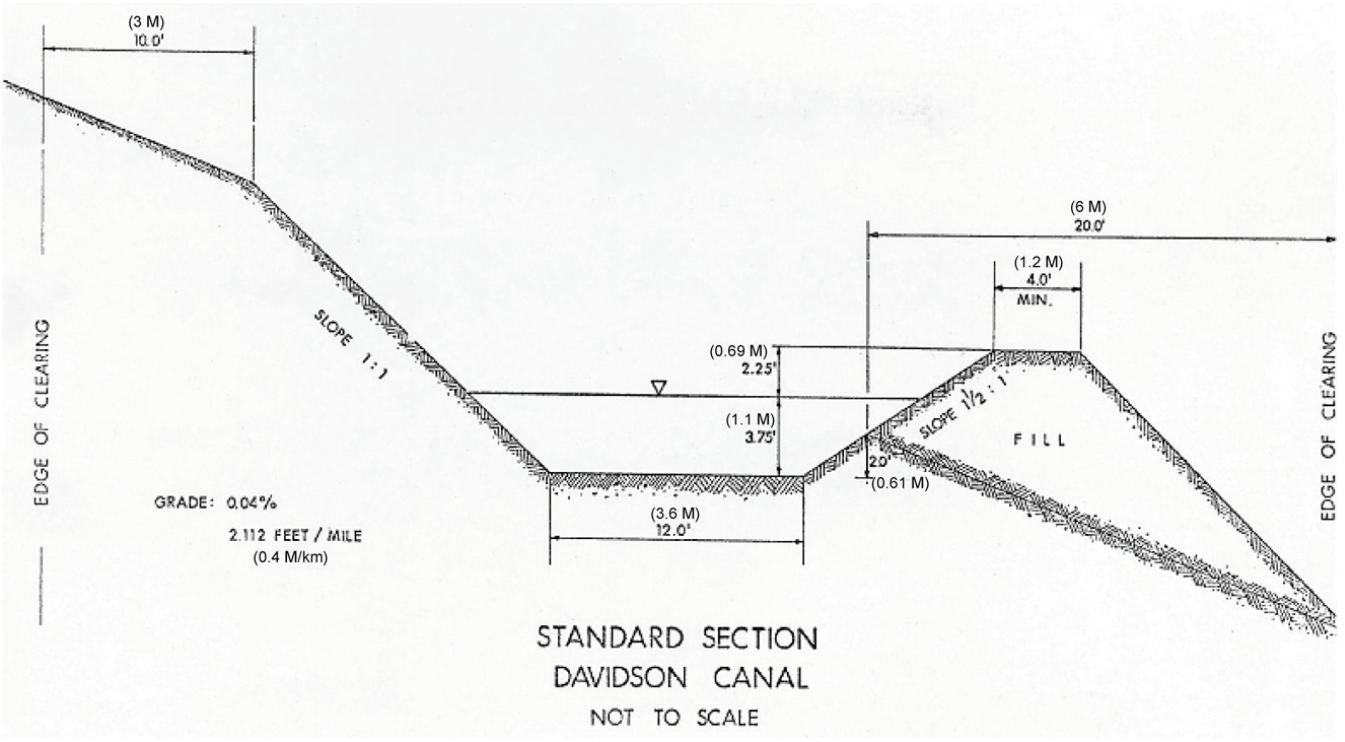

Figure 2. Davidson Canal standard section.

Soil and loose rock	1,455,324 y^3 (1,112,675 m^3)
Solid rock	118,401 y^3 (90,524 m^3)
Total:	1,573,725 y^3 (1,203,199 m^3)

The valley siphon crossings were accomplished through the frozen soils, noted in the above quote, using the pile bents to support the siphon pipe above flood flow levels and anticipated surface icing conditions. Other than comments on evident frost-jacking of the timber piles, little information has been provided on the overall performance of these pile supports. Each siphon crossing was restrained at the center point by a weighted and braced anchor system for restraining excessive siphon pipe movement. This restraint system was placed in an excavation of the frozen soil and supported as shown on Figure 3. While long-term performance of the anchor system appears to have been acceptable, it would be interesting to learn what ground conditions now exist after over 80 years.

Operation Issues

Operation of the ditch required considerable maintenance efforts as a result of ground deformation, soil and ice thaw instability, and berm washouts. Ditch tending personnel were utilized along the grade to maintain and repair the ditches throughout the summer. The ditches and siphons were drained each fall under controlled conditions in order to minimize potential sudden drawdown or freeze damage to the siphon pipe. The extent of ground thawing below and around the ditch construction zone over the period does not appear to have been documented and the current thermal state after over thirty years of abandonment is unknown. It would seem worthwhile to review current ground conditions, past climate as well as site-specific history in order to develop a better understanding of our modeling capabilities and improve our ability to define potential future project impacts.

The Davidson Ditch operated until it was closed in 1942, due to the closing of major placer mining during World War II. It was reopened in 1945. The Davidson Ditch was again in operation until 1952. At that time, the system was acquired by the Chatanika Power Company which utilized the water supply head, at approximately 1,068 N of pressure, to generate an average 9,000 MJ of electricity. The Davidson Ditch continued to function until August, 1967 when major flooding took out the arch bridge supporting the siphon and also collapsed over 213 m of uphill pipe.

Some project photographs taken during early operations, and shown in Figures 4 through 8, identify: the intake and diversion dam, siphon pipe, a typical siphon pipe support, anchor and outlet penstock, and the Chatanika River bridge that supported the siphon pipe.

Closure

Evidence of the ditch and some pile bents may still be observed along segments of the route. Photos of the abandoned project, taken by the senior author in the fall of 1970, are included as Figures 9 through 13. These identify some selected features that remained at that time. These include: the ditch itself, siphon pipe penstock inlet and outlet structures, and a siphon pipe valley crossing. The siphon pipe was salvaged in 1974 and many features of the project were obliterated (Fradley 1974). Consideration was given to making the Davidson Ditch a national historical site that would have

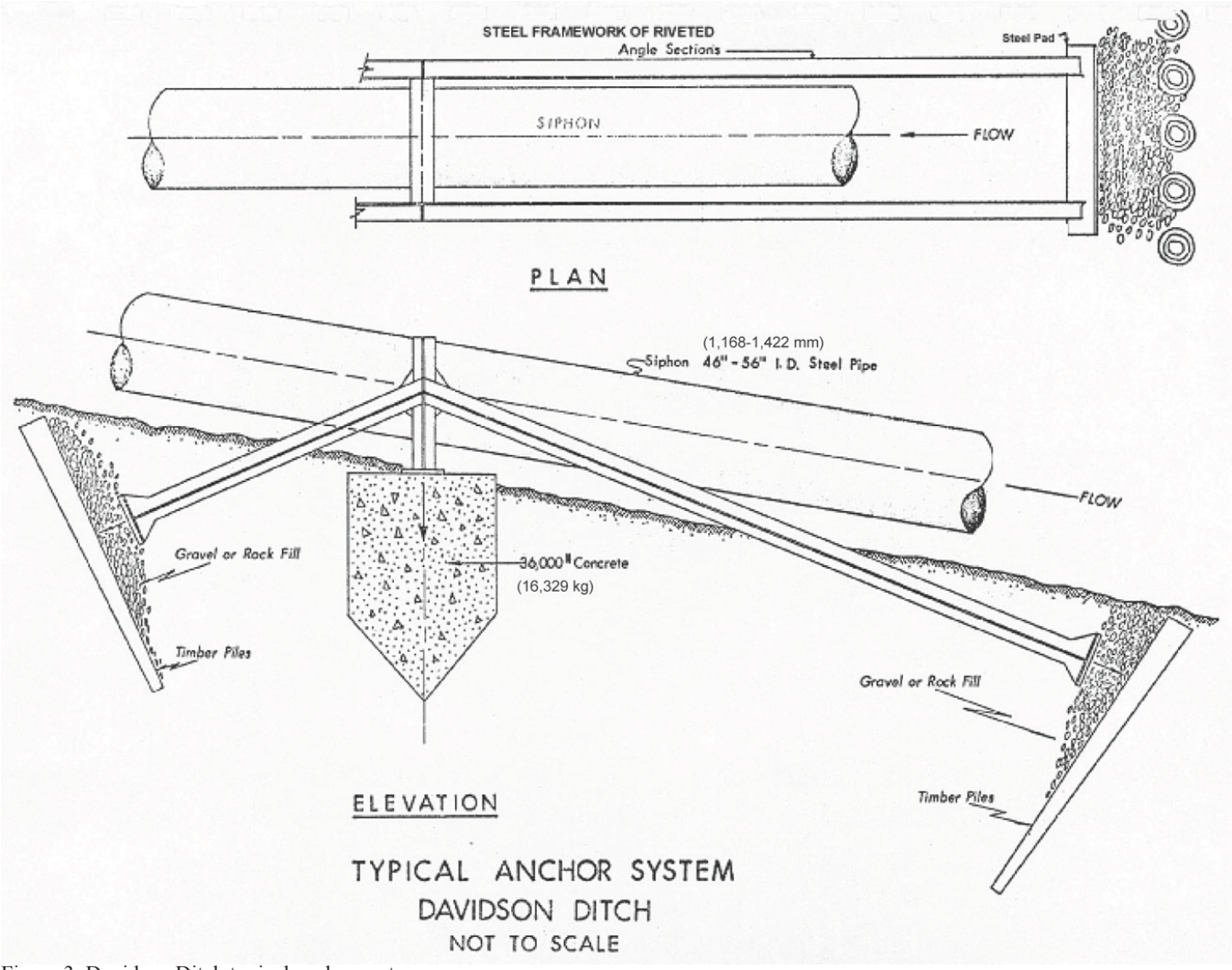

Figure 3. Davidson Ditch typical anchor system.

Figure 4. Intake and diversion dam at headwaters of Chatanika River.

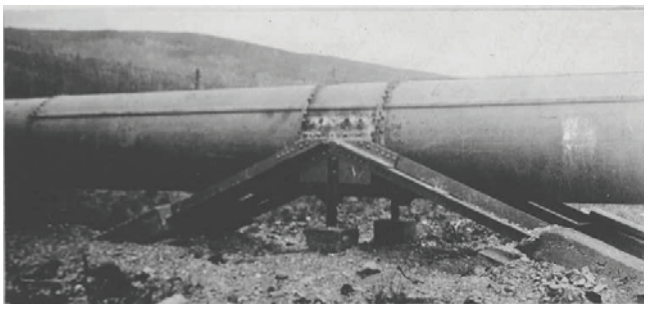

Figure 5. Typical siphon pipe anchor.

included a trail system along the route. Unfortunately, property ownership issues did not allow this to happen.

Details associated with the FE Company's earthwork effort and the economic impact of the Davidson Ditch because of its capability to deliver water to the Fairbanks mining region was documented by Boswell (1979) and Deyos (1925) as follows:

Est. stripping of overburden	7,000,000 y^3 (5,351,884 m^3)
Est. dredging of gravel	5,500,000 y^3 (4,205,052 m^3)
Est. initial investment	$10,000,000
(included cost of Davidson Ditch at $1,773,800)	
Est. total payroll 1926 to 1969	$50,552,175
Est. total gold value recovery (at $35/oz.) from all dredges in the Fairbanks area	$125,000,000

Most of the areas dredged by the FE Company were generally covered by frozen, relatively unstable soils that were totally modified by the mining operations. Much of the

Figure 6. Typical siphon pipe support on timber pile trestle bent.

impacted areas have since been developed and are now the site of both residential and business activities.

In closing, it seems the total socio-economic and environmental impact of the FE Company's Davidson Ditch operations should be reviewed and assessed for both historical value, its possible modeling value, and with regard to estimating any potential future impacts associated with climate-warming trends.

References

Boswell, J.C. 1979. *History of Alaskan Operations of United States Smelting, Refining and Mining Company*. University of Alaska, Fairbanks: Minerals Industries Research Laboratory, Special Publications, Spring 1979, 126 pp.

Davidson, J.M. 2006. *Alaska Mining Hall of Fame Foundation (1853–1928)*.

Deyos, M.C. 1925. Waste Gold, *Fairbanks Daily News Miner*, Fairbanks, Alaska Dec. 24, 1925.

O'Donnell, H.W. 1970. *Report on the Davidson Ditch*, Fairbanks, Alaska: Trans Alaska Pipeline System, June, 1970.

Stines, Norman C. 2006. *Alaska Mining Hall of Fame Foundation (1881–1955)*.

Fradley, Dennis. 1974 Davidson Ditch Pipe Salvaged, *Fairbanks Daily News Miner*, Fairbanks, Alaska, April 18, 1974.

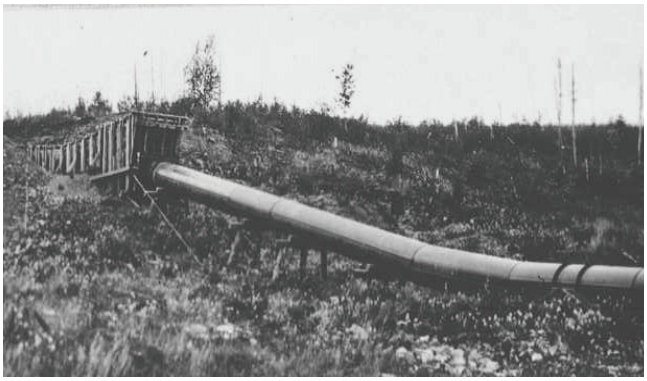

Figure 7. Typical outlet penstock at siphon valley crossing.

Figure 8. Chatanika River siphon and steel arch bridge crossing.

Davidson Ditch – Early Project Photos

Figure 9. Abandoned ditch, fall, 1970.

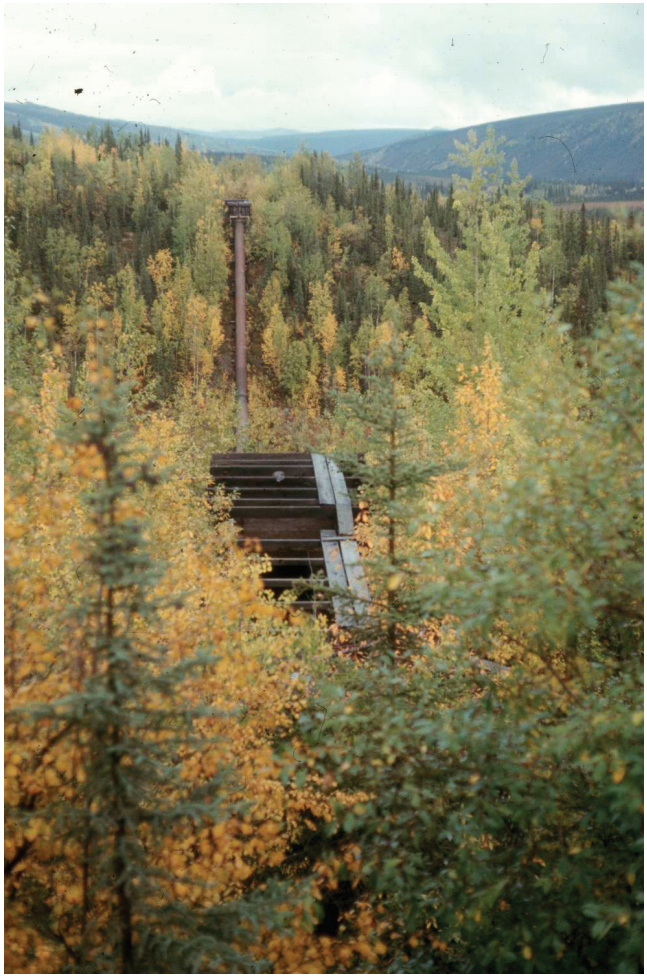

Figure 10. Siphon intake and outlet structures, at a valley crossing, fall, 1970.

Figure 11. Siphon pipe valley crossing, fall, 1970.

Figure 12. Inlet structure and siphon pipe, fall, 1970.

Figure 13. Wood outlet structure at siphon valley crossing, fall, 1970.

Davidson Ditch – Photos of Abandoned Project